Université de Toulouse

THÈSE

En vue de l'obtention du

DOCTORAT DE L'UNIVERSITÉ DE TOULOUSE

Délivré par :

Institut National Polytechnique de Toulouse (Toulouse INP)

Discipline ou spécialité :

Dynamique des fluides

Présentée et soutenue par :

M. GORKEM OZTARLIK

le mardi 20 octobre 2020

Titre :

Numerical and Experimental Investigations of Combustion Instabilities of Swirled Premixed Methane-Air Flames With Hydrogen Addition

---

Ecole doctorale :

Mécanique, Energétique, Génie civil, Procédés (MEGeP)

Unité de recherche :

Institut de Mécanique des Fluides de Toulouse (IMFT)

Directeur(s) de Thèse :

M. THIERRY POINSOT

M. LAURENT SELLE

Rapporteurs :

M. JAMES R. DAWSON, NORWEGIAN UNI OF SCE AND TECHN TRONDHEIM

M. RONAN VICQUELIN, CENTRALESUPELEC GIF SUR YVETTE

Membre(s) du jury :

M. FRANCK NICOUD, UNIVERSITE DE MONTPELLIER, Président

M. LAURENT SELLE, CNRS TOULOUSE, Membre

Mme BENEDICTE CUENOT, CERFACS, Membre

M. THIERRY POINSOT, CNRS TOULOUSE, Membre

M. THIERRY SCHULLER, UNIVERSITE PAUL SABATIER, Invité

To my family; including present and future members,
all my friends and all tango lovers in the multiverse

FOREWORD

The adventure of this thesis started in Princeton during the Combustion Summer School, where my thesis director Dr. Thierry Poinsot invited me to L'Institut de Mécanique des Fluides de Toulouse (IMFT) for a doctorate thesis. I don't know exactly what put me ahead among other candidates, but the idea of learning a new language and a new culture while contributing to research in a distinguished research group quickly attracted my attention. Thanks for the opportunity Thierry.

Here, I would like to seize the occasion to thank my thesis directors Thierry Poinsot and Laurent Selle for their support, being not only research related, but also personal, like helping me to get settled at the beginning of my thesis, not something easy for someone not yet speaking the language. I also had the opportunity to work with Thierry Schuller to whom I cannot thank enough for all the professional and personal support, not only for the thesis but in the job application processes also. Forever grateful to you all. This work would not have been possible without any of you. I shared the office with Benoit Bedat and Enrica Masi, thanks for your scientific support and company.

The first day in the lab, I was greeted by Thomas Kaiser (in my native language too) who introduced me to everybody in the group. Pradip Xavier, Daniel Mejia, Christian Kraus, Maxence Miguel-Brebion, Ainur Nigmetova, Ziad Hamidouche, François Audard, Solène Chevrier, Elhadji Thiam and Quentin Douasbin. In research the members of the teams move in and out frequently, so I also had the chance to meet Jimmy Suarez, Francois Muller, Sylvain Marragou, Mohamed Zekad and Andrea Aniello also. Special thanks to Pradip here, one of the people I enjoyed working with the most, who thought me about LIP. Furthermore, thanks to Sylvain for being a student who learns fast, you saved me valuable time at the end of my thesis. Thomas, I hope we can see each other in Istanbul one day to enjoy the Bosphorus and the food. I also had the possibility to work with Davide Laera from Cerfacs to whom I am very grateful for his support on the CFD side of this thesis. I wish you all a fulfilling and pleasant careers and joy and happiness in your personal lives.

Glad Licsandru, Julien Lefort. I don't know how many times that you have saved my day by finding material that was there probably before you were born, helping me clean the quartz and opening me the 3D printing room door :) Thank you for your friendship and Bamboleo!

As this work contains a lot of experimental results, there were a lot of pieces to manufacture and a lot of equipment to buy. I cannot overstate the joy of working with technicians and engineers both in the workshop and the labs. Ilyass Loukili, Ruddy Soeparno, Laurent Mouneix, Gilles Albert. I hope your workload is a bit less now without the guy who was "bugging" you always with pieces to manufacture that were needed yesterday. Not all the experimental work I have performed is written in this thesis, my work also involved lasers, different cameras, countless optical elements. Tkanks to "SIGNAUX ET IMAGES" for their help. Special thanks to Herve Ayroles here, I don't know how many times I visited your lab for countless equipment and your talent is beyond my understanding. This work would not have been possible without your interest, THANK YOU.

I would also like to thank the reviewers of my thesis; Ronan Vicquelin and James R. Dawson. Thank you for taking the time for reading my dissertation. Also the jury members Franck Nicoud and Bénédicte Cuenot. I am honored to prepare my thesis defense with your presence. Thank you all very much for your quick responses in a time when planning is especially difficult because of the epidemic.

Thanks to Stephanie Mathys, Pınar Başbuğ, Marion Prime, Sophie Malbreil, Irene Breunig, Julie Lazuli, Caroline Landrevie, Marc Androulët, Elizabeth Popow, Thomas Viron, Rodolphe Reiss and Anne Derrien for their support, friendship and making my stay so pleasant and safe, even picking me up from hospitals and everything :) Although I am very proud of the scientific work that was performed during this thesis, I appreciate even more the gentle and sweet people that I have met during my stay. Thanks for your friendship, hospitality and kindness. Toulouse and the people that I have met there will always have a special place in my heart. Thanks to everyone I met in Tangueando Toulouse for making my stay in France so pleasant and also helping me to learn French. The first years of trying to speak a new language and not really getting at it brings out the necessity of kind, patient friends, who show kind interest in sentences that take ages to come out of a beginner. Special thanks to Marc here for teaching me the subtleties of the French slang.

Chloé Rueff, there is not enough number of pages in the multiverse to express my gratitude to you. I feel very lucky to have met you and to share my life with you. Indeed it took a PhD. thesis and the biggest tango festival in Europe for us to meet. Thank you for supporting me, especially when I had to work with superhuman dedication to finish my thesis, resembling probably closer to a vegetable with a beard than a human being during the COVID-19 outbreak. "Il n'y a pas de hasard, il n'y a que des rendez-vous."

I would like to thank my brother Berkay, my mother Filiz, and my father Haluk Oztarlik and all my family for their support all along. I cannot wait to get together and celebrate the end of the thesis. I hope the days that we can see each other more frequently are near. Thanks to you all.

Finally, I would like to thank the European Research Council for the funding (European Union's Seventh Framework Programme (FP/2007-2013)/ERC Grant Agreement ERC-AdG 319067-INTECOCIS) that enabled this thesis.

TABLE OF CONTENTS

Page

ABBREVIATIONS

FDF : Flame Describing Function
FFT : Fast Fourier Transform
FTF : Flame Transfer Function
LES : Large Eddy Simulation

SYMBOLS

Symbols	Description and Units
a	: Molar N_2/O_2 ratio in the air
A_e	: Einstein coefficient, m^2
A_e	: Einstein coefficient, m^2
γ	: Heat capacity ratio
c	: Sound speed, m/s
c_p	: Specific heat capacity at constant pressure, $J/kg-K$
D	: Diameter, m or mm as indicated
$\mathscr{E}$	: Expansion Ratio
f	: Frequency, Hz
i	: Imaginary unit, $i^2=-1$
$\dot{i}$	: Photon emission rate, $kmolephotons/m^3/s$
I	: Pixel intensity/Chemiluminescent light emission
λ	: Thermal conductivity, $W/m-K$
L	: Length, m or mm as indicated
$\dot{m}$	: mass flow rate, kg/s.
μ	: Dynamic viscosity, $Pa-s$.
$\dot{n}$	: Molar flow rate $kmole/s$
N	: Number of
∇	: Gradient operator
$\dot{q}$	: Heat release rate, W/m^3
Pr	: Prandtl number
ϕ	: Equivalence ratio
ψ	: Phase, radians
V	: Cell volume, m^3
$\mathscr{P}$	: Thermal power, W
ρ	: Density, kg/m^3
R,r	: Radial position - Radius, m or mm as indicated
$\mathscr{R}$	: Rayleigh index
S	: Swirl number
S_L	: Laminar flame speed, m/s
σ	: Growth rate, $1/s$
θ	: Angular position - Angle, deg
$\mathfrak{t}$	: Time-stamp, s
u	: Axial velocity, m/s
U	: Axial bulk velocity, m/s
v	: Velocity vector, m/s
$\dot{V}$	: Volumetric flow rate, m^3/s

Symbols	Description and Units
X, x	**:** X Position, *m* or *mm* as indicated
X_s	**:** Molar fraction of species *s*
Y, y	**:** Y Position, *m* or *mm* as indicated
Z, z	**:** Z Position, *m* or *mm* as indicated
Y_X	**:** Mass fraction of species *X*
$\dot{Q}$	**:** Volume integrated heat release rate, *W*
$\dot{q}$	**:** Heat release rate, W/m^3
$\{X\}$	**:** Concentration of species X, $kmole/m^3$
ω	**:** Angular frequency, rad/s
Z	**:** Acoustic impedance, $Pa\,s/m$
$\lfloor \bar{\mathbf{V}} \rfloor$	**:** Phase averaged variable
$\bar{\mathbf{V}}$	**:** Time averaged variable
$\langle \mathbf{V} \rangle$	**:** Angle averaged variable

Subscripts	Description
a	**:** Air
f	**:** Fuel
$\mathfrak{f}$	**:** Forcing frequency
G	**:** Global
h	**:** holes
LS_y	**:** Line of Sight Integration (y-direction)
M	**:** Measured value
N	**:** Normal conditions
rms	**:** Root-mean-square
R	**:** Reference condition
$\mathcal{T}$	**:** Period
V	**:** Molar

Functions	Description
IA	**:** Inverse Abel Transform
Im	**:** Imaginary part of complex number
Re	**:** Real part of complex number

LIST OF TABLES

Page

LIST OF FIGURES

Page

NUMERICAL AND EXPERIMENTAL INVESTIGATIONS OF COMBUSTION INSTABILITIES OF SWIRLED PREMIXED METHANE-AIR FLAMES WITH HYDROGEN ADDITION

SUMMARY

In this work, hydrogen assisted (hydrogen enrichment and piloting) swirl stabilized flames are studied experimentally via MIRADAS experiment. First of all, static stability characteristics, such as flame lengths and flame attachment characteristics are studied via CH* chemiluminescence flame images and cases with hydrogen piloting, methane piloting and hydrogen enrichment are compared to the reference case of perfectly premixed methane-air combustion for a wide range of equivalence ratios and bulk velocities. It is found out that hydrogen piloting is the most efficient method to attach the flames and extend operating ranges of the combustion chamber.

Next the dynamic stability characteristics of the setup is studied experimentally via stability maps and it is shown that injection of a very small portion of the thermal power worth of hydrogen results in a more stable system and an extension in the stable operating points in the stability maps, meaning safer overall operation. Hydrogen enrichment and methane piloting are also explored, and it is demonstrated that these methods are not effective in changing stability maps, stability maps are not effected.

Subsequently, the forced flame responses are studied experimentally and it is shown that hydrogen piloting and hydrogen enrichment causes a drop in the global time delay of the flame transfer function. With hydrogen piloting, there is a global drop in the flame transfer function gain, however for hydrogen enriched cases, the gain is increased. For methane piloted cases, there is a global reduction in the flame transfer function gain, however the time delay is not affected.

Consequently, to explore why and how the global flame transfer function is changed with different injection strategies, forced flame images are studied. It is shown that the changes in flame transfer function is caused by the competition behavior between the local heat release responses for hydrogen piloted cases. Simply put, there is a phase difference between the local responses near the injection tube and the flame edges, causing a "pull-back" effect, which in turn causes a drop in the flame transfer function gain.

Next the effect of different injection strategies on the pollutant emissions are investigated. It is demonstrated that adding hydrogen, in pilot injection or hydrogen enrichment configuration, causes a drop in CO_2 emissions for the same thermal power. Piloting strategies cause a slight increase in NOx emissions, however results show that an optimization is possible to obtain flames that are stable, low CO_2 and low NOx.

Finally, LES calculations and their comparisons with experimental results are presented. The capability of LES calculations in predicting flame responses is demonstrated and it is shown that the flame responses originate from the interactions of the vortices that are formed as a result of acoustic pulsations and the flames. Flames are wrapped around these vortices which increase the flame surface area. Further down

the forcing cycle, the rolled up portions of the flames start touching the combustion chamber walls and gets quenched which causes a loss of flame surface area. These changes in flame surface area result in a fluctuating heat release rate, consisting the flame response.

ÉTUDES NUMÉRIQUES ET EXPÉRIMENTALES DES INSTABILITÉS DE COMBUSTION DE FLAMMES PRÉMÉLANGÉES SWIRLÉES DE MÉTHANE-AIR AVEC ADDITION D'HYDROGÈNE

RÉSUMÉ

Dans ce travail, les flammes stabilisées par tourbillonnement, assistées par hydrogène (enrichissement en hydrogène et pilotage) sont étudiées expérimentalement via l'expérience MIRADAS. Tout d'abord, les caractéristiques de stabilité statique, telles que les longueurs de flamme et les caractéristiques d'attachement de la flamme sont étudiées via des images de chimiluminescence CH * de flamme et les cas avec pilotage à l'hydrogène, pilotage au méthane et enrichissement en hydrogène sont comparés au cas de référence; d'une combustion méthane-air parfaitement prémélangée, pour une large gamme des richesse et des vitesses. On constate que le pilotage de l'hydrogène est la méthode la plus efficace pour fixer les flammes et étendre les plages de fonctionnement stables de la chambre de combustion.

Ensuite, les caractéristiques de stabilité dynamique de l'installation sont étudiées expérimentalement via des cartes de stabilité et il est démontré que l'injection d'une très petite partie de la puissance thermique de l'hydrogène se traduit par un système plus stable ; une extension des points de fonctionnement stables dans les cartes de stabilité, ce qui signifie un fonctionnement global plus sûr. L'enrichissement en hydrogène et le pilotage du méthane sont également explorés et il est démontré que ces méthodes ne sont pas efficaces pour changer les cartes de stabilité, les cartes de stabilité ne sont pas effectuées.

Par la suite, les réponses des flammes forcées sont étudiées expérimentalement et il est démontré que le pilotage de l'hydrogène et l'enrichissement en hydrogène provoquent une baisse du délai global de la fonction de transfert de flamme. Avec le pilotage de l'hydrogène, il y a une baisse globale du gain de la fonction de transfert de flamme, mais pour les cas enrichis en hydrogène, le gain est augmenté. Pour les cas pilotés au méthane, il y a une réduction globale du gain de la fonction de transfert de flamme, mais le délai n'est pas affectée.

Par conséquent, pour explorer pourquoi et comment la fonction globale de transfert de flamme est modifiée avec différentes stratégies d'injection, des images de flamme forcée sont étudiées. Il est démontré que les changements dans la fonction de transfert de flamme sont causés par le comportement de compétition entre les réponses locales de dégagement de chaleur pour les cas pilotés par l'hydrogène. Autrement dit, il y a une différence de phase entre les réponses locales près du tube d'injection et les bords de la flamme, provoquant un effet de baisse, qui à son tour provoque une baisse du gain de la fonction de transfert de flamme.

Ensuite, l'effet de différentes stratégies d'injection sur les émissions de polluants est étudié. Il est démontré que l'ajout d'hydrogène, en configuration d'injection pilote ou d'enrichissement d'hydrogène, entraîne une baisse des émissions de CO_2 pour la même puissance thermique. Les stratégies de pilotage provoquent une légère augmentation

des émissions de NOx, mais les résultats montrent qu'une optimisation est possible pour obtenir des flammes stables, à faible CO_2 et à faible NOx.

Enfin, les calculs LES et leurs comparaisons avec les résultats expérimentaux sont présentés. La capacité des calculs LES à prédire les réponses de la flamme est affichée et il est démontré que les réponses de la flamme proviennent des interactions des tourbillons qui se forment à la suite des pulsations acoustiques et des flammes. Des flammes sont enroulées autour de ces tourbillons, ce qui augmente la surface de la flamme. Plus loin dans le cycle de forçage, les parties enroulées des flammes commencent à toucher les parois de la chambre de combustion et s'éteignent, ce qui entraîne une perte de surface de la flamme. Ces changements dans la surface de la flamme se traduisent par un taux de dégagement de chaleur fluctuant, consistant en la réponse de la flamme.

1. INTRODUCTION

Charles Darwin wrote "The discovery of fire, probably the greatest ever made by man, excepting language, dates from before the dawn of history" [10] in his pioneering work The Descent of Man. This phrase summarizes the importance of combustion for the existence and development of humanity. Some scientists even suggest that earliest controlled fire use by hominins surpasses homo sapiens, reaching far to homo erectus [11, 12].

Like early homo sapiens, we use combustion to cook our food and for heating but also in more advanced ways like transport, industry and construction and unlike early hominins, the variety of the fuels we use are pretty much limitless. The widespread use of advanced technology brings along the need for more power, intrinsically more sources of fuel that is filled in with worldwide search for fossil fuel reserves. In Fig.1.1, the worldwide total primary energy supply by sources in the period 1971-2017 is presented. The first striking indication is that the total energy produced in the world is always increasing, although the weight of different sources changes from time to time. The energy produced from renewable sources is increasing, however, energy produced from fossil fuels except coal is also on the rise.

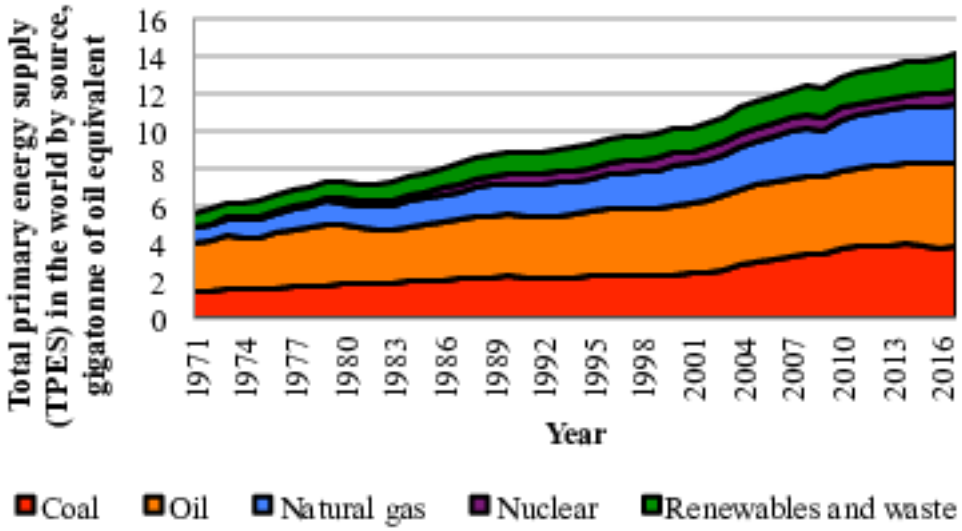

Figure 1.1: Total primary energy supply in the world by sources in the period 1971-2017 [2] [2].

Today, ≈80% of the total energy produced in the world comes from combustion and the most widely used fuel in 2017 in the world is oil. Taking into account biofuels and energy produced from waste, hydro, wind and solar power, the energy produced from renewable sources amounts to 14% of the total energy supply in the world. Coal, oil and natural gas together they make up 81% of the total energy supply, emitting the infamous CO_2 in the atmosphere that was underground before being burnt. Finally 5% of the global energy supply comes from nuclear reactions [2]. This is an indication that we need very efficient systems to reduce CO_2 emissions.

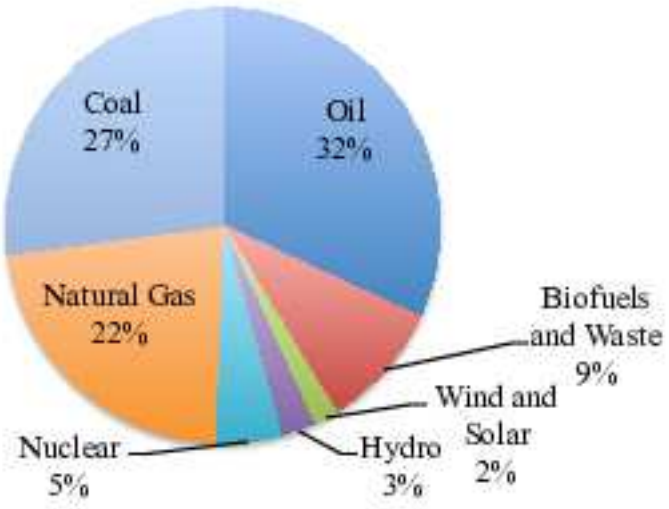

Figure 1.2: Pie chart of total primary energy supply by sources in the world in 2017 [2].

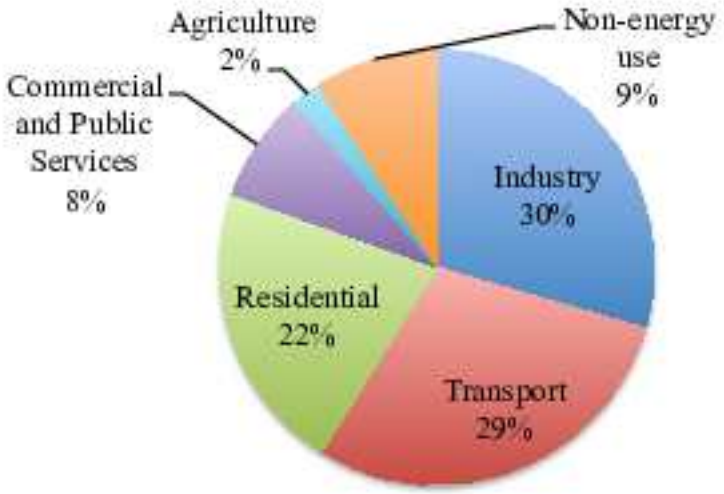

Figure 1.3: Total final consumption (TFC) by sector in the world in 2017. IEA defines non-energy use as petroleum products such as white spirit, paraffin waxes, lubricants, bitumen and other products, exclusively produced for non-energy use [2].

In Fig. 1.3 the end use of the fuels is presented. Here it can be seen that the bulk of the energy is spent on industry, transportation and residential areas. One point to make here is that in heating, transport and industry, what is needed generally is the heat rather than electrical power, unlike most of residential applications. This makes it possible to apply different types of fuels directly, meaning that they do not need to be converted to electrical power to be useful. Different fuels from different sources can be directly used in combustion chambers to produce heat. This is of course not a simple task, most of the heat producing machines today are designed for specific fuels; natural gas, propane or different oil products and they rarely allow changes in fuel composition.

One of the topics that has gained a lot of momentum in the last years is the power-to-gas projects, where the idea is to produce hydrogen via electrolysis using electricity obtained from renewable sources [13, 14]. This is also a renewable answer to the industry standard methods like steam reforming from natural gas [15] and steam gasification from coal and biomasses [16] which use fossil fuels as feedstocks and produce CO_2 [17]. Moreover, using methanation processes and hydrogen produced from renewable resources, it is even possible to remove CO_2 from the atmosphere and produce methane to be used in the energy network [18]. Synthesis processes cal also be added to this processes to produce valuable chemicals for the pharmaceutical industry [19] and diesel and gasoline for the transportation sector [20].

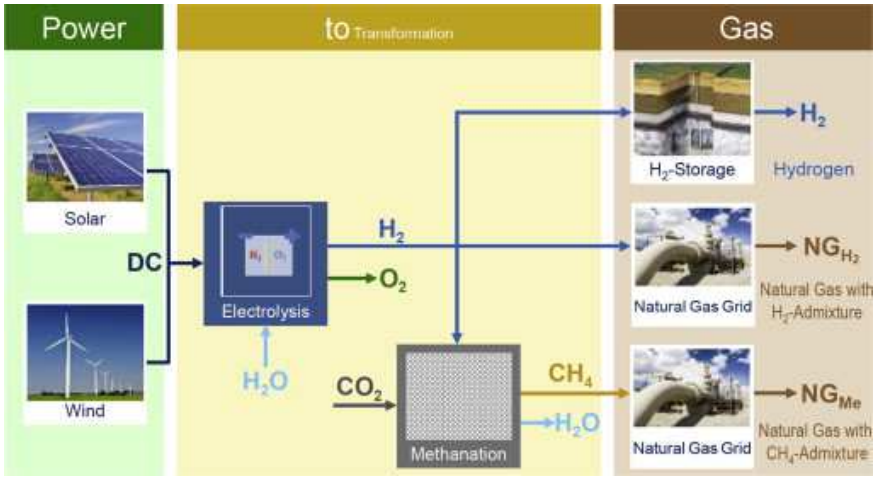

Figure 1.4: Overview of the working principle of power-to-gas concept [3]

The leader being Germany in these developments, projects like P2X [21] in the Kopernikus framework received funding from the German Federal Ministry of Education and Research on the order of 120 million Euros until 2018 and a further 280 million is foreseen until 2025 [22]. Furthermore STORE&GO project which is

aimed to produce natural gas using electricity produced from renewable resources obtained 28 million Euros from from the European Union's Horizon 2020 research and innovation programme [23]. Boiler manufacturers like Bosch are already building hydrogen capable systems in the 20 MW range [24]. Additionally Wärtsilä is building engines for power production that fire with 100% hydrogen [25]. In power applications hydrogen functions like a battery, storing energy to be used when the electricity supply falls below current demand, to stabilize the power grid.

For the short term shift towards an hydrogen economy, hydrogen enrichment being hydrogen mixed in with fossil fuels like natural gas has been suggested [26–28]. This is logical as although there are big investments and a lot of scientific research pointed towards developing renewable energies, in the short term, hydrogen production from renewable resources will not be enough instantly to totally replace the fossil fuels the world currently consumes.

1.1 Hydrogen as a Fuel and a Way to Store Power

Hydrogen is an energy carrier with low molecular weight large diffusion coefficient, high thermal conductivity and low viscosity and has interesting combustion properties including high flame speed, small quenching distance, and low ignition energy [17]. Among the practical alternative fuels, hydrogen offers the most benefits, especially when added to fossil fuels [29].

Hydrogen can be utilized in practical systems in the following ways:

- Hydrogen powered engines
- Fuel cells
- Hydrogen enrichment
- Syngas

Hydrogen has some advantageous properties when used as fuel for combustion, these are summed up as:

- Can be Renewable
- No carbon emission
- High energy density on mass basis
- Extended flammability limits
- Increased resistance to strain and extinction

- Higly diffusive [30]
- Lower ignition energy
- Smaller quenching distance

Along with these advantages, there are some disadvantages when hydrogen is used as fuel:

- Transportation and storage is expensive [16]
- Somewhat dangerous to have around [31] [30]
- Low energy content on a volume basis
- Increased flashback propensity [16]
- High potential crossover from deflagration to detonation
- Potential unwanted autoignition
- Not readily available from a natural source

Hydrogen has many beneficial properties of combustion including high flame speed, small quenching distance, low ignition energy, high autoignition temperature, and high octane [17]. Some properties of hydrogen compared to other fuels are given in table 1.1.

Table 1.1: Combustion properties of hydrogen [1] at 25 °C and 1atm

Property	Hydrogen	CNG	Gasoline	Methane
Density (kg/m^3)	0.0824	0.72	730 [a]	0.651
Flammability limits (volume % in air)	4-75	4.3-15	1.4-7.6	5.5-15
Flammability limits (ϕ)	0.1-7.1	0.4-1.6	∼0.7-4	0.4-1.6
Autoignition temperature in air (K)	858	723	550	813
Minimum ignition energy in air (mJ) [b]	0.02	0.28	0.24	0.29
Flame velocity (m/s) [b]	1.85	0.38	0.37-0.43	0.4
Adiabatic flame temperature (K) [b]	2480	2214	2580	2226
Quenching distance (mm) [b]	0.64	2.1[c]	∼2	2.5
Stoichiometric fuel/air mass ratio	0.029	0.069	0.068	0.058
Stoichiometric volume fraction (%)	29.53	9.48	∼2 [d]	9.48
Lower heating value (MJ/m^3)	9.9	32.6	42.0–44.0	32.6
Lower heating value (MJ/kg)	119.7	45.8	44.79	50
Heat of combustion (MJ/kg air) [b]	3.37	2.9	2.83	2.9

[a] Liquid at 0 °C; [b] At stoichiometry; [c] Methane; [d] Vapor

One of the ways that hydrogen can be used in existing combustion systems is hydrogen enrichment, being the addition of hydrogen to other fuels, typically the goal

Figure 1.5: Bus used in hydrogen/natural gas blend tests [4].

being either to enhance complete combustion, stability or to extend lean operability. Hydrogen enrichment can be applied to many practical stems, including aeronautical and industrial gas turbines, piston engines and all sort of burners. Some research even involved on road experimental tests of hydrogen/natural gas blends [4].

Hydrogen enrichment increases the ratio of specific heats through lean operability which in turn enables higher compression ratio improving thermal effiiency [32], burn rates [33] [34] and decreases cycle-to-cycle variations [32] [35] [36] and throttling losses and all these add up to increase efficiency of the combustion systems . Emission reduction is another benefit of hydrogen enrichment, hydrogen aids in more complete combustion therefore reducing unburnt hydrocarbon emissions, and with increased lean operability leads to reduced CO and NOx emissions.

Hydrogen enrichment has applications on primary fuels such as gasoline [37] [32] [38] [34] [39] [30], diesel [40] [41], natural gas [32] [42] [33] [43] [44] and kerosene [45] [46].

Hydrogen also finds applications in exhaust gas fuel reforming, where primary fuel such as gasoline and a fraction of the engine exhaust gas is reformed by endothermic catalytic reforming which is then fed into the intake manifold [37]. Moreover, hydrogen enrichment increases free radical production with extention of the lean limit, shortening the flame nucleation period, thereby increasing the heat release/burn rate [16].

The development of hydrogen and hydrogen enriched hydrocarbon fuels in combustion holds interest as hydrogen containing fuels are readily being produced as a byproduct of coal gasification and fluidized bed combustion systems and the utilization of hydrogen produced this way would provide a cost effective fuel and ultra-lean combustion holds a great promise in reducing NOx emissions [47].

Hydrogen promises performance benefits in high performance aircrafts also. In addition to its combustion properties, because of the fact that it is stored in liquid state means that it can also be used as a coolant for suction air in scramjet engines in which the compressor stage outlet temperature is the cause of degregation in high speed flight conditions [48]. Another application of cryogenic cooling with hydrogen is engine component cooling [49] and laminarization control of aeroplanes aerodynamic surfaces for drag reduction [50]. Researchers investigated the effect of H_2 addition tokerosene on a Snecma engine combustor and found out that when injected in a partially premixed configuration and forming a hydrogen pilot flame, hydrogen improves lean blow off limits [45]. Research also shows the levels of CO concentrations can be reduced without adversely affecting the NO_2 emissions in laboratory swirl combustors. It is also stated that hydrogene even low values as 12% of hydrogene enrichement provided a shorter and a more robust flame [47]. Gas turbines can also be modified to burn hydrogen instead of liquid fuels [51].

As hydrogen enrichment or hydrogen combustion modifies the properties of the flame, the stability of combustion systems is also modified. The literature is rich with cases suggesting that hydrogen makes systems more prone to instabilities [47, 52–55]. However with the current investments and the real possibility of using hydrogen in industrial systems, more research is needed to explore the ways to use and the effect of hydrogen in combustion systems.

1.2 Combustion Instabilities

Gas turbines burning natural gas is one the most efficient solution for power production with limited pollutant emissions levels and reduced carbon emissions, compared to other power generation units burning a hydrocarbon fuel [56–58]. Typical industrial gas turbines operate on natural gas in a lean premixed regime to cut down NOx emissions with swirl stabilised flames, but these systems suffer from

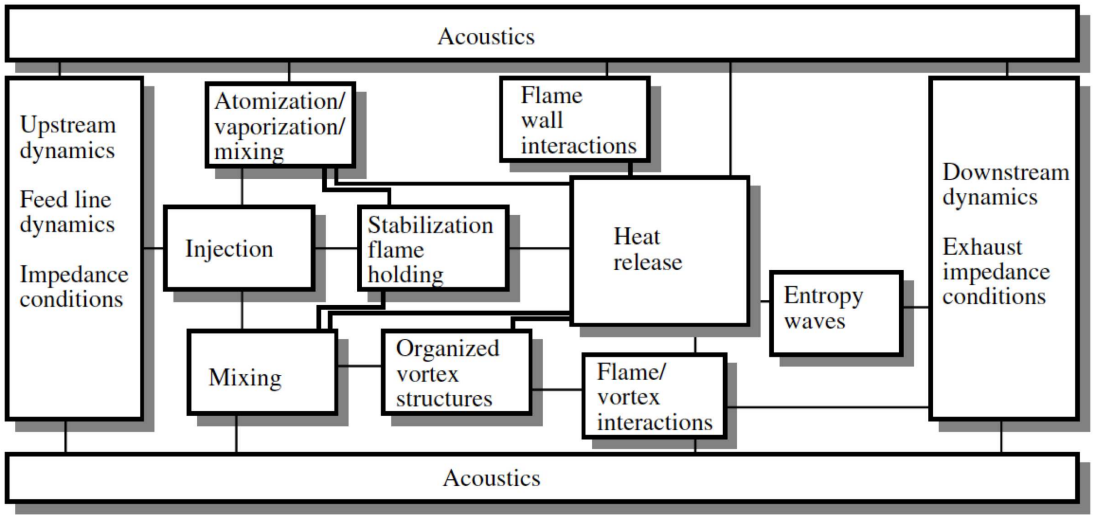

Figure 1.6: Basic interactions leading to combustion instabilities [5].

dynamical problems mainly associated to combustion instabilities [6, 59, 60]; large scale fluctuations in heat release, velocity and pressure in combustion systems.

Instances of heat shields (splash plates) breaking due to high cycle fatigue, damaged burners, liners and transition pieces are regularly reported [6]. With the introduction of new gases from intermittent renewable ressources in the fuel supply line, like biogas or syngas, these issues become more stringent due to changes in the fuel composition powering the engine [61–64]. Combustion instabilities also exist in rocket engines, especially at high frequencies, however the focus in this work is on gas turbines, gas generators and boilers.

Figure 1.7: Damage caused by combustion instabilities in gas turbines [6].

The strategies developed to mitigate combustion instabilities can be grouped into two; active and passive control strategies. In active control strategies, the instability is suppressed by a feedback control system which drives either an acoustic actuator [65–70] or a pulsation of the fuel line flow [69, 71, 72]. Full scale gas turbine applications were also designed and tested by success [7, 71, 73–75], but active control strategies were found to be rather expensive and difficult to certificate as an ultimate solution [76]. For passive control approaches, acoustic manipulation of the combustion

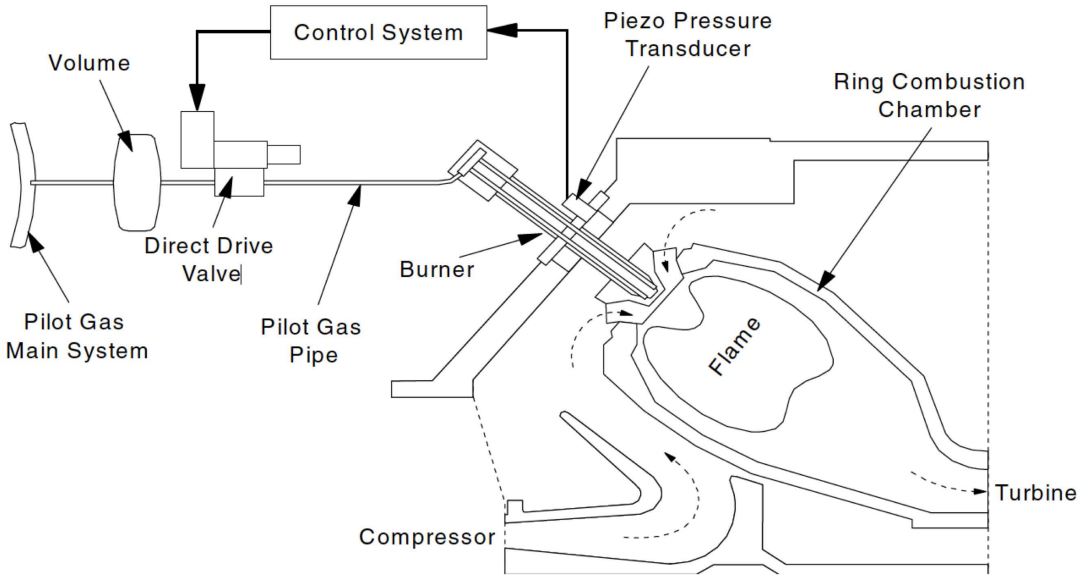

Figure 1.8: Schematic of the active instability control setup for Siemens gas turbines with annular combustors [7]

system as use of dampers such as Helmholtz resonators [77–83] and perforated liners [84, 85] and acoustic impedance tuning [86] techniques can be listed. Other methods such as pilot fuel injection [87, 88] bluff body assisted combustion [89, 90], time lag distribution and symmetry breaking techniques [7, 91–93] and different fuel staging techniques that change the temperature and sound speed field and flame response in the combustors [91, 94–98] can be listed. Additionaly modifications made to burner geometries to reduce vortex generated combustion instabilities were also applied [99, 100].

It is also well known that the dynamics of flames depend on the shapes of flames, so any modification that changes the shape of the flames is expected to alter the stability characteristecs of the combustion systems [101]. Flame holder temperature is shown to be a driving mechanism in combustion instabilities [102, 103]. Axial and radial fuel staging is one of the passive control strategies that is applied, primarily to change the sound speed field in the combustion [91, 94, 95] and also asymmetric fuel distribution was implemented to reduce combustion instabilities [98].

The use of a hydrogen pilot fuel jet has been considered in a few studies. Hussain et al. [104] recently made a clear review of these studies in their introduction. In one of the pioneering works, Anderson et al. [105] noted that it would make flames quieter and more stable in a perforated-plate flame holder configuration. More recently, Barbosa et

al. [106] showed that a swirled injection of hydrogen into a combustor operated with a lean propane-air mixture can be used to reduce combustion oscillations, without impairing NOx emissions but with a drastic increase in CO emissions. Hussain et al. [104] analyzed the response to acoustic perturbations of methane-air and ethylene-air flames stabilized by a large bluff body in a dump combustor, when secondary hydrogen is injected through the bluff body. They found that the Flame Describing Function (FDF) linking the acoustic velocity modulation to the resulting heat release rate oscillation at 30, 255 and 315 Hz could be lowered compared to operation without hydrogen for all acoustic forcing levels tested. However, NOx emissions rapidly increase when the hydrogen concentration exceeds 5%. Their analysis carried out without swirl is also limited to selected forcing frequencies.

1.3 Purpose and Objective of Thesis

The purpose of this thesis is to explore the ways that hydrogen can be used in swirl stabilized flames. This includes static aerodynamic stability of flames, dynamic stability of flames; flame response to acoustic fluctuations and resistance to combustion instabilities and different strategies of introducing hydrogen into flames; practically premixed and pilot injection. The final goal is the reduction of CO_2 emissions, without adversely effecting NOx emissions and the creation of even more stable systems with hydrogen applied. To achieve these goals a highly modular and fuel flexible MIRADAS setup is constructed.

Firstly, the static instability characteristics are studied. Subsequently, the dynamic stability characteristics are studied via stability maps. Afterwards the heat release response to acoustic fluctuations and the local flame responses are studied to explain the effect of different injection strategies. Then the emission measurements and the effect of hydrogen are presented. Finally, the heat release response mechanisms and LES calculations of the setup are presented.

2. INTRODUCTION TO MIRADAS EXPERIMENT, FUEL PILOTING, HYDROGEN ENRICHMENT STRATEGIES AND CONTROL

The objective of the MIRADAS (Mitigation of Instabilities by Radially and/or Axially Directed Addition of Species) setup is to study the stability characteristics of premixed swirled flames and to come up with innovative ideas to suppress thermo-acoustic instabilities, such as hydrogen piloting. Many gas turbines, being one of the most commonly used industrial combustion systems, operate on natural gas in a lean premixed regime to cut down NOx emissions, but these systems suffer from dynamical problems mainly associated to combustion instabilities [60]. Instances of heat shields breaking due to high cycle fatigue, damaged burners, liners and transition pieces are regularly reported [6].

With the introduction of new gases from renewable sources in the fuel supply line, such as biogas or syngas, instability issues become more critical due to (1) changes in the fuel composition powering the engine and altering the heat release distribution for a given thermal power output [61–64] and (2) intermittent changes of the supply and power demand leading to operation with high turn-down ratios [**?**].

Blending hydrogen from renewable sources into natural gas can be used to reduce carbon dioxyde emissions without impairing pollutant emissions. In this strategy, hydrogen is premixed with natural gas prior to combustion. But it was found out that although hydrogen addition widens the static operability range of the combustor by improving blow-off characteristics, it tends to make combustion systems more prone to flashback and more sensitive to combustion instabilities even at low power regimes and more quickly compared to natural gas [47, 52–55].

One of the targets of the MIRADAS setup is to use hydrogen to suppress combustion instabilities. In most operating regimes the fraction of hydrogen is kept low because high amounts of hydrogen are not available with the current infrastructure installed in most of the cities, even if significant, investments are being made to increase the applications of hydrogen in practical systems [107–110].

As in most practical combustion systems used to produce electricity or heat [56–58], the main source of power comes from methane; used as a surrogate to natural gas to resemble industrial configurations. Hydrogen can be introduced to create a hydrogen-methane-air mixture resulting in perfectly premixed combustion, or can be injected directly into the combustion chamber, creating a small pilot flame assisting a premixed flame.

The MIRADAS experiment is modular. It is very easy to change the setup to perform different experiments. For example, the 3D printed swirlers permit testing different levels of swirl and the replacement of pieces can be done in minutes. In a similar way, it is easy to change the setup from a long configuration used to measure self sustained instabilities to a shorter configuration equipped with a loud speaker to measure flame transfer functions. The details of these configurations will be given in their respective sections, but a general description of the experimental setup and its aerodynamic constituents, the control algorithm and the conventions of the different cases is first presented. The information on the diagnostics systems and experimental measurement techniques is given in their respective sections.

2.1 Aerodynamic Elements of MIRADAS Setup

The MIRADAS setup consists of a swirling injector fed with a gaseous mixture, plugged into a cylindrical flame tube. The schematic of the setup is presented in Fig. 2.1. The main mixture of fuel and air is injected at the bottom of a plenum with a circular cross section of diameter D_p=65 mm through two poly-amide tubes of 10 mm internal diameter separated symmetrically by 180°. Inside the plenum a honeycomb panel is fitted to break the turbulent structures resulting from the injection. The L_p=147 mm long plenum is presented in Fig. 2.1, but different lengths of plenums are available to change the inlet impedance permitting the study of the stability characteristics of the setup. The flow then goes through a convergent nozzle that ensures a laminar flow with less than 1% velocity fluctuation with a top hat velocity profile, followed by a short annular tube of 12 mm internal diameter.

It then flows through a radial swirler with a 22 mm internal diameter and with circular holes off the swirler axis to give a tangential component to the flow. Different angles between the holes and the swirler axis are possible to study the effect of swirl on

mean flames and forced flame responses. After the swirler, the mixture follows the main annular injection channel with a reduced external diameter of 12 mm to avoid flashbacks. In the middle of the injection channel, a stainless steel injection tube aligned with the burner axis with an external diameter of 6 mm and an internal diameter of 4 mm permits injection of fuel directly into the combustion chamber.

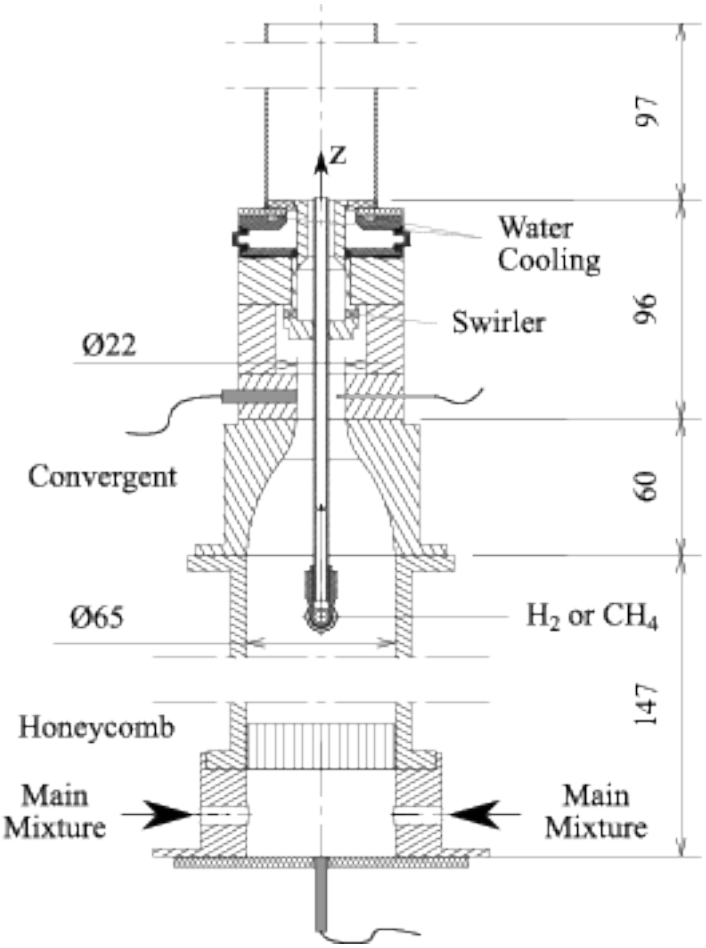

Figure 2.1: Schematic representation and relevant dimensions of the experimental setup. Dimensions are in millimeters. This configuration is used to obtain the mean flame images for different swirlers and different chamber diameters.

The top of the central injection tube protrudes by 1.25 mm inside the chamber to ensure the full visibility of the flame. A detailed view of this component is given in Fig. 2.2, together with its main dimensions. The flame is formed in the cylindrical combustion chamber consisting of a quartz tube with an internal diameter of 46 mm which provides full visual access to the flame at all times. Different combustion chamber lengths (L_c) are possible to change the impedance downstream of the flame to study combustion instabilities as well as different internal diameters (D_c). The top of the burner is water

cooled in order to maintain the thermal equilibrium of the plenum at room temperature, T_u=292 K.

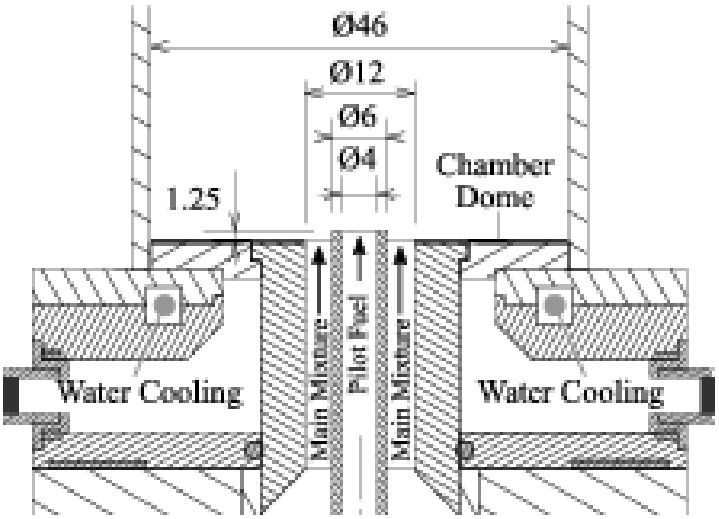

Figure 2.2: Detailed view of the injection system with the main dimensions are in millimeters.

It is also possible to inject air, methane, hydrogen or a mixture of these gasses via the small chamber fed using 4 poly-amide tubes and using an annular injection channel with small holes. Furthermore, pulsation of this small jet is also achieved by using acoustic actuators. This part of the will be briefly presented in the corresponding section. When they are not in use, the tubes are plugged and completely sealed so that there is no flow in and out the small chamber.

To investigate the effect of swirl, swirlers are 3D printed with a 3D Systems Projet HD 3500 3D printer (≈30 µm precision), offering multiple choices of swirl number by changing the angle between the axis of the radial holes and the swirler axis. The main configurations studied are the 15° and 35° swirlers, which correspond to geometrical a swirl number of 0.33 and 0.86 respectively according to the expression in Eq. 2.1 taken from [111] and modified to express the MIRADAS setup.

$$S = \frac{1}{1-\beta} \tan\theta_{SW} \frac{r_1}{4r_h} \left[1 - \left(\frac{r_t}{r_1} \right)^2 \right] \tag{2.1}$$

where β is the blockage factor defined as:

$$\beta = 1 - \frac{N_h r_h}{4r_0} \tag{2.2}$$

The schematic representations of the different swirlers used in this work is presented in Fig. 2.3.

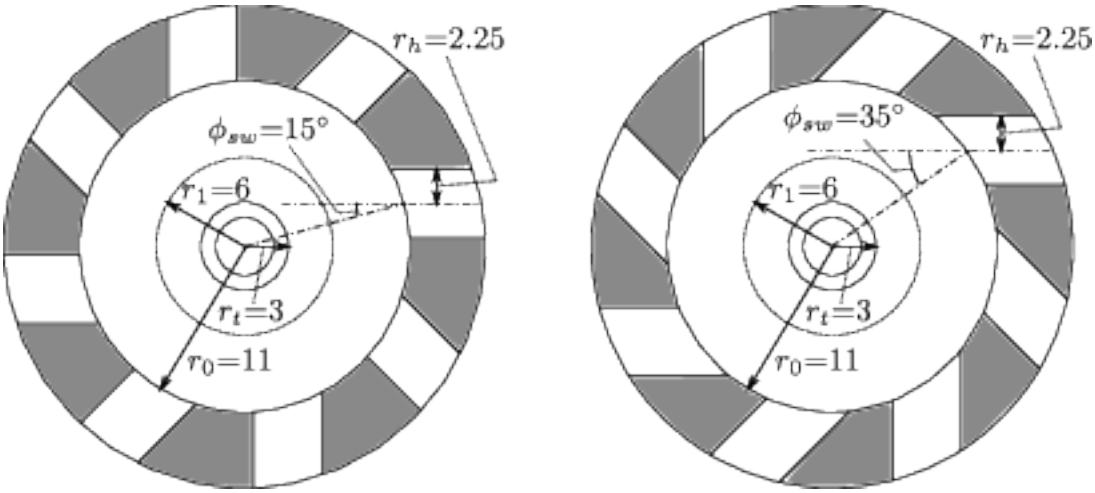

Figure 2.3: Schematic representation of the two different swirlers used in this work. The dimensions are in milimeters. One on the left; the swirler with holes 15° of the swirler axis corresponding to a geometrical swirl number of S=0.33 and on the right; the swirler with holes 35° of the swirler axis corresponding to a geometrical swirl number of S=0.86.

Another important parameter for the aerodynamic stability of the flames is the expansion ratio between the combustion chamber and the swirler exit, defined as the ratio of the cross-sectional area of the combustion chamber to the cross-sectional area of the swirled annular injection channel. This parameter has a first order effect on the length of the flame and the size of the side and middle recirculation zones. Different chamber diameters are possible for MIRADAS setup, so it is possible to change this the expansion ratio. The definition of the expansion ratio $\mathscr{E}$ is given in Eq. 2.3.

$$\mathscr{E} = \frac{r_c^2}{r_1^2 - r_t^2} \tag{2.3}$$

2.2 Mass Flow Control Strategy and Definitions of Conventions Used To Describe Different Configurations

With MIRADAS, it is possible to investigate the effect of different fuels, and the strategy applied in their combustion. The base case is methane-air perfectly premixed flame. The flow-rates of methane and air are controlled by their respective mass flow controllers and methane and air are mixed in a T junction long before the plenum to have a perfectly premixed mixture in the experiment. Furthermore hydrogen can be injected through the injection tube to create a small hydrogen pilot flame where the flow-rate is of hydrogen is controlled with a dedicated mass flow controller. To investigate the effect of hydrogen enrichment, mixing of hydrogen before the

experiment as in perfectly premixed combustion is also possible. This is done by mixing methane and hydrogen in a T junction and then mixing the fuel mixture with air in another T junction. Switching between two different regimes are possible with a 3 way valve, directing the hydrogen through the injection tube or the

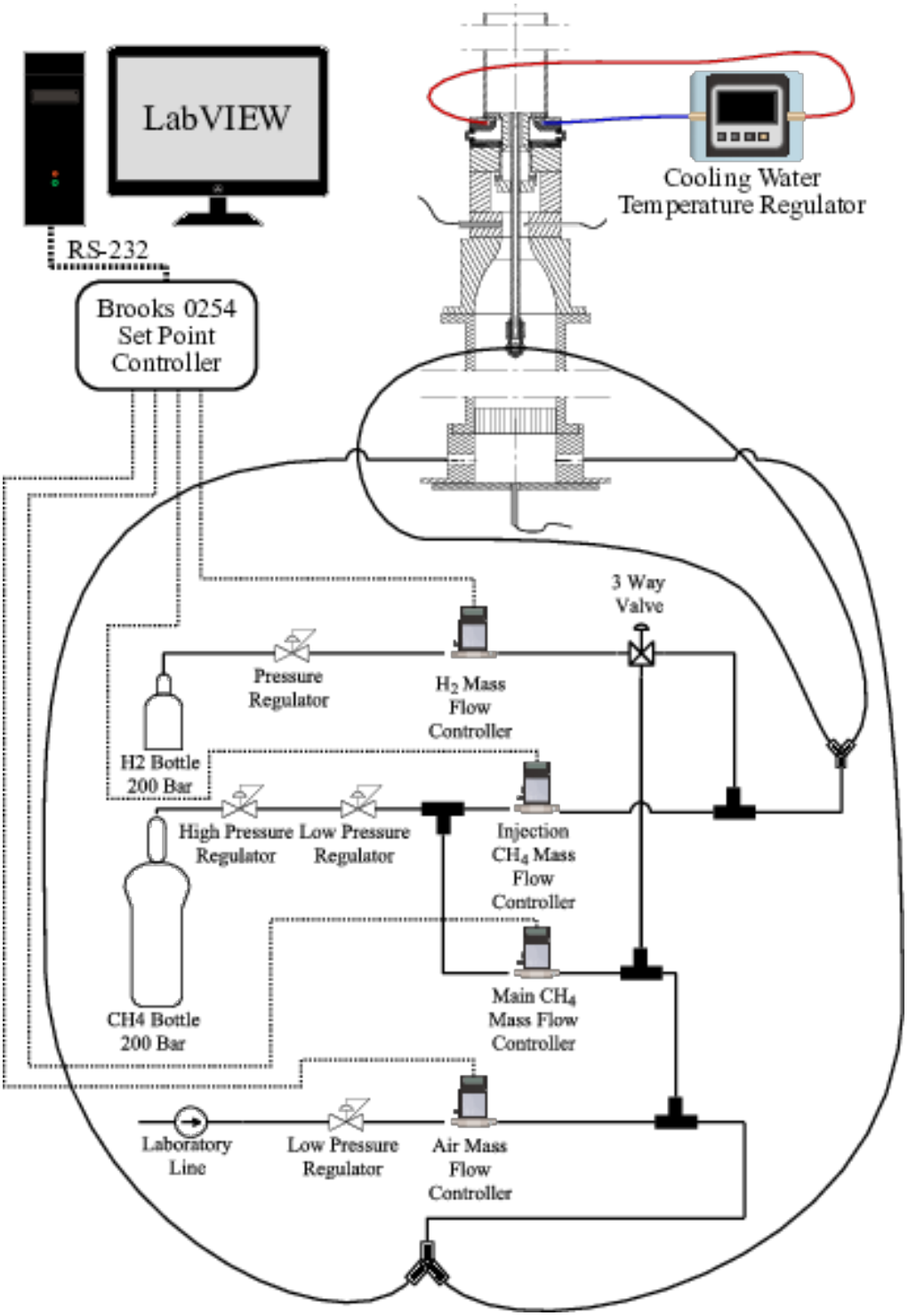

Figure 2.4: Schematic representation of the gas and cooling water lines of MIRADAS setup.

mixing T junction. Finally, methane can also be injected through the middle injection tube, with a flow-rate controlled by a dedicated mass flow controller. The schematic representation of the gas, water and control-communication lines are presented in Fig. 2.4.

The different fuels used brings the need of utilizing different mass flow controllers, each one controlling the flow its respective gas. This way the global equivalence ratio, the power or the velocity at the exit of the burner, the power that is coming from different fuels or the power coming from the main mixture or the injected fuel can be precisely controlled. The mass flow controllers used in this work are summarized in Table 2.1. All controllers are driven via a Brooks 0254 set-point controller with 4 control channels.

Table 2.1: Different mass flow controllers used in MIRADAS experiment.

Fluid	Brand	Model
Air	Brooks	SLA 5358
Main Methane	Brooks	SLA 5851
Hydrogen	Brooks	SLA 5851
Injection Methane	Brooks	SLA 5850

When investigating scenarios including different injection strategies and fuels, it is useful to define certain conventions for clarity of descriptions. The reference case is defined as the methane-air perfectly premixed flame, where the mixture is prepared before entering the plenum, denoted as REF. The case when hydrogen is injected through the injection tube at the middle of the swirler to form a small hydrogen pilot flame in a premixed methane-air flame is called PH, meaning that it is piloted by a small hydrogen flame. "*" signifies the percentage of power coming from the injection. To differentiate the effect of fuel composition and the injection strategy, the hydrogen-methane-air perfectly premixed flame cases for which the mixture is prepared before being introduced in the plenum are also explored. This configuration is called MH. Similarly to differentiate between the injection strategy and the fuel that is injected, methane is injected through the injection tube, creating a small methane pilot flame. This configuration is termed PC, meaning that the premixed methane-air flame is piloted by a small methane pilot flame. It should be noted that for REF and MH cases, there is no mean flow through the injection tube. A schematic summary is presented in Fig. 2.5.

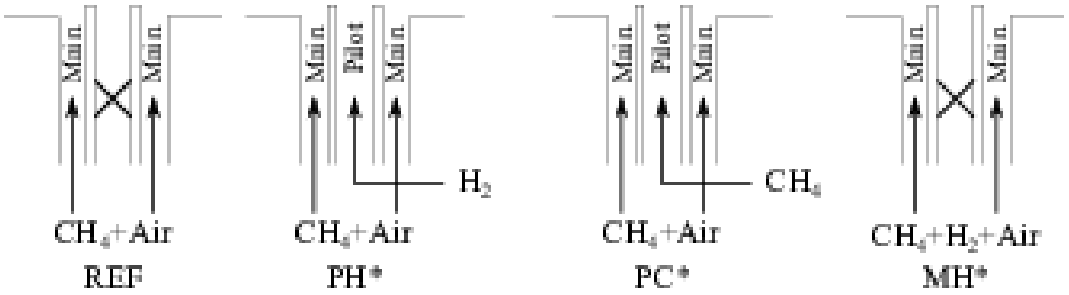

Figure 2.5: Representation of the injection strategies. The cross indicates that the pilot fuel stage is not used, there is no mean flow through the tube.

The control of the experiment is done via a labview program which drives all the necessary equipment except the cooling system, which is separately controlled with its dedicated controller controlling the temperature and the flow-rate of the cooling water. The LabVIEW control algorithm is constructed in a way that it takes the mean velocity in the annular injecting channel and the global equivalence ratio then calculates the respective flow-rates of respective gasses in normal conditions to set the set-points of the mass flow meters. Mass flows are closely followed and the program warns the user not to use any of the experiments if there is more than 1% difference between the set-point and the measured flow rate. This warning is respected at all times during this thesis. Furthermore, to be able to reproduce same flame shapes with varying temperatures and pressures throughout the year, the parameter chosen to keep constant is the mean axial velocity of the gasses at their respective sections. The flow-rate of the gasses are pressure corrected and as the experiment is in a air conditioned room with sufficiently long tubing, the variations in temperature of the gasses and unwanted variations in flame speeds are negligible. Before going forward with the control algorithm, some conventions need to be given necessary for the calculations of mass flows. The balance equation for lean methane-air combustion is presented by the following balance equation (in moles).

$$\phi_G^0 \mathrm{CH_4} + 2\left(\mathrm{O_2} + a\mathrm{N_2}\right) \longrightarrow \phi_G^0\left(\mathrm{CO_2} + 2\mathrm{H_2O}\right) + 2\left(\left(1-\phi_G^0\right)\mathrm{O_2} + a\mathrm{N_2}\right) \qquad (2.4)$$

where ϕ_G^0 is the global equivalence ratio when methane fuel is used, called initial equivalence ratio from now onward, which signifies that this balance equation holds true when the total flow-rates of methane and air is accounted for, independent of the combustion regime being premixed or non-premixed, when only methane fuel is used. $a = 3.76$ is the molar ratio of nitrogen to oxygen in the air.

This work contains the hydrogen-methane-air perfectly premixed flames; deemed as hydrogen enriched combustion and hydrogen injection in a methane-air flame. Both are done by keeping the air flow-rate and the thermal power constant, taking out a defined percentage of methane from the global flow and replacing it with the equivalent amount of hydrogen giving the same amount of thermal power corresponding to the amount of methane taken out. The thermal power and the air flow rate for all cases incuding REF, PH, PC and MH cases are constant. This signifies that the ratio of the thermal power coming from the hydrogen to the total thermal power is an input parameter for the algorithm controlling the fuel flow-rates, which is presented in Fig. 2.6.

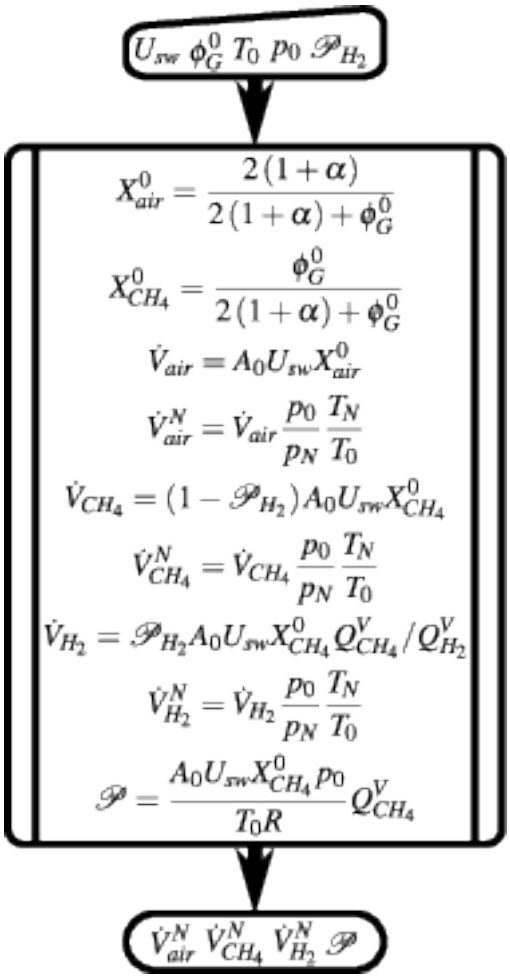

Figure 2.6: Schematic representation of the mass flow control algorithm applied in the software controlling the MIRADAS experiment. The descriptions of the symbols are given in Table 2.2.

Table 2.2: Descriptions of the symbols used in flow-rate calculations of hydrogen, methane and air.

A_0	: Area at the exit of the annular injection channel
T_N	: Temperature at normal conditions, 273.15 K
p_N	: Pressure at normal conditions, 101 325 Pa
U_{sw}	: Average axial flow velocity at the exit of the annular injection channel
ϕ_G^0	: Global equivalence ratio when only methane fuel is used
T_0	: Fresh gas temperature
p_0	: Atmospheric pressure at the time of experiment
$\mathscr{P}_{H_2}$	: Ratio of the thermal power coming from Hydrogen
X_{air}^0	: Air molar fraction for methane-air combustion
$X_{CH_4}^0$	: Methane molar fraction for methane-air combustion
$\dot{V}_{air}$	: Air volumetric flow-rate
$\dot{V}_{air}^N$	: Air volumetric flow-rate at normal conditions
$\dot{V}_{CH_4}$	: Methane volumetric flow-rate
$\dot{V}_{CH_4}^N$	: Methane volumetric flow-rate at normal conditions
$\dot{V}_{H_2}$	: Hydrogen volumetric flow-rate
$\dot{V}_{H_2}^N$	: Hydrogen volumetric flow-rate at normal conditions
$\mathscr{P}$	: Thermal power

When multiple fuels are used simultaneously, care is required for a consistent definition of basic combustion parameters. Whether the fuels are premixed or injected separately, one may define the molar fraction of each species in the hypothetical fuel mixture. In this study considering hydrogen and methane oxidized in air, the molar fraction of hydrogen in the hypothetical global fuel mixture is:

$$X_{H_2}^f = \frac{\dot{n}_{H_2}}{\dot{n}_{H_2} + \dot{n}_{CH_4}} \tag{2.5}$$

where $\dot{n}_j$ denotes the molar flow rate of species j. Then, the balance equation for lean combustion of this multicomponent fuel may be written:

$$\begin{aligned}\phi_G \left(X_{CH_4}^f \mathrm{CH_4} + X_{H_2}^f \mathrm{H_2} \right) + \left(2 - \frac{3}{2} X_{H_2}^f \right) (\mathrm{O_2} + a\mathrm{N_2}) \longrightarrow \\ \phi_G \left(X_{CH_4}^f \mathrm{CO_2} + \left(2 - X_{H_2}^f \right) \mathrm{H_2O} \right) + \left(2 - \frac{3}{2} X_{H_2}^f \right) ((1-\phi_G)\,\mathrm{O_2} + a\mathrm{N_2})\end{aligned} \tag{2.6}$$

where $X_{CH_4}^f = 1 - X_{H_2}^f$ is the molar fraction of methane in the global hypothetical fuel mixture. The global equivalence ratio is defined as $\phi_G = \alpha/\alpha_s$, where $\alpha = \dot{m}_f/\dot{m}_a$ is the ratio between the fuel and air mass flow rates injected in the burner. The stoichiometric value of α is:

$$\alpha_s = \frac{X_{CH_4}^f W_{CH_4} + X_{H_2}^f W_{H_2}}{\left(2 - \frac{3}{2} X_{H_2}^f \right) (W_{O_2} + a W_{N_2})}, \tag{2.7}$$

where W_j is the molar mass of species j. It should be noted that, even though they differ slightly, ϕ_G^0 is different than ϕ_G. ϕ_G is the real equivalence ratio of the hypothetical fuel air mixture with or without hydrogen addition, defined taking into account all the constituents, and ϕ_G^0 is the equivalence ratio of the mixture with just methane, before the replacement of a certain percentage of methane by power equivalent by hydrogen. When a certain percentage of methane is taken away and it is replaced by the equivalent flow-rate of hydrogen with the same power, the equivalence ratio changes. There is a simple relationship between the two equivalence ratios defined as presented in Eq.2.8.

$$\phi_G = \phi_G^0 \left(1 + \mathscr{P}_{H_2} \left(\frac{Q_{CH_4}^V}{4 Q_{H_2}^V} - 1 \right) \right) \tag{2.8}$$

where Q_j^V is the molar lower heating value of species j. Finally, for the analysis conducted in this paper, it is relevant to define the link between the fraction of the total thermal power attributed to hydrogen $\mathscr{P}_{H_2}$ to the molar fractions of the fuels in the global fuel mixture:

$$\mathscr{P}_{H_2} = \frac{X_{H_2}^f Q_{H_2}^V}{X_{H_2}^f Q_{H_2}^V + X_{CH_4}^f Q_{CH_4}^V}, \tag{2.9}$$

All the cases presented in Fig. 2.5 are conducted at constant thermal power $\mathscr{P}$ and constant air flow rate. This strategy is chosen because the thermal power is usually the most important parameter in systems constructed to recover the heat or the mechanical power and also has a first-order impact on the magnitude of combustion instabilities. The air flow-rate is kept constant, because for most naturally aspirated systems, the air flow-rate is a function of thermal power. Therefore, the control parameters are the fraction of the thermal power from hydrogen, $\mathscr{P}_{H_2}$ and that from the pilot flame, $\mathscr{P}_{pilot}$. Accordingly, the fraction of power from the main mixture is $\mathscr{P}_{main} = 1 - \mathscr{P}_{H_2}$. All these cases are summarized in Table 2.3 and allow a systematic investigation of effects of fuel composition, injection strategy and pilot fuel.

Table 2.3: Details of the operating points.

Case	Main		Pilot		$\mathscr{P}_{main}$ [%]	$\mathscr{P}_{pilot}$ [%]	$\mathscr{P}_{H_2}$ [%]
	$X^f_{H_2}$ [%]	$X^f_{CH_4}$ [%]	$X^f_{H_2}$ [%]	$X^f_{CH_4}$ [%]			
REF	0.0	100.0	0.0	0.0	100.0	0.0	0.0
PH1	0.0	96.8	3.2	0.0	99.0	1.0	1.0
PH2	0.0	93.7	6.3	0.0	98.0	2.0	2.0
PH4	0.0	87.9	12.1	0.0	96.0	4.0	4.0
PH10	0.0	73.1	26.9	0.0	90.0	10.0	10.0
PC1	0.0	99.0	0.0	1.0	99.0	1.0	0.0
PC2	0.0	98.0	0.0	2.0	98.0	2.0	0.0
PC4	0.0	96.0	0.0	4.0	96.0	4.0	0.0
PC10	0.0	90.0	0.0	10.0	90.0	10.0	0.0
MH1	3.2	96.8	0.0	0.0	100.0	0.0	1.0
MH2	6.3	93.7	0.0	0.0	100.0	0.0	2.0
MH4	12.1	87.9	0.0	0.0	100.0	0.0	4.0
MH10	26.9	73.1	0.0	0.0	100.0	0.0	10.0

3. STABILIZATION OF SWIRLED PREMIXED FLAMES AND THE EFFECT OF INJECTION STRATEGIES AND HYDROGEN ENRICHEMENT

In most combustion systems, the flow speeds are faster compared to turbulent flame speeds. This imposes the necessity to use stabilization elements, like sudden expansions, bluff bodies and swirlers to stabilize the flames that otherwise would be blown-out by the flow. In this work the term static stability is used to explore the ability of flames to resist lift-off and blow-off and flashback. Oscillations that are weakly periodic such as local flame quenching and bifurcations that occur at very low equivalence ratios are present in MIRADAS setup, however these phenomenons are left out from the scope of this work.

In MIRADAS setup the three basic elements are used to stabilize the flames. The swirler creates a re-circulation region in the middle along the combustion chamber axis that helps the flame to stabilize. Furthermore, the sudden expansion from the annular injection channel to the combustion chamber creates the outer recirculation zones, which helps the flame to be stabilized at low equivalence ratios. Moreover the injection tube in the middle also creates a wake that helps to stabilize the flames for non-piloted flames and for low injection velocities.

In this chapter the effect of hydrogen piloting, methane piloting and hydrogen enrichment on swirled premixed flames is studied. Furthermore the effect of geometrical parameters such as swirl number and chamber diameters, is explored along with injection strategies to conclude the efficiency of the injection strategies for different flames which are characterized by expansion ratios and swirl numbers.

3.1 Flame Images of the Stable Configuration - Effect of Hydrogen and Methane Piloting, Hydrogen Enrichment, Swirl Number and Chamber Diameter

Mean flame images are taken with a configuration with the short plenum and short combustion chamber which is stable for all the operating conditions studied. The long exposure flame images are recorded with a PI-MAX4 emICCD intensified camera

(GaAsP type photo-cathode) equipped with a Opto Engineering TC4M120 telecentric lens and a ASAHI XHQA430 high transmission band-pass filter centered at the wavelength of λ=430 nm. This wavelength corresponds to the chemiluminescent light emitted by excited CH radicals, denoted as CH* which emit a photon upon relaxing to their ground states, giving up a bluish light, which is used as a marker of heat release rate [112–116]. The schematic representation of the setup is presented in Fig. 3.1.

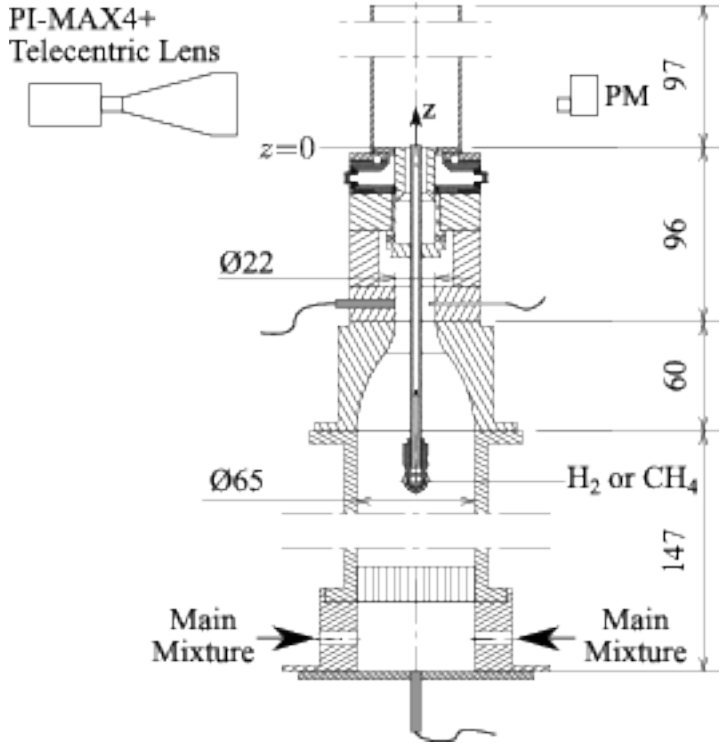

Figure 3.1: Schematic representation of the configuration used in mean flame imaging.

Mean flame images are taken for 15° (S=0.33) and 35° (S=0.86) swirlers for a variety of operating points with different bulk velocities, equivalence ratios and fraction of hydrogen powers and are compared to study the respective effects. The entirety of the flame is in the field of view of the camera, giving an image where the intensity of the pixels are proportional to the line of sight integrated heat release rate.

Furthermore, to obtain the magnification ratio which permits the conversion from pixel units to SI units and to locate the combustion chamber in the frame of the image, a calibration target is used. The calibration target has 5 mmx5 mm squares, which enable to calculate how many pixels make a millimeter and the lines along the middle axis of the combustion chamber can be used to verify that the camera vertical axis is aligned well with the axis of the combustion chamber. The calibration target used is presented in Fig. 3.2.

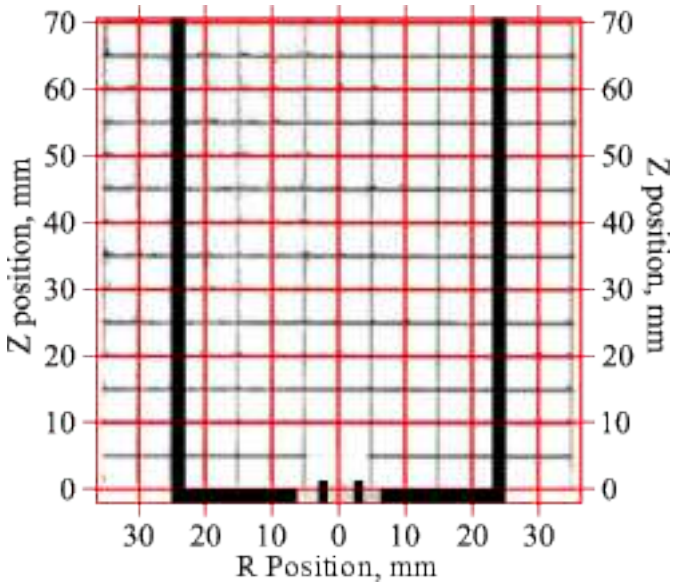

Figure 3.2: Calibration target used to obtain the magnification ratio.

3.2 Flame Images with 15° Swirler, D_c=46 mm Combustion Chamber

Firstly, the flames obtained with a low swirl configuration (θ_{sw}=15° corresponding to a geometrical swirl number of S=0.33) are presented. The bulk velocity U_{sw} is set to 18 m/s and the initial equivalence ratio is ϕ_G^0=0.8. The fraction of hydrogen percentage is increased and its effect is observed. This corresponds to a Reynolds number of 7120 based on the hydraulic diameter of D_h=6 mm and a thermal power of 3910 W.The resulting images are presented in Fig. 3.3.

Looking at Fig. 3.3 the most important aspect is that with increasing hydrogen piloting (PH cases), the length of the flame decreases. This also holds true for hydrogen enrichment as in MH cases. Methane injection also very slightly shortens the flame, but it is not nearly as effective as hydrogen injection. Another important aspect is that the general shape of the flames are not changed, the conical shape of the line of sight integrated flame images stays practically the same, especially for low levels of piloting or enrichment.

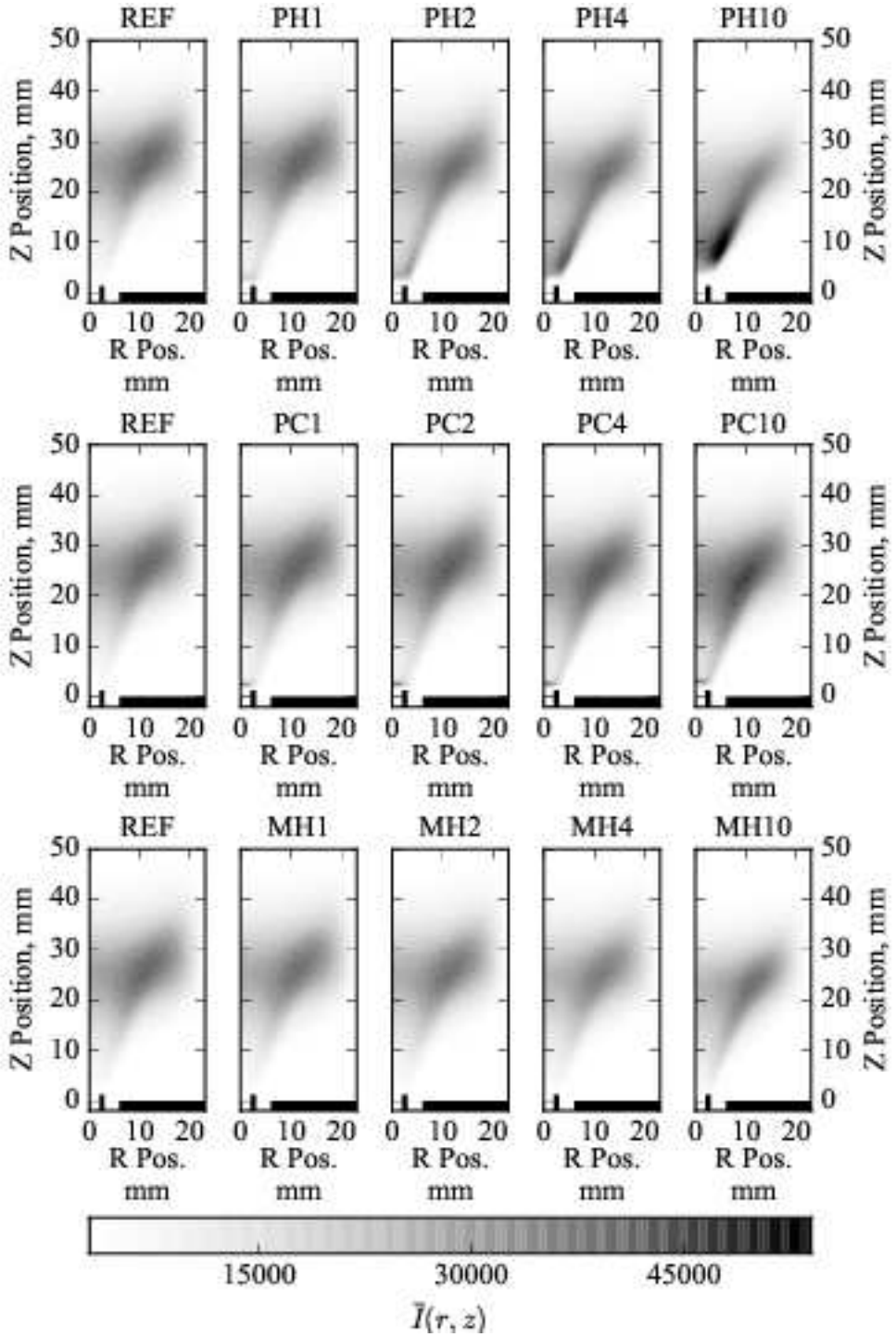

Figure 3.3: Mean flames corresponding to a geometrical swirl number of S=0.33 and a chamber diameter of D_c=46 mm. The bulk velocity at the exit of the swirled annular injection channel is U_{sw}=18 m/s and the initial equivalence ratio is ϕ_G^0=0.8. Right side of the images are presented for comparison.

For MH cases with increased hydrogen enrichment, the length of the flame shortens, this is due to the higher flame speed of hydrogen. Laminar flame speeds (S_L) for 300 K unburnt gas temperature atmospheric flames obtained with GRI-Mech 3.0 [117] using Cantera [118] are presented in Fig. 3.4.

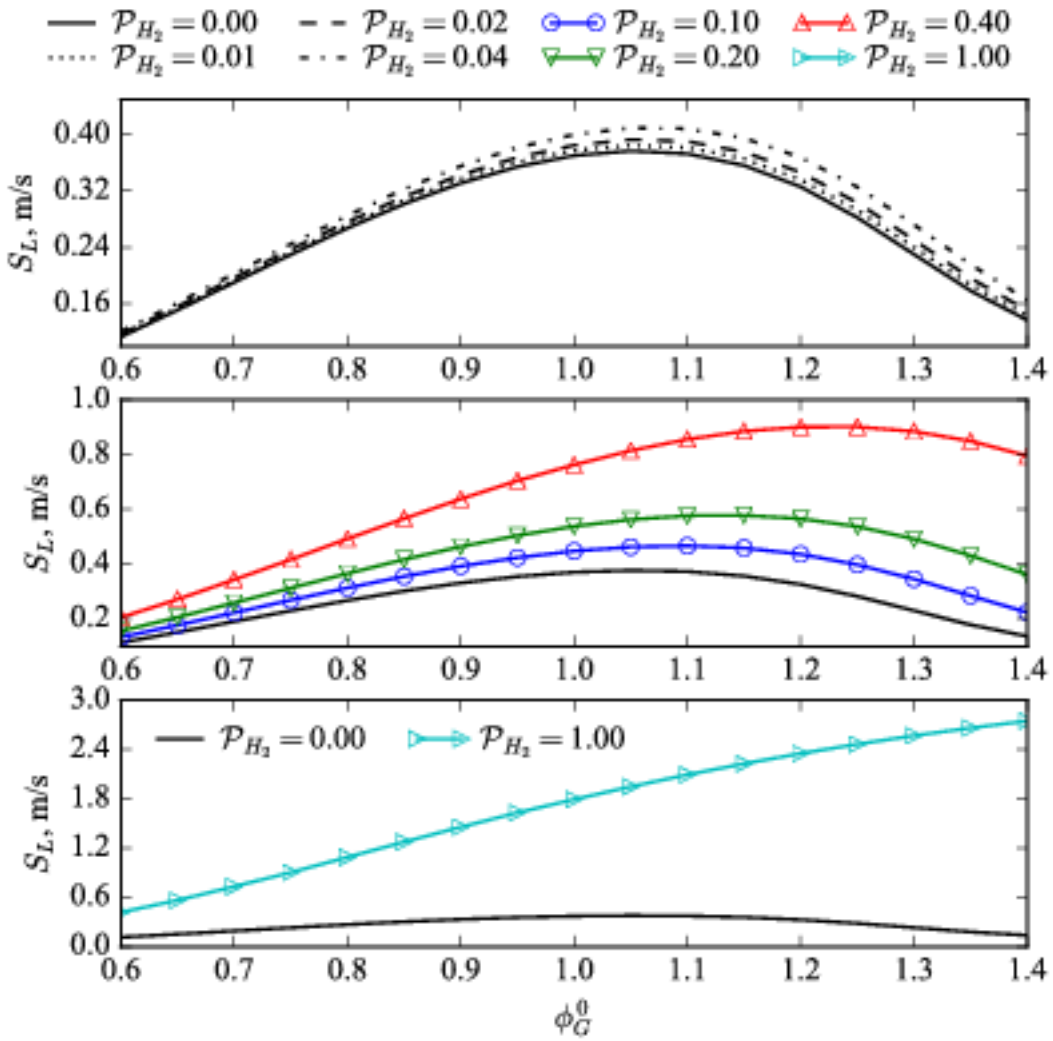

Figure 3.4: Laminar Flame Speeds as a function of initial equivalence ratio ϕ_G^0 and hydrogen power fraction $\mathscr{P}_{H_2}$.

With injection, the intensity near the injection tube increases both for PC and PH cases, as this high equivalence ratio region produces CH* intensely. When the injection power rate is increased, the lift-off distance increases both for PH and PC cases, as the bulk velocity of fuel in the injection tube is increased, however the increase in lift-off distance is more pronounced for PH cases. This is due to a competition between diffusion of fuel in the premixed mixture, flame speed and flow velocity. The lift-off distance is longer for PH cases compared to PC cases for the same power of injection $\mathscr{P}_{pilot}$. However, this shouldn't be confused with the ability of hydrogen to resist lift-off, which is discussed further down the text.

Another way to explore these flame images is to perform an Inverse Abel transform [119, 120] to reconstruct a slice of the half conical shaped flame. As the flame has a half conical shape, the line of sight integrated images include the effect of increasing

radius along the combustion chamber axis. At the edges of the flame, the flame radius is higher, so the picture taken with the camera which is integrating the CH* emissions along the line of sight results in data that is weighted by the radius, not just the local intensity. The reconstructed slice obtained with an Inverse-Abel transform shows the local CH* chemiluminescent intensity, which can be correlated to the local heat release. The resulting Inverse-Abel transformed images are presented in Fig. 3.5. The Inverse-Abel transformations are done using PyAbel Python package [121].

For the REF case, the Inverse-Abel transformed image shows a more uniform distribution of local CH* chemiluminescent emissions along the combustion chamber axis as the effect of increase of CH* emission caused by the increase in radius at the edges of the flame is removed. With hydrogen piloting, the local intensity at the base of the flame increases. This suggest that the injection of hydrogen at the base of the flame, increases the production of CH* radicals. With increased hydrogen injection as in PH10 case, the local CH* emissions along the flame is increased as well, as the flame length itself is reduced for the same power, the intensity is accordingly increased.

With increased methane injection (PC), the intensity at the flame base is increased as well. Compared to the hydrogen cases, the intensity just at the tip of the injection tube is higher, as the methane fuel can produce CH* radicals that the hydrogen cannot, the increased intensity in hydrogen injected cases comes from the methane which is providing the bulk of the power. The intensity at the base of the flame until 20 mm of axial distance is increased as well, but not as much as hydrogen injection cases.

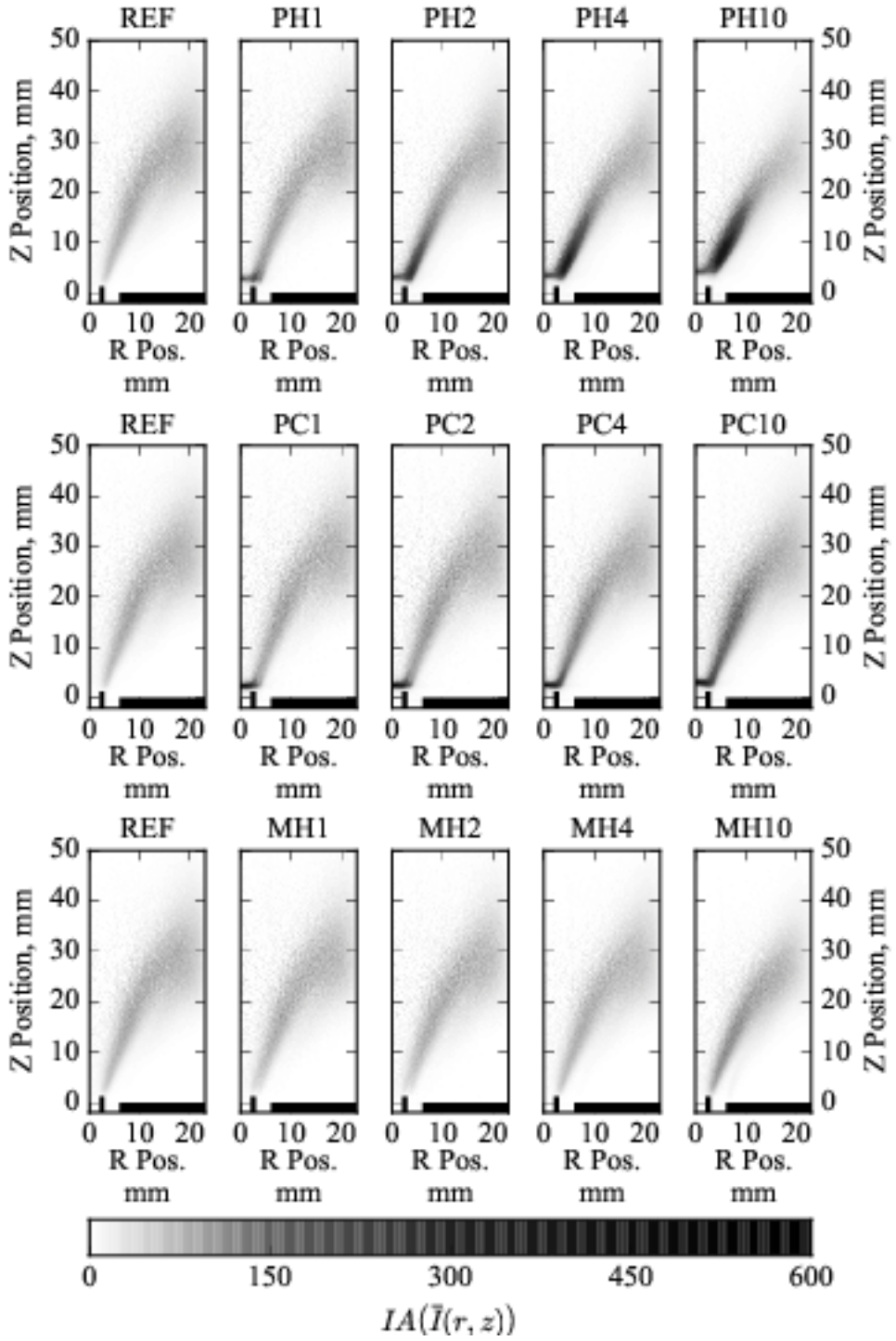

Figure 3.5: Inverse-Abel transformed mean flame images of cases corresponding to a geometrical swirl number of S=0.33 and a chamber diameter of D_c=46 mm. The bulk velocity at the exit of the swirled annular injection channel is U_{sw}=18 m/s and the initial equivalence ratio is ϕ_G^0=0.8. Right side of the images are presented for ease of comparison.

Moreover, hydrogen enrichment does not change the flames drastically until 10% of hydrogen power fraction. For MH10 case, the local intensity is slightly increased compared to the REF case, as a result of shorter flame length. For MH10 case, flames start to stabilize on the outer side of the burner wall and start to resemble an M-shape

as a result of increased reactivity. This is a characteristic of hydrogen enriched swirled flames [122].

As described before, the replacement of methane by hydrogen with the amount equivalent in thermal power changes the global equivalence ratio. Even though the change is very small for low levels of hydrogen power fraction, when increased it lowers the global equivalence ratio ϕ_G. The global equivalence ratio versus hydrogen power fraction for an initial equivalence ratio of 0.8 is presented in Table 3.1.

Table 3.1: Change of equivalence ratio with increasing hydrogen power fraction

$\mathscr{P}_{H_2}$, %	0	1	2	4	10	20	40
ϕ_G	0.800	0.799	0.797	0.795	0.786	0.773	0.745

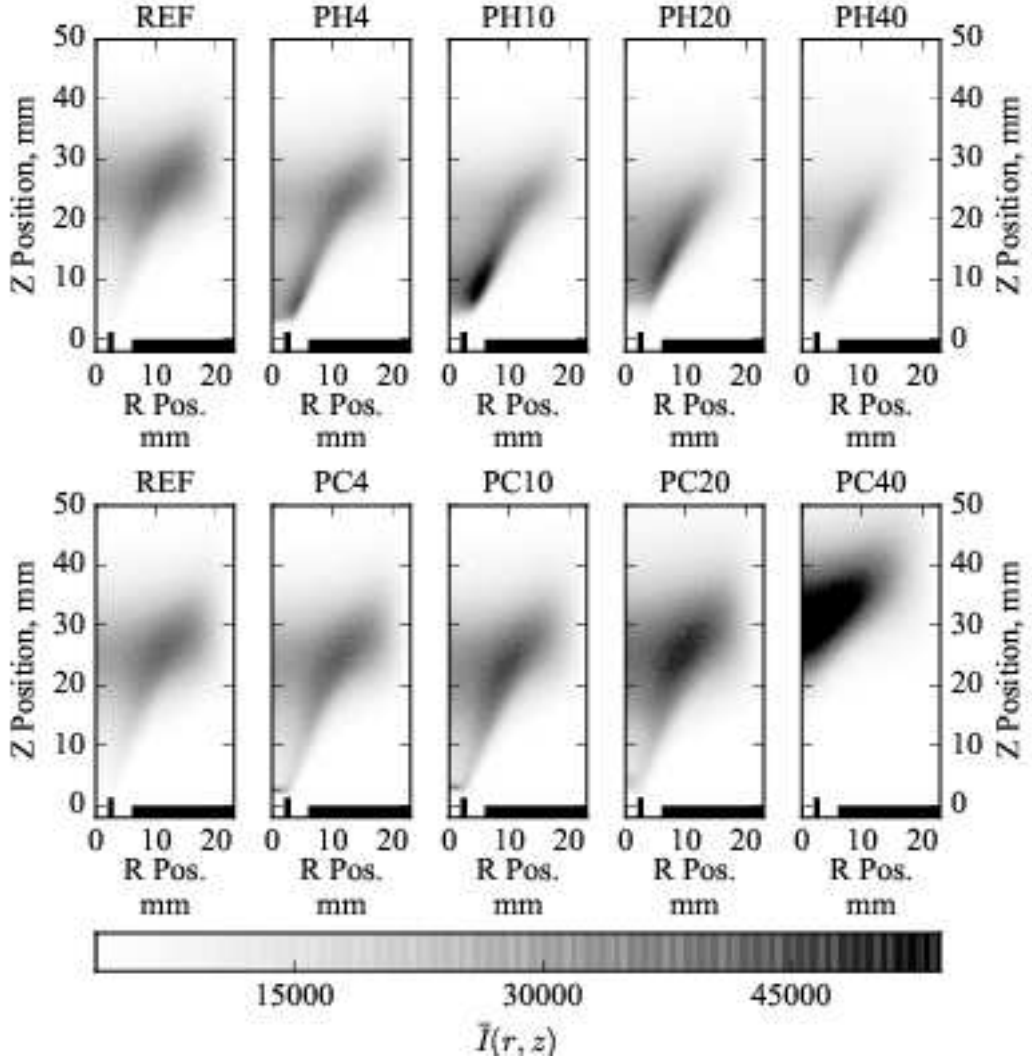

Figure 3.6: Flames with increased piloting ratio, U_{sw}=18 m/s and ϕ_G^0=0.8, S=.33

Furthermore, even though hydrogen as a higher lift-off distance for lower power fractions, for higher piloting power fractions hydrogen piloted flame rests attached to the injection tube when the methane piloted flame is lifted off. This phenomenon

is presented in Fig. 3.6. The CH* intensity increases as the flames get shorter until PH20, and for PH40, the CH* intensity is less compared to others. This is due to the decrease in CH* concentrations as methane is replaced by hydrogen, which does not contain carbon atoms to produce CH* radicals. The remainder of CH* radicals come from combustion of methane which provides 60% of the thermal power for PH40 case.

The resistance of hydrogen to lift-off is partly due to the ability of hydrogen to resist high strain rates. Opposed-flow diffusion flame calculations with Cantera [118] using GRI-Mech 3.0 [117] and San Diego Mechanism [123] has been performed to compare the extinction strain rates of hydrogen and methane flames. The fuel and air temperatures are set to 300 K and pressure is atmospheric. The results are presented in Fig.3.7; H_2/Air diffusion flames can resist up to ≈40 times of the extinction strain rates of CH_4/Air diffusion flames.

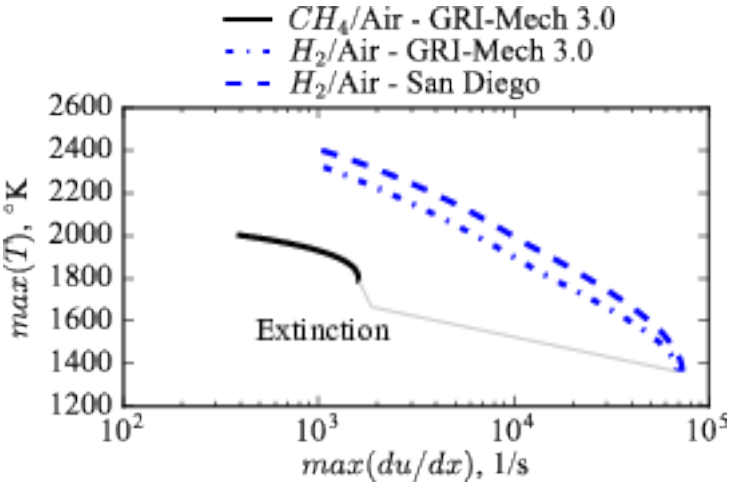

Figure 3.7: Maximum temperatures vs. strain rates for atmospheric pressure CH_4/Air and H_2/Air flames. Unburnt gas temperatures are set to 300 K. Horizontal axis is on a logarithmic scale.

3.3 Flame Images with 35° Swirler, D_c=46 mm Combustion Chamber

High levels of swirl allow to obtain shorter, more intense flames, however they also bring along the danger of flashbacks, so a compromise needs to be done between aerodynamic combustion stability and flame length. Flames obtained with the 35° swirler (S=0.86) and D_c=46 mm chamber with U_{sw}=18 m/s and ϕ_G^0=0.8 is presented in Fig. 3.8.

Fig 3.8 shows that, as expected, the flames obtained with 35° swirler are shorter for the same injection power fraction or hydrogen power fraction compared to the flames

obtained with 15° swirler. Another important aspect is the reduced attachment distance in all cases compared to their corresponding low swirl counterparts. Furthermore, the edges of the flames are more smeared on the chamber walls, as there is more swirl in the flow. The same behavior observed as in 15° swirler cases of reduced flame length with increasing hydrogen power fraction is present for 35° swirler cases as well.

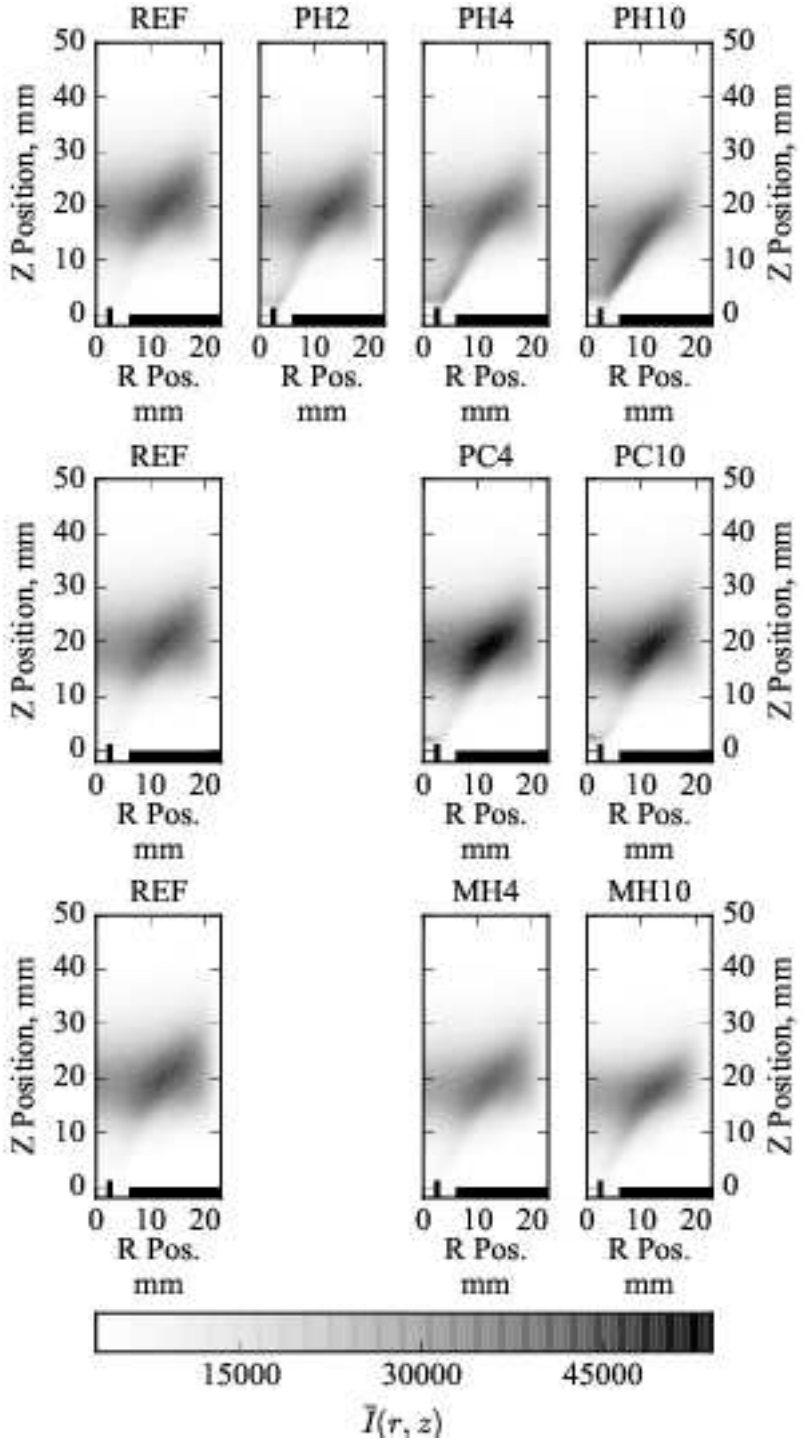

Figure 3.8: Mean flames corresponding to a geometrical swirl number of S=0.86 and a chamber diameter of D_c=46 mm. The bulk velocity at the exit of the swirled annular injection channel is U_{sw}=18 m/s and the initial equivalence ratio is ϕ_G^0=0.8. Right side of the images are presented for comparison.

Looking at the Inverse-Abel transformed images presented in Fig. 3.9, it can be seen that compared to the low swirl case, the flames are almost folded at the edges, creating the more intense regions on the line of sight integrated images. The REF flame starts to fold on itself at the edges, resembling a hook shape. Hydrogen injection flattens the flame edges and for PH10 case, the edge of the flame is straightened out.

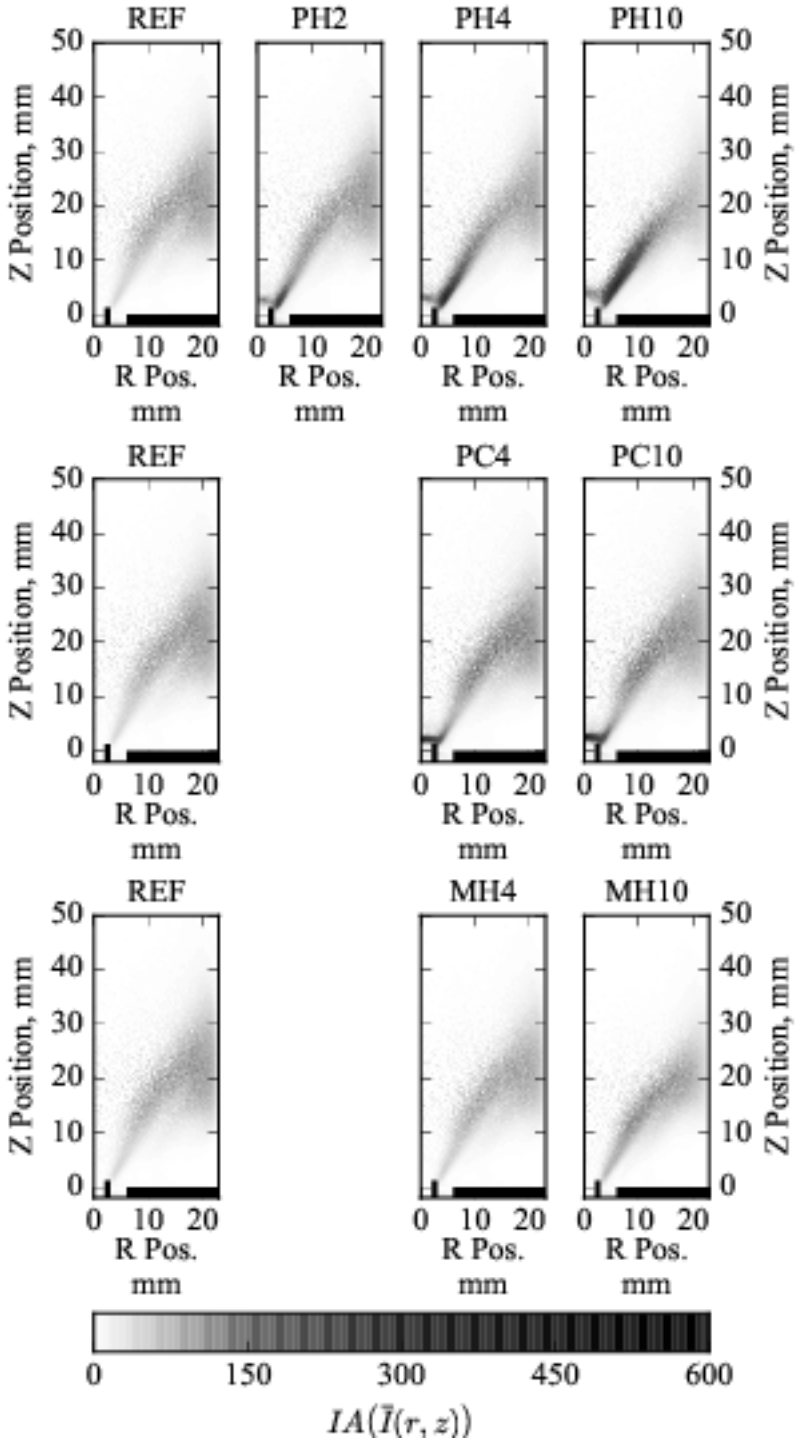

Figure 3.9: Inverse-Abel transformed mean flame images corresponding to a geometrical swirl number of S=0.86 and a chamber diameter of D_c=46 mm. The bulk velocity at the exit of the swirled annular injection channel is U_{sw}=18 m/s and the initial equivalence ratio is ϕ_G^0=0.8.

These flames are also attached closer to the walls of the injection tube and the attachment point is further in the radial direction, almost going past the edge of the injection tube compared to low swirl configuration. The lift-off height of the flame at the center-line of the chamber moves very slightly upstream, but it is not as greatly effected as the edges of the base of the flame.

Furthermore, the effect of bulk velocity at the exit of the annular injection channel and the equivalence ratio on the shapes of the flames are studied as well. This is done by building mean line of sight integrated flame image maps for different injection and hydrogen enrichment strategies. The images are normalized by the maximum value of the flame images 14 m/s of each initial equivalence ratio ϕ_G^0 of the REF case. For example all the flame images of ϕ_G^0=0.65 with bulk velocities from 14 m/s to 30 m/s are normalized by the maximum pixel intensity of ϕ_G^0=0.65 and U_{sw}=14 m/s. Similarly the cases corresponding to an initial equivalence ratio of ϕ_G^0=0.7 are normalized by the maximum pixel intensity of U_{SW}=14 m/s case. When the injection strategy or the hydrogen enrichment is applied as in PH, PC and MH cases, the same normalization strategy is applied, however cases are normalized by the maximum values of the corresponding initial equivalence ratios of the REF cases. For example the PH10 cases with ϕ_G^0=0.7 and changing bulk velocities are normalized by the maximum pixel intensity of REF case with ϕ_G^0=0.7 and U_{sw}=14 m/s. Eventually, this normalization strategy results in images that can be compared between all injection and hydrogen enrichment strategies for all bulk velocities by keeping initial equivalence constant. However the images cannot be intensity compared between different equivalence ratios. This technique is chosen as the CH* intensity is strongly dependent on equivalence ratio and increases in a near exponential fashion and when images obtained for different equivalence ratios are normalized by a constant value, the resulting images are very bright for high equivalence ratios and very dark for low equivalence ratios. The image maps for all cases are presented in Figs. 3.10 to 3.13.

Looking at Fig. 3.10, the most important observation is that the flame shape and the flame length is nearly independent of the bulk velocity. Even when the bulk velocity is doubled the shape and the length of the flames change very slightly. However, this is not the case for changes in equivalence ratio, the changes in equivalence ratio completely changes the topology of the flames. Another important observation is the

CH* emissions in the side re-circulation zones; for ϕ_G^0=0.65, there is no combustion in the side re-circulation zone. When the equivalence ratio is increased to ϕ_G^0=0.7, the side re-circulation zone becomes able to sustain the reactions as the temperature of the walls of the combustion chamber is increased and the flame itself becomes more robust

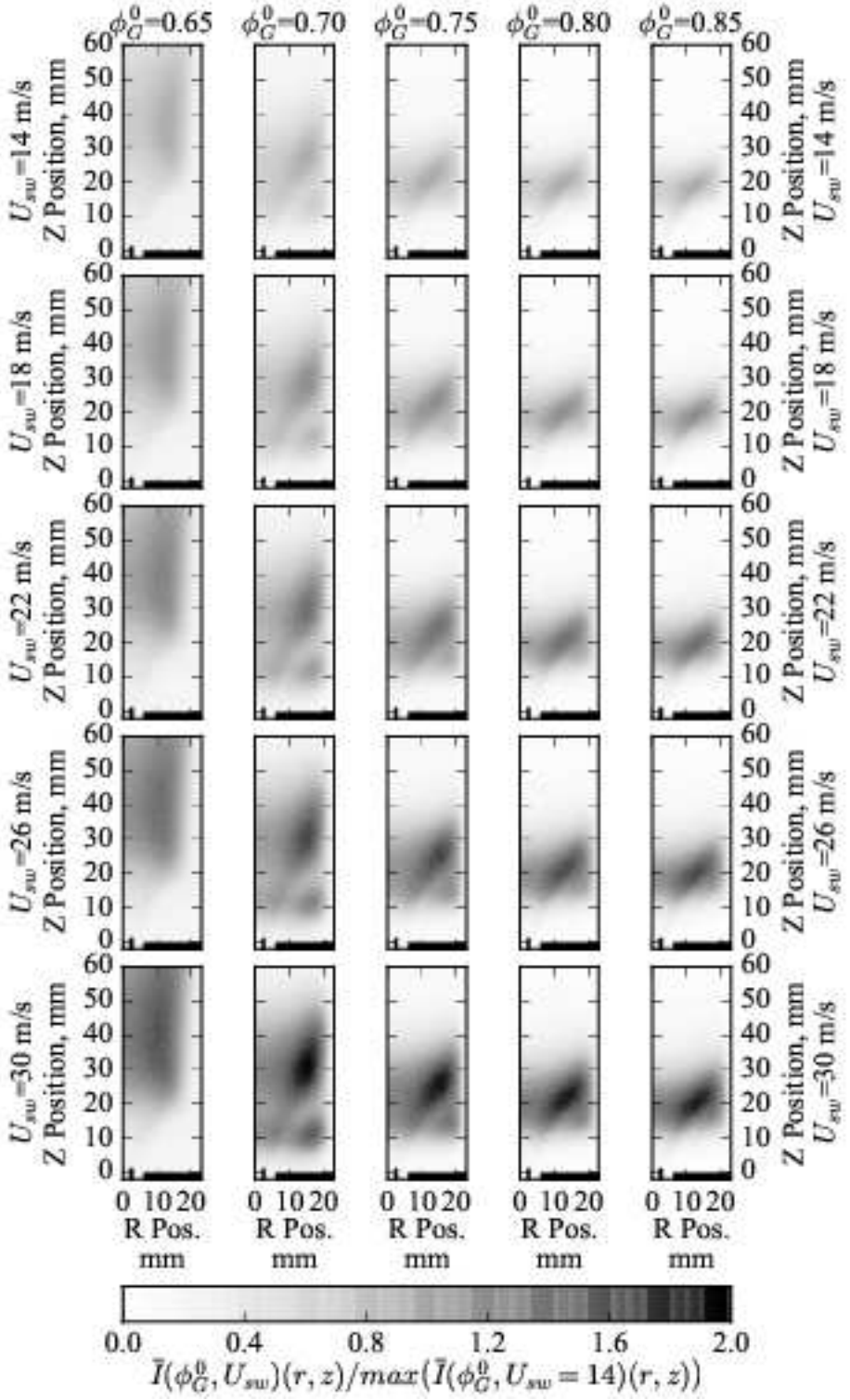

Figure 3.10: Mean flame image map of the REF cases corresponding to a geometrical swirl number of S=0.86 and a chamber diameter of D_c=46 mm. The pixel intensities are normalized by the maximum pixel intensity of the averaged images of the 14 m/s cases for each equivalence ratio.

to heat losses. When the equivalence ratio is further increased, the center flame is able to consume the reactants as the speed of the flame increases, so that the fresh gasses are burnt before transported to this side re-circulation region.

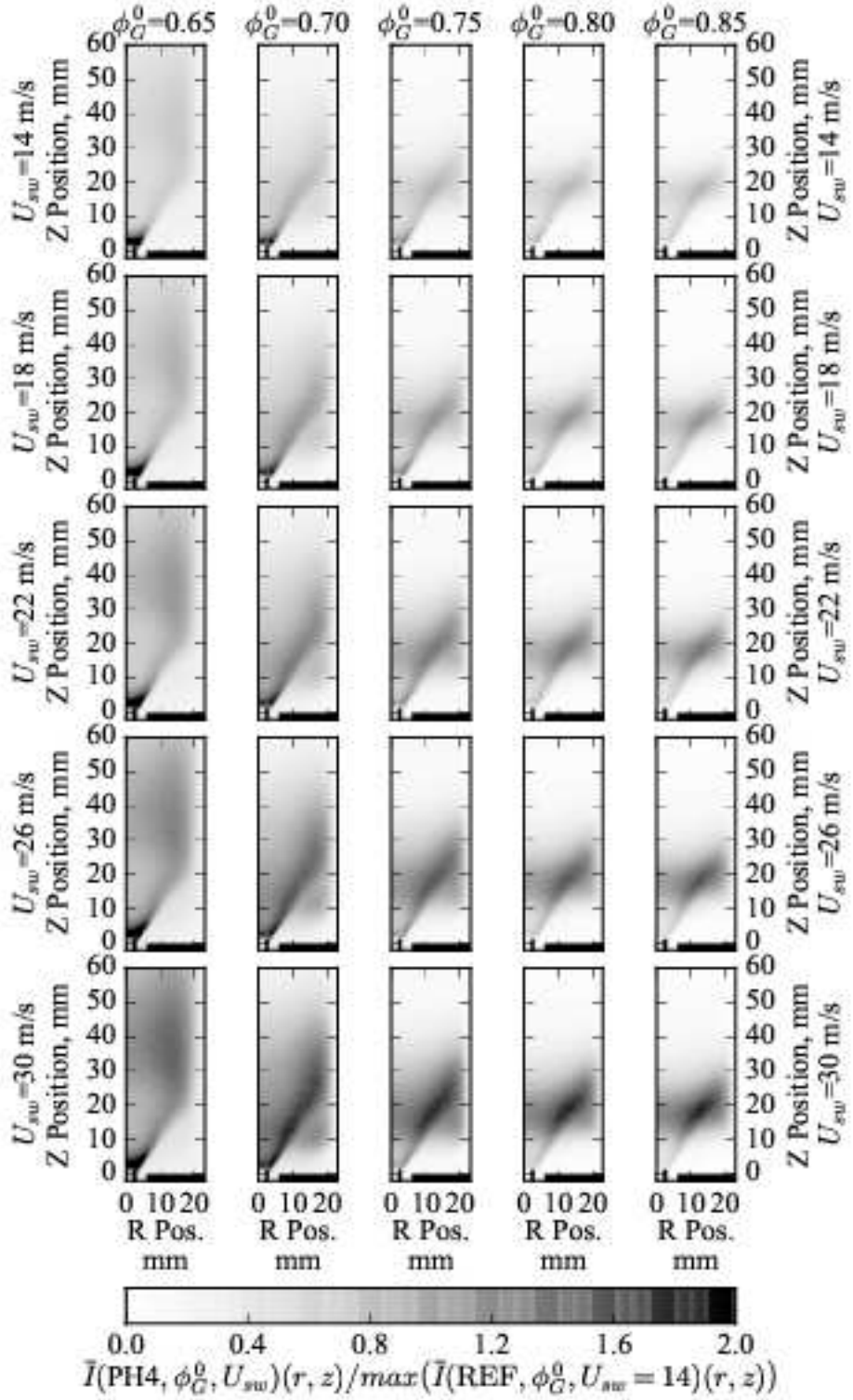

Figure 3.11: Mean flame image map of the PH4 cases, S=0.86, D_c=46 mm. Pixel intensities are normalized by the maximum pixel intensity of 14 m/s flames of REF cases for each equivalence ratio.

For low levels of hydrogen injection as in PH4 cases (Fig. 3.11), this side recirculation zones are moved downstream, however the overall flame topologies are similar to REF cases. CH* emissions are higher near the injection tube outlet as the injected hydrogen burns in this region, it helps along the combustion of the methane-air mixture.

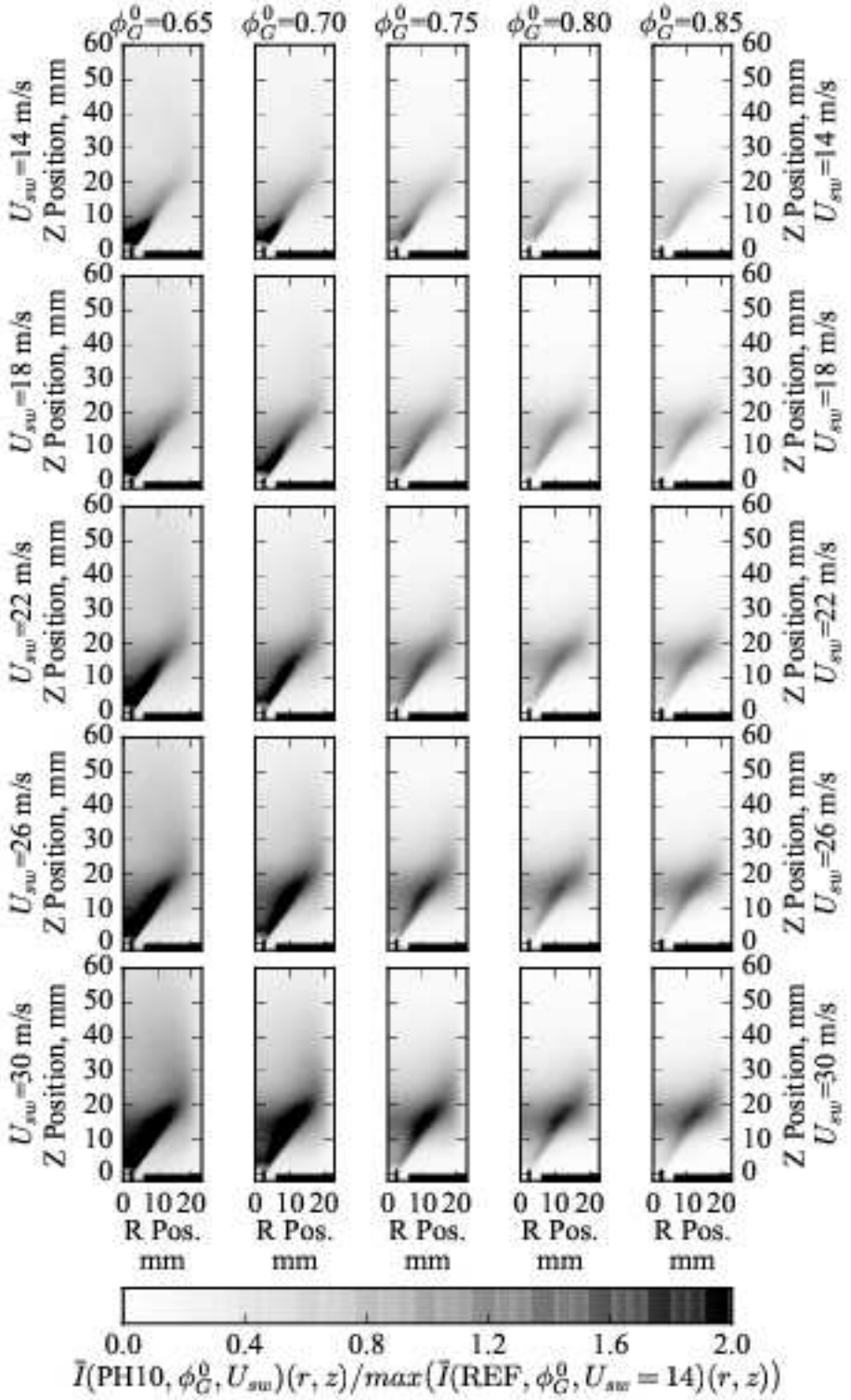

Figure 3.12: Mean flame image map of the PH10 cases; S=0.86, D_c=46 mm. Pixel intensities are normalized by the maximum pixel intensity of 14 m/s flames of REF cases for each equivalence ratio.

When hydrogen injection level is increased to 10% (PH10 cases, Fig. 3.12) the topology of the flames are completely changed. All the flames are well attached to the injection tube and are much shorter. Even for the ϕ_G^0=0.65 case, the long, lazy flame of the REF case becomes an intense, shorter flame with 10% hydrogen injection.

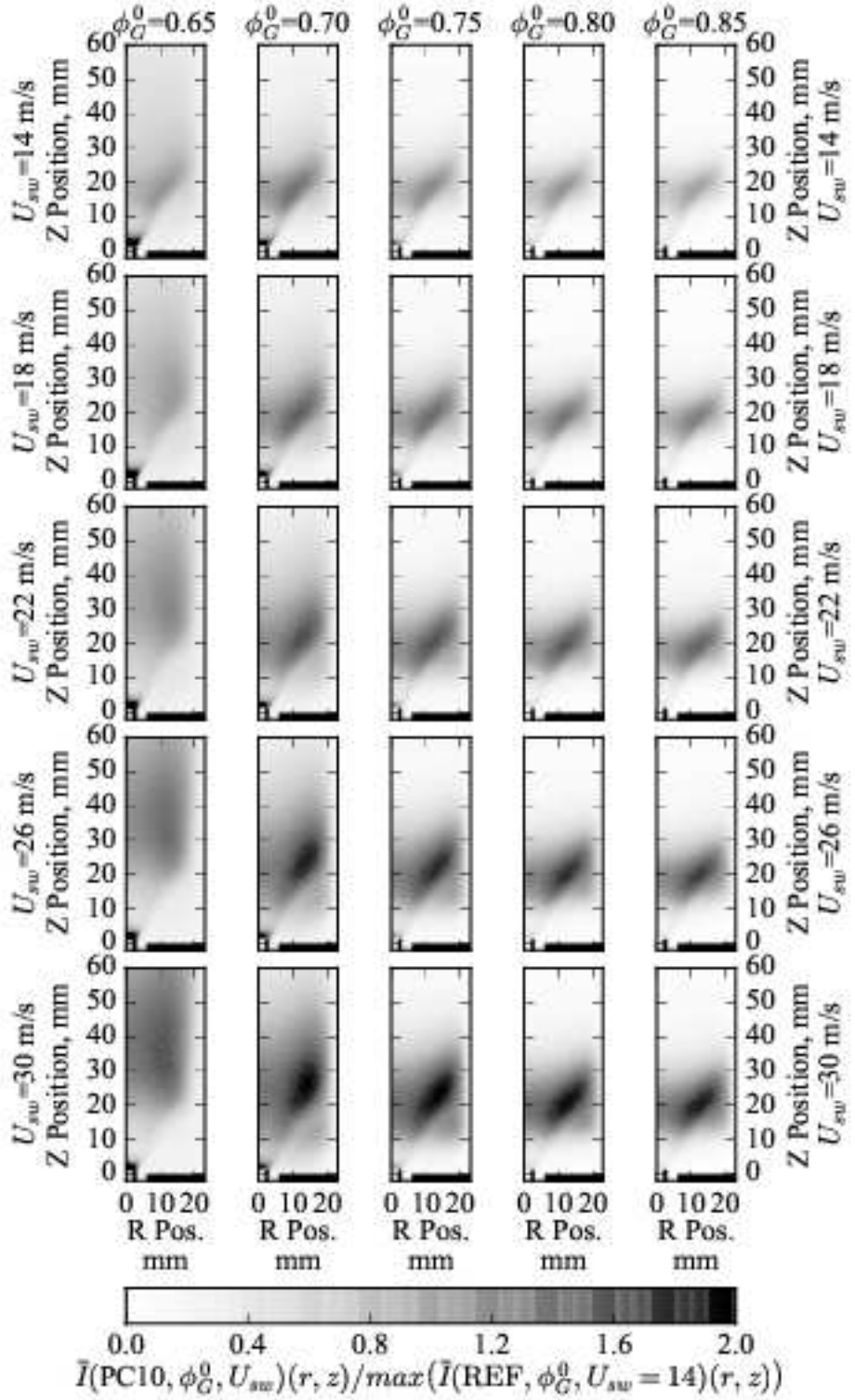

Figure 3.13: Mean flame image map of the PC10 cases; S=0.86, D_c=46 mm. Pixel intensities are normalized by the maximum pixel intensity of 14 m/s flames of REF cases for each equivalence ratio.

When methane is injected through the injection tube (Fig. 3.13), the flame length is reduced for $U_{sw} \leq$18 m/s for ϕ_G^0=0.65 and all ϕ_G^0=0.7 flames of PC10 cases compared to the corresponding REF flames, however methane injection is not nearly as effective as reducing flame lengths compared to hydrogen injection.

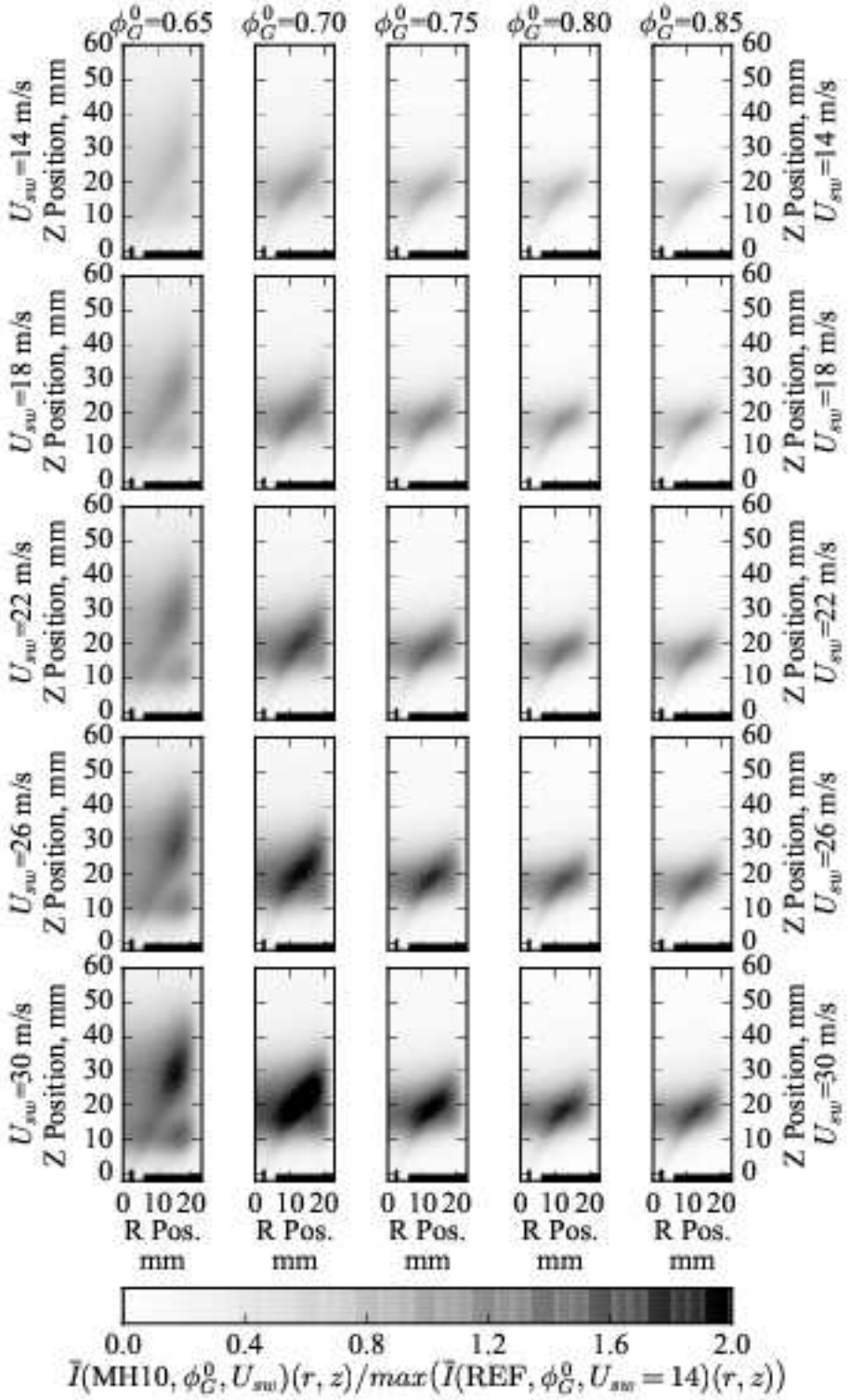

Figure 3.14: Mean flame image map of the MH10 cases; S=0.86, D_c=46 mm. Pixel intensities are normalized by the maximum pixel intensity of 14 m/s flames of REF cases for each equivalence ratio.

When hydrogen enrichment is applied (Fig. 3.14), the flames become shorter compared to REF cases, however still taller compared to PH10 cases. Moreover the reactions can be sustained in the side re-circulation zone for ϕ_G^0=0.65 flames, which is not present for the ϕ_G^0=0.65 REF flames. For all other equivalence ratios the MH10 flames are shorter compared to the REF flames and the side recurculation zones move downstream.

3.4 Flame Images with 35° Swirler, D_c=64 mm Combustion Chamber

It is logical to think that when the diameter of the combustion chamber is increased the length of the flame would be shorter as the bulk velocity in the combustion chamber is lower, but of course swirled flames are never that simple. The length of the flames are strongly dependent on combustion aerodynamics, mainly the size of the center and size re-circulation zones. Flame images obtained with combustion chamber of D_c=64 mm inner diameter is presented in Fig. 3.15.

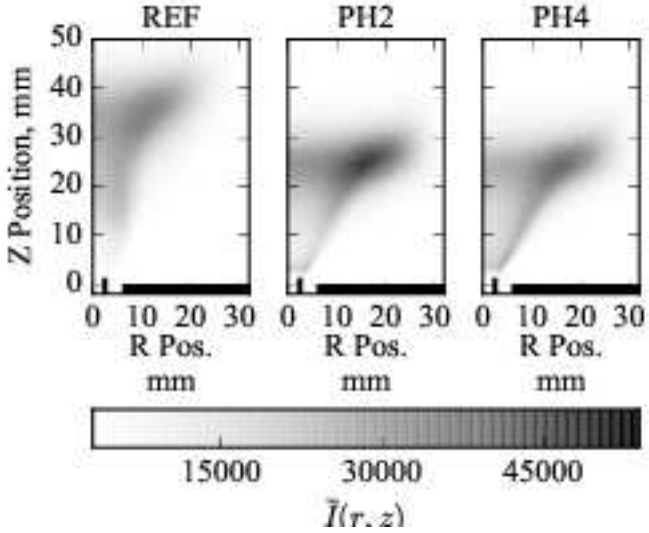

Figure 3.15: Mean flames corresponding to a geometrical swirl number of S=0.86 and a chamber diameter of D_c=64 mm. The bulk velocity at the exit of the swirled annular injection channel is U_{sw}=18 m/s and the initial equivalence ratio is ϕ_G^0=0.8.

Fig. 3.15 shows that the REF flame of the 64 mm chamber is taller compared to the REF flame of the 46 mm chamber (Fig. 3.8), even though the bulk velocity inside the chamber is lower, suggesting that it is extremely difficult to predict the length of flames using geometrical and flame speed expressions. Moreover, when 2% hydrogen is injected, the length of the flames are reduced by 25% for 64 mm chamber. The Inverse-Abel transformed images are presented in Fig. 3.16.

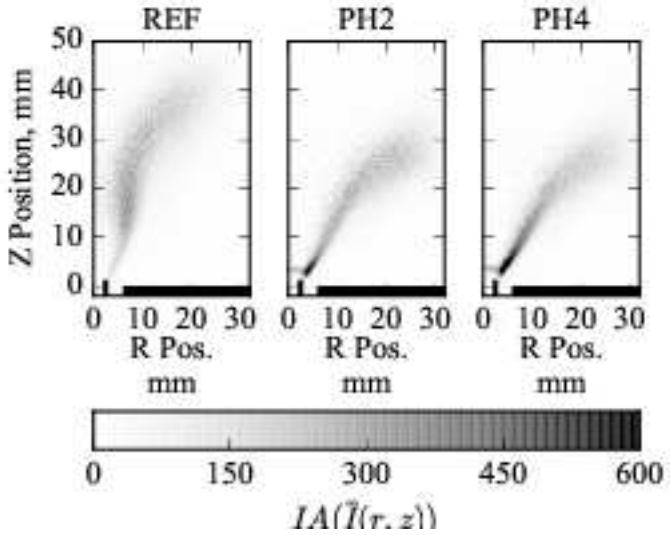

Figure 3.16: Inverse-Abel transformed mean flame images of respectable cases corresponding to a geometrical swirl number of S=0.86 and a chamber diameter of D_c=64 mm. The bulk velocity at the exit of the swirled annular injection channel is U_{sw}=18 m/s and the initial equivalence ratio is ϕ_G^0=0.8.

Looking at the Inverse-Abel transformed images obtained with the D_c=64 mm chamber presented in Fig. 3.16, one can see that the edges of the flames are not folded as in flames D_c=46 mm chamber for the same conditions. Which is more surprising is the S shape flame of the REF case, which is not present for the smaller combustion chamber D_c=46 mm cases. When hydrogen is injected, this S shape is straightened out and the flames become much shorter.

Similarly, the image maps for S=0.86, D_c=64 mm configuration for all cases studied are presented in Figs. 3.17 to 3.19. Investigating the flame image maps, the ϕ_G^0=0.65 and ϕ_G^0=0.7 flames for all bulk velocities and ϕ_G^0=0.75 flames for $U_{sw} \geq$26 m/s flames are lifted for REF cases. With 2% hydrogen injection (PH2), all these flames become attached to the injection tube except ϕ_G^0=0.65 and $U_{sw} \geq$26 m/s flames, where the roots and the tops of the flames are nearly separated as the flame speed is low and the flow velocity is high. With increased hydrogen injection of 4%, all the flames become attached to the injection tube, implying that hydrogen injection can be used to increase lean blow-off limits of combustion chambers.

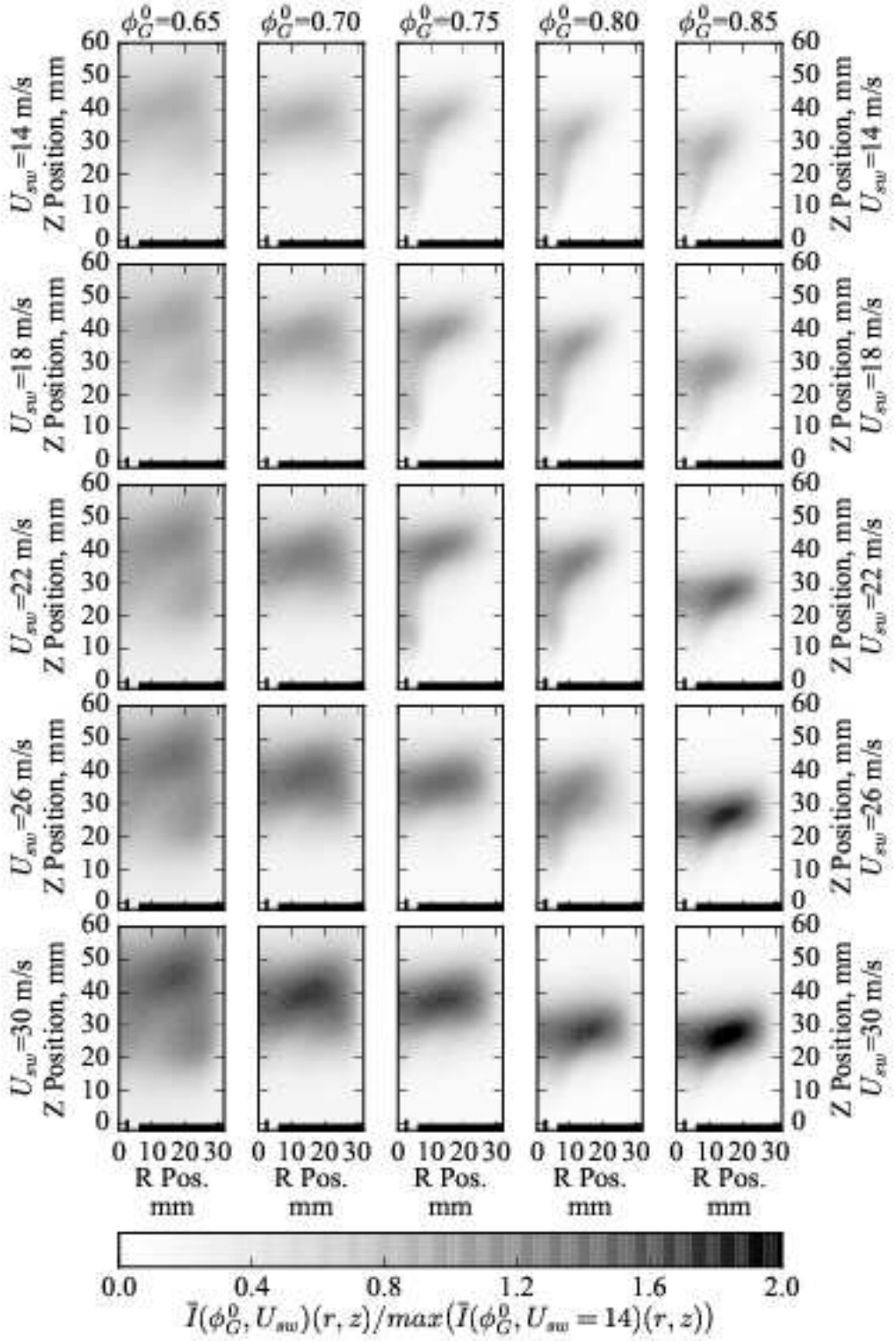

Figure 3.17: Mean flame image map of the REF cases corresponding to a geometrical swirl number of S=0.86 and a chamber diameter of D_c=64 mm. The pixel intensities are normalized by the maximum pixel intensity of the averaged images of the 14 m/s cases for each equivalence ratio.

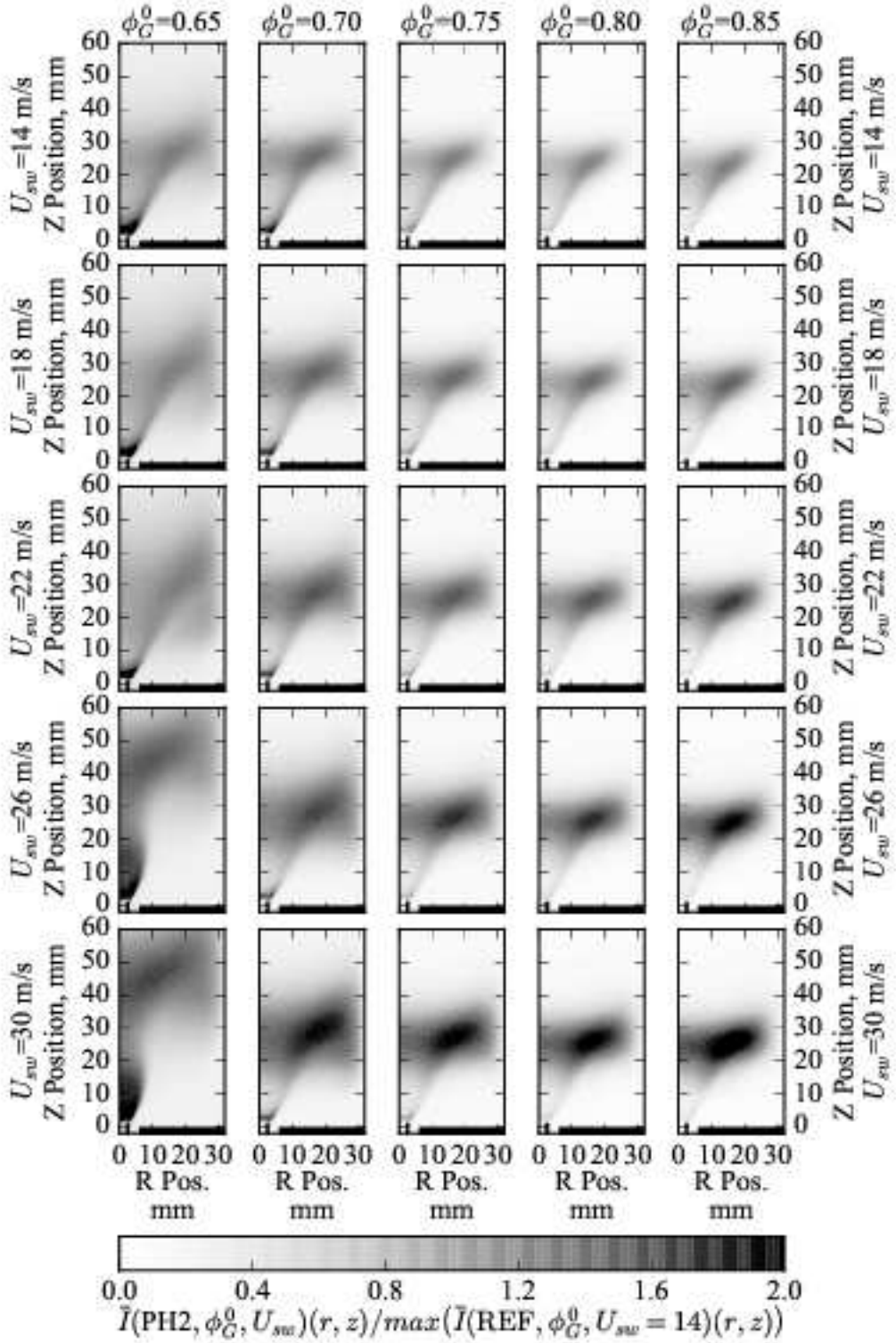

Figure 3.18: Mean flame image map of the PH2 cases; S=0.86, D_c=64 mm. Pixel intensities are normalized by the maximum pixel intensity of 14 m/s flames of REF cases for each equivalence ratio.

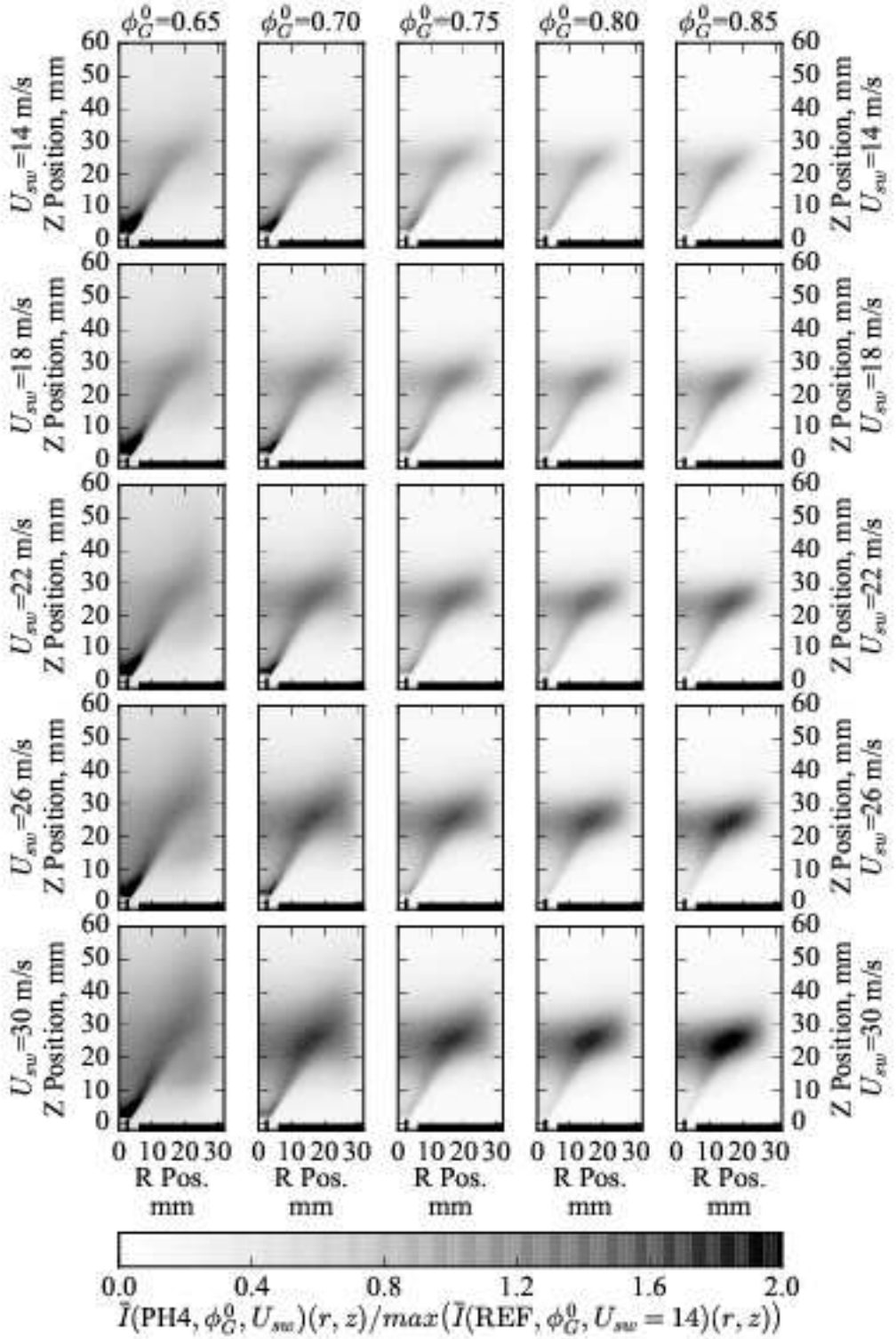

Figure 3.19: Mean flame image map of the PH4 cases; S=0.86, D_c=64 mm. Pixel intensities are normalized by the maximum pixel intensity of 14 m/s flames of REF cases for each equivalence ratio.

3.5 Conclusions

Examining the flames with hydrogen and methane injection and hydrogen enrichment, the following conclusions can be derived.

- Hydrogen addition to methane, either in the form of hydrogen enrichment (perfectly premixed with methane/air mixture) or hydrogen piloting (injected directly into the combustion chamber) makes the flames shorter. This is due to the higher flame speed of hydrogen.

- Hydrogen piloting (PH cases) is much more efficient in reduction of flame lengths and flame anchoring compared to hydrogen enrichment (MH cases) and methane piloting (PC cases), especially for lower equivalence ratios. Causing a redistribution of the volumetric heat release toward the root of the flame, even for very low fractions of pilot power such as 4%, hydrogen can be used to attach flames that are otherwise detached, meaning that low amounts of hydrogen can be used to extend stability limits of combustion systems.

- As the extinction strain rate and diffusivity of hydrogen in air is much higher compared to methane, hydrogen can be injected at much higher power fractions (or velocities) without blow-off compared to methane.

- As expected, increased swirl makes the flames shorter for the same combustion chamber diameter. However, when combustion chamber diameter is increased for the same swirl, it has been observed that the flame topology changes completely and flames become longer, although this should not be interpreted as a general trend.

- For swirled flames, the flame topology is much more sensitive to changes in equivalence ratio and injection strategies compared to changes in bulk velocity. There are some cases where the flames are lifted of when bulk velocity is increased for the same equivalence ratio, but globally, the topology of most of the flames are very similar with changing bulk velocities with an increase in CH* emissions proportional to thermal power.

4. DYNAMIC STABILITY CHARACTERISTICS OF MIRADAS SETUP

Dynamic instabilities in combustion systems are defined as large scale oscillations in pressure, velocity and heat release which have distinct frequencies, associated to the natural acoustic modes of the combustion systems, referred generally as combustion instabilities. More specifically, as they are linked to acoustic modes of the system, dynamical instabilities are referred to as self sustained thermo-acoustic instabilities. They are a product of the feedback loop between the unsteady pressure and velocity and unsteady heat release [5, 6, 124–126].

In this chapter, the dynamic stability characteristics of MIRADAS setup will be explored. Firstly an introduction to the configuration used is given in Section 4.1. Then, the stability maps are presented in Section 4.2. Next, the low order model constructed to study the mode shapes is presented in Section 4.3. Afterwards, spectral analysis of unstable modes and the classification of modes are presented in Section 4.4.

4.1 Configuration Used to Study Dynamic Combustion Instabilities

It is well known that the acoustic characteristics of the combustion system play a first order role in combustion dynamics, most importantly the impedances downstream and upstream of the flame [86, 127–132]. In MIRADAS setup, the modifications of acoustic impedances are achieved by changing the length of the plenum and the combustion chamber. Flame stabilization in the MIRADAS setup is studied using a "shorter" configuration, the dynamic stability is studied using a "longer" configuration, with a plenum length of L_p=258 mm and a combustion chamber length of L_c=297 mm. The schematic representation of the configuration used to study self sustained thermo-acoustic instabilities is presented in Fig. 4.1.

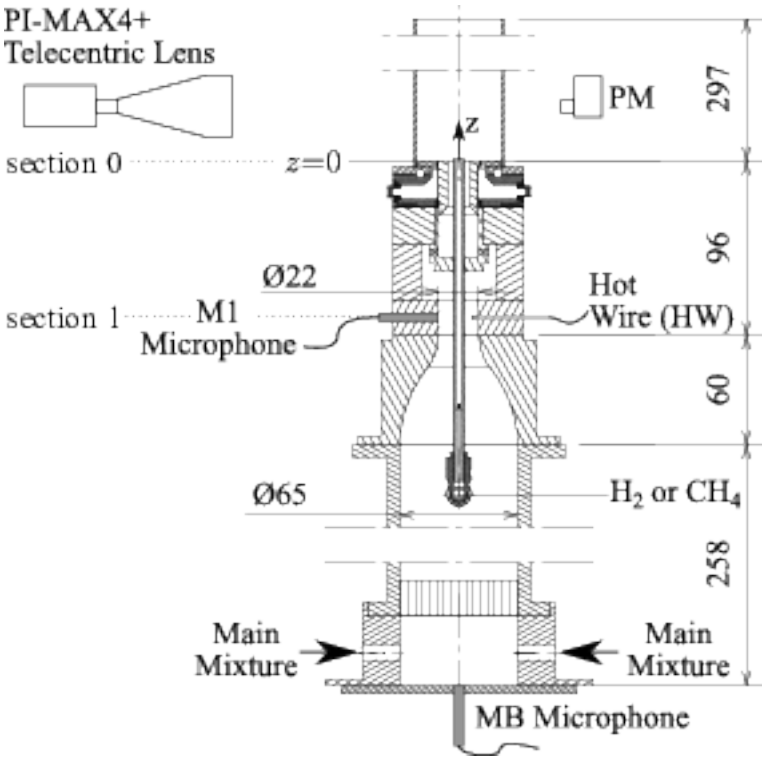

Figure 4.1: Schematic representation of the configuration used in thermo-acoustic stability studies.

Experimental investigations of thermo-acoustic instabilities brings forward the necessity of acoustics diagnostics systems. The base configuration of MIRADAS setup is equipped with Brüel & Kjær-TYPE 4954 microphones at the bottom of the plenum; marked MB and in the 22 mm section channel, designated as section 1; marked M1, capturing acoustic pressure fluctuations. The pressure signal is amplified with a Brüel & Kjær-TYPE 1704-A-002 signal conditioner. Furthermore the instantaneous velocity is also recorded with a constant-temperature anemometer (Dantec 55P16 miniature hot wire probe and a Dantec 54T42 MiniCTA), denoted HW in Fig. 4.1). Care has been taken to set the hot wire probe outside of the boundary layer, where the velocity is almost uniform with a top hat velocity profile.

Heat release rate fluctuations of the flame are deduced from the emission intensity of CH^* radicals. They are recorded with a photomultiplier along with a band-pass filter centered on the CH^* emission spectrum peak λ=430 $\pm$ 10 nm (THORLABS FB430-10) marked PM in Fig. 4.1. Flame images are also taken with a camera (PI-MAX4) along with an appropriate filter (ASAHI XHQA430) and a telecentric lens (Opto Engineering TC4M120), which provide valuable information on the shape and heat release distribution of the flame.

All the signals are recorded using National Instruments PCI-6052E Data Acquisition Card and BNC 2120 shielded connector block with in house LabVIEW programs which run side by side with the main control LabVIEW program. Temperature measurements are also taken NI-9213 Temperature Input Module using k-type TC Direct thermocouples to provide temperature input for the hot wire measurements. With this control strategy, it is possible to construct the stability maps of MIRADAS setup for a wide variety of operating conditions.

4.2 Dynamic Stability Maps of MIRADAS Setup

The stability maps are constructed with different injection and enrichment strategies, as presented in Fig. 2.5. The stability maps cover a range of equivalence rations between $0.70 \leq \phi_G^0 \leq 0.85$, bulk velocities between $14\,\text{m/s} \leq U_{sw} \leq 40\,\text{m/s}$, corresponding to thermal powers in the range $2700\,\text{W} \leq \mathscr{P} \leq 9300\,\text{W}$. Gases are injected in the setup at room temperature $T_u = 292$ K. These conditions correspond to injection Reynolds numbers $5541 \leq \text{Re}_{D_h} \leq 15831$ based on the hydraulic diameter $D_h = 6$ mm of the main annular injection channel (Fig. 2.2).

The variations in injection strategies and hydrogen enrichment are conducted at constant thermal power $\mathscr{P}$ because this parameter has a first-order impact on the magnitude of combustion instabilities. Therefore, the control parameters are the fraction of the thermal power from hydrogen, $\mathscr{P}_{H_2}$ and that from the pilot flame, $\mathscr{P}_{pilot}$. Accordingly, the fraction of power from the main mixture is $\mathscr{P}_{main} = 1 - \mathscr{P}_{pilot}$. The reference is a fully premixed methane-air case without piloting, labelled REF in Fig. 2.5. Then piloting with hydrogen is considered in cases PH1 and PH2 corresponding to $\mathscr{P}_{H_2} = 1\%$ and 2%, respectively. Cases PC1 and PC2 correspond to injection of methane in the pilot tube, with the same levels of power $\mathscr{P}_{pilot}$. Finally, in cases MH1 and MH2 the pilot is turned off and the hydrogen is premixed in the main stream, with corresponding power fractions $\mathscr{P}_{H_2}$. All these cases are summarized in Tab. 2.3. They allow a systematic investigation of fuel composition, piloting and pilot fuel at low levels of hydrogen addition.

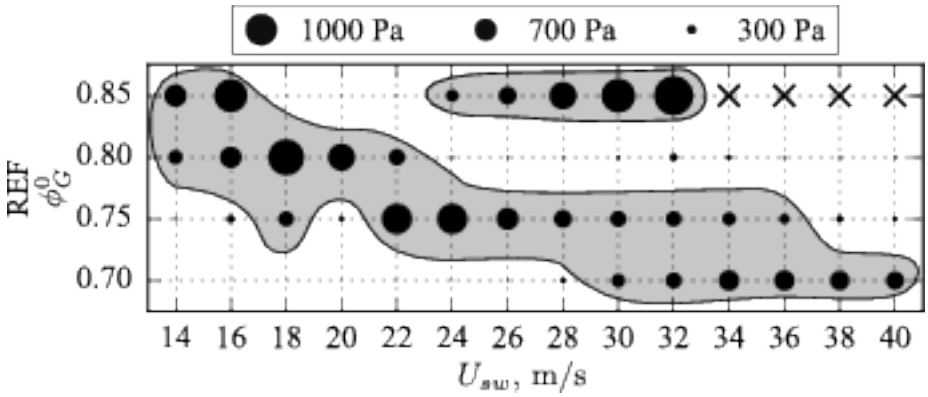

Figure 4.2: Stability map of the methane-air fully premixed flame. Case REF in Tab. 2.3 and Fig. 2.5. Root-mean-square fluctuations of pressure at MB versus bulk velocity U_{sw} and equivalence ratio ϕ_G^0.

The stability map of the reference case is presented in Fig. 4.2. It shows the evolution of the magnitude of pressure fluctuations recorded by the microphone MB for variations in bulk velocity U_{sw} and equivalence ratio ϕ_G^0. The radii of the disks in Fig. 4.2 are proportional to the root-mean-square (RMS) value of the pressure fluctuations measured by microphone MB. The grey shaded regions delineate the regions of instability, defined here as the operating conditions where RMS pressure fluctuations are higher than 300 Pa. This threshold level was chosen as representative of established self-sustained combustion oscillations. Changing this threshold leads to similar results even though the boundaries of the unstable regions are slightly shifted. For some operating conditions, hysteresis takes place in which cases the instability jumps from one intensity to another. These operating conditions are marked with half circles. Finally, a X indicates a condition that was not explored because the instability is too strong and may damage the burner. This nomenclature is used for Figs. 4.2 through 4.5. Figure 4.2 shows that the reference configuration exhibits two regions of instability, one at ϕ_G^0=0.85 for flow velocities higher than $U_{sw} \geq 24$ m.s^{-1} ($\mathrm{Re}_{D_h} \geq 9500$) and another one along the descending diagonal covering a large fraction of the operational domain. The peak frequency of these self-sustained modes lies between 520 Hz and 680 Hz depending on the operating point considered.

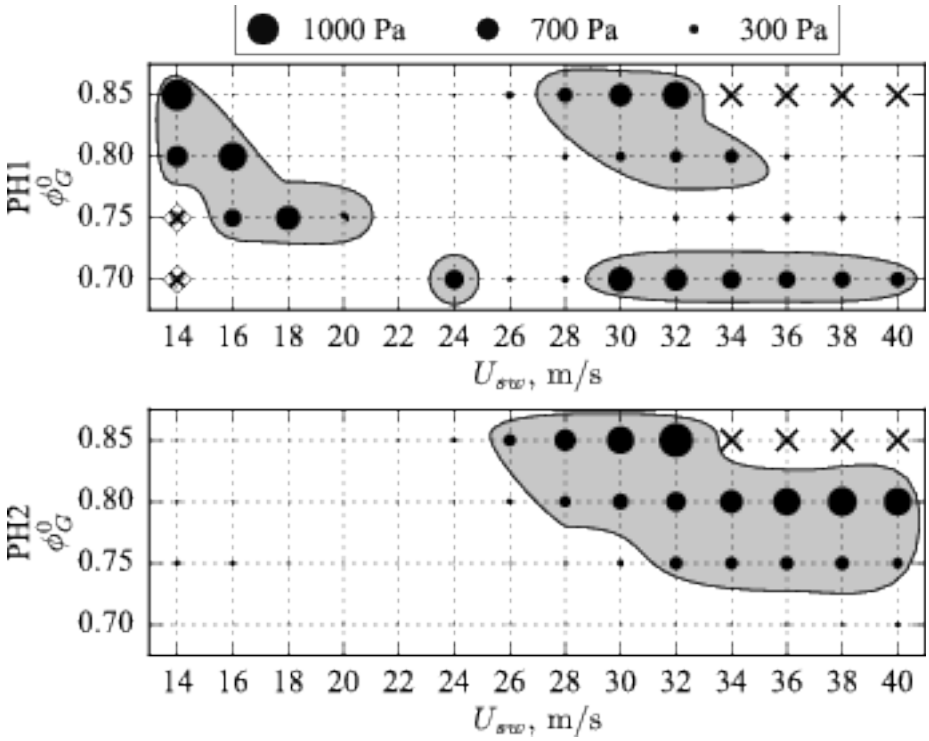

Figure 4.3: Stability maps of the configurations with hydrogen pilot injection. Cases PH1 and PH2 in Tab. 2.3 and Fig. 2.5. Root-mean-square fluctuations of pressure at MB versus bulk velocity U_{sw} and equivalence ratio ϕ_G^0.

The control strategy explored here is the pilot injection of hydrogen in small quantities. For PH1 (respectively PH2), 1% (respectively 2%) of the methane flow rate is removed from the main mixture and the hydrogen pilot flow rate is adjusted to compensate for the loss in thermal power. Because of the large differences in molecular weight between H_2 and CH_4, this yields a molar fraction of hydrogen in the total fuel flow $X_{H_2}^f = 3.2\%$ for PH1 and $X_{H_2}^f = 6.3\%$ for PH2 (see Tab. 2.3). The corresponding stability maps are shown in Fig. 4.3. Markers ✱ correspond to operating conditions that could not be explored because the pilot mass flow rates are too small for a stable regulation by the mass-flow controllers.

For PH1 there is a reduction of the acoustic pressure level in the system for velocities in the range $18 \leq U_{sw} \leq 28$ m.s^{-1} and the total number of unstable points has been reduced by one third. This is a very significant impact of the hydrogen injection for it contributes to only 1% of the thermal power. A further increase in the hydrogen content (case PH2 in Fig. 4.3) results in the complete suppression of all unstable points for $U_{sw} \leq 24$ m.s^{-1} and ϕ_G^0=0.7. The conclusion is that a minimal level of hydrogen piloting has allowed to stabilize the unstable operating points at low thermal power. However, the stability of the combustor at high power, i.e. the upper-right quadrant

in Fig. 4.3), gets worse as the pilot hydrogen is increased. Interestingly, in these conditions, the bulk flow velocity U_{H_2} of the hydrogen flow in the pilot tube is less than 3% of the bulk velocity U_{sw} of swirled flow in the main annular injection channel. This rules out that direct modifications of the flow field caused by the pilot jet would be the cause for the modified stability.

In order to mimic a practical situation, it was chosen to keep the air flow rate and the thermal power constant. Therefore, hydrogen piloting yields small changes in global equivalence ratio ϕ_G^0 and bulk velocity U_{sw} in the main annular injection channel. One can show that for PH1 (respectively PH2), U_{sw} is reduced to 99.9% (respectively 99.8%) of the bulk velocity of case REF. The reduction of ϕ_G^0 is less than 0.1%.

It is well known that fuel piloting affects the stability of swirl burners. In order to assess the influence of hydrogen, methane piloting is considered with cases PC1 and PC2, by replacing H_2 with CH_4. The corresponding stability maps are shown in Fig. 4.4. The comparison with the reference case in Fig. 4.2 indicates that the stability is marginally impacted, even for case PC2, which has the largest methane pilot flowrate.

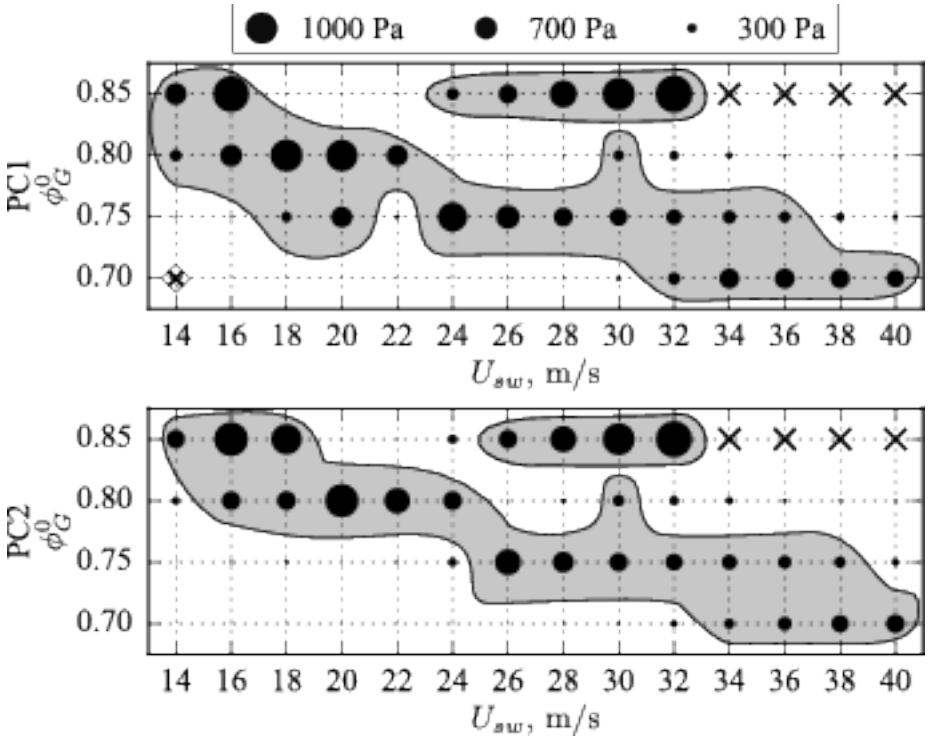

Figure 4.4: Stability maps of the configurations with methane pilot injection. Cases PC1 and PC2 in Tab. 2.3 and Fig. 2.5. Root-mean-square fluctuations of pressure at MB versus bulk velocity U_{sw} and equivalence ratio ϕ_G^0.

The two cases with pilot injection suggest that the change in the global composition of the fuel, namely hydrogen addition, is the driving factor for the improved stability. A

third set of cases is devised where the hydrogen content is identical to piloting cases, but fully premixed within the main injection stream. In MH1 and MH2, the pilot is closed and the hydrogen is premixed with the methane and air, and sent through the swirler. The corresponding stability maps are presented in Fig. 4.5. As for the PC cases, the stability is not affected and the maps are virtually identical to the reference case (Fig. 4.2).

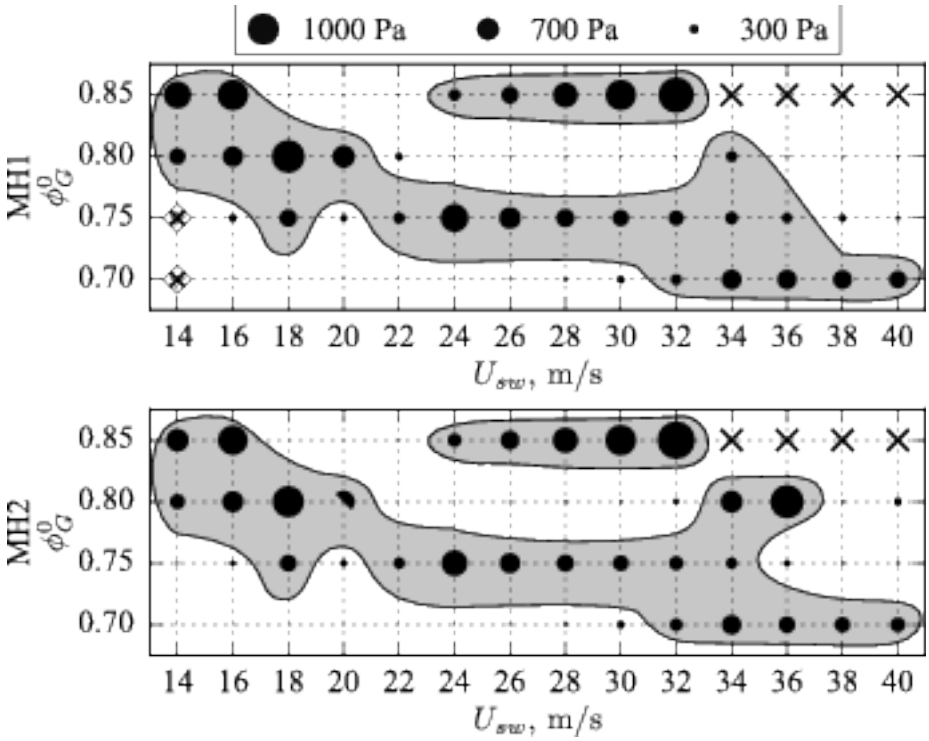

Figure 4.5: Stability maps of configurations with the hydrogen-enriched methane/air mixtures. Cases MH1 and MH2 in Tab. 2.3 and Fig. 2.5. Root-mean-square fluctuations of pressure at MB versus bulk velocity U_{sw} and equivalence ratio ϕ_G^0.

As a conclusion, it was shown that pilot hydrogen injection has a strong influence on the stability maps of the present swirl combustor, even at very low flow rates. With 2% of the thermal power from hydrogen, stability is greatly increased for low power operating conditions but degrades for high power. It should be noted that the hydrogen injected in the burner provides only up to 2% of the total power, which is minute. In previous investigations, conducted with fully premixed systems, hydrogen addition between 3.2%-9.1% of the total power was shown to make the system more unstable even at low equivalence ratios [52, 54, 55]. Comparing between hydrogen injection, methane injection and hydrogen premixing, it can be concluded that for low flow-rates, hydrogen injection is the most efficient method to change the stability characteristics.

Images of the unstable flames are shown in Fig. 4.6, corresponding to time-averaged line-of-sight integration of the CH^* signal over a long duration. 50 snapshots are taken for each case with a total exposure time of 40 ms. For cases REF, PH and MH, the CH^* signal is spread out over the view frame because of the flame motion associated to the combustion instability. For the PH cases, which are stable, the image is much sharper. For the cases with hydrogen, there is no obvious difference between $\mathscr{P}_{H_2} = 1\%$ and 2%. However between PC1 and PC2, the increase of the methane flow rate enhances the emission of CH^* in the streak of the pilot tube.

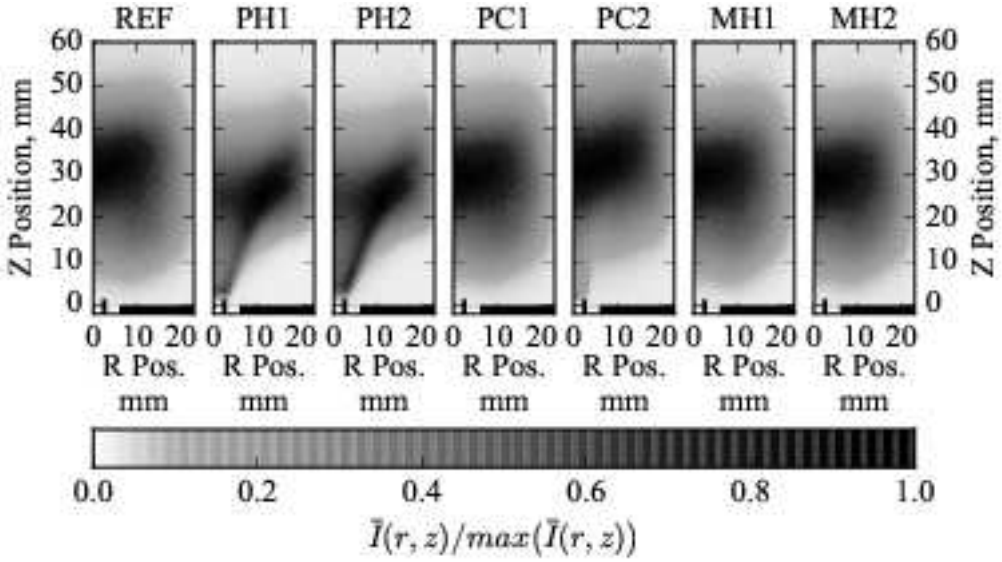

Figure 4.6: Flame images with a long chamber and a long plenum for $\phi_G = 0.80$ and $U_{sw} = 18$ m.s^{-1} (Tab. 2.3). Only the right sides of the images with respect the burner axis is presented. The intensities are normalized by their maximum values to increase the contrast. The location of the burner is added in black at the bottom of each image.

4.3 Low Order Model of MIRADAS Setup and Comparison with Experimental Data

The previous experimental sections have shown that H2 injection was able to decrease instabilities. We now try to provide theoretical explanations for these observations. The stability of a combustion system can be explored by reduced order models, where the system is expressed as a series of discrete acoustic elements connected by transfer matrices [133–135]. These types of analyses are quicker to perform compared to full geometry LES calculations [136–138] or Helmholtz solvers [139–141] and are efficient methods to asses the acoustic behavior of combustion systems.

To perform the acoustic stability analysis of the setup, a low order instability simulator called OSCILOS, developed by Imperial College London, is used [142–144]. In the low order model, the geometry is represented by a series of ducts connected by transfer matrices. The speed of sound and density field are calculated from thermodynamic relations. The flames are represented by flame transfer functions and the reflection coefficients at the boundaries needs to be specified to complete the model.

To validate the numerical model, the modes of the system without combustion have first been calculated. This is done by setting $T = 292$ K in the whole combustor, without an active flame and temperature jump. One needs to define reflection coefficients at the boundaries. A reflection coefficient of $R = 1$ has been applied at the inlet corresponding to a fully reflecting closed end boundary. For all the low order model calculations, the reflection coefficients at the flame tube outlet are represented by linear system fits, where the reflection coefficient is a function of frequency. To deduce the reflection coefficient at the outlet of the combustion chamber, measurements without flow are performed with three microphone measurement techniques [145, 146]. For hot operation with mean flow, the reflection coefficient needs to be corrected for the change in the speed of sound and the effect of mean Mach. To express the reflection coefficient, a modified version of the model of Levine and Schwinger [147] has been applied:

$$Z_s(k,0) = \mathscr{C}(ka)^2 + ik\delta_0 \quad \text{and} \quad R(k,0) = \frac{Z_s - 1}{Z_s + 1} \tag{4.1}$$

where a is the radius of the pipe, $\mathscr{C} = 0.25$ for unflanged and $\mathscr{C} = 0.5$ for flanged pipes, δ_0 is the end correction without mean flow and k is the wavelength. A fit has been applied to determine this constant for MIRADAS setup. To account for the change in the speed of sound for hot operation, the wavelength needs to be corrected and it is assumed that the end correction δ does not change with temperature. As there is mean flow in hot operation, one needs to apply a correction to the refleclection coefficient as well. Davies proposed the following expression for the correction of the mean Mach number [148]:

$$R(k,M) = R(k,0)\left[(1-\alpha M)/(1+\alpha M)\right]^{0.9} \tag{4.2}$$

where M is the mach number at the outlet and $\alpha = 1$ has been implemented. The measured reflection coefficient and the corrected reflection coefficient is presented in 4.7.

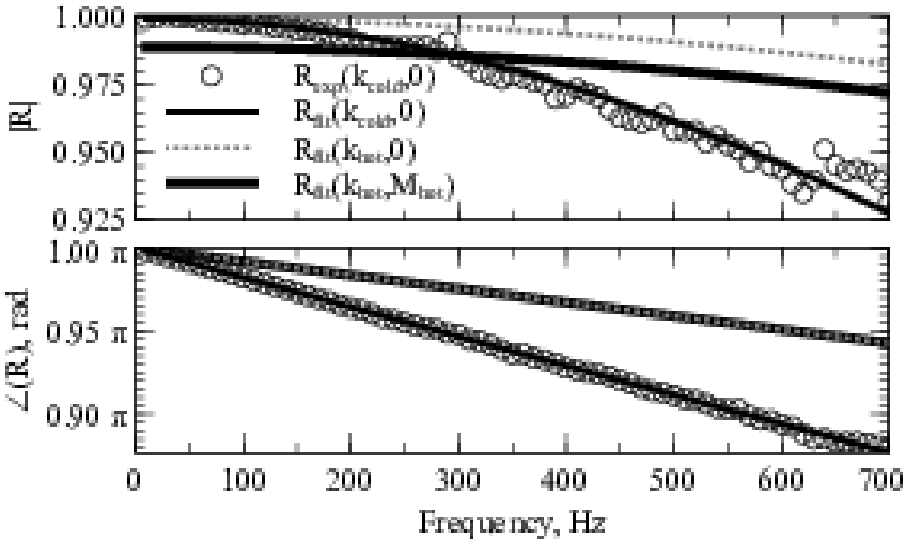

Figure 4.7: Measured and fitted reflection coefficients at the flame tube outlet for $U_{sw} = 18$ m.s^{-1}. The subscript "hot" and "cold" depict the cases with and without combustion, and the "M" signifies the Mach number with combustion.

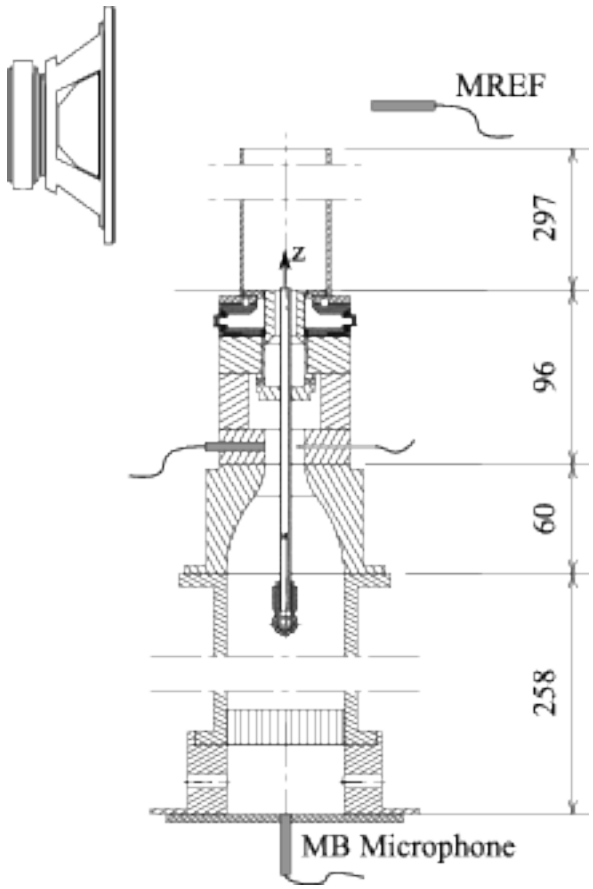

Figure 4.8: Setup used to measure the acoustic modes of the system without combustion.

Validation of the numerical model is carried out first without combustion with the long plenum $L_p = 221$ mm and the long flame tube $L_c = 300$ mm. The modes of the system without combustion are determined with microphone MB at the bottom of the plenum and a reference microphone MREF located near the outlet of the flame tube. The schematic of the experiment is given in Fig. 4.8. The system is excited with an external speaker positioned near the outlet of the chamber and the signals from MREF and MB are recorded.

The modes of the system without combustion are also determined with OSCILOS using fits to the measured reflection coefficients measured without combustion at the outlet boundary condition. The measurements and the results of these calculations are compared in Fig. 4.9, where the peaks of $|\tilde{p}_{MB}/\tilde{p}_{REF}|$ represent the modes of the system. This comparison validates the acoustic model of the combustor without combustion. The frequencies of the three first pressure peaks are well retrieved by the model at 62, 304 and 572 Hz.

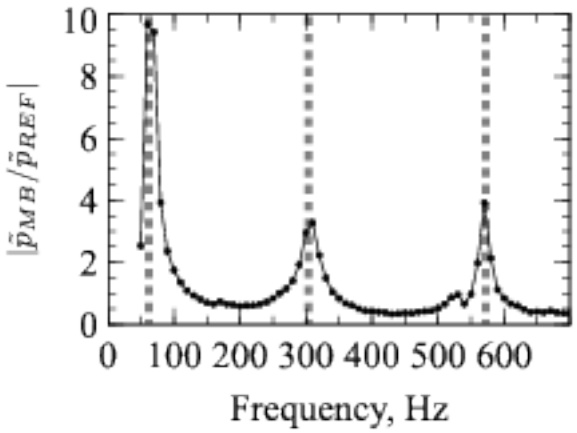

Figure 4.9: Modes of the acoustic setup without combustion. The line represents the measured pressure ratio and the dotted lines are the predictions of the low order model.

To investigate the modes in hot operation, the case of a 'passive' flame where combustion is steady and does not pulsate is studied first. This model incorporates the temperature jump caused by the flame, however the flame is non-responsive to acoustics (flame transfer function has zero gain). The modes formed in the chamber will be around these modes, however the delay and the gain of the flame will modify slightly the frequencies and the mode-shapes of these passive modes towards the limit cycle oscillations. Two of the modes frequently encountered in MIRADAS studies are

presented in Fig. 4.10 and Fig. 4.11. The mode shapes shown in Fig. 4.10 and Fig. 4.11 will be referred to as MODE-1 and MODE-2 respectively further down the text.

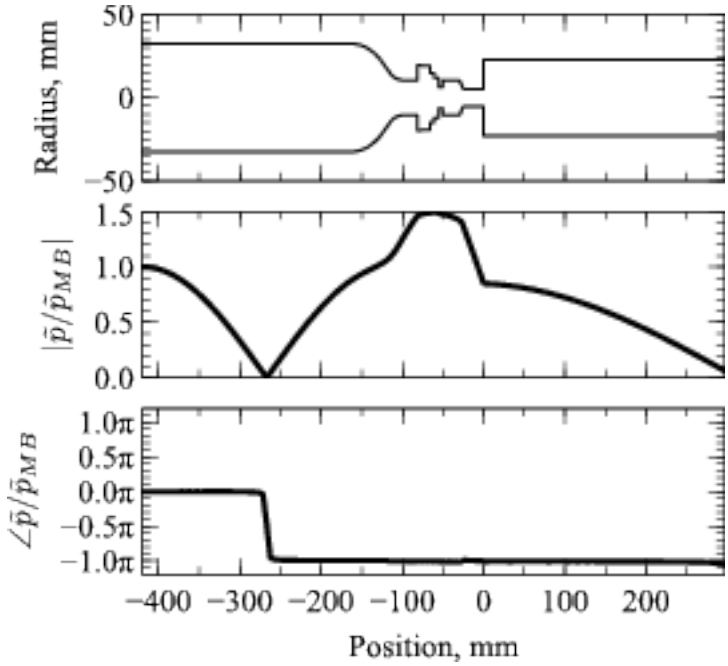

Figure 4.10: Mode shape for passive flame at 560 Hz with 1425 K chamber temperature, designated as MODE-1.

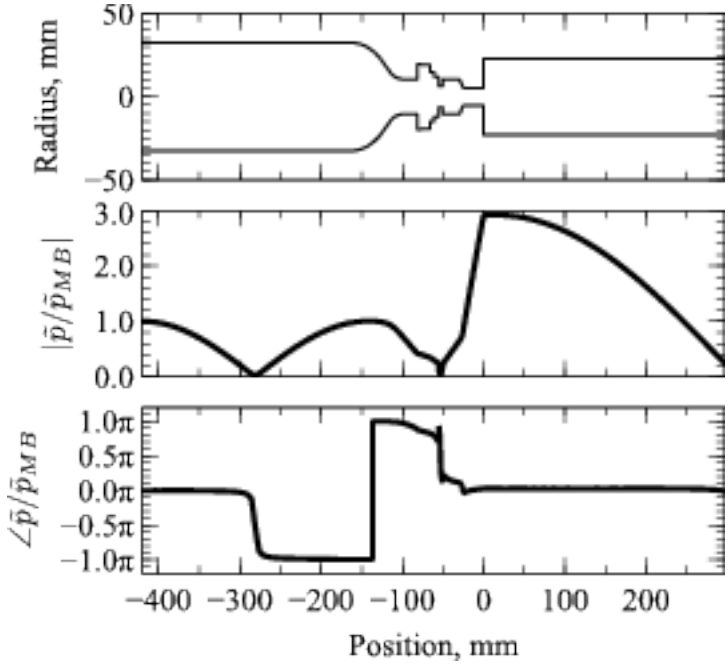

Figure 4.11: Mode shape for passive flame at 618 Hz with 1425 K chamber temperature, designated as MODE-2.

This passive flame low order modal analysis was performed for different chamber temperatures. Although the frequencies of the modes change slightly with temperature, the phase of acoustic pressure in the chamber remains the same for the respective modes; for MODE-1, (Fig. 4.10) the chamber pressure is in phase opposition with the

acoustic pressure at the bottom of the plenum and MODE-2, (Fig. 4.11) the chamber pressure is in phase with the acoustic pressure at the bottom of the plenum. This property will be later used to classify the modes.

4.4 Analysis of Instability Signals and Unstable Modes

The RMSs of the pressure signals give an overall view of the strength of instability of the combustion system, however neither frequency information nor information on transitory modes, which can switch between different modes (frequencies) or the amplitudes which oscillate cannot be obtained from analyzing RMS values. This behavior needs to be studied with spectral analysis methods.

Typical pressure and velocity signals recorded during the limit cycle all cases (Table 2.3) for a bulk velocity of U_{sw}=18 m/s and an initial equivalence ratio of ϕ_G^0=0.8 are presented in Fig. 4.12. The total recording time is 10 seconds, so this 4 ms window in Fig. 4.12 corresponds to a small part of the recorded signals. For the REF case, the traces are sinusoidal despite the large magnitude of the oscillations. The oscillation level reaches around 25% for the heat release rate (HRR) recorded by the PM and 20% for the velocity measured by HW for the REF case. The RMS of pressure fluctuations recorded by microphone MB at the bottom of the plenum is 1124 Pa. This signal is also in phase with the heat release rate fluctuations in Fig. 4.12.

Using the raw signals presented in Fig. 4.12, it is difficult to distinguish between MODE-1 and MODE-2 as the phase of the pressure at M1 location is nearly the same for both modes, measurements inside the chamber is needed to classify the modes. For this, an acoustic reconstruction technique is developed and validated with pressure measurements inside the combustion chamber which will be presented further down the text. What makes the situation more complicated is that these two modes sometimes co exist for certain regimes and we will now study these issues.

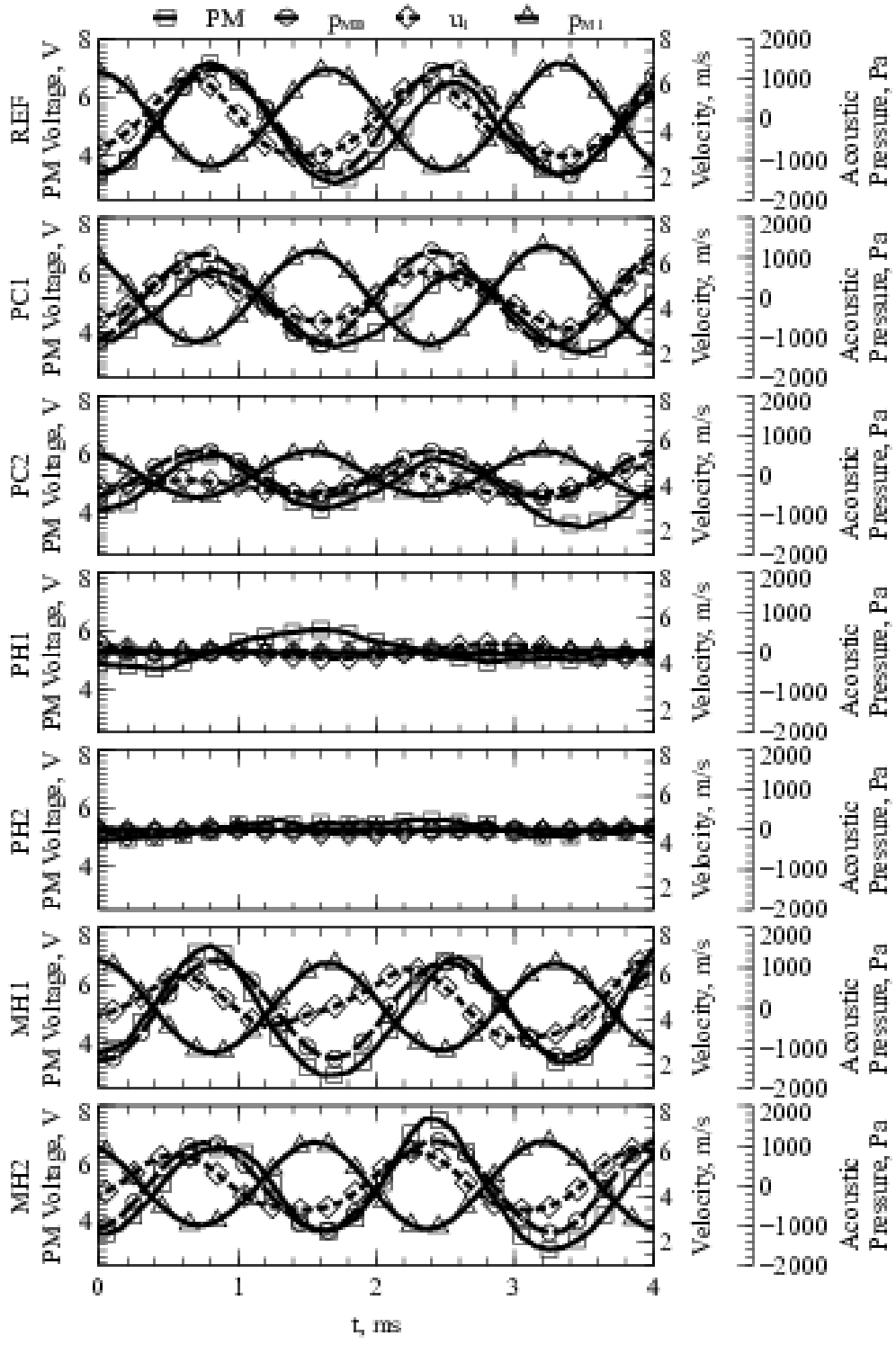

Figure 4.12: Pressure, velocity and heat release signals for the respective cases. The bulk velocity at the exit of the swirled annular injection channel is U_{sw}=18 m/s and the initial equivalence ratio is ϕ_G^0=0.8.

The spectra of the pressure signals recorded by microphone MB at the bottom of the plenum are presented in Fig. 4.13. The most dominant frequencies and their respective amplitudes are listed in Tab. 4.1. As expected from the stability maps, the spectra for cases PC and MH are very close to that of the REF case. There is however a notable

reduction of the amplitude for PC2 (Tab. 4.1), which is coherent with the knowledge that fuel piloting usually damps combustion instabilities.

The first remarkable effect of hydrogen injection in the pilot tube (PH cases) is a strong reduction of the peak pressure around 590 Hz. Smaller peaks emerge, at 641 Hz for PH1 and 339 Hz for PH2 but the associated RMS values are low (Tab. 4.1) so these conditions are considered stable. These peaks correspond to acoustic modes of the setup that are excited by the noise from the turbulent flame. Finally, the spectra for the fully premixed (MH) and methane piloting (PC) cases are almost identical to the REF case.

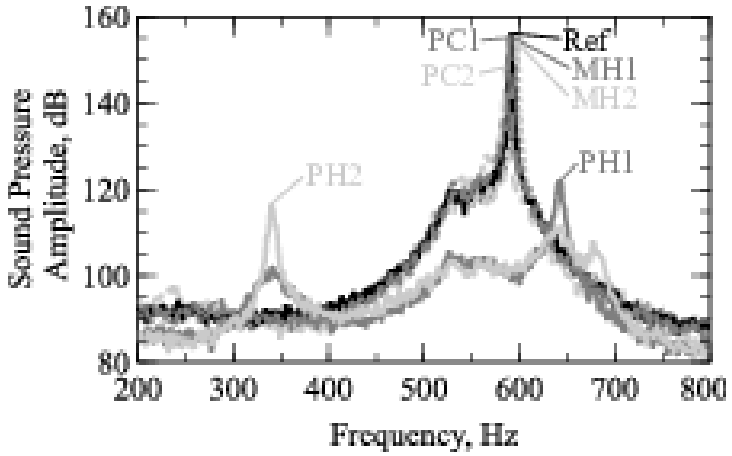

Figure 4.13: Power spectra of pressure signals recorded by MB for the cases in Table 2.3 for U_{sw}=18 m/s ϕ_G^0=0.8.

Table 4.1: Dominant frequencies and corresponding pressure amplitudes for the cases in Table 2.3 at $\phi_G^0 = 0.80$ and $U_{sw} = 18$ m.s^{-1}.

Case	Amplitude, Pa	Frequency, Hz
REF	1304	591
PH1	25	641
PH2	13	339
PC1	1140	590
PC2	520	586
MH1	1112	596
MH2	1024	597

Similarly, the dominant frequencies for all cases are presented in Fig. 4.14. It can be seen that with hydrogen injection (PH1 and PH2 cases) the stability map is completely changed. In addition, there are big frequency jumps on the order of 100 Hz for the operating points at at $\phi_G^0 = 0.80$ between REF and PH2 cases. This will be investigated later in the text. Comparing PC2 and REF cases shows that methane injection causes

a weak tendency to reduce the frequencies on the order of 10 Hz. Additionally, comparing MH2 and REF cases, it can be seen that hydrogen enrichment generally increases the frequency of unstable modes by 10 Hz.

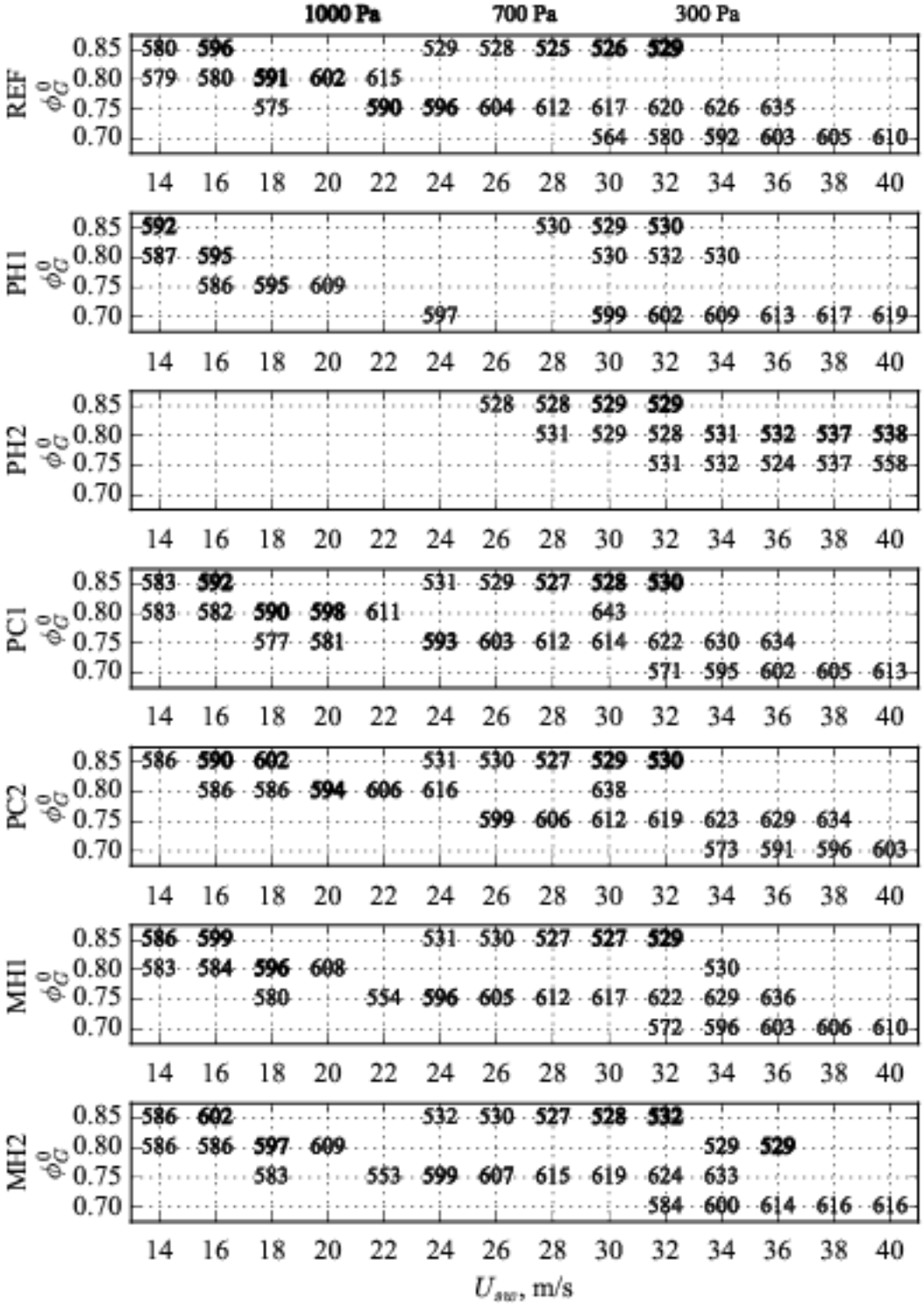

Figure 4.14: Dominant frequencies of pressure signals recorded by MB for the cases in Table 2.3 for U_{sw}=18 m/s ϕ_G^0=0.8. The thickness of the font of the text depends on RMS of pressure oscillations measured by MB microphone.

Furthermore, by short time fast Fourier transform analysis, the changes that occur quickly can be examined as well. For example, there are operating points where the instability reaches a quasi limit cycle, then it's is dissipated for a short amount of time and then re-initiated. Additionally switches in frequencies where the instability switches from a frequency to another frequency also occurs. For the MIRADAS setup, three different classes are defined; established limit cycles where the frequency and the amplitude of the oscillations are stable over a long time scale, short-lived limit cycles where the frequency of the instability does not change but the instability fades out and fades in with time and intermittent limit cycles where different modes compete and the frequency and the amplitude of the oscillations change with time. Additionally, classifications between mode shapes are done corresponding to MODE-1 and MODE-2. This is done by evaluating the phase of the pressure fluctuations between the annular injection channel exit and the MB microphone. For MODE-1, acoustic pressure fluctuations at the annular injection channel outlet is in phase opposition with the pressure fluctuations at MB microphone and for MODE-2, they are in phase. This property is used to classify different modes in MIRADAS setup.

The established limit cycles are defined as where the RMS of the amplitude of the pressure fluctuations are less than 30% of the average and the phase of the pressure fluctuations at the chamber do not vary more than 20°. An example of the established limit cycle is given in Fig. 4.15. Furthermore, as the pressure fluctuations in the combustion chamber are in phase with the pressure fluctuations at the bottom of the plenum, this mode is defined as MODE-2. For this operating point, acoustic pressure measurements taken inside the combustion chamber are available and they are compared to the acoustic pressure at the exit of the annular injection channel reconstructed using the technique described in Appendix A. A for verification.

The classified modes for the REF cases are presented in Fig. 4.16. Intermittent limit cycles are defined as the cases where the RMS of the amplitude of the pressure fluctuations does not change more than 30/% of the mean amplitude of pressure fluctuations during 10 seconds, however the phase between the pressure fluctuations at the bottom of the plenum and the exit of the annular injection chamber changes more than 20°. The short lived limit cycles are defined as the operating points where the

RMS of the amplitude of the pressure fluctuations are more than 30% of the mean pressure fluctuations during 10 seconds.

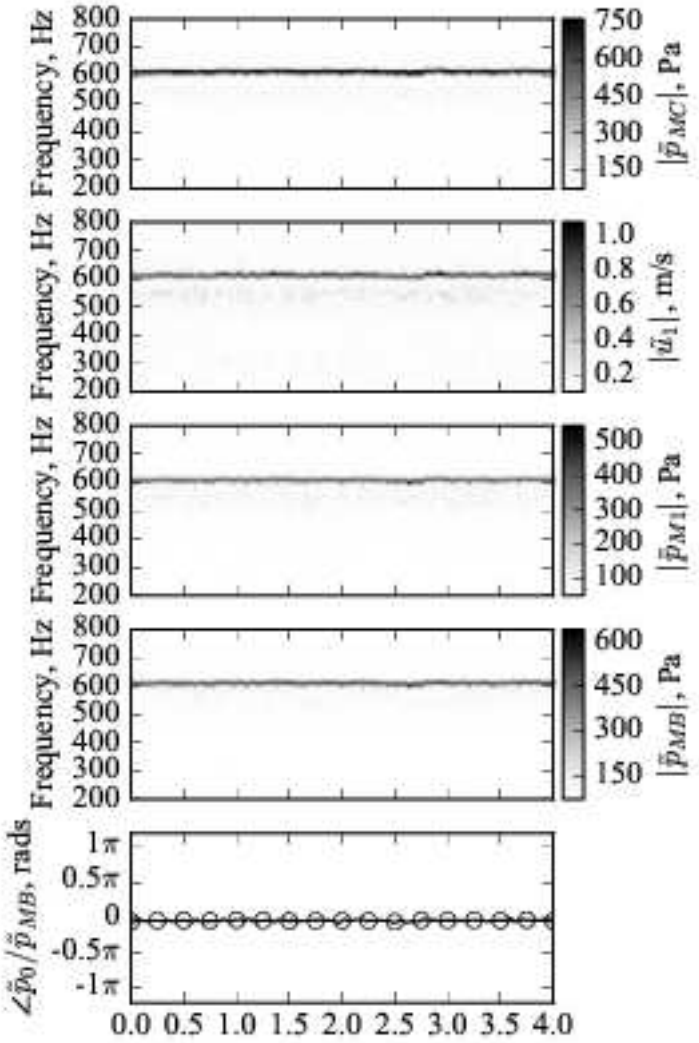

Figure 4.15: Short time FFT analysis of the pressure and velocity signals obtained for the REF case at U_{sw}=18 m/s ϕ_G^0=0.8. The line represents the reconstructed acoustic pressure using the model presented in A, the circular markers are measurements.

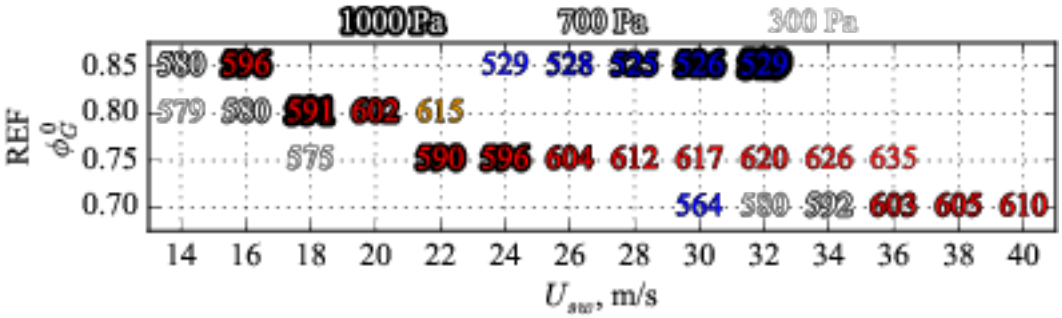

Figure 4.16: Classified unstable modes of MIRADAS setup for REF cases. Blue corresponds to MODE-1 (Fig.4.10) and established limit cycles, red corresponds to MODE-2 (Fig.4.11) and established limit cycles, orange corresponds MODE-2 (Fig.4.11) and short-lived limit cycles, white corresponds to competing intermittent limit cycles. The thickness of the outlines of text is proportional to the RMS amplitude of the fluctuations. A legend is provided at the top of the figure for comparison.

Fig. 4.15 shows that the phase of the reconstructed and measured acoustic pressure match well. For the rest of the cases, the acoustic pressure measurements inside the combustion chamber are not available, so the reconstructed acoustic pressure at the exit of the annular injection channel is used for classification of instabilities.

In Fig. 4.16 the classified modes are presented. This classification shows a mode jump at ϕ=0.7 at U_{sw}=30 m/s from the mode shown in Fig. 4.10 to the mode shown in Fig. 4.11 at U_{sw}=36 m/s. The operating points in between shown as white fonts in Fig. 4.16 show that the phase between the acoustic pressure at the bottom of the plenum and the exit of the annular injection channel is not constant, it changes more than 20°. Short time FFT analysis of these signals are presented in figures 4.17 to 4.20.

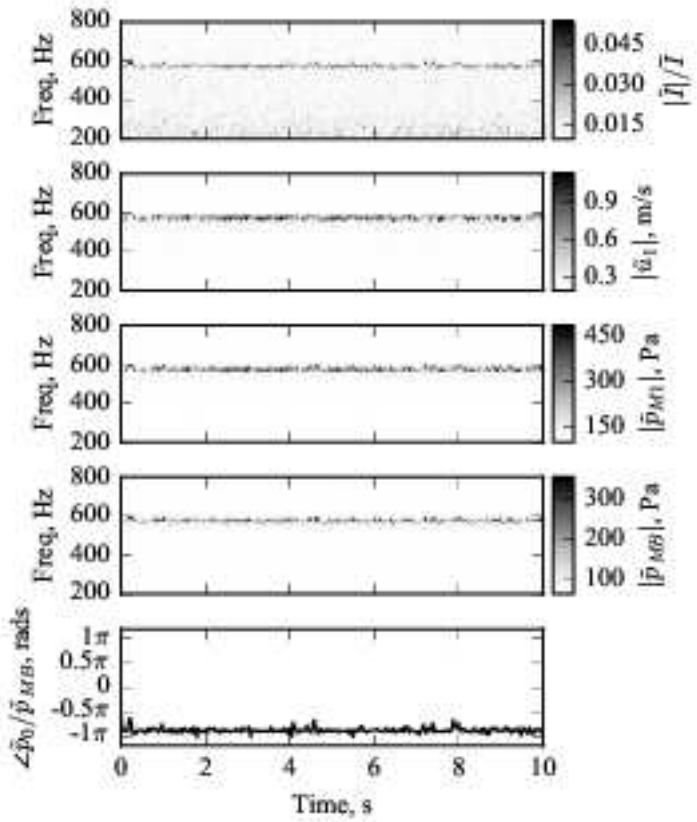

Figure 4.17: Short time FFT analysis of the pressure, velocity and CH* signals obtained for the REF case at U_{sw}=30 m/s ϕ_G^0=0.7.

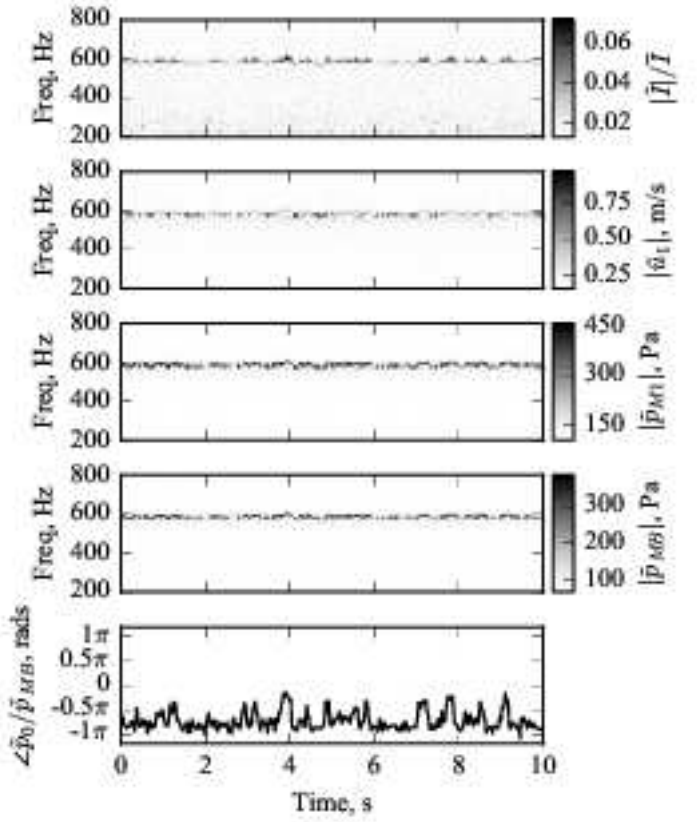

Figure 4.18: Short time FFT analysis of the pressure, velocity and CH* signals obtained for the REF case at U_{sw}=32 m/s ϕ_G^0=0.7.

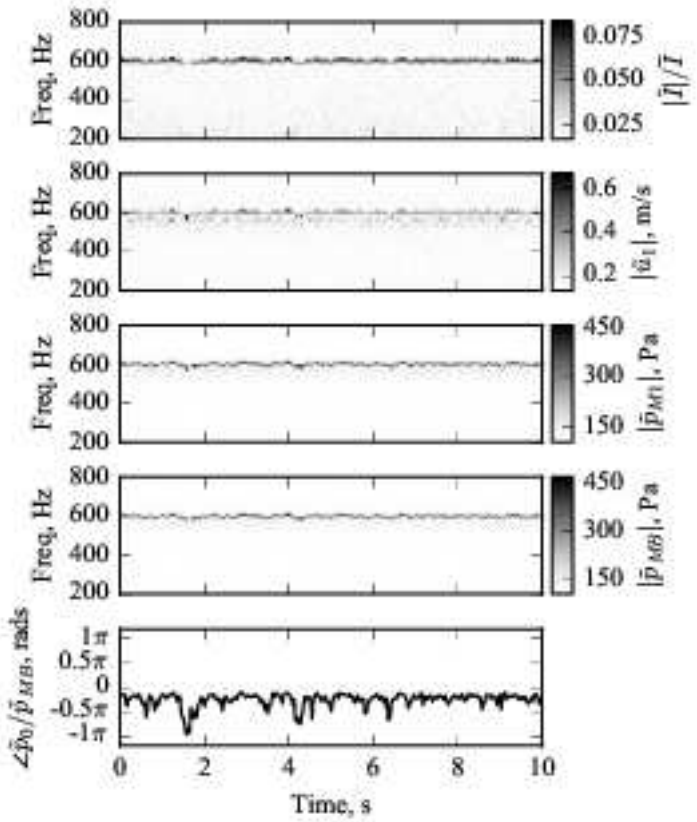

Figure 4.19: Short time FFT analysis of the pressure, velocity and CH* signals obtained for the REF case at U_{sw}=34 m/s ϕ_G^0=0.7.

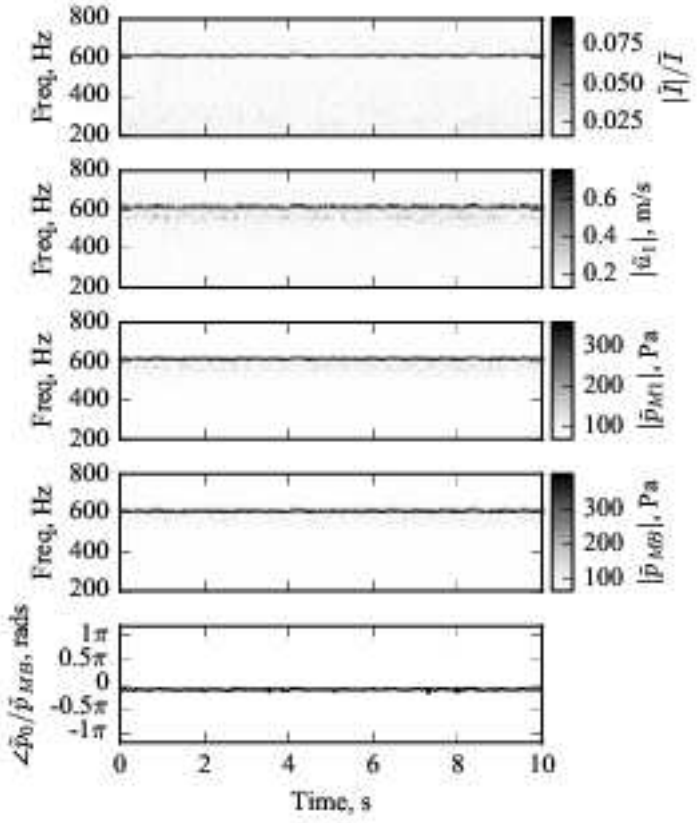

Figure 4.20: Short time FFT analysis of the pressure, velocity and CH* signals obtained for the REF case at U_{sw}=36 m/s ϕ_G^0=0.7.

Examining Fig. 4.17, it can be seen for the REF case at U_{sw}=30 m/s ϕ_G^0=0.7, the mode shape corresponds to MODE-1 (Fig. 4.10) as judged from the phase between the annular injection channel outlet and the MB pressure. When the bulk velocity at the annular injection channel is increased to U_{sw}=32 m/s for the same equivalence ratio, a competitive behavior between MODE-1 (Fig. 4.10) and MODE-2 (Fig. 4.11) occurs. The instability jumps from MODE-1 towards MODE-2 for short periods of time. This behavior can be observed from the time dependent frequency in short time FFT plot of acoustic variables and the phase plot of $\angle\tilde{p}_0/\tilde{p}_{MB}$. The phase $\angle\tilde{p}_0/\tilde{p}_{MB}$ jumps from $-\pi$ as in MODE-1 towards 0 as in MODE-2. Increasing the velocity to U_{sw}=34 m/s shows an instability where a jump to MODE-2 has happened, but the instability is not completely established, it falls back to MODE-1 from time to time as can be observed in $\angle\tilde{P}_0/\tilde{P}_{MB}$ plot presentedin Fig. 4.19. When the velocity is further to U_{sw}=36 m/s, a fully established instability corresponding to MODE-2 is observed, where the transition towards MODE-1 never occurs anymore.

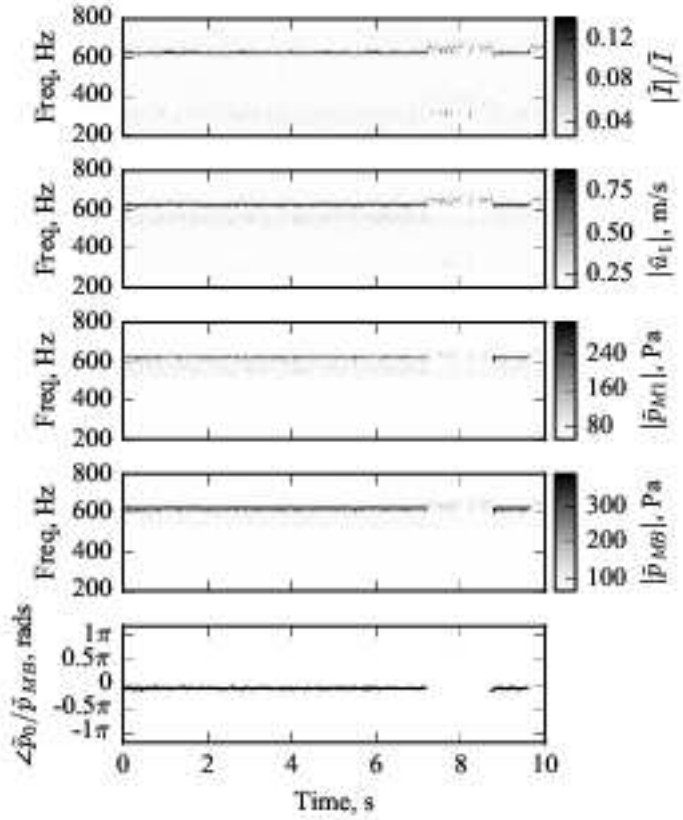

Figure 4.21: Short time FFT analysis of the pressure, velocity and CH* signals obtained for the REF case at U_{sw}=22 m/s ϕ_G^0=0.8.

In Fig. 4.21 the REF case for U_{sw}=22 m/s ϕ_G^0=0.8 is presented. Here the mode shape corresponds to MODE-2 and does not change with time, however the instability

kicks-in and fades-out with time. This operating point is classified as a short-lived limit cycle and colored orange in Fig. 4.16.

The classified modes for PH1 and PH2 cases are presented in Fig. 4.22. Examining Fig. 4.16 and Fig. 4.22, it can be seen that hydrogen injection is more effective on instabilities locked on MODE-2. 1% of hydrogen injection (PH1) suppresses most of the instabilities at ϕ_G^0=0.75 which are locked on MODE-2. 1% of hydrogen injection (PH2) suppresses all of the instabilities at ϕ_G^0=0.7 again locked on MODE-2, to the result that there are no MODE-2 instabilities for PH2 cases.

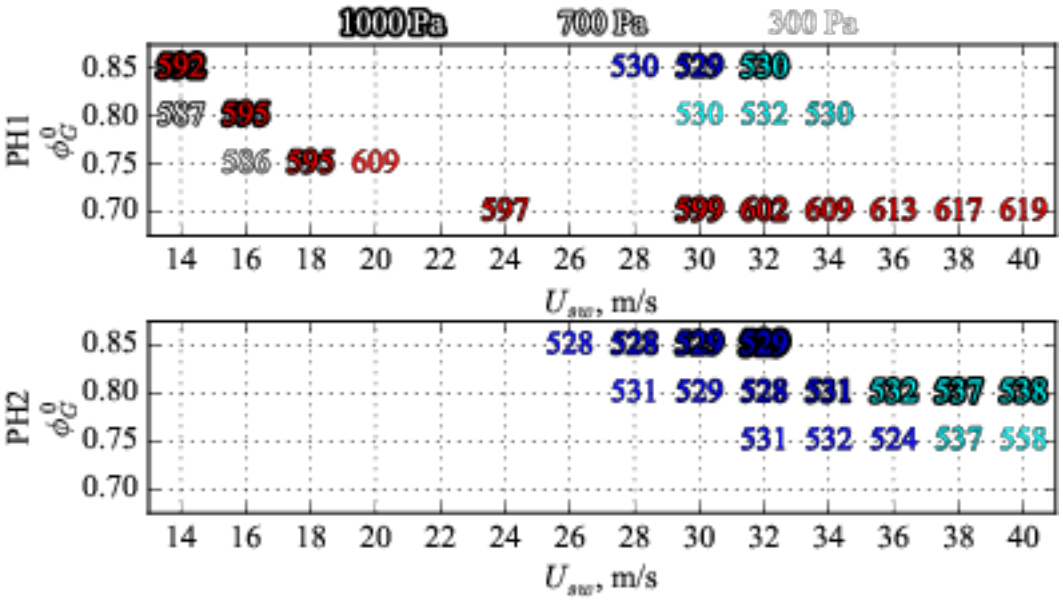

Figure 4.22: Classified unstable modes of MIRADAS setup for PH1 and PH2 cases. Blue corresponds to MODE-1 (Fig.4.10) and established limit cycles, red corresponds to MODE-2 (Fig.4.11) and established limit cycles, cyan corresponds to MODE-1 (Fig.4.11) and short-lived limit cycles, white corresponds to competing intermittent limit cycles. The thickness of the outlines of text is proportional to the RMS amplitude of the fluctuations. A legend is provided at the top of the figure for comparison.

Another interesting observation is that the time scale of the short lived limit cycles become much more jittery for the cases with 2% hydrogen injection. The amplitude of the fluctuations change significantly with short periods of time. An example of this behavior is presented in Fig. 4.23 for PH2 case with U_{sw}=40 m/s ϕ_G^0=0.8.

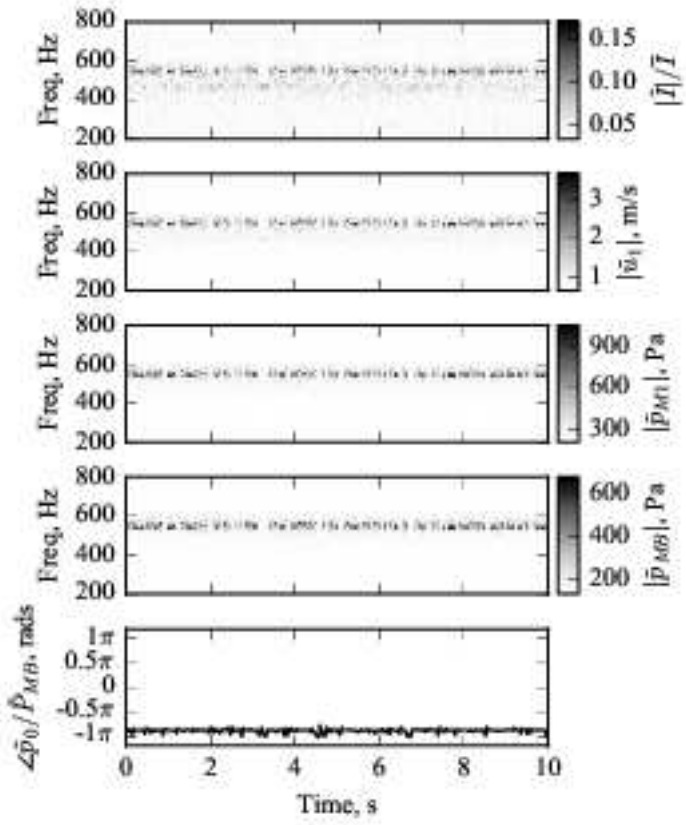

Figure 4.23: Short time FFT analysis of the pressure, velocity and CH* signals obtained for the PH2 case at U_{sw}=40 m/s ϕ_G^0=0.8.

4.5 Conclusions

In this chapter, self sustained thermo-acoustic instabilities encountered in MIRADAS experiment have been analyzed and classified. The following conclusions can be deduced.

- For low levels of hydrogen power fraction $\mathscr{P}_{H_2} \leq 0.02$, hydrogen enrichment ($\mathscr{P}_{pilot} = 0$) does not affect the dynamic stability of the setup for the fully premixed mode.

- This is also true for methane piloting, for low levels of methane piloting ($\mathscr{P}_{pilot} \leq 0.02$, $\mathscr{P}_{H_2} = 0$) , the dynamic stability of the setup remains unchanged.

- For low levels of hydrogen piloting ($\mathscr{P}_{H_2} \leq 0.02$, $\mathscr{P}_{pilot} \leq 0.02$), the dynamic stability behavior completely changes. With 1% (PH1) and 2% (PH2) hydrogen injection respectively 30% and 40% of the operating points that are unstable for the REF case become stable operating points. Hydrogen injection is found out to be

most effective for MODE-2 at a higher frequency, For PH2 cases, all the instabilities locked to this mode are eliminated.

5. HEAT RELEASE RESPONSE TO ACOUSTIC FLUCTUATIONS

Determining the forced response of flames is a powerful way to infer the susceptibility of combustors to thermo-acoustic instabilities [139, 149, 150]. In the frequency space, this response corresponds to the Flame Transfer Functions (FTF) in the linear regime or Flame Describing Functions (FDF) for finite amplitude perturbations [151, 152].

The pioneering work in this field is done by Crocco which links the unsteady velocity to unsteady heat release rate by a gain n and a time lag τ [153] as $\dot{Q}' = nu'(t-\tau)$. When a perturbation in velocity upstream of the flame occurs, the flame reacts accordingly with a heat release rate response after a time τ. The strength of this response depends on the gain n.

Further developments lead to the notion of linear Flame Transfer Functions, where the harmonic response of flames are measured by introducing sinusoidal acoustic fluctuations and measuring the heat release response [154–157]. In addition, Flame Describing Functions, where the effect of the amplitude of the velocity fluctuations were included in flame response models were constructed to better represent limit cycle flame dynamics [158–162].

For an operating point kept at U_{sw} and ϕ, the flame describing functions for MIRADAS setup are expressed in the form as presented in Eq.5.1.

$$\frac{\tilde{I}}{\bar{I}} \cong \frac{\tilde{\dot{Q}}}{\bar{\dot{Q}}} = G(\omega, \tilde{u}_0)\exp(i\varphi(\omega, \tilde{u}_0))\frac{\tilde{u}_0}{U_{sw}} \tag{5.1}$$

where $\dot{Q}$ and u_0 denote the global heat release rate and the velocity at the burner outlet in section 0 respectively. The operator $\tilde{\cdot}$ stands for the Fourier component of the signal at the angular forcing frequency ω and $\bar{\cdot}$ means the time averaged value. In this framework, the heat release rate fluctuation $\tilde{\dot{Q}}$, deduced from the PM equipped with the CH* filter, features a gain G and a phase lag φ with respect to the acoustic velocity $\tilde{u}_0$. Then the Flame Describing Function (FDF) and the Flame Transfer Function (FTF)

for a constant forcing amplitude can be expressed as presented in Eq.5.2.

$$\begin{aligned} FDF &= G(\omega,\tilde{u}_0)\exp(i\varphi(\omega,\tilde{u}_0)) \\ FTF &= G(\omega)\exp(i\varphi(\omega)) \quad G = |\mathrm{FTF}|, \quad \varphi = \angle\mathrm{FTF} \end{aligned} \tag{5.2}$$

The prerequisite for this task is a stable flame, which is again obtained with the flame tube and plenum lengths $l_f = 97$ mm and $l_p = 147$ mm, respectively. In this case the system is void of thermo-acoustic instabilities for all operating points studied. The bottom cap of the plenum is replaced with an extension housing a loud-speaker as shown in Fig. 5.1. Using this configuration, the flow in the main annular injection channel is submitted to harmonic modulation with a controllable level.

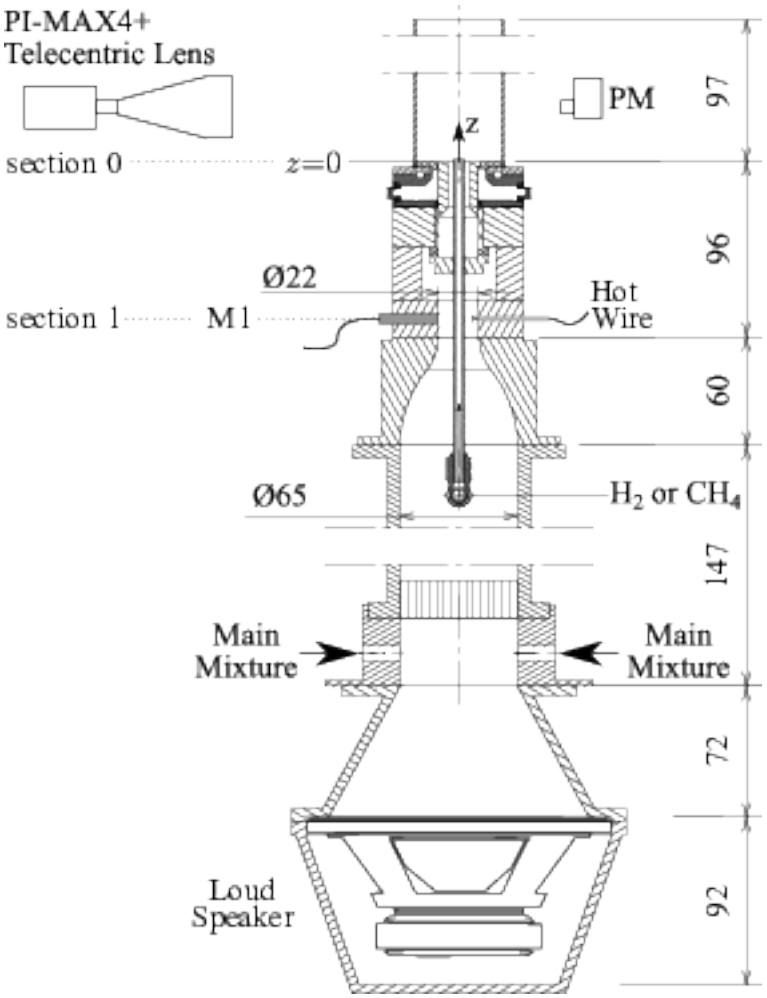

Figure 5.1: Schematic representation of the configuration used to measure FTFs.

The FTF should be determined with a reference velocity as close as possible to the burner outlet [163]. In a swirling injector, it is difficult to instrument the burner at this location and a similar technique as used by [164] to reconstruct the acoustic velocity $\tilde{u}_0$ at the burner outlet from the hot-wire probe HW and the pressure M1 signals upstream of the swirler. This reconstructed velocity is used to measure FTFs.

This is an important aspect of the method because the distance $l_i = 87$ mm between sections 0 and 1 is not short. Even at relatively low frequencies there may be a node in the acoustic field between HW and the flame. The methodology is fully described in Annex A. For all the FTFs obtained, the forcing by the loudspeaker is tuned so that the ratio of amplitude of the velocity fluctuation at the burner outlet to the bulk velocity $|\tilde{u}_0|/U_{sw}$ is constant for all frequencies for a given forcing amplitude.

5.1 Flame Transfer Functions with 15° Swirler, D_c=46 mm Combustion Chamber

For single-fuel lean premixed flames, it is known that the heat release rate is proportional to the light emission of OH* or CH*, but in this study the application of hydrogen piloting brings into question the methodology for the determination of heat release rate. Firstly the mean flame images obtained with Nikon UV-105, 105mm f/4.5 Multispectral Imaging Lens (transparent at UV and visible wavelengths) and a PI-MAX4 emICCD intensified camera that can be equipped either with an Edmund optics 310nm CWL, 50mm Dia., Hard Coated OD 4.0 10nm Bandpass Filter or a 430nm CWL, 50mm Dia., Hard Coated OD 4.0 10nm Bandpass Filter to measure the emission of chemiluminescent light of CH* and OH* radicals are compared in Fig.5.2. Here, the left half of the flame corresponds to the CH* light emission and the right half to OH*. First, the increase in hydrogen content leads to a shortening of the flame, which is consistent with the larger flame speed of hydrogen enriched mixtures versus pure methane as can be seen in Fig. 3.4. The overall flame shape and length are very similar using CH* or OH* emissions. However, with increasing hydrogen content, OH* images show higher intensities, either spatially distributed, for MH cases, or closer to the pilot tube in the PH cases. This is consistent with the region where one would expect that hydrogen oxidation occurs. Overall, both emissions give very similar results.

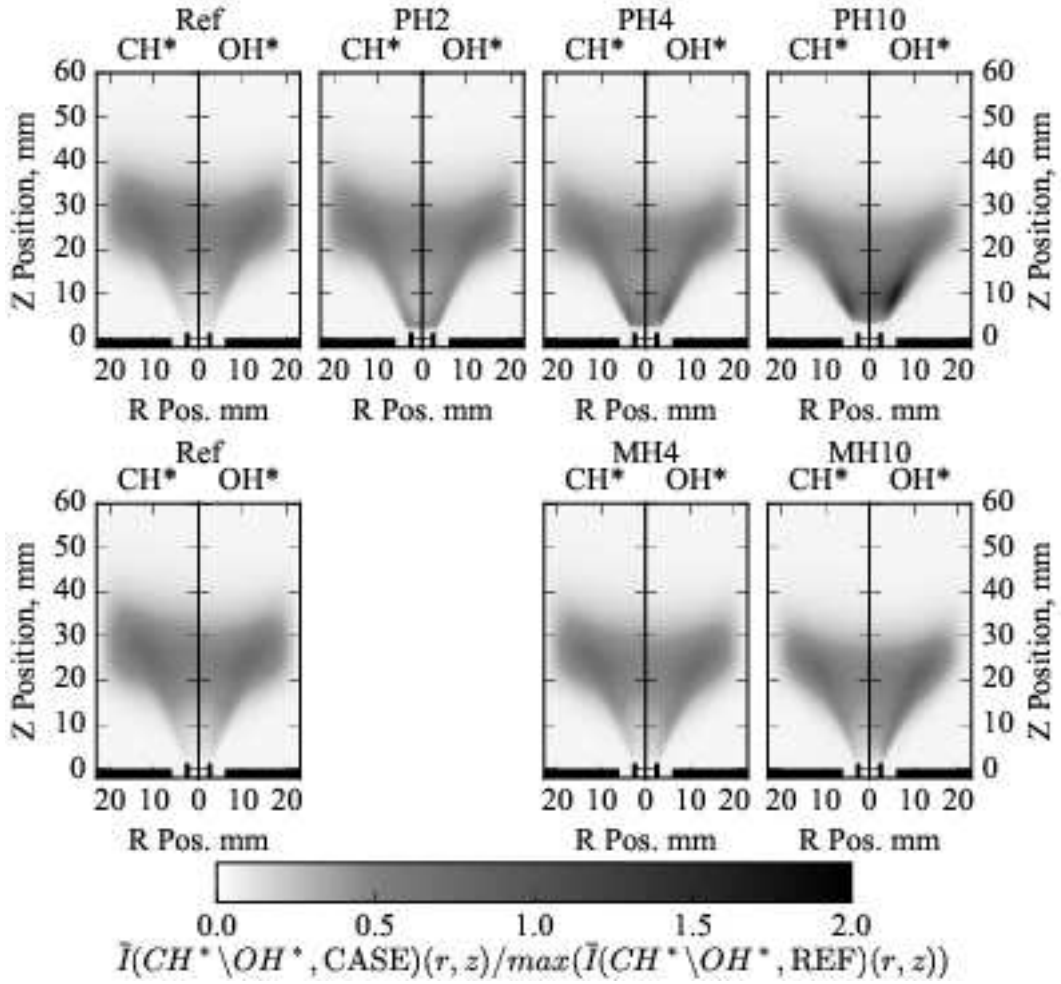

Figure 5.2: Comparison of mean flame structure determined from CH* and OH* emissions. Influence of injection strategy (PH versus MH) and hydrogen content (in % of the total thermal power), U_{sw}=18 m/s, ϕ_G^0=0.8, S=0.33.

Moving on to the determination of FTF from CH* or OH* emissions, the objective is to assess whether or not classical techniques are still valid in such configuration with two fuels. Indeed, the link between radical emissions and heat release has been studied for a long time for single fuels (REF) but here we are actually burning two fuels at the same time. The FTF gain and phase lag of cases PH10 and MH10, with the highest hydrogen content, are presented in Fig.5.3. The FTF determined using CH* or OH* light intensity are virtually identical giving high confidence that the methodology is robust to these changes in fuel composition and injection strategy. Of course, this statement only pertains to these cases with hydrogen concentrations in the fuel blend lower than 10% of the thermal power and higher hydrogen content or other flame configurations may lead to different conclusions. All the other measurements presented in this work are performed with the CH* emissions for both flame images and FTFs if explicitly precised otherwise.

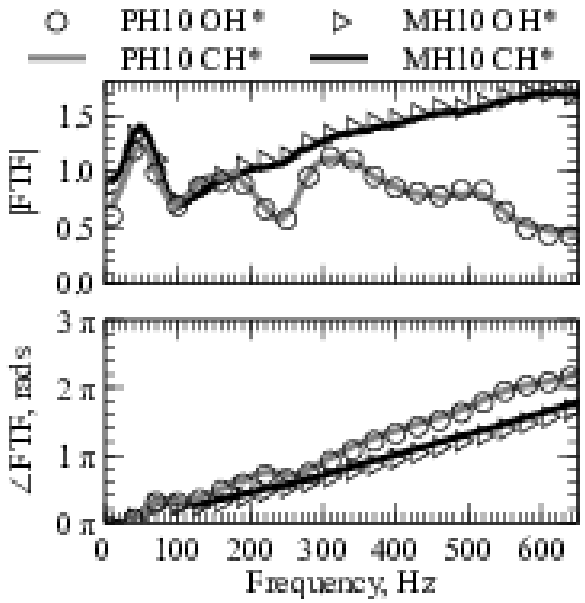

Figure 5.3: Comparison of FTFs measured with CH* and OH* emissions for a constant forcing level $\tilde{u}_0/U_{sw} = 0.10$ for U_{sw}=18 m/s, ϕ_G^0=0.8, S=0.33.

The resulting flame transfer function for all the cases obtained with 15° swirler and D_c=46 mm combustion chamber at a forcing level of $\tilde{u}_0/U_{sw} = 0.10$ are presented in Fig. 5.4. For the REF case (premixed methane-air), the flame is very responsive with large FTF gains exceeding unity over almost the entire frequency range explored from 10 to 700 Hz, with a dip at 100 Hz and a peak at 360 Hz. Regarding the fully premixed MH cases, hydrogen addition in the fuel at low concentration levels does not impact the flame response. This observation is also consistent with the stability maps presented in Section 4.2 and the flame visualizations shown in Fig. 3.3. A fuel blend with a few percent of hydrogen, $X_{H_2}^f < 2\%$ does not alter the dynamic stability of the system. However when the injection power is increased to 4% and beyond, the maximum of the FTF is shifted towards higher frequencies. The cross-over frequencies where the gain of the hydrogen enriched cases surpasses REF case can be defined as 450 Hz and 510 Hz for MH4 and MH10 cases respectively. Concurrently the delay of the flames become significantly shorter, at 600 Hz, the FTF phase lag is close to 3π for the REF case and drops to 2π for MH10. This is attributed to increase in flame speed and decrease in flame length.

Methane injection in the central pilot fuel line (PC cases) decreases the FTF gain |FTF| for a broad range of frequencies, however, the FTF phase lag ∠FTF is marginally altered. This is consistent with the modest reduction in the magnitude of the limit-cycle amplitude of the unstable modes observed for the PC cases in Fig. 4.13. The Rayleigh

index is barely modified because the FTF phase lag is identical for the REF case and the PC cases. However, a slight reduction in FTF gain |FTF| leads to unstable modes with lower pressure amplitudes. For PC4 and PC10 cases there are two dips at 80 Hz 170 Hz.

The strongest alteration of the FTF is obtained with hydrogen piloting for PH cases. The most obvious impact is the large reduction of the FTF gain in the range 150 Hz to 300 Hz, which is more pronounced when the flowrate of hydrogen injection is increased. The large dip of the gain |FTF| around 220-240 Hz with a change in the slope of the phase lag ∠FTF is characteristic of interferences between acoustic waves and azimuthal convective waves downstream the swirler [165–167].

Above 300 Hz, the FTF gain for the PH cases lies below the REF case and decreases with increased hydrogen injection. For frequencies higher than ≥300 Hz, the FTF phase lags between the PH and REF cases begin to deviate and the difference increases with the forcing frequency, resulting in a large difference at the frequency of the instability at this operating point (U_{sw}=18 m/s ϕ_G^0=0.8.). Around 590 Hz, one reads in Fig. 5.4: $\varphi(590) = 8.2$ rad for the REF, PC1, PC2, MH1 and MH2 cases and $\varphi(590) = 6.3$ rad for the PH1 and PH2 cases.

Comparing REF, PH, PC and MH cases, it can be seen that introduction of hydrogen (PH and MH cases) reduces the time delay of the flame response, and fuel piloting reduces the gain of the FTFs in a broadband manner. Hydrogen enrichment reduces the delay of flame responses; however makes the flames more reactive at higher frequencies with higher FTF gains. Methane piloting reduces FTF gain in a broadband manner, however does not effect the delays of the flame responses. Only hydrogen piloting (PH cases) reduces the time delay and gain simultaneously in a broadband manner.

This large difference of the FTF phase lag φ is at the origin of the augmented stability margins of the PH cases. This is highlighted by conducting a simplified acoustic energy balance. For a compact flame, the thermo-acoustic energy release at frequency $f = 1/T$ in the system is determined by the Rayleigh index:

$$\mathscr{R} = \frac{1}{T}\int_T \frac{\gamma-1}{\gamma\overline{p}} p'\dot{Q}'dt = \frac{(\gamma-1)}{2\gamma\overline{p}}\mathrm{Re}\left(Z\tilde{u}_0\tilde{\dot{Q}}^*\right) \tag{5.3}$$

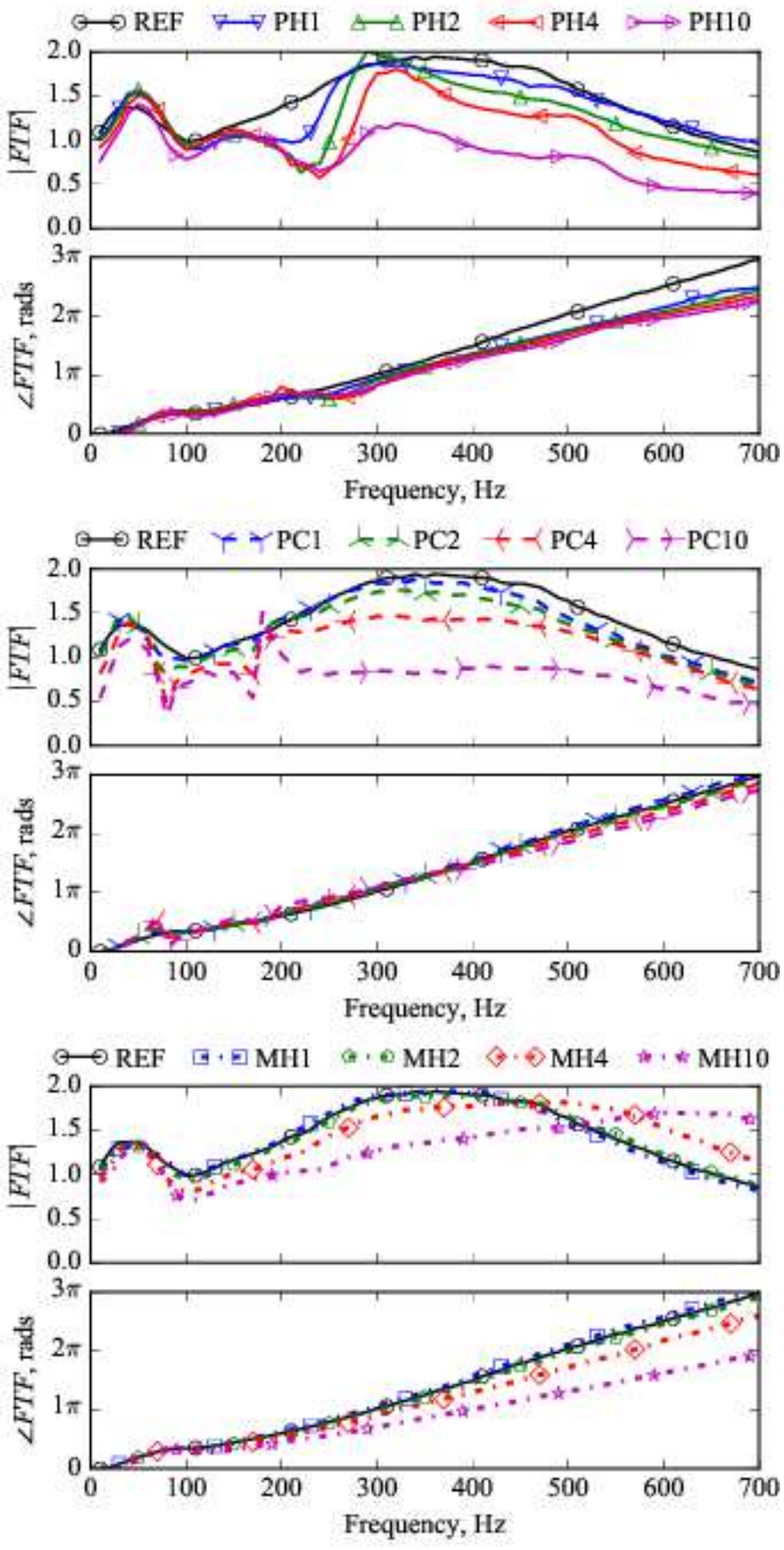

Figure 5.4: FTFs for a constant forcing level $\tilde{u}_0/U_{sw} = 0.10$ for U_{sw}=18 m/s, ϕ_G^0=0.8, S=0.33.

In Eq. 5.3 Re$[\cdot]$ is the real component of the complex argument and the star denotes the complex conjugate. It makes use of the complex burner impedance Z at the instability frequency f:

$$Z = \frac{\tilde{p}_0}{\tilde{u}_0} = |Z| \exp(i\varphi_0) \tag{5.4}$$

where $\tilde{p}_0$ and $\tilde{u}_0$ denote the acoustic pressure and velocity at the burner outlet in section (0). In this study, the phase lag φ_0 in section 0 is deduced from acoustic field reconstructions from $\tilde{p}_0$ and $\tilde{u}_0$ with measurements of $\tilde{p}_1$ and $\tilde{u}_1$ made in section (1). This reconstruction of the acoustic field at the burner outlet was verified with pressure measurements taken from inside the chamber.

When the Rayleigh index is positive $\mathscr{R} > 0$ the combustion dynamics destabilizes the system. When $\mathscr{R} < 0$, the flame damps acoustic perturbations and the system is stable. Equations (5.2) and (5.4) are used to rewrite the Rayleigh source term as a function of the phase lags from the burner impedance Z and FTF:

$$\mathscr{R} = \frac{(\gamma-1)\overline{\dot{Q}}}{2\gamma\overline{p}U_{sw}} |\tilde{u}_0|^2 |Z| G \cos(\varphi_0 - \varphi) \tag{5.5}$$

When the burner impedance Z, the FTF or the acoustic velocity $\tilde{u}_0$ at the burner outlet vanishes, there is no thermo-acoustic energy release $\mathscr{R} = 0$. For all other conditions, the thermo-acoustic source may damp $\mathscr{R} < 0$ or amplify $\mathscr{R} > 0$ acoustic perturbations, depending on the phase lags φ_0 and φ from the burner impedance Z and FTF, respectively. According to Eq. (5.5) and neglecting other damping mechanisms, unstable modes need to comply with:

$$-\frac{\pi}{2}[2\pi] < \varphi - \varphi_0 < \frac{\pi}{2}[2\pi] \tag{5.6}$$

Knowing that the burner impedance at $f \simeq 590$ Hz is $\varphi_0 \simeq 1.96$ rad, one deduces that to trigger an instability the FTF phase lag necessarily belongs to:

$$0.39 < \varphi < 3.53 \quad \text{or} \quad 6.67 < \varphi < 9.82 \tag{5.7}$$

For the Ref methane/air case, methane piloting PC1, PC2 cases and the fully premixed hydrogen/methane MH1 and MH2 cases, the FTF phase lag $\varphi(590) \sim 7.69$ rad falls within the second instability region. With hydrogen piloting, PH1 and PH2, $\varphi(590) \sim 6.36$ rad falls within the stable band $3.53 < \varphi < 6.67$. This analysis shows that minimal hydrogen injection through a pilot jet is an efficient way to alter the FTF

with significant changes of the gain at low forcing frequencies and phase lag at high forcing frequencies. This in turn can be used to drastically change the stability margins of the combustor.

Flame transfer functions at different forcing levels are also studied. In Fig. 5.5 flame transfer functions with a forcing level of $\tilde{u}_0/U_{sw} = 0.30$ are presented. With increased forcing levels, there is a broadband reduction in the FTF gain for nearly all frequencies except PH2 case, where the gain slightly increases around 220 Hz where thedip occurs. Furthermore an augmentation of FTF phase is observed for all cases except PH10 case, where the phase drops very slightly. This behaviour is due to the saturation of FTF gain and a property often reported [161,162]. For the REF case, the frequency of maximum FTF gain drops from 360 Hz at 10% pulsation to to 280 Hz for 30% pulsation.

For PH cases, the difference in the phase of FTF $\angle$FTF with increased levels of hydrogen piloting becomes more pronounced with the increased forcing level of $\tilde{u}_0/U_{sw} = 0.30$ compared to the forcing level of $\tilde{u}_0/U_{sw} = 0.10$. FTF phase $\angle$FTF drops with increased level of hydrogen piloting. For PH2 case, the gain around the dip at 220 Hz increases slightly, however for frequencies higher than 260 Hz, there is a consistent drop in FTF gain.

For PC4 and PC10 cases, the same behavior of reduced gains with increased levels of methane piloting as with the forcing level of $\tilde{u}_0/U_{sw} = 0.10$ is also observed with a forcing level of $\tilde{u}_0/U_{sw} = 0.30$. As the forcing level is increased, the gain of the FTFs drops, however this drop occurs for frequencies larger than 180 Hz and 300 Hz for PC4 and PC10 cases respectively. Below these frequencies the drop in gain with increased forcing level is obscure.

For MH cases, the increase in phase is less compared to the REF case and the cross-over frequency drops down to 340 Hz and 430 Hz for MH4 and MH10 cases respectively. The frequency of maximum gain FTF gain drops from 450 Hz for 10% forcing level Hz to 300 Hz for 30% frocing level for MH4 case. The FTF gain demonstrates a plateau behavior between 200 Hz and 650 Hz with near unity gains over this frequency range for MH10 case.

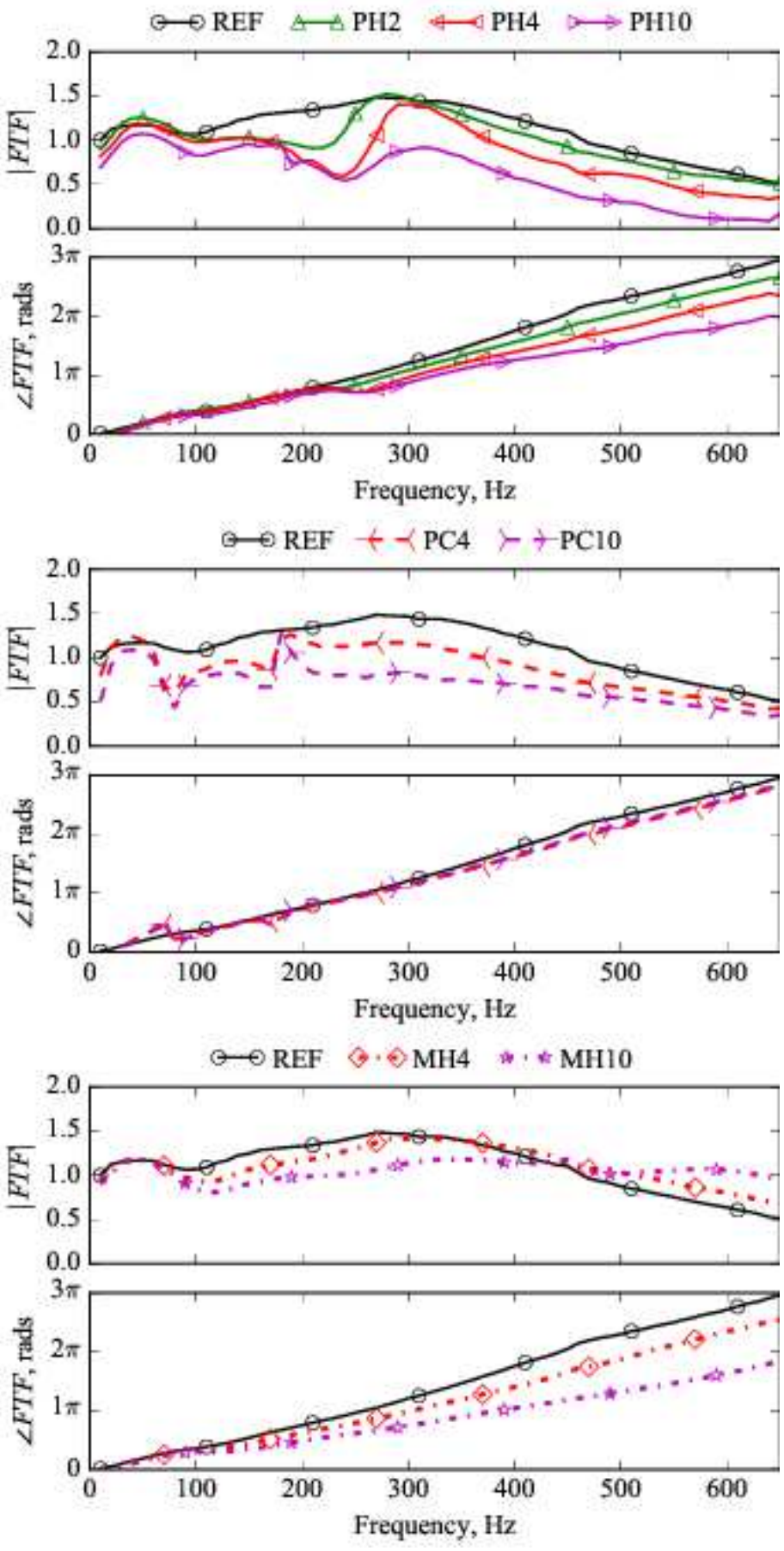

Figure 5.5: FTFs for a constant forcing level $\tilde{u}_0/U_{sw} = 0.30$ for U_{sw}=18 m/s, ϕ_G^0=0.8, S=0.33.

When the forcing level is further increased, to $\tilde{u}_0/U_{sw} = 0.60$ (Fig. 5.6), gains are reduced even further. For the REF case, there is a steep fall in the gain plot and a bump in the phase plot at around 450 Hz. This point coincides with the point where the flame is lifted because of high levels of forcing and will be explained further down the text. This behavior is not present with 4% of hydrogen enrichment and all levels of hydrogen piloting, where the flames are attached for the frequency range of 10 Hz to 600 Hz and the forcing levels studied. This shows the efficiency of hydrogen in flame holding even for high forcing levels.

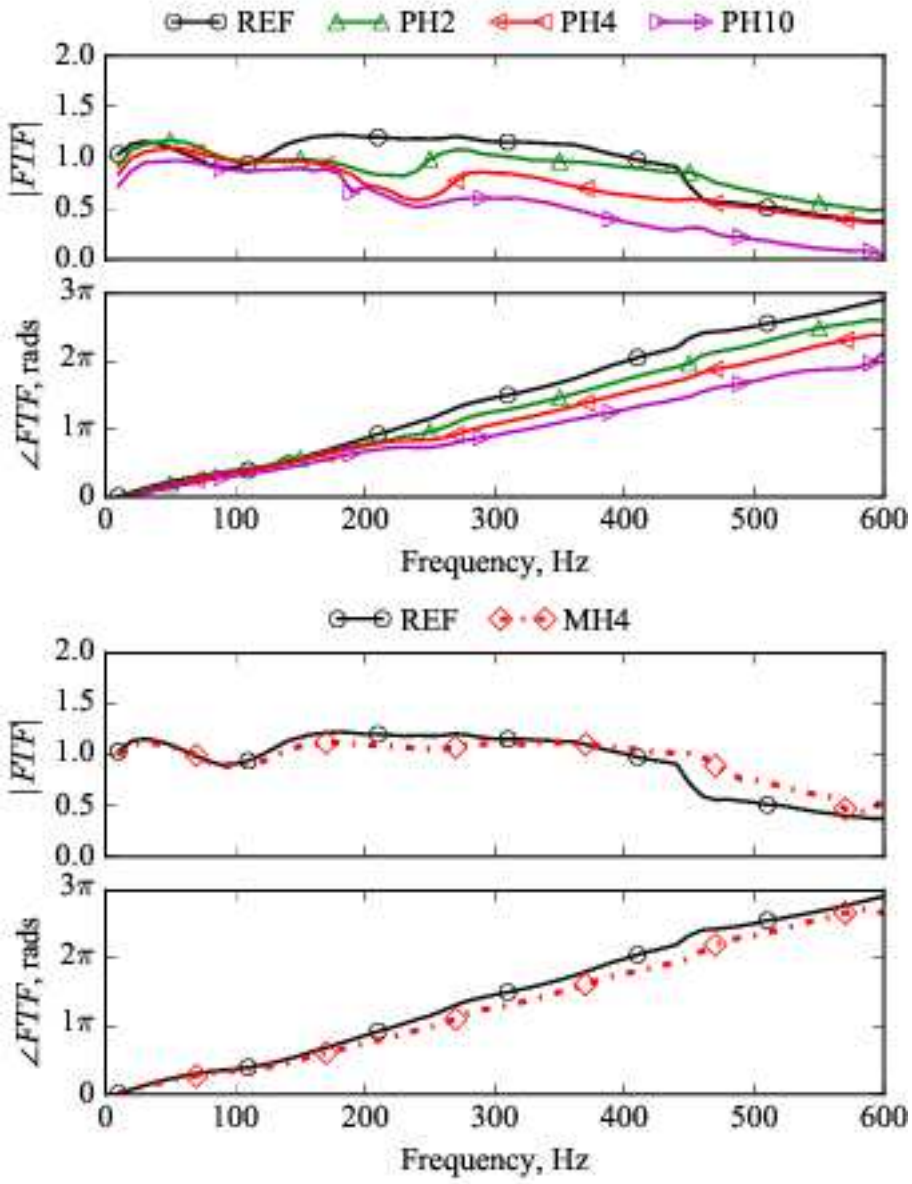

Figure 5.6: FTFs for a constant forcing level $\tilde{u}_0/U_{sw} = 0.60$ for U_{sw}=18 m/s, ϕ_G^0=0.8, S=0.33.

5.2 Flame Transfer Functions with 35° Swirler, D_c=46 mm Combustion Chamber

When the swirl number is increased to S=0.86, there is a broadband reduction in gain for mid range frequencies (120 Hz to 500 Hz) and increase in gain at high frequencies >500 Hz for the REF case compared to the REF case of S=0.33. Furthermore the dip at around 90 Hz for the swirl number of S=0.33 moves to 170 Hz for S=0.86. The maximum FTFs gain is not reported for the swirl number of S=0.86 as the FTF gain resembles a plateau for frequencies greater than 300 Hz for the REF case. This shows that when the swirl number is increased, the FTF gain drops for lower frequencies, however, there is more activity at high frequencies.

For hydrogen injection, the dip at 240 Hz is still present for all PH cases, and the saturation of drop in FTF gain happens at PH2 rather than PH4 for the lower swirl number. The delay of the flame response is reduced with increased hydrogen injection, however the drops in phase with increased levels of hydrogen injection is less pronounced. There is also a broadband increase in gain for frequencies higher than 400 Hz 360 Hz and 320 Hz for PH2, PH4 and PH10 cases respectively.

For PC cases, the bump at low frequency moves from 40 Hz for S=0.33 to 60 Hz for S=0.86. The dips at 70 Hz and 180 Hz persist at the same frequencies similar to S=0.33 cases, however for S=0.86 cases the dip at 180 Hz is more pronounced. As in S=0.33 cases, the methane injection does not change the delay of the flame response.

For MH cases, the behavior of the gain resembles to the gain of the REF case for S=0.86, meaning the increase in activity at higher frequencies with hydrogen enrichment is less pronounced, however the time lag of the flames is greatly reduced with hydrogen enrichment. This is due to the reduction in flame length as the flame speed is increased as can be observed in Fig. 3.8.

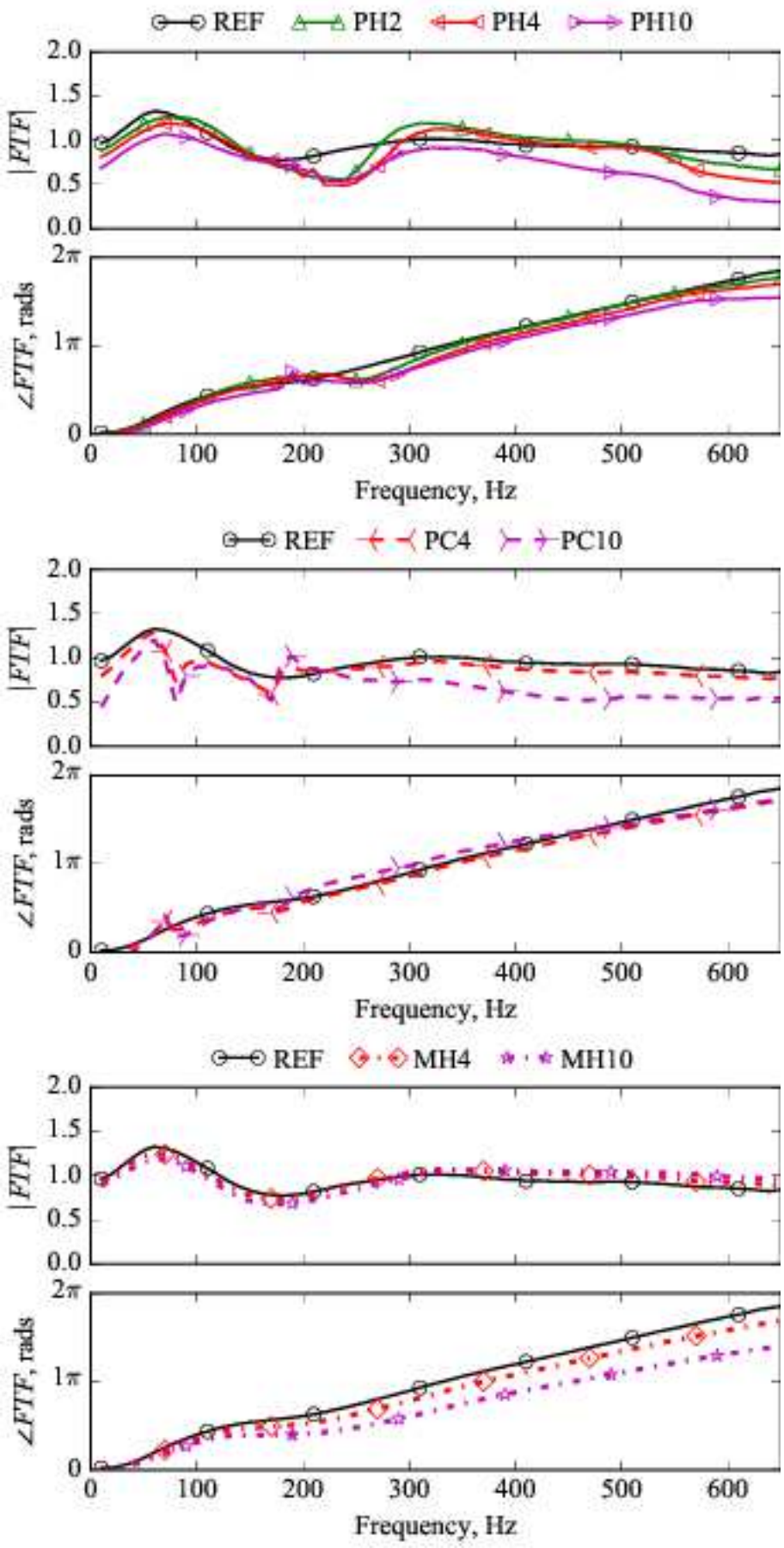

Figure 5.7: FTFs for a constant forcing level $\tilde{u}_0/U_{sw} = 0.30$ for U_{sw}=18 m/s, ϕ_G^0=0.8, S=0.86.

5.3 Low Order Model With Active Flame

With the measured flame transfer functions, it is possible to assess the stability of the combustion system using the low order model constructed. This is done by representing the contribution of the flame to the acoustic activity by Flame Describing Functions which consist of Flame Transfer Functions at multiple forcing amplitudes. Here the flame is assumed to be compact and infinitely thin, separating the fresh gasses in the plenum and the burner and the burnt gasses in the combustion chamber. With this representation, the heat release rate fluctuations are linked to the velocity perturbations at the burner outlet.

In OSCILOS, the contributions of the flames are represented by fitting time invariant linear system models to the experimental measured transfer functions. To calculate the modes of the system with combustion and active flames, the temperature of the gases in the plenum and the burner are set to $T_u = 292.15$ K. The temperature of the gasses is measured at the center of the outlet of the flame tube with a thermocouple and radiation corrected which corresponds to $T_b = 1425$ K. This value is set in the numerical model for the burnt gases filling the flame tube. The corresponding speeds of sound at the respective sections are deduced from ideal gas relations.

The modes of the cases with a temperature jump, active flames and corrected reflection coefficients were calculated with OSCILOS software and are presented in Fig. 5.8. The imaginary parts of these eigenvalues are the angular frequencies $w_n = 2\pi f_n = \mathrm{Im}(s_n)$ of the modes and the real parts $\mathrm{Re}(s_n) = \sigma_n$ are the growth rates σ_n. Here the instantaneous signal of any acoustic variable of a single eigenvalue system can be expressed as $a(t) = \mathrm{Re}(\tilde{a}e^{s_0 t}) = \mathrm{Re}\left(\tilde{a}e^{\sigma_0 t}e^{i\omega_0 t}\right)$ where $\tilde{a}$ is an arbitrary complex amplitude evaluated at $t = 0$.

For the REF case, at 10% forcing ($\tilde{u}_0/U_{sw} = 0.10$), the model predicts a mode locked at 620 Hz with a positive growth rate of σ=191 1/s. When the forcing level is increased to $\tilde{u}_0/U_{sw} = 0.30$ and $\tilde{u}_0/U_{sw} = 0.50$, this mode goes to f =604 Hz - σ=103 1/s and f =605 Hz - σ=78 1/s respectively. To asses the model at the limit cycle, the FTF gain and phase has been calculated from the limit cycle data and fed to the model, which results in a mode at f =611 Hz - σ=50 1/s contrary to the limit cycle measurements at

591 Hz. This result brings forward the conclusion that the acoustic losses in the model are under-predicted, as the low order model of the limit cycle measurements predict a positive growth rate.

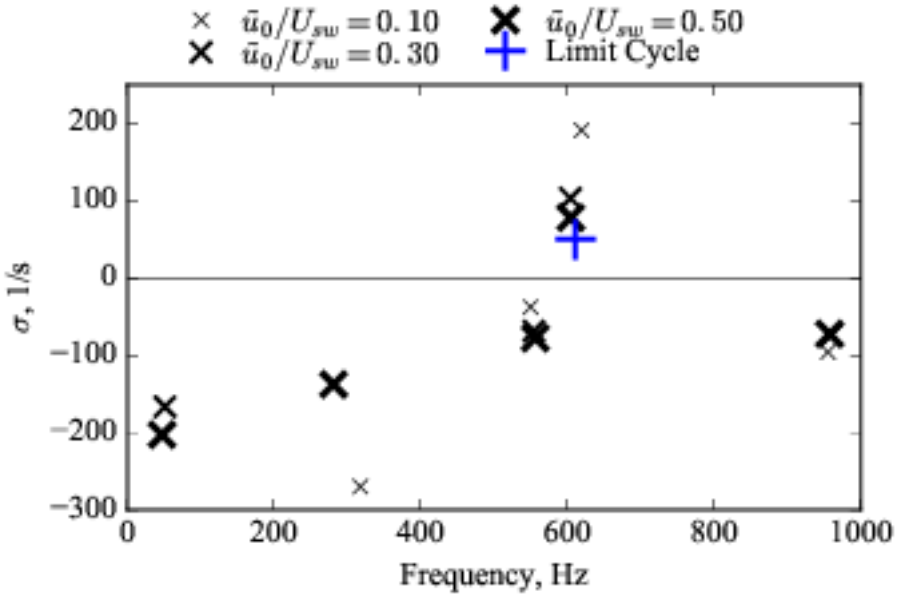

Figure 5.8: Eigenfrequencies and growth rates of the reduced order acoustic model calculated with OSCILOS of the REF case as a function of the forcing level, U_{sw}=18 m/s, ϕ_G^0=0.8, S=0.33.

Furthermore, the modes at 10% forcing for all cases studied in stability maps are also calculated. The results are presented in Fig. 5.9. The model captures that hydrogen enrichment at low levels $\mathscr{P}_{H_2} \leq 2$ does not alter the stability behavior of the system. Furthermore, with 2% methane injection (PC2 case), the modeled growth rate drops to σ=150 1/s from σ=191 1/s for the REF case. This is consistent with the drop in the limit cycle pressure amplitude measured with the MB microphone which drops to 520 Pa for the PC2 case from the limit cycle amplitude of 1140 Pa of the REF case. More interestingly, the increase in frequency for PH1 case is also captured. The frequency of the instability goes to 649 Hz for PH1 case with a reduced growth rate. This is also consistent with the measurements, as the limit cycle frequency of the PH1 case goes to 641 Hz with an amplitude reduced to 25 Pa as measured by MB microphone. PH1 case is marked as stable in stability maps as RMS of limit cycle pressure fluctuations is less than 300 Pa. The models predicts a positive growth rate for the completely stable PH2 case, however with a simple analogy that the acoustic losses are constant, it can be shown that the growth rate is lower than the acoustic losses deduced from the limit cycle measurements of the REF case.

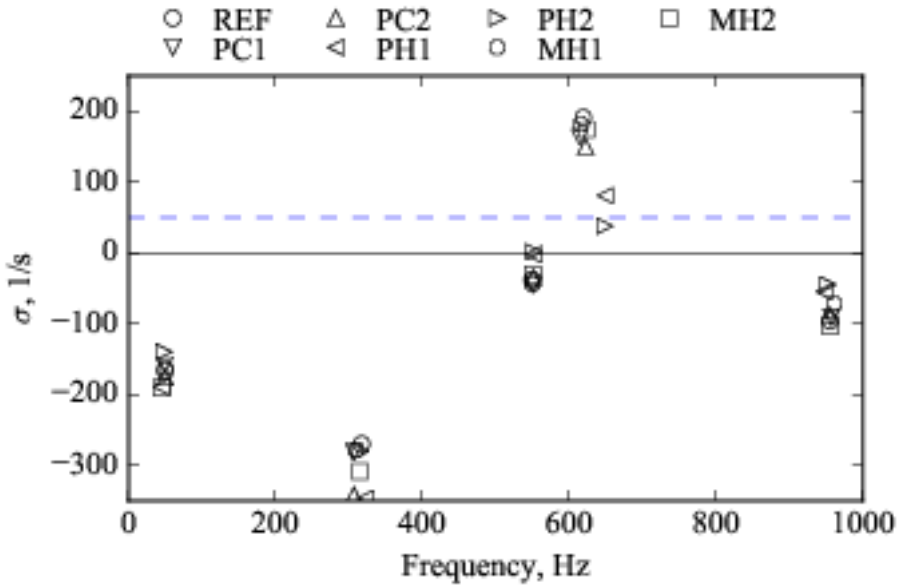

Figure 5.9: Eigenfrequencies and growth rates of the reduced order acoustic model calculated with OSCILOS of the respective cases at 10% forcing. The horizontal dashed line represents the acoustic losses obtained form the limit cycle analysis of the REF case (blue plus in Fig. 5.8).

Moreover, the comparison of the measured limit cycle structure and the model is given in Fig.5.10. The top image shows a schematic of the burner cavities. The middle plot shows the pressure amplitude with respect to that measured by microphone MB at the bottom of the plenum. The bottom plot shows the phase lag with respect to that

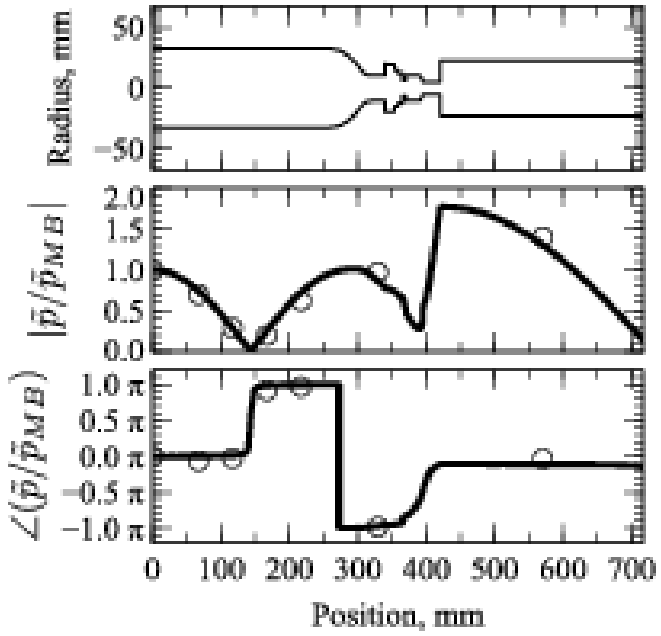

Figure 5.10: Comparison between measurements (circles) and predictions (full line) of the acoustic pressure distribution along the combustor of the unstable mode of the REF case calculated with OSCILOS.

measured by microphone MB. This figure confirms that the acoustic pressure in the flame tube is in phase with the pressure signal measured by microphone MB.

5.4 Radial Injection, Multi Input Flame Transfer Functions and Flame Response Control

As the name suggests, MIRADAS (Mitigation of Instabilities by Radially and/or Axially Directed Addition of Species) setup is designed in a way that also permits radial injection of gasses. Furthermore, with the chamber and a speaker, the flow-rate of the gasses can be pulsated. This configuration of MIRADAS setup is not heavily exploited and left for future studies. However initial interesting results are also obtained with this configuration which will be presented in this section. A brief technical description is presented in Fig.5.11.

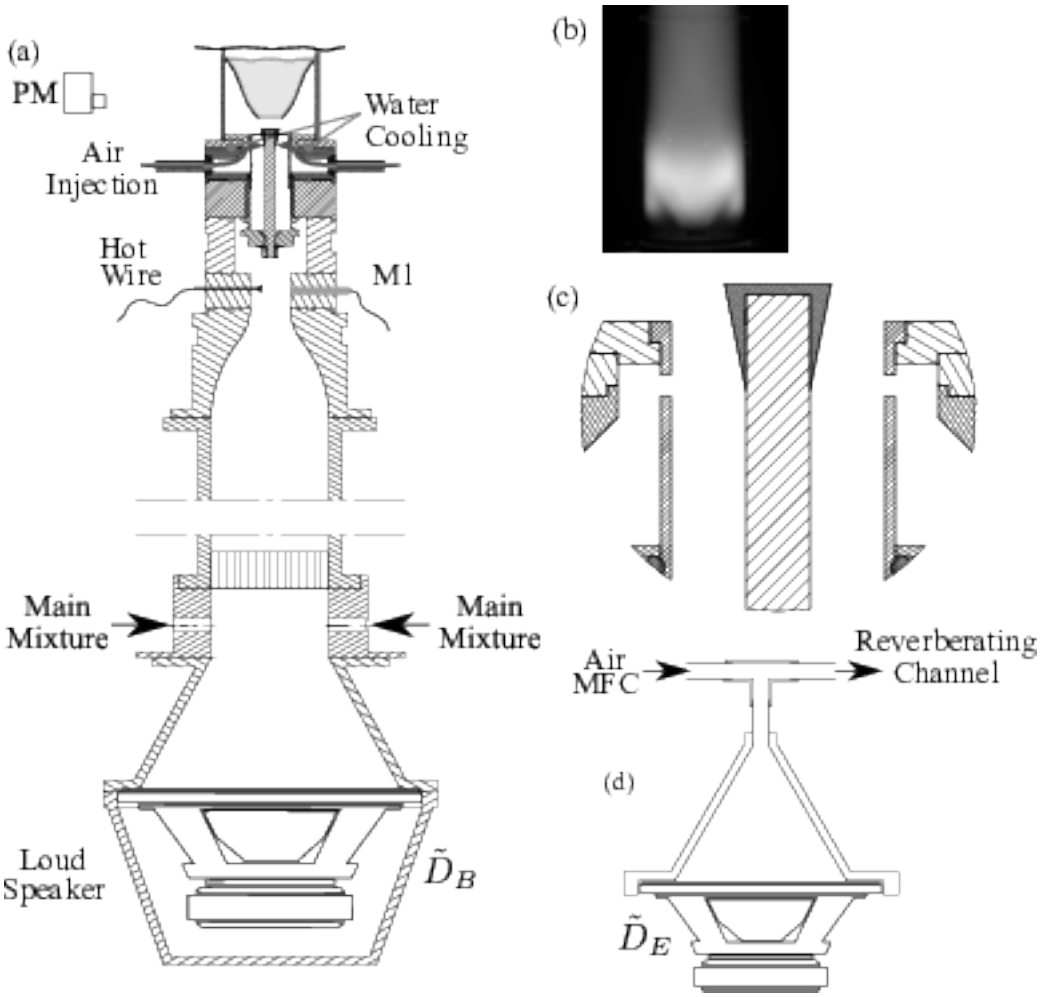

Figure 5.11: MIRADAS setup in radial injection configuration. (a) Overview of the experiment, (b) direct visualization (without optical filter) of the flame image with $\bar{U}_{sw}$=8 m/s and ϕ_G=0.75 (c) detail view of the injection system, (d) External speaker used to modulate injected flowrate.

The operating point presented in Fig. 5.11 is obtained by fixing the equivalence ratio ϕ_G=0.75 and injecting 10% of the total air flow by the 4 radial injection holes of 1 mm diameter separated by 90° around the axis. Evidently, 10% of the airflow is removed from the main flow to keep the equivalence ratio constant. With the aid of a second speaker, the injection flowrate can also be pulsated, creating a modulation in instantaneous equivalence ratio at the outlet of the burner similar to [168]. This equivalence ratio modulation also creates fluctuations in the instantaneous heat release as well. When two speakers are used simultaneously, the heat release fluctuations are caused by both velocity modulation (bottom speaker) and equivalence ratio fluctuations (external speaker and reverberating chamber) which act on the flame response together. The contributions of each of these modulations can be decomposed to give a multi-input-single-output system with two flame transfer functions, one for the velocity modulation and one for the equivalence ratio modulation as presented in Eq.5.8 [169, 170].

$$\frac{\tilde{\dot{Q}}}{\bar{\dot{Q}}} = FTF_u(\omega)\frac{\tilde{u}}{\bar{u}} + FTF_\phi(\omega)\frac{\tilde{\phi}}{\bar{\phi}} \tag{5.8}$$

In MIRADAS setup, by adjusting the phase between two speakers ($\tilde{D}_E/\tilde{D}_B$) driven at the same frequency, the phase between $FTF_u(\omega)\frac{\tilde{u}}{\bar{u}}$ and $FTF_\phi(\omega)\frac{\tilde{\phi}}{\bar{\phi}}$ can be changed to investigate the effect on the amplitude of the global heat release response $\frac{|\tilde{\dot{Q}}|}{\bar{\dot{Q}}}$. First of all, the drive signals of each speaker are set one by one to give a heat release response of $|\tilde{q}/\bar{q}| = .2$ individually. Then, both speakers are driven at the same time with the calibrated drive signal amplitudes $|\tilde{D}_E|$ and $|\tilde{D}_B|$ and the phase between the driving signals $\angle\tilde{D}_E/\tilde{D}_B$ are changed to modify the phase between $FTF_u(\omega)\frac{\tilde{u}}{\bar{u}}$ and $FTF_\phi(\omega)\frac{\tilde{\phi}}{\bar{\phi}}$ and the heat release response $\frac{\tilde{\dot{Q}}}{\bar{\dot{Q}}} \equiv \frac{\tilde{I}}{\bar{I}}$ for each phase is recorded. The results of this experiment are presented in Fig. 5.12.

Fig. 5.12 shows that the amplitude of the global heat release response changes as a function of the phase between the drive signals of speakers $\angle\tilde{D}_E/\tilde{D}_B$. This is a result of the competition between the two parts of the decomposed FTF, one caused by the equivalence ratio modulation $FTF_\phi(\omega)\frac{\tilde{\phi}}{\bar{\phi}}$ and the other caused by velocity modulation $FTF_u(\omega)\frac{\tilde{u}}{\bar{u}}$. At $\angle\tilde{D}_E/\tilde{D}_B = \pi/4$ these two parts are in phase meaning that the angle between these decomposed FTFs that are complex numbers are close to zero, and their amplitudes are accumulated, resulting in a maximum in the heat release response $\frac{|\tilde{Q}|}{\bar{Q}} \equiv \frac{|\tilde{I}|}{\bar{I}}$. At $\angle\tilde{D}_E/\tilde{D}_B = 5\pi/4$ they are out of phase and the angle between decomposed FTFs

is close to π and the amplitudes are canceled out resulting in a near zero heat release rate response $\frac{|\tilde{Q}|}{\bar{Q}} \equiv \frac{|\tilde{I}|}{\bar{I}} \approx 0$. This phenomenon can be used to control instabilities, however with the present setup an active control system is needed. Development of a passive control system using equivalence ratio modulations are left to future studies.

It should be noted that, this canceling out effect in the heat release response is not due to the canceling out of the acoustic waves, but really the canceling out of the heat release fluctuations caused by equivalence ratio modulation and velocity modulation. This behavior can be observed by investigating the acoustic velocity or acoustic pressure signal. The non-dimensional acoustic velocity amplitude $|\tilde{u}|/\bar{u}$ goes from 25.6% at the phase of maximum global heat release response to 20.4% at the phase of minimum global heat release response, meaning that the acoustic activity in the chamber is still as strong. The difference in amplitude is caused by the activity of the flame, acting as a third speaker, injecting acoustic energy into the system. When the global heat release is zero, the acoustic energy put onto the system by the flame is diminished.

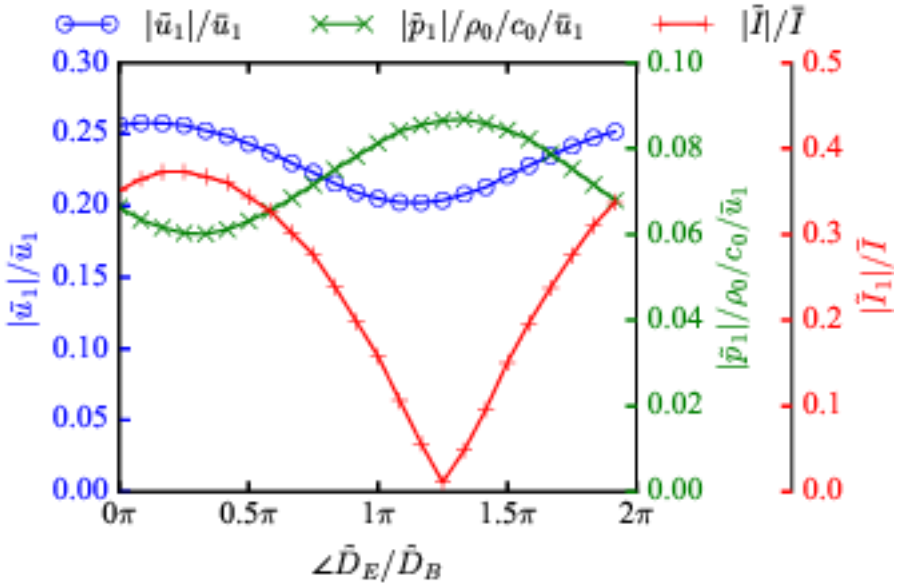

Figure 5.12: Amplitude of global heat release response $\frac{|\tilde{Q}|}{\bar{Q}} \equiv \frac{|\tilde{I}|}{\bar{I}}$ with competing $FTF_u(\omega)\frac{\tilde{u}}{\bar{u}}$ and $FTF_\phi(\omega)\frac{\tilde{\phi}}{\bar{\phi}}$ transfer functions. The acoustic velocity and pressure measurements are taken at Section 1 as marked in Fig.5.11.

5.5 Conclusions

In this chapter, the effect of hydrogen and methane piloting and hydrogen enrichment on flame dynamics has been experimentally studied by measured Flame Transfer Functions. The following conclusions can be derived.

- Hydrogen, when premixed with methane, in perfectly premixed regime (MH cases) reduces the delay of the flame responses, however causes higher FTF gains at high frequencies.

- High levels of methane piloting causes a broadband drop in the Flame Transfer Function gain for mid-range injection fractions $0.04 \leq \mathscr{P}_{pilot} \leq 0.1$, however does not change the phase of the FTF, limitings its potential to be used as an efficient passive control parameter as the Rayleigh criteria remains practically unchanged. For low levels of methane injection $\mathscr{P}_{pilot} \leq 0.02$, the FTF remains quasi-unchanged.

- Hydrogen in piloting regime (PH cases) reduces the gain of the flame transfer functions in a broadband manner for mid-range injection fractions $0.04 \leq \mathscr{P}_{H_2} = \mathscr{P}_{pilot} \leq 0.1$. However the most remarkable observation is the effectiveness of hydrogen injection on changing the phase of the flame transfer functions even for low injection power fractions $\mathscr{P}_{H_2} = \mathscr{P}_{pilot} \leq 0.02$.

- With its effectiveness on the phase of the FTFs, hydrogen piloting can be used to passively control combustion instabilities, without the application of flow-rate pulsation mechanisms.

- As expected, increased swirl causes shorter flames with shorter delays. However these flames are on the limit of flashback for low flow velocities.

- Low order acoustic models are an efficient method to predict the stability behavior of combustion systems, offering easy to set up calculations with easy to set up geometries and quick results with acceptable accuracy.

6. SPATIAL ANALYSIS OF FLAME RESPONSES

In the previous chapter, a global overview on the responses of flame responses with different injection strategies are presented. The heat release responses are measured with a photomultiplier, which integrates spatially the CH* chemiluminescent light signal, and giving a signal proportional to the integrated heat release rate. Using these measurements it is possible to comment on the global response of the different flames, however the reason why there are dips in the FTF gains, or why the global delays of the flame change is not possible.

Further investigations are done by recording phase locked flame images to investigate the reason behind the dips and the changes in phase of the Flame Transfer Functions. Three frequencies of interest are explored; 240 Hz where the dip in the FTFs occur, 590 Hz where there is a big difference in the phase of the FTFs with the introduction of hydrogen and also the frequency of instability, and a mid range frequency of 400 Hz. This chapter is organized into two sections, the first investigating the local flame responses for low swirl flames and the second one providing a similar analysis for high swirl flames.

6.1 Spatial Spectral Analysis of Flame Responses for 15° Swirler, D_c=46 mm Combustion Chamber

Phase locked flame images of forced flames are recorded to investigate the differences in flame transfer functions for each case. This is done by forcing the flow with a speaker using a sinusoidal signal and at the same time triggering the camera using a TTL signal. The phase of the trigger is changed wrt. the drive signal to obtain images at different phases. These images are than aligned with the velocity signal at the outlet of the annular injection channel, so that the delays are reported wrt. to the velocity fluctuations, as in flame transfer functions. An example of these images are given in Fig. 6.1. Here the angles represent the phase of the instant at which the pictures are taken wrt. the velocity signal at the burner outlet.

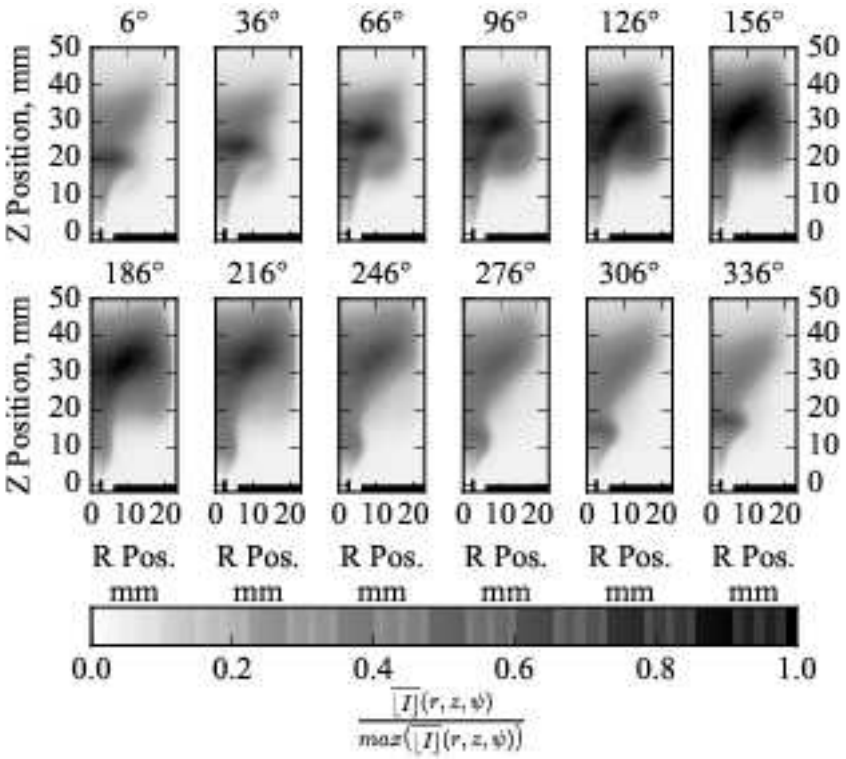

Figure 6.1: Phase locked images of the REF case at a forcing level of $\tilde{u}_0/U_{sw} = 0.30$ at 240 Hz for U_{sw}=18 m/s, ϕ_G^0=0.8, S=0.33. $\overline{\lfloor I \rfloor}$ designates phase averaged CH* chemiluminescent light emission.

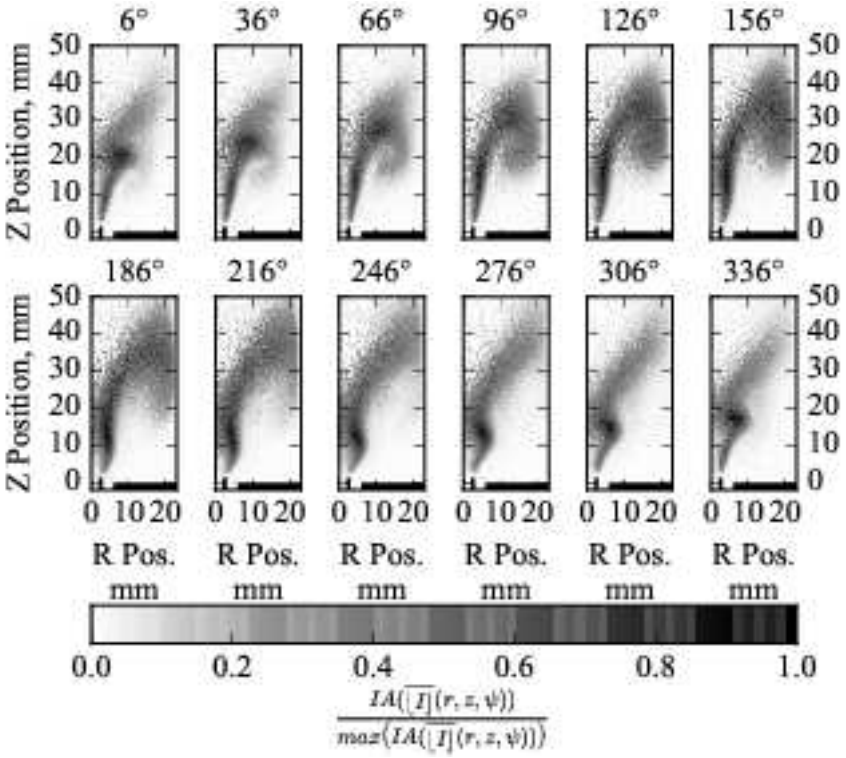

Figure 6.2: Inverse Abel Transformed phase locked images of the REF case at a forcing level of $\tilde{u}_0/U_{sw} = 0.30$ at 240 Hz for U_{sw}=18 m/s, ϕ_G^0=0.8, S=0.33. $IA\left(\overline{\lfloor I \rfloor}(r,z,\psi)\right)$ designates phase averaged inverse Abel Transformed CH* chemiluminescent light emission.

Another way to look at these images is to take the Inverse Abel Transform to get a cut of the axially symmetric swirled flame. These Inverse Abel transformed images show more clearly the distortion of the flame sheet by the perturbation created at the bottom of the image and transported downstream. Additionally the vortex roll-up phenomenon is more visible.

From Fig. 6.2, it can be observed that a perturbation is formed at around 180° of phase; the root of the flame starts to advance upstream towards the burner as the velocity at the outlet of the burner is at its minimum. Moving along further in phase, the velocity increases and this distorted part of the flame is blown further downstream. This perturbation is transported with the mean flow, growing in amplitude as it is transported. At around 30°, this perturbation is rolled upon itself and greatly increases the flame surface area which is proportional to the global integrated heat release rate, reaching to a maximum of heat release rate at around 150°. Later on, at ≈180°, the sides of this rolled up part of the flame start touching the combustion chamber walls and gets extinguished, causing a drop in the instantaneous global heat release. This behavior is repeated periodically, for the next cycles that follow.

An important step in recording of these flame images is to set the exposure time of the camera. The camera integrates the light intensity emitted by the fame in time in the limits of the exposure time. To get instantaneous chemiluminescent light images, it is important to set this exposure time low enough not to get a flame image integrated in time. Exposure time is set to 10 µs for all the images, which is low enough to get instantaneous emission of CH* chemiluminescence for the frequencies studied. The comparison of the space integrated intensity signal from the camera and the PM signal, which captures the light coming from the whole image is compared in Fig. 6.3.

Fig. 6.3 shows that the phase locked flame images represents quite well the instantaneous CH* intensity signal and can be used with confidence to examine the local flame response of the forced flames. Here all the signals are aligned to have zero phase angle for the velocity signal at the outlet of the burner.

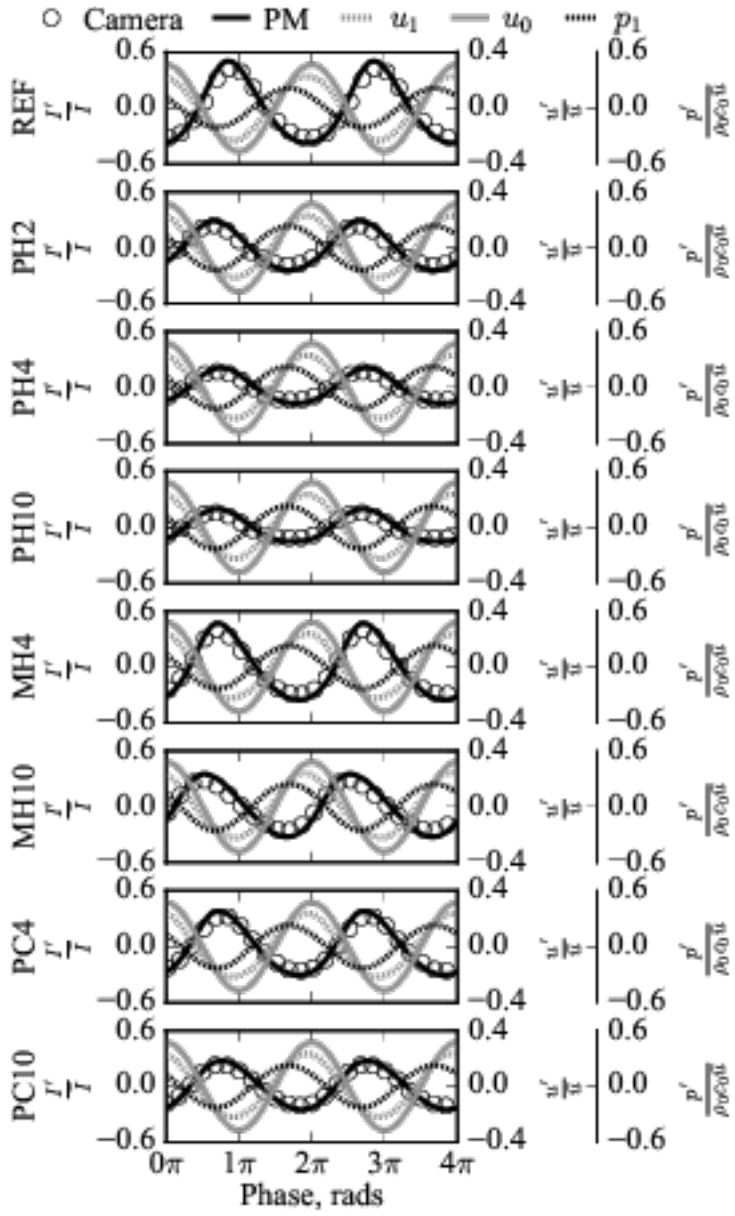

Figure 6.3: Comparison of the signals obtained with camera and PM for a forcing level of $\tilde{u}_0/U_{sw} = 0.30$ at 240 Hz for U_{sw}=18 m/s, ϕ_G^0=0.8, S=0.33.

Furthermore, using time (phase) dependent intensities for each pixel of the phase locked flame images, the amplitude and phase at each pixel location can be obtained. All the post processing in this chapter is summed up in Appendix A.2.

Firstly the amplitudes are presented for all cases from Fig. 6.4 to Fig. 6.6. It can be seen that for all frequencies, with hydrogen piloting (PH cases) there is increased activity with increased amplitudes at the roots of the flames near the injection tube outlet compared to REF cases. Moreover, there is a shift of heat release response activity towards upstream of the combustion chamber, towards the burner. This is attributed to the flame length getting shorter with the injection of hydrogen.

With methane injection (PC cases) there is increased activity at the roots of the flames near the injection tube outlet, however not as pronounced as PH cases. Furthermore, the shift of the heat release response towards the upstream is quasi-nonexistent with methane injection, as the flame length is not modified with methane injection.

With hydrogen enrichment (MH cases), as the flame lengths get shorter with increased hydrogen fraction, the heat release response activity shifts towards upstream. As these cases are perfectly-premixed, the increase in amplitude of heat release fluctuations as in hydrogen piloted cases (PH cases) does not occur, instead, the heat release response activity is shifted downstream as a result of the increased flame speed.

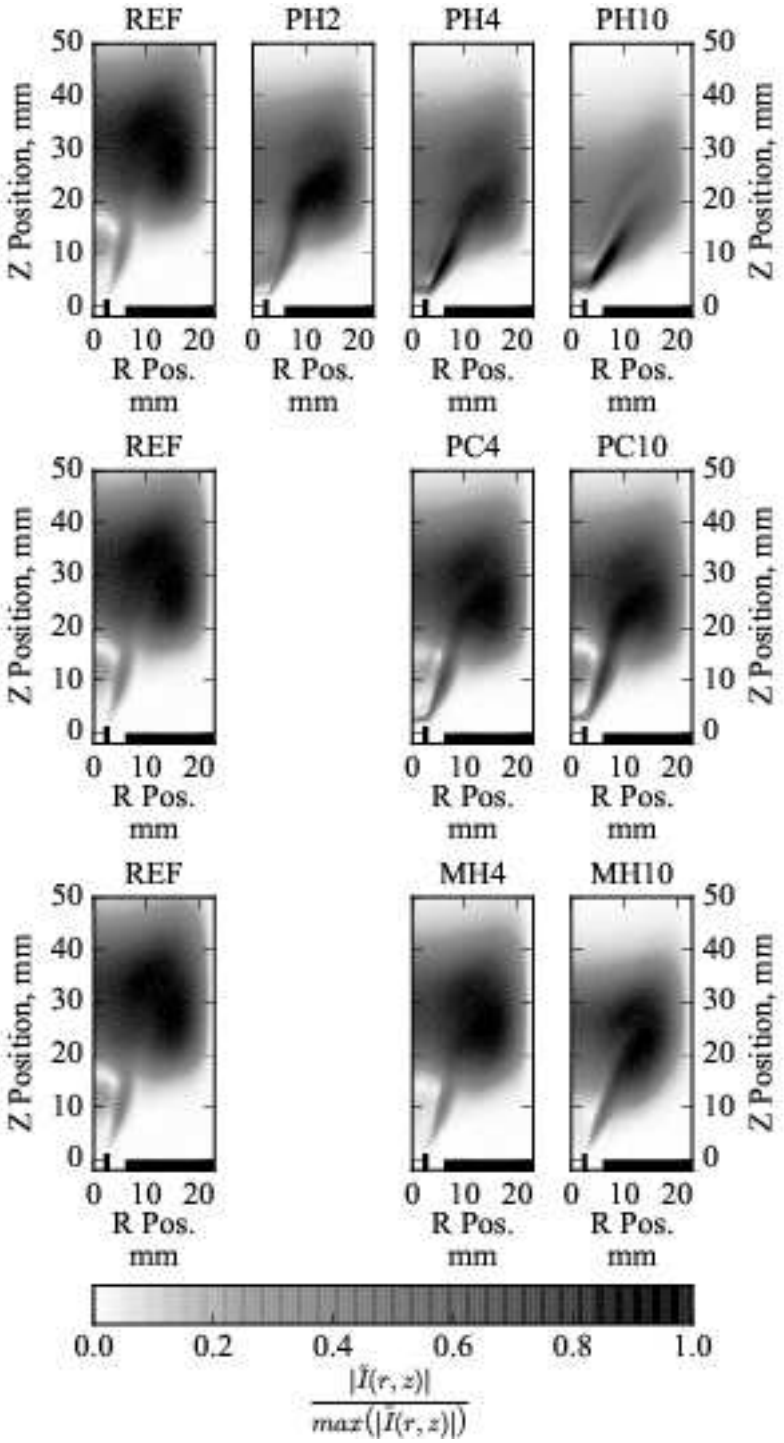

Figure 6.4: Amplitudes of the complex heat release signal with acoustic forcing, $\tilde{u}_0/U_{sw} = 0.30$ at 240 Hz for U_{sw}=18 m/s, ϕ_G^0=0.8, S=0.33.

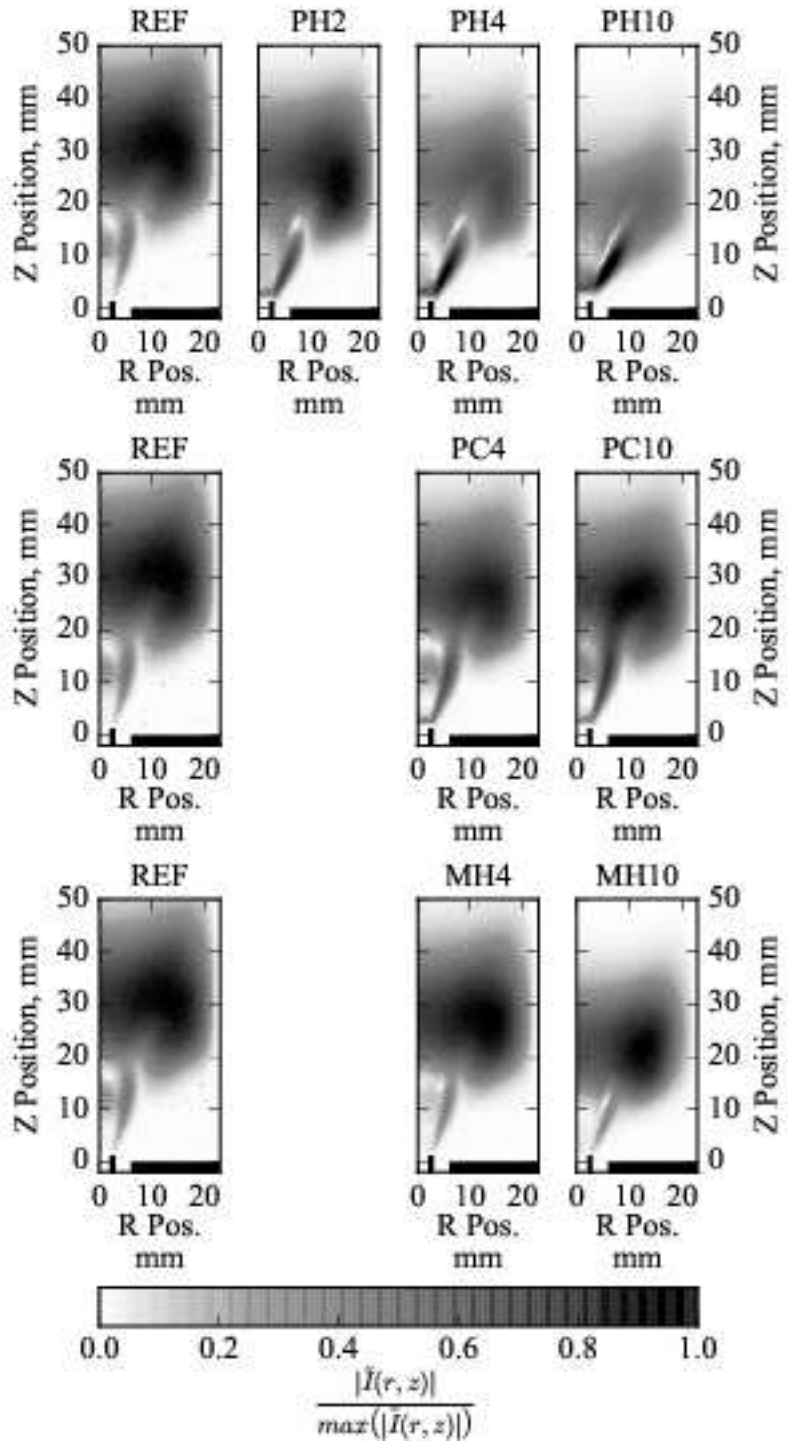

Figure 6.5: Amplitudes of the complex heat release signal with acoustic forcing, $\tilde{u}_0/U_{sw} = 0.30$ at 400 Hz for U_{sw}=18 m/s, ϕ_G^0=0.8, S=0.33.

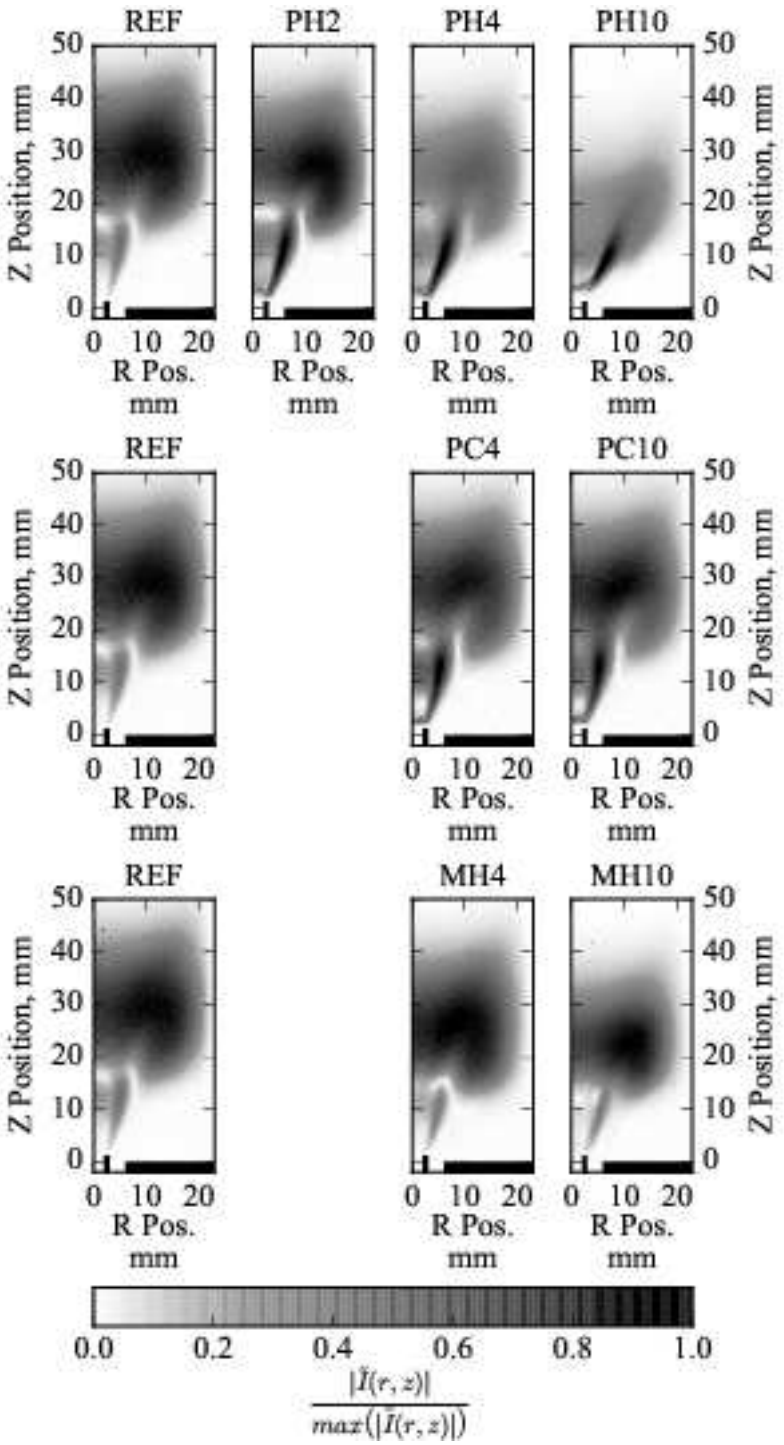

Figure 6.6: Amplitudes of the complex heat release signal with acoustic forcing, $\tilde{u}_0/U_{sw} = 0.30$ at 590 Hz for U_{sw}=18 m/s, ϕ_G^0=0.8, S=0.33.

Subsequently the delays are presented in figures Fig. 6.7 to Fig. 6.9.

For cases with hydrogen piloting (PH cases), as the activity at the roots of the flames are increased, the weight of the phase of the heat release fluctuations at the root of the flames on the global phase of the flame transfer function increases. This creates a

competition between the bottom and top parts of the flames that have different phase lags and results in a drop in the phase and the gain of the flame transfer function.

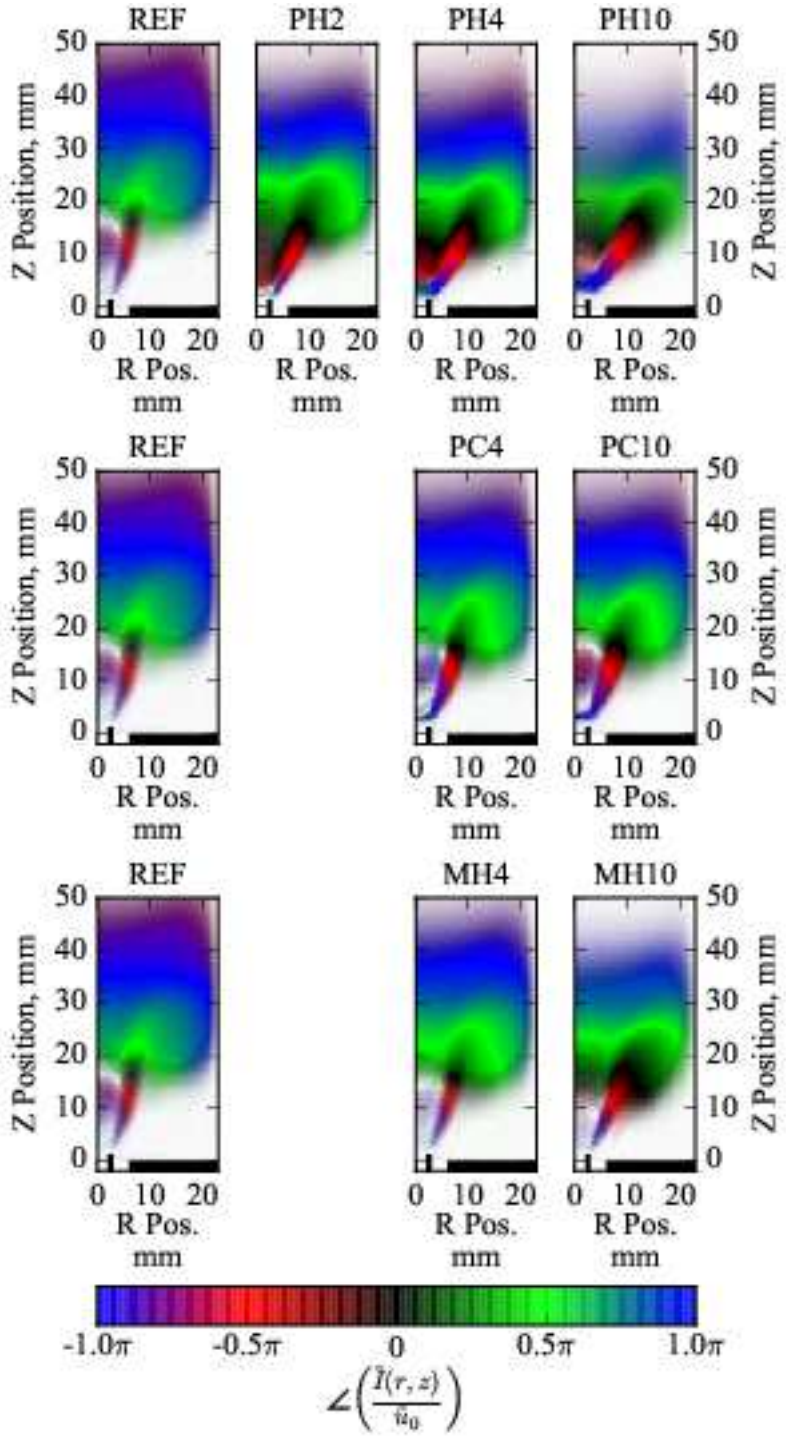

Figure 6.7: Phases wrt. velocity at the burner outlet of the complex flame response to acoustic forcing, $\tilde{u}_0/U_{sw} = 0.30$ at 240 Hz for U_{sw}=18 m/s, ϕ_G^0=0.8, S=0.33.

For methane piloting (PC) cases, because of methane piloting, the weight at the root of the flames increases as well, however this is not nearly as strong as hydrogen piloting.

This is consistent with the FTFs presented in Fig. 5.5; the phase of the FTFs is not altered with methane piloting.

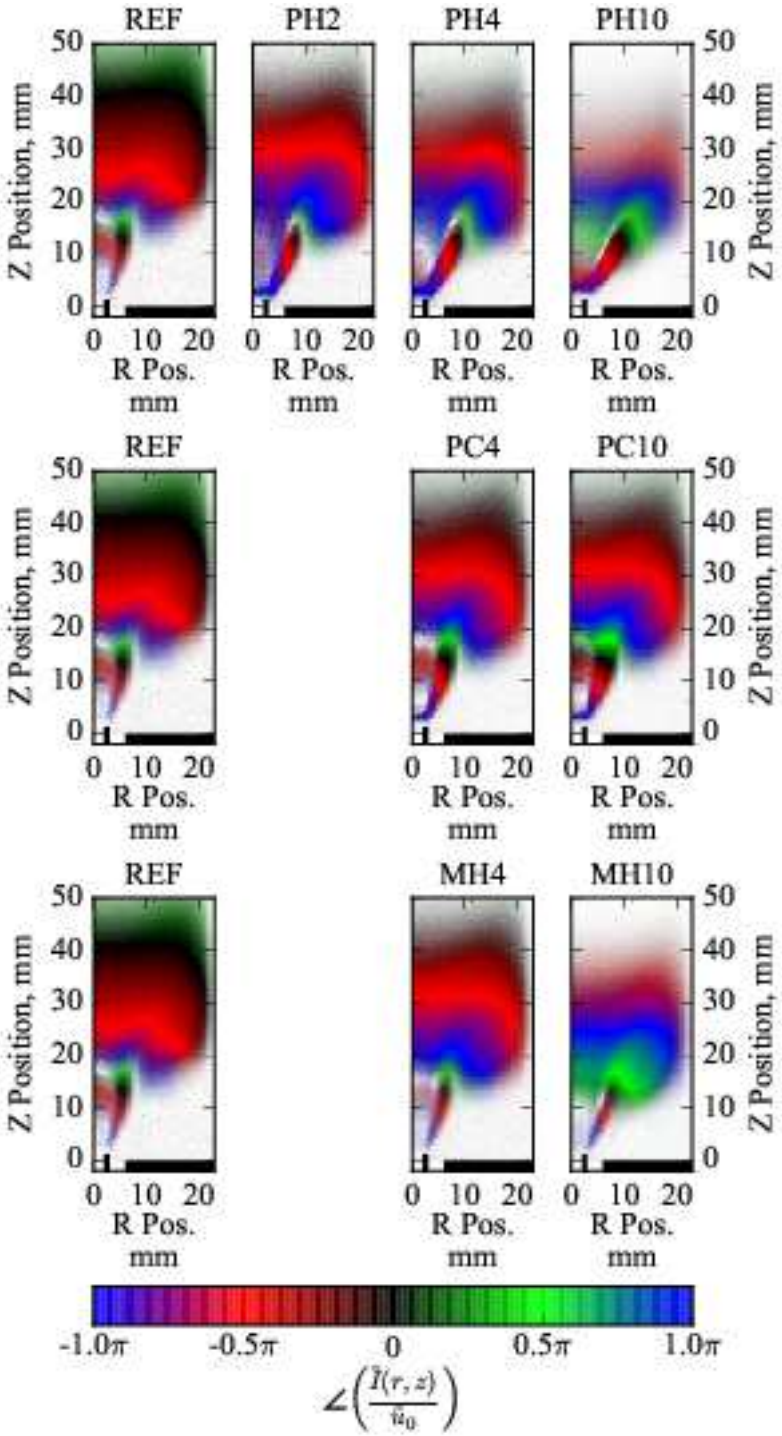

Figure 6.8: Phases wrt. velocity at the burner outlet of the complex flame response to acoustic forcing, $\tilde{u}_0/U_{sw} = 0.30$ at 400 Hz for U_{sw}=18 m/s, ϕ_G^0=0.8, S=0.33.

With hydrogen enrichment (MH cases), as the flames get shorter, the disturbance has a smaller distance to travel to reach the edges of the flames, which reduces the global phase lag of the flame response. Furthermore, the speed that the disturbance

is transported downstream increases. This is more pronounced in higher frequencies and can be seen by comparing the phase lags to the REF case, for example of Fig. 6.9. The phase bands are elongated for MH cases compared to REF case, meaning that the disturbance moves faster in the axial direction for MH cases.

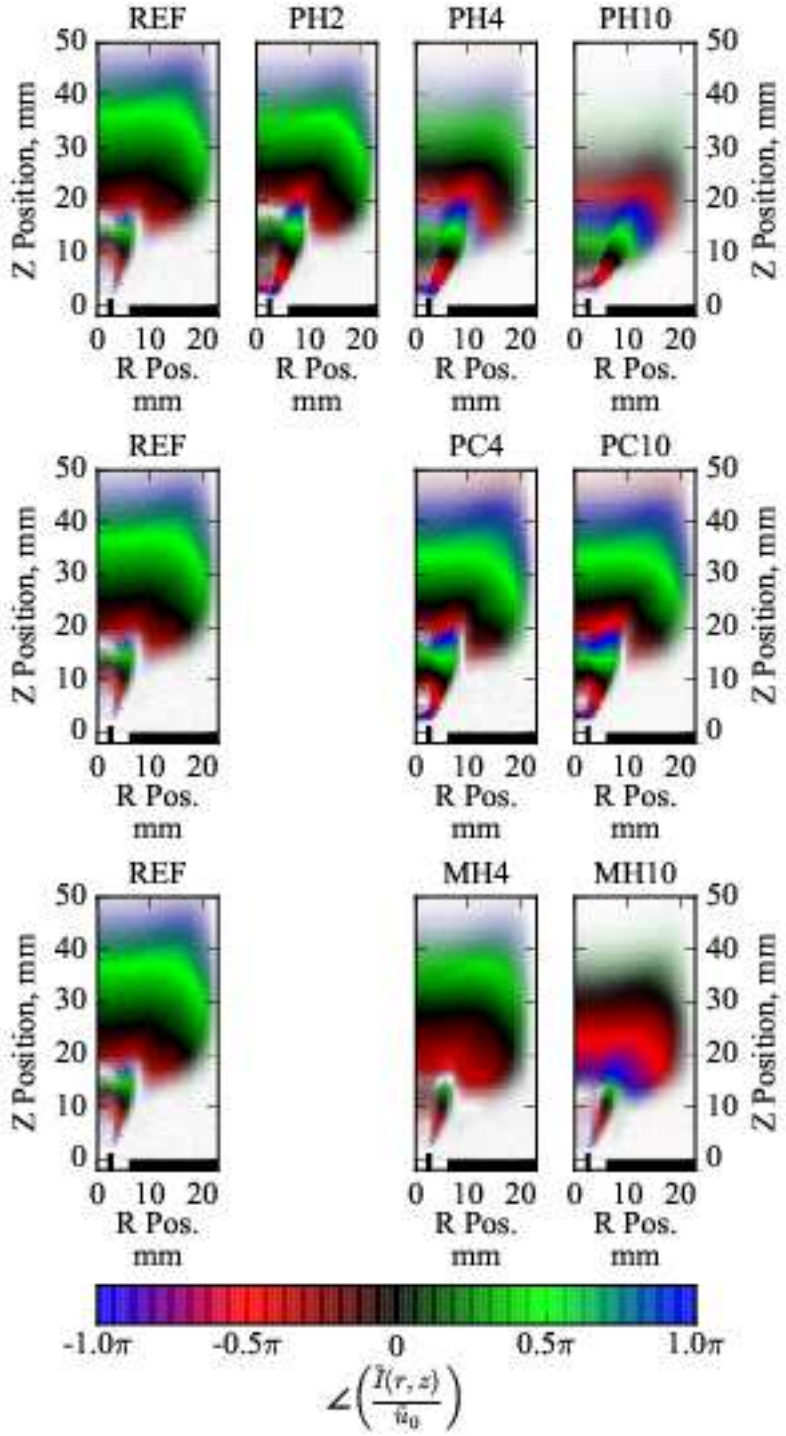

Figure 6.9: Phases wrt. velocity at the burner outlet of the complex flame response to acoustic forcing, $\tilde{u}_0/U_{sw} = 0.30$ at 590 Hz for U_{sw}=18 m/s, ϕ_G^0=0.8, S=0.33.

Next the RMS of pixel intensities are presented in figures Fig. 6.7 to Fig. 6.9. The RMS figures are presented to mention briefly the Noise component in Eq. **A.2.5**. Although it exists, this component is very small compared to the amplitude, resulting in RMS figures (Figs. 6.7 to 6.9) exhibiting the same behavior as the amplitude figures (Figs. 6.4 to 6.6).

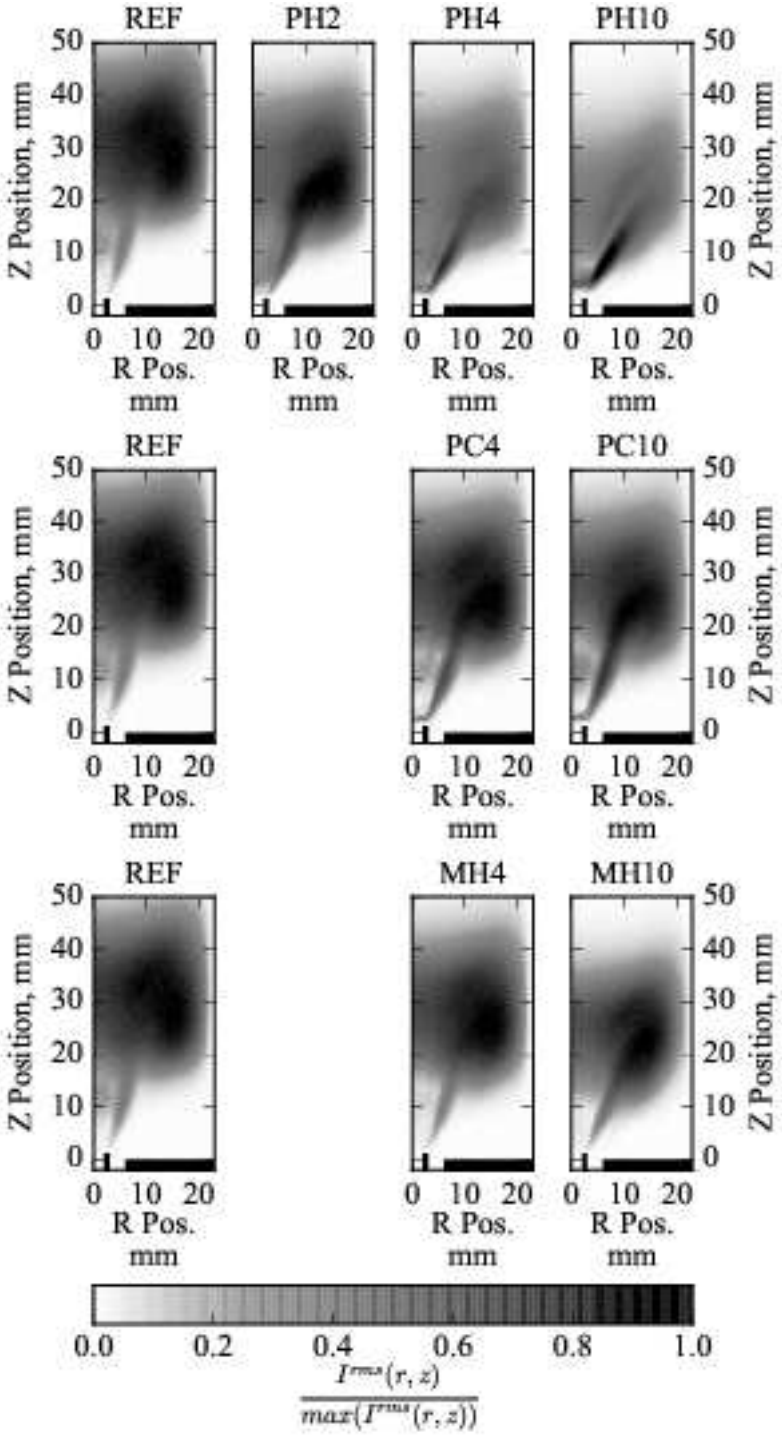

Figure 6.10: RMS values of pixel intensities of flame response to acoustic forcing, $\tilde{u}_0/U_{sw} = 0.30$ at 240 Hz for U_{sw}=18 m/s, ϕ_G^0=0.8, S=0.33.

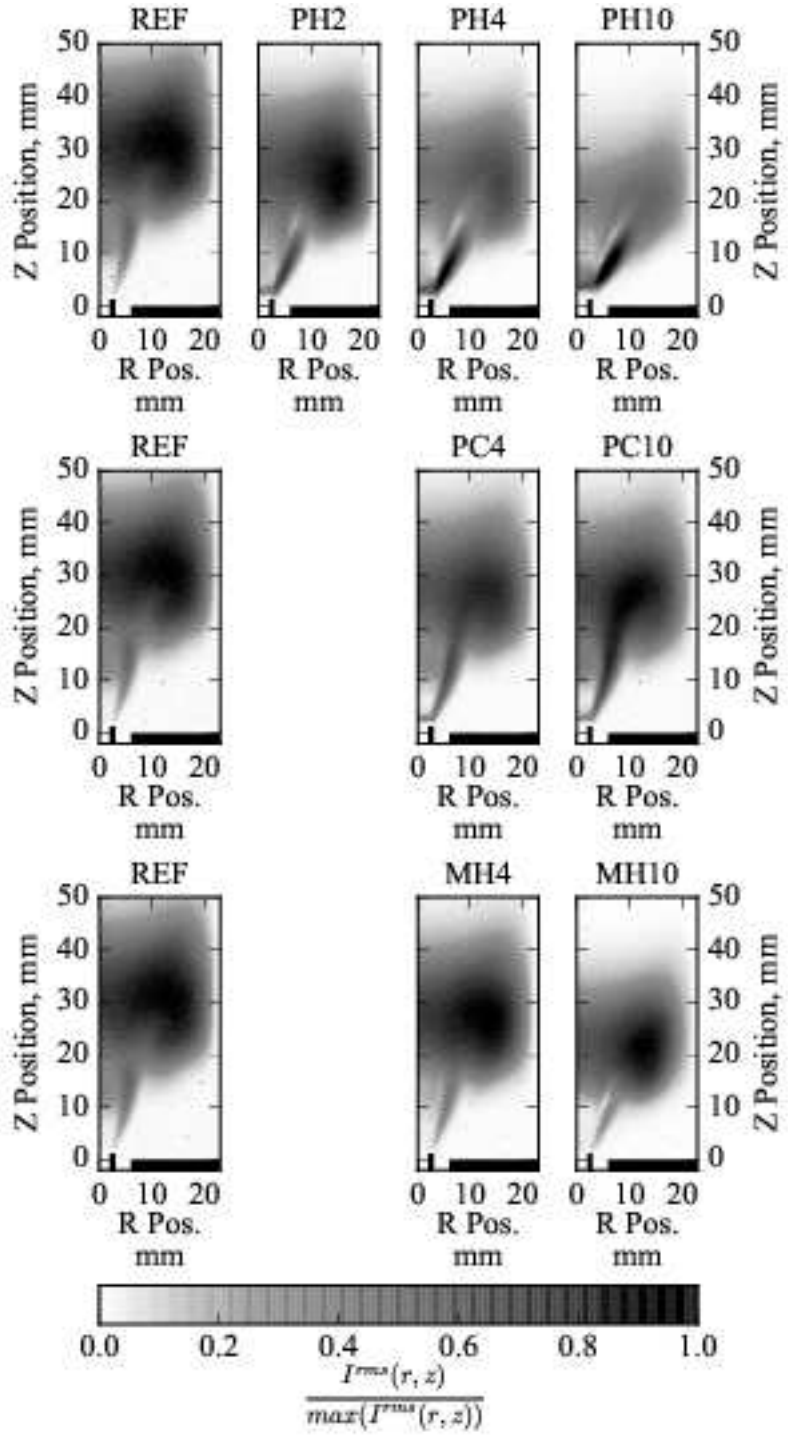

Figure 6.11: RMS values of pixel intensities of flame response to acoustic forcing, $\tilde{u}_0/U_{sw} = 0.30$ at 400 Hz for U_{sw}=18 m/s, ϕ_G^0=0.8, S=0.33.

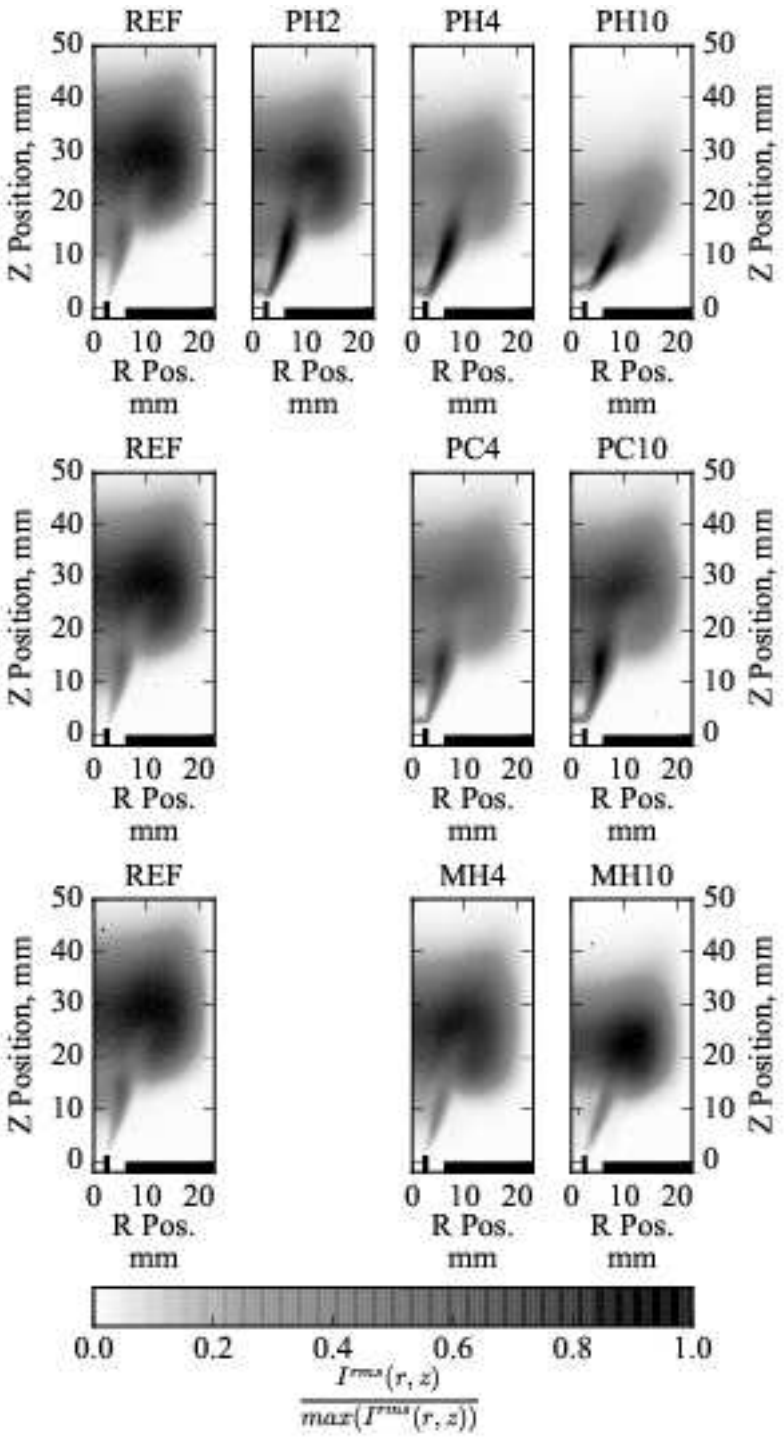

Figure 6.12: RMS values of pixel intensities of flame response to acoustic forcing, $\tilde{u}_0/U_{sw} = 0.30$ at 590 Hz for U_{sw}=18 m/s, ϕ_G^0=0.8, S=0.33.

Although the local delays and amplitudes give a very detailed view of the local responses of forced flames, an easier to present method which offers a broader view on the responses of forced flames is possible. To accomplish this, profiles of radially integrated heat release fields are used. This is easy for experimental measurements, as the forced flame images consist of spatially uniform pixels with pixel intensities proportional to the chemiluminescent light coming from the flame, representing line

of sight integrated the heat release. The pixel intensities in a row can be summed to get the radially integrated heat release at the axial position representing the pixel row. The procedure to obtain the radially integrated variables are presented in Appendix A.2.

With the conventions given in Appendix A.2, it is possible to examine the phase difference between the radially integrated heat release at a point z and the global heat release rate by projecting the radially integrated heat release response on the global response. This shows the if the axial point along the combustion chamber are ahead or behind in phase compared to the global heat release fluctuations, showing regions of phase opposition that reduce the amplitude of the global heat release response and regions that are in phase with the global heat release, that increase the amplitude of the global heat release response. The definition of the projection procedure is summarized in **A.2.15**.

6.1.1 Inspection of Local Flame Responses for 30% Forcing at 240 Hz

Using the conventions presented, the longitudinal distribution of the radially integrated heat release rate responses for forcing at %30 amplitude at 240 Hz are presented in Figs. 6.13 to 6.15 for the PH, PC and MH cases, respectively. REF case is also present in each of the figures as a reference for comparison and all the comparisons are made wrt. to REF case. The normalized time-averaged magnitudes plotted in subplots a in the respective figures show similar trends with the maximum of heat release rate moving upstream as the fraction of hydrogen increases. This is also true for PC cases plotted in Fig.6.14.a however, not nearly as pronounced as hydrogen piloting (PH cases) or hydrogen enrichment (MH cases). Hydrogen is much more effective in reducing flame lengths.

Furthermore, the normalized root-mean-square fluctuations are plotted in Figs. 6.13.b 6.14.b and 6.15.b for PH, PC and MH cases respectively. Here it can be seen that the activity of the flame is shifted upstream with increased levels of hydrogen power fraction, both for PH and MH cases. Although there is a small increase in flame RMS heat release fluctuations at the root of the flames wrt. REF case, however this is not nearly as strong as PH cases. Additionally there is a reduction in flame activity towards the edges of the flames with increased methane injection. One may however note that close to the burner outlet, between $0 \leq z \leq 10$ mm, the redistribution of heat release

towards upstream is much more pronounced with hydrogen piloting than in hydrogen enrichment or methane piloting.

The phases presented in Figs. 6.13.c 6.14.c and 6.15.c, demonstrate that the introduction of hydrogen causes a redistribution of the phase lag between the heat release rate fluctuations and the local heat release rate, however the global change in FTF delays and phases occur as a combined effect of the amplitude and phase redistribution.

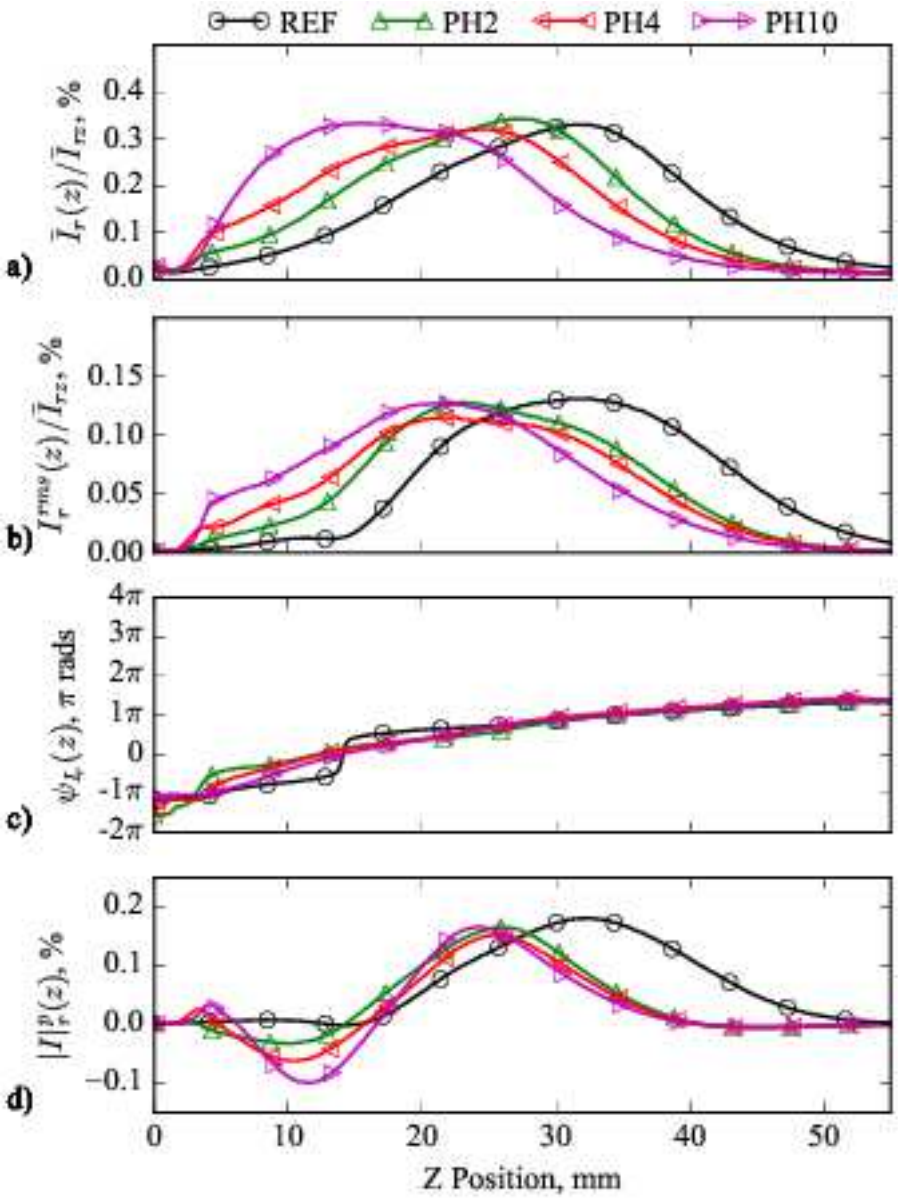

Figure 6.13: Longitudinal evolution of the radially integrated heat release rate for hydrogen piloted (PH) cases forced at 240 Hz with a forcing level of %30. a) normalized time-averaged heat release rate; b) normalized root-mean-square fluctuations; c) phase of heat release fluctuations; d) projection of the radially integrated heat release on the global heat release, U_{sw}=18 m/s, ϕ_G^0=0.8, S=0.33.

Furthermore, in Figs. 6.13.d, 6.14.d and 6.15.d show the projection of complex amplitude of radially integrated heat release fluctuations $\tilde{I}_r(z)$ on complex amplitude of global heat release fluctuations $\tilde{I}_{rz} = \tilde{I}$ are presented. Positive values of $|I|_r^p(z)$ indicate that the local radially integrated heat release fluctuations contributes positively to the global response. Conversely, negative values of $|I|_r^p(z)$ indicate a local contribution that is "pulling backwards" the global response. Additionally, here the effects of the local amplitude of the heat release fluctuations are also accounted for, giving the notion of the strength of the local contribution.

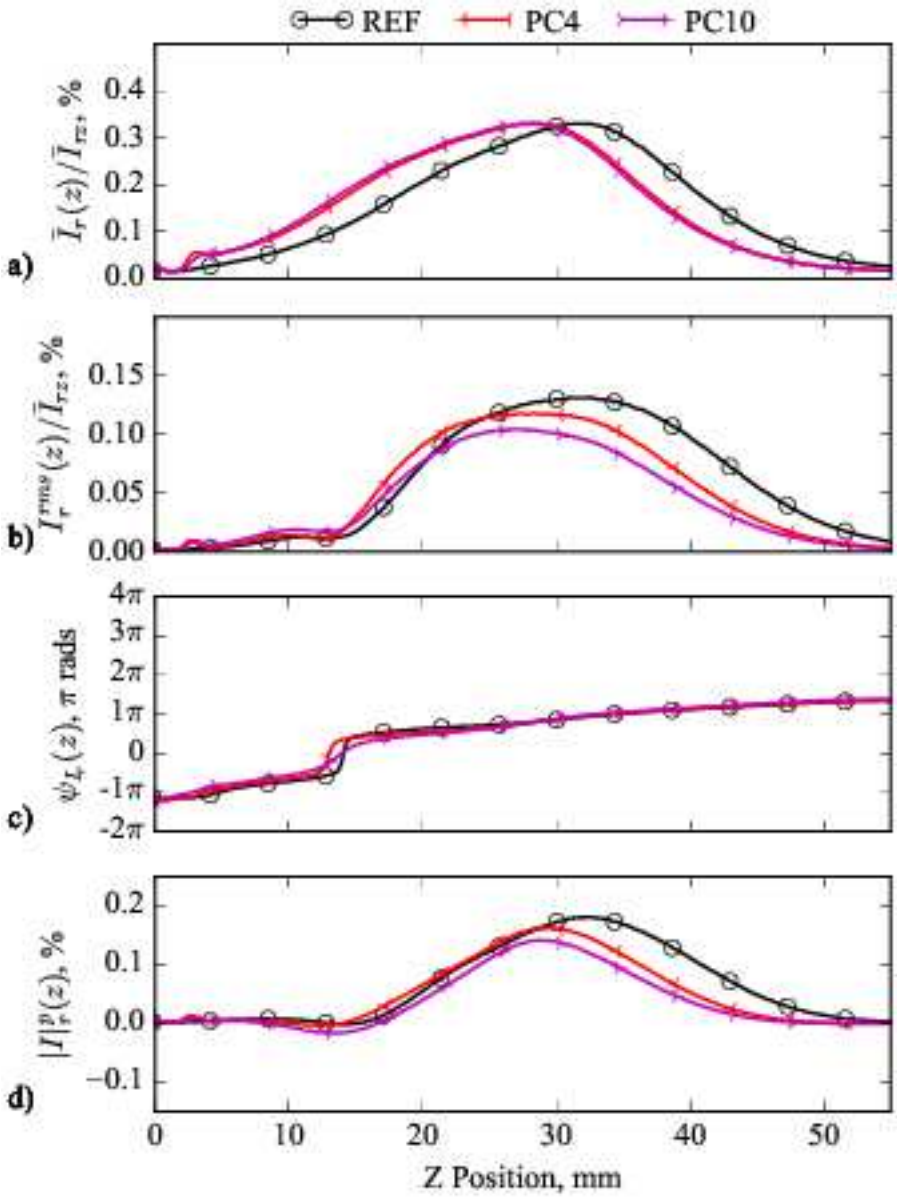

Figure 6.14: Longitudinal evolution of the radially integrated heat release rate for methane piloted (PC) cases forced at 240 Hz with a forcing level of %30. a) normalized time-averaged heat release rate; b) normalized root-mean-square fluctuations; c) phase of heat release fluctuations; d) projection of the radially integrated heat release on the global heat release, U_{sw}=18 m/s, ϕ_G^0=0.8, S=0.33.

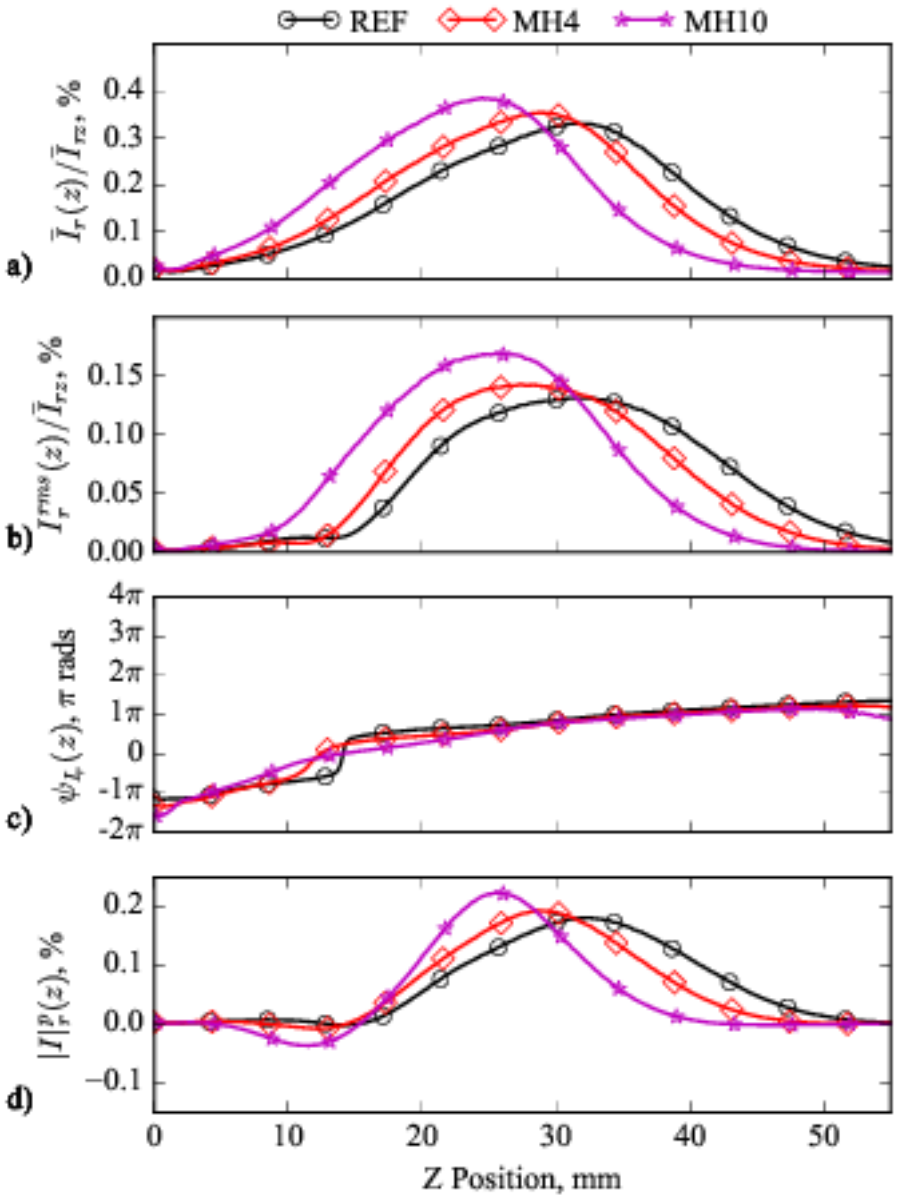

Figure 6.15: Longitudinal evolution of the radially integrated heat release rate for hydrogen enriched (MH) cases forced at 240 Hz with a forcing level of %30. a) normalized time-averaged heat release rate; b) normalized root-mean-square fluctuations; c) phase of heat release fluctuations; d) projection of the radially integrated heat release on the global heat release, U_{sw}=18 m/s, ϕ_G^0=0.8, S=0.33.

For the REF case, this projection is always positive, $|I|_r^p(z) \geq 0$, meaning that there is no competition between the local heat release rates affecting the global heat release response. With hydrogen piloting (PH cases), a competition between the roots and the edges of the flames occur, which reduces the amplitude of the global heat release response (FTF gain) at 240 Hz as can be observed in Fig. 5.7. This reduction through competition of local heat release responses is proportional to the hydrogen injection fraction. For PC cases, this competition behavior is very discrete, that is it is not the

reason of the drop in the FTF gains, however there is a distributed reduction in heat release response amplitude without a significant change in local and global phases. With hydrogen enrichment, this competition between local responses is also present for high injection fractions (PH10), but not nearly as strong as hydrogen piloted cases.

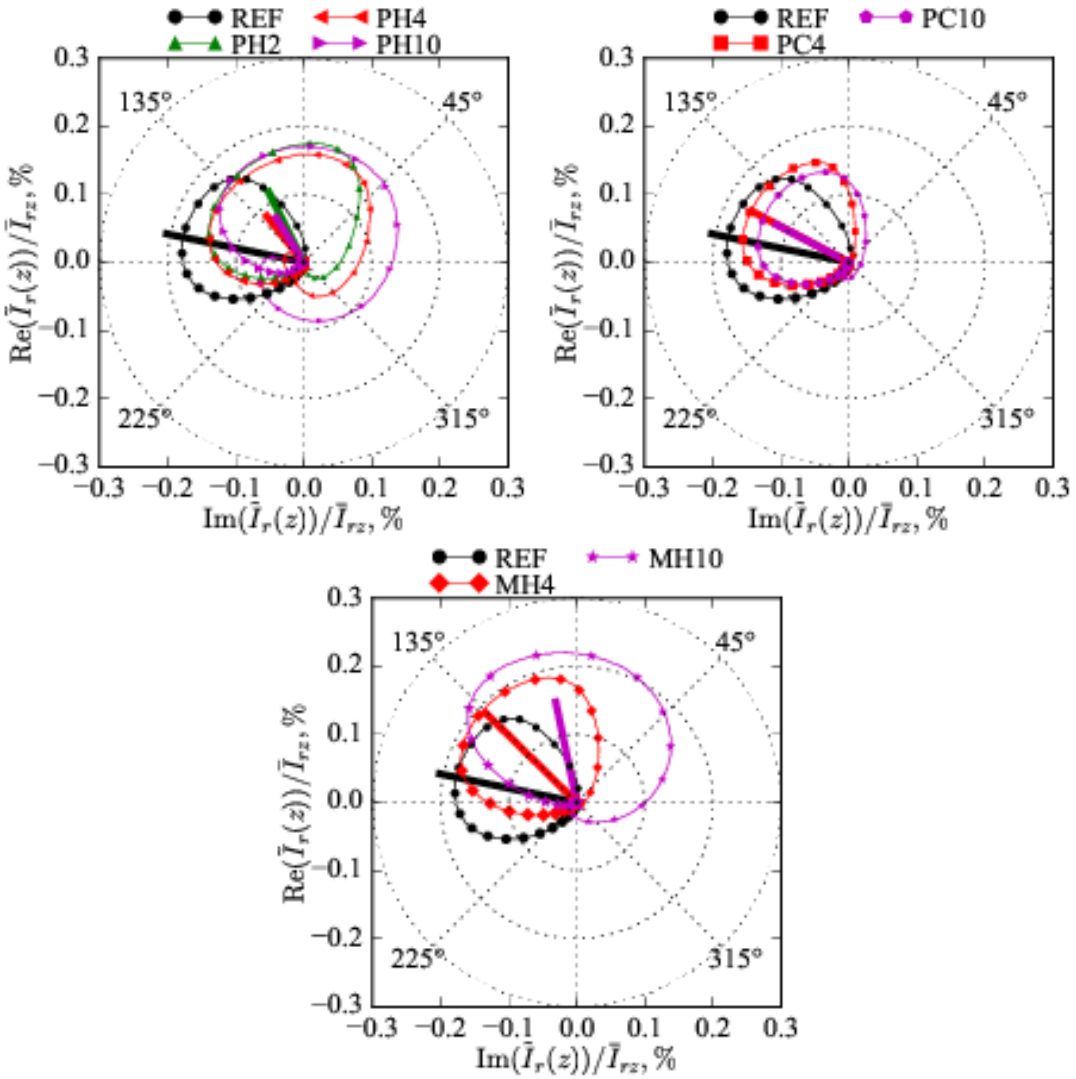

Figure 6.16: Polar plots of the local heat release rate for 30% forcing at 240 Hz. The size of the markers are as a function of the axial distance. The thick lines represent the spatially integrated global response scaled by 1/200, U_{sw}=18 m/s, ϕ_G^0=0.8, S=0.33.

Furthermore, polar plots showing the contribution of each pixel row on the phase and the gain of the global response are shown in Fig. 6.16. The REF case has a guitar pick shape. This shape that lives in a quarter of the polar coordinate plane is an indication that there is limited "pull back effect" (local complex amplitudes that have phase opposition), also true for MH4 case. However for PH cases, the shape resembles more to an apple, which is extended over most of the three quadrants of the polar

plane. As the opposing quadrants mean phase opposition this spread out apple shape is a precursor of the reduction of the global FTF gain and phase. A deformed version of this shape is also present for MH10 case, however this shape is not well spread into opposite quadrants to cause a big effect of "pull back". However because it is spread enough into two quadrants, the phase of the global FTF changes.

6.1.2 Inspection of Local Flame Responses for 30% Forcing at 400 Hz

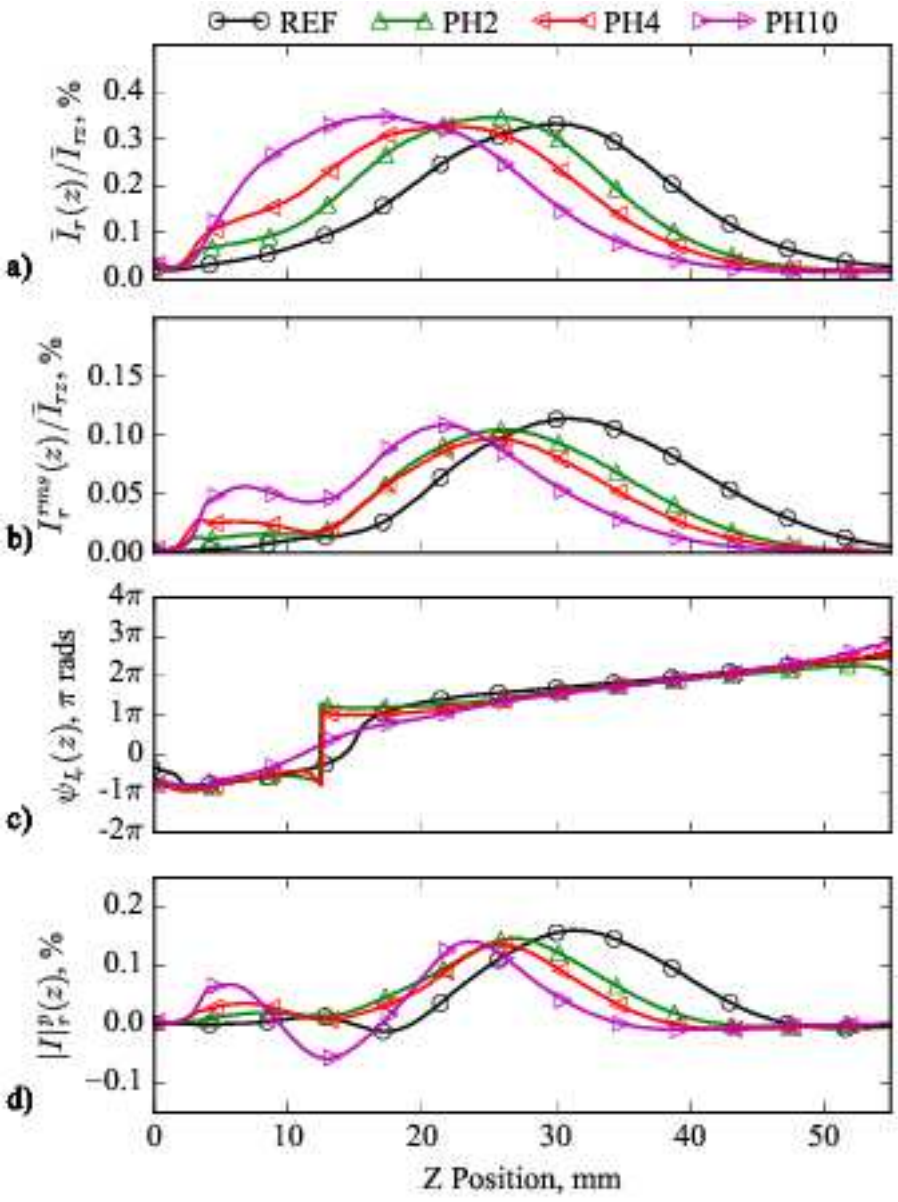

Figure 6.17: Longitudinal evolution of the radially integrated heat release rate for hydrogen piloted (PH) cases forced at 400 Hz with a forcing level of 30%. a) normalized time-averaged heat release rate; b) normalized root-mean-square fluctuations; c) phase of heat release fluctuations; d) projection of the radially integrated heat release on the global heat release, U_{sw}=18 m/s, ϕ_G^0=0.8, S=0.33.

Similarly, the effect of local response to forcing on the global FTF of flames forced at 400 Hz is explored in this section. All the cases are compared to REF case which is plotted in all the figures.

Hydrogen piloted (PH) cases are presented in Fig. 6.17. The effect of hydrogen making flames shorter are visible in Fig. 6.17.a showing profiles of radially integrated time averaged local heat release rates. The roots of the flames also respond stronger as it can be seen in the RMS profiles of radially integrated local heat release demonstrated in Fig. 6.17.b. The phase lag profiles show an interference behavior at around 12 mm axial position, this is due to the competition of the local heat release rate in the radial direction as can be seen in Fig. 6.8. It is also observed that hydrogen injection by 10% of thermal power fraction alters the local phase between 5 mm to 30 mm where most of the heat release occurs. Moreover by inspecting Fig. 6.17.d, it can be seen that the competition behavior between local responses at the root and the edges of the flames similar to forcing at 240 Hz is also present for forcing at 400 Hz. This competition goes in favor of the roots of the flame with increased hydrogen injection fraction.

Methane piloted (PC) cases for 30% forcing at 400 Hz are presented in Fig. 6.18. With methane injection, flames and flame activity mores towards upstream slightly, however the local phases are marginally effected. The artifact in the phase at 15 mm axial position is due to the competition between the local heat release responses in the radial direction as can be seen in Fig. 6.8. Additionally for PC cases the competition behavior between the roots and the edges of the flames is not pronounced.

Hydrogen enriched (MH) cases for 30% forcing at 400 Hz are presented in Fig. 6.19. As discussed before, hydrogen enrichment also makes flames shorter with increased responsivity at the roots of the flames. Furthermore, it also reduces the local phase where significant heat release occurs. For MH cases forced at 400 Hz, there is a very slight competition behavior for MH10 case, the middle of the flame competes with the root and the edge, however not nearly as strong as PH cases. For MH4 case, $|I|_r^p(z) \geq 0$ nearly for all along the axial coordinate.

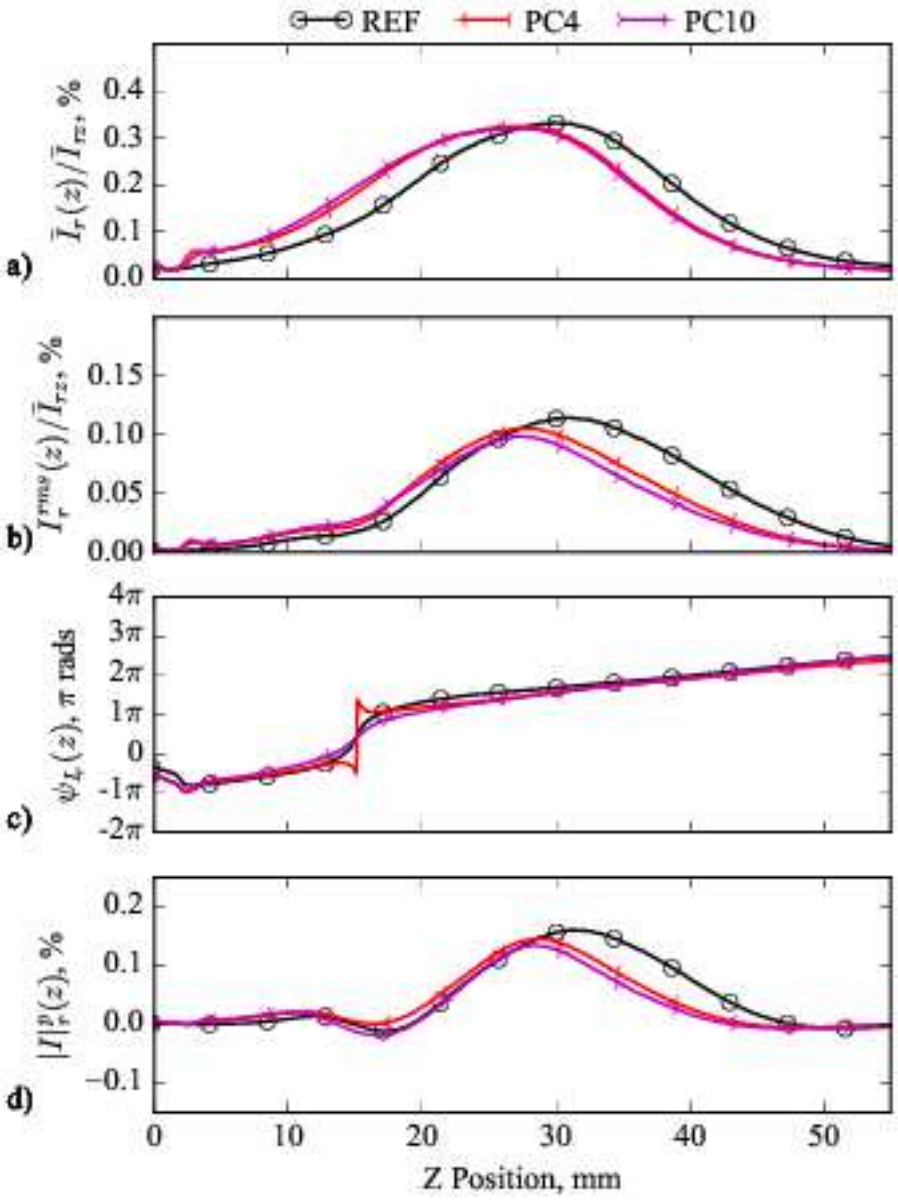

Figure 6.18: Longitudinal evolution of the radially integrated heat release rate for methane piloted (PC) cases forced at 400 Hz with a forcing level of %30. a) normalized time-averaged heat release rate; b) normalized root-mean-square fluctuations; c) phase of heat release fluctuations; d) projection of the radially integrated heat release on the global heat release, U_{sw}=18 m/s, ϕ_G^0=0.8, S=0.33.

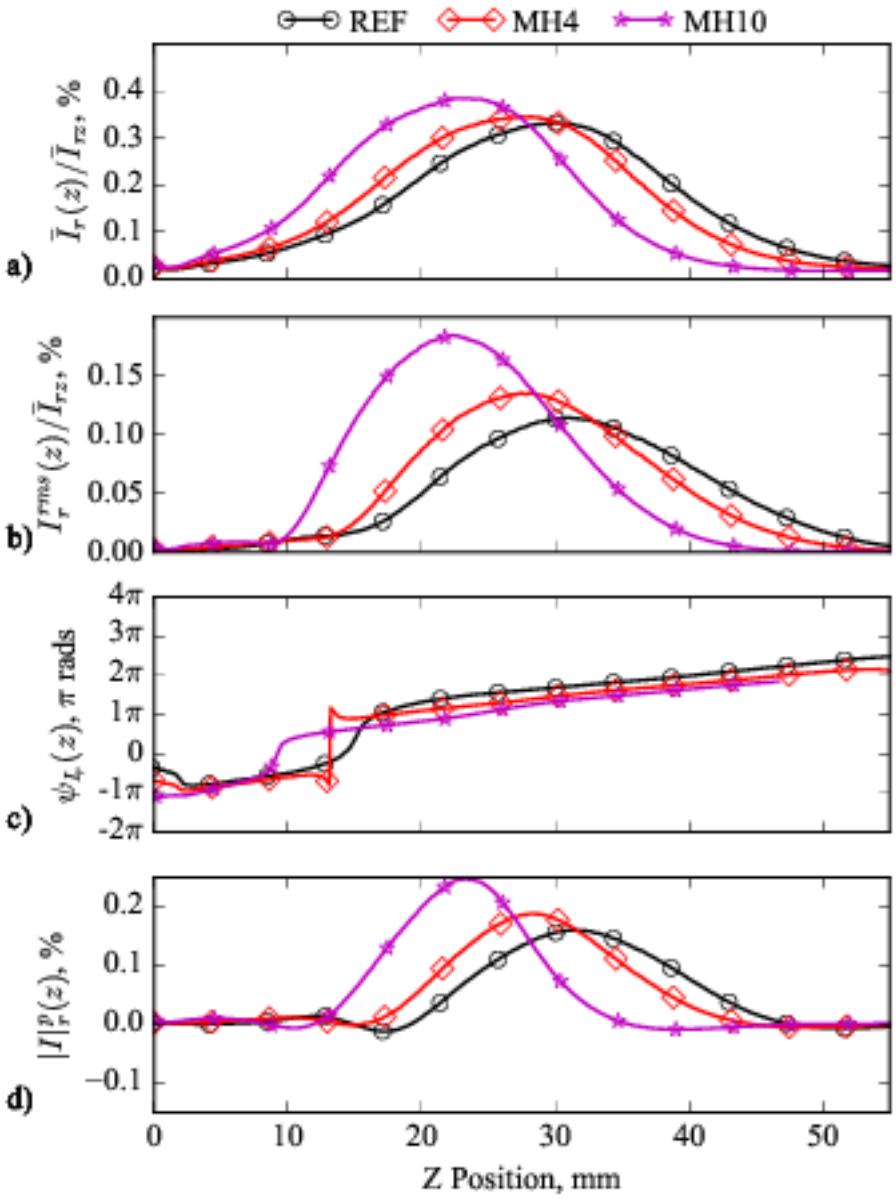

Figure 6.19: Longitudinal evolution of the radially integrated heat release rate for hydrogen enriched (MH) cases forced at 400 Hz with a forcing level of %30. a) normalized time-averaged heat release rate; b) normalized root-mean-square fluctuations; c) phase of heat release fluctuations; d) projection of the radially integrated heat release on the global heat release, U_{sw}=18 m/s, ϕ_G^0=0.8, S=0.33.

Moreover, polar plots showing the contribution of each pixel row on the phase and the gain of the global response are shown in Fig. 6.20. It is observed that MH4 and PH4 cases have nearly the same global phase lag however very different local heat release response profiles. Additionally, MH4 case has nearly 1.5 times the gain of PH4 case. It can also be seen that methane injection modifies the global phase slightly, however increasing methane injection fraction from 4% to 10% does not change the global phase lag, there is a saturation phenomenon. This is not true for hydrogen injection,

increasing hydrogen fraction always reduces FTF phase lag up to 10% power fraction, with redistributed local phase lags.

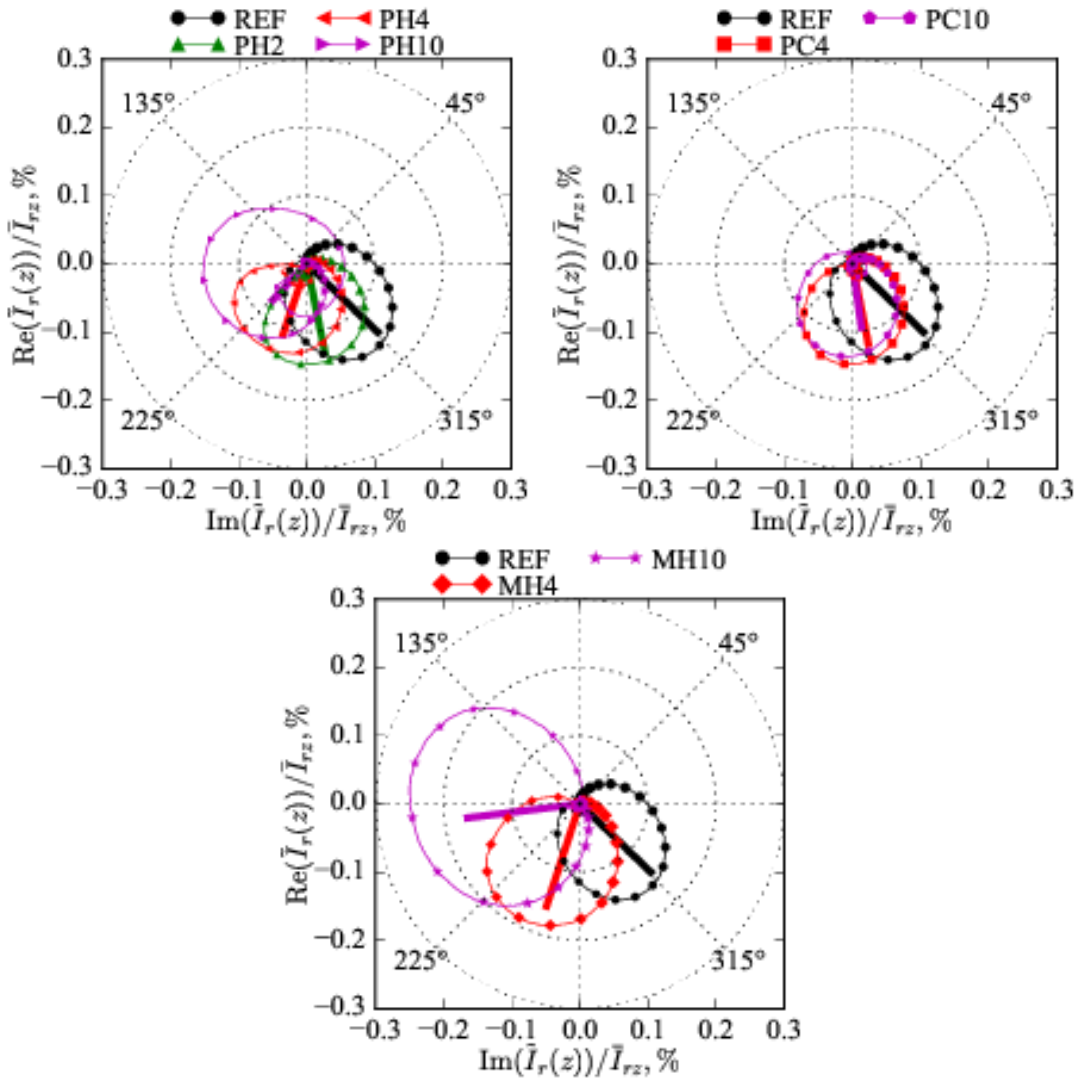

Figure 6.20: Polar plots of the local heat release rate for 30% forcing at 400 Hz. The size of the markers are as a function of the axial distance. The thick lines represent the spatially integrated global response scaled by 1/200, U_{sw}=18 m/s, ϕ_G^0=0.8, S=0.33.

6.1.3 Inspection of Local Flame Responses for 30% Forcing at 590 Hz

Finally, the effect of local response to forcing on the global FTF of flames forced at the frequency of instability (590 Hz) is explored in this section. Axial profiles of radially integrated local heat release rates are plotted in Figs. 6.21 to 6.23.

Similarly, hydrogen injection shortens the flames with increased levels of hydrogen fraction and displaces flame activity upstream as can be seen in time averaged heat release rate and normalized RMS fluctuation profiles in Fig. 6.21. Furthermore, with hydrogen injection, the projection of the radially integrated heat release on the global

heat release shows strong competition behavior for PH10 case, $|I|_r^p(z)$ starts as positive, crosses over to the negative side at 10 mm axial position, and again to positive at 10 mm. This is the reason of the low FTF gains for PH10 case as can be seen in Fig. 5.5 Additionally, for PH2 case, at $|I|_r^p(z)$ is positive along the chamber axis, however there is a drop in heat release rate fluctuation diffused along the chamber axis, which drops the gain of the global FTF.

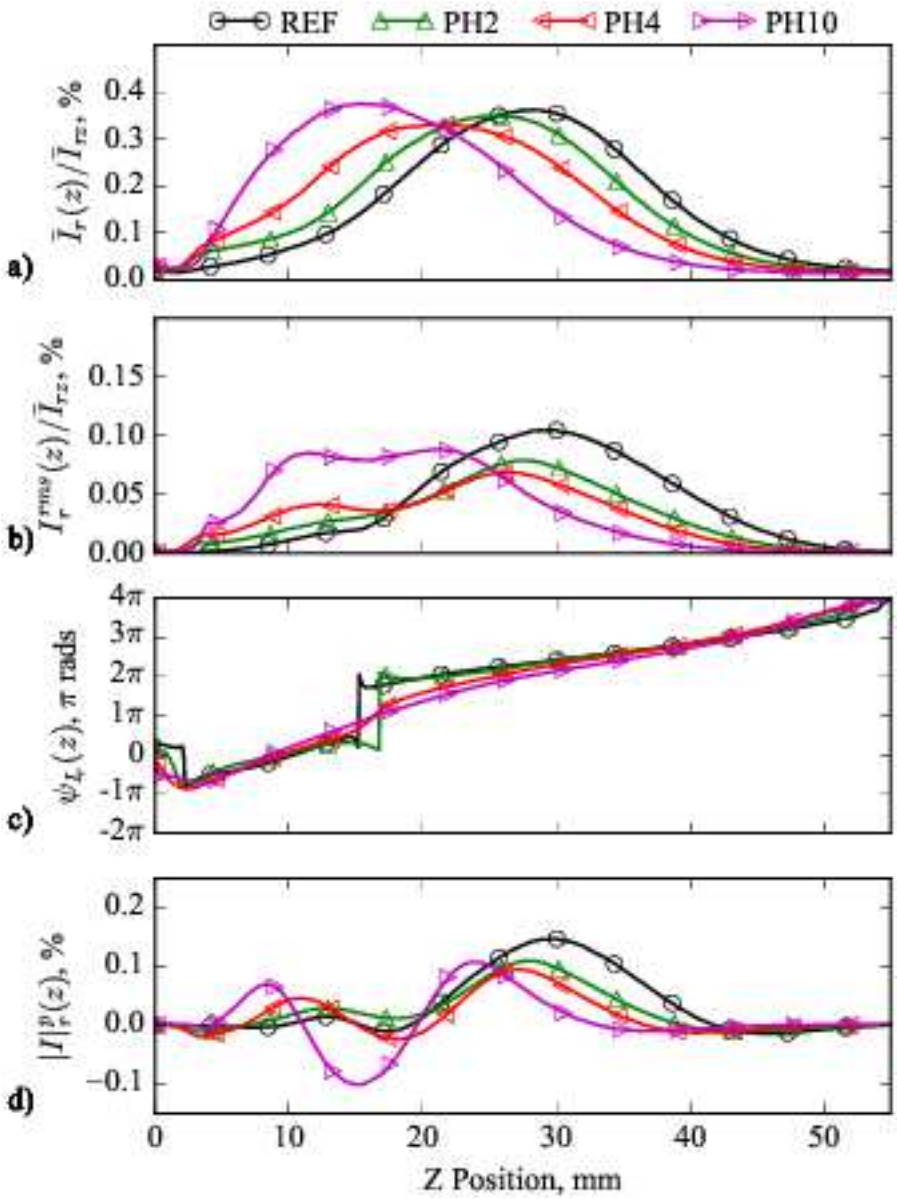

Figure 6.21: Longitudinal evolution of the radially integrated heat release rate for hydrogen piloted (PH) cases forced at 590 Hz with a forcing level of %30. a) normalized time-averaged heat release rate; b) normalized root-mean-square fluctuations; c) phase of heat release fluctuations; d) projection of the radially integrated heat release on the global heat release, U_{sw}=18 m/s, ϕ_G^0=0.8, S=0.33.

For PC4 and PC10 cases presented in Fig. 6.22, the maximums of the time averaged heat release and RMS of the local heat release rates drop and the time averaged heat release rate is shifted upstream. Additionally there is an increase in flame activity at the root of the flames and a drop at the edges. Additionally $|I|_r^p(z)$ is positive along the chamber axis for the two cases, meaning that there is no pull-back effect on the global FTF.

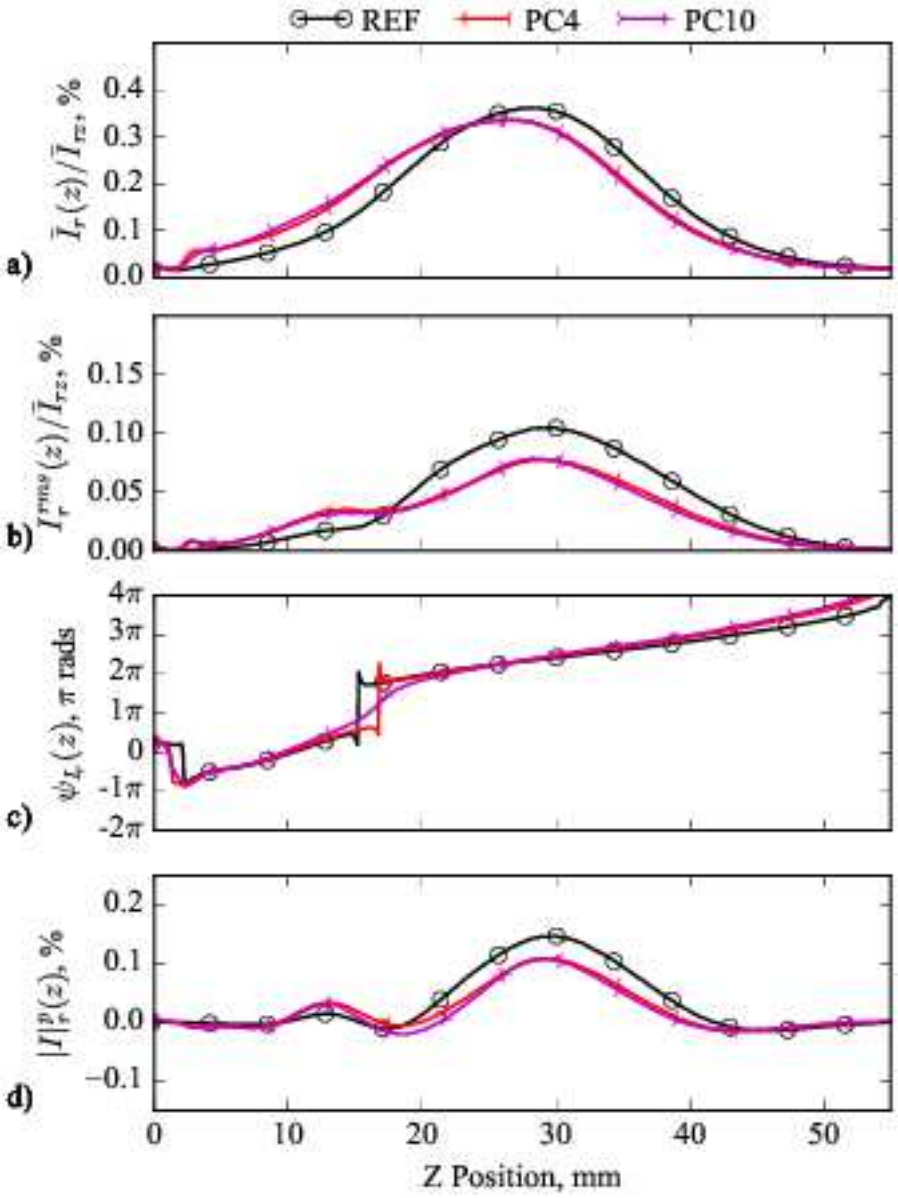

Figure 6.22: Longitudinal evolution of the radially integrated heat release rate for methane piloted (PC) cases forced at 590 Hz with a forcing level of %30. a) normalized time-averaged heat release rate; b) normalized root-mean-square fluctuations; c) phase of heat release fluctuations; d) projection of the radially integrated heat release on the global heat release, U_{sw}=18 m/s, ϕ_G^0=0.8, S=0.33.

With increased hydrogen enrichment, flames respond more violently at 590 Hz. The maximum of RMS of fluctuations increases and is shifted upstream. Furthermore, there is a significant drop in the local phase of the heat release fluctuations. There are axial locations where $|I|_r^p(z)$ is negative indicating that there is pull-back on the global FTF, however $|I|_r^p(z)$ does not fall back too far from zero, meaning that this pull-back behavior is not very strong. Similarly to other cases, the flame is shortened by the addition of hydrogen.

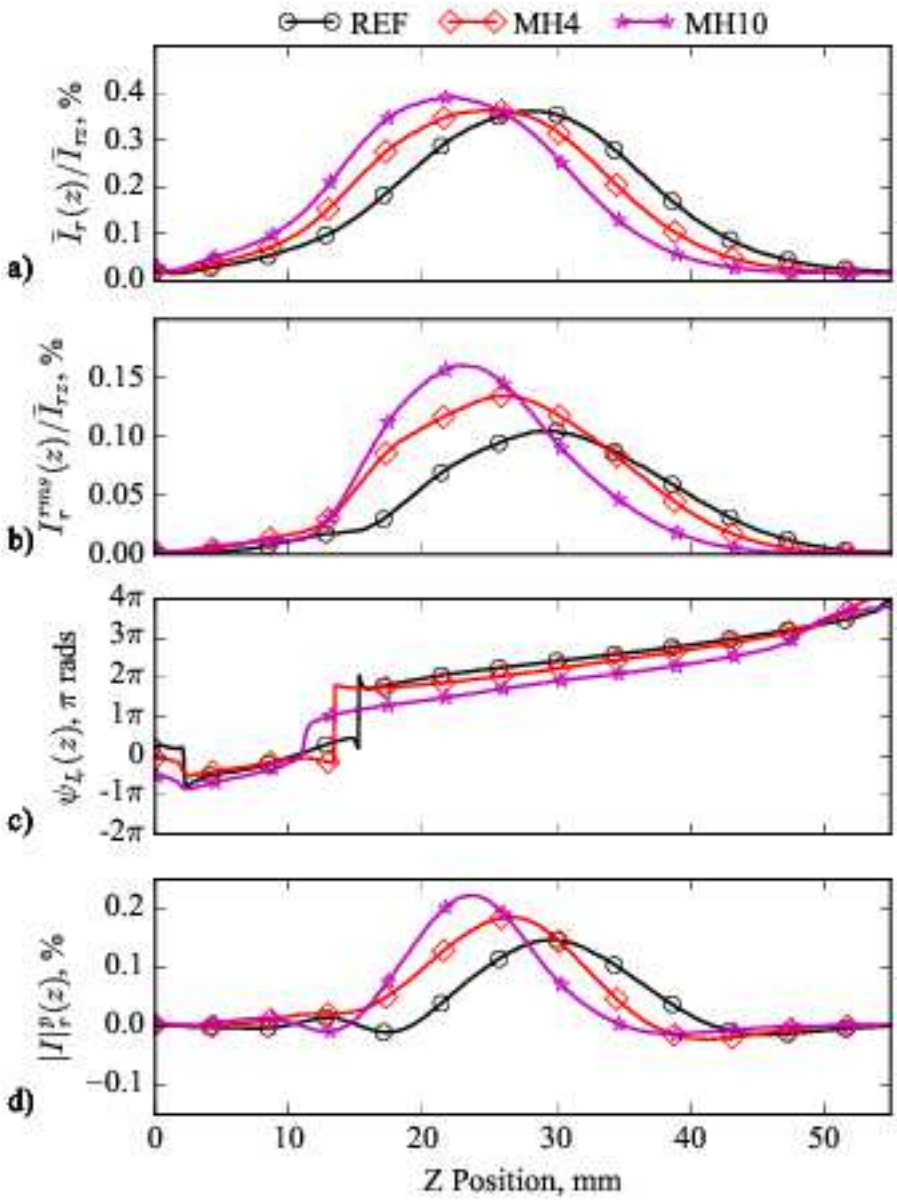

Figure 6.23: Longitudinal evolution of the radially integrated heat release rate for methane piloted (MH) cases forced at 590 Hz with a forcing level of %30. a) normalized time-averaged heat release rate; b) normalized root-mean-square fluctuations; c) phase of heat release fluctuations; d) projection of the radially integrated heat release on the global heat release, U_{sw}=18 m/s, ϕ_G^0=0.8, S=0.33.

Furthermore, the polar plot of the local complex amplitudes of heat release fluctuations are presented in Fig. 6.24. Here it can be seen that with 10% hydrogen injection, there is a strong competition behavior between local heat release rate responses, dropping the global FTF gain and reducing its phase. Methane injection globally lowers the local heat release rate amplitudes at the flame edges, this in turn reduces the gain and the phase of the global FTF. Methane enrichment causes flames that respond more violently throughout the combustion chamber axis with reduced phase lags throughout.

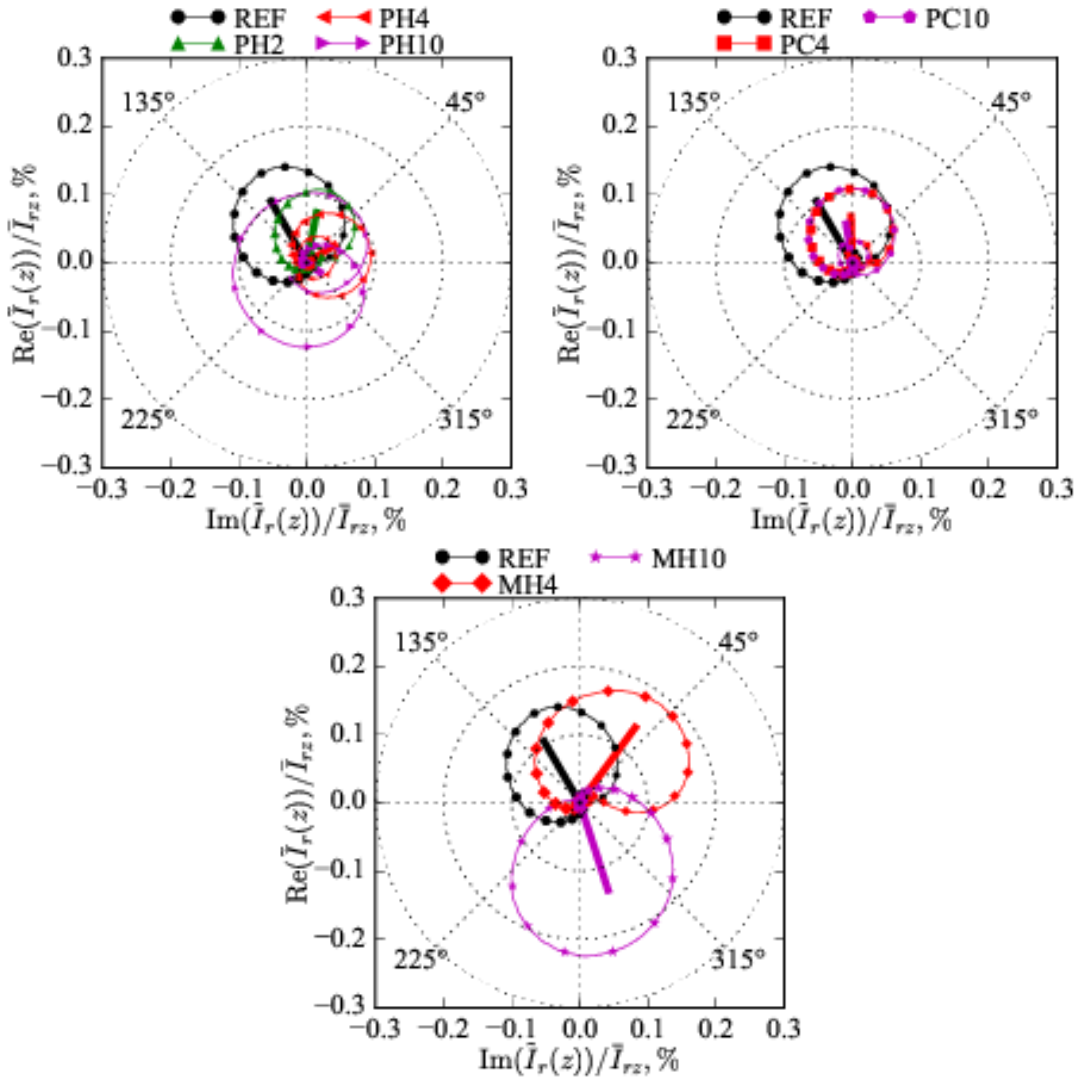

Figure 6.24: Polar plots of the local heat release rate for 30% forcing at 590 Hz. The size of the markers are as a function of the axial distance. The thick lines represent the spatially integrated global response scaled by 1/200, U_{sw}=18 m/s, ϕ_G^0=0.8, S=0.33.

The effectiveness of hydrogen in reducing the phase lag of the neat release response is demonstrated. Next section is reserved for higher forcing levels.

6.1.4 Inspection of Local Flame Responses for 60% Forcing

For forcing at 240 Hz and a forcing level of $\tilde{u}_0/U_{sw} = 0.60$, the phase locked flame images for the REF case are presented in Fig. 6.25. Compared to forcing at $\tilde{u}_0/U_{sw} = 0.30$ (Fig. 6.1), the response of the flame the flame response is much more erratic at $\tilde{u}_0/U_{sw} = 0.60$ forcing. The Vortex roll-up is much more pronounced and the flame edges travel much farther as a result of increased forcing amplitude, the flame flaps its wings much more. For example, comparing two flames at $\approx 30^\circ$ of phase, edges of the REF flame forced at $\tilde{u}_0/U_{sw} = 0.60$ forcing are completely rolled upon themselves (Fig. 6.25), while this rolled up part of the flame edges is much more smaller for forcing at $\tilde{u}_0/U_{sw} = 0.30$ (Fig. 6.1).

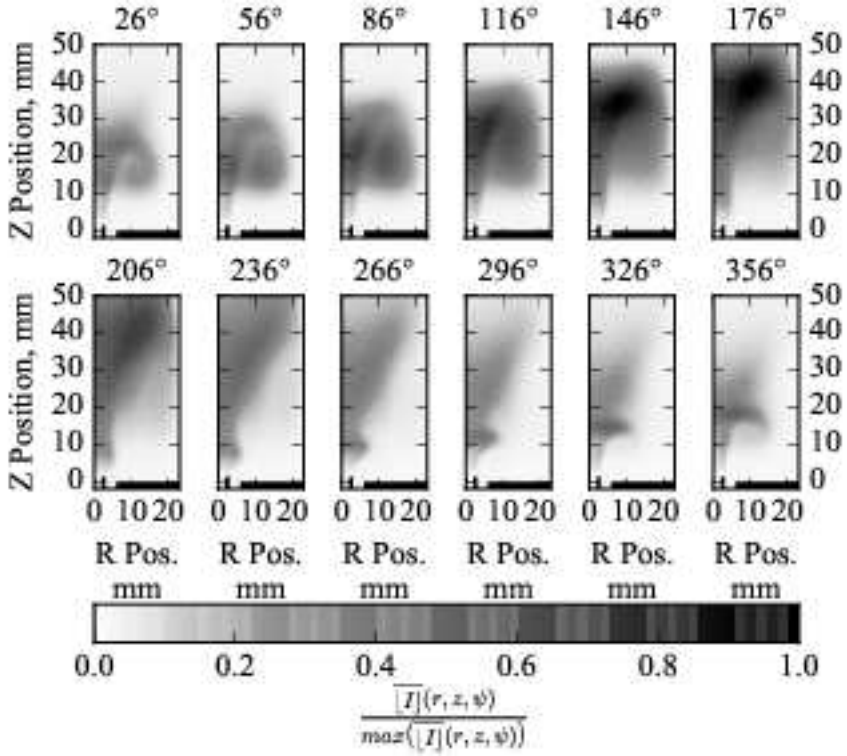

Figure 6.25: Phase locked images of the REF case at a forcing level of $\tilde{u}_0/U_{sw} = 0.60$ at 240 Hz for U_{sw}=18 m/s, ϕ_G^0=0.8, S=0.33.

Furthermore for forcing at 400 Hz and $\tilde{u}_0/U_{sw} = 0.60$, the flame is detached at 236° of phase. The forcing cycle is always sampled with 12 flame images in this thesis and this is the only point (400 Hz, $\tilde{u}_0/U_{sw} = 0.60$, 236°) where the flame is lifted, all other flames forced at 400 Hz with a forcing level of $\tilde{u}_0/U_{sw} = 0.60$ are attached to the injection tube for all instances recorded. Furthermore, there is no residual heat release rate signal near the injection tube in the 236° phase image, indicating that this behavior

is repeatable for each cycle. This partial lifting at one instance of the forcing cycle can be interpreted as a precursor, this flame becomes more susceptible to detachment when the forcing frequency is increased for a constant level of forcing.

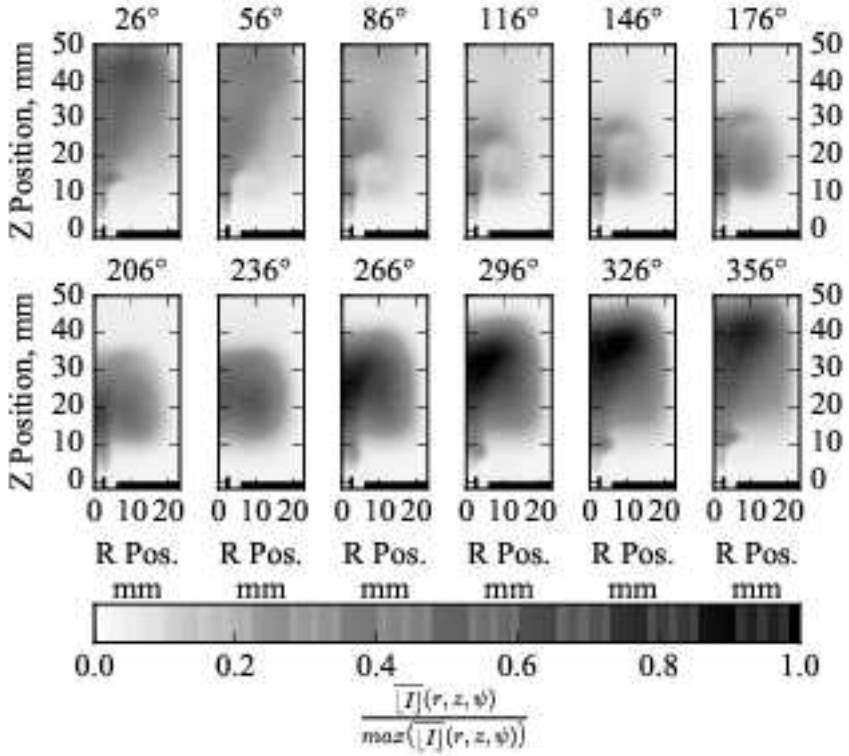

Figure 6.26: Phase locked images of the REF case at a forcing level of $\tilde{u}_0/U_{sw} = 0.60$ at 400 Hz for U_{sw}=18 m/s, ϕ_G^0=0.8, S=0.33.

When the forcing frequency is increased to 590 Hz the REF flame is detached for all instances of the forcing cycle as presented in Fig.6.27. The forced flame has no longer the distorted V-shape and resembles a distorted ball. Again, the non-presence of residual heat release signal near the injection tube means that the flame is lifted throughout the forcing cycle. The flame still responds to a vortex, however, the vortex roll-up less pronounced, as there is no attached root of the flame. In Fig.6.28, Inverse Abel transformed flame images are presented, where the presence of the vortex can be clearly seen.

This detachment from the injection tube causes a drop in FTF gain and an increase in FTF phase as can be seen in Fig.5.6. At 450 Hz there is a deflection and a drop in FTF gain and a slight increase in FTF phase for REF case; after this point the forced flames are detached at the base.

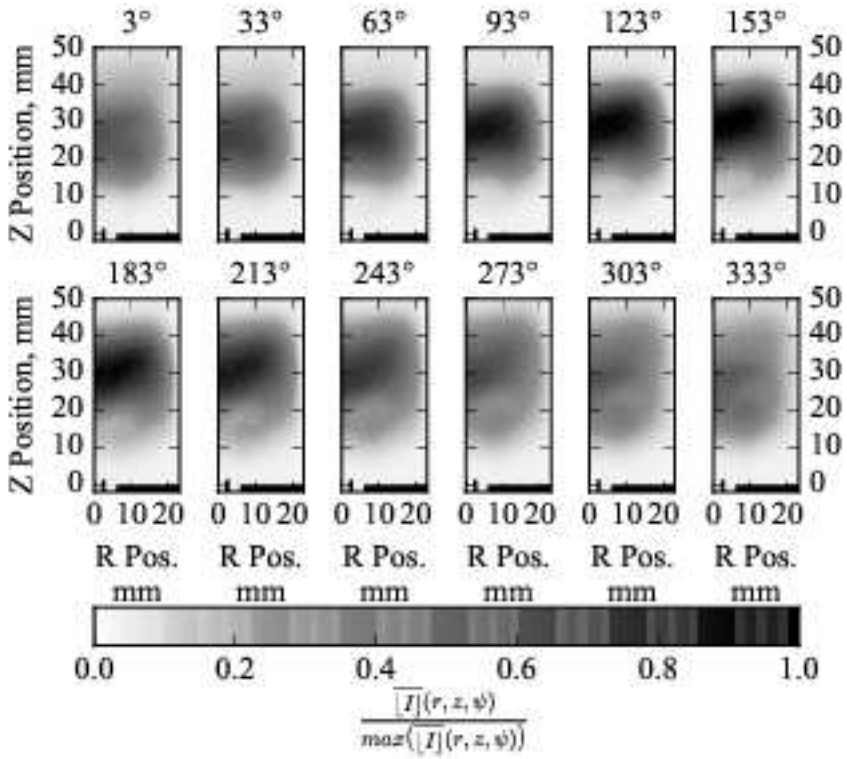

Figure 6.27: Phase locked images of the REF case at a forcing level of $\tilde{u}_0/U_{sw} = 0.60$ at 590 Hz for U_{sw}=18 m/s, ϕ_G^0=0.8, S=0.33.

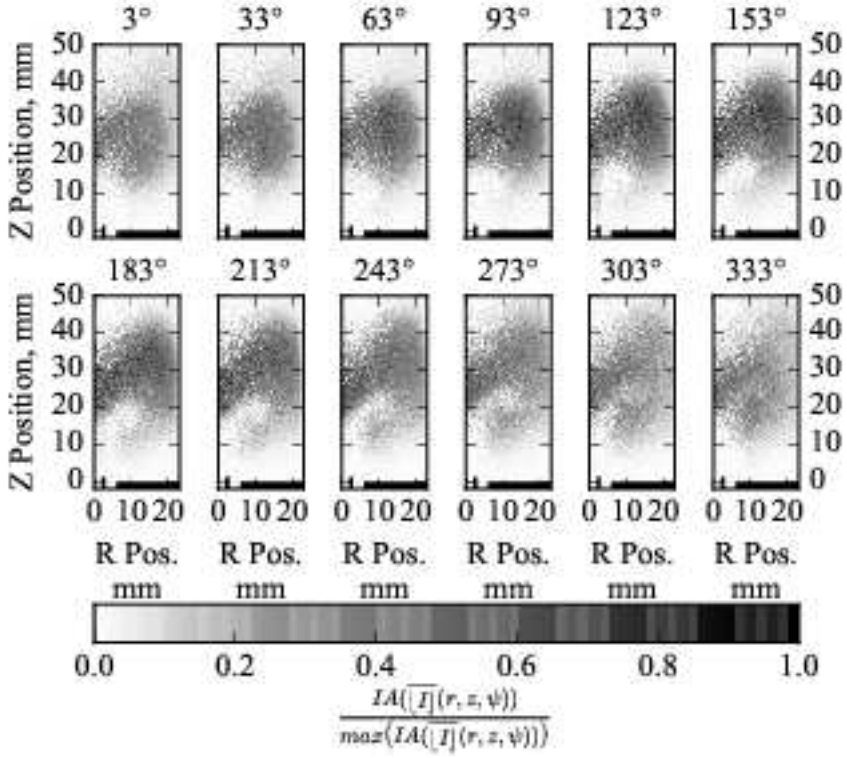

Figure 6.28: Inverse Abel Transformed phase locked images of the REF case at a forcing level of $\tilde{u}_0/U_{sw} = 0.60$ at 590 Hz for U_{sw}=18 m/s, ϕ_G^0=0.8, S=0.33. $IA\left(\overline{[I]}(r,z,\psi)\right)$ designates phase averaged inverse Abel Transformed CH* chemiluminescent light emission.

With 2% hydrogen injection (PH2), this detachment behavior is completely suppressed, flames are strongly attached to the injection tube as presented in Fig. 6.29.

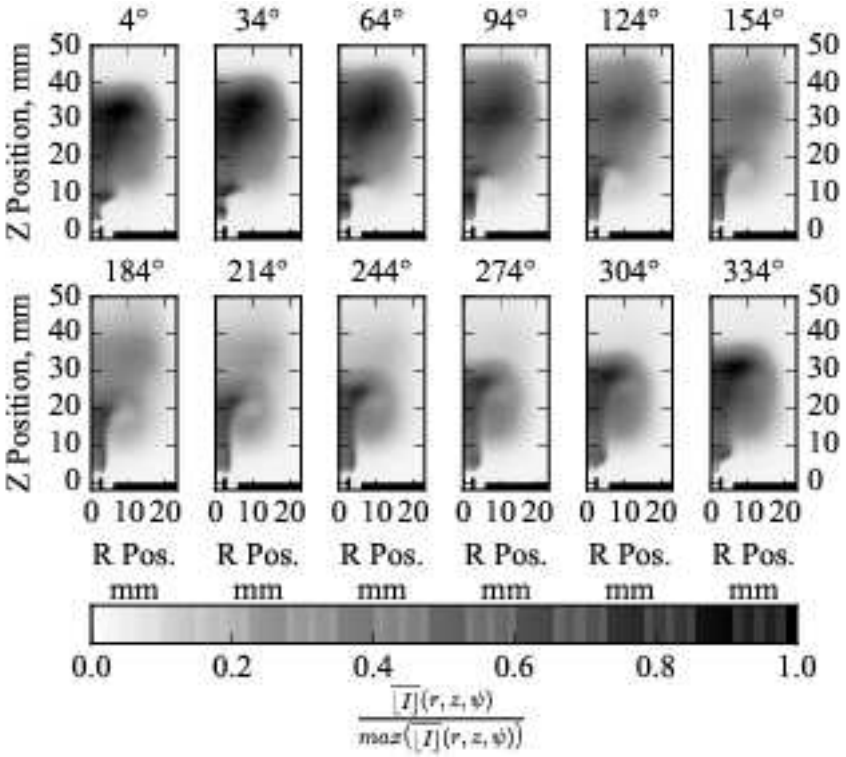

Figure 6.29: Phase locked images of the PH2 case at a forcing level of $\tilde{u}_0/U_{sw} = 0.60$ at 590 Hz for U_{sw}=18 m/s, ϕ_G^0=0.8, S=0.33.

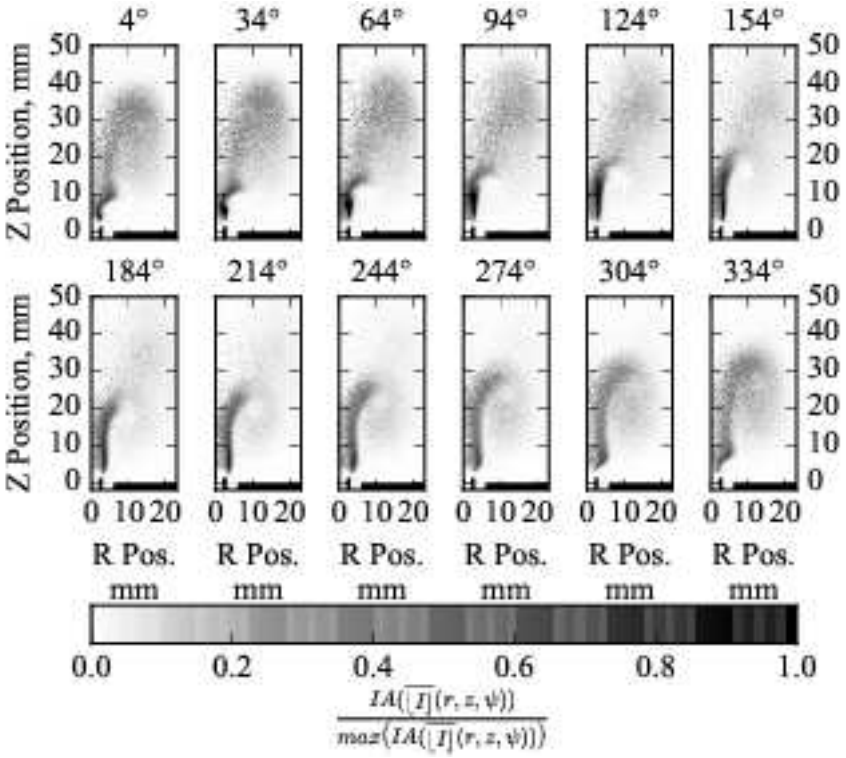

Figure 6.30: Inverse Abel Transformed phase locked images of the PH2 case at a forcing level of $\tilde{u}_0/U_{sw} = 0.60$ at 590 Hz for U_{sw}=18 m/s, ϕ_G^0=0.8, S=0.33. $IA\left(\overline{\lfloor I \rfloor}(r,z,\psi)\right)$ designates phase averaged inverse Abel Transformed CH* chemiluminescent light emission.

This shows the ability of hydrogen in resisting lift-off; even for a very low hydrogen power fraction of $\mathscr{P}_{H_2}$=0.02. For a better comparison Inverse Abel transformed images are also shown in Fig. 6.30. Here the roll-up of the edge of the flame is clearly present as there is a clear root of the flame.

However when 2% of hydrogen in thermal power is fully premixed with the flow (MH2 case, Fig. 6.31), the flame is still lifted-off. Hydrogen enrichment to methane-air mixtures increases the resistance to strain of the mixture, however for this case this slight increase is not enough to attach the flame.

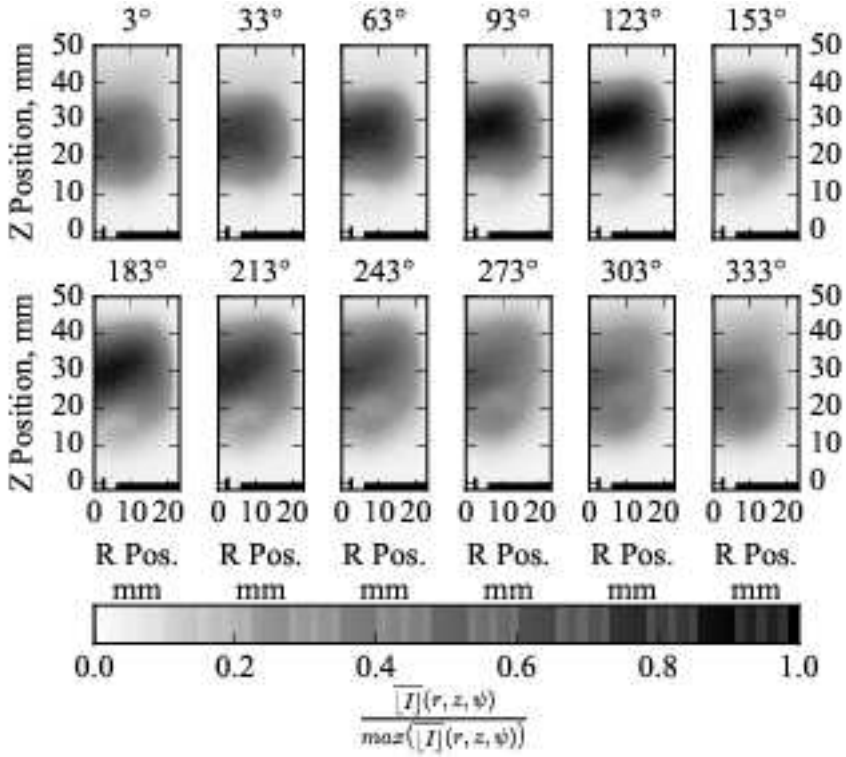

Figure 6.31: Phase locked images of the MH2 case at a forcing level of $\tilde{u}_0/U_{sw} = 0.60$ at 590 Hz for U_{sw}=18 m/s, ϕ_G^0=0.8, S=0.33.

In Fig. 6.32 hydrogen enriched by 4% power fraction is presented. Here it can be seen that 4% of hydrogen enrichment is enough to attach the flame. As hydrogen flames are much more resistant to strain compared to methane flames, the increase of hydrogen fraction in hydrogen-methane-air flames increases the resistance to strain.

Furthermore, in Fig. 6.33, PC10 case with 10% methane piloting is presented. Even-though the injection power fraction is much higher, methane does not succeed in attaching the flame root. The flame is lifted-off and resembles very closely REF case. This is partly because of partial premixing of the injected methane before combustion, as the flame is further downstream. The proves that hydrogen is much more efficient in

stabilization of flames even in the presence of perturbations. While hydrogen piloted flame is attached to the injection tube, methane piloted flame is lifted-off.

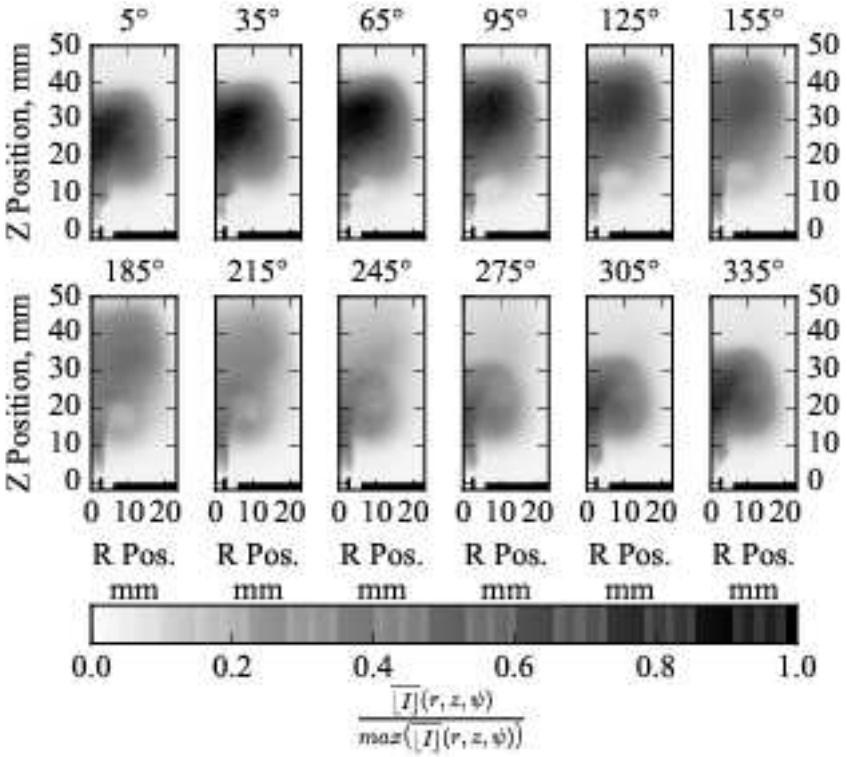

Figure 6.32: Phase locked images of the MH4 case at a forcing level of $\tilde{u}_0/U_{sw} = 0.60$ at 590 Hz for U_{sw}=18 m/s, ϕ_G^0=0.8, S=0.33.

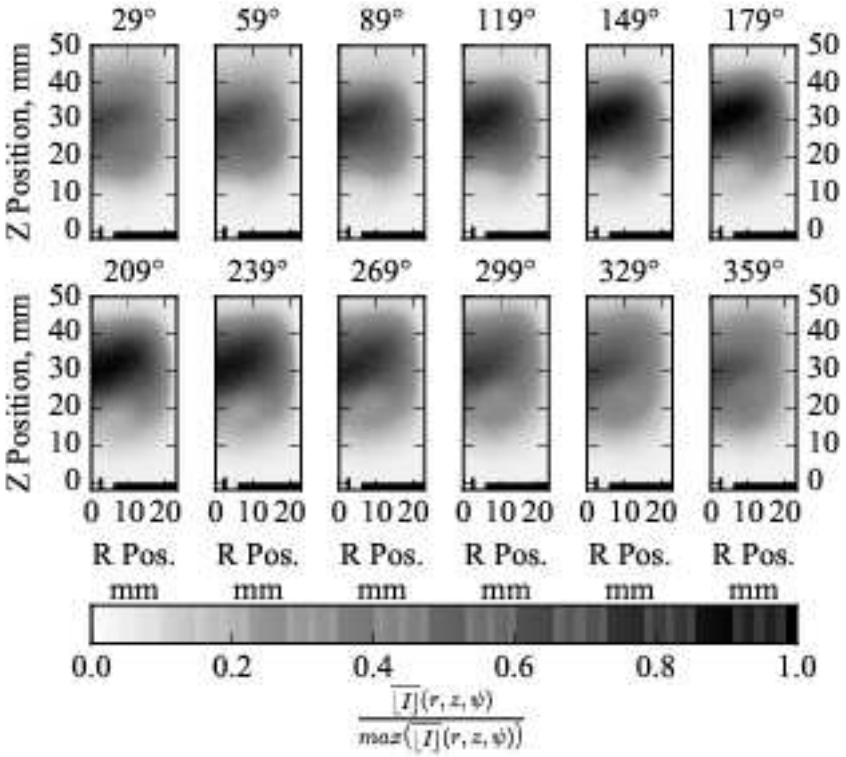

Figure 6.33: Phase locked images of the PC10 case at a forcing level of $\tilde{u}_0/U_{sw} = 0.60$ at 590 Hz for U_{sw}=18 m/s, ϕ_G^0=0.8, S=0.33.

6.2 Spatial Spectral Analysis of Flame Responses for 35° Swirler, D_c=46 mm Combustion Chamber

In this section a brief analysis of the high swirl cases will be presented. When swirl is increased, the flames become shorter, therefore the delay of the flame response decreases as the disturbance has less axial distance to travel to traverse the flame. In this section the scope is fixed to forcing at 240 Hz and a level of 30%. This is where

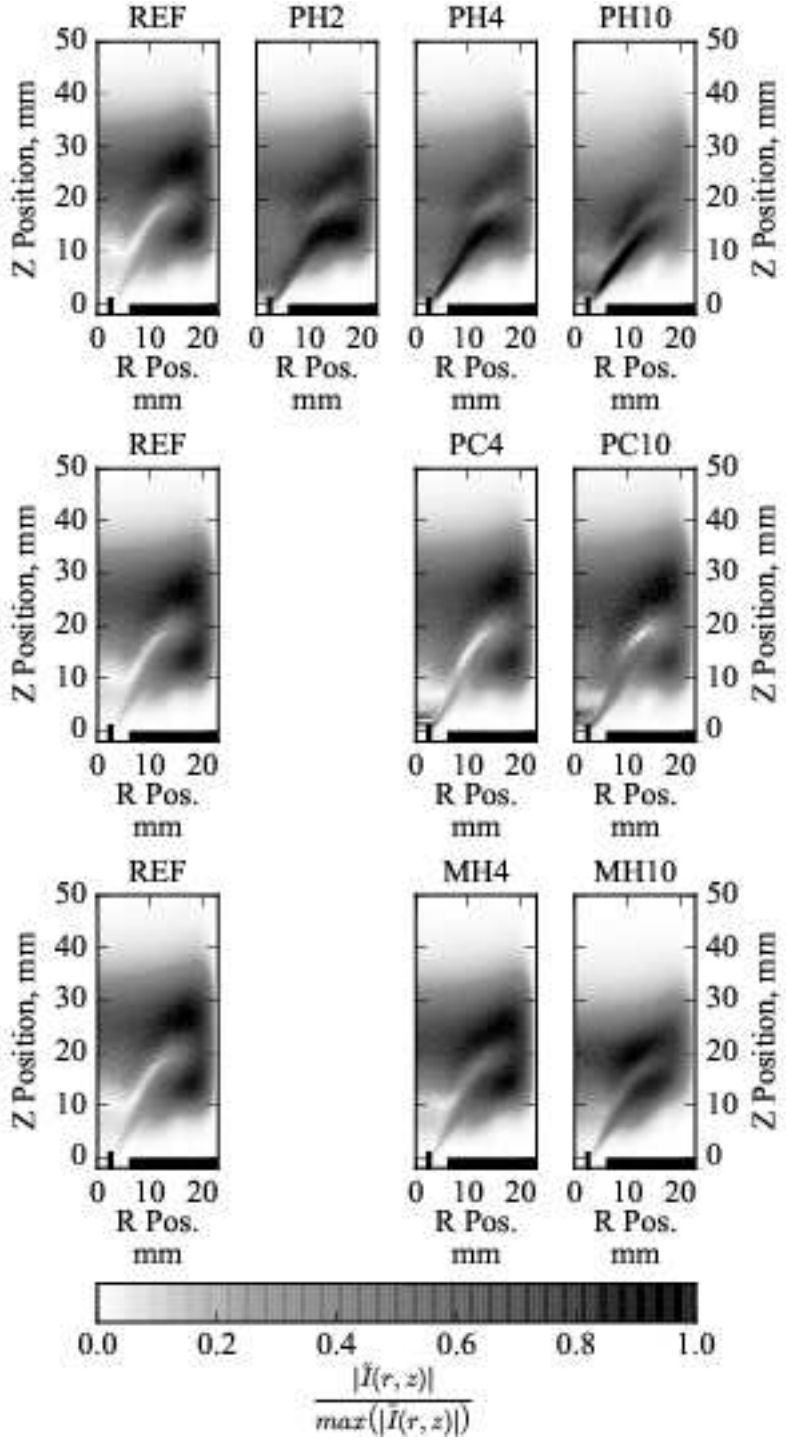

Figure 6.34: Amplitudes of the complex heat release signal with acoustic forcing, $\tilde{u}_0/U_{sw} = 0.30$ at 240 Hz for U_{sw}=18 m/s, ϕ_G^0=0.8, S=0.86.

the dip in the FTF occurs with hydrogen injection as can be seen in Fig. 5.7. Performing a similar analysis, the resulting heat release rate amplitudes are presented in Fig. 6.34. Here, it can be seen that not only the flame length gets shorter with hydrogen (Fig. 3.8), also the flame activity is shifted upstream. Additionally, there are node like structures, where the amplitude is nearly zero, which are not present with the lower swirl configuration of S=0.33 (Fig. 6.4) for the same forcing level and frequency.

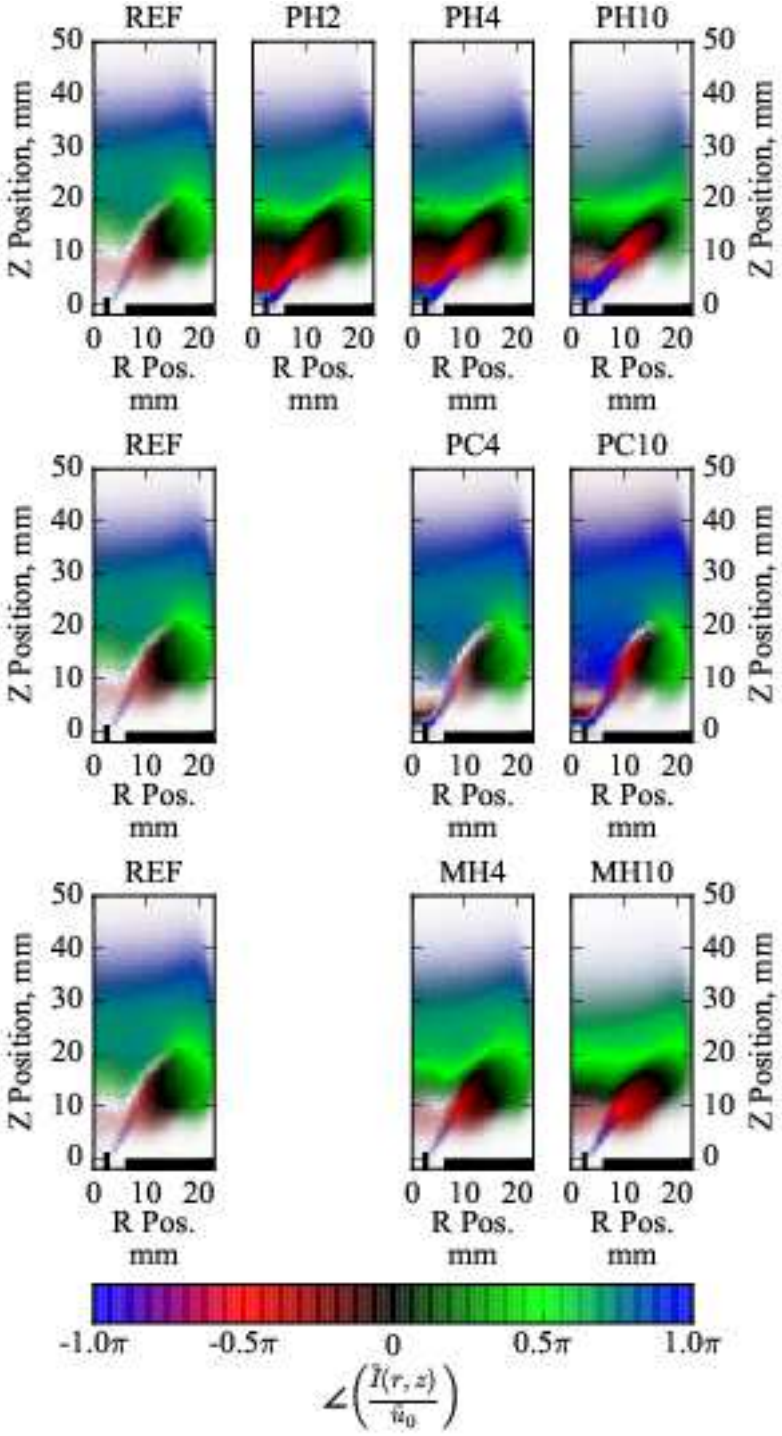

Figure 6.35: Phases wrt. velocity at the burner outlet of the complex flame response to acoustic forcing, $\tilde{u}_0/U_{sw} = 0.30$ at 240 Hz for U_{sw}=18 m/s, ϕ_G^0=0.8, S=0.86.

Next the delays are presented in Fig. 6.35. The effect of shortening of the flames with increased swirl can also be observed here. Furthermore the phases are much less uniform in the radial direction for all cases compared to low swirl configuration. For example for REF case at 10 mm axial location, the phase changes from $-\pi/2$ to $\pi/2$ going from center to chamber walls. Obviously this creates a competitive behavior between the amplitudes and causes a drop in the FTF gain. This is even more pronounced for 10% methane injection (PC10 case), at 15 mm axial location, the phase goes from $-\pi$ to $\pi/2$ following from center to chamber walls.

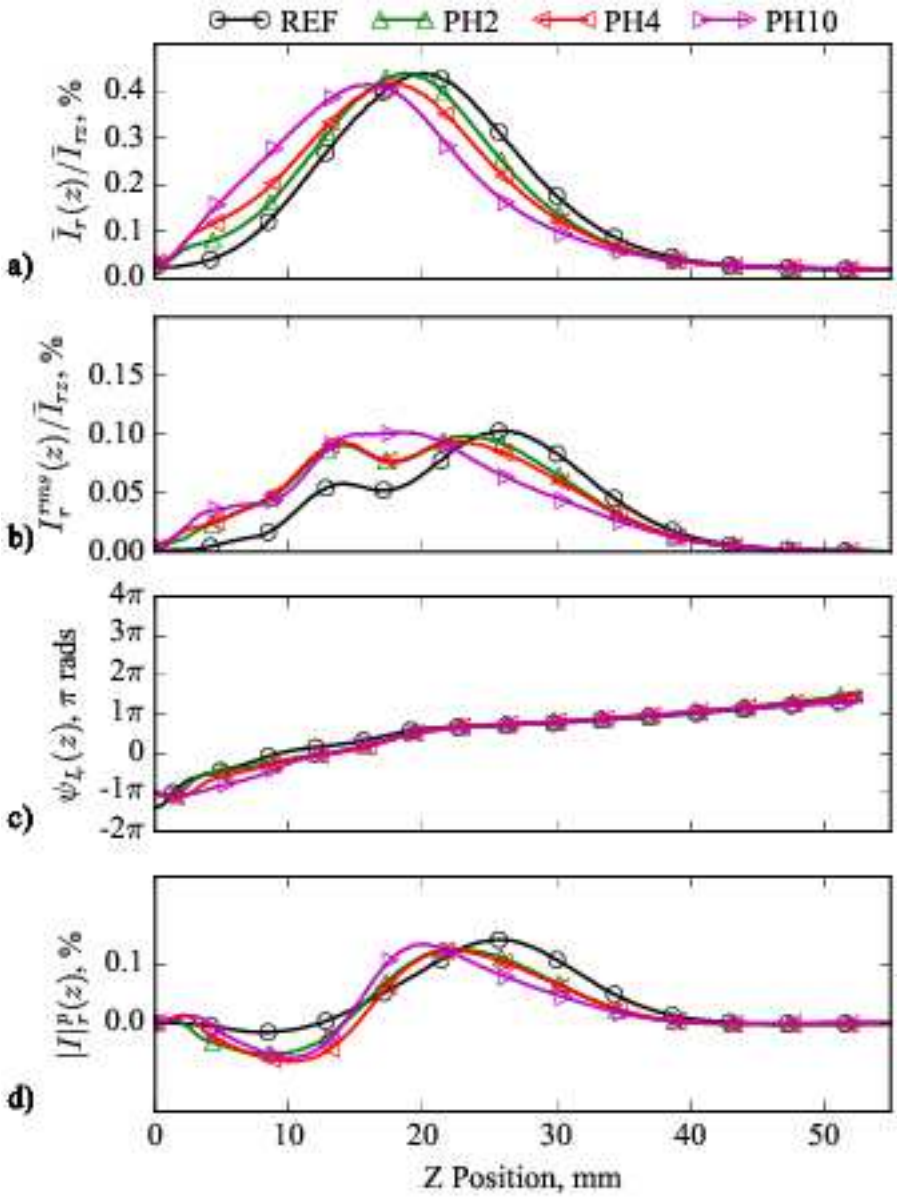

Figure 6.36: Longitudinal evolution of the radially integrated heat release rate for hydrogen piloted (PH) cases forced at 240 Hz with a forcing level of %30. a) normalized time-averaged heat release rate; b) normalized root-mean-square fluctuations; c) phase of heat release fluctuations; d) projection of the radially integrated heat release on the global heat release, U_{sw}=18 m/s, ϕ_G^0=0.8, S=0.86.

Using the same technique, the longitudinal distribution of the radially integrated heat release rate responses for forcing at %30 amplitude and 240 Hz are presented in Figs. 6.36 to 6.38 for the PH, PC and MH cases, respectively.

First of all, by comparing the high swirl cases of S=0.86 (Figs 6.36 to 6.38) to the low swirl cases of S=0.33 (Figs 6.13 to 6.15), it can be seen that increased swirl shortens the flames and increases the maximum of the radially integrated time averaged heat release rate, resulting in flames that are more compact and more intense. However the local delays are nearly identical, suggesting that the reduction of the phase with increased swirl is due to the redistribution of the heat release amplitudes rather than reduction in the local phase.

Examining Fig. 6.36, it can be seen that hydrogen injection once again results in shorter flames, but also increases heat release response activity at the base of the flames. Additionally local phases are not greatly affected by hydrogen injection. Moreover, the flames respond as strongly with hydrogen injection (Fig. 6.36.b), however looking at the projection of the radially integrated heat release on the global heat release, it can be seen that the reduction in the global FTF at 240 Hz (Fig. 5.7) is due to this competition behavior between different axial locations explained earlier.

PC cases with methane injection are presented in Fig. 6.37. Similar to low swirl cases, methane injection reduces slightly the maximum of the mean local heat release (Fig. 6.37.a) and reduces the flame activity along the chamber axis (Fig. 6.37.b). Local phases are not greatly effected and the artifact at 8 mm axial distance is caused by the competition of the complex amplitudes in the radial direction as can be observed in Fig. 6.35. There is no axial competition between local heat release responses, as $|I|_r^p(z) \geq 0$ nearly for all along the axial coordinate in Fig. 6.37.d.

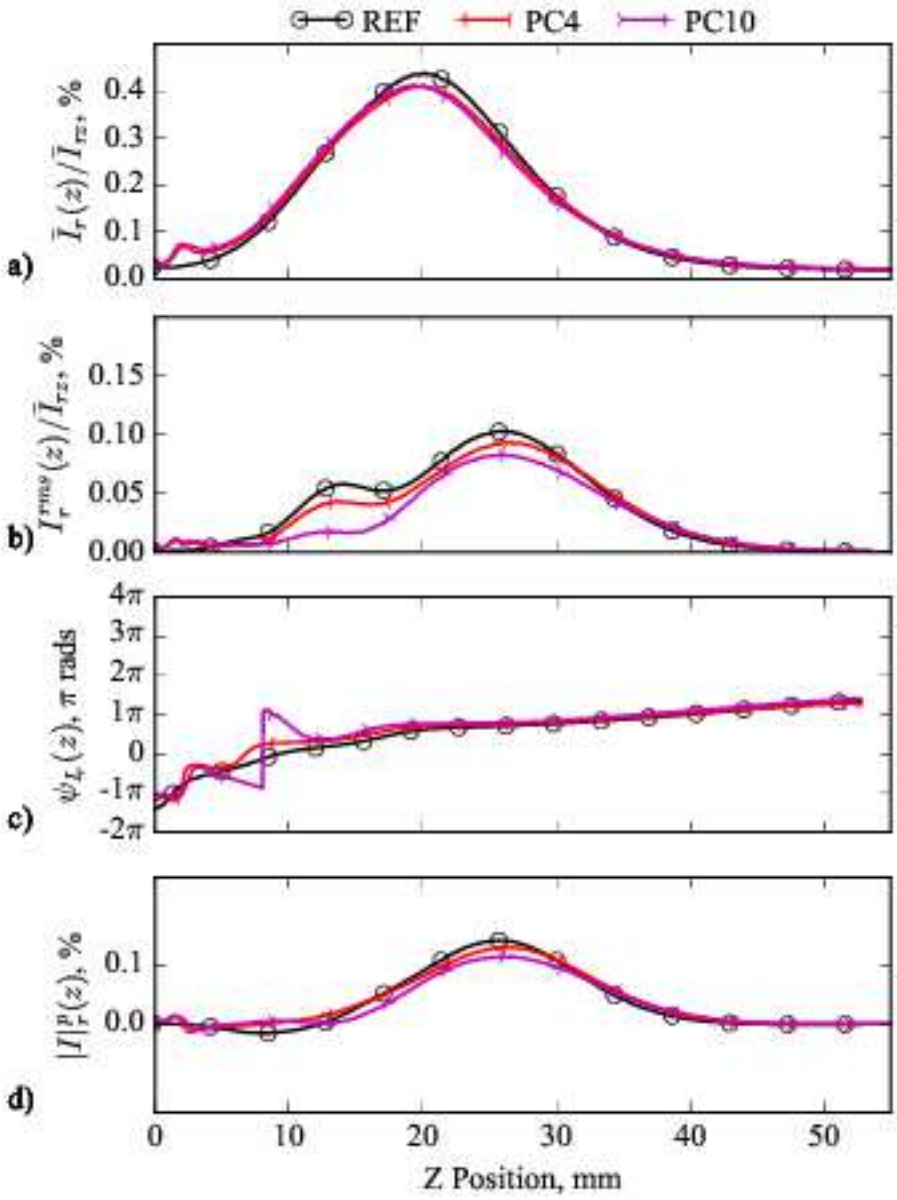

Figure 6.37: Longitudinal evolution of the radially integrated heat release rate for methane piloted (PC) cases forced at 240 Hz with a forcing level of %30. a) normalized time-averaged heat release rate; b) normalized root-mean-square fluctuations; c) phase of heat release fluctuations; d) projection of the radially integrated heat release on the global heat release, U_{sw}=18 m/s, ϕ_G^0=0.8, S=0.86.

For MH cases, hydrogen injection increases the maximum of the mean heat release presented in Fig. 6.38.a and RMS of fluctuations presented in Fig. 6.38.b. Local delays are not affected at all. For MH10 case there is competition between local heat release responses as can be seen in Fig. 6.38.d where $|I|_r^p(z)$ drops below zero 5 mm to 12 mm.

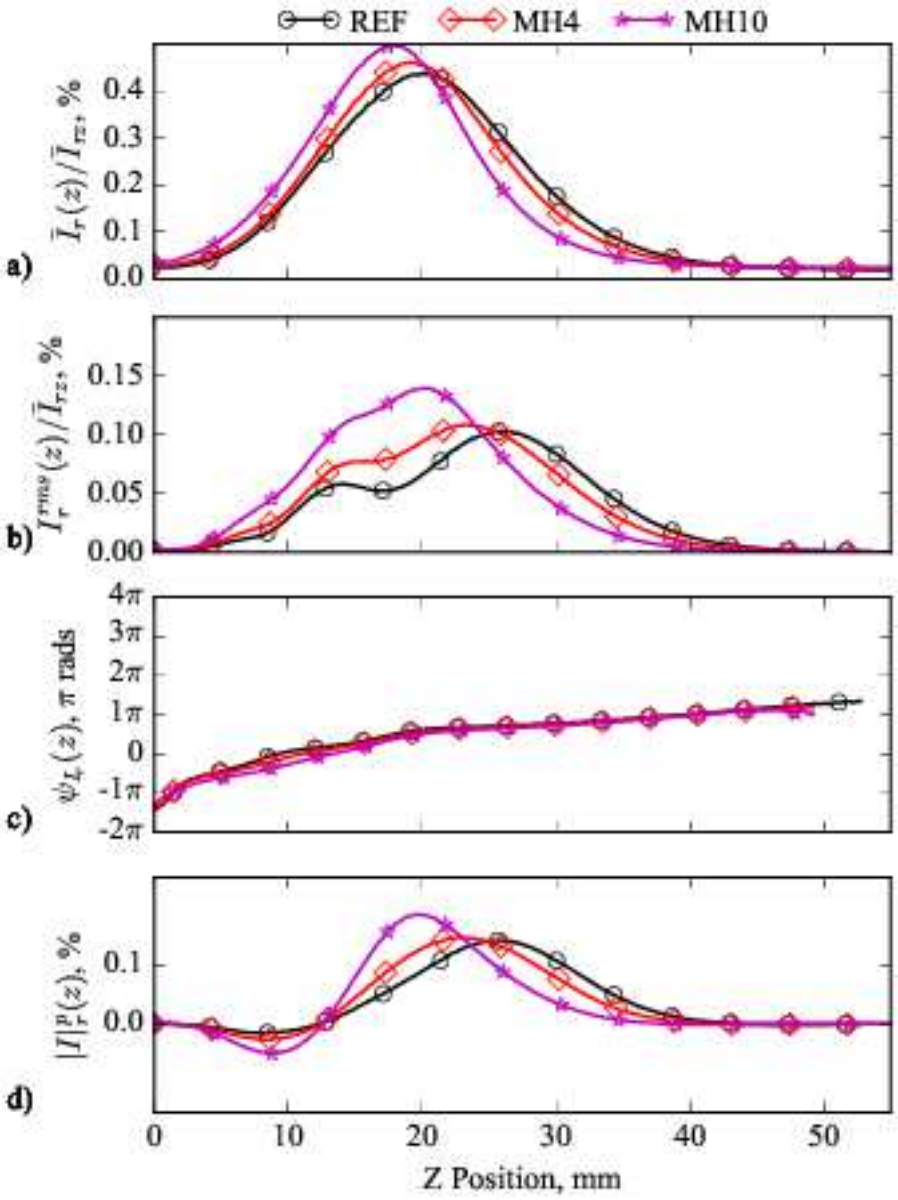

Figure 6.38: Longitudinal evolution of the radially integrated heat release rate for hydrogen enriched (MH) cases forced at 240 Hz with a forcing level of %30. a) normalized time-averaged heat release rate; b) normalized root-mean-square fluctuations; c) phase of heat release fluctuations; d) projection of the radially integrated heat release on the global heat release, U_{sw}=18 m/s, ϕ_G^0=0.8, S=0.86.

Additionally, polar plots showing the contribution of each pixel row on the phase and the gain of the global response are shown in Fig. 6.16. The REF case is spread over two quadrants, which limits the reduction of FTF gain by competition of local complex amplitudes. For PH cases, the maximum amplitude of the local responses stays the same, however with hydrogen injection there is competition between local heat release responses as the local complex amplitudes are spread over three quadrants. For PC10 case, the small reduction in FTF gain is caused by a general reduction in the amplitude

of local heat release responses rather than reduction by competition. The reduction in phase for MH cases are caused by the increase in amplitude at the root of the flame which has a smaller phase lag as it is closer to the burner outlet. The weight of the delay at the base of the flame increases as the amplitude here increases. This phenomenon lets MH10 case be spread over the fourth quadrant, which in turn causes a drop in the global FTF phase lag.

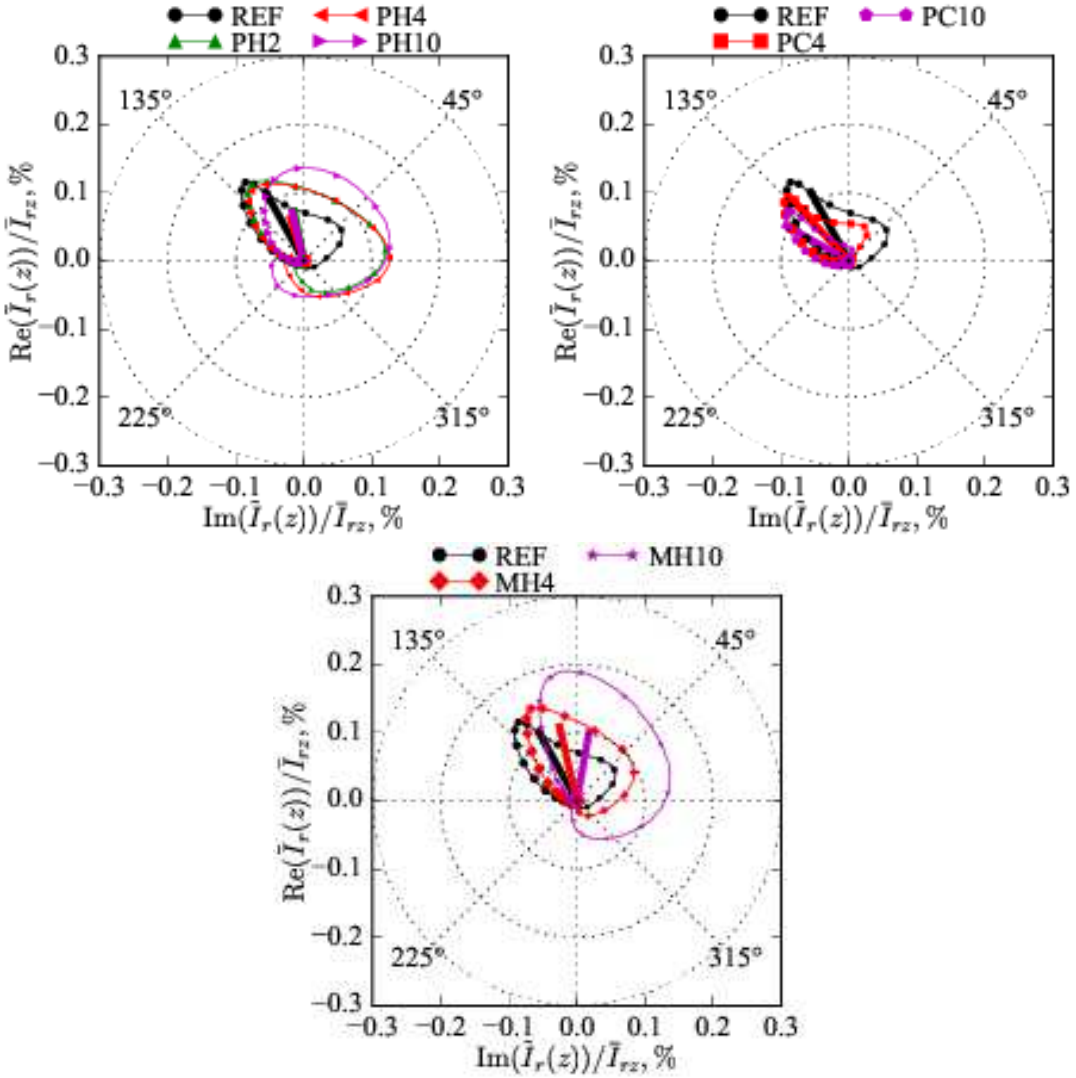

Figure 6.39: Polar plots of the local heat release rate for 30% forcing at 240 Hz. The size of the markers are as a function of the axial distance. The thick lines represent the spatially integrated global response scaled by 1/200, U_{sw}=18 m/s, ϕ_G^0=0.8, S=0.86.

6.3 Conclusions

In this chapter, the spatial heat release response of flames to acoustic forcing is studied using phase locked flame images and spectral analysis techniques for various frequencies and for different swirl numbers. The following conclusions can be drawn.

- Hydrogen injection increases heat release response activity at the roots of flames. As the local phases at the bases of the flames are lower than the edges, hydrogen injection also causes a drop in the phase of the global FTFs. Furthermore, this difference in phase creates a competition behavior, diminishing the gain of the global FTFs.

- This competition behavior is not present with methane injection, however methane injection causes a slight increase at the base activity and a slight decrease in the activity towards the edges of the flames. This redistribution of local amplitudes results in a slightly dropped phase for high levels of methane piloting.

- Hydrogen enrichment increases the maximum of the time averaged heat release rate and the RMS of the heat release fluctuations, resulting in flames that respond more violently to acoustic forcing, especially at high frequencies. Additionally, as flame length is reduced by methane enrichment, the global phase of the FTF is reduced. Although the competition between local heat release rate responses is observed for MH10 cases, it is not nearly enough to cause a significant reduction in FTF gain.

- High forcing levels cause detachment of the flame root for REF cases. Hydrogen injection with thermal power fractions as low as 2% re-attaches these flames. For hydrogen enrichment thermal power fraction necessary increases to 4%. Up to 10% thermal power fraction is tested for methane injection, however methane injection appears ineffective to reattach these flames.

- Increasing swirl reduces the flame length resulting in more compact, more intense flames and shifts the heat release response towards upstream, resulting in higher maximums in time averaged heat release rates compared to lower swirl flames. This causes a reduction in FTF phase lags. However because competition of the local heat release rate in the radial direction, the global FTF gains are reduced.

7. EMISSION MEASUREMENTS AND EFFECT OF HYDROGEN

The most important aspect of hydrogen combustion for engineering applications is the possibility of zero carbon emissions. Although it is the most abundent element in the universe, hydrogen is not readily available in its molecular form H_2 and needs to be produced. The word "possibility" is there to emphasize the necessity of producing hydrogen using renewable resources. As the world is trying to limit the global warming to 2 °C with the Paris Agreement [171], and effort is being made to lower the limit to 1.5 °C [172] the importance of hydrogen is on the rise and investments are being made to initiate a hydrogen based carbon free economy [173–175].

Another source of renewable energy that is gaining momentum by governmental support is biogas, produced from fermentation of plants, organic waste or manure. Biogas is composed mainly of methane and carbon dioxide but also with environmentally harmful H_2S. The final composition of biogas depends heavily on stock [176, 177], production and purification processes [178–181].

With all these different fuels with varying compositions, flexible fuel combustion systems are needed to supply the power need taking into consideration the need of using renewable fuels. With this in mind, MIRADAS experiment can be run with methane-hydrogen mixtures with widely varying compositions and injection strategies. This chapter is dedicated to emission measurements and the effect of hydrogen and injection strategies.

Emissions are measured with a gas analyzer (ECOM J2KN PRO) equipped with electrochemical cells capable of measuring CO, NO, NO_2 and a nondispersive infrared sensor capable of measuring CO_2 and hydrocarbons. Firstly the effect of different injection strategies on emissions are studied. Then, the effect of equivalence ratio and power on fully premixed flames are explored.

7.1 Effect of Injection Strategies on Emissions

For all the operating points presented in this section, the thermal power is kept constant at 3910 W. The effects of injection strategies on emissions are explored.

Fig. 7.1 displays the evolution of NOx emissions with different injection strategies is presented. The values presented are parts per million by volume in dried burnt gasses. Here no O2 correction is applied as the flow-rate of air is kept constant. As expected injection of H_2 as well as CH_4 causes an increase in NOx emissions, as a result of partially premixed combustion. Furthermore, the increase in NOx emissions is slightly higher for hydrogen injection up to 15% in thermal power, after which a slight drop occurs for hydrogen. This drop is thought to be caused by partial mixing before combustion, as the lift-off distance for increased injection rates are greater. Hydrogen premixing (cases MH in Fig. 7.1)marginally effects NOx emissions and the differences between the REF case are within error bars.

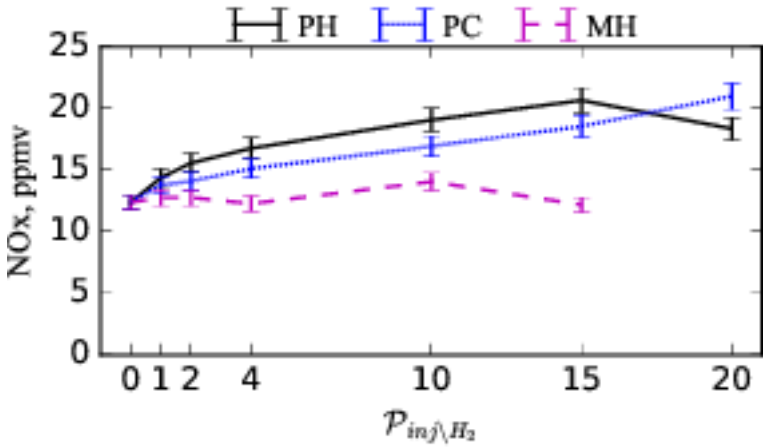

Figure 7.1: NO emissions in dry exhaust gasses as a function of hydrogen and/or injection fraction for PH, PC and MH cases, for a bulk velocity of U_{sw}=18 m/s and an equivalence ratio of ϕ=0.8.

Fig. 7.2 also shows CO emissions. Methane injection causes an increase in CO emissions as a result of deviation from perfectly premixed regime. Hydrogen injection reduces CO emissions. This is caused partly by hydrogen aiding in achieving complete combustion and partly by the fact that replacing methane by hydrogen reduces the number of carbon atoms that can create CO emissions.

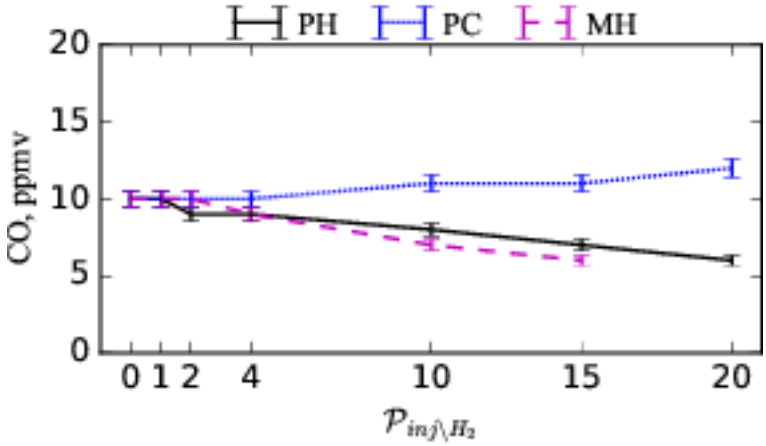

Figure 7.2: CO emissions in dry exhaust gasses as a function of hydrogen and/or injection fraction for PH, PC and MH cases, for a bulk velocity of U_{sw}=18 m/s and an equivalence ratio of ϕ=0.8.

When burning hydrocarbon fuels, there are no escape from CO_2 emissions. An option to reduce CO_2 emissions is to use carbon-free fuels such as hydrogen. Fig. 7.3 displays CO_2 emissions for PH, PC and MH cases as summarized in Table 2.3. Here the effect of using carbon free hydrogen can be clearly seen. For the same power, replacing methane by hydrogen reduces CO_2 emissions proportionally.

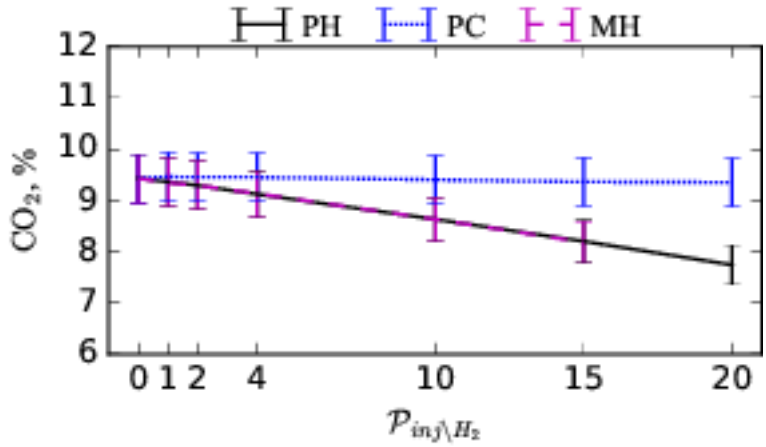

Figure 7.3: CO_2 emissions in dry exhaust gasses as a function of hydrogen and/or injection fraction for PH, PC and MH cases, for a bulk velocity of U_{sw}=18 m/s and an equivalence ratio of ϕ=0.8.

Fig. 7.3 may invoke the idea of using hydrogen from renewable sources to replace some part of the fossil fuels in combustion systems without the need of costly heavy modifications to reduce CO_2 emissions. The hydrogen economy is not the reality of today, however a progressive shift towards a sustainable energy economy is possible

by introducing renewable sources into existing combustion systems with significant reduction in pollutant emissions.

7.2 Effect of Equivalence Ratio on Emissions

Emission measurements are generally presented with respect to a fixed reference to prevent injection of air in the exhaust gasses to reduce NOx emissions in a misleading way. When air is added to exhaust gasses, the volumetric fraction of emissions drop as a result of dilution, however the mass flow of polluting gasses is not reduced. This can create a hole in the regulations fixing emission standards. To fix this issue, engineers decided to report emissions wtr. to a reference O2 fraction, to which all measurements are corrected as given in Eq. 7.1.

$$NOx_R = NOx_M \frac{20.9 - O_{2R}}{20.9 - O_{2M}} \tag{7.1}$$

In Fig. 7.4 pollutant emissions as a function of equivalence ratio for a fixed bulk velocity of U_{sw}=18 m/s are reported. Here, it can be observed that NOx emissions increase exponentially as a function of the equivalence ratio between $0.55 \leq \phi \leq 0.90$. CO emissions exhibit a similar behavior. Here the effectiveness of lean combustion in reducing pollutant emissions can be observed.

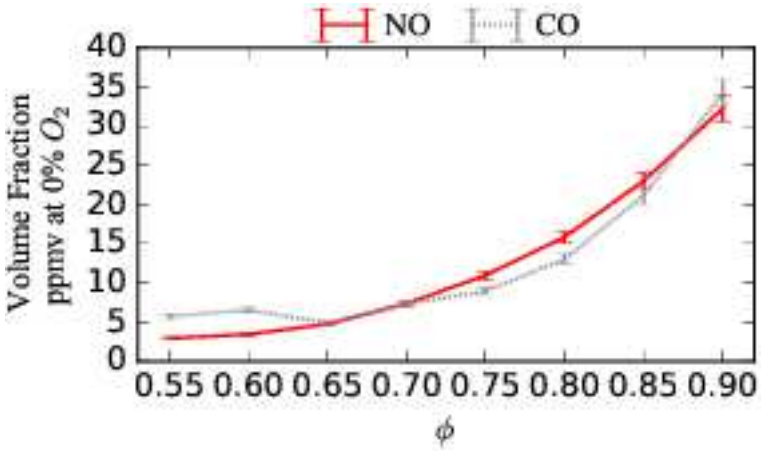

Figure 7.4: PPMv volume fraction of NO and CO in dry exhaust gasses as a function of equivalence ratio for a fixed bulk velocity of U_{sw}=18 m/s.

7.3 Conclusions

In this chapter, the effects of hydrogen, different injection strategies and equivalence ratio on pollutant emissions are studied experimentally. The following conclusions can be drawn:

- Although hydrogen injection can be used to control combustion instabilities, it causes an increase in NOx emissions.
- Methane injection increases emissions without a significant gain.
- Replacing methane by hydrogen keeping the thermal power constant reduces significantly CO_2 emissions.
- NOx emissions increase exponentially as a function of the equivalence ratio. CO emissions exhibit a similar behavior.
- Introduction of hydrogen $\mathscr{P}_{H_2} \leq 0.2$ into existing natural gas burning combustion systems is possible without heavy modifications.

8. LES CALCULATIONS, COMPARISON TO EXPERIMENTS AND HEAT RELEASE RESPONSE MECHANISMS OF HARMONICALLY FORCED METHANE / AIR FLAMES

This chapter summarizes 3D reacting compressible Large Eddy Simulations done with AVBP code [182] to show the capabilities of LES in predicting harmonic responses of fully premixed and lightly piloted methane air flames and the mechanism of heat release response of harmonically forced flames. No hydrogen/methane flame is computed here because the computation of such flames would have required too many developments in the LES code (this is actually the topic of an ongoing ERC grant at IMFT/CERFACS : cerfacs.fr/scirocco). The flame responses for different flames are presented in the experimental chapters. Here, the mechanism leading to the heat release response will be analyzed using LES calculations. Firstly, general information on the code AVBP, the mesh and the boundary conditions used has been presented in the section General Description of AVBP, Mesh and Boundary Conditions. Subsequently, stable (without forcing) flame calculations and their comparison to experiments are studied and flow and combustion characteristics of swirled premixed and lightly piloted flames are investigated. Finally forced flame calculations, heat release response mechanisms and comparisons of numerical and experimental flame transfer functions are analyzed.

8.1 General Description of AVBP, Mesh and Boundary Conditions

AVBP is an unstructured mesh flow solver with finite volume and finite element capabilities [182]. It has third order finite elements [183] and second order finite volume schemes [184] in both space and time along with a thickened flame model [185–189] to numerically solve Navier-Stokes equations for turbulent reacting flows. More information on conservation equations and can be found readily available in the literature [190] and will not be repeated in this thesis. Instead, the mesh and different boundary conditions applied in LES calculations and comparisons between experiments and calculations to study the physics of harmonically forced flames will

be emphasized. The mesh used in all the calculations contains ~24 Million cells and has been refined in the flame regions to better resolve the steep gradients present. It starts at the outlet of the convergent section of MIRADAS setup and also contains a part of the ambient air at the outlet of the chamber as needed for better representation of acoustic reflection at the exit of the combustion chamber. The CFL condition has

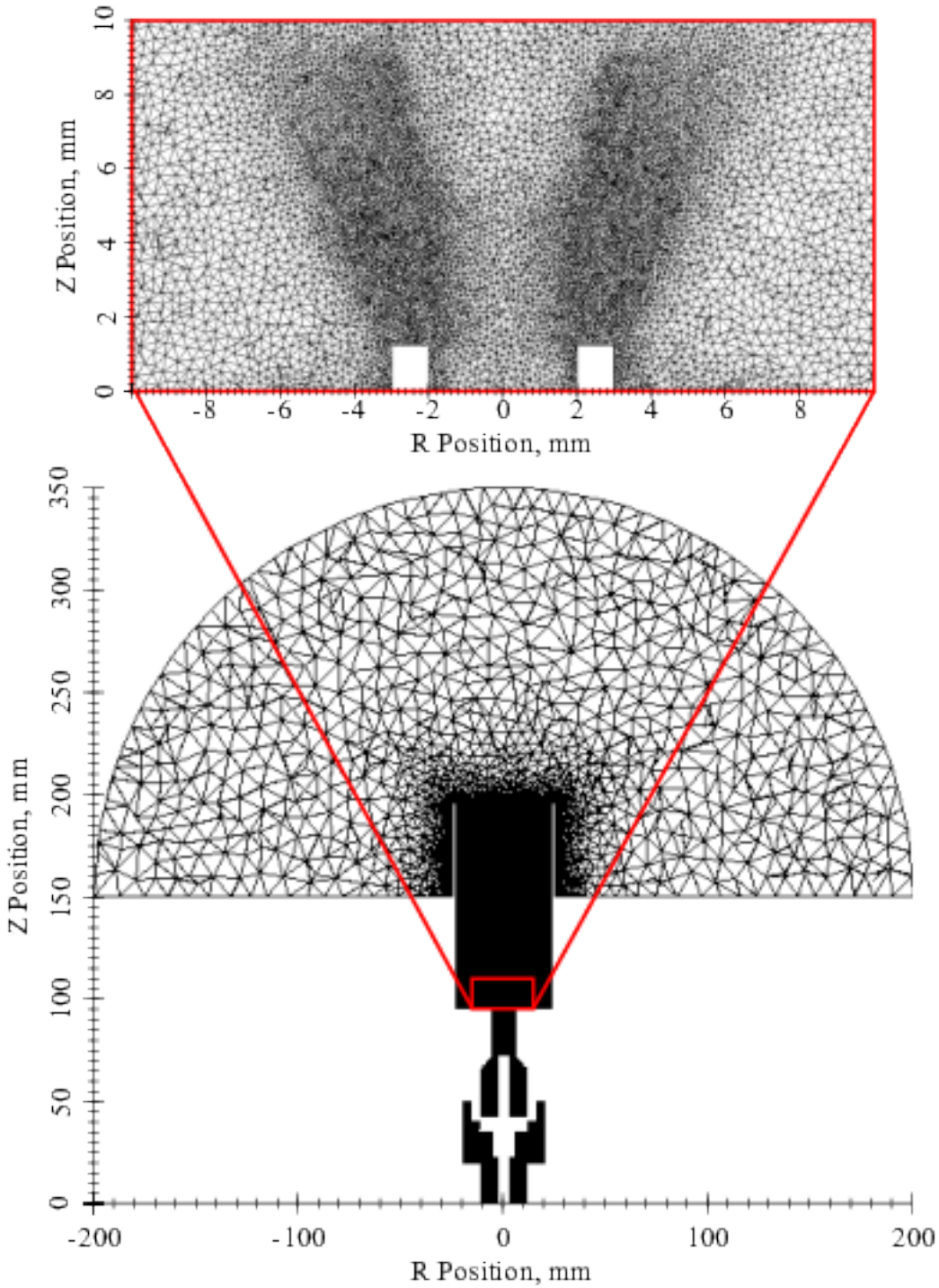

Figure 8.1: Overview of the mesh used in reacting compressible LES calculations of MIRADAS setup.

been fixed to 0.7 and it drives the time-step, which in all simulations is calculated from the acoustic CFL number $CFL = |u + c|\Delta t/\Delta x$. The Sigma LES model is used to model sub-grid stresses [191]. To represent chemical kinetics, a simplified two-step scheme consisting of methane oxidation and CO-CO_2 equilibrium with 6 species [136] has been implemented for all calculations. Along with this chemical scheme the assumption of constant Prandtl number $Pr = \mu c_p/\lambda = 0.7$ and a power law viscosity definition has been applied for thermodynamic and transport properties.

High fidelity compressible reacting LES calculations which include acoustic phenomena, require quality boundary conditions alongside with high order low-dissipative schemes. This requires handling waves in CFD while keeping the mean flow variables from drifting away. This requires characteristic non-reflecting boundary conditions as proposed in the NSCBC method [192], where rather than fixing absolute values for flow variables, the variation of flow variables are controlled by injected and outgoing waves. Firstly a brief introduction of boundary conditions in AVBP will be presented. The full derivations of the boundary conditions will not be given here, as they can be easily found in literature [192–195].

- INLET_RELAX_UVW_T_Y: Non-Reflecting inlet with imposed velocity, temperature, and species profiles. The in-going acoustic wave is given as: $2K\Delta t(U_n^t - U_n)$ where U_n is the boundary normal component of instantaneous velocity, U_n^t the boundary normal component of the target velocity, Δt the time-step and K is the relaxation coefficient applied to keep the velocity from drifting from its target mean value.

- INLET_RELAX_UVW_T_Y_PULSE: Non-Reflecting inlet with imposed velocity, temperature, and species profiles with a superimposed acoustic excitation to inject acoustic waves for forced LES calculations. The in-going acoustic wave is given as
  $4|U_n^w|\pi f cos(2\pi ft)\Delta t + 2K\Delta t((U_n^t + |U_n^w|sin(2\pi ft)) - U_n)$ where $|U_n^w|$ the amplitude of the acoustic forcing, f the frequency of excitation.

- INLET_RELAX_RHOUVW_T_Y: Non-Reflecting mass flow rate, temperature, and species imposed inlet. This boundary condition works like INLET_RELAX_UVW_T_Y, however instead of velocity, mass flow is imposed.

The in-going acoustic wave is given as $\frac{2Ku_n\Delta t}{\rho(1-M_n)}((\rho U_n)^t - (\rho U_n))$ where M_n is the boundary normal Mach number and ρ is the density at the inlet.

- WALL_NOSLIP_ADIAB: No-slip, adiabatic wall.
- WALL_NOSLIP_LOSS: No-slip wall with heat losses to impose experimentally measured temperature profile.
- OUTLET_RELAX_P: Non-Reflecting pressure imposed subsonic outlet. The in-going acoustic wave is expressed as: $2\frac{K_p\delta t(P^t - P^n)}{\rho c}$ where P^n is the instantaneous pressure, P^t the target pressure, c the sound speed and K_p is the relaxation coefficient applied to keep the pressure from drifting from its target mean value.

A schematic representation of the boundary conditions applied is given in Fig. 8.2.

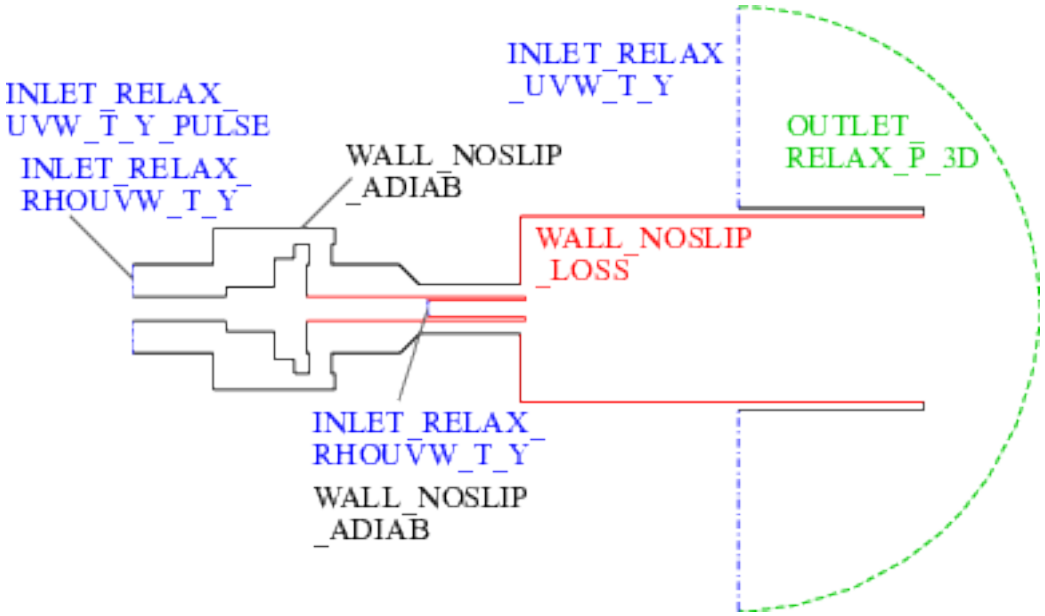

Figure 8.2: Boundary conditions applied in LES calculations. The volume of the ambient air around the combustion chamber is reduced for ease of presentation.

Combustion chamber walls, back-plate and injection tube temperatures have been measured with k-type thermocouples in the experiments and have been implemented in CFD calculations. Different boundary conditions depending on the injection and presence of forcing needs to be implemented to represent the different operating and forcing conditions. The boundary conditions which depend on the operating and forcing conditions has been presented in Table 8.1.

Table 8.1: Boundary conditions applied in LES calculations. PC* represents the calculations with fuel injection in the middle tube.

		REF	PC*
Mean Flame Calculations	Main Inlet	INLET_RELAX_ RHOUVW_T_Y	INLET_RELAX_ RHOUVW_T_Y
	Pilot Fuel Inlet	WALL_NOSLIP _ADIAB	INLET_RELAX_ RHOUVW_T_Y
FTF Calculations	Main Inlet	INLET_RELAX_ UVW_T_Y_PULSE	INLET_RELAX_ UVW_T_Y_PULSE
	Pilot Fuel Inlet	WALL_NOSLIP _ADIAB	INLET_RELAX_ RHOUVW_T_Y

The temperature of the combustion chamber dome (450 K) and the tip of the injection tube (720 K) are measured in the experiment and applied in LES calculations. The chamber heat losses are implemented by measuring the external wall temperatures of the quartz and applying the measured temperature along with a thermal resistance of $R_{ch} = 9e^{-4}$ computed using a thermal conductivity of $\lambda = 2.17\,\mathrm{W/mK}$ for the 2 mm quartz windows.

To produce an easier to read text, the post processing steps are summed up in Appendix A.3.

8.2 Mean Flame Calculations

Mean (without forcing) flame LES calculations are performed for REF, PC4 and PC10 cases and are compared with experimental results. In experiments multiple long exposure flame images are taken and then averaged to get the mean CH* emission field. The CH* chemiluminescent light is a good marker of the heat release of the flame [112] and is compared to heat release information directly available in LES calculations, in AVBP, the mean heat release is obtained by:

$$\overline{\dot{q}}(x,y,z) = \sum_{n_t=0}^{N_t} \dot{q}(x,y,z,t)/N_t \tag{8.1}$$

where x, y, z and r are coordinates and N_t is the number of time-steps used in averaging. As mean flame CH* emission images of experiments are obtained using a telecentric lens with a depth of field greater compared to the dimensions of the chamber, to compare with CFD calculations, mean CFD flames must be line of sight integrated by integrating the data on evenly distributed slices. As the camera outputs measurements

in pixel intensities, which for 16 bit depth goes from 0 to 65535 for every pixel and CFD calculations output heat release data in SI units, a maximum value normalization has been performed for comparison as presented in **A.3.2** for clarity and ease of comparison. The normalized heat release expression $\bar{\dot{q}}_{LS_{y_{Norm}}}$ in Eq. **A.3.2** has been plotted for REF case in Fig. 8.3.

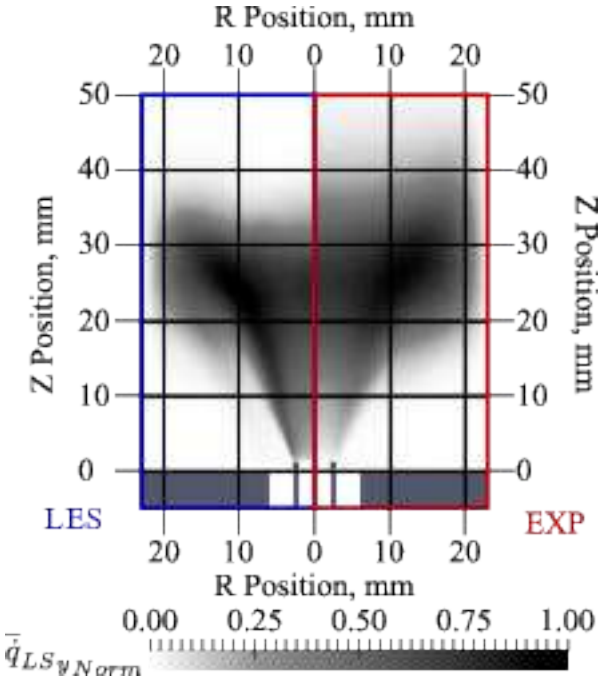

Figure 8.3: Comparison of calculated and measured mean flames for the REF case. On the left side of z-axis; LES calculations, on the right side; measurements from MIRADAS experiment.

As seen in Fig. 8.3, there is a good agreement between the experiments and the LES calculations for the REF case. The flame in the LES calculation is very slightly shorter and the high intensity (darker regions in Fig. 8.3) is marginally more downstream, but the mean flame height and the flame angle are represented very well and the spatial distribution of normalized heat release in CFD calculations and normalized CH* intensity in experiments match quite well for the turbulent premixed methane-air flame.

The results of PC4 and PC10 cases are presented in Fig. 8.4.

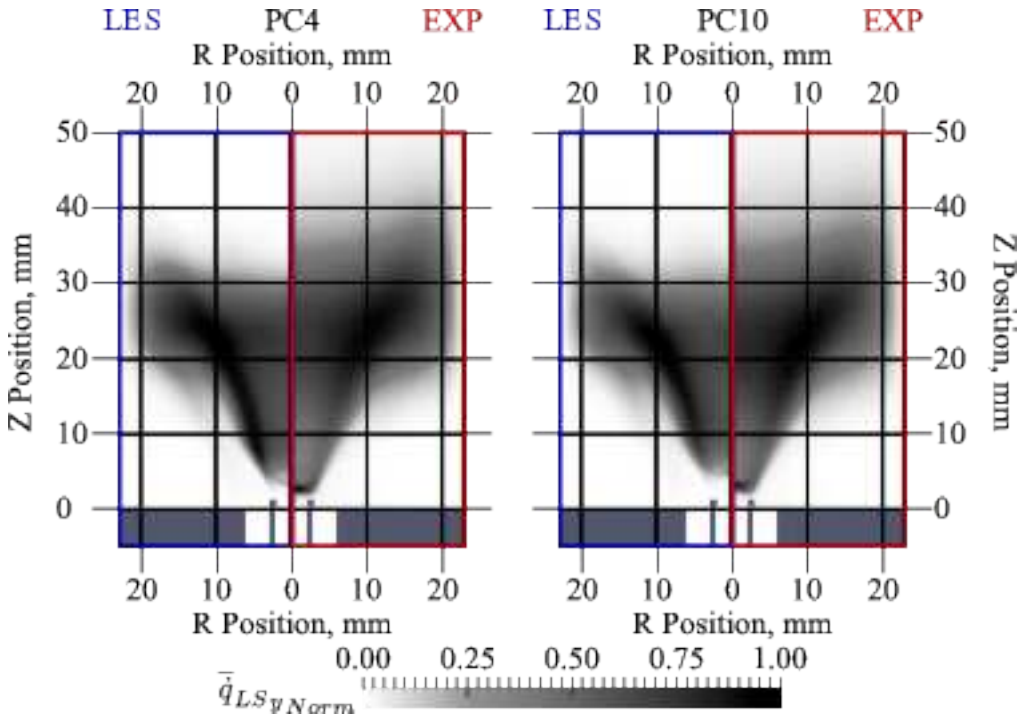

Figure 8.4: Comparison of calculated and measured mean flames for the PC4 and PC10 cases. On the left side of z-axis; LES calculations, on the right side; measurements from MIRADAS experiment.

Comparison of experimental and LES fields of PC4 and PC10 cases presented in Fig. 8.4 shows that LES calculations reproduce the flame length and flame angle quite well. Furthermore, comparing PC4 and PC10 cases to the REF case presented in Fig. 8.4, reveals that with pilot methane injection, the burning intensity increases near the injection tube both for LES and experimental flames. The shortening of flames caused by pilot injection in PC10 and PC4 cases, can be seen in experimental measurements and is well reproduced by LES calculations.

However, the edges of the LES flames burns more intensely compared to experimental measurements both for PC4 and PC10 cases. Furthermore, there is more intensity (darker regions in Fig. 8.3) at the flame base in experimental measurements compared to LES calculations both for PC4 and PC10 cases. This small difference is partly caused by comparison of normalized fields of heat release which is directly available in LES calculations to CH* emission in experiments which is not directly heta release, but a strong marker of heat release and partly by the effect of line of sight integration of axi-symmetric flames. This effect is investigated by taking inverse abel transform of experimental flame images and comparing them to angle averaged heat release field obtained from LES calculations. To obtain inverse abel transforms of flame images,

PyAbel package is used [121]. The resulting angle averaged normalized heat release field is presented in Fig. 8.5.

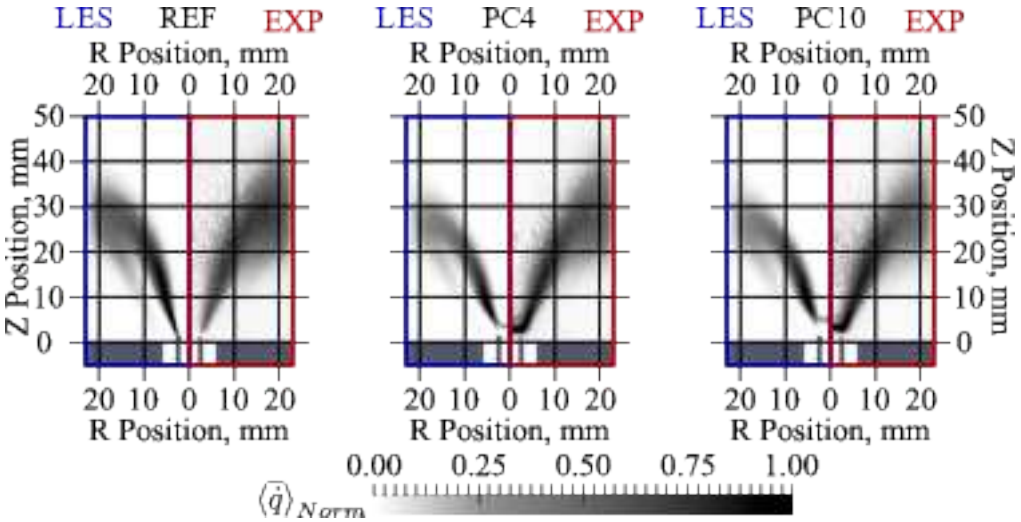

Figure 8.5: Comparison of calculated and measured angle averaged mean flames for REF, PC4 and PC10 cases. On the left side of z-axis angle averaged LES calculations, on the right side inverse abel transformed flame images from MIRADAS experiment.

Images shown in Fig. 8.5 are free of the effect of line of sight integration, so that the local variation of intensity along the flame can be observed. Comparing REF, PC4 and PC10, the shortening of the flames with pilot methane injection can be observed both for experimental measurements and LES calculations. Another effect is the increase in the local burning intensity at the vicinity of the injection tube.

The pilot flame in a premixed methane-air mixture brings along the question whether if CH* emissions are a good marker of heat release in the vicinity of the injection tube. First of all, a chemical mechanism that contains excited states of CH* species has been chosen to conclude the reliability of CH* light emission as a heat release marker. The chemical mechanism constructed by Guiberti et. al. is based on the Lindstedt mechanism [196] and includes CH* chemiluminescence [8]. This is done be adding reaction paths for CH* and OH* [116], and CO_2* [197]. Firstly 1D perfectly premixed free flames are calculated and the chemical mechanism is validated by comparing with experimental results of Nori et al [9]. Experimental results are given as a function of the CH* chemiluminescence emission power normalized by the mass flow of methane fuel as presented in Eq. 8.2.

$$\frac{P_{CH*}}{\dot{m}_f} = A_E \int_0^{L_c} [CH*]\, dz \frac{1+\dot{m}_a/\dot{m}_f}{\rho_u S_L} \tag{8.2}$$

Where P_{CH*} [kmole photons/s] is the emission of CH* chemiluminescence, $\dot{m}_f$ and $\dot{m}_a$ are fuel and air mass flow rates, A_E is the Einstein coefficient for CH*, L_c is the length of the calculation domain for 1D flame simulations, $[CH*]$ [kmole/m^3] is the concentration of CH*, ρ_u is the density of the unburnt gasses, S_L is the laminar flame speed. The comparison of the experimental emission curve and numerical results is presented as a function of the equivalence ratio in Eq. 8.6.

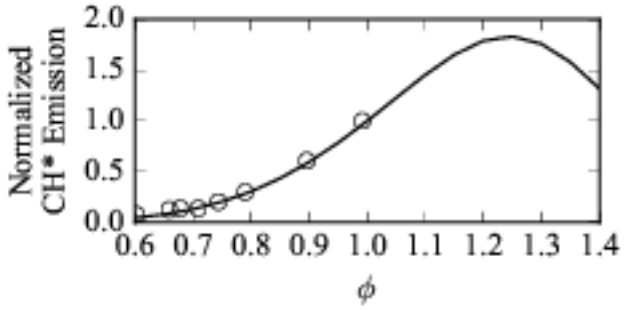

Figure 8.6: Comparison of CH* emissions of flames calculated with CH* extended Lindstedt mechanism [8] and experimental results of Nori et. al. [9]. Data points are normalized by dividing the emission data by the value at stoichiometry as direct comparison is not possible coming from the fact that the details of the measurement system is not given.

Fig. 8.6 shows that the CH* extended Lindstedt mechanism represents the experiments quite nicely, leading to the conclusion that the CH* extended Lindstedt mechanism [8] can be used to study the link between heat release and CH* emissions. Furthermore, as the normalized CH* emission fields from the experiments are compared to normalized heat release rates, the spatial agreement of CH* emission and heat release fields comes into question. Fig.8.7 shows the heat release and CH* emission profiles along the PC10 1D counter-flow flame calculated with the extended Lindstedt mechanism. The maximums of CH* emission rates and heat release rates match well, meaning that a comparison for piloted flames can be done with confidence.

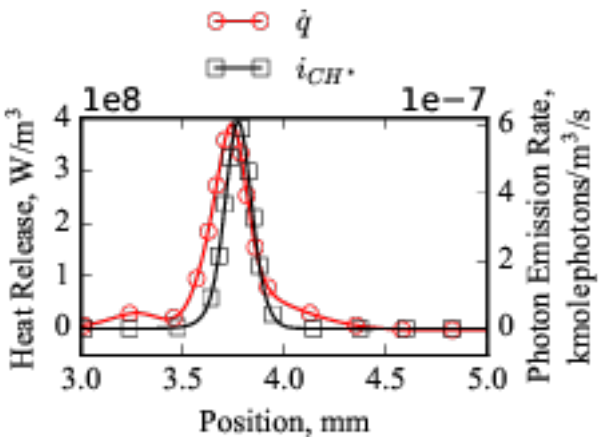

Figure 8.7: CH* emission and heat release profiles along the counter-flow PC10 flame, showing the proximity of the maximums of CH* photon emission rate and heat release rate.

Now, LES results are used to study flow and combustion characteristics of the setup. Comparisons of the flow field measurements and LES results could not be performed as PIV measurements of the MIRADAS setup is not yet available, so LES results are used to compare the flow fields of the corresponding cases. The velocity fields are presented in Fig. 8.8.

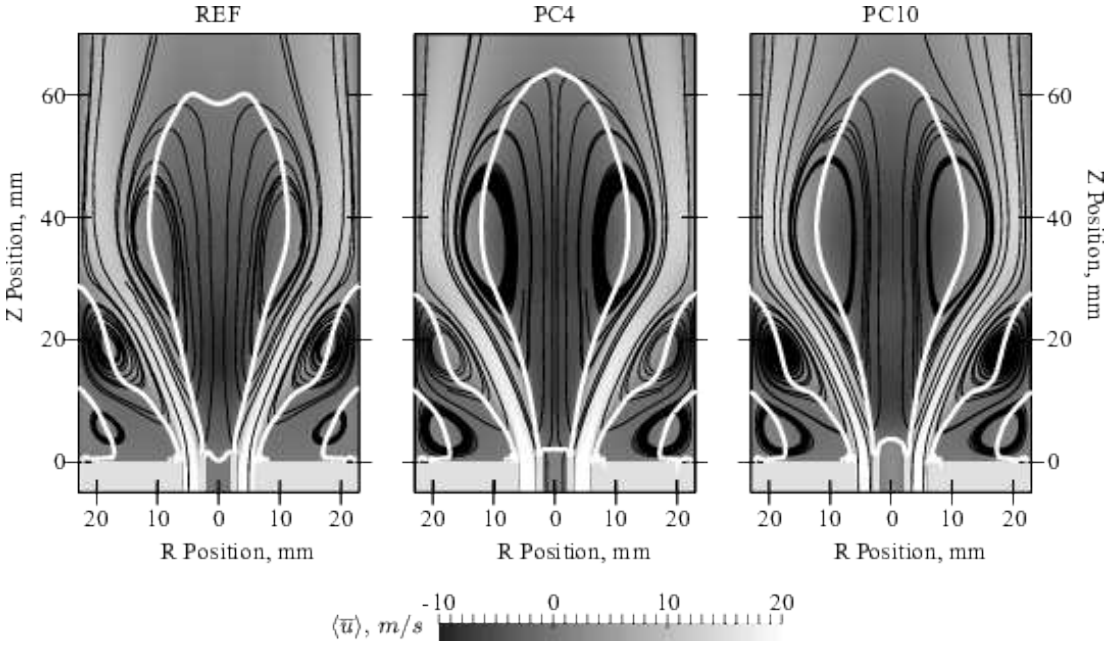

Figure 8.8: Angle averaged - time averaged axial velocity fields of REF, PC4 and PC10 cases obtained from LES calculations. The thick white lines are contours of zero axial velocity, the black lines are streamlines of the time averaged field.

The flow fields displayed in Fig. 8.8, show that all the cases contain a large recirculation region in the middle of the combustion chamber and two smaller recirculation regions

on each side. These recirculation regions transport hot combustion products into the fresh gasses and help the flame stabilize.

Furthermore, the injection of methane in the middle tube while keeping the global equivalence and the airflow constant does not change the flow field drastically. For comparison, the mean velocity at the burner exit is ≈18 m/s for all cases and in the injection tube is 0.38 and 0.95 m/s for PC4 and PC10 cases respectively. As the jet velocities are very low, the characteristic recirculation zones of the swirled flames are not changed drastically, however with increasing injection velocity, the middle recirculation zone gets wider at around 40 mm of the axial (Z) position. As expected, the zero axial velocity line at the outlet of the injection tube moves up in the axial direction.

As PC4 and PC10 cases encompass pilot fuel injection, there are portions of these flames burning in partially premixed mode, however as 96% for PC4 case and 90% of the methane fuel is premixed with air long before the combustion chamber, the diffusion portions should be very small. These diffusion and premixed portions of flames can be examined using the Takeno criteria [198–200] :

$$\zeta = \frac{\nabla Y_{CH_4} \cdot \nabla Y_{O_2}}{|\nabla Y_{CH_4} \cdot \nabla Y_{O_2}|} \tag{8.3}$$

where ζ is the flame index, ∇ is the gradient operator, Y_{CH_4} and Y_{O_2} are mass fractions of CH_4 and O_2 respectively. The positive parts of this flame index $\zeta > 0$ signify parts of flames burning in premixed mode and negative parts signify parts of flames burning in non-premixed mode. The heat release fields separated to premixed and non-premixed parts of flames are presented in Fig. 8.9.

Fig. 8.9 shows that the non-premixed portions of flames PC10 and PC4 are very small compared to the premixed portions of the respective cases. The non-premixed portions of the heat release represents 0.8% and 1.4% of the total heat mean release of the flames of PC4 and PC10 cases respectively. This feature of the flames suggest that they should follow premixed flame characteristics in their responses to acoustic forcing.

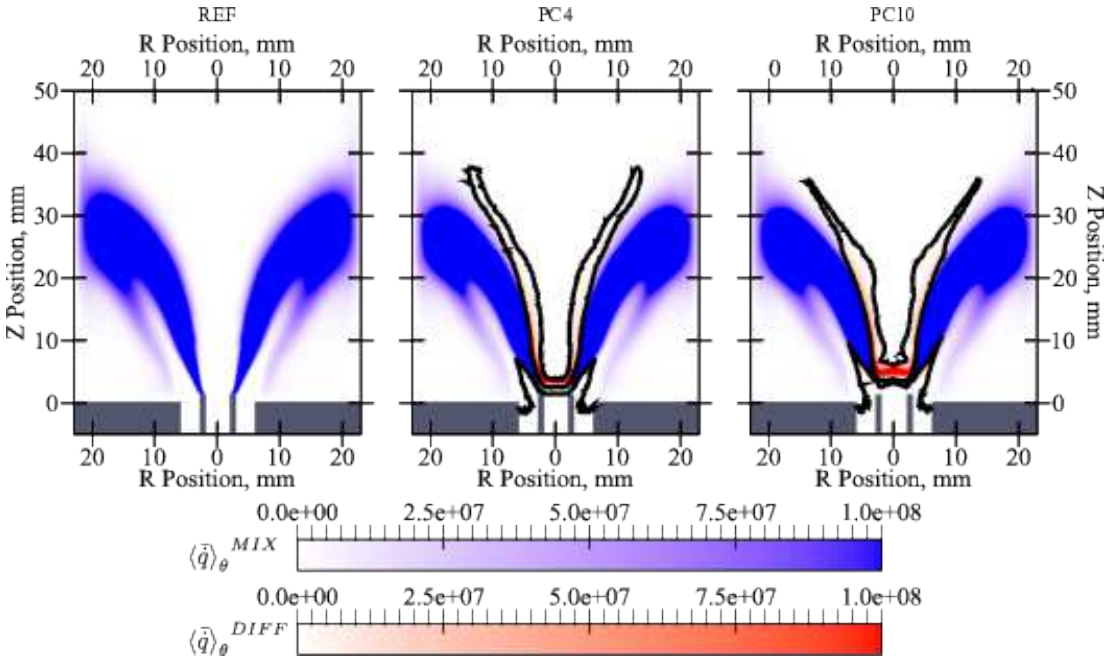

Figure 8.9: Flames separated into premixed burning and non-premixed burning regions using normalized Takeno index. The black corresponds to null Takeno index $\zeta = 0$.

This small heat release coming from the non-premixed parts of the flames also shows that mixing of the injected methane is fast. The equivalence ratio field calculated using the passive scalar (mixture fraction) is presented in Fig.8.10. The mixture fraction and the equivalence ratio are defined as [201]:

$$Z = \frac{Z_C/(mW_C) + Z_H/(nW_H) + 2(Y_{O_2,2} - Z_O)/(\nu'_{O_2} W_{O_2})}{Z_{C,1}/(mW_C) + Z_{H,1}/(nW_H) + 2Y_{O_2,2}/(\nu'_{O_2} W_{O_2})} \qquad \phi = \frac{Z}{1-Z}\frac{1-Z_{st}}{Zst} \tag{8.4}$$

where Z_x is the elemental mass fraction of element x, W_x is the elemental mass of element x, m and n are the number of carbon and hydrogen atoms in the fuel molecule respectively, $Y_{O_2,2}$ is the O_2 mass fraction in the oxidizer stream, ν'_{O_2} is the stoichiometric coefficient of the oxidizer stream in the chemical balance equation and subscripts 1 and 2 defines the fuel and oxidizer streams respectively. Z_st is the stoichiometric mixture fraction.

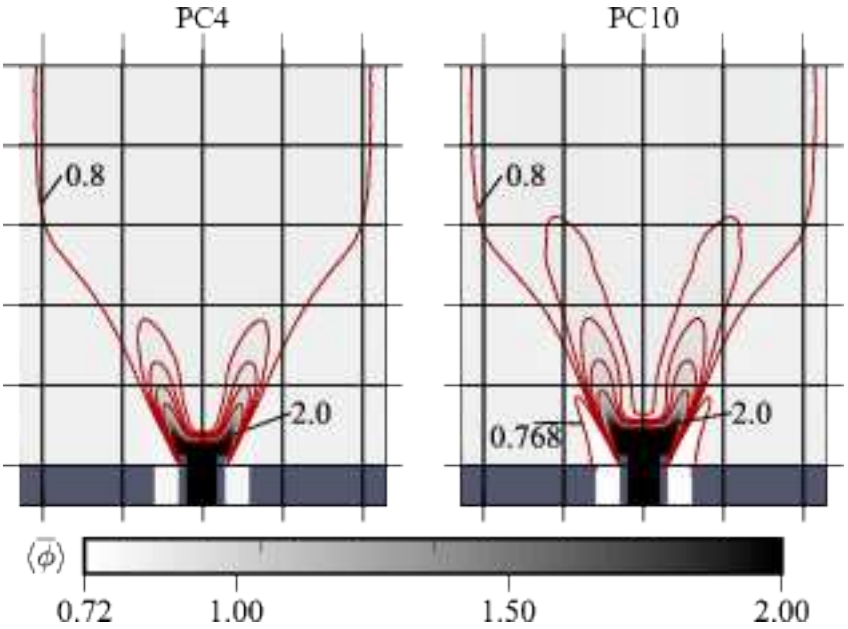

Figure 8.10: Equivalence ratio field for PC4 and PC10 cases. Contour lines are labeled with their respective values. The equivalence ratio field for REF case is not shown as the case is perfectly premixed, the field is completely uniform.

Inspection of Fig.8.10 leads to the conclusion that the methane injected changes the equivalence ratio of the flames at the vicinity of the injection tube, where a very small portion of the flame burns in diffusion mode. As expected, when the flowrate of the injection is increased, the spatial variation of the equivalence ratio increases. However, the mixing happens quite rapidly in the swirled hot flow and the global equivalence ratio is quickly reached.

8.3 Response of Flames to Acoustic Forcing and Mechanisms Driving Heat Release Response

To explore the effects of acoustic forcing on the heat release response of the flames, LES calculations and experimental measurements are performed. PID measurements are not available to explore the mechanism leading to forced heat release response, so LES results are first validated wrt. experimental results and LES fields will be used to explore the flow field. Experimental results are already discussed in the previous chapters, so only a brief description will be given here. To obtain experimental flame images, the camera is triggered with a TTL signal separated which separates the forcing period $\mathcal{T}$ into 12 instants. The exposure time of the camera is set to 10 ns to get an instantaneous image not integrated in time by the exposure time. As the

light captured with such a small exposure time is very low, multiple images triggered at the same phase of the forcing cycle are accumulated on the sensor to get a phase averaged image. It should be noted that all the phases presented either obtained from LES calculations or experimental measurements are wrt. to the velocity signal at the outlet of the burner. For LES calculations, instantaneous solutions taken at respective time-stamps separated by 30° in the period has been taken and they are averaged to obtain the phase averaged variables. The procedure is summed up in Appendix A.3.

As the camera is looking at the transparent quartz chamber and it sees the light emitted by every point of the flame, a line of sight integration has been performed to represent flame images. This integration technique also enables the comparison of the photomultiplier measurements, as the photomultiplier looks at the integrated luminosity coming from all the flame.

Further down the text the heat release and CH* emission values will be used interchangeably when experiments are compared to LES calculations. The information obtained from the flame images are in pixel intensity values in contrary to LES calculations, where the heat release of the flame is directly accessible. To be able to compare the two, a normalization needs to be performed. This is done by normalizing the respective fields by their maximums in space and phase. The normalization is presented in Eq. **A.3.7**. With this convention, we can compare the LES results to the experimental measurements. For the REF case, the phase locked line of sight integrated heat release fields are presented in Fig. 8.11.

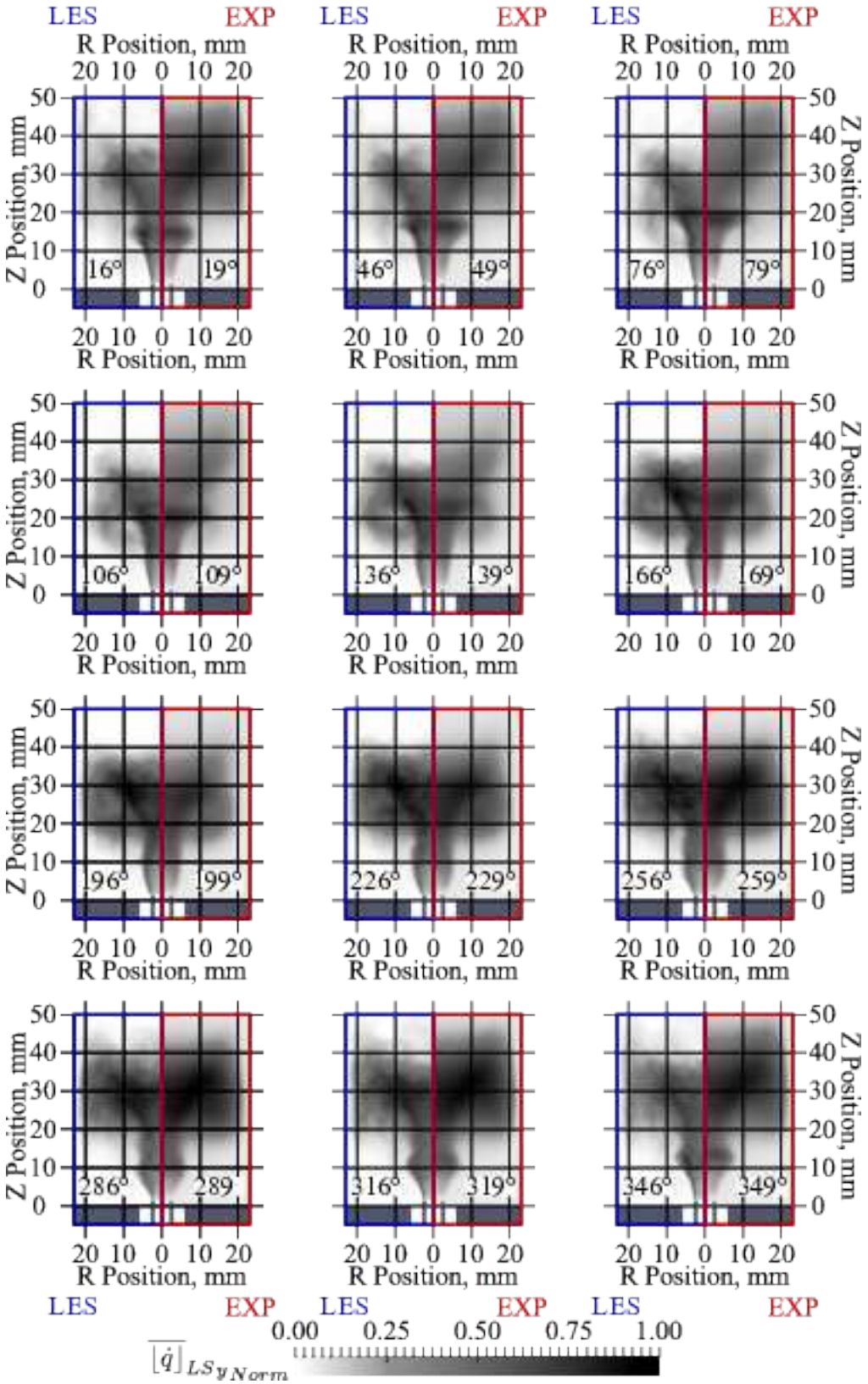

Figure 8.11: Phase locked normalized heat release rate as presented in Eq. **A.3.7** for a forced flame at a frequency of 400 Hz for the REF case. Left sides of the images are LES results and right sides are the experimental flame CH* chemiluminescence images. Phase angles wrt. the velocity signal at the outlet of the burner are indicated at the bottom of the images.

Fig. 8.11 shows that the response of the REF flame is well represented in LES calculations. There are two main shapes which are linked to the flame response in these flames. Firstly, the perturbation which is located in the vicinity of the injection tube that becomes clear around 300 $^{\circ}$ of phase with respect to the periodic velocity perturbation. The agreement in the phase between the experiment and the LES calculations strongly supports the validity of the technique used to reconstruct the experimental flame responses and the velocity reconstruction at the exit of the combustion chamber. This perturbation is convected downstream of the flame with the flow, continuing the deformation of the flame and getting amplified as it is transported. As it reaches $\approx$140 $^{\circ}$ of phase, this perturbation is wrapped around itself constituting a vortex roll-up phenomenon. Towards the end of the cycle, the rolled-up vortex is transported even further downstream, continuing to deform the edges of the flame, at the same time the perturbation of the next period is generated. The flame responses obtained from LES calculations and experimental flame images agree very well, with a very slight phase difference, but all the phenomena are well captured in space and time.

In Fig. 8.12, phase locked normalized heat release rates for PC4 case are presented. As in REF case, the perturbation which becomes clear around 300 $^{\circ}$ of phase is transported downstream, causes a vortex roll-up and deforms the flame as it is ejected downstream followed by the perturbation of the next cycle. Compared to the REF case, the pulsed flame gets shorter and there is more activity at the base of the flames both for LES calculations and experimental flame images. The flames get a bit wider, caused by injection flow pushing the flame towards the sides and changing the flame speed slightly at the base of the flame. This widening and slight increase at the base of the flame suggests the fact that the flames with injection are a bit shorter compared to REF flames. The most evident change compared to REF case is the fact that the flame is brighter and the amplitude of the fluctuations increase at the base of the flame, in the vicinity of the secondary injection. Once again the phase and the amplitude of the pulsations are very well predicted in LES calculations, supporting the fact that the LES calculations can be used to further explain the phenomenon of flame response.

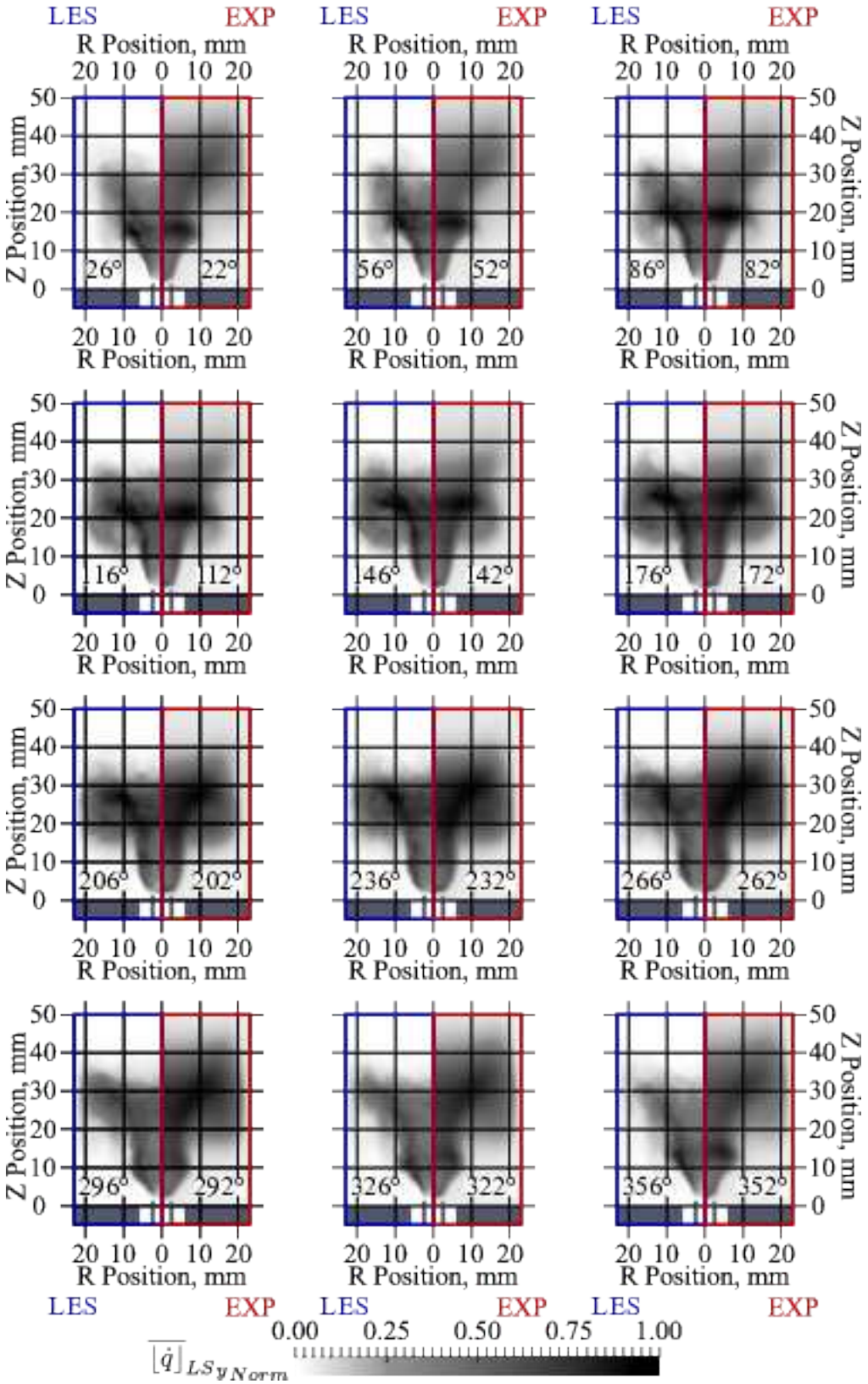

Figure 8.12: Phase locked normalized heat release rate as presented in Eq. **A.3.7** for a forced flame at a frequency of 400 Hz for the PC4 case. Left sides of the images are LES results and right sides are the experimental flame CH* chemiluminescence images. Phase angles wrt. the velocity signal at the outlet of the burner are indicated at the bottom of the images.

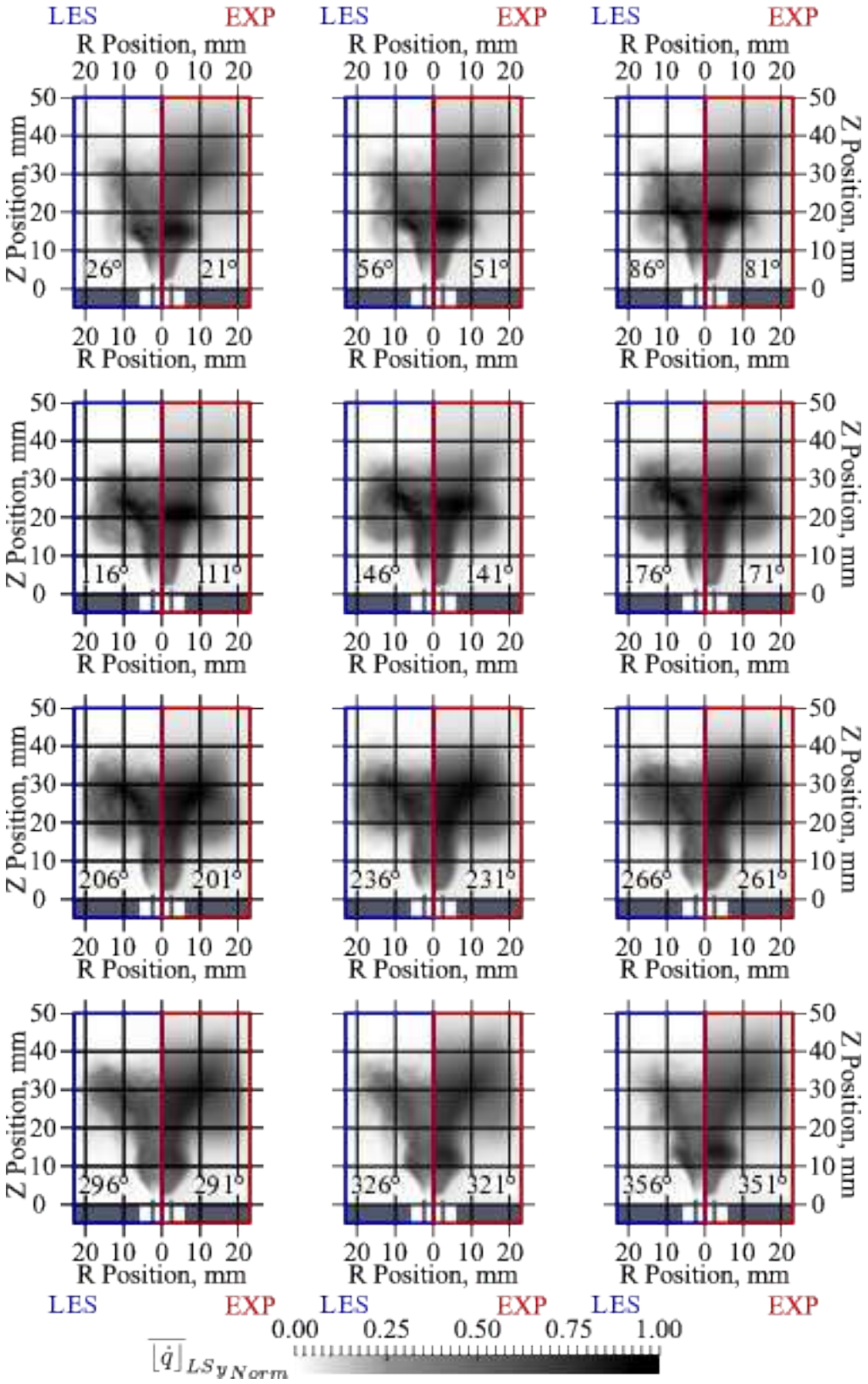

Figure 8.13: Phase locked normalized heat release rate as presented in Eq. **A.3.7** for a forced flame at a frequency of 400 Hz for the PC10 case. Left sides of the images are LES results and right sides are the experimental flame CH* chemiluminescence images. Phase angles wrt. the velocity signal at the outlet of the burner are indicated at the bottom of the images.

For PC10 case (Fig. 8.13), as methane injection flow rate is increased, the activity at the base of the flame is increased even more both for LES calculations and experimental measurements. The flame cone is moved slightly downstream as the attachment point is slightly further downstream, coming from the fact that the injection velocity is increased. However the fact that the flame length does not get shorter suggests that the displacement of the flame cone is balanced out by the increase in flame speed at the base of the flame. Even though the changes between PC4 and PC10 are small, they are well captured by LES calculations.

Examining figures 8.11, 8.12 and 8.13, it can be seen that the heat release response in the measurements and the LES calculations are in agreement and the phenomenons attributed with forced flame responses are well recovered. This idea will be used to explain how the flames are responding to acoustic perturbations.

One other interesting way to look at these flame images is to perform an inverse-abel transform to obtain a slice of the the axially symmetric flame. These images show more clearly how the flame is deformed and are more intuitive to post process. This pseudo angle-averaged phase averaged slice from experiments can be compared to an angle-averaged phase-averaged field obtained from LES calculations.

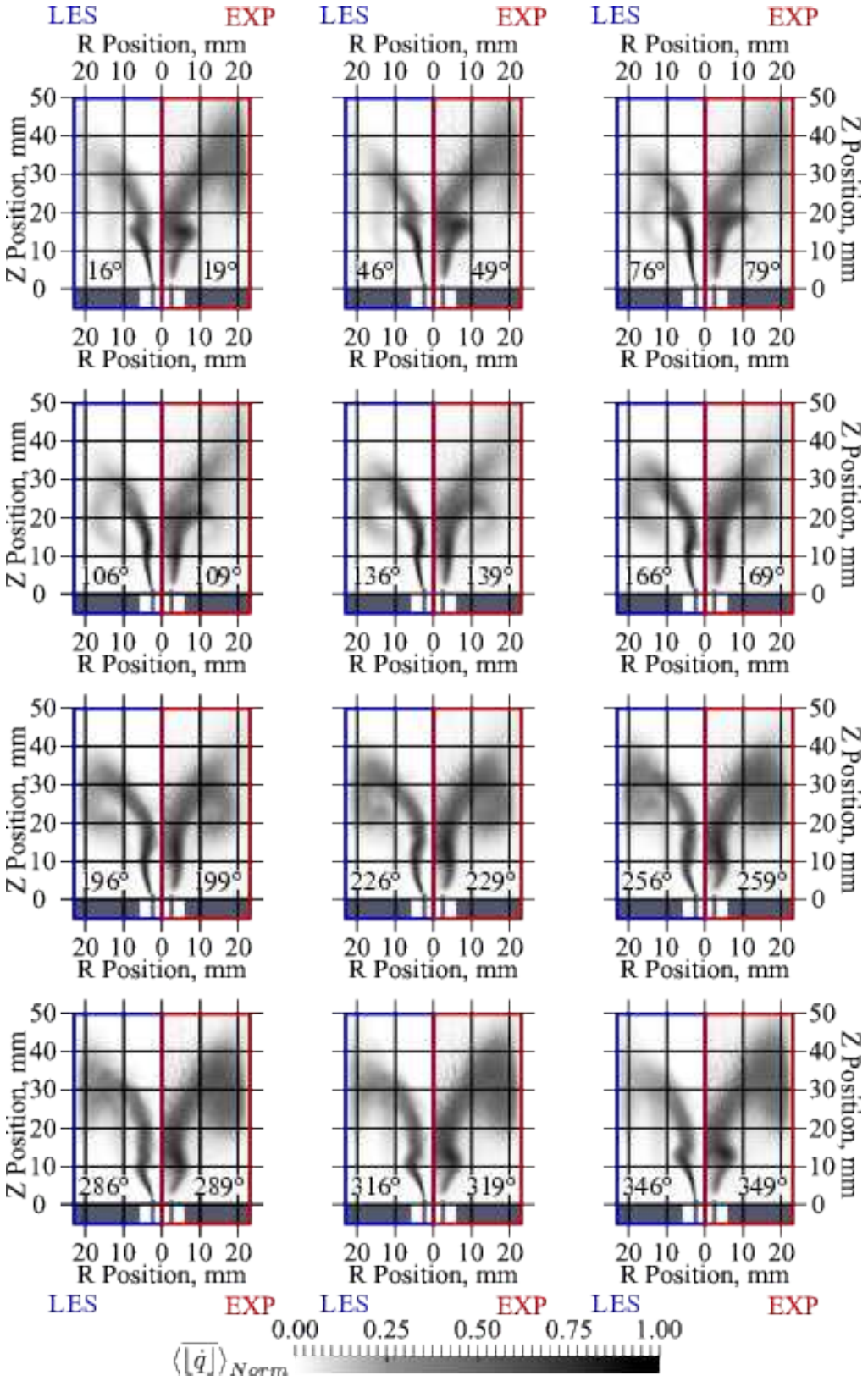

Figure 8.14: Phase locked normalized heat release rate as presented in Eq. **A.3.2** for a forced flame at a frequency of 400 Hz for the REF case. Left sides of the images are LES results and right sides are the experimental flame CH* chemiluminescence images. Phase angles are indicated at the bottom of the images.

Fig.8.14 displays the comparison of inverse abel transformed phase locked flame images to angle averaged phase averaged heat release field for REF case. The flame responds with its entire surface, with deformations varying in space. A disturbance at the flame front base close to the injection tube travels downstream with time, deforming the flame. The flame starts getting wrapped at around 140° of phase and $r = 10$, $z = 20$ mm in space. This wrapped portion of the flame is transported downstream with the flow, getting bigger as it is transported. At around 200° of phase the outer part of this wrapped part of the flame starts touching the walls of the combustion chamber. As the walls of the combustion chamber are colder, this part starts getting quenched at around 200° in phase. As it is transported upstream, the center of this wrapped part of the flame moves outwards and downstream more and more of the flame surface is lost by heat losses. At around 0° in phase the center traverses the combustion chamber walls and this rolled up portion of the flame is lost and the process is repeated for the new cycle.

In Fig.8.15 the same post processing for PC4 case has been presented. The intensity and activity at the flame base increases and the flame gets a bit wider at the base, both for LES calculations and experimental values wrt. the REF case. The same phenomenon of vortex roll-up is present, the formation of the rolled up flame can be seen at around 140° of phase. However, as a result of the widening at the base, the center of the rolled up part of the flame is moved slightly outwards of the combustion chamber on the order of 3 mm both for LES calculations and experimental measurements. As this rolled up part of the flame is transported downstream of the flame, it reaches the combustion chamber walls sooner than the REF case, and the loss of the flame surface happens sooner in the cycle compared to the REF case. This is one of the reasons why there is a small phase difference in FTFs of REF and PC4 cases, being this phase ifference is much smaller compared to the phase difference caused by hydrogen injection. Furthermore, the flame burns more intensely in the vicinity of the injection tube and less intensely along the axis of the combustion chamber, this changes the amplitude of the fluctuations in space. A phase difference appears between the base of the flame and the edges of the flame, this changes the global phase difference between the velocity fluctuations at the exit of the burner and the global heat release response of the flame.

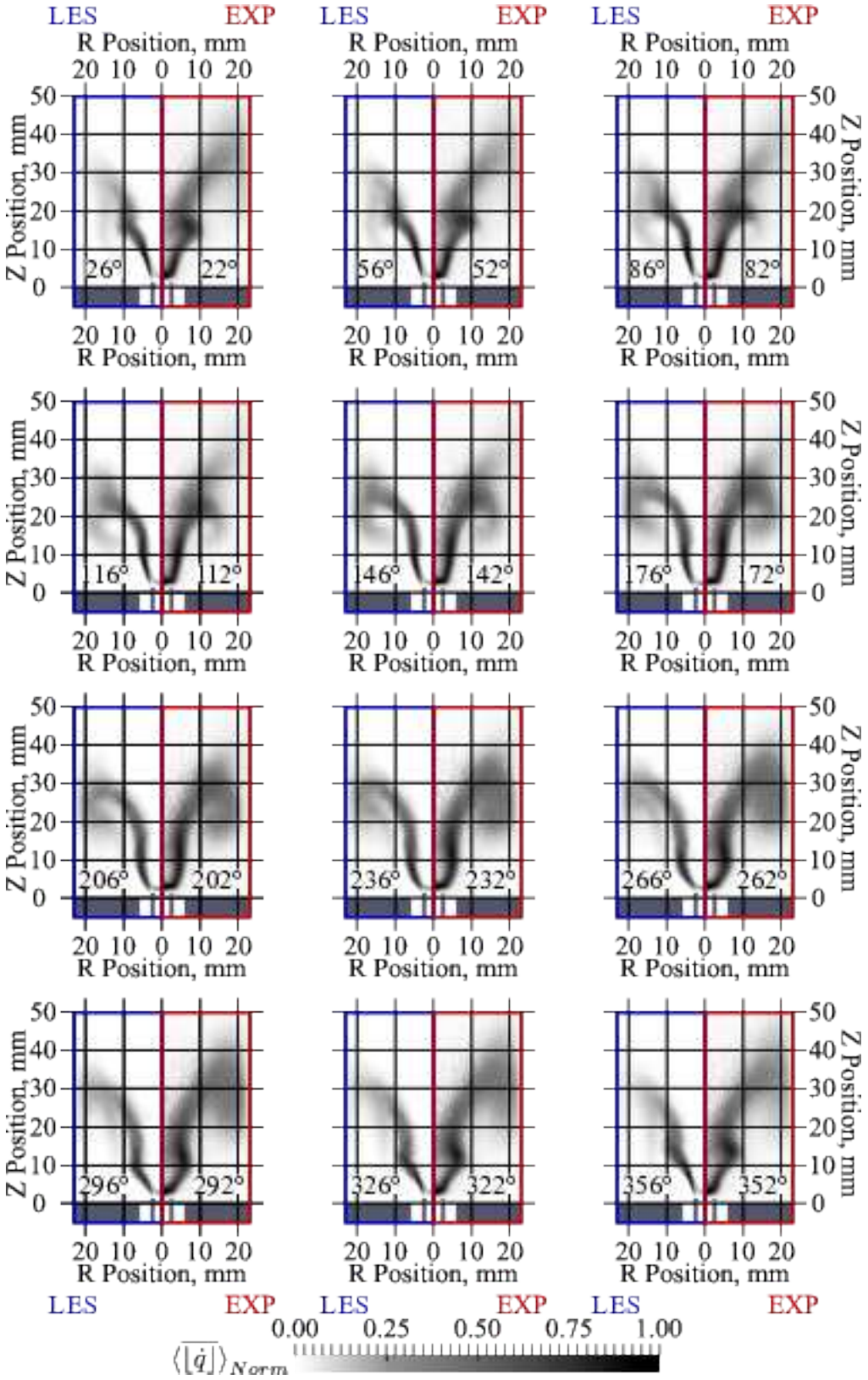

Figure 8.15: Phase locked normalized heat release rate as presented in Eq. **A.3.2** for a forced flame at a frequency of 400 Hz for the PC4 case. Left sides of the images are LES results and right sides are the experimental flame CH* chemiluminescence images. Phase angles are indicated at the bottom of the images.

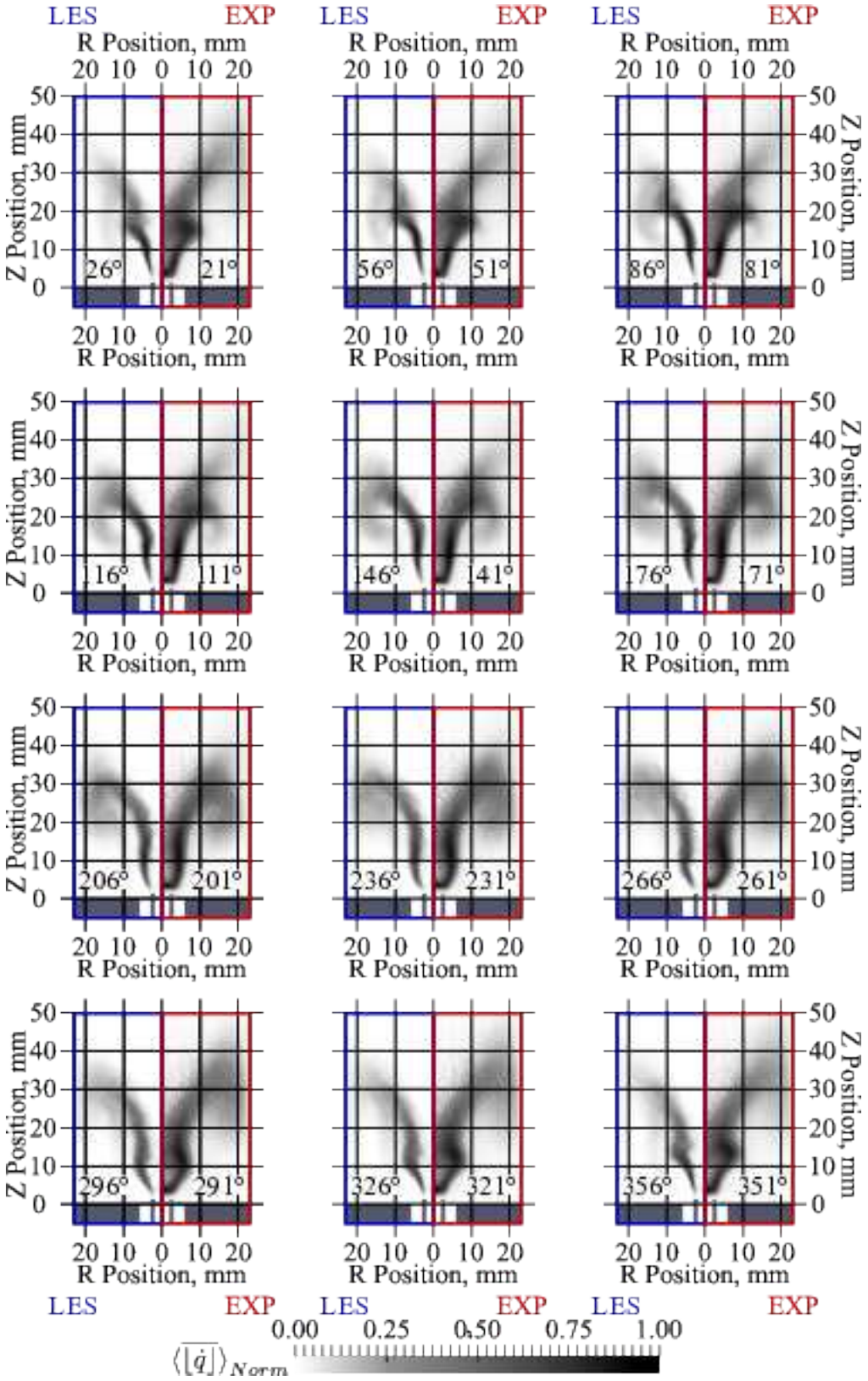

Figure 8.16: Phase locked normalized heat release rate as presented in Eq. **A.3.2** for a forced flame at a frequency of 400 Hz for the PC10 case. Left sides of the images are LES results and right sides are the experimental flame CH* chemiluminescence images. Phase angles are indicated at the bottom of the images.

PC10 case is presented in Fig. 8.16. Compared to REF and PC4 cases, PC10 burns even more intensely at the flame base, as a result flame response activity at the base of the flame is stronger. The pulsated flame of PC10 case is narrower compared to PC4 case, and wider compared to REF, however the formation of the rolled up flame at around 140° of phase for PC10 case is nearly the same as PC4 case, meaning the difference of phase of the FTF between PC10 and PC4 cases is less compared to the difference between PC4 and REF cases.

The comparisons of experimental and numerical flame responses to acoustic forcing were presented and the agreement between the experiments and LES calculations were established. As experimental PIV measurements including combustion are not available, LES calculations are used now to explain the response of the flame to acoustic forcing. This is done by calculating phase locked angle averaged fields of velocity like done for heat release. Then, the vorticity field was calculated from the velocity field. The conversion from cartesian to cylindrical coordinates are presented in Eq. 8.5.

$$\theta = \arctan(y/x), \quad \langle\overline{\lfloor v_r \rfloor}\rangle(r,z,\psi) = \langle\overline{\lfloor v_x \rfloor}\rangle\cos(\theta) + \langle\overline{\lfloor v_y \rfloor}\rangle\sin(\theta) \tag{8.5}$$

then the x-component of the vorticity field can be calculated as:

$$\text{Vorticity X}(r,z,\psi) = \frac{\partial\langle\overline{\lfloor u \rfloor}\rangle}{\partial y} - \frac{\partial\langle\overline{\lfloor v_r \rfloor}\rangle}{\partial z} \tag{8.6}$$

Where i represents the mesh points where the fields are evaluated. The resulting vorticity and axial velocity u fields and superimposed heat release contours are presented in Fig. 8.17 for all cases.

In Fig. 8.17, all the images presented are phase averaged angle averaged fields of the respective fields and the contours obtained from the averaged fields. On the left side of the images for a given phase angle, the vorticity field and the superimposed heat release contours are presented. On the right side, the axial velocity contours and the and the superimposed heat release contours are presented for ease of comparison. It can be seen that there is a strong vortex that is formed at around ≈290 °, turning counter clock-wise for all cases. This vortex is transported downstream with the flow, distorting the flame as it goes along. At around ≈ 110 °, the edges of the flame starts getting wrapped around this vortex, establishing the foundation of the vortex roll-up

phenomenon and creating additional flame surface. At the same time, this vortex starts getting shed while it is transported with the flow. At around $\approx$200 $^\circ$ the flame is wrapped around the vortex and it can be seen that the outer edges of the rolled up flame towards the combustion chamber walls gets compressed as there is flame surface loss due to heat losses to the chamber walls. At the same time, as expected, the kinetic energy of the vortex is diffused as it is transported downstream as it can be seen that the amplitude of the vorticity is diminished. At around $\approx$290 $^\circ$ the flame vortex gets closer to the wall and the outer side of the flame rapped around the vortex is lost, creasing a big loss of flame surface. At around $\approx$20 $^\circ$ the vortex is at the chamber wall and its kinetic energy is much less, as it is diffused at the chamber walls while traversing the flame edge. This process is repeated for each cycle, resulting in creation of flame surface and flame surface loss, constituting flame response.

At the vicinity of the injection tube, the flame is at a position where it is closer to a field of vorticity which is turning clockwise, contrary to the main vortex causing vortex roll-up phenomenon turning counter clockwise, suggesting that the base of the flame is more susceptible to the velocity fluctuations at the base compared to the vortex that is formed. At the beginning of the cycle when the axial velocity at the burner outlet is at its maximum, the flame angle (between the flame and the axis of the combustion chamber) in the vicinity of the injection tube is much lower for all cases compared to further along the cycle where the axial velocity at the burner exit is lower resulting in a steeper flame angle.

Comparing between cases, it can be seen that injecting low amounts of methane through the injection tube changes slightly the phase of creation and loss of flame surface, however, increasing the injection flow-rate while keeping the same power does not change it further, resulting in a saturation phenomenon. The dominant change between REF and PC4 cases of FTF phase happens due to the movement of the vortex roll-up towards the chamber walls, for PC10 case this vortex roll-up does not move resulting in the nearly same phase response as PC4 case.

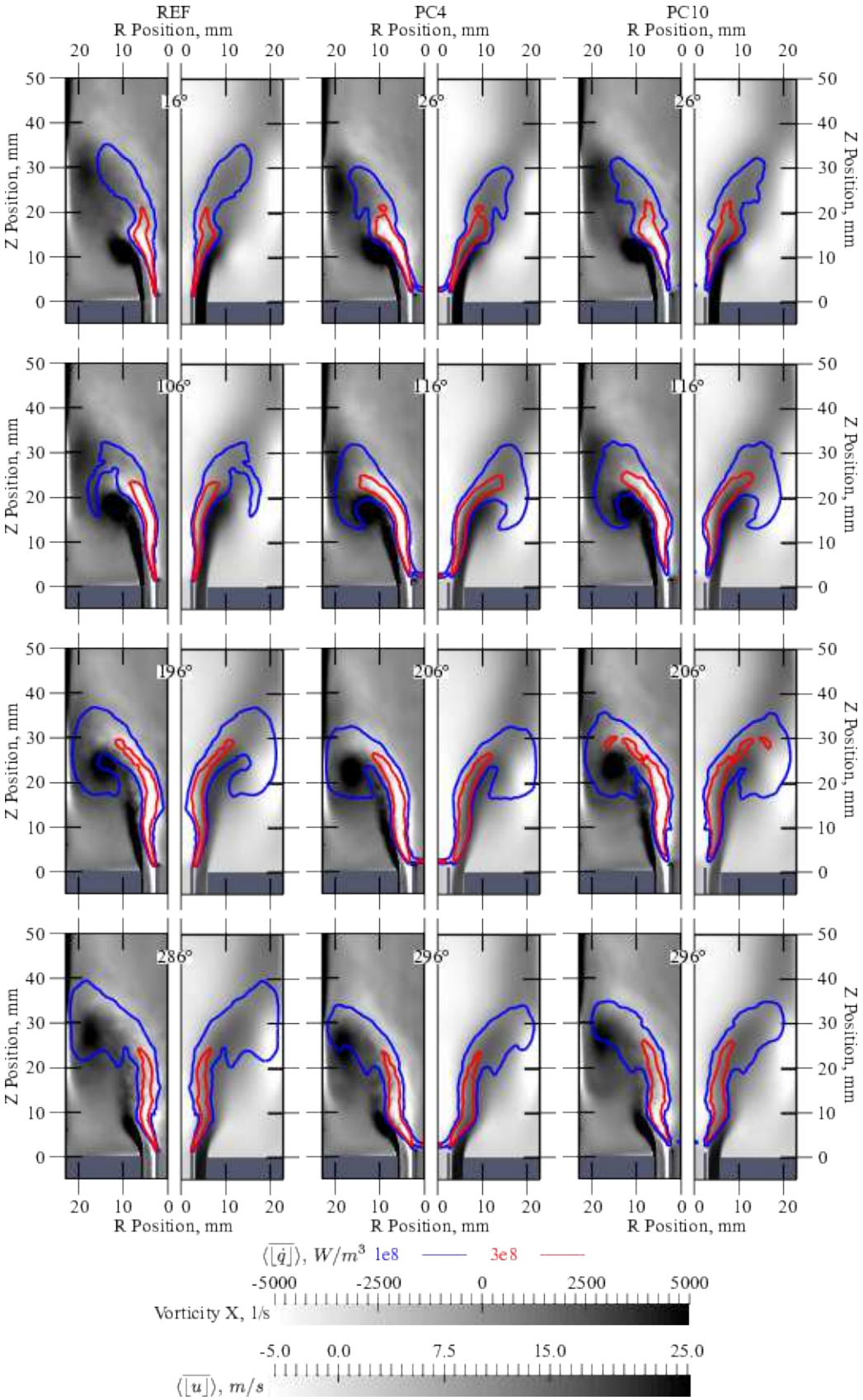

Figure 8.17: Mechanism leading to deformation of the flame during a forcing cycle. On the left of each image vorticity field with heat release contours superimposed on top, on the right of each image the velocity field with heat release contours superimposed on top has been presented.

8.4 Spectral Analysis of Flame Response

To conclude the effect of pilot injection on the flame dynamics, spectral analysis of phase locked flame images and forced LES calculations has been performed. As the disturbance at the flame root is convected along the flame, it bends and contorts the flame. When there is pilot injection, the response of the root of the flame changes. To explore this effect, spectral analysis of the flame heat release response to acoustic pulsations along the combustion chamber has been performed. First of all, to show where the flame is most active during a forcing cycle, the root mean squares of line of sight integrated heat release fluctuations is investigated in Fig. 8.18.

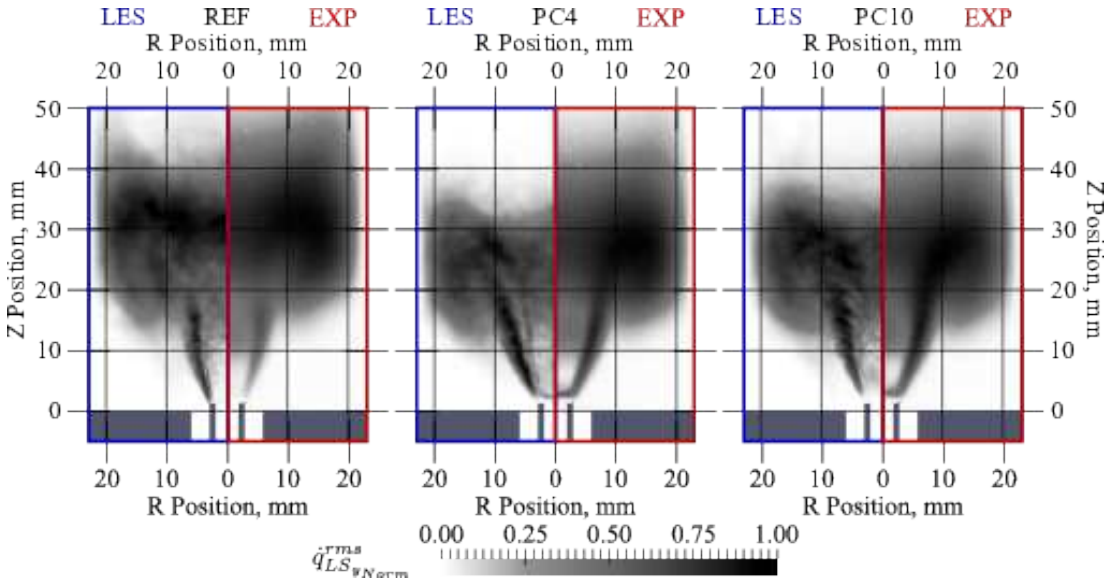

Figure 8.18: Normalized RMS field of heat release fluctuations during a forcing cycle. On the left side of the images, LES calculations, on the right side of the images, experimental measurements are presented.

Fig. 8.18 shows that there is more activity at the bases of the flames with secondary methane injection both for LES calculations and experimental measurements, and increasing injection flow-rate increases this activity or root mean square of heat release field further. The capabilities of LES calculations in predicting flame responses are once again upheld; the shortening of the flame activity of PC4 and PC10 cases with respect to REF case is well predicted.

The local amplitude and phase fields are extracted using techniques summed up in Appendix A.3. These fields offer a more intuitive view of the local responses an how the global response is constituted as the global heat release response is the integral of the local complex amplitudes.

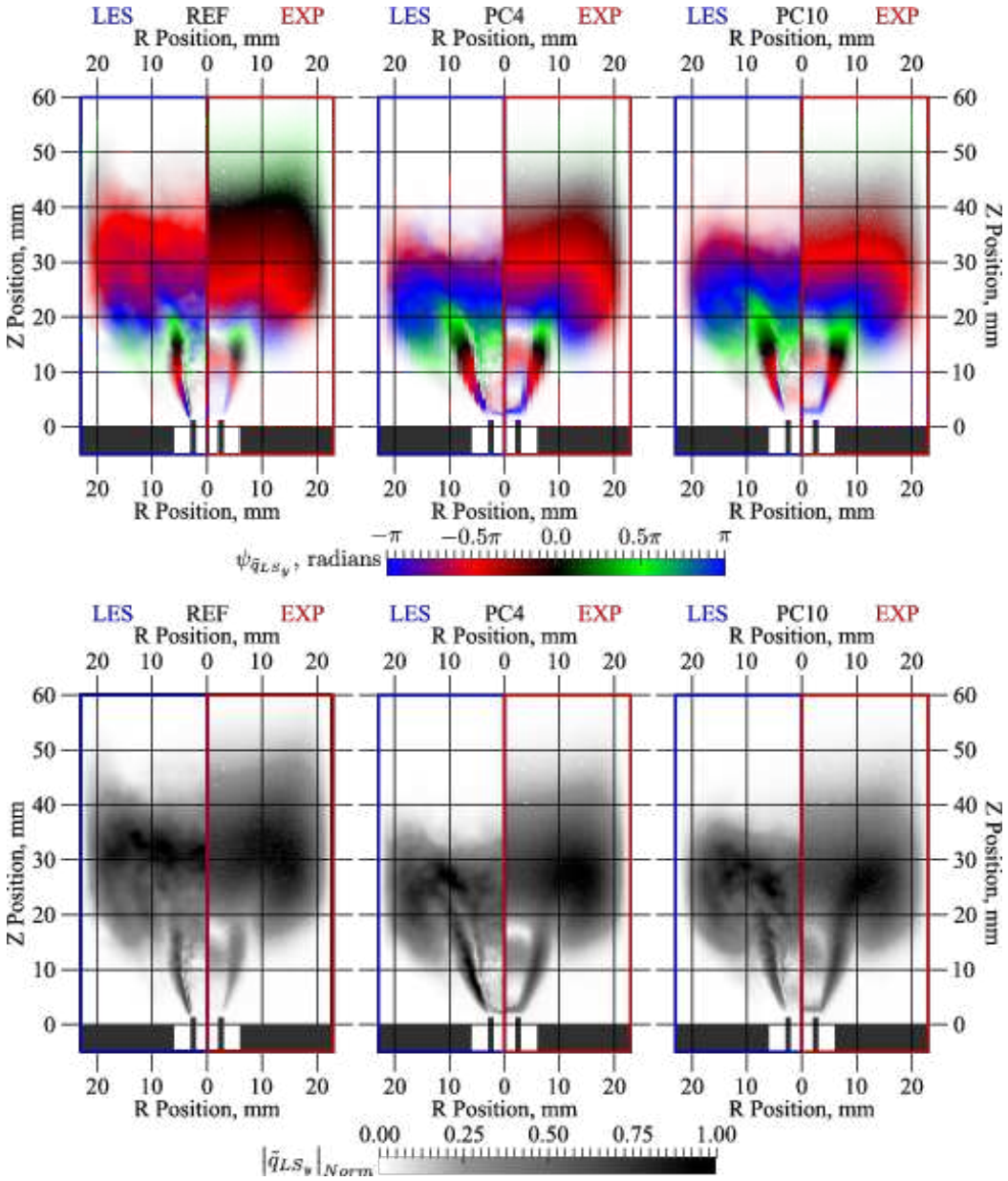

Figure 8.19: Complex field of heat release fluctuations represented by phase (Eq. **A.3.16**) at the top and by normalized amplitude (Eq. **A.3.15**) at the bottom. On the left side of each figure, LES results and on the right side experimental measurements are presented.

Convention shown in Fig. 8.19 leads to the harmonic instantaneous heat release rate as shown in Eq. 8.7.

$$\dot{q}_{LS_y}(r,z,t) = Re\left\{\tilde{q}_{LS_y}(r,z)e^{-i\omega t}\right\} + \bar{\dot{q}}_{LS_y}(r,z) + \text{Noise} \tag{8.7}$$

To further analyze the spectral response and the effect of injection on the responses of the flames, profiles of radially integrated heat release fields will be used as presented in Chapter 6. Thiis is straightforward for experimental flame images as the pixels are uniformly located in space, however in LES calculations, neither mesh points not the

size of the cells are uniform, leading to the integration by volume of the cells that are in a thin slice that the height equal to magnification ratio of the camera representing the field of view of a row of pixels to get the radially integrated heat release response profiles. The procedure is summed up in Appendix A.3. The axial profiles of flame response characteristics for REF case are shown in Fig. 8.20.

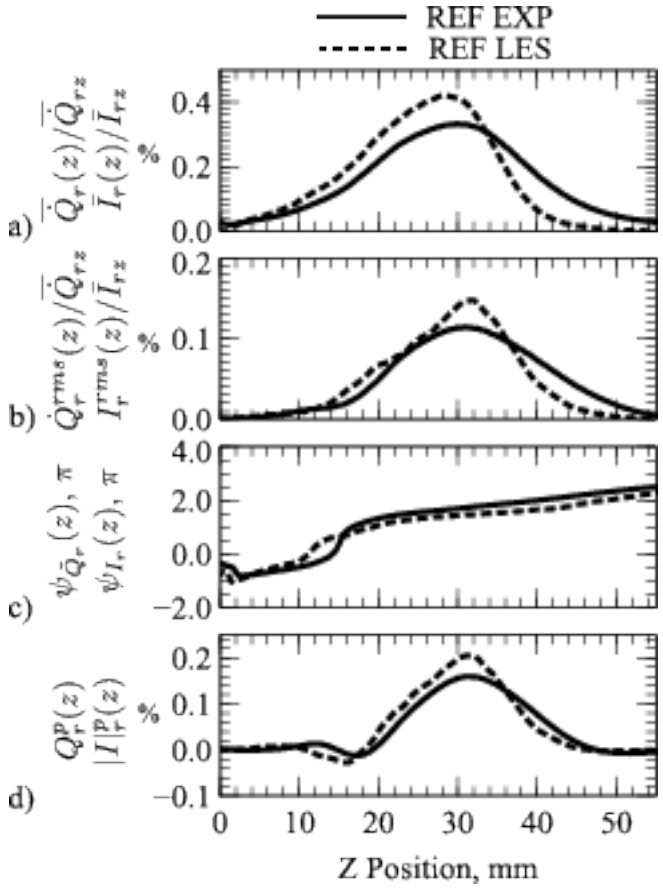

Figure 8.20: REF case at 400 Hz: longitudinal evolution of the cross-stream averaged heat release rate. a) normalized time-averaged heat release rate; b) normalized root-mean-square fluctuations; c) phase of heat release fluctuations; d) projection of the the radially integrated heat release on the global heat release.

Examining Fig. 8.20.a), it can be seen that the mean forced LES flame is marginally shorter compared to the mean forced experimental flame. The bulk of the flame response happens at around 30 mm of axial position where the maximum of the RMS fluctuations are reached, without much interference coming from the base of the flames, both for LES calculations and experimental measurements. The RMS of heat release fluctuations are marginally higher in LES calculations compared to experimental measurements so that the LES flames are marginally more responsive to acoustic forcing. The phase is very well represented in LES calculations, validating

that the acoustic forcing response calculated using LES represents the physics quite well. Looking at the projection of the radially integrated heat release on the global heat release, it can be seen that the flames respond in unison with its entirety in LES calculations and experimental measurements, there is not much phase contribution from the base of the flame. The gains and phases obtained from experimental measurements and LES calculations are presented in Table 8.2.

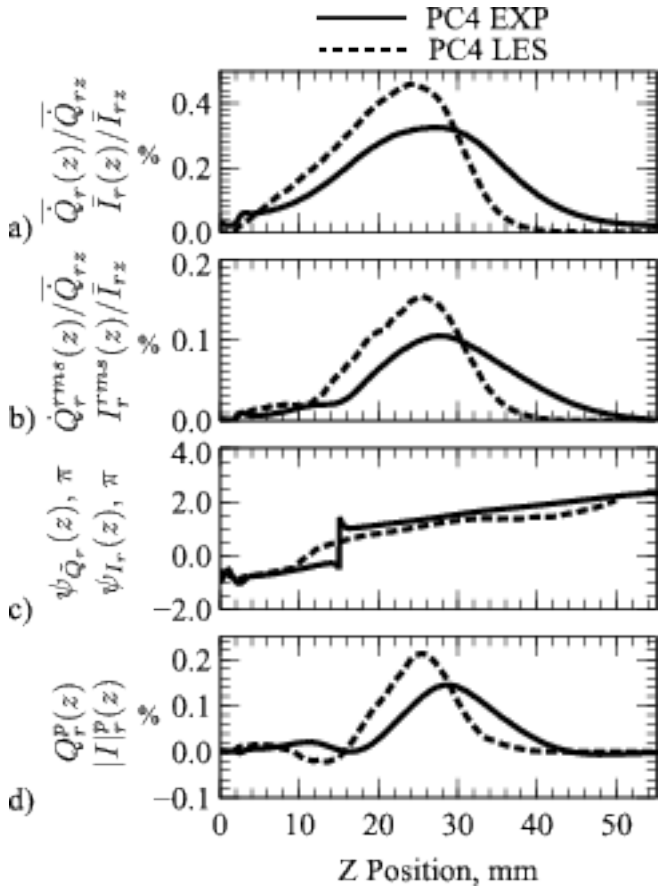

Figure 8.21: PC4 case at 400 Hz: longitudinal evolution of the cross-stream averaged heat release rate. a) normalized time-averaged heat release rate; b) normalized root-mean-square fluctuations; c) phase of heat release fluctuations; d) projection of the the radially integrated heat release on the global heat release.

In Fig. 8.21, the axial profiles of the characteristic flame response parameters for the PC4 case are shown. Compared to the REF case (8.20), the PC4 flames are shorter and they are more responsive closer to the injection tube at around 27 mm compared to the maximum of the RMS fluctuations of 30 mm of the REF case both for LES calculations and experimental measurements. The LES flame of PC4 case is slightly shorter and more responsive at the base compared to the experimental measurements, however the general tendency is quite well reproduced. The artifact in the phase in

Fig. 8.21 is caused by the competition of the middle and exterior parts of the flame having different phases as can be seen in Fig. 8.19. The phase plot of the LES flame is cut at 49 mm, as after this point there is no heat release, so the phase does not hold information. There is slight increase in heat release fluctuation activity at the base of the injection tube, but the increase in activity is much less compared to hydrogen injection presented in Chapter 6. Interestingly, the wide but less intense response in the calculations matches quite well with the FTF gains of the narrower but more intense response of the LES calculations as presented in Table 8.2.

Fig. 8.22 displays the axial profiles of the characteristic flame response parameters for the PC10 case. The change in length of the averaged flames are much less between PC10 and PC4 cases compared to the change in lengths between PC4 and REF cases and this holds true for RMS of the heat release fluctuations. The base of the flames becomes more active and contributes to the global heat release response. In Fig. 8.22.d the projection of the the radially integrated heat release on the global heat release is presented. The negative parts of this curve mark the parts of the flames responding with a phase difference that is destructive, meaning these parts cause a drop in the FTF gain, and the positive parts cause a increase in the FTF gain. With the increased flowrates of injection, the base of the flames start to respond and start to 'pull back' the global gain of the FTF. Although this 'pull back' effect is there for 10% methane injection, it is much less compared to hydrogen injection as presented in Chapter 6. The LES flame of PC10 case is more responsive along all the axis of the combustion chamber compared to experimental measurements, however the phase is once again very well represented.

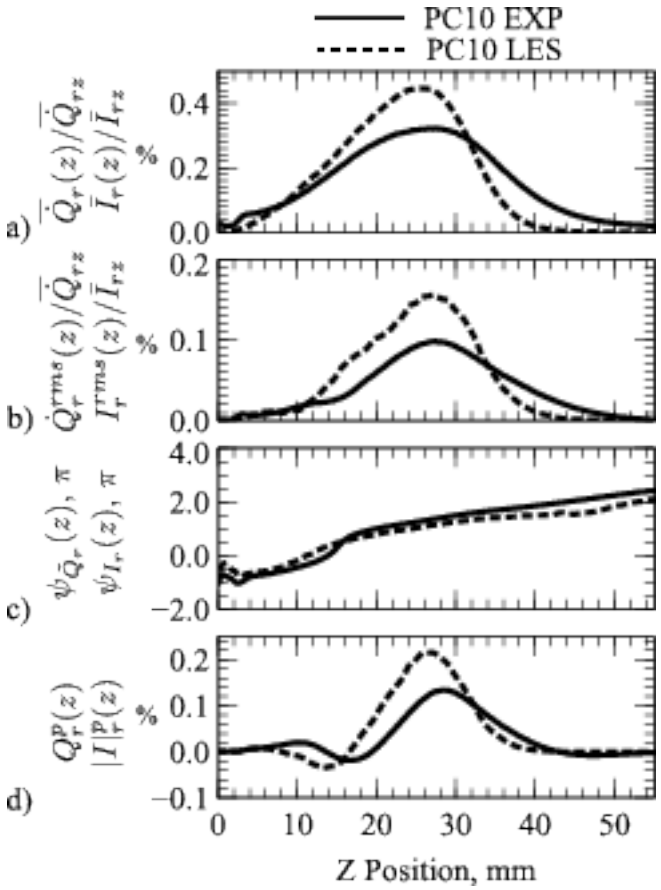

Figure 8.22: PC10 case at 400 Hz: longitudinal evolution of the cross-stream averaged heat release rate. a) normalized time-averaged heat release rate; b) normalized root-mean-square fluctuations; c) phase of heat release fluctuations; d) projection of the the radially integrated heat release on the global heat release.

The FTF gains and phases obtained from LES calculations and experimental measurements are summed up in Table 8.2 for all cases studied experimentally and computationally. There are slight differences between the experimental and LES gains and phases, however the drop in the phase of the FTF as the flowrate of methane injection is increased is well predicted by LES calculations.

Table 8.2: Flame transfer function gains and phases obtained from experimental measurements and LES calculations for a forcing level of %30 at 400 Hz of frequency for respective cases.

	Gain		Phase, radians	
	EXP	LES	EXP	LES
REF	1.23	1.30	5.62	4.44
PC4	1.04	1.07	4.46	3.52
PC10	0.83	1.13	4.67	3.57

Finally, to conclude the validity of the velocity reconstruction technique presented in Appendix A.1 the same technique is applied to LES calculations. In experimental measurements, acoustic velocity measurements at the burner outlet is not available as the position is not accessible and measurements at this location is quite difficult. So a model has been developed to reconstruct the acoustic velocity at the outlet of the burner to measure flame transfer functions. The validity of this model can be verified using LES calculations, where both pressure and velocity information both at the hot wire location and the burner outlet is readily available. The reconstructed and sampled (measured in LES) time traces of the velocity at the burner outlet has been presented in figures 8.23, 8.24 and 8.25 for the respective cases.

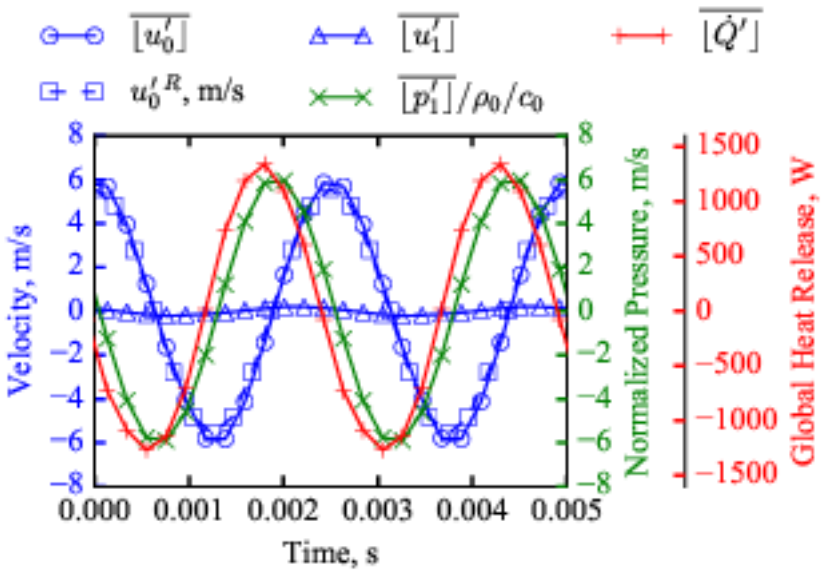

Figure 8.23: Phase averaged signals of the LES calculations and the reconstructed velocity for REF case. $\overline{\lfloor u_0' \rfloor}$ is the acoustic velocity measured at the HW location in Fig. 5.1, $\overline{\lfloor p_1' \rfloor}/\rho_0/c_0$ is the normalized acoustic pressure, $\overline{\lfloor u_1' \rfloor}$ is the velocity measured in LES at the burner exit and $u_0'^R$ is the acoustic velocity at the burner outlet reconstructed using the technique presented in Appendix A.1

Figures 8.23, 8.24 and 8.25 show the validity of the velocity reconstruction technique and its convenience in measuring flame transfer functions.

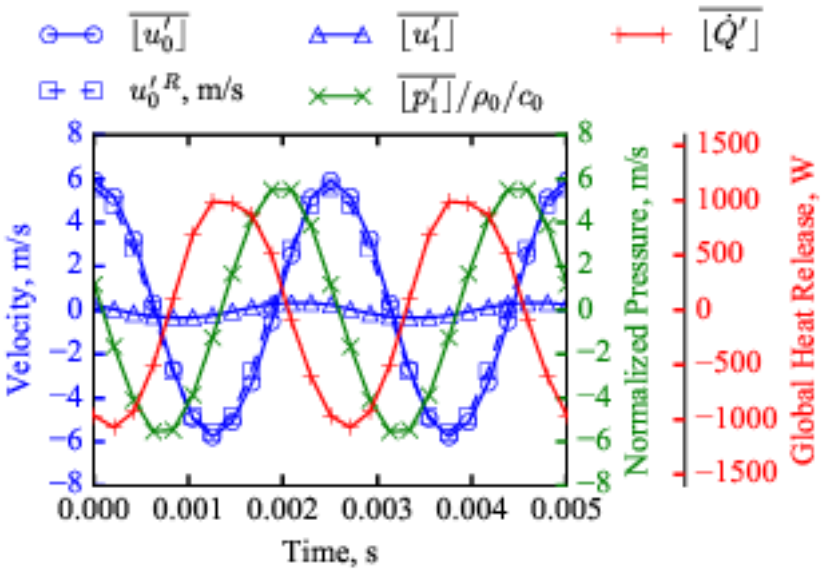

Figure 8.24: Phase averaged signals of the LES calculations and the reconstructed velocity for PC4 case. $\overline{\lfloor u_0' \rfloor}$ is the acoustic velocity measured at the HW location in Fig. 5.1, $\overline{\lfloor p_1' \rfloor}/\rho_0/c_0$ is the normalized acoustic pressure, $\overline{\lfloor u_1' \rfloor}$ is the velocity measured in LES at the burner exit and $u_0'^R$ is the acoustic velocity at the burner outlet reconstructed using the technique presented in Appendix A.1

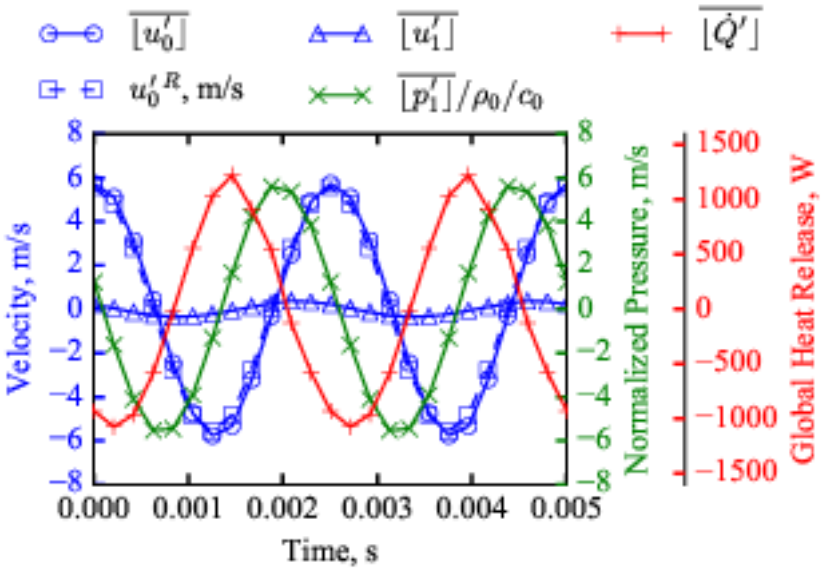

Figure 8.25: Phase averaged signals of the LES calculations and the reconstructed velocity for PC10 case. $\overline{\lfloor u_0' \rfloor}$ is the acoustic velocity measured at the HW location in Fig. 5.1, $\overline{\lfloor p_1' \rfloor}/\rho_0/c_0$ is the normalized acoustic pressure, $\overline{\lfloor u_1' \rfloor}$ is the velocity measured in LES at the burner exit and $u_0'^R$ is the acoustic velocity at the burner outlet reconstructed using the technique presented in Appendix A.1

8.5 Conclusions

In this chapter, experimental and LES techniques are used to study the flow and forced flame response characteristics of perfectly premixed (REF) and piloted premixed PC4, PC10) flames. Using flame imaging techniques, experimental fields of CH* emission (a marker of heat release) are compared to heat release fields obtained from LES calculations. The agreement between LES calculations and experimental measurements shows that flame response characteristics and the vortex roll-up phenomenon can be studied using flow fields obtained from LES calculations for all the configurations studied. It has been shown that the main cause of the heat release response is the destruction of the flame surface as the rolled-up vortex approaches the combustion chamber walls. The effects of secondary methane injection on the heat release responses of acoustically forced flames were also examined, and it has been shown that the injection increases the flame response at the base of the flames, creating a pull-back effect at high injection flowrates of 10%. Additionally, the acoustic field reconstruction technique is verified using LES calculations and is deemed reliable even for moderate frequencies.

9. Concluding Remarks

In this thesis, the static stability characteristics of swirl stabilized premixed flames with different injection strategies were investigated in a setup called MIRADAS. It has been concluded that hydrogen, either injected directly into the combustion chamber (pilot injection) either mixed in with the main flow, reduces the length of the flames. However pilot hydrogen injection is much more effective in flame attachment compared to methane piloting and hydrogen enrichment.

Subsequently, the dynamic stability characteristics of the MIRADAS setup were explored and it has been shown that hydrogen injection at very low fractions of thermal power ($\leq 2\%$) changes the stability characteristics, resulting in more stable flames for a wide range of operating conditions. This is not true for hydrogen enrichment and methane injection, the stability characteristics are not altered with low levels of enrichment or methane piloting.

Next, the global heat release response of flames with different injection strategies were studied: hydrogen injection and hydrogen enrichment lowers the heat release delay of flame responses to acoustic fluctuations and piloting strategies changes the gain of the flame transfer functions. Here hydrogen piloting is again the most effective option; causing a reduction in time delays of flame responses and a broadband reduction in FTF gain. It is demonstrated that hydrogen injection can be used to passively control combustion instabilities. Subsequently, the local flame responses are studied and it is shown that this broadband reduction in the gain of FTFs is caused by competition of heat release responses, mainly the region close to the injection tube and the flame edges. The reduction in time delay is caused by increased flame speeds, resulting in shorter flames.

Thereafter, emission measurements are presented and it is shown that hydrogen injection causes a very slight increase in NOx emissions. it was found out that keeping the thermal power constant, hydrogen enrichment does not change NOx emissions. However hydrogen addition in both configurations result in a remarkable drop in

CO_2 emissions. This configuration can be taken further as introducing hydrogen in both premixed main stream and a very low power injection to stabilize combustion instabilities, resulting in flames that are low NOx, low CO_2 and stable.

Finally, LES calculations and their comparisons with experimental results were displayed. It is demonstrated that the heat release response is caused by the increase in the flame surface area caused by the vortex roll-up mechanism and the destruction of the flame surfave area when the rolled up parts of the flame touches the combustion chamber walls. Furthermore the acoustic reconstruction technique to measure actual flame transfer functions has been validated.

It has been shown that hydrogen can be used to make systems more stable, rather than making them unstable. This technique can easily be applied in existing systems with flow partitioning techniques and simple valves that eliminate the need of high precision, but highly expensive thermal mass flow meters that also increase pressure drop. In high power systems like gas turbines and boilers, the air-fuel ratio is closely monitored and kept to a set point, so that a simple pre-designed injection systems can be used to stage hydrogen and natural gas to needs, rather than controlling the flow of each injection point corresponding to hydrogen injection and hydrogen enrichment. This makes the application of hydrogen piloting highly applicable in gas powered systems. In this thesis, pure hydrogen and pure methane piloting is explored, further experiments are needed to conclude the effect of fuel piloting when hydrogen enrichment is applied. Furthermore the effect of swirl on pilot fuel flow can be explored, as it would increase mixing, it should reduce NOx emissions when piloting is applied, while still benefiting from increased stability.

REFERENCES

[1] **Dunn-Rankin, D.** (2011). *Lean Combustion: Technology and Control*, Elsevier Science, https://books.google.fr/books?id=qVg51XOpiOEC.

[2] **IEA** (2019). World Energy Outlook 2019, **Technical Report**, Paris.

[3] **Stolten, D. and Scherer, V.** (2013). *Transition to Renewable Energy Systems*, Wiley, https://books.google.fr/books?id=fEjqL9gIVCkC.

[4] **Genovese, A.**, **Contrisciani, N.**, **Ortenzi, F. and Cazzola, V.** (2011). On road experimental tests of hydrogen/natural gas blends on transit buses, *International Journal of Hydrogen Energy*, *36*(2), 1775–1783, http://www.sciencedirect.com/science/article/pii/S0360319910022044.

[5] **Candel, S.** (2002). Combustion dynamics and control: Progress and challenges, *Proceedings of the Combustion Institute*, *29*(1), 1–28, http://www.sciencedirect.com/science/article/pii/S1540748902800074.

[6] **Lieuwen, T.C. and Yang, V.** (2005). *Combustion instabilities in gas turbine engines: operational experience, fundamental mechanisms and modeling*, Progress in astronautics and aeronautics, American Institute of Aeronautics and Astronautics, https://books.google.fr/books?id=4{_}pTAAAAMAAJ.

[7] **Berenbrink, P. and Hoffmann, S.**, (2000), Suppression of Dynamic Combustion Instabilities by Passive and Active Means, http://dx.doi.org/10.1115/2000-GT-0079.

[8] **Guiberti, T.F.**, **Durox, D. and Schuller, T.** (2017). Flame chemiluminescence from CO2- and N2-diluted laminar CH4/air premixed flames, *Combustion and Flame*, *181*, 110–122, http://www.sciencedirect.com/science/article/pii/S0010218017300974.

[9] **Nori, V.N. and Seitzman, J.M.** (2009). CH* chemiluminescence modeling for combustion diagnostics, *Proceedings of the Combustion Institute*, *32*(1), 895–903, http://www.sciencedirect.com/science/article/pii/S1540748908001089.

[10] **Darwin, C.** (1872). *The Descent of Man, and Selection in Relation to Sex*, numberv. 1 in Marilee E. Thomas and Robert C. Thomas Science and Related Subjects Collection, D. Appleton, https://books.google.fr/books?id=LYEQAAAAYAAJ.

[11] **Berna, F.**, **Goldberg, P.**, **Horwitz, L.K.**, **Brink, J.**, **Holt, S.**, **Bamford, M. and Chazan, M.** (2012). Microstratigraphic evidence of in situ fire in the Acheulean strata of Wonderwerk Cave, Northern Cape province, South Africa, *Proceedings of the National Academy of Sciences*, *109*(20), E1215 LP – E1220, http://www.pnas.org/content/109/20/E1215.abstract.

[12] **Hlubik, S.**, **Berna, F.**, **Feibel, C.**, **Braun, D. and Harris, J.W.K.** (2017). Researching the Nature of Fire at 1.5 Mya on the Site of FxJj20 AB, Koobi Fora, Kenya, Using High-Resolution Spatial Analysis and FTIR Spectrometry, *Current Anthropology*, *58*(S16), S243–S257, https://doi.org/10.1086/692530.

[13] **Götz, M.**, **Lefebvre, J.**, **Mörs, F.**, **McDaniel Koch, A.**, **Graf, F.**, **Bajohr, S.**, **Reimert, R. and Kolb, T.** (2016). Renewable Power-to-Gas: A technological and economic review, *Renewable Energy*, *85*, 1371–1390, http://www.sciencedirect.com/science/article/pii/S0960148115301610.

[14] **Lehner, M.**, **Tichler, R.**, **Steinmüller, H. and Koppe, M.** (2014). *Power-to-Gas: Technology and Business Models*, SpringerBriefs in Energy, Springer International Publishing, https://books.google.fr/books?id=X8okBAAAQBAJ.

[15] **Steinberg, M. and Cheng, H.C.** (1989). Modern and prospective technologies for hydrogen production from fossil fuels, *International Journal of Hydrogen Energy*, *14*(11), 797–820, http://www.sciencedirect.com/science/article/pii/0360319989900189.

[16] **De Falco, M. and Basile, A.** (2015). *Enriched Methane: The First Step Towards the Hydrogen Economy*, Green Energy and Technology, Springer International Publishing, https://books.google.fr/books?id=fyHUCgAAQBAJ.

[17] **Sherif, S.A.**, **Goswami, D.Y.**, **Stefanakos, E.K. and Steinfeld, A.** (2014). *Handbook of Hydrogen Energy*, Mechanical and Aerospace Engineering Series, Taylor & Francis, https://books.google.fr/books?id=jGkLBAAAQBAJ.

[18] **Vázquez, F.V.**, **Koponen, J.**, **Ruuskanen, V.**, **Bajamundi, C.**, **Kosonen, A.**, **Simell, P.**, **Ahola, J.**, **Frilund, C.**, **Elfving, J.**, **Reinikainen, M.**, **Heikkinen, N.**, **Kauppinen, J. and Piermartini, P.** (2018). Power-to-X technology using renewable electricity and carbon dioxide from ambient air: SOLETAIR proof-of-concept and improved process concept, *Journal of CO2 Utilization*, *28*, 235–246, http://www.sciencedirect.com/science/article/pii/S2212982018305213.

[19] **Bailera, M.**, **Lisbona, P.**, **Romeo, L.M. and Espatolero, S.** (2017). Power to Gas projects review: Lab, pilot and demo plants for storing renewable energy and CO2, *Renewable and Sustainable Energy Reviews*, *69*, 292–312, http://www.sciencedirect.com/science/article/pii/S1364032116307833.

[20] **König, D.H.**, **Freiberg, M.**, **Dietrich, R.U. and Wörner, A.** (2015). Techno-economic study of the storage of fluctuating renewable energy in liquid hydrocarbons, *Fuel*, *159*, 289–297, http://www.sciencedirect.com/science/article/pii/S0016236115006651.

[21] **Kopernikus-Projekte**, (2020), Kopernikus-Projekt P2X, https://www.kopernikus-projekte.de/projekte/p2x.

[22] **RWTH Aachen**, (2016), Power-To-X: Entering the Energy Transition with Kopernikus, https://www.rwth-aachen.de/go/id/kvyv/lidx/1.

[23] **German Technical and Scientific Association for Gas and Water (DVGW)**, (2016), STORE&GO Project kick-off in Karlsruhe.

[24] **Bosch Industriekessel GmbH**, (2020), Universal Steam Boiler UL-S, UL-SX, https://www.bosch-thermotechnology.com/global/en/ocs/commercial-industrial/universal-steam-boiler-ul-s-ul-sx-669474-p/.

[25] **Wärtsilä Corporation**, (2020), Wärtsilä gas engines to burn 100% hydrogen, https://www.wartsila.com/media/news/05-05-2020-wartsila-gas-engines-to-burn-100-hydrogen-27009

[26] **Villante, C. and Genovese, A.** (2012). Hydromethane: A bridge towards the hydrogen economy or an unsustainable promise?, *International Journal of Hydrogen Energy*, *37*(15), 11541–11548, http://www.sciencedirect.com/science/article/pii/S0360319912007136.

[27] **Moliner, R.**, **Lázaro, M.J. and Suelves, I.** (2016). Analysis of the strategies for bridging the gap towards the Hydrogen Economy, *International Journal of Hydrogen Energy*, *41*(43), 19500–19508, http://www.sciencedirect.com/science/article/pii/S0360319916303287.

[28] **Melaina, M.W.**, **Antonia, O. and Penev, M.** (2013). Blending Hydrogen into Natural Gas Pipeline Networks. A Review of Key Issues, **Technical Report**, United States, https://www.osti.gov/servlets/purl/1219920.

[29] **Tang, C.**, **Zhang, Y. and Huang, Z.** (2014). Progress in combustion investigations of hydrogen enriched hydrocarbons, *Renewable and Sustainable Energy Reviews*, *30*, 195–216, http://www.sciencedirect.com/science/article/pii/S1364032113007041.

[30] **MacLean, H.L. and Lave, L.B.** (2003). Evaluating automobile fuel/propulsion system technologies, *Progress in Energy and Combustion Science*, *29*(1), 1–69, http://www.sciencedirect.com/science/article/pii/S0360128502000321.

[31] **Poulton, M.L.** (1994). Alternative fuels for road vehicles.

[32] **Ma, F. and Wang, Y.** (2008). Study on the extension of lean operation limit through hydrogen enrichment in a natural gas spark-ignition engine, *International Journal of Hydrogen Energy*, *33*(4), 1416–1424, http://www.sciencedirect.com/science/article/pii/S0360319907007665.

[33] **Dimopoulos, P.**, **Bach, C.**, **Soltic, P. and Boulouchos, K.** (2008). Hydrogen–natural gas blends fuelling passenger car engines: Combustion, emissions and well-to-wheels assessment, *International Journal of Hydrogen Energy*, *33*(23), 7224–7236, http://www.sciencedirect.com/science/article/pii/S0360319908008185.

[34] **Ji, C. and Wang, S.** (2010). Combustion and emissions performance of a hybrid hydrogen–gasoline engine at idle and lean conditions, *International Journal of Hydrogen Energy*, *35*(1), 346–355, http://www.sciencedirect.com/science/article/pii/S0360319909016723.

[35] **Ma, F.**, **Wang, Y.**, **Liu, H.**, **Li, Y.**, **Wang, J. and Ding, S.** (2008). Effects of hydrogen addition on cycle-by-cycle variations in a lean burn natural gas spark-ignition engine, *International Journal of Hydrogen Energy*, *33*(2), 823–831, http://www.sciencedirect.com/science/article/pii/S0360319907006404.

[36] **Huang, B.**, **Hu, E.**, **Huang, Z.**, **Zheng, J.**, **Liu, B. and Jiang, D.** (2009). Cycle-by-cycle variations in a spark ignition engine fueled with natural gas–hydrogen blends combined with EGR, *International Journal of Hydrogen Energy*, *34*(19), 8405–8414, http://www.sciencedirect.com/science/article/pii/S0360319909012440.

[37] **Fennell, D.**, **Herreros, J. and Tsolakis, A.** (2014). Improving gasoline direct injection (GDI) engine efficiency and emissions with hydrogen from exhaust gas fuel reforming, *International Journal of Hydrogen Energy*, *39*(10), 5153–5162, http://www.sciencedirect.com/science/article/pii/S0360319914001153.

[38] **Ji, C. and Wang, S.** (2009). Effect of hydrogen addition on combustion and emissions performance of a spark ignition gasoline engine at lean conditions, *International Journal of Hydrogen Energy*, *34*(18), 7823–7834, http://www.sciencedirect.com/science/article/pii/S0360319909010519.

[39] **Ji, C.**, **Wang, S. and Zhang, B.** (2010). Combustion and emissions characteristics of a hybrid hydrogen–gasoline engine under various loads and lean conditions, *International Journal of Hydrogen Energy*, *35*(11), 5714–5722, http://www.sciencedirect.com/science/article/pii/S0360319910004775.

[40] **Hairuddin, A.A.**, **Yusaf, T. and Wandel, A.P.** (2014). A review of hydrogen and natural gas addition in diesel HCCI engines, *Renewable and Sustainable Energy Reviews*, *32*, 739–761, http://www.sciencedirect.com/science/article/pii/S136403211400029X.

[41] **Shirk, M.G.**, **McGuire, T.P.**, **Neal, G.L. and Haworth, D.C.** (2008). Investigation of a hydrogen-assisted combustion system for a light-duty diesel vehicle, *International Journal of Hydrogen Energy*, *33*(23), 7237–7244, http://www.sciencedirect.com/science/article/pii/S0360319908009683.

[42] **Ma, F.**, **Wang, Y.**, **Liu, H.**, **Li, Y.**, **Wang, J. and Zhao, S.** (2007). Experimental study on thermal efficiency and emission characteristics of a lean burn hydrogen enriched natural gas engine, *International Journal of Hydrogen Energy*, *32*(18), 5067–5075, http://www.sciencedirect.com/science/article/pii/S0360319907004144.

[43] **Ma, F.**, **Wang, M.**, **Jiang, L.**, **Chen, R.**, **Deng, J.**, **Naeve, N. and Zhao, S.** (2010). Performance and emission characteristics of a turbocharged CNG engine fueled by hydrogen-enriched compressed natural gas with high hydrogen ratio, *Renewable Energy*, *35*(12), 6438–6447, http://www.sciencedirect.com/science/article/pii/S0360319910006282.

[44] **Deng, J.**, **Ma, F.**, **Li, S.**, **He, Y.**, **Wang, M.**, **Jiang, L. and Zhao, S.** (2011). Experimental study on combustion and emission characteristics of a hydrogen-enriched compressed natural gas engine under idling condition, *International Journal of Hydrogen Energy*, *36*(20), 13150–13157, http://www.sciencedirect.com/science/article/pii/S036031991101696X.

[45] **Burguburu, J.**, **Cabot, G.**, **Renou, B.**, **Boukhalfa, A.M. and Cazalens, M.** (2011). Effects of H2 enrichment on flame stability and pollutant emissions for a kerosene/air swirled flame with an aeronautical fuel injector, *Proceedings of the Combustion Institute*, *33*(2), 2927–2935, http://www.sciencedirect.com/science/article/pii/S1540748910002506.

[46] **Frenillot, J.P.**, **Cabot, G.**, **Cazalens, M.**, **Renou, B. and Boukhalfa, M.A.** (2009). Impact of H2 addition on flame stability and pollutant emissions for an atmospheric kerosene/air swirled flame of laboratory scaled gas turbine, *International Journal of Hydrogen Energy*, *34*(9), 3930–3944, http://www.sciencedirect.com/science/article/pii/S0360319909003000.

[47] **Schefer, R.W.**, **Wicksall, D.M. and Agrawal, A.K.** (2002). Combustion of hydrogen-enriched methane in a lean premixed swirl-stabilized burner, *Proceedings of the Combustion Institute*, *29*(1), 843–851, http://www.sciencedirect.com/science/article/pii/S1540748902801080.

[48] **Tsujikawa, Y. and Hirano, M.** (1988). Effects of precooling of suction air on the performance of liquid hydrogen-fueled supersonic aircraft engine, *International Journal of Hydrogen Energy*, *13*(11), 691–700, http://www.sciencedirect.com/science/article/pii/0360319988900808.

[49] **Mikolowsky, W.T. and Noggle, L.W.** (1978). The potential of liquid hydrogen as a military aircraft fuel, *International Journal of Hydrogen Energy*, *3*(4), 449–460, http://www.sciencedirect.com/science/article/pii/0360319978900058.

[50] **Reshotko, E.** (1979). Drag Reduction by Cooling in Hydrogen-Fueled Aircraft, *Journal of Aircraft*, *16*(9), 584–590, http://arc.aiaa.org/doi/abs/10.2514/3.58571.

[51] **Gupta, K.K.**, **Rehman, A. and Sarviya, R.M.** (2010). Bio-fuels for the gas turbine: A review, *Renewable and Sustainable Energy Reviews*, *14*(9), 2946–2955, http://www.sciencedirect.com/science/article/pii/S1364032110002054.

[52] **Figura, L.**, **Lee, J.G.**, **Quay, B.D. and Santavicca, D.A.**, (2007), The Effects of Fuel Composition on Flame Structure and Combustion Dynamics in a Lean Premixed Combustor, http://dx.doi.org/10.1115/GT2007-27298.

[53] **Wicksall, D.M. and Agrawal, A.K.** (2007). Acoustics measurements in a lean premixed combustor operated on hydrogen/hydrocarbon fuel mixtures, *International Journal of Hydrogen Energy*, *32*(8), 1103–1112, http://www.sciencedirect.com/science/article/pii/S0360319906002989.

[54] **Taamallah, S.**, **Vogiatzaki, K.**, **Alzahrani, F.M.**, **Mokheimer, E.M.A.**, **Habib, M.A. and Ghoniem, A.F.** (2015). Fuel flexibility, stability and emissions in premixed hydrogen-rich gas turbine combustion: Technology, fundamentals, and numerical simulations, *Applied Energy*, *154*, 1020–1047, http://www.sciencedirect.com/science/article/pii/S0306261915004997.

[55] **Taamallah, S.**, **LaBry, Z.A.**, **Shanbhogue, S.J. and Ghoniem, A.F.** (2015). Thermo-acoustic instabilities in lean premixed swirl-stabilized combustion and their link to acoustically coupled and decoupled flame macrostructures, *Proceedings of the Combustion Institute*, *35*(3), 3273–3282, http://www.sciencedirect.com/science/article/pii/S1540748914003125.

[56] **Jaramillo, P.**, **Griffin, W.M. and Matthews, H.S.** (2007). Comparative Life-Cycle Air Emissions of Coal, Domestic Natural Gas, LNG, and SNG for Electricity Generation, *Environmental Science & Technology*, *41*(17), 6290–6296, https://doi.org/10.1021/es063031o.

[57] **Viebahn, P.**, **Nitsch, J.**, **Fischedick, M.**, **Esken, A.**, **Schüwer, D.**, **Supersberger, N.**, **Zuberbühler, U. and Edenhofer, O.** (2007). Comparison of carbon capture and storage with renewable energy technologies regarding structural, economic, and ecological aspects in Germany, *International Journal of Greenhouse Gas Control*, *1*(1), 121–133, http://www.sciencedirect.com/science/article/pii/S1750583607000242.

[58] **Odeh, N.A. and Cockerill, T.T.** (2008). Life cycle GHG assessment of fossil fuel power plants with carbon capture and storage, *Energy Policy*, *36*(1), 367–380, http://www.sciencedirect.com/science/article/pii/S0301421507004120.

[59] **Krebs, W.**, **Flohr, P.**, **Prade, B. and Hoffmann, S.** (2002). Thermoacoustic stability chart for high-intensity gas turbine combustion systems, *Combustion Science and Technology*, *174*(7), 99–128, https://www.tandfonline.com/doi/abs/10.1080/00102200208984089.

[60] **Poinsot, T.** (2017). Prediction and control of combustion instabilities in real engines, *Proceedings of the Combustion Institute*, *36*(1), 1–28, http://www.sciencedirect.com/science/article/pii/S1540748916300074.

[61] **Speth, R.L. and Ghoniem, A.F.** (2009). Using a strained flame model to collapse dynamic mode data in a swirl-stabilized syngas combustor, *Proceedings of the Combustion Institute*, *32*(2), 2993–3000, http://www.sciencedirect.com/science/article/pii/S1540748908003283.

[62] **Liu, K. and Sanderson, V.** (2013). The influence of changes in fuel calorific value to combustion performance for Siemens SGT-300 dry low emission combustion system, *Fuel*, *103*, 239–246, http://www.sciencedirect.com/science/article/pii/S0016236112006291.

[63] **Mordaunt, C.J. and Pierce, W.C.** (2014). Design and preliminary results of an atmospheric-pressure model gas turbine combustor utilizing varying CO2 doping concentration in CH4 to emulate biogas combustion, *Fuel*, *124*, 258–268, http://www.sciencedirect.com/science/article/pii/S0016236114001161.

[64] **García-Armingol, T. and Ballester, J.** (2015). Operational issues in premixed combustion of hydrogen-enriched and syngas fuels, *International Journal of Hydrogen Energy*, *40*(2), 1229–1243, http://www.sciencedirect.com/science/article/pii/S0360319914031206.

[65] **POINSOT, T.**, **CANDEL, S.**, **ESPOSITO, E.**, **LANG, W. and BOURIENNE, F.** (1989). Suppression of combustion instabilities by active control, *Journal of Propulsion and Power*, *5*(1), 14–20, https://doi.org/10.2514/3.23108.

[66] **Lang, W.**, **Poinsot, T. and Candel, S.** (1987). Active control of combustion instability, *Combustion and Flame*, *70*(3), 281–289, http://www.sciencedirect.com/science/article/pii/001021808790109X.

[67] **Poinsot, T.**, **Veynante, D.**, **Bourienne, F.**, **Candel, S.**, **Esposito, E. and Surget, J.** (1989). Initiation and suppression of combustion

instabilities by active control, *Symposium (International) on Combustion*, *22*(1), 1363–1370, http://www.sciencedirect.com/science/article/pii/S008207848980147X.

[68] **Paschereit, C.O.**, **Gutmark, E. and Weisenstein, W.** (1999). Coherent structures in swirling flows and their role in acoustic combustion control, *Physics of Fluids*, *11*(9), 2667–2678, https://doi.org/10.1063/1.870128.

[69] **PASCHEREIT, C.O.**, **GUTMARK, E. and WEISENSTEIN, W.** (1998). Structure and Control of Thermoacoustic Instabilities in a Gas-turbine Combustor, *Combustion Science and Technology*, *138*(1-6), 213–232, https://doi.org/10.1080/00102209808952069.

[70] **Paschereit, C.O.**, **Gutmark, E. and Weisenstein, W.** (1998). Control of thermoacoustic instabilities and emissions in an industrial-type gas-turbine combustor, *Symposium (International) on Combustion*, *27*(2), 1817–1824, http://www.sciencedirect.com/science/article/pii/S0082078498800234.

[71] **Seume, J.R.**, **Vortmeyer, N.**, **Krause, W.**, **Hermann, J.**, **Hantschk, C.C.**, **Zangl, P.**, **Gleis, S.**, **Vortmeyer, D. and Orthmann, A.** (1998). Application of Active Combustion Instability Control to a Heavy Duty Gas Turbine, *Journal of Engineering for Gas Turbines and Power*, *120*(4), 721–726, http://dx.doi.org/10.1115/1.2818459.

[72] **Johnson, C.**, **Neumeier, Y.**, **Lubarsky, E.**, **Lee, J.**, **Neumaier, M. and Zinn, B.**, (2000). Suppression of combustion instabilities in a liquid fuel combustor using a fast adaptive control algorithm, 38th Aerospace Sciences Meeting and Exhibit, Aerospace Sciences Meetings, American Institute of Aeronautics and Astronautics, https://doi.org/10.2514/6.2000-476.

[73] **Hibshman, J.R.**, **Cohen, J.M.**, **Banaszuk, A.**, **Anderson, T.J. and Alholm, H.A.**, (1999), Active Control of Combustion Instability in a Liquid–Fueled Sector Combustor, http://dx.doi.org/10.1115/99-GT-215.

[74] **Banaszuk, A.**, **Ariyur, K.B.**, **Krstić, M. and Jacobson, C.A.** (2004). An adaptive algorithm for control of combustion instability, *Automatica*, *40*(11), 1965–1972, http://www.sciencedirect.com/science/article/pii/S0005109804001815.

[75] **Johnson, C.E.**, **Neumeier, Y.**, **Neumaier, M.**, **Zinn, B.T.**, **Darling, D.D. and Sattinger, S.S.**, (2001), Demonstration of Active Control of Combustion Instabilities on a Full-Scale Gas Turbine Combustor, http://dx.doi.org/10.1115/2001-GT-0519.

[76] **Poinsot, T.** (2016). Prediction and control of combustion instabilities in real engines, *Proceedings of the Combustion Institute*, *000*(1), 1–28, http://linkinghub.elsevier.com/retrieve/pii/S1540748916300074.

[77] **Dupere, I.D.J. and Dowling, A.P.** (2005). The Use of Helmholtz Resonators in a Practical Combustor, *Journal of Engineering for Gas Turbines and Power*, *127*(2), 268–275, http://dx.doi.org/10.1115/1.1806838.

[78] **Bellucci, V.**, **Flohr, P.**, **Paschereit, C.O. and Magni, F.** (2004). On the Use of Helmholtz Resonators for Damping Acoustic Pulsations in Industrial Gas Turbines, *Journal of Engineering for Gas Turbines and Power*, *126*(2), 271–275, http://dx.doi.org/10.1115/1.1473152.

[79] **Richards, G.A.**, **Straub, D.L. and Robey, E.H.** (2003). Passive Control of Combustion Dynamics in Stationary Gas Turbines, *Journal of Propulsion and Power*, *19*(5), 795–810, https://doi.org/10.2514/2.6195.

[80] **Gysling, D.L.**, **Copeland, G.S.**, **McCormick, D.C. and Proscia, W.M.** (1999). Combustion System Damping Augmentation With Helmholtz Resonators, *Journal of Engineering for Gas Turbines and Power*, *122*(2), 269–274, http://dx.doi.org/10.1115/1.483205.

[81] **Lepers, J.**, **Krebs, W.**, **Prade, B.**, **Flohr, P.**, **Pollarolo, G. and Ferrante, A.**, (2005), Investigation of Thermoacoustic Stability Limits of an Annular Gas Turbine Combustor Test-Rig With and Without Helmholtz-Resonators, http://dx.doi.org/10.1115/GT2005-68246.

[82] **Krebs, W.**, **Bethke, S.**, **Lepers, J.**, **Flohr, P.**, **Prade, B.**, **Johnson, C. and Sattinger, S.** (2005). Thermoacoustic design tools and passive control: Siemens power generation approaches, *Combustion Instabilities in Gas Turbine Engines Operational Experience, Fundamental Mechanisms and Modeling*.

[83] **Bellucci, V.**, **Schuermans, B.**, **Nowak, D.**, **Flohr, P. and Paschereit, C.O.** (2005). Thermoacoustic Modeling of a Gas Turbine Combustor Equipped With Acoustic Dampers, *Journal of Turbomachinery*, *127*(2), 372–379, http://dx.doi.org/10.1115/1.1791284.

[84] **Rupp, J.**, **Carrotte, J. and Macquisten, M.** (2012). The Use of Perforated Damping Liners in Aero Gas Turbine Combustion Systems, *Journal of Engineering for Gas Turbines and Power*, *134*(7), 71502–71510, http://dx.doi.org/10.1115/1.4005972.

[85] **Lei, L.**, **Zhihui, G.**, **Chengyu, Z. and Xiaofeng, S.** (2010). A Passive Method to Control Combustion Instabilities with Perforated Liner, *Chinese Journal of Aeronautics*, *23*(6), 623–630, http://www.sciencedirect.com/science/article/pii/S1000936109602636.

[86] **Tran, N.**, **Ducruix, S. and Schuller, T.** (2009). Damping combustion instabilities with perforates at the premixer inlet of a swirled burner, *Proceedings of the Combustion Institute*, *32*(2), 2917–2924, http://www.sciencedirect.com/science/article/pii/S1540748908002356.

[87] **Steele, R.C.**, **Cowell, L.H.**, **Cannon, S.M. and Smith, C.E.** (2000). Passive Control of Combustion Instability in Lean Premixed Combustors, *Journal of Engineering for Gas Turbines and Power*, *122*(3), 412–419, http://dx.doi.org/10.1115/1.1287166.

[88] **Paschereit, C.O.**, **Flohr, P.**, **Knopfel, H.**, **Geng, W.**, **Steinbach, C.**, **Stuber, P.**, **Bengtsson, K. and Gutmark, E.**, (2002), Combustion Control by Extended EV Burner Fuel Lance, http://dx.doi.org/10.1115/GT2002-30462.

[89] **Kendrick, D.W.**, **Anderson, T.J.**, **Sowa, W.A. and Snyder, T.S.** (1999). Acoustic Sensitivities of Lean-Premixed Fuel Injectors in a Single Nozzle Rig, *Journal of Engineering for Gas Turbines and Power*, *121*(3), 429–436, http://dx.doi.org/10.1115/1.2818491.

[90] **Gatti, M.**, **Gaudron, R.**, **Mirat, C.**, **Zimmer, L. and Schuller, T.** (2019). Impact of swirl and bluff-body on the transfer function of premixed flames, *Proceedings of the Combustion Institute*, *37*(4), 5197–5204, http://www.sciencedirect.com/science/article/pii/S1540748918303316.

[91] **Scarinci, T. and Halpin, J.L.** (2000). Industrial Trent Combustor—Combustion Noise Characteristics, *Journal of Engineering for Gas Turbines and Power*, *122*(2), 280–286, http://dx.doi.org/10.1115/1.483207.

[92] **Lovett, J.A. and Uznanski, K.T.**, (2002), Prediction of Combustion Dynamics in a Staged Premixed Combustor, http://dx.doi.org/10.1115/GT2002-30646.

[93] **Straub, D.L. and Richards, G.A.**, (1998), Effect of Fuel Nozzle Configuration on Premix Combustion Dynamics, http://dx.doi.org/10.1115/98-GT-492.

[94] **Joshi, N.D.**, **Epstein, M.J.**, **Durlak, S.**, **Marakovits, S. and Sabla, P.E.**, (1994), Development of a Fuel Air Premixer for Aero-Derivative Dry Low Emissions Combustors, http://dx.doi.org/10.1115/94-GT-253.

[95] **Joshi, N.D.**, **Mongia, H.C.**, **Leonard, G.**, **Stegmaier, J.W. and Vickers, E.C.**, (1998), Dry Low Emissions Combustor Development, http://dx.doi.org/10.1115/98-GT-310.

[96] **Mongia, H.C.**, **Held, T.J.**, **Hsiao, G.C. and Pandalai, R.P.** (2003). Challenges and Progress in Controlling Dynamics in Gas Turbine Combustors, *Journal of Propulsion and Power*, *19*(5), 822–829, https://doi.org/10.2514/2.6197.

[97] **Pandalai, R. and Mongia, H.**, (1998). Combustion instability characteristics of industrial engine dry low emission combustion systems, 34th AIAA/ASME/SAE/ASEE Joint Propulsion Conference and Exhibit, Joint Propulsion Conferences, American Institute of Aeronautics and Astronautics, https://doi.org/10.2514/6.1998-3379.

[98] **James, D.**, (2002), A Solution for Noise Associated With a Series Staged DLE Combustion System, http://dx.doi.org/10.1115/IPC2002-27342.

[99] **Paschereit, C. and Gutmark, E.**, (2003). Passive Combustion Control for Enhanced Stability and Reduced Emissions in a Swirl-Stabilized Burner, 41st Aerospace Sciences Meeting and Exhibit, Aerospace Sciences Meetings, American Institute of Aeronautics and Astronautics, https://doi.org/10.2514/6.2003-1011.

[100] **Paschereit, C. and Gutmark, E.**, (2004). Control of Combustion Instability and Emissions by Burner's Exit Geometry Modifications, 42nd AIAA Aerospace Sciences Meeting and Exhibit, Aerospace Sciences Meetings, American Institute of Aeronautics and Astronautics, https://doi.org/10.2514/6.2004-636.

[101] **Durox, D.**, **Schuller, T.**, **Noiray, N. and Candel, S.** (2009). Experimental analysis of nonlinear flame transfer functions for different flame geometries, *Proceedings of the Combustion Institute*, *32*(1), 1391–1398, http://www.sciencedirect.com/science/article/pii/S1540748908001818.

[102] **Mejia, D.**, **Miguel-Brebion, M.**, **Ghani, A.**, **Kaiser, T.**, **Duchaine, F.**, **Selle, L. and Poinsot, T.** (2018). Influence of flame-holder temperature on the acoustic flame transfer functions of a laminar flame, *Combustion and Flame*, *188*, 5–12, http://www.sciencedirect.com/science/article/pii/S0010218017303462.

[103] **Mejia, D.**, **Selle, L.**, **Bazile, R. and Poinsot, T.** (2015). Wall-temperature effects on flame response to acoustic oscillations, *Proceedings of the Combustion Institute*, *35*(3), 3201–3208, http://www.sciencedirect.com/science/article/pii/S1540748914003253.

[104] **Hussain, T.**, **Talibi, M. and Balachandran, R.** (2019). Investigating the effect of local addition of hydrogen to acoustically excited ethylene and methane flames, *International Journal of Hydrogen Energy*, *44*(21), 11168–11184, http://www.sciencedirect.com/science/article/pii/S0360319919308407.

[105] **Anderson, D.N.** (1975). Effect of hydrogen injection stability and emissions of an experimental premixed prevaporized propane burner.

[106] **Barbosa, S.**, **de La Cruz Garcia, M.**, **Ducruix, S.**, **Labegorre, B. and Lacas, F.** (2007). Control of combustion instabilities by local injection of hydrogen, *Proceedings of the Combustion Institute*, *31*(2), 3207–3214, http://www.sciencedirect.com/science/article/pii/S1540748906001039.

[107] **Cocchi, S. and Sigali, S.**, (2010), Development of a Low-NOX Hydrogen-Fuelled Combustor for 10 MW Class Gas Turbines, https://doi.org/10.1115/GT2010-23348.

[108] **Balestri, M.**, **Benelli, G.**, **Donatini, F.**, **Arlati, F. and Conti, G.** (2007). Enel's Fusina hydrogen-fed power generation plant, *2007 International Conference on Clean Electrical Power*, pp.456–463.

[109] **Glickenstein, H.** (2019). March 2019 Land Transportation News [Transportation Systems], *IEEE Vehicular Technology Magazine*, *14*(1), 18–26.

[110] **Miller, S.**, **Collet, C. and Thibaut, S.**, (2020), Alstom's hydrogen train Coradia iLint completes successful tests in the Netherlands, https://www.alstom.com/press-releases-news/2020/3/alstoms-hydrogen-train-coradia-ilint-completes-successful-tests.

[111] **Galley, D.**, **Ducruix, S.**, **Lacas, F. and Veynante, D.** (2011). Mixing and stabilization study of a partially premixed swirling flame using laser induced fluorescence, *Combustion and Flame*, *158*(1), 155–171, http://www.sciencedirect.com/science/article/pii/S0010218010002300.

[112] **Vagelopoulos, C.M. and Frank, J.H.** (2005). An experimental and numerical study on the adequacy of CH as a flame marker in premixed methane flames, *Proceedings of the Combustion Institute*, *30*(1), 241–249, http://www.sciencedirect.com/science/article/pii/S0082078404002826.

[113] **Kojima, J.**, **Ikeda, Y. and Nakajima, T.** (2005). Basic aspects of OH(A), CH(A), and C2(d) chemiluminescence in the reaction zone of laminar methane–air premixed flames, *Combustion and Flame*, *140*(1), 34–45, http://www.sciencedirect.com/science/article/pii/S0010218004002081.

[114] **DANDY, D.S. and VOSEN, S.R.** (1992). Numerical and Experimental Studies of Hydroxyl Radical Chemiluminescence in Methane-Air Flames, *Combustion Science and Technology*, *82*(1-6), 131–150, https://doi.org/10.1080/00102209208951816.

[115] **Nikolaou, Z.M. and Swaminathan, N.** (2014). Heat release rate markers for premixed combustion, *Combustion and Flame*, *161*(12), 3073–3084, http://www.sciencedirect.com/science/article/pii/S0010218014001606.

[116] **Luque, J.**, **Jeffries, J.B.**, **Smith, G.P.**, **Crosley, D.R.**, **Walsh, K.T.**, **Long, M.B. and Smooke, M.D.** (2000). CH(A-X) and OH(A-X) optical emission in an axisymmetric laminar diffusion flame, *Combustion and Flame*, *122*(1), 172–175, http://www.sciencedirect.com/science/article/pii/S0010218000001127.

[117] **Smith, G.P.**, **Golden, D.M.**, **Frenklach, M.**, **Moriarty, N.W.**, **Eiteneer, B.**, **Goldenberg, M.**, **Bowman, C.T.**, **Hanson, R.K.**, **Song, S.**, **Gardiner, Jr, W.C.**, **Lissianski, V.V. and Qin, Z.**, GRI-Mech 3.0, http://www.me.berkeley.edu/gri{_}mech/.

[118] **Goodwin, D.G.**, **Moffat, H.K. and Speth, R.L.**, (2016), Cantera: An Object-oriented Software Toolkit for Chemical Kinetics, Thermodynamics, and Transport Processes, \url{http://www.cantera.org}.

[119] **Yuan, R.**, **Kariuki, J.**, **Dowlut, A.**, **Balachandran, R. and Mastorakos, E.** (2015). Reaction zone visualisation in swirling spray n-heptane flames, *Proceedings of the Combustion Institute*, *35*(2), 1649–1656, http://www.sciencedirect.com/science/article/pii/S1540748914001709.

[120] **Palies, P.**, **Durox, D.**, **Schuller, T.**, **Morenton, P. and Candel, S.** (2009). Dynamics of premixed confined swirling flames, *Comptes Rendus Mécanique*, *337*(6), 395–405, http://www.sciencedirect.com/science/article/pii/S1631072109000655.

[121] **Hickstein, D.D.**, **Yurchak, R.**, **Das, D.**, **Shih, C.Y. and Gibson, S.T.**, (2016), PyAbel (v0. 7): A Python Package for Abel Transforms.

[122] **Guiberti, T.F.**, **Durox, D.**, **Scouflaire, P. and Schuller, T.** (2015). Impact of heat loss and hydrogen enrichment on the shape of confined swirling flames, *Proceedings of the Combustion Institute*, *35*(2), 1385–1392, http://www.sciencedirect.com/science/article/pii/S1540748914001746.

[123] **San Diego Mechanism, Mechanical and Aerospace Engineering (Combustion Research), U.o.C.a.S.D.**, Chemical-Kinetic Mechanisms for Combustion Applications, http://combustion.ucsd.edu.

[124] **Lieuwen, T.C.** (2012). *Unsteady Combustor Physics*, Cambridge University Press, https://books.google.fr/books?id=ewKJs{_}16FhMC.

[125] **Dunn-Rankin, D. and Therkelsen, P.** (2016). *Lean Combustion: Technology and Control*, Elsevier Science, https://books.google.fr/books?id=kd2cBAAAQBAJ.

[126] **McManus, K.R.**, **Poinsot, T. and Candel, S.M.** (1993). A review of active control of combustion instabilities, *Progress in Energy and Combustion Science*, *19*(1), 1–29, http://www.sciencedirect.com/science/article/pii/036012859390020F.

[127] **Noiray, N.**, **Durox, D.**, **Schuller, T. and Candel, S.** (2007). Passive control of combustion instabilities involving premixed flames anchored on perforated plates, *Proceedings of the Combustion Institute*, *31*(1), 1283–1290, http://www.sciencedirect.com/science/article/pii/S1540748906001052.

[128] **Hobson, D.E.**, **Fackrell, J.E. and Hewitt, G.** (2000). Combustion Instabilities in Industrial Gas Turbines—Measurements on Operating Plant and Thermoacoustic Modeling, *Journal of Engineering for Gas Turbines and Power*, *122*(3), 420–428, https://doi.org/10.1115/1.1287238.

[129] **Noiray, N.**, **Durox, D.**, **Schuller, T. and Candel, S.** (2006). Self-induced instabilities of premixed flames in a multiple injection configuration, *Combustion and Flame*, *145*(3), 435–446, http://www.sciencedirect.com/science/article/pii/S0010218006000368.

[130] **Tran, N.**, **Ducruix, S. and Schuller, T.** (2009). Passive Control of the Inlet Acoustic Boundary of a Swirled Burner at High Amplitude Combustion Instabilities, *Journal of Engineering for Gas Turbines and Power*, *131*(5), 51502–51507, http://dx.doi.org/10.1115/1.3078206.

[131] **Tran, N.**, **Ducruix, S. and Schuller, T.**, (2007). Analysis and Control of Combustion Instabilities by Adaptive Reflection Coefficients, 13th AIAA/CEAS Aeroacoustics Conference (28th AIAA Aeroacoustics Conference), Aeroacoustics Conferences, American Institute of Aeronautics and Astronautics, https://doi.org/10.2514/6.2007-3716.

[132] **Lieuwen, T. and Zinn, B.**, (1998). Theoretical investigation of combustion instability mechanisms in lean premixed gas turbines, 36th AIAA Aerospace Sciences Meeting and Exhibit, Aerospace Sciences Meetings, American Institute of Aeronautics and Astronautics, https://doi.org/10.2514/6.1998-641.

[133] **Dowling, A.P. and Stow, S.R.** (2003). Acoustic Analysis of Gas Turbine Combustors, *Journal of Propulsion and Power*, *19*(5), 751–764, https://doi.org/10.2514/2.6192.

[134] **Dowling, A.P. and Mahmoudi, Y.** (2015). Combustion noise, *Proceedings of the Combustion Institute*, *35*(1), 65–100, http://www.sciencedirect.com/science/article/pii/S1540748914004003.

[135] **Parmentier, J.F.**, **Salas, P.**, **Wolf, P.**, **Staffelbach, G.**, **Nicoud, F. and Poinsot, T.** (2012). A simple analytical model to study and control azimuthal instabilities in annular combustion chambers, *Combustion and Flame*, *159*(7), 2374–2387, http://www.sciencedirect.com/science/article/pii/S0010218012000569.

[136] **Franzelli, B.**, **Riber, E.**, **Gicquel, L.Y.M. and Poinsot, T.** (2012). Large Eddy Simulation of combustion instabilities in a lean partially premixed swirled flame, *Combustion and Flame*, *159*(2), 621–637, http://www.sciencedirect.com/science/article/pii/S0010218011002525.

[137] **Wolf, P.**, **Balakrishnan, R.**, **Staffelbach, G.**, **Gicquel, L.Y.M. and Poinsot, T.** (2012). Using LES to Study Reacting Flows and Instabilities in Annular Combustion Chambers, *Flow, Turbulence and Combustion*, *88*(1), 191–206, https://doi.org/10.1007/s10494-011-9367-7.

[138] **Zellhuber, M.**, **Schwing, J.**, **Schuermans, B.**, **Sattelmayer, T. and Polifke, W.** (2014). Experimental and Numerical Investigation of Thermoacoustic Sources Related to High-Frequency Instabilities, *International Journal*

of Spray and Combustion Dynamics, *6*(1), 1–34, https://doi.org/10.1260/1756-8277.6.1.1.

[139] **Nicoud, F.**, **Benoit, L.**, **Sensiau, C. and Poinsot, T.** (2007). Acoustic Modes in Combustors with Complex Impedances and Multidimensional Active Flames, *AIAA Journal*, *45*(2), 426–441, https://doi.org/10.2514/1.24933.

[140] **Wolf, P.**, **Staffelbach, G.**, **Gicquel, L.Y.M.**, **Müller, J.D. and Poinsot, T.** (2012). Acoustic and Large Eddy Simulation studies of azimuthal modes in annular combustion chambers, *Combustion and Flame*, *159*(11), 3398–3413, http://www.sciencedirect.com/science/article/pii/S0010218012001964.

[141] **Roux, S.**, **Lartigue, G.**, **Poinsot, T.**, **Meier, U. and Bérat, C.** (2005). Studies of mean and unsteady flow in a swirled combustor using experiments, acoustic analysis, and large eddy simulations, *Combustion and Flame*, *141*(1), 40–54, http://www.sciencedirect.com/science/article/pii/S0010218005000039.

[142] **Han, X.**, **Li, J. and Morgans, A.S.** (2015). Prediction of combustion instability limit cycle oscillations by combining flame describing function simulations with a thermoacoustic network model, *Combustion and Flame*, *162*(10), 3632–3647, http://www.sciencedirect.com/science/article/pii/S0010218015002011.

[143] **Yang, D. and Morgans, A.S.** (2017). Acoustic Models for Cooled Helmholtz Resonators, *AIAA Journal*, *55*(9), 3120–3127, https://doi.org/10.2514/1.J055854.

[144] **Li, J.**, **Xia, Y.**, **Morgans, A.S. and Han, X.** (2017). Numerical prediction of combustion instability limit cycle oscillations for a combustor with a long flame, *Combustion and Flame*, *185*, 28–43, http://www.sciencedirect.com/science/article/pii/S0010218017302390.

[145] **Tran, N.** (2009). Influence of inlet acoustic boundary condition on large amplitude combustion instabilities : design of a robust impedance control system, Theses, Ecole Centrale Paris, https://tel.archives-ouvertes.fr/tel-00677071.

[146] **Chung, J.Y.** (1978). Cross-spectral method of measuring acoustic intensity without error caused by instrument phase mismatch, *The Journal of the Acoustical Society of America*, *64*(6), 1613.

[147] **Levine, H. and Schwinger, J.** (1948). On the Radiation of Sound from an Unflanged Circular Pipe, *Physical Review*, *73*(4), 383–406, http://link.aps.org/doi/10.1103/PhysRev.73.383.

[148] **Davies, P.** (1988). Practical flow duct acoustics, *Journal of Sound and Vibration*, *124*(1), 91–115, http://www.sciencedirect.com/science/article/pii/S0022460X8881407X.

[149] **Laera, D.**, **Schuller, T.**, **Prieur, K.**, **Durox, D.**, **Camporeale, S.M. and Candel, S.** (2017). Flame Describing Function analysis of spinning and standing modes in an annular combustor and comparison with experiments, *Combustion and Flame*, *184*, 136–152, http://www.sciencedirect.com/science/article/pii/S0010218017301967.

[150] **Camporeale, S.M.**, **Fortunato, B. and Campa, G.** (2010). A Finite Element Method for Three-Dimensional Analysis of Thermo-acoustic Combustion Instability, *Journal of Engineering for Gas Turbines and Power*, *133*(1), https://doi.org/10.1115/1.4000606.

[151] **NOIRAY, N.**, **DUROX, D.**, **SCHULLER, T. and CANDEL, S.** (2008). A unified framework for nonlinear combustion instability analysis based on the flame describing function, *Journal of Fluid Mechanics*, *615*, 139–167, https://www.cambridge.org/core/article/unified-framework-for-nonlinear-combustion-instability-analysis-EC71018216E8E14BF27A7F607DB799F4.

[152] **DOWLING, A.P.** (1999). A kinematic model of a ducted flame, *Journal of Fluid Mechanics*, *394*, 51–72, https://www.cambridge.org/core/article/kinematic-model-of-a-ducted-flame/AD4434E57C8C33E4811FE07A4EE9DC2A.

[153] **CROCCO, L.** (1951). Aspects of Combustion Stability in Liquid Propellant Rocket Motors Part I: Fundamentals. Low Frequency Instability With Monopropellants, *Journal of the American Rocket Society*, *21*(6), 163–178, https://doi.org/10.2514/8.4393.

[154] **Lohrmann, M.**, **Büchner, H.**, **Zarzalis, N. and Krebs, W.**, (2003), Flame Transfer Function Characteristics of Swirl Flames for Gas Turbine Applications, https://doi.org/10.1115/GT2003-38113.

[155] **Ranalli, J.A.**, **Martin, C.R.**, **Black, P.R.**, **Vandsburger, U. and West, R.** (2009). Measurement of Flame Transfer Functions in Swirl-Stabilized, Lean-Premixed Combustion, *Journal of Propulsion and Power*, *25*(6), 1350–1354, https://doi.org/10.2514/1.44187.

[156] **Guyot, D.**, **Moeck, J.**, **Paschereit, C. and Schuermans, B.**, (2009). Optical Transfer Function Measurement for a Premixed Swirl-Stabilized Flame at Atmospheric Conditions, 47th AIAA Aerospace Sciences Meeting including The New Horizons Forum and Aerospace Exposition, Aerospace Sciences Meetings, American Institute of Aeronautics and Astronautics, https://doi.org/10.2514/6.2009-1236.

[157] **Kim, K.T. and Santavicca, D.A.** (2013). Generalization of Turbulent Swirl Flame Transfer Functions in Gas Turbine Combustors, *Combustion Science and Technology*, *185*(7), 999–1015, https://doi.org/10.1080/00102202.2012.752734.

[158] **Bellows, B.D.**, **Bobba, M.K.**, **Seitzman, J.M. and Lieuwen, T.**, (2006), Nonlinear Flame Transfer Function Characteristics in a Swirl-Stabilized Combustor, https://doi.org/10.1115/GT2006-91119.

[159] **Harper, J.**, **Johnson, C.**, **Neumeier, Y.**, **Lieuwen, T. and Zinn, B.**, (2001). Experimental investigation of the nonlinear flame response to flow disturbances in a gas turbine combustor, 39th Aerospace Sciences Meeting and Exhibit, Aerospace Sciences Meetings, American Institute of Aeronautics and Astronautics, https://doi.org/10.2514/6.2001-486.

[160] **Schimek, S.**, **Moeck, J.P. and Paschereit, C.O.** (2011). An Experimental Investigation of the Nonlinear Response of an Atmospheric Swirl-Stabilized Premixed Flame, *Journal of Engineering for Gas Turbines and Power*, *133*(10), https://doi.org/10.1115/1.4002946.

[161] **Palies, P.**, **Durox, D.**, **Schuller, T.**, **Morenton, P. and Candel, S.** (2009). Dynamics of premixed confined swirling flames, *Comptes Rendus Mécanique*, *337*(6), 395–405, http://www.sciencedirect.com/science/article/pii/S1631072109000655.

[162] **Durox, D.**, **Schuller, T.**, **Noiray, N. and Candel, S.** (2009). Experimental analysis of nonlinear flame transfer functions for different flame geometries, *Proceedings of the Combustion Institute*, *32*(1), 1391–1398, http://www.sciencedirect.com/science/article/pii/S1540748908001818file:///C:/Users/Gorkemo.TEIDOM/Workfolder/TechnologyDevelopment/Library/Mendeley/Organize/Duroxetal/Experimentalanalysisofnonlinearflametransferfunctionsfordif

[163] **Truffin, K. and Poinsot, T.** (2005). Comparison and extension of methods for acoustic identification of burners, *Combustion and Flame*, *142*(4), 388–400, http://www.sciencedirect.com/science/article/pii/S0010218005001057.

[164] **Gaudron, R.**, **Gatti, M.**, **Mirat, C. and Schuller, T.** (2019). Flame Describing Functions of a Confined Premixed Swirled Combustor With Upstream and Downstream Forcing, *Journal of Engineering for Gas Turbines and Power*, *141*(5), 51016–51019, http://dx.doi.org/10.1115/1.4041000.

[165] **Komarek, T. and Polifke, W.** (2010). Impact of Swirl Fluctuations on the Flame Response of a Perfectly Premixed Swirl Burner, *Journal of Engineering for Gas Turbines and Power*, *132*(6), https://doi.org/10.1115/1.4000127.

[166] **Palies, P.**, **Durox, D.**, **Schuller, T. and Candel, S.** (2010). The combined dynamics of swirler and turbulent premixed swirling flames, *Combustion and Flame*, *157*(9), 1698–1717, http://www.sciencedirect.com/science/article/pii/S001021801000057X.

[167] **Bunce, N.A.**, **Quay, B.D. and Santavicca, D.A.** (2013). Interaction Between Swirl Number Fluctuations and Vortex Shedding in a Single-Nozzle Turbulent Swirling Fully-Premixed Combustor, *Journal of Engineering for Gas Turbines and Power*, *136*(2), https://doi.org/10.1115/1.4025361.

[168] **Ćosić, B.**, **Terhaar, S.**, **Moeck, J.P. and Paschereit, C.O.** (2015). Response of a swirl-stabilized flame to simultaneous perturbations in equivalence ratio and velocity at high oscillation amplitudes, *Combustion and Flame*, *162*(4), 1046–1062, http://www.sciencedirect.com/science/article/pii/S001021801400306X.

[169] **Huber, A. and Polifke, W.** (2009). Dynamics of Practical Premixed Flames, Part I: Model Structure and Identification, *International Journal of Spray and Combustion Dynamics*, *1*(2), 199–228, https://doi.org/10.1260/175682709788707431.

[170] **Huber, A. and Polifke, W.**, (2008), Impact of Fuel Supply Impedance on Combustion Stability of Gas Turbines, https://doi.org/10.1115/GT2008-51193.

[171] **UNCC** (2015). The Paris Agreement, **Technical Report**, https://unfccc.int/files/essential{_}background/convention/application/pdf/english{_}paris{_}agreement.pdf.

[172] **IPCC**, (2019), Special report on global warming of 1.5 C (SR15), https://www.ipcc.ch/site/assets/uploads/sites/2/2019/06/SR15{_}Full{_}Report{_}High{_}Res.pdf.

[173] **Hansen, L.**, (2018), Der Erste ohne Emissionen: Brennstoffzellen-Zug startet, https://www.dw.com/de/der-erste-ohne-emissionen-brennstoffzellen-zug-startet/a-45516725.

[174] **Wärtsilä**, (2020), Wärtsilä gas engines to burn 100% hydrogen, https://www.wartsila.com/media/news/05-05-2020-wartsila-gas-engines-to-burn-100-hydrogen-2700995?utm{_}campaign=59d9ceb49849f839e101fec4{&}utm{_}content=5eb1249cbf6d2a0001e21f1c{&}utm{_}medium=smarpshare{&}utm{_}source=linkedin{&}utm{_}term=energy.

[175] **Wärtsilä** (2020). Wärtsilä X-Ahead project gets government funding to promote carbon-neutral economy, https://www.wartsila.com/media/news/20-04-2020-wartsila-x-ahead-project-gets-government-funding-to-p

[176] **Tanimu, M.I.**, **Ghazi, T.I.M.**, **Harun, R.M. and Idris, A.** (2014). Effect of carbon to nitrogen ratio of food waste on biogas methane production in a batch mesophilic anaerobic digester, *International journal of innovation, management and technology*, *5*(2), 116.

[177] **Wang, X.**, **Yang, G.**, **Feng, Y.**, **Ren, G. and Han, X.** (2012). Optimizing feeding composition and carbon–nitrogen ratios for improved methane yield during anaerobic co-digestion of dairy, chicken manure and wheat straw, *Bioresource Technology*, *120*, 78–83, http://www.sciencedirect.com/science/article/pii/S0960852412009625.

[178] **Fernández-Delgado Juárez, M.**, **Mostbauer, P.**, **Knapp, A.**, **Müller, W.**, **Tertsch, S.**, **Bockreis, A. and Insam, H.** (2018). Biogas purification with biomass ash, *Waste Management*, *71*, 224–232, http://www.sciencedirect.com/science/article/pii/S0956053X17307067.

[179] **Peluso, A.**, **Gargiulo, N.**, **Aprea, P.**, **Pepe, F. and Caputo, D.** (2019). Nanoporous Materials as H2S Adsorbents for Biogas Purification: a Review, *Separation & Purification Reviews*, *48*(1), 78–89, https://doi.org/10.1080/15422119.2018.1476978.

[180] **Bharathiraja, B.**, **Sudharsana, T.**, **Jayamuthunagai, J.**, **Praveenkumar, R.**, **Chozhavendhan, S. and Iyyappan, J.** (2018). Biogas production–A review on composition, fuel properties, feed stock and principles of anaerobic digestion, *Renewable and Sustainable Energy Reviews*, *90*(C), 570–582.

[181] **Jegede, A.O.**, **Zeeman, G. and Bruning, H.** (2019). A review of mixing, design and loading conditions in household anaerobic digesters, *Critical Reviews in Environmental Science and Technology*, *49*(22), 2117–2153, https://doi.org/10.1080/10643389.2019.1607441.

[182] **Schönfeld, T. and Rudgyard, M.** (1999). Steady and Unsteady Flow Simulations Using the Hybrid Flow Solver AVBP, *AIAA Journal*, *37*(11), 1378–1385, https://doi.org/10.2514/2.636.

[183] **Colin, O. and Rudgyard, M.** (2000). Development of High-Order Taylor–Galerkin Schemes for LES, *Journal of Computational Physics*, *162*(2), 338–371, http://www.sciencedirect.com/science/article/pii/S0021999100965380.

[184] **Schoenfeld, T.**, **Angelberger, C.**, **Legier, J.P. and Ducruix, S.**, (1999). Numerical simulation of compressible reactive flows on unstructured grids, 37th Aerospace Sciences Meeting and Exhibit, Aerospace Sciences Meetings, American Institute of Aeronautics and Astronautics, https://doi.org/10.2514/6.1999-414.

[185] **Veynante, D. and Poinsot, T.** (1997). Large eddy simulation of combustion instabilities in turbulent premixed burners, *Annual Research Briefs*, 253–274.

[186] **Angelberger, C.**, **Veynante, D.**, **Egolfopoulos, F. and Poinsot, T.** (1998). Large eddy simulations of combustion instabilities in premixed flames, *Proc. of the Summer Program*, pp.61–82.

[187] **Legier, J.P.**, **Poinsot, T. and Veynante, D.** (2000). Dynamically thickened flame LES model for premixed and non-premixed turbulent combustion, *Proceedings of the summer program*, volume 12, Center for Turbulence Research Stanford, CA.

[188] **Colin, O.**, **Ducros, F.**, **Veynante, D. and Poinsot, T.** (2000). A thickened flame model for large eddy simulations of turbulent premixed combustion,

Physics of Fluids, *12*(7), 1843–1863, https://doi.org/10.1063/1.870436.

[189] **Legier, J.P.** (2001). Simulations numériques des instabilités de combustion dans les foyers aéronautiques, *Ph.D. thesis*.

[190] **Poinsot, T. and Veynante, D.** (2011). *Theoretical and Numerical Combustion*, CNRS, https://books.google.fr/books?id=6u5rNAEACAAJ.

[191] **Nicoud, F.**, **Toda, H.B.**, **Cabrit, O.**, **Bose, S. and Lee, J.** (2011). Using singular values to build a subgrid-scale model for large eddy simulations, *Physics of Fluids*, *23*(8), 85106, https://doi.org/10.1063/1.3623274.

[192] **Poinsot, T.J. and Lelef, S.K.** (1992). Boundary conditions for direct simulations of compressible viscous flows, *Journal of Computational Physics*, *101*(1), 104–129, arXiv:1011.1669v3.

[193] **Kaufmann, A.**, **Nicoud, F. and Poinsot, T.** (2002). Flow forcing techniques for numerical simulation of combustion instabilities, *Combustion and Flame*, *131*(4), 371–385, http://www.sciencedirect.com/science/article/pii/S0010218002004194.

[194] **Selle, L.**, **Nicoud, F. and Poinsot, T.** (2004). Actual Impedance of Nonreflecting Boundary Conditions: Implications for Computation of Resonators, *AIAA Journal*, *42*(5), 958–964, https://doi.org/10.2514/1.1883.

[195] **Moureau, V.**, **Lartigue, G.**, **Sommerer, Y.**, **Angelberger, C.**, **Colin, O. and Poinsot, T.** (2005). Numerical methods for unsteady compressible multi-component reacting flows on fixed and moving grids, *Journal of Computational Physics*, *202*(2), 710–736, http://www.sciencedirect.com/science/article/pii/S0021999104003134.

[196] **Lindstedt, P.** (1998). Modeling of the chemical complexities of flames, *Symposium (International) on Combustion*, *27*(1), 269–285, http://www.sciencedirect.com/science/article/pii/S0082078498804141.

[197] **Kopp, M.**, **Brower, M.**, **Mathieu, O.**, **Petersen, E. and Güthe, F.** (2012). CO2 chemiluminescence study at low and elevated pressures, *Applied Physics B*, *107*(3), 529–538, https://doi.org/10.1007/s00340-012-5051-4.

[198] **Yamashita, H.**, **Shimada, M. and Takeno, T.** (1996). A numerical study on flame stability at the transition point of jet diffusion flames, *Symposium (International) on Combustion*, volume 26, Elsevier, pp.27–34.

[199] **Knudsen, E. and Pitsch, H.** (2009). A general flamelet transformation useful for distinguishing between premixed and non-premixed modes of combustion, *Combustion and Flame*, *156*(3), 678–696,

http://www.sciencedirect.com/science/article/pii/S0010218008003246.

[200] **Knudsen, E. and Pitsch, H.** (2012). Capabilities and limitations of multi-regime flamelet combustion models, *Combustion and Flame*, *159*(1), 242–264, http://www.sciencedirect.com/science/article/pii/S0010218011001982.

[201] **Bilger, R.W.** (1989). The structure of turbulent nonpremixed flames, *Symposium (International) on Combustion*, *22*(1), 475–488, http://www.sciencedirect.com/science/article/pii/S0082078489800542.

APPENDICES

APPENDIX A.1 : Methodology for FTF reconstruction
APPENDIX A.2 : Experimental Post Processing
APPENDIX A.3 : LES Post Processing

APPENDIX A.1 Methodology for FTF reconstruction

The method developed in [164] is used to infer the FTF at the burner outlet in section 0 from measurements of the acoustic velocity $\tilde{u}_1$ and pressure $\tilde{p}_1$ with HW and M1 made in section 1 below the swirling vane, in a region where the velocity has a top hat profile. The velocity $\tilde{u}_0$ differs from $\tilde{u}_1$ because the distance $l_i = 87$ mm between section 0 and 1 is quite large and the burner is not compact for the range of frequencies of interest $0 \leq f \leq 700$ Hz. At $f = 700$ Hz, He$= 2\pi f l_i/c \sim 1$. The method is based on the low order model of the burner cavities presented in Fig. A.1.

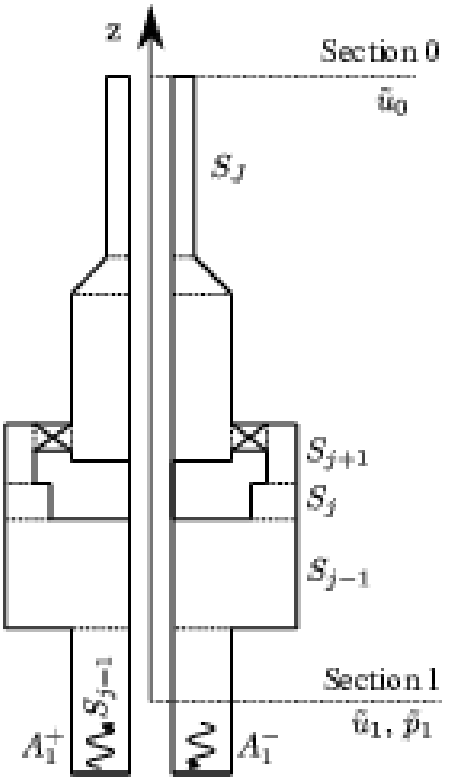

Figure A.1: Schematic representation of acoustic reconstruction through the different sections of the swirled injector.

At low harmonic forcing frequencies, the acoustic field inside the combustor cavities can be assumed to be 1D and can be represented by the complex amplitudes A^+ and A^- of upstream and downstream waves in each cavity. For an harmonic perturbation in the Fourier space at angular frequency ω, $a' = \mathrm{Re}\left[\tilde{a}e^{-i\omega t}\right]$, one has along the burner z-axis:

$$\tilde{p}_j = A_j^+ e^{ik_j z} + A_j^- e^{-ik_j z} \quad \textbf{(A.1.1)}$$

$$\rho_j c_j \tilde{u}_j = A_j^+ e^{ik_j z} - A_j^- e^{-ik_j z} \quad \textbf{(A.1.2)}$$

where $k_j = \omega/c_j$ is the wave number, c_j the speed of sound, ρ_j the density of the medium and z_j is the position in the jth section. As the sound speed and density do not change in the sections considered, the subscripts are removed. With these complex

wave amplitudes, the acoustic pressure $\tilde{p}_j$ and acoustic velocity $\tilde{u}_j$ at any section S_j of the combustor can be reconstructed.

The wave amplitudes A_1^+ and A_1^- in section 1 are determined from the microphone M1 and HW measurements:

$$A_1^+ e^{ik_1 z_1} + A_1^- e^{-ik_1 z_1} = \tilde{p}_1 \quad \textbf{(A.1.3)}$$

$$A_1^+ e^{ik_1 z_1} - A_1^- e^{-ik_1 z_1} = \rho c \tilde{u}_1 \quad \textbf{(A.1.4)}$$

where $\tilde{p}_1$ and $\tilde{u}_1$ are the Fourier components of the pressure and velocity signals evaluated at the forcing frequency f respectively. This linear system of equations is solved for A_1^+ and A_1^-. Subsequently, using continuity of acoustic pressure and of acoustic volumetric flow rate, the jump conditions at abrupt section changes are given by [190]:

$$\tilde{p}_j\left(z_{j+1}\right) = \tilde{p}_{j+1}\left(z_{j+1}\right) \quad \textbf{(A.1.5)}$$

$$S_j \tilde{u}_j\left(z_{j+1}\right) = S_{j+1}\tilde{u}_{j+1}\left(z_{j+1}\right) \quad \textbf{(A.1.6)}$$

where l_j the length and S_j is the cross-sectional area of the j-th section. With these relations the transfer matrix relating the wave amplitudes of the subsequent sections can be constructed as:

$$\begin{bmatrix} A_{j+1}^+ \\ A_{j+1}^- \end{bmatrix} = T_j \begin{bmatrix} A_j^+ \\ A_j^- \end{bmatrix} \quad \textbf{(A.1.7)}$$

where T_j is defined as:

$$T_j = \frac{1}{2}\begin{bmatrix} e^{ikl_j}(1+\Gamma) & e^{-ikl_j}(1-\Gamma) \\ e^{ikl_j}(1-\Gamma) & e^{-ikl_j}(1+\Gamma) \end{bmatrix} \quad \textbf{(A.1.8)}$$

and $\Gamma = S_J/S_{j+1}$. Using these relations a global matrix relating any two sections connected with multiple sections in between can be constructed. These relations are used to calculate the complex wave amplitudes in the main annular injection channel as:

$$\begin{bmatrix} A_0^+ \\ A_0^- \end{bmatrix} = G \begin{bmatrix} A_1^+ \\ A_1^- \end{bmatrix} \quad \textbf{(A.1.9)}$$

where G is the global transfer matrix cast as:

$$G = \prod_{j=1}^{J-1} T_j \quad \textbf{(A.1.10)}$$

where $j = 1$ stands for the HW duct and $J-1$ denotes the duct just before the injector annular channel. After the wave amplitudes at the main annular injection channel are determined, the acoustic velocity $\tilde{u}_0$ at the burner outlet in section 0 corresponds to:

$$\tilde{u}_0 = A_0^+ + A_0^- \quad \textbf{(A.1.11)}$$

The Flame Transfer Function is deduced from the light intensity I from CH^* radicals recorded by the PM and the velocity u_0 at the burner outlet:

$$FTF = \frac{\tilde{I}}{\bar{I}}\frac{U_{sw}}{\tilde{u}_0} = G\left(f, |\tilde{u}_0/U_{sw}|\right) e^{i\varphi\left(f,|\tilde{u}_0/U_{sw}|\right)} \quad \textbf{(A.1.12)}$$

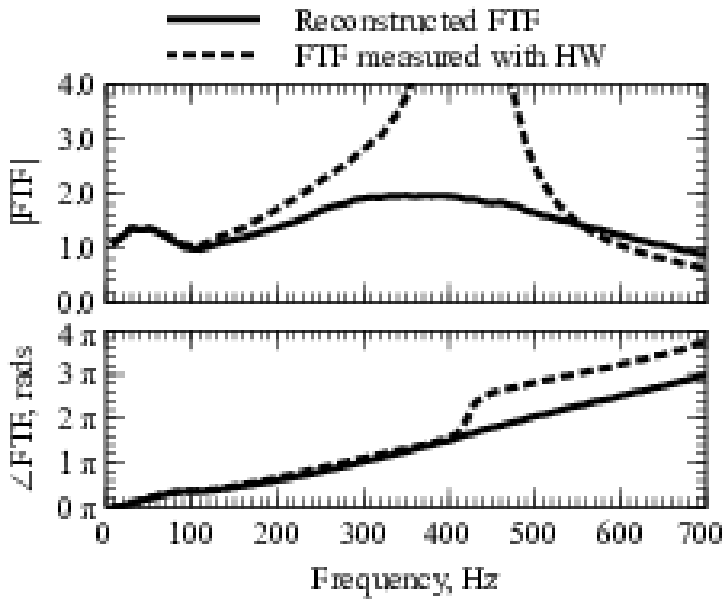

Figure A.2: Flame Transfer Functions for the Ref case. The dotted line is the FTF determined with the HW signal. The straight line is the FTF using the reconstructed velocity at the burner outlet from the low order model and the HW and M1 signals.

Figure A.2 compares the FTF determined with the reference signals $\tilde{u}_0$ and $\tilde{u}_1$. The FTF deduced from the hot wire measurements in section 1 is obviously incorrect. The hot wire lies 87 mm below the burner outlet leading to different acoustic velocity fluctuations at the outlet of the main annular injection channel and the channel where the HW is located. There is also a velocity node near the HW position when the system is pulsated at 420 Hz and the FTF gain determined with HW gain diverges around this forcing frequency.

Another important feature when determining the FTF is to keep the same forcing level at the burner outlet [101]. An iterative algorithm was developed to keep this perturbation level equal to $\tilde{u}_0/U_{sw} = 0.10$. The difference between the velocity fluctuation amplitude recorded with the hot wire HW and the reconstructed velocity amplitude $|\tilde{u}_0|$ in section 0 is presented in Fig. A.3. This last test validates the FTF reconstruction technique and the results shown in Fig. A.2.

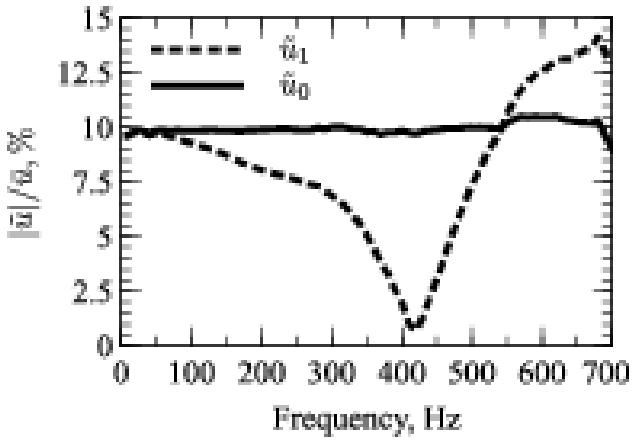

Figure A.3: Velocity fluctuation level in section 1 and 0 used for the FTF determination. The operator $\bar{\cdot}$ denotes here the bulk flow velocity in the corresponding section.

APPENDIX A.2 Experimental Post Processing

The mean of the phase locked images are expressed as shown in Eq. **A.2.1**.

$$\bar{I}(r,z) = \sum_{n_\psi=0}^{N_\psi} I(r,z,\psi)/N_\psi \tag{A.2.1}$$

With the mean of phase locked images defined, the RMS of the pixel intensity fluctuations can be defined as in Eq. **A.2.2**.

$$I^{rms}(r,z) = \sqrt{\overline{|I(r,z,\psi) - \bar{I}(r,z)|^2}} \tag{A.2.2}$$

Furthermore, using the pixel intensities of the phase locked images, it is possible to calculate the complex amplitudes $\tilde{I}(r,z)$ of the fluctuations as presented in Eq.**A.2.3**. With these complex amplitudes, it is also possible to calculate the delays of each pixel during the forcing cycle.

$$\tilde{I}(r,z) = \{I(r,z,\psi)\}\Big|_{\mathfrak{f}} \tag{A.2.3}$$

where $\{I(r,z,\psi)\}\Big|_{\mathfrak{f}}$ is the Fourier component of the instantaneous pixel intensities evaluated at the forcing frequency f. Finally the delays wrt. the velocity fluctuations at the outlet of the burner can be represented as given in Eq. **A.2.4**.

$$\psi_I(r,z) = \angle\left(\frac{\tilde{I}(r,z)}{\tilde{u}_0}\right) \tag{A.2.4}$$

Using this complex amplitude representation, the instantaneous pixel intensities can be expressed as given in Eq.**A.2.5**.

$$I(r,z,t) = \mathrm{Re}\left\{\tilde{I}(r,z)e^{-i\omega t}\right\} + \bar{I}(r,z) + \mathrm{Noise} \tag{A.2.5}$$

Here all the fluctuations around the mean that are not locked to the forcing frequency are lumped into the noise component.

The phase locked mean of the images can be represented as:

$$\lfloor \bar{I}_r \rfloor(z,\psi) = \sum_{n_r=0}^{N_r} \lfloor \bar{I} \rfloor(r,z,\psi) \tag{A.2.6}$$

In the same way, the integrated time average in a pixel row can be calculated as in Eq. **A.2.7**.

$$\bar{I}_r(z) = \sum_{n_t=0}^{N_\psi} \sum_{n_r=0}^{N_r} \lfloor \bar{I} \rfloor(r,z,\psi)/N_\psi \tag{A.2.7}$$

The time units are given in phase as in the experiments images are triggered at a determined phase rather than time. Similarly, the same procedures can be applied

to get the volume integrated phase averaged and time averaged CH* emissions in the chamber as presented in equations **A.2.8** and **A.2.9** respectively.

$$\lfloor \bar{I}_{rz} \rfloor(\psi) = \sum_{n_z}^{N_z} \sum_{n_r}^{N_r} \lfloor \bar{I} \rfloor(r,z,\psi) \tag{A.2.8}$$

$$\bar{I}_{rz} = \sum_{n_t=0}^{N_\psi} \sum_{n_z=0}^{N_z} \sum_{n_r=0}^{N_r} \lfloor \bar{I} \rfloor(z,r,\psi)/N_\psi \tag{A.2.9}$$

Furthermore, the complex amplitude of the radially integrated and volume integrated heat release fluctuations are given in equations **A.2.10** and **A.2.11** respectively.

$$\tilde{I}_r(z) = \left\{ \lfloor \bar{I}_r \rfloor(z,\psi) \right\} \big|_{\mathfrak{f}} \tag{A.2.10}$$

$$\tilde{I}_{rz} = \tilde{I} = \left\{ \lfloor \bar{I}_{rz} \rfloor(\psi) \right\} \big|_{\mathfrak{f}} \tag{A.2.11}$$

From the complex amplitudes, the delays can also be calculated as shown in equations **A.2.12** and **A.2.13**.

$$\psi_{I_r}(z) = \angle\left(\tilde{I}_r/\tilde{u}_0\right) \tag{A.2.12}$$

$$\psi_{I_{rz}} = \psi_I = \angle\left(\tilde{I}_{rz}/\tilde{u}_0\right) \tag{A.2.13}$$

where $\tilde{u}_0$ is the complex amplitude of the velocity fluctuations at the burner outlet. This definition leads to the instantaneous harmonic heat release fluctuations presented in Eq. **A.2.14**.

$$I_r(z,t) = Re\left\{\tilde{I}_r(z)e^{-i\omega t}\right\} + \bar{I}_r(z) + \text{Noise} \quad I_{rz}(t) = Re\left\{\tilde{I}_{rz}e^{-i\omega t}\right\} + \bar{I}_{rz} + \text{Noise} \tag{A.2.14}$$

The projection of the radially integrated heat release response on the global response is given as:

$$|I|_r^p(z) = \frac{|\tilde{I}_r(z)|}{\bar{I}_{rz}} \cos\left(\angle\left(\tilde{I}_r(z), \tilde{I}_{rz}\right)\right) \tag{A.2.15}$$

Furthermore, profiles of RMS of radially integrated heat release field are calculated as presented in Eq.**A.2.16**.

$$I_r^{rms}(z) = \sqrt{\overline{|I_r(z,t) - \bar{I}_r(z)|^2}} \tag{A.2.16}$$

APPENDIX A.3 LES Post Processing

The line of sight integration has been performed by the trapezoidal rule:

$$\bar{\dot{q}}_{LS_y}(x\backslash r,z) = \sum_{n_{slice}=1}^{N_{slice}} \frac{\bar{\dot{q}}(x,y_{n_{slice}-1},z) + \bar{\dot{q}}(x,y_{n_{slice}},z)}{2}\Delta y \qquad \textbf{(A.3.1)}$$

where N_{slice} is the number of slices used to calculate the line of sight integrated heat release, $\dot{q}$ is the heat release and $x\backslash r$ signifies that after line of sight information, the x coordinate can be interpreted as radial coordinate assuming axial periodicity.

The normalized heat release rate is presented as:

$$\bar{\dot{q}}_{LS_{y_{Norm}}}(r,z) = \frac{\bar{\dot{q}}_{LS_y}(r,z)}{\max\left(\bar{\dot{q}}_{LS_y}(r,z)\right)} \cong \frac{\bar{I}(r,z)}{\max\left(\bar{I}(r,z)\right)} \qquad \textbf{(A.3.2)}$$

The expressions used to obtain angle averaged heat release field is presented in Eq. **A.3.3**.

$$\langle\bar{\dot{q}}\rangle(r,z) = \frac{\sum_{n_{slice}=0}^{N_{slice}} \bar{\dot{q}}(r,\theta_{n_{slice}},z)}{N_{slice}} \qquad \textbf{(A.3.3)}$$

A similar normalization process has been applied as expressed in Eq. **A.3.4** to compare experimental and LES results.

$$\langle\bar{\dot{q}}\rangle_{Norm}(r,z) = \frac{\langle\bar{\dot{q}}\rangle(r,z)}{max\left(\langle\bar{\dot{q}}\rangle(r,z)\right)} \equiv \frac{IA\left(\bar{I}\right)(r,z)}{max\left(IA\left(\bar{I}(r,z)\right)\right)} \qquad \textbf{(A.3.4)}$$

The phase averaged heat release rate field in LES calculations are presented as:

$$\overline{\lfloor\dot{q}\rfloor}(x,y,z,\psi) = \sum_{n_{\mathfrak{T}}=0}^{N_{\mathfrak{T}}} \dot{q}(x,y,z,\psi)/N_{\mathfrak{T}} \qquad \textbf{(A.3.5)}$$

As the camera is looking at the transparent quartz chamber and it sees the light emitted by every point of the flame, a line of sight integration has been performed to represent flame images. This integration technique also enables the comparison of the photomultiplier measurements, as the photomultiplies looks at the integrated luminosity coming from all the flame.

$$\overline{\lfloor\dot{q}\rfloor}_{LS_y}(x\backslash r,z,\psi) = \sum_{n_{slice}=1}^{N_{slice}} \frac{\lfloor\bar{\dot{q}}\rfloor(x,y_{n_{slice}-1},z,\psi) + \lfloor\bar{\dot{q}}\rfloor(x,y_{n_{slice}},z,\psi)}{2}\Delta y \qquad \textbf{(A.3.6)}$$

$x\backslash r$ is used to represent the periodic characteristic of the setup.

To compare experimental measurements and LES calculations, a normalization procedure is applied:

$$\overline{\lfloor\dot{q}\rfloor}_{LS_{y_{Norm}}}(x\backslash r,z,\psi) = \frac{\overline{\lfloor\dot{q}\rfloor}_{LS_y}(x\backslash r,z,\psi)}{max\left(\overline{\lfloor\dot{q}\rfloor}_{LS_y}(x\backslash r,z,\psi)\right)} \equiv \frac{\overline{\lfloor I\rfloor}(x\backslash r,z,\psi)}{max\left(\overline{\lfloor I\rfloor}(x\backslash r,z,\psi)\right)} \qquad \textbf{(A.3.7)}$$

The angle-averaged-phase-averaged fields are obtained as averages of 360 slices separated by 1 $^\circ$ as presented in Eq. **A.3.8**.

$$\langle\overline{\lfloor\dot{q}\rfloor}\rangle(r,z,\psi) = \frac{\sum_{n_{slice}=0}^{N_{slice}} \overline{\lfloor\dot{q}\rfloor}(r,\theta_{n_{slice}},z,\psi)}{N_{slice}} \tag{A.3.8}$$

To compare experimental and numerical fields, a similar maximum normalization procedure has been applied as shown in Eq. **A.3.9**.

$$\langle\overline{\lfloor\dot{q}\rfloor}\rangle_{Norm}(r,z,\psi) = \frac{\langle\overline{\lfloor\dot{q}\rfloor}\rangle(r,z,\psi)}{max\left(\langle\overline{\lfloor\dot{q}\rfloor}\rangle(r,z,\psi)\right)} \equiv \frac{IA\left(\overline{\lfloor I\rfloor}\right)(r,z,\psi)}{max\left(IA\left(\overline{\lfloor I\rfloor}(r,z,\psi)\right)\right)} \tag{A.3.9}$$

here *IA* is the inverse abel transformation of the field.

The line of sight average of an instantaneous solution is defined in Eq. **A.3.10**.

$$\dot{q}_{LS_y}(x\backslash r,z,t\backslash(\psi,\mathcal{T})) = \sum_{n_{slice}=1}^{N_{slice}} \frac{\dot{q}(x\backslash r,y_{n_{slice}-1},z,t\backslash(\psi,\mathcal{T})) + \dot{q}(x\backslash r,y_{n_{slice}},z,t\backslash(\psi,\mathcal{T}))}{2}\Delta y \tag{A.3.10}$$

where $\dot{q}_{LS_y}(x\backslash r,z,t\backslash(\psi,\mathcal{T}))$ represents the instantaneous integrated heat release for a given time. $x\backslash r$ is there to show that this integrated field can be represented in cylindrical or cartesian coordinates and $t\backslash(\psi,\mathcal{T})$ signifies that the time-stamps can be also described as a given period and phase. Then the mean of the line of sight integrated heat release is presented in Eq. **A.3.11**.

$$\overline{\dot{q}}_{LS_y}(x\backslash r,z) = \sum_{n_t=0}^{N_t} \dot{q}_{LS_y}(x\backslash r,z,t)/N_t \tag{A.3.11}$$

Definitions of RMS procedure and normalization step are given in equations **A.3.12** and **A.3.13** respectively.

$$\dot{q}^{rms}_{LS_y}(r,z) = \sqrt{\overline{|\dot{q}_{LS_y}(r,z,t) - \overline{\dot{q}}_{LS_y}(r,z)|^2}}, \quad I^{rms}(r,z) = \sqrt{\overline{|I(r,z,t) - \overline{I}(r,z)|^2}} \tag{A.3.12}$$

$$\dot{q}^{rms}_{LS_{y_{Norm}}}(r,z) = \frac{\dot{q}^{rms}_{LS_y}(r,z)}{max(\dot{q}^{rms}_{LS_y})(r,z)} \equiv \frac{I^{rms}(r,z)}{max(I^{rms}(r,z))} \tag{A.3.13}$$

where $\overline{\dot{q}}_{LS_y}$ is the mean of all the timesteps in the forcing cycle.

To perform the spectral analysis, first of all the complex amplitude of the heat release fluctuations in space are defined in Eq. **A.3.14**.

$$\tilde{q}_{LS_y}(r,z) = \left\{\dot{q}_{LS_y}(r,z,t)\right\}\Big|_f \tag{A.3.14}$$

where $\left\{\dot{q}_{LS_y}(r,z,t)\right\}\Big|_f$ is the fourier component of the instantaneous line of sight integrated heat release field evaluated at the forcing frequency f. Similarly, the complex heat release field from the experiments can be obtained from CH* emission images as presented in Eq. **A.2.3**.

To permit the comparison of experimental and numerical values, a normalization step on the amplitude of heat release fluctuations is applied as defined in Eq **A.3.15**.

$$\left|\tilde{q}_{LS_y}\right|_{Norm}(r,z) = \frac{|\tilde{q}_{LS_y}|}{max\left(|\tilde{q}_{LS_y}|\right)} \equiv \frac{|\tilde{I}|}{max\left(|\tilde{I}|\right)} \tag{A.3.15}$$

This definition also leads to the definition of the phase field in space, which is in Eq. **A.3.16**, where $\tilde{u}_0$ is the complex amplitude of axial velocity at the burner outlet.

$$\psi_{\tilde{q}_{LS_y}} = \angle\left(\frac{\tilde{q}_{LS_y}}{\tilde{u}_{0_{LES}}}\right) \equiv \angle\left(\frac{\tilde{I}}{\tilde{u}_{0_{EXP}}}\right) \tag{A.3.16}$$

The expression of the volume integrated heat release in the thin slice is presented in Eq. **A.3.17**.

$$\dot{Q}_r(z,t\backslash(\psi,\mathcal{T})) = \sum_{n_{i_{cell}}=0}^{N_{i_{cell}}^{slice}} \dot{q}_{i_{cell}}((x,y)\backslash(r,\theta),z,t\backslash(\psi,\mathcal{T}))V_{i_{cell}} \tag{A.3.17}$$

here $V_{i_{cell}}$ signifies the volume of any of all the cells i_{cell} that falls inside the slice of interest and $t\backslash(\psi,\mathcal{T})$ is to convey the idea that these timesteps can be expressed as a function of time t or a phase ψ and period $\mathcal{T}$. The time average can be represented as shown in Eq. **A.3.18**.

$$\overline{\dot{Q}}_r(z) = \sum_{n_t=0}^{N_t} \dot{Q}_r(z,t\backslash(\psi,\mathcal{T}))/N_t \tag{A.3.18}$$

where N_t signifies the number of all the time-steps recorded including 12 steps per period and 10 periods. The dependence on the number of periods have been checked to ensure statistically converged flame response calculations. Furthermore, the phase averaged integrated heat release can be represented as shown in Eq. **A.3.19**.

$$\lfloor\overline{\dot{Q}}_r\rfloor(z,\psi) = \sum_{n_{\mathcal{T}}=0}^{N_{\mathcal{T}}} \dot{Q}_r(z,\psi,\mathcal{T})/N_{\mathcal{T}} \tag{A.3.19}$$

where $N_{\mathcal{T}}$ signifies the number of the periods recorded. The complex amplitude of the integrated fluctuating heat release in the thin slice can be expressed as presented in Eq. **A.3.20**.

$$\tilde{Q}_r(z) = \left\{\dot{Q}_r(z,t)\right\}\Big|_{\mathfrak{f}} \tag{A.3.20}$$

From the complex amplitude the phase of heat release fluctuations wrt.to the velocity fluctuations at the burner outlet can be calculated, this is shown in Eq. **A.3.21**.

$$\psi_{\tilde{Q}_r}(z) = \angle\left(\tilde{Q}_r/\tilde{u}_0\right) \tag{A.3.21}$$

Furthermore, the definition of RMS of radially integrated heat release fluctuations are presented in Eq.**A.3.22**.

$$\dot{Q}_r^{rms}(z) = \sqrt{\overline{|\dot{Q}_r(z,t) - \overline{\dot{Q}}_r(z)|^2}} \tag{A.3.22}$$

Similar variables are calculated for the whole chamber for normalization and projection purposes. The mean heat release in all the chamber can be obtained as

shown in Eq. **A.3.24**.Firstly, the volume integrated instantaneous heat release field is defined in Eq.**A.3.23**.

$$\dot{Q}_{rz}(t\backslash(\psi,\mathcal{T})) = \sum_{n_{i_{cell}}=0}^{N_{i_{cell}}^{chamber}} \dot{q}_{i_{cell}}((x,y)\backslash(r,\theta),z,t\backslash(\psi,\mathcal{T}))V_{i_{cell}} \tag{A.3.23}$$

Similarly the mean, the phase average, the complex amplitude and the phase of the of the chamber volume integrated heat release fluctuations are defined in equations **A.3.24**, **A.3.25**, **A.3.26** and **A.3.27** respectively.

$$\overline{\dot{Q}}_{rz} = \sum_{n_t=0}^{N_t} \dot{Q}_{rz}(t\backslash(\psi,\mathcal{T}))/N_t \tag{A.3.24}$$

$$\lfloor\overline{\dot{Q}}_{rz}\rfloor(\psi) = \sum_{n_{\mathcal{T}}=0}^{N_{\mathcal{T}}} \dot{Q}_{rz}(t\backslash(\psi,\mathcal{T}))/N_{\mathcal{T}} \tag{A.3.25}$$

$$\tilde{Q}_{rz} = \left\{\dot{Q}_{rz}(t)\right\}\Big|_{\mathrm{f}} \tag{A.3.26}$$

$$\psi_{\tilde{Q}_{rz}} = \angle\left(\tilde{Q}_{rz}/\left(\tilde{u}_0/|\tilde{u}_0|\right)\right) \tag{A.3.27}$$

With these definitions, it is possible once again to calculate the projection of the the radially integrated heat release on the global heat release as presented in Eq. **A.3.28**.

$$Q_r^p(z) = \frac{|\tilde{Q}_r(z)|}{\overline{\dot{Q}}_{rz}} \cos\left(\angle\left(\tilde{Q}_r(z),\tilde{Q}_{rz}\right)\right) \tag{A.3.28}$$

Combustion and Flame 214 (2020) 266–276

Contents lists available at ScienceDirect

Combustion and Flame

journal homepage: www.elsevier.com/locate/combustflame

Suppression of instabilities of swirled premixed flames with minimal secondary hydrogen injection

Gorkem Oztarlik, Laurent Selle, Thierry Poinsot, Thierry Schuller*

Institut de Mécanique des Fluides de Toulouse, IMFT, Université de Toulouse, CNRS, Toulouse, France

ARTICLE INFO

Article history:
Received 20 September 2019
Revised 4 November 2019
Accepted 21 December 2019

Keywords:
Hydrogen injection
Combustion instabilities
Instability mitigation
Flame transfer function
Swirled turbulent flames

ABSTRACT

The impact of hydrogen addition on the dynamics of a methane-air premixed flame is explored for different injection strategies. The configuration is a swirled injector with a central tube for pilot fuel injection. Keeping the air flow rate and thermal power of the burner constant, it is shown that even for very small flow rates of hydrogen, as low as one percent of the thermal power, flame stabilization and combustor stability are greatly altered when pure hydrogen is injected through the central tube as a pilot jet. It is also shown that fully premixing the same quantity of hydrogen with methane or use of methane for the pilot jet has no significant effects compared to hydrogen pilot injection strategy. The flame response to forced flow perturbations is use to interpret the observed features. It is shown that hydrogen piloting drastically changes the gain of the flame transfer function at low frequencies and its phase lag at high frequencies, while other injection strategies barely change the flame response for these minute flowrates. CO and NOx emissions are finally examined for the different injection strategies. NOx emissions are found to drastically increase with hydrogen piloting compared to other injection strategies. These experiments indicate that pure hydrogen injected in minute fractions may be used as an efficient passive control means to mitigate combustion instabilities, but a compromise needs to be made with emissions.

1. Introduction

Gas turbines fired with natural gas is one the most efficient solution for power generation with limited pollutant emissions and reduced carbon dioxide emissions, compared to other power generation units burning hydrocarbon fuels [1–3]. Typical industrial gas turbines operate on natural gas in a lean premixed regime to cut down NOx emissions, but these systems suffer from dynamical problems mainly associated to combustion instabilities [4]. Instances of heat shields breaking due to high cycle fatigue, damaged burners, liners and transition pieces are regularly reported [5]. With the introduction of new gases from renewable sources in the fuel supply line, such as biogas or syngas, these issues become more critical due to (1) changes in the fuel composition powering the engine and altering the heat release distribution for a given thermal power output [6–9] and (2) intermittent changes of the supply and power demand leading to operation with high turndown ratios [10].

Blending hydrogen from renewable sources into natural gas can be used to reduce carbon dioxide emissions without impairing pollutant emissions. In this strategy, hydrogen is premixed with natural gas prior to combustion. But it was found out that although hydrogen addition widens the static operability range of the combustor by improving blow-off characteristics, it tends to make combustion systems more prone to flashback and more sensitive to combustion instabilities even at low power regimes and more quickly compared to natural gas [11–15].

An alternative way to avoid flashback issues and mitigate combustion instabilities is to use a pilot fuel circuit, burning a fraction of the fuel in partially premixed or non-premixed mode, while the main fuel stage burns in a lean premixture. This strategy helps achieving more stable flames [16–19] and has also been proven on full scale engine tests [20,21]. Because hydrogen has a higher extinction strain rate compared to methane and natural gas, it is a good candidate to serve as a pilot fuel.

The use of a hydrogen pilot fuel jet has been considered in a few studies. Hussain et al. [22] recently made a clear review of these studies in their introduction. In one of the pioneering works, Anderson et al. [23] noted that it would make flames quieter and more stable in a perforated-plate flame holder configuration. More recently, Barbosa et al. [24] showed that a swirled injection of hydrogen into a combustor operated with a lean propane-air mixture can be used to reduce combustion oscillations, without impairing NOx emissions but with a drastic increase in CO

* Corresponding author.
E-mail address: thierry.schuller@imft.fr (T. Schuller).

https://doi.org/10.1016/j.combustflame.2019.12.032

emissions. Hussain et al. [22] analyzed the response to acoustic perturbations of methane-air and ethylene-air flames stabilized by a large bluff body in a dump combustor, when secondary hydrogen is injected through the bluff body. They found that the Flame Describing Function (FDF) linking the acoustic velocity modulation to the resulting heat release rate oscillation at 30, 255 and 315 Hz could be lowered compared to operation without hydrogen for all acoustic forcing levels tested. However, NOx emissions rapidly increase when the hydrogen concentration exceeds 5% in volume. Their analysis carried out without swirl is also limited to selected forcing frequencies.

In this study, an experimental setup with separate injection of hydrogen is considered with the objective to alter the dynamic stability of a swirled combustor operated with methane, used here as a surrogate for natural gas. The fraction of hydrogen injected in the system is kept very low to limit NOx emissions. The goal is to change the distribution of heat release in order to affect flame stabilization and its dynamics without altering the global thermal power and the air flow rate through the system. The effectiveness of this strategy is compared by replacing hydrogen with methane for the pilot fuel or by fully premixing methane and hydrogen in order to discriminate between the effects of fuel composition and injection strategies. The flame response to acoustic perturbations is then analyzed for these different injection strategies. Use of the burner impedance and Flame Transfer Function (FTF) is finally made to identify the mechanisms through which the combustor stability is affected.

This paper is organized as follows. First some generic definitions and theoretical considerations about hydrogen-enriched combustion are given in Section 2. The experimental setup and diagnostics are then presented in Section 3, followed by a detailed comparison of stability maps in Section 4 for the various fuel injection configurations. A deeper analysis of one selected unstable operating point is finally conducted in Section 5 through the scrutiny of pressure traces, flame visualisations and FTF. Pollutant emissions are finally examined in Section 6 for the different injection strategies.

2. Definitions for hydrogen-enriched systems

When multiple fuels are used simultaneously, care is required for a consistent definition of basic combustion parameters. Whether the fuels are premixed or injected separately, one may define the molar fraction of each species in the hypothetical fuel mixture. In this study considering hydrogen and methane, the molar fraction of hydrogen in the fuel is:

$$X^f_{H_2} = \frac{\dot{n}_{H_2}}{\dot{n}_{H_2} + \dot{n}_{CH_4}} \tag{1}$$

where $\dot{n}_j$ denotes the molar flow rate of species j. Then, the balance equation for lean combustion of this multicomponent fuel may be written:

$$\begin{aligned}\phi_G\left(X^f_{CH_4}CH_4 + X^f_{H_2}H_2\right) + \left(2 - \frac{3}{2}X^f_{H_2}\right)(O_2 + aN_2)\\ \longrightarrow \phi_G\left(X^f_{CH_4}CO_2 + \left(2 - X^f_{H_2}\right)H_2O\right)\\ + \left(2 - \frac{3}{2}X^f_{H_2}\right)((1-\phi_G)O_2 + aN_2)\end{aligned} \tag{2}$$

where $a = 3.76$ is the molar fraction of nitrogen in air and $X^f_{CH_4} = 1 - X^f_{H_2}$ is the molar fraction of methane in the fuel blend. The global equivalence ratio is defined as $\phi_G = \alpha/\alpha_s$, where $\alpha = \dot{m}_f/\dot{m}_a$ is the ratio between the fuel and air mass flow rates injected in the burner. The stoichiometric value of α is:

$$\alpha_s = \frac{X^f_{CH_4}W_{CH_4} + X^f_{H_2}W_{H_2}}{\left(2 - \frac{3}{2}X^f_{H_2}\right)(W_{O_2} + aW_{N_2})} \tag{3}$$

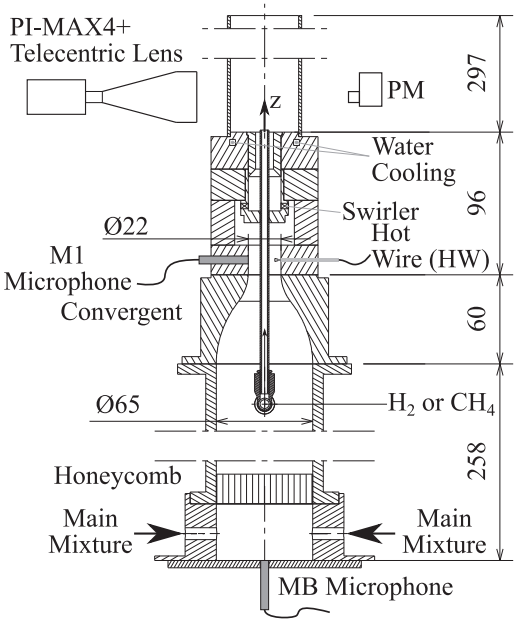

Fig. 1. Schematic representation and relevant dimensions of the experimental setup. Dimensions are in millimeters.

where W_j is the molar mass of species j. Finally, for the analysis conducted in this paper, it is relevant to define the fraction of the total thermal power $\mathcal{P}_{H_2}$ attributed to hydrogen combustion:

$$\mathcal{P}_{H_2} = \frac{X^f_{H_2}Q_{H_2}}{X^f_{H_2}Q_{H_2} + X^f_{CH_4}Q_{CH_4}} \tag{4}$$

where Q_j is the molar lower heating value of species j.

3. Experimental setup and diagnostics

The objective of the study is to alter the dynamics of a burner equipped with a radial swirling vane with the addition of hydrogen. Therefore, the configuration that is presented in Fig. 1 consists of a swirled injector fed with a gaseous mixture, plugged into a cylindrical flame tube. This burner is an evolution of that used in [25–27] operating in fully premixed mode. Here the central insert is replaced by a pilot fuel line aligned with the swirler axis.

The main mixture of fuel and air is injected at the bottom of a plenum with a circular cross section of diameter $D_p = 65$ mm. The acoustic pressure is recorded at the bottom of the plenum via a Brüel & Kjær-TYPE 4954 microphone (MB) and a honeycomb panel is fitted in the plenum to break the turbulent structures resulting from the injection. Two plenum lengths $l_p = 258$ mm and $l_p = 147$ mm are available to modify the acoustic response of the setup.

The flow then goes through a convergent nozzle that ensures a laminar flow with less than 1% velocity fluctuation with a top hat velocity profile, followed by a short annular tube of diameter $D = 22$ mm. In this tube, the acoustic pressure and the velocity are recorded with microphone M1 flush mounted to the wall and a constant temperature anemometer (Dantec 55P16 miniature hot wire probe and a Dantec 54T42 MiniCTA), denoted HW. The microphone M1 and the hot wire probe HW are located in the same section in front of each other as shown in Fig. 1. This section is designated in the following by section (1). Care has been taken to set the hot wire probe outside of the boundary layer, where the velocity is uniform with a top hat velocity profile.

Then follows a radial swirler with 8 feed channels of 4.5 mm diameter each, which are 15^o off the swirler axis. The flow leaves

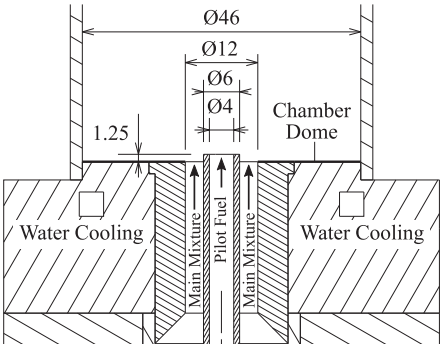

Fig. 2. Detailed view of the injection system with the main dimensions are in millimeters.

the swirler through the main annular injection channel with a reduced external diameter of 12 mm to avoid flashback. A detailed view of this component is given in Fig. 2, together with its main dimensions.

The bulk velocity U_{sw} that is used to define the operating conditions is determined in the main mixture annular injection channel at temperature $T_u = 292$ K. It has a cross section area $A = 84.82$ mm^2 with 6 mm internal diameter and 12 mm external diameter. The swirl number determined from numerical flow simulations is $S_w = 0.4$ at the injector outlet. The top of the burner is water cooled in order to maintain the thermal equilibrium of the plenum at room temperature, $T_u = 292$ K. The outlet of the annular injection channel defines section (0) of the burner at altitude $z = 0$. The piloting system consists of a central stainless steel tube with a 6 mm external diameter and a 4 mm internal diameter, aligned with the burner axis where pure fuel can be injected. The tube protrudes $z = 1.25$ mm inside the combustion chamber to ease flame visualization at its base when the flame is anchored at this location. The combustion chamber consists of cylindrical quartz tubes with an internal diameter of 46 mm. Two flame tube lengths are available, $l_f = 300$ mm and $l_f = 100$ mm, the smaller being used for the measurement of flame responses to acoustic perturbations as described in Section 5.3.

The mass flow rates of methane, air and hydrogen are controlled separately (Brooks SLA 585x series), so that the fraction of the thermal power from hydrogen $\mathcal{P}_{H_2}$ can be regulated as well as the global equivalence ratio ϕ_G. Hydrogen can be added in the main mixture to operate in fully premixed mode or through the pilot tube. Methane can also be used as the pilot fuel for comparison, meaning that this system is versatile for the development of control strategies via fuel composition and injection.

Heat release rate fluctuations of the flame are deduced from the emission intensity of CH* radicals. They are recorded with a photomultiplier along with a band-pass filter centered on the CH* emission spectrum peak $\lambda = 430 \pm 10$ nm (THORLABS FB430-10). Flame images are also taken with a camera (PI-MAX4) along with an appropriate filter (ASAHI XHQA430) also centered on $\lambda = 430 \pm 10$ nm and a telecentric lens (Opto Engineering TC4M120), which provide valuable information on the shape and heat release distribution of the flame. The telecentric lens avoids image distortion due to perspective effects compared to classical lenses.

Table 1
Operating conditions.

Case	Main		Pilot		$\mathcal{P}_{main}$ [%]	$\mathcal{P}_{pilot}$ [%]	$\mathcal{P}_{H_2}$ [%]
	$X^f_{H_2}$ [%]	$X^f_{CH_4}$ [%]	$X^f_{H_2}$ [%]	$X^f_{CH_4}$ [%]			
Ref	0.0	100.0	0.0	0.0	100.0	0.0	0.0
PC1	0.0	99.0	0.0	1.0	99.0	1.0	0.0
PC2	0.0	98.0	0.0	2.0	98.0	2.0	0.0
PH1	0.0	96.8	3.3	0.0	99.0	1.0	1.0
PH2	0.0	93.7	6.6	0.0	98.0	2.0	2.0
MH1	3.3	96.8	0.0	0.0	100.0	0.0	1.0
MH2	6.6	93.7	0.0	0.0	100.0	0.0	2.0

The experiments presented in this paper are conducted at lean operating conditions, $0.70 \leq \phi_G \leq 0.85$, and for bulk flow velocities, $14\ \text{m.s}^{-1} \leq U_{sw} \leq 40\ \text{m.s}^{-1}$, corresponding to thermal powers in the range $2700\ \text{W} \leq \mathcal{P} \leq 9300\ \text{W}$. Gases are injected in the setup at room temperature $T_u = 292$ K. These conditions correspond to injection Reynolds numbers $5541 \leq \text{Re}_{D_h} \leq 15831$ based on the hydraulic diameter $D_h = 6$ mm of the main annular injection channel (Fig. 2).

4. Stability maps

The dynamic stability of the combustor is examined for the operating range given in Section 3. In order to evaluate the effect of hydrogen on the stability of each operating point, different injection strategies are tested as illustrated in Fig. 3. These variations are conducted at constant thermal power $\mathcal{P}$ because this parameter has a first-order impact on the magnitude of combustion instabilities. Therefore, the control parameters are the fraction of the thermal power from hydrogen, $\mathcal{P}_{H_2}$ and that from the pilot flame, $\mathcal{P}_{pilot}$. Accordingly, the fraction of power from the main mixture is $\mathcal{P}_{main} = 1 - \mathcal{P}_{pilot}$. The reference is a fully premixed methane-air case without piloting, labelled 'Ref' in Fig. 3. Then piloting with hydrogen is considered in cases PH1 and PH2 corresponding to $\mathcal{P}_{H_2} = 1\%$ and 2%, respectively. Cases PC1 and PC2 correspond to the replacement of hydrogen by methane in the pilot tube, with the same levels of power $\mathcal{P}_{pilot}$. Finally, in cases MH1 and MH2 the pilot is turned off and the hydrogen is premixed in the main stream, with corresponding power fractions $\mathcal{P}_{H_2}$. All these cases are summarized in Table 1. They allow a systematic investigation of effects of fuel composition, injection strategy and pilot fuel at low levels of hydrogen addition. These experiments are conducted with a long flame tube, $l_f = 300$ mm and a long plenum $l_p = 221$ mm (see Fig. 1).

The stability map of the reference case is presented in Fig. 4. It shows the evolution of the magnitude of pressure fluctuations

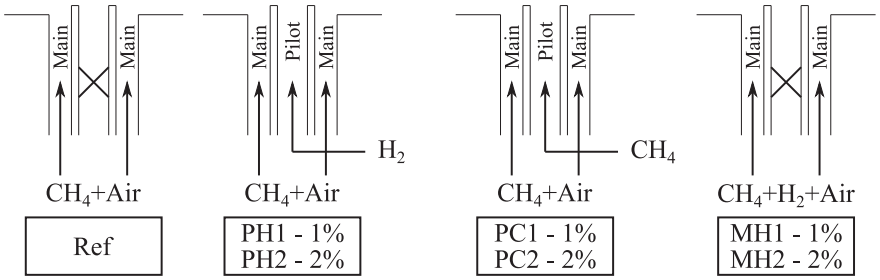

Fig. 3. Representation of the injection strategies that are tested. The cross indicates that the pilot fuel stage is not used.

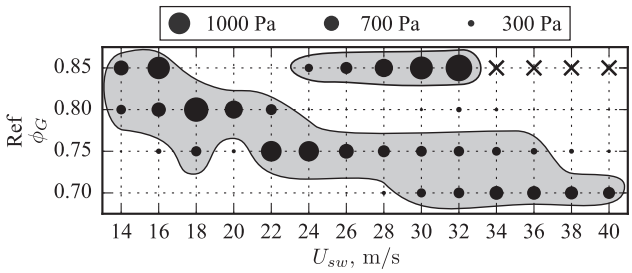

Fig. 4. Stability map of the methane-air fully premixed flame. Case Ref in Table 1 and Fig. 3. Root-mean-square fluctuations of pressure at MB versus bulk velocity U_{sw} and equivalence ratio ϕ_G.

recorded by the microphone MB for variations in bulk velocity U_{sw} and equivalence ratio ϕ_G. The radii of the disks in Fig. 4 are proportional to the root-mean-square (RMS) value of the pressure fluctuations measured by microphone MB. The grey shaded regions delineate the regions of instability, defined here as the operating conditions where RMS pressure fluctuations are higher than 300 Pa. This threshold level was chosen as representative of established self-sustained combustion oscillations associated to a coherent peak in the recorded power spectra. Variations of this threshold show similar results even though the boundaries of the unstable regions are slightly shifted. For some operating conditions, hysteresis takes place in which cases the instability jumps from one intensity to another. These operating conditions are marked with half circles. Finally, a X indicates a condition that was not explored because the instability is too strong and may damage the burner. This nomenclature is used for Figs. 4 through 7. Figure 4 shows that the reference configuration exhibits two regions of instability, one at ϕ_G=0.85 for flow velocities higher than $U_{sw} \geq 24$ m.s^{-1} ($\mathrm{Re}_{D_h} \geq 9500$) and another one along the descending diagonal covering a large fraction of the operational domain. The peak frequency of these self-sustained modes lies between 520 Hz and 680 Hz depending on the operating point considered.

The control strategy that is explored is the pilot injection of hydrogen in small quantities. For PH1 (respectively PH2), 1% (respectively 2%) of the methane flow rate is removed from the main mixture and the hydrogen pilot flow rate is adjusted to compensate for the loss in thermal power. Because of the large differences in molecular weight between H_2 and CH_4, this yields a molar fraction of hydrogen in the total fuel flow $X^f_{H_2} = 3.3\%$ for PH1 and $X^f_{H_2} = 6.6\%$ for PH2 (see Table 1). The corresponding stability maps are shown in Fig. 5. Markers ❖ correspond to operating conditions that could not be explored because the pilot mass flow rates are too small for a stable regulation by the mass-flow controllers. The peak frequency of the unstable modes lies close to those found for the same bulk flow velocity and equivalence ratio in the Ref stability map.

For PH1 there is a reduction of the acoustic pressure level in the system for velocities in the range 18 m.s^{-1} $\leq U_{sw} \leq$ 28 m.s^{-1} and the total number of unstable points has been reduced by one third. This is a very significant impact of the hydrogen injection for it contributes to only 1% of the thermal power. A further increase in the hydrogen content (case PH2 in Fig. 5) results in the complete suppression of all unstable points for $U_{sw} \leq 24$ m.s^{-1} and ϕ_G=0.7. The conclusion is that a minimal level of hydrogen piloting has allowed to stabilize the unstable operating points at low thermal power. However, the stability of the combustor at high power, i.e. the upper-right quadrant in Fig. 5, gets worse as the pilot hydrogen is increased. Interestingly, in these conditions, the bulk flow velocity U_{H_2} of the hydrogen flow in the pilot tube is less than 3% of the bulk velocity U_{sw} of the swirled flow in the main annular injection channel. This rules out that direct modifications of the flow field caused by the pilot jet would be the cause for the modified stability.

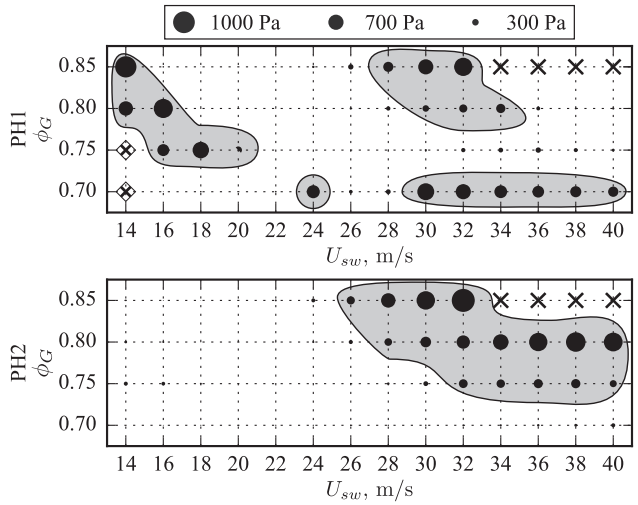

Fig. 5. Stability maps of the configurations with hydrogen pilot injection. Cases PH1 and PH2 in Table 1 and Fig. 3. Root-mean-square fluctuations of pressure at MB versus bulk velocity U_{sw} and equivalence ratio ϕ_G.

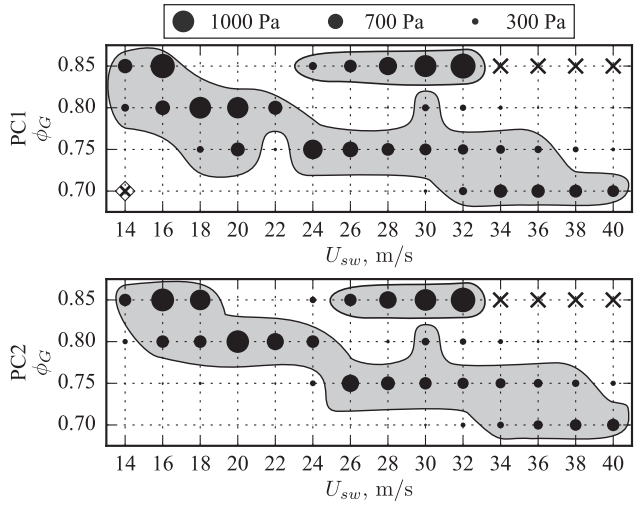

Fig. 6. Stability maps of the configurations with methane pilot injection. Cases PC1 and PC2 in Table 1 and Fig. 3. Root-mean-square fluctuations of pressure at MB versus bulk velocity U_{sw} and equivalence ratio ϕ_G.

In order to mimic a practical situation, it was chosen to keep the air flow rate and the thermal power constant. Therefore, hydrogen piloting yields small changes in global equivalence ratio ϕ_G and bulk velocity U_{sw} in the main annular injection channel. One can show that for PH1 (respectively PH2), U_{sw} is reduced to 99.9% (respectively 99.8%) of the bulk velocity of case Ref. The reduction of ϕ_G is less than 0.1% so that these differences are neglected in the present study.

It is well known that fuel piloting affects the stability of swirl burners. In order to assess the influence of hydrogen, methane piloting is considered with cases PC1 and PC2, by replacing H_2 with CH_4. The corresponding stability maps are shown in Fig. 6. The comparison with the reference case in Fig. 4 indicates that the stability is marginally impacted, even for case PC2, which has the largest methane pilot flowrate.

The two cases with pilot injection suggest that the change in the global composition of the fuel, namely hydrogen addition, is the driving factor for the improved stability. A third set of cases is

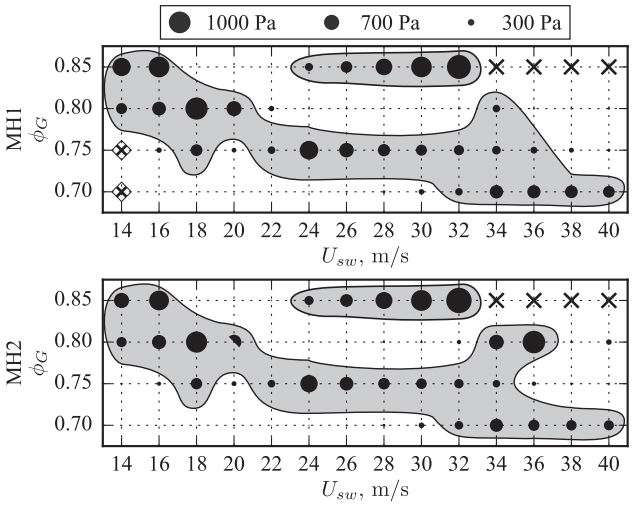

Fig. 7. Stability maps of configurations with the hydrogen-enriched methane/air mixtures. Cases MH1 and MH2 in Table 1 and Fig. 3. Root-mean-square fluctuations of pressure at MB versus bulk velocity U_{sw} and equivalence ratio ϕ_G.

devised where the hydrogen content is identical to piloting cases, but fully premixed within the main injection stream. In MH1 and MH2, the pilot is closed and the hydrogen is premixed with the methane and air, and sent through the swirler. The corresponding stability maps are presented in Fig. 7. As for the PC cases, the stability is not affected and the maps are virtually identical to the reference case shown in Fig. 4.

As a conclusion, it was shown that pilot hydrogen injection has a strong influence on the stability maps of the present swirl combustor, even at very low flow rates. With 2% of the thermal power from hydrogen, stability is greatly increased for low power operating conditions but degrades for high power. It should be noted that the hydrogen injected in the burner provides only up to 2% of the total power, which is minute. In previous investigations, conducted with fully premixed systems, hydrogen addition between 3.2%-9.1% of the total power was shown to make the system more unstable even at low equivalence ratios [12,14,15]. Comparing between hydrogen injection, methane injection and hydrogen premixing, it can be concluded that for low flow-rates, hydrogen injection is the most efficient method to change the stability characteristics.

5. Analysis

In the remainder of this paper, a specific operating point is considered with the objective to explain the mechanism leading to stable operation with pilot hydrogen. It corresponds to $U_{sw} = 18$ m.s^{-1} and $\phi_G = 0.80$. As can be seen by comparing Figs. 4 and 5, this operating point corresponds to a strong instability in the Ref case that is damped with the PH1 and PH2 hydrogen pilot injections.

5.1. Pressure traces

Typical pressure and velocity signals recorded during the limit cycle of case Ref (Table 1) are presented in Fig. 8. The traces are all sinusoidal at a frequency $f = 595$ Hz, despite the large magnitude of the oscillations. The oscillation level reaches around 25% for the heat release rate (HRR) recorded by the PM and 20% for the velocity measured by HW. The RMS of pressure fluctuations recorded by microphone MB at the bottom of the plenum is 1124 Pa. This signal is also in phase with the HRR fluctuations in Fig. 8. Appendix B shows that the acoustic pressure inside the

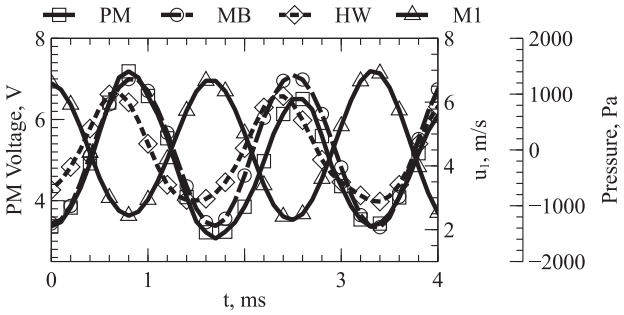

Fig. 8. Pressure (MB, M1), velocity (HW) and heat release rate (PM) time traces for case Ref at $\phi_G = 0.80$ and $U_{sw} = 18$ m.s^{-1}.

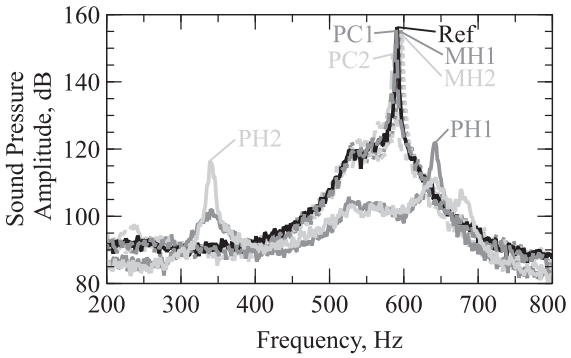

Fig. 9. Power spectra of pressure signals recorded by MB for the cases in Table 1 at $\phi_G = 0.80$ and $U_{sw} = 18$ m.s^{-1}.

combustion chamber is also in phase with the pressure recorded by microphone MB.

The fact that the acoustic pressure and the CH* signals remain close to sine waves indicates that the saturation of the system is not due to a redistribution of the acoustic energy into higher harmonics. A full description of mechanisms leading to limit cycle would require to determine the flame describing function for different pulsation levels $u'_0/\bar{u}_0$, which is out of the scope of the study. One may however make the following qualititative analysis. The HHR and acoustic pressure inside the chamber being in phase, the Rayleigh index is positive and the instability still feeds acoustic energy in the system at the limit cycle. Therefore saturation is probably due to acoustic fluxes at the boundaries or acoustic losses inside the injector or to a change of the flame response to acoustic disturbances, but the nonlinearity of the flame response remains here weak. It is also worth noting that the pressure traces recorded by microphones MB and M1 are in phase opposition in Fig. 8. An acoustic analysis indicates that the corresponding mode has the structure of a 3/4-wave like mode, featuring at $f = 591$ Hz a pressure node slightly upstream the section where the signals M1 and HW are recorded. A full characterization of the structure of this mode is given in Appendix B.

The spectra of the pressure signals recorded by microphone MB at the bottom of the plenum are presented in Fig. 9. The most dominant frequencies and their respective amplitudes are listed in Table 2. As expected from the stability maps, the spectra for cases PC and MH are very close to that of the REF case. There is however a notable reduction of the amplitude for PC2 (Table 2), which is coherent with the knowledge that fuel piloting usually damps combustion instabilities. The first remarkable effect of hydrogen injection in the pilot tube (PH cases) is a strong reduction of the peak pressure around 590 Hz. Smaller peaks emerge, at 641 Hz for PH1 and 339 Hz for PH2 but the associated RMS values are low (Table 2) so these conditions are considered stable. These peaks

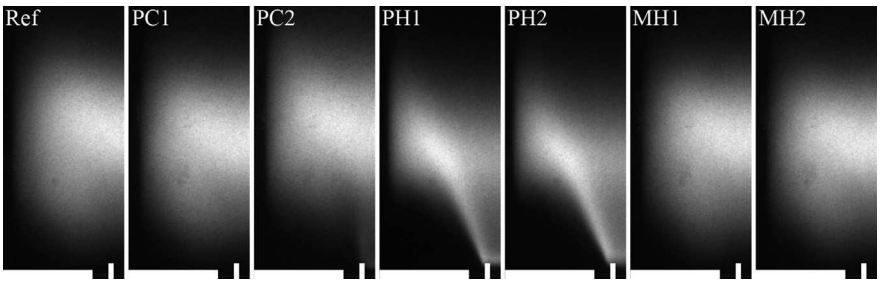

Fig. 10. Flame images with a long chamber and a long plenum for $\phi_G = 0.80$ and $U_{sw} = 18$ m.s^{-1} (Table 1). Only the left side of the image with respect the burner axis is presented. The intensity is scaled in order to increase the overall contrast. The location of the burner is added in white at the bottom of each image.

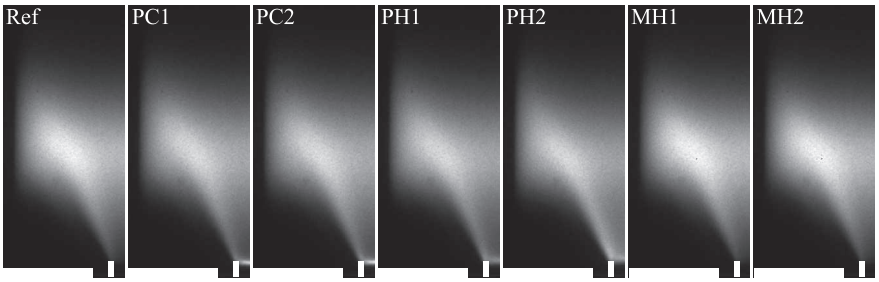

Fig. 11. Flame images with a short combustion chamber and a short plenum for $\phi_G = 0.80$ and $U_{sw} = 18$ m.s^{-1} (Table 1). Only the left side image with respect to the burner axis is presented. Camera settings are the identical for all cases meaning that their intensity can be compared. The location of the burner is added in white at the bottom of each image.

Table 2
Dominant frequencies and corresponding pressure amplitudes for the cases in Table 1 at $\phi_G = 0.80$ and $U_{sw} = 18$ m.s^{-1}.

Case	Amplitude, Pa	Frequency, Hz
Ref	1304	591
PH1	25	641
PH2	13	339
PC1	1140	590
PC2	520	586
MH1	1112	596
MH2	1024	597

correspond to acoustic modes of the setup that are excited by the noise from the turbulent flame. Finally, the spectra for the fully premixed (MH) and methane piloting (PC) cases are almost identical to the Ref case.

5.2. Direct visualisations

Images of the flames are shown in Fig. 10, corresponding to time-averaged line-of-sight integration of the CH* signal over a long duration. 50 snapshots are taken for each case with a total exposure time of 40 ms. For cases Ref, PC and MH, the CH* signal is spread out over the view frame because of the flame motion associated to the combustion instability. A closer look at PC1 and PC2 however shows that the increase of the methane flow rate slightly enhances the emission of CH* in the wake of the pilot injection tube. For the PH cases, which are stable, the image is much sharper. The two flames are anchored at the outlet of the central pilot tube and there is no obvious difference between $\mathcal{P}_{H_2} = 1\%$ and 2%.

For a meaningful comparison of the flame shapes and the analysis of the influence of the injection strategies on the flame stabilization, all the cases need to be made stable. This is achieved by changing the acoustic properties of the setup by modifying the lengths of the plenum and flame tube. Experiments are carried out with the short plenum $l_p = 147$ mm and the short flame tube $l_f = 100$ mm. Time-averaged images of the CH* signal integrated in the line-of-sight are shown in Fig. 11 for these stable flames. As expected, all cases are now comparably sharp. The flames are all anchored at the outlet of the central pilot fuel injection tube and the most striking feature is that these flames are very similar at first glance. The shape of the PC, PH and MH flames is almost identical to the Ref case. For the premixed MH cases, this can be explained by the very small increase in the flame speed with hydrogen enrichment. The laminar burning velocity calculated with Cantera and the GRI-mech 3.0 chemistry mechanism is $S_L = 0.269$ m.s^{-1} for the Ref case and barely increases for MH1 and MH2 cases, $S_L = 0.275$ m.s^{-1} (+1.6%) and $S_L = 0.275$ m.s^{-1} (+3.2%), respectively. This is due to the fact that the maximum variation in fuel injection is 2% of the total power corresponding $X^f_{H_2} = 6.6\%$.

A closer inspection reveals that the distribution of CH* intensity along the flame arms for the cases with piloting exhibit a more intense CH* emission near the flame base compared to the Ref and MH cases. This zone is more intense for the PC cases than the PH cases, which relates to the fact that hydrogen combustion does not generate CH* radicals.

For a more quantitative evaluation of the changes in flame shape, contours at 35% of the CH* peak intensity are plotted for cases Ref, PH1 and PH2 in Fig. 12. Variations of this threshold level slightly modifies the boundary of these contours, but does not change the difference in flame patterns. The stronger attachement of the flame base is quite obvious but it also appears that the flame height is slightly reduced by the injection of hydrogen. This is a consequence of the increased burning rate when replacing CH_4 by H_2 and altogether, these slight modifications of the flame geometry and the redistribution of the volumetric heat release rate through the reaction zone alter the flame response.

5.3. Flame Transfer Functions

The forced response of the flames to acoustic excitation is examined by measuring its Flame Transfer Function (FTF):

$$\frac{\tilde{\dot{Q}}}{\bar{\dot{Q}}} = G\exp(i\varphi)\frac{\tilde{u}_0}{\bar{u}_0} \tag{5}$$

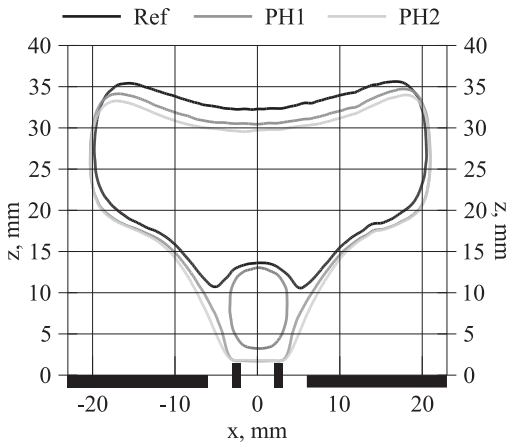

Fig. 12. Contours of 35% of the maximum of CH* intensity from images in Fig. 11.

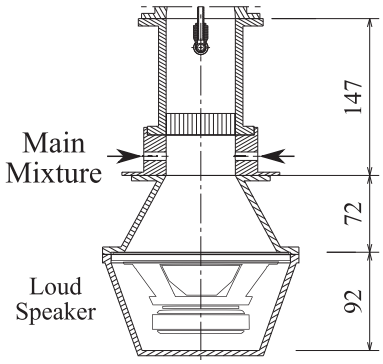

Fig. 13. Schematic representation of the configuration used to measure FTFs.

where $\dot{Q}$ and u_0 denote the heat release rate and the velocity at the burner outlet in section (0). In this expression, $\overline{u}_0$ corresponds to U_{sw}. The operator $\tilde{}$ stands for the Fourier component of the signal at the forcing frequency ω and $\bar{}$ means the time averaged value. In this framework, the heat release rate fluctuation $\tilde{\dot{Q}}$, deduced from the PM equipped with the CH* filter, features a gain G and a phase lag φ with respect to the acoustic velocity $\tilde{u}_0$.

The prerequisite for this task is a stable flame, which is again obtained with the flame tube and plenum lengths $l_f = 100$ mm and $l_p = 147$ mm, respectively. In this case the system is void of thermo-acoustic instabilities for all operating points studied. The bottom cap of the plenum is replaced with an extension housing a loudspeaker as shown in Fig. 13. Using this configuration, the flow in the main annular injection channel is submitted to harmonic modulation with a controllable level.

The FTF should be determined with a reference velocity as close as possible to the burner outlet [28]. In a swirling injector, it is difficult to instrument the burner at this location and the technique used in [29] to reconstruct the acoustic velocity $\tilde{u}_0$ at the burner outlet from the hot wire probe HW and the pressure M1 signals upstream of the swirler is used instead. This is an important aspect of the method because the distance $l_i = 87$ mm between sections (0) and (1) is not short. Even at relatively low frequencies there may be a node in the acoustic field between HW and the flame. The methodology is fully described in Appendix A.

The forcing by the loudspeaker is tuned so that the amplitude of the velocity fluctuation at the burnet outlet is 10% of the bulk velocity for all frequencies $\tilde{u}_0/U_{sw} = 0.10$. The resulting FTFs are presented in Fig. 14. For the premixed methane-air Ref case, the flame is very responsive with large FTF gains exceeding unity over almost the entire frequency range explored from 10 Hz to 700 Hz.

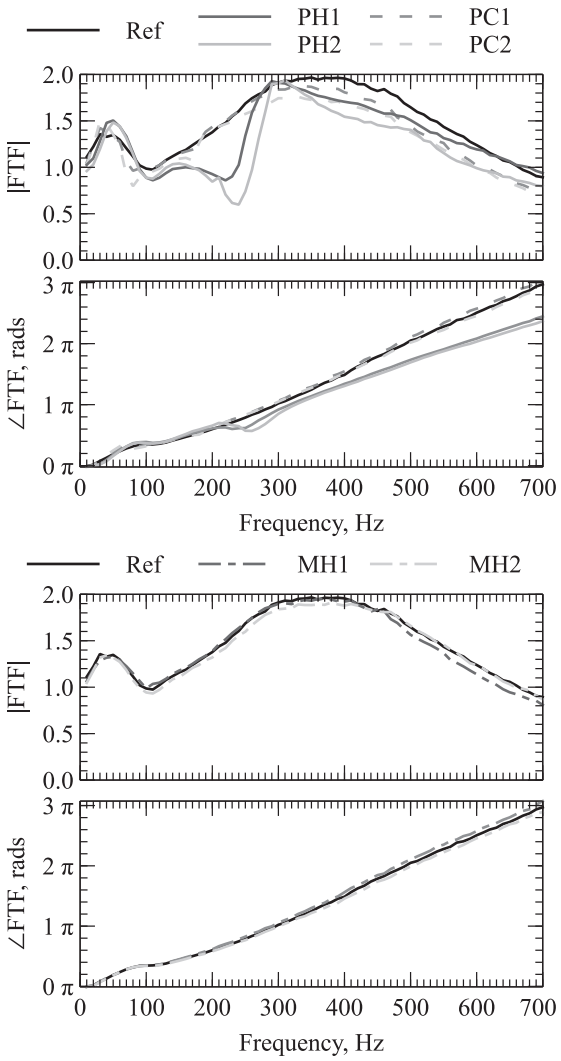

Fig. 14. Flame transfer functions for a constant forcing level $\tilde{u}_0/U_{sw} = 0.10$ at the burner outlet.

Regarding the fully premixed MH cases, hydrogen addition in the fuel at such low concentration levels does not impact the flame response in Fig. 14. This observation is consistent with the stability maps and the flame visualizations. A fuel blend with a few percent of hydrogen, $X^f_{H_2} < 7\%$ does not alter the dynamic stability of the system. The laminar burning velocity was already shown to change less than 3.3% for MH2. Changes of the adiabatic flame temperature for mixtures Ref, MH1 and MH2 are also smaller than 1%.

Methane injection in the central pilot fuel line corresponding to cases PC1 and PC2 has more effect and visibly decreases the FTF gain G for frequencies higher than 250 Hz in Fig. 14. The FTF phase lag φ is marginally altered. The Rayleigh index, that has been shown to take a positive value for the Ref case at this operating condition, remains positive for PC1 and PC2 because the FTF phase lag is identical for the Ref case and the PC cases. The small drop in the FTF gain around 600 Hz is consistent with the modest reduction of the limit-cycle amplitude of the unstable mode observed for the PC cases in Fig. 9 (see also Table 2). For case PC2, there is a small bump in the FTF gain at 30 Hz followed by a dip at 80 Hz, but these features are not explained.

The strongest alteration of the FTF is obtained with hydrogen piloting for cases PH1 and PH2. The most obvious impact is the large reduction of the FTF gain in the range 150–300 Hz, which is more pronounced for PH2 than PH1 when the hydrogen flowrate

Table 3
CO and NOx emissions measured at the flame tube outlet for U_{sw}=18 m.s^{-1} and ϕ=0.8.

ppm	Ref	PH1	PH2	MH1	MH2	PC1	PC2
NOx	12.4 ± 0.6	14.4 ± 0.7	15.6 ± 0.8	12.8 ± 0.6	12.8 ± 0.6	13.8 ± 0.7	14.1 ± 0.7
CO	10.0 ± 1	10.0 ± 1	9.0 ± 1	10.0 ± 1	10.0 ± 1	10.0 ± 1	10.0 ± 1

is increased. This could be an effective control strategy but at this operating point, the instability is not in this frequency range. The large dip of the gain G around 220–240 Hz with a change in the slope of the phase lag φ is characteristic of interferences between acoustic waves and azimuthal convective waves downstream the swirler [25,30,31]. This feature is not discussed here since our focus is on the influence of piloting and hydrogen addition. The scrutiny of this mechanism is left to further studies.

Above 300 Hz, the FTF gain for the PH cases lies below the Ref case in Fig. 14, but the difference is not sufficient to explain the difference in stability. For frequencies higher than 300 Hz, the FTF phase lags between the PH and Ref cases begin to deviate and the difference increases with the forcing frequency, resulting in a large difference at the frequency of the instability. Around 590 Hz, one reads in Fig. 14: $\varphi(590) \sim 7.75$ rad for the Ref, PC1, PC2, MH1 and MH2 cases and $\varphi(590) = 6.36$ rad for the PH1 and PH2 cases.

This large difference of the FTF phase lag φ is at the origin of the augmented stability margins of the PH cases. This is highlighted by conducting a simplified acoustic energy balance. For a compact flame, the thermo-acoustic energy release at frequency $f = 1/T$ in the system is determined by the Rayleigh index:

$$\mathcal{R} = \frac{1}{T}\int_T \frac{\gamma-1}{\gamma\bar{p}} p'\dot{Q}'dt = \frac{\gamma-1}{2\gamma\bar{p}}\mathrm{Re}\left[Z\tilde{u}_0\tilde{Q}^*\right] \tag{6}$$

In this expression Re[·] is the real component of the complex argument and the star denotes the complex conjugate. It makes use of the complex burner impedance Z at the instability frequency f:

$$Z = \frac{\tilde{p}_0}{\tilde{u}_0} = |Z|\exp(i\varphi_0) \tag{7}$$

where $\tilde{p}_0$ and $\tilde{u}_0$ denote the acoustic pressure and velocity at the burner outlet in section (0). In this study, the phase lag φ_0 in section (0) is deduced from reconstructions of $\tilde{p}_0$ and $\tilde{u}_0$ with measurements of $\tilde{p}_1$ and $\tilde{u}_1$ made in section (1). This reconstruction of the acoustic field at the burner outlet was verified with pressure measurements taken from inside the chamber as explained in Appendix B.

When the Rayleigh index is positive $\mathcal{R} > 0$ the combustion dynamics destabilizes the system. When $\mathcal{R} < 0$, the flame damps acoustic perturbations and the system is stable. Eqs. (5) and (7) are used to rewrite the Rayleigh source term as a function of the phase lags from the burner impedance Z and FTF:

$$\mathcal{R} = \frac{(\gamma-1)\bar{\dot{Q}}}{2\gamma\bar{p}U_{sw}}|\tilde{u}_0|^2|Z|G\cos(\varphi_0-\varphi) \tag{8}$$

When the burner impedance Z, the FTF or the acoustic velocity $\tilde{u}_0$ at the burner outlet vanishes, there is no thermo-acoustic energy release $\mathcal{R} = 0$. For all other conditions, the thermo-acoustic source may damp $\mathcal{R} < 0$ or amplify $\mathcal{R} > 0$ acoustic perturbations, depending on the phase lags φ_0 and φ from the burner impedance Z and FTF, respectively. According to Eq. (8) and neglecting other damping mechanisms, unstable modes need to comply with:

$$-\frac{\pi}{2}[2\pi] < \varphi - \varphi_0 < \frac{\pi}{2}[2\pi] \tag{9}$$

Knowing that the burner impedance at $f \simeq 590$ Hz is $\varphi_0 \simeq 1.96$ rad, one deduces that to trigger an instability the FTF phase lag necessarily belongs to:

$$0.39 < \varphi < 3.53 \quad \text{or} \quad 6.67 < \varphi < 9.82 \tag{10}$$

For the REF methane/air case, methane piloting PC1 and PC2 cases and the fully premixed hydrogen/methane MH1 and MH2 cases, the FTF phase lag $\varphi(590) \sim 7.69$ rad falls within the second instability region. With hydrogen piloting, PH1 and PH2, $\varphi(590) \sim 6.36$ rad falls within the stable band $3.53 < \varphi < 6.67$.

This analysis shows that minimal hydrogen injection through a pilot jet is an efficient way to alter the FTF with significant changes of the gain at low forcing frequencies and phase lag at high forcing frequencies. This in turn can be used to drastically change the stability margins of the combustor.

Experiments, not shown here, have also been repeated by replacing the CH* filter by an OH* filter to deduce the heat release rate fluctuations. It was found that the measured FTF is independent of the selected filter to deduce heat release rate fluctuations for all injection strategies tested (PM, PH and PC) with $\mathcal{P}_{H_2}$=1% and 2%.

6. Emissions

Another aspect that needs to be considered is the pollutant emissions. NOx emissions are a known issue for hydrogen enriched flames. CO and NOx concentration measurements in the burnt gases have been performed with a gas analyzer ECOM J2KN PRO by probing the flow at the outlet of a 200 mm length combustion chamber. Care has been taken to prevent combustion products mixing with the ambient air. Results for U_{sw}=18 m.s^{-1} and ϕ=0.8 and the different injection strategies are presented in Table 3.

Injection of hydrogen premixed with the main methane/air mixture does not modify emissions for the MH cases. Methane and hydrogen piloting do not alter CO emissions, but they increase NOx emissions even for these small flowrates. PC2 and PH2 injection strategies with only 2% of the power originating from combustion of the pilot fuel, lead to an increase of NOx concentrations in the flue gases of +16% for methane and +25% for hydrogen injection. These results put in forward that an optimization needs to be performed between the benefits of the change in the FTF obtained from the injection of hydrogen, and the increase of NOx emissions coming from the non-premixed part of the flame when pure hydrogen is injected.

7. Conclusion

In this work, the control of combustion instabilities via separate hydrogen injection was studied. The configuration is a swirled premixed methane/air burner, tested over a wide range of operating conditions through variations of bulk flow velocity and equivalence ratio. The goal was to assess control strategies that would require very low fractions of hydrogen, therefore the maximum investigated is 2% of the thermal power. For each operating condition, the air flow rate and total thermal power are kept constant. The reference being the fully premixed methane case, three alternatives are considered: pilot injection of hydrogen (PH), pilot injection of methane (PC) and fully premixed methane hydrogen (MH). These allow to discriminate between fuel composition effects and injection strategies.

The analysis of stability maps, pressure traces, flame images and Flame Transfer Functions led to the following conclusions:

1. When the hydrogen is fully premixed with methane and air the stability map is not affected.
2. Pilot injection of pure hydrogen strongly affects the stability map with a significant reduction of the unstable zones.
3. Classical pilot injection of methane has a weak stabilizing effect at such low fraction of the total power ($<$ 2%).
4. Piloting with hydrogen affects the flame anchoring resulting in slightly shorter flames with a redistribution of the volumetric heat release toward the bottom of the flame.
5. Both the gain and phase lag of the FTF are massively affected by pilot hydrogen addition with different behaviors depending on the frequency range.
6. NOx emissions need to monitored to select the best compromise between augmented stability margins and reduced emission levels.

It is concluded that hydrogen injection can be used as an efficient passive control means to mitigate thermo-acoustic instabilities. Small changes in the percentage of hydrogen addition result in stable regimes, otherwise unstable without injection for the same thermal power and air flow rate. This effect is more pronounced at low power regimes, resulting in a system that has augmented stability margins.

Declaration of Competing Interest

We, the authors, declare that we have no known competing financial interests or personal relationships that could have appeared to influence the work reported in this paper.

Acknowledgments

The research leading to these results has received funding from the European Research Council under the European Union's Seventh Framework Programme (FP/2007-2013)/ERC Grant Agreement ERC-AdG 319067-INTECOCIS.

Appendix A. Methodology for FTF reconstruction

The method developed in [29] is used to infer the FTF at the burner outlet in section (0) from measurements of the acoustic velocity $\tilde{u}_1$ and pressure $\tilde{p}_1$ with HW and M1 in section (1) below the swirling vane. In section (1), the flow is laminar with a top hat velocity profile. The velocity $\tilde{u}_0$ at the burner outlet differs from $\tilde{u}_1$ because the distance $l_i = 87$ mm between sections (0) and (1) is quite large and the burner is not compact for the range of frequencies of interest $0 \leq f \leq 700$ Hz. At $f = 700$ Hz, He$= 2\pi f l_i/c \sim 1$. The method is based on the low order model of the burner cavities presented in Fig. 15.

At low harmonic forcing frequencies, the acoustic field inside the combustor cavities can be assumed to be 1D and can be represented by the complex amplitudes A^+ and A^- of upstream and downstream waves in each cavity. For an harmonic perturbation in the Fourier space at angular frequency ω, $a' = \mathrm{Re}\left[\tilde{a}e^{-i\omega t}\right]$, one has along the burner z-axis:

$$\tilde{p}_j = A_j^+ e^{ik_j z} + A_j^- e^{-ik_j z} \tag{A.1}$$

and

$$\rho_j c_j \tilde{u}_j = A_j^+ e^{ik_j z} - A_j^- e^{-ik_j z} \tag{A.2}$$

where $k_j = \omega/c_j$ is the wave number, c_j the speed of sound, ρ_j the density of the medium and z_j is the position in the jth section. As the sound speed and density do not change in the sections considered, the subscripts are removed. With these complex wave amplitudes, the acoustic pressure $\tilde{p}_j$ and acoustic velocity $\tilde{u}_j$ at any section S_j of the combustor can be reconstructed.

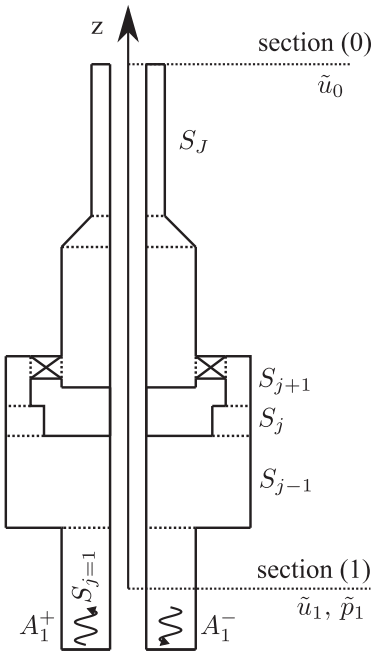

Fig. 15. Schematic representation of acoustic reconstruction through the different sections of the swirled injector.

The wave amplitudes A_1^+ and A_1^- in section (1) are determined from the microphone M1 and HW measurements:

$$A_1^+ e^{ik_1 z_1} + A_1^- e^{-ik_1 z_1} = \tilde{p}_1 \tag{A.3}$$

$$A_1^+ e^{ik_1 z_1} - A_1^- e^{-ik_1 z_1} = \rho c \tilde{u}_1 \tag{A.4}$$

where $\tilde{p}_1$ and $\tilde{u}_1$ are the Fourier components of the pressure and velocity signals evaluated at the forcing frequency f respectively. This linear system of equations is solved for A_1^+ and A_1^-. Subsequently, using continuity of acoustic pressure and of acoustic volumetric flow rate, the jump conditions at abrupt section changes are given by [32]:

$$\tilde{p}_j\left(z_{j+1}\right) = \tilde{p}_{j+1}\left(z_{j+1}\right) \tag{A.5}$$

$$S_j \tilde{u}_j\left(z_{j+1}\right) = S_{j+1}\tilde{u}_{j+1}\left(z_{j+1}\right) \tag{A.6}$$

where l_j is the length and S_j is the cross-sectional area of the jth section. With these relations the transfer matrix relating the wave amplitudes of the subsequent sections can be constructed as:

$$\begin{bmatrix} A_{j+1}^+ \\ A_{j+1}^- \end{bmatrix} = T_j \begin{bmatrix} A_j^+ \\ A_j^- \end{bmatrix} \tag{A.7}$$

where T_j is defined as:

$$T_j = \frac{1}{2}\begin{bmatrix} e^{ikl_j}(1+\Gamma) & e^{-ikl_j}(1-\Gamma) \\ e^{ikl_j}(1-\Gamma) & e^{-ikl_j}(1+\Gamma) \end{bmatrix} \tag{A.8}$$

and $\Gamma = S_j/S_{j+1}$. A global matrix relating any two sections connected with multiple sections in between can be constructed. These relations are used to calculate the complex wave amplitudes in the main annular injection channel as:

$$\begin{bmatrix} A_0^+ \\ A_0^- \end{bmatrix} = M \begin{bmatrix} A_1^+ \\ A_1^- \end{bmatrix} \tag{A.9}$$

where M is the global transfer matrix cast as:

$$M = \prod_{j=1}^{J-1} T_j \tag{A.10}$$

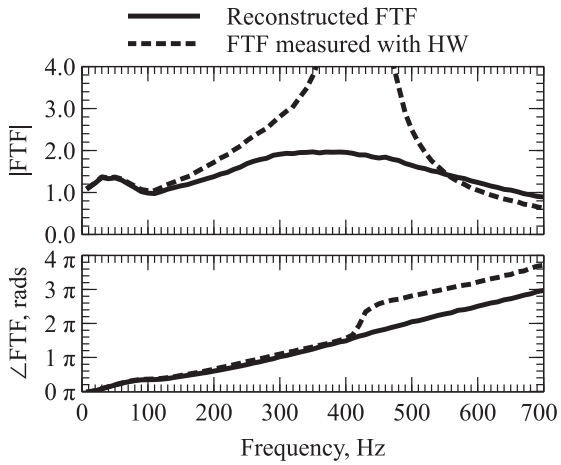

Fig. 16. FTF for the Ref case. The dotted line is the FTF determined with the HW signal measured in section (1). The straight line is the FTF using the reconstructed velocity u_0' at the burner outlet in section (0) from the low order model and the HW and M1 signals.

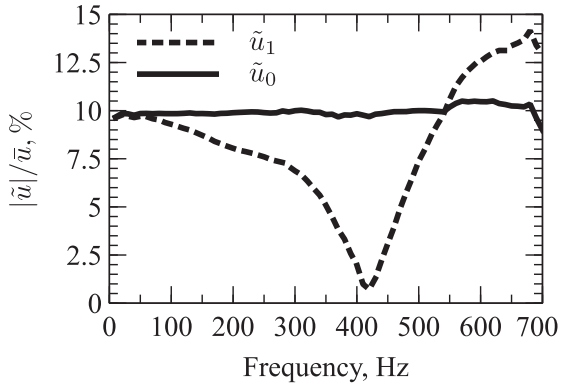

Fig. 17. Velocity fluctuation level in sections (1) and (0) used for the FTF determination. The operator $\bar{\cdot}$ denotes here the bulk flow velocity in the corresponding section.

where $j = 1$ stands for the HW duct and $J - 1$ denotes the duct just before the injector annular channel. After the wave amplitudes at the main annular injection channel are determined, the acoustic velocity $\tilde{u}_0$ at the burner outlet in section (0) corresponds to:

$$\tilde{u}_0 = A_0^+ + A_0^- \tag{A.11}$$

The FTF is deduced from the light intensity I from CH^* radicals recorded by the PM and the velocity u_0 at the burner outlet:

$$FTF = \frac{\tilde{I}}{\bar{I}}\frac{U_{sw}}{\tilde{u}_0} = G(f, |\tilde{u}_0/U_{sw}|)e^{i\varphi(f,|\tilde{u}_0/U_{sw}|)} \tag{A.12}$$

Figure 16 compares the FTF determined with the reference signals $\tilde{u}_0$ and $\tilde{u}_1$. The FTF deduced from the hot wire measurements in section (1) is obviously incorrect. The hot wire lies 87 mm below the burner outlet leading to different acoustic velocity fluctuations at the outlet of the main annular injection channel and the channel where the HW is located. There is also a velocity node near the HW position when the system is pulsated at 420 Hz and the FTF gain determined with HW diverges around this forcing frequency.

Another important feature when determining the FTF is to keep the same forcing level at the burner outlet [33]. An iterative algorithm was developed to keep this perturbation level equal to $\tilde{u}_0/U_{sw} = 0.10$. The difference between the velocity fluctuation amplitude recorded with the hot wire HW in section (1) and the reconstructed velocity amplitude $|\tilde{u}_0|$ in section (0) is presented in Fig. 17. This last test validates the FTF reconstruction technique and the results shown in Fig. 14.

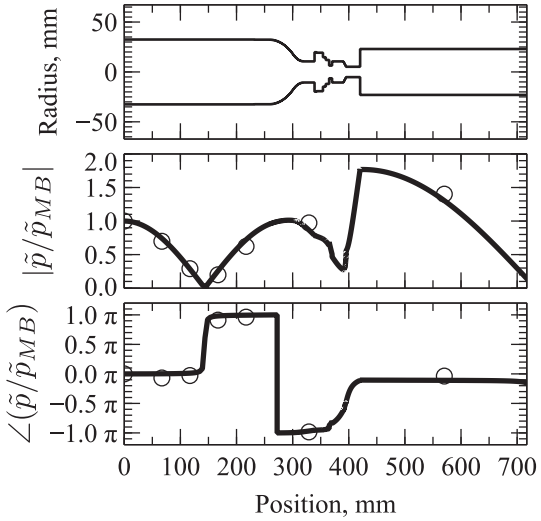

Fig. 18. Comparison between measurements (circles) and predictions (full line) of the acoustic pressure distribution along the combustor of the unstable mode calculated with OSCILOS (http://www.oscilos.com).

Appendix B. Acoustic Structure of the Mode

A low order thermo-acoustic model of the combustor has been constructed with the help of the OSCILOS simulator [34]. This model includes the flame response with the gain and the phase lag measured at the limit cycle of the Ref case. The reflection coefficient at the inlet has been taken to be a fully reflecting velocity node. The outlet of the combustion chamber exhausting burnt gases is open to atmosphere. Measurements of the outlet reflection coefficient in hot conditions were made and a fit was included in the numerical model. The temperature at the outlet of the 300 mm combustion chamber has been measured with a thermocouple. Temperature measurements corrected for thermal radiation were used to calculate the speed of sound and density in the flame tube. The fresh mixture in the plenum is at ambient conditions. The structure of the instability observed for the Ref case at $U_{sw} = 18$ m.s^{-1} and $\phi = 0.8$ is presented in Fig. 18. The top image shows a schematic of the burner cavities. The middle plot shows the pressure amplitude with respect to that measured by microphone MB at the bottom of the plenum. The bottom plot shows the phase lag with respect to that measured by microphone MB. This figure confirms that the acoustic pressure in the flame tube is in phase with the pressure signal measured by microphone MB.

References

[1] P. Jaramillo, W.M. Griffin, H.S. Matthews, Comparative life-cycle air emissions of coal, domestic natural gas, LNG, and SNG for electricity generation, Environ. Sci. Technol. 41 (17) (2007) 6290–6296.
[2] P. Viebahn, J. Nitsch, M. Fischedick, A. Esken, D. Schüwer, N. Supersberger, U. Zuberbühler, O. Edenhofer, Comparison of carbon capture and storage with renewable energy technologies regarding structural, economic, and ecological aspects in germany, Int. J. Greenh. Gas Control 1 (1) (2007) 121–133.
[3] N.A. Odeh, T.T. Cockerill, Life cycle GHG assessment of fossil fuel power plants with carbon capture and storage, Energy Policy 36 (1) (2008) 367–380.
[4] T. Poinsot, Prediction and control of combustion instabilities in real engines, Proc. Combust. Inst. 36 (1) (2017) 1–28.
[5] T.C. Lieuwen, V. Yang, Combustion instabilities in gas turbine engines: operational experience, fundamental mechanisms and modeling, Progress in Astronautics and Aeronautics, American Institute of Aeronautics and Astronautics (2005).
[6] R.L. Speth, A.F. Ghoniem, Using a strained flame model to collapse dynamic mode data in a swirl-stabilized syngas combustor, Proc. Combust. Inst. 32 (2) (2009) 2993–3000.

[7] K. Liu, V. Sanderson, The influence of changes in fuel calorific value to combustion performance for siemens SGT-300 dry low emission combustion system, Fuel 103 (2013) 239–246.
[8] C.J. Mordaunt, W.C. Pierce, Design and preliminary results of an atmospheric–pressure model gas turbine combustor utilizing varying CO2 doping concentration in CH4 to emulate biogas combustion, Fuel 124 (2014) 258–268.
[9] T. García-Armingol, J. Ballester, Operational issues in premixed combustion of hydrogen-enriched and syngas fuels, Int. J. Hydrogen Energy 40 (2) (2015) 1229–1243.
[10] P. Jansohn (Ed.), Modern gas turbine systems: high efficiency, low emission, fuel flexible power generation, Woodhead publishing, 2013.
[11] R.W. Schefer, D.M. Wicksall, A.K. Agrawal, Combustion of hydrogen-enriched methane in a lean premixed swirl-stabilized burner, Proc. Combust. Inst. 29 (1) (2002) 843–851.
[12] L. Figura, J.G. Lee, B.D. Quay, D.A. Santavicca, The effects of fuel composition on flame structure and combustion dynamics in a lean premixed combustor, GT2007-27298, ASME Turbo Expo, May 14–17, 2007 Montreal, Canada, no. 47918 (2007), pp. 181–187.
[13] D.M. Wicksall, A.K. Agrawal, Acoustics measurements in a lean premixed combustor operated on hydrogen/hydrocarbon fuel mixtures, Int. J. Hydrogen Energy 32 (8) (2007) 1103–1112.
[14] S. Taamallah, K. Vogiatzaki, F.M. Alzahrani, E.M.A. Mokheimer, M.A. Habib, A.F. Ghoniem, Fuel flexibility, stability and emissions in premixed hydrogen-rich gas turbine combustion: Technology, fundamentals, and numerical simulations, Appl. Energy 154 (2015) 1020–1047.
[15] S. Taamallah, Z.A. LaBry, S.J. Shanbhogue, A.F. Ghoniem, Thermo-acoustic instabilities in lean premixed swirl-stabilized combustion and their link to acoustically coupled and decoupled flame macrostructures, Proc. Combust. Inst. 35 (3) (2015) 3273–3282.
[16] G.A. Richards, R.S. Gemmen, M.J. Yip, A test device for premixed gas turbine combustion oscillations, J. Eng. Gas Turb. Power 119 (4) (1997) 776–782.
[17] D.W. Kendrick, T.J. Anderson, W.A. Sowa, T.S. Snyder, Acoustic sensitivities of lean-premixed fuel injectors in a single nozzle rig, J. Eng. Gas Turb. Power 121 (3) (1999) 429–436.
[18] K.O. Smith, D.C. Rawlins, R.C. Steele, Developments in dry low emissions systems, 3rd International Pipeline Conference, October 1–5, 2000, Calgary, Alberta, Canada, no. 40252 (2000). p. V002T09A010
[19] R.C. Steele, L.H. Cowell, S.M. Cannon, C.E. Smith, Passive control of combustion instability in lean premixed combustors, J. Eng. Gas Turb. Power 122 (3) (2000) 412–419.
[20] C.J. Etheridge, Mars soloNOx: Lean premix combustion technology in production, in: 94-GT-255, ASME Turbo Expo 1994, June 13–16, 1994 The Hague, Netherlands, no. 78859 (1994). p. V003T06A013.
[21] C.O. Paschereit, P. Flohr, H. Knopfel, W. Geng, C. Steinbach, P. Stuber, K. Bengtsson, E. Gutmark, Combustion control by extended EV burner fuel lance, in: GT2002-30462, ASME Turbo Expo 2002, June 3–6, 2002 Amsterdam, the Netherlands, no. 36061 (2002), pp. 721–730.
[22] T. Hussain, M. Talibi, R. Balachandran, Investigating the effect of local addition of hydrogen to acoustically excited ethylene and methane flames, Int. J. Hydrogen Energy 44 (21) (2019) 11168–11184.
[23] D.N. Anderson, Effect of hydrogen injection stability and emissions of an experimental premixed prevaporized propane burner, in: Nasa Technical Memorandum, NASATM X-3301.
[24] S. Barbosa, M. de La Cruz Garcia, S. Ducruix, B. Labegorre, F. Lacas, Control of combustion instabilities by local injection of hydrogen, Proc. Combust. Inst. 31 (2) (2007) 3207–3214.
[25] P. Palies, D. Durox, T. Schuller, S. Candel, The combined dynamics of swirler and turbulent premixed swirling flames, Combust. Flame 157 (9) (2010) 1698–1717.
[26] D. Durox, J.P. Moeck, J.-F. Bourgouin, P. Morenton, M. Viallon, T. Schuller, S. Candel, Flame dynamics of a variable swirl number system and instability control, Combust. Flame 160 (9) (2013) 1729–1742.
[27] M. Gatti, R. Gaudron, C. Mirat, L. Zimmer, T. Schuller, Impact of swirl and bluff–body on the transfer function of premixed flames, Proc. Combust. Inst. 37 (4) (2019) 5197–5204.
[28] K. Truffin, T. Poinsot, Comparison and extension of methods for acoustic identification of burners, Combust. Flame 142 (4) (2005) 388–400.
[29] R. Gaudron, M. Gatti, C. Mirat, T. Schuller, Flame describing functions of a confined premixed swirled combustor with upstream and downstream forcing, J. Eng. Gas Turb. Power 141 (5) (2019) 51016–51019.
[30] T. Komarek, W. Polifke, Impact of swirl fluctuations on the flame response of a perfectly premixed swirl burner, J. Eng. Gas Turb. Power 132 (6) (2010) 061503.
[31] N.A. Bunce, B.D. Quay, D.A. Santavicca, Interaction between swirl number fluctuations and vortex shedding in a single-nozzle turbulent swirling fully-premixed combustor, J. Eng. Gas Turb. Power 136 (2) (2013) 021503.
[32] T. Poinsot, D. Veynante, Theoretical and Numerical Combustion, CNRS, 2011.
[33] D. Durox, T. Schuller, N. Noiray, S. Candel, Experimental analysis of nonlinear flame transfer functions for different flame geometries, Proc. Combust. Inst. 32 (1) (2009) 1391–1398.
[34] X. Han, J. Li, A.S. Morgans, Prediction of combustion instability limit cycle oscillations by combining flame describing function simulations with a thermoacoustic network model, Combust. Flame 162 (10) (2015) 3632–3647.

Computers and Fluids 190 (2019) 503–513

Contents lists available at ScienceDirect

Computers and Fluids

journal homepage: www.elsevier.com/locate/compfluid

A generalized non-reflecting inlet boundary condition for steady and forced compressible flows with injection of vortical and acoustic waves

G. Daviller[a,*], G. Oztarlik[b], T. Poinsot[b]

[a] CERFACS, Toulouse 31100, France
[b] IMF Toulouse, INP de Toulouse and CNRS, France

ARTICLE INFO

Article history:
Received 19 February 2019
Revised 14 May 2019
Accepted 24 June 2019
Available online 24 June 2019

Keywords:
Characteristic boundary conditions
Non reflecting boundary conditions
Turbulence injection
Acoustic forcing

ABSTRACT

This paper describes a new boundary condition for subsonic inlets in compressible flow solvers. The method uses characteristic analysis based on wave decomposition and the paper discusses how to specify the amplitude of incoming waves to inject simultaneously three-dimensional turbulence and one-dimensional acoustic waves while still being non-reflecting for outgoing acoustic waves. The non-reflecting property is ensured by using developments proposed by Polifke et al. [1, 2]. They are combined with a novel formulation to inject turbulence and acoustic waves simultaneously at an inlet. The paper discusses the compromise which must be sought by the boundary condition formulation between conflicting objectives: respecting target unsteady inlet velocities (for turbulence and acoustics), avoiding a drift of the mean inlet velocities and ensuring non-reflecting performances for waves reaching the inlet from the computational domain. This well-known limit of classical formulations is improved by the new approach which ensures that the mean inlet velocities do not drift, that the unsteady components of velocity (turbulence and acoustics) are correctly introduced into the domain and that the inlet remains non-reflecting. These properties are crucial for forced unsteady flows but the same formulation is also useful for unforced cases where it allows to reach convergence faster. The method is presented by focusing on the expression of the ingoing waves and comparing it with the classical NSCBC approach [3]. Four tests are then described: (1) the injection of acoustic waves through a non reflecting inlet, (2) the compressible flow establishment in a nozzle, (3) the simultaneous injection of turbulence and ingoing acoustic waves into a duct terminated by a reflecting outlet and (4) a turbulent, acoustically forced Bunsen-type premixed flame.

1. Introduction

Specifying boundary conditions for compressible flow simulations is still a major issue in many fields such as astrophysics [4,5], aerodynamics and aeroacoustics [6–11] or combustion instabilities and noise [2,12–16]. The present paper focuses on a limited part of this problem: the specification of inlet boundary conditions in subsonic compressible flows. Its objective is to construct a boundary condition which should satisfy three properties:

- P1 - Provide a well-posed formulation for the Navier–Stokes equations as well as perfectly non-reflecting inlet properties
- P2 - Allow to inject plane acoustic waves
- P3 - Allow to inject three-dimensional turbulence

It is important to satisfy P1, P2 and P3 simultaneously: the capability to inject ingoing acoustic waves and turbulence at the same time on an inlet patch while letting outgoing acoustic waves cross the boundary without reflection is crucial in many configurations. Well-known examples include the determination of the transfer function of turbulent flames [15,17], the prediction of combustion noise in gas turbines [18–20] or the evaluation of the acoustic transfer matrix of singular elements in turbulent flows [21–24]. All these studies require to introduce harmonic acoustic forcing and turbulence on the same inlet boundary while letting acoustic waves propagate from the computational domain to the outside without reflection (Fig. 1). Similarly, studies of combustion noise in gas turbines [20,25,26] require to perform simulations of the noise produced by a jet forced simultaneously by turbulence and by acoustic waves generated in the combustion chamber.

This paper uses characteristic boundary conditions [3,4,27] which have become the standard approach in most

* Corresponding author.
E-mail address: daviller@cerfacs.fr (G. Daviller).

https://doi.org/10.1016/j.compfluid.2019.06.027
0045-7930/

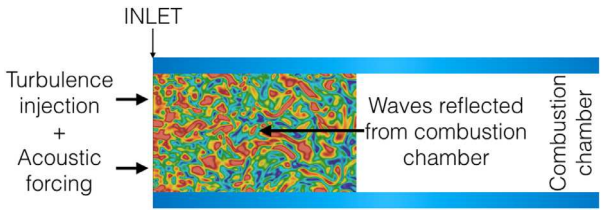

Fig. 1. An example where turbulence and acoustic waves must be introduced through the inlet of a compressible simulation while acoustic waves reflected from the computational domain must propagate without reflection through the same surface: the computation of the Flame Transfer Function of a turbulent flame [15].

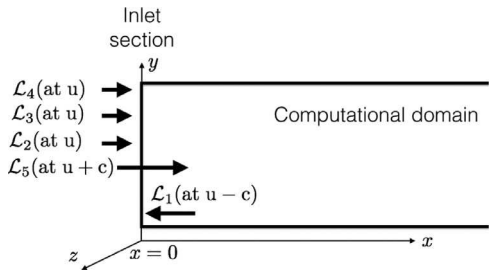

Fig. 2. Characteristic waves at a subsonic inlet (inlet at $x = 0$).

compressible solvers [11,28–30]. These methods use characteristic analysis to decompose the Navier–Stokes equations at the boundary[1] and identify waves going into the domain and waves leaving the domain. Wave amplitudes can be expressed as spatial derivatives of the primitive variables. The amplitudes of waves leaving the domain depend only on the flow within the computational domain: they can be computed using one-sided derivatives of the resolved field inside this domain. Inversely, the amplitudes of the waves entering the computational domain can not be obtained by differentiating the field in the domain because this would lead to an ill-posed problem: they must be imposed using information given by the boundary conditions. Fig. 2 shows that, for a subsonic inlet, only the outgoing acoustic wave $\mathcal{L}_1$ (see Section 2 for wave definitions) is leaving the computational domain at speed $u - c$ where u is the local convection velocity and c the local sound speed. All other waves (the acoustic wave $\mathcal{L}_5$ at speed $u + c$, the entropy wave $\mathcal{L}_2$ at speed u and the two transverse waves $\mathcal{L}_3$ and $\mathcal{L}_4$ at speed u) are entering the domain and must be specified using the boundary conditions. This paper focuses on the determination of these incoming wave amplitudes.

Section 2 recalls the basis of the NSCBC (Navier Stokes Characteristic Boundary Conditions) technique applied to an inlet. The specification of the incoming waves is presented in Section 3 and a novel inlet condition able to satisfy properties P1–P3 is discussed (called NRI-NSCBC for Non Reflecting Inlet NSCBC). Before performing any simulation, a simple theoretical approach is used to predict the reflection coefficient of the standard NSCBC formulation and of the new NRI-NSCBC condition for the injection of acoustic waves in one dimension (Section 4). These results are validated using a one-dimensional simulation of a forced duct in Section 5. The impact of the NRI-NSCBC formulation is then illustrated through three examples[2]:

- Section 6 shows that, for an unforced multi-dimensional flow (a nozzle case), using the NRI-NSCBC condition allows to eliminate acoustic waves and to converge much faster to steady state, a crucial property for compressible flow solvers which often remain limited by small time steps and long computation times before convergence.
- Section 7 presents an example of simultaneous acoustic forcing and turbulence injection in a three-dimensional channel and shows that the NRI-NSCBC is able to satisfy Properties 1–3 simultaneously.
- Finally Section 8 proposes a DNS of a premixed turbulent flame which is forced acoustically using both boundary conditions formulations.

2. Characteristic inlet boundary condition for subsonic flows

Consider a subsonic inlet (Fig. 2) where the boundary plane is the (y, z) plane. The velocity components to impose at this inlet are (u^t, v^t, w^t). These components can be steady or change with time when turbulence and/or acoustic waves are injected through the inlet. Note that these fields are "target" values: they correspond to the injected velocity signals which must be imposed at the inlet, not necessarily to the values (u, v, w) which will be actually reached during the computation because outgoing reflected waves (coming from the computational domain) also change the velocity and pressure field on the inlet patch (Fig. 1).

The Navier–Stokes equations at the inlet can be recast in terms of waves propagating in the x direction, leaving the other two directions unchanged:

$$\frac{\partial \rho}{\partial t} + d_1 + \frac{\partial}{\partial y}(\rho v) + \frac{\partial}{\partial z}(\rho w) = 0 \tag{1}$$

$$\frac{\partial (\rho E)}{\partial t} + \frac{1}{2}\left(u^2 + v^2 + w^2\right) d_1 + \frac{d_2}{\gamma - 1} + \rho u d_3 + \rho v d_4 + \rho w d_5 + \frac{\partial}{\partial y}[v(\rho e_s + p)] + \frac{\partial}{\partial z}[w(\rho e_s + p)] = \nabla(\lambda \nabla T) + \nabla(u.\tau) \tag{2}$$

$$\frac{\partial (\rho u)}{\partial t} + u d_1 + \rho d_3 + \frac{\partial}{\partial y}(\rho v u) + \frac{\partial}{\partial z}(\rho w u) = \frac{\partial \tau_{1j}}{\partial x_j} \tag{3}$$

$$\frac{\partial (\rho v)}{\partial t} + v d_1 + \rho d_4 + \frac{\partial}{\partial y}(\rho v v) + \frac{\partial}{\partial z}(\rho w v) + \frac{\partial p}{\partial y} = \frac{\partial \tau_{2j}}{\partial x_j} \tag{4}$$

$$\frac{\partial (\rho w)}{\partial t} + w d_1 + \rho d_5 + \frac{\partial}{\partial y}(\rho v w) + \frac{\partial}{\partial z}(\rho w w) + \frac{\partial p}{\partial z} = \frac{\partial \tau_{3j}}{\partial x_j} \tag{5}$$

where τ is the viscous stress tensor. e_s and E are the sensible and total energies respectively:

$$e_s = \int_{To}^{T} C_v dT \quad \text{and} \quad E = e_s + \frac{1}{2}(u^2 + v^2 + w^2) \tag{6}$$

The system of Eqs. (1) to (5) contains derivatives normal to the x boundary (d_1 to d_5), derivatives parallel to the x boundary (called "transverse terms"), and viscous terms. The vector $\mathbf{d}$ is given by characteristic analysis:

[1] Note that more sophisticated methods such as Perfectly Matched Layers [31–33] can be used to make boundaries fully non-reflecting for multidimensional flows in other fields such as electromagnetism or aeroacoustics. These methods are used mainly in infinite domains while characteristic-based methods are usually preferred in inlet/outlet/ configurations.

[2] Note that the present paper focuses on inlet boundary conditions: readers are referred to [2,34,35] which discuss similar methods for outlets.

$$\mathbf{d} = \begin{pmatrix} d_1 \\ d_2 \\ d_3 \\ d_4 \\ d_5 \end{pmatrix} = \begin{pmatrix} \frac{1}{c^2}\left[\mathcal{L}_2 + \frac{1}{2}(\mathcal{L}_5 + \mathcal{L}_1)\right] \\ \frac{1}{2}(\mathcal{L}_5 + \mathcal{L}_1) \\ \frac{1}{2\rho c}(\mathcal{L}_5 - \mathcal{L}_1) \\ \mathcal{L}_3 \\ \mathcal{L}_4 \end{pmatrix} = \begin{pmatrix} \frac{\partial(\rho u)}{\partial x} \\ \rho c^2 \frac{\partial u}{\partial x} + u\frac{\partial p}{\partial x} \\ u\frac{\partial u}{\partial x} + \frac{1}{\rho}\frac{\partial p}{\partial x} \\ u\frac{\partial v}{\partial x} \\ u\frac{\partial w}{\partial x} \end{pmatrix} \tag{7}$$

where c is the local speed of sound given by $c^2 = \gamma p/\rho$ and the $\mathcal{L}_i$'s are the amplitudes of characteristic waves propagating at the characteristic velocities $u - c$, u and $u + c$:

$$\mathcal{L}_1 = (u - c)\left(\frac{\partial p}{\partial x} - \rho c \frac{\partial u}{\partial x}\right) \tag{8}$$

$$\mathcal{L}_2 = u\left(c^2 \frac{\partial \rho}{\partial x} - \frac{\partial p}{\partial x}\right) \tag{9}$$

$$\mathcal{L}_3 = u\frac{\partial v}{\partial x} \quad \text{and} \quad \mathcal{L}_4 = u\frac{\partial w}{\partial x} \tag{10}$$

$$\mathcal{L}_5 = (u + c)\left(\frac{\partial p}{\partial x} + \rho c \frac{\partial u}{\partial x}\right) \tag{11}$$

3. Specification of incoming waves

For a subsonic three-dimensional inlet, the problem is well posed if four conditions are imposed [3,36]. In a characteristic based method such as NSCBC, this means that the four incoming waves $\mathcal{L}_2, \mathcal{L}_3, \mathcal{L}_4$ and $\mathcal{L}_5$ must be imposed. The outgoing wave $\mathcal{L}_1$ does not depend on the boundary conditions and can be computed using one-sided derivatives of the field inside the computational domain. Therefore, the solution can be advanced in time on the inlet, using the system of Eqs. (1) to (5) for boundary values if an evaluation for $\mathcal{L}_2$ to $\mathcal{L}_5$ can be found. The principle of NSCBC is to evaluate these wave amplitudes as if the flow was locally one-dimensional and inviscid (LODI). LODI equations provide an estimation of the wave amplitudes $\mathcal{L}_i$ which is usually chosen so that the physical boundary condition is satisfied. Usual LODI equations are:

$$\frac{\partial \rho}{\partial t} + \frac{1}{c^2}\left(-\mathcal{L}_2 + \frac{1}{2}(\mathcal{L}_5 + \mathcal{L}_1)\right) = 0 \tag{12}$$

$$\frac{\partial u}{\partial t} + \frac{1}{2\rho c}(\mathcal{L}_5 - \mathcal{L}_1) = 0 \tag{13}$$

$$\frac{\partial v}{\partial t} + \mathcal{L}_3 = 0 \tag{14}$$

$$\frac{\partial w}{\partial t} + \mathcal{L}_4 = 0 \tag{15}$$

$$\frac{\partial p}{\partial t} + \frac{1}{2}(\mathcal{L}_5 + \mathcal{L}_1) = 0 \tag{16}$$

The difficult question and the differentiating factor between characteristic methods is the specification of the ingoing wave amplitudes $\mathcal{L}_2, \mathcal{L}_3, \mathcal{L}_4$ and $\mathcal{L}_5$ as a function of the chosen inlet conditions. For example, for a constant velocity inlet, the LODI equation (13) would suggest that the incoming acoustic wave amplitude $\mathcal{L}_5$ should be equal to the outgoing wave $\mathcal{L}_1$ but this approach is often too simple for unsteady cases.[3] For the sake of simplicity, the presentation is limited now to an isentropic inlet where the entropy wave $\mathcal{L}_2$ is set to zero. Using Eqs. (13)–(15), the LODI expression for such an isentropic inlet is to write the incoming waves as:

$$\mathcal{L}_5 = -2\rho c \frac{\partial u^t}{\partial t},\ \mathcal{L}_3 = -\frac{\partial v^t}{\partial t} \text{ and } \mathcal{L}_4 = -\frac{\partial w^t}{\partial t} \tag{17}$$

which allows to inject an unsteady signal of components (u^t, v^t, w^t). Unfortunately, Eq. (17) does not work in practice for three reasons:

1. For a steady inlet ($u^t = v^t = w^t =$ constant), this condition is perfectly reflecting as the ingoing waves $\mathcal{L}_3$, $\mathcal{L}_4$ and $\mathcal{L}_5$ are all exactly zero: the solver knows that the inlet velocity is constant but it has no information on the values of the target velocities so that, in multidimensional configurations, the mean inlet velocities usually drift because of transverse and viscous terms present in the system of Eqs. (1) to (5). This is usually corrected by adding a linear relaxation term to the target values u^t, v^t and w^t as proposed initially by Rudy and Strikwerda [36,38]. For the normal velocity u, the ingoing acoustic wave $\mathcal{L}_5$ becomes:
$$\mathcal{L}_5 = \rho c\left(-2\frac{\partial u^t}{\partial t} + 2\ K(u - u^t)\right) \tag{18}$$
while the two transverse waves are written:
$$\mathcal{L}_3 = -\frac{\partial v^t}{\partial t} + 2\ K(v - v^t) \quad \text{and} \quad \mathcal{L}_4 = -\frac{\partial w^t}{\partial t} + 2K(w - w^t) \tag{19}$$
Terms such as $(u - u^t)$ are called "relaxation" terms [36,38]. They do not have a theoretical basis[4]: they offer the simplest linear correction form which can be added to the NSCBC theory to avoid a drift of mean values as it forces the instantaneous velocity u to go to its target value u^t with a relaxation time $1/K$. Independently of its exact form, this term in Eq. (18) is sufficient to avoid drifting mean inlet speed values when K is "sufficiently" large but it also deteriorates the non-reflecting character of the inlet as will be shown later. Transverse waves ($\mathcal{L}_3$ and $\mathcal{L}_4$) raise no difficulty as they are not associated to any axial acoustic wave and will not be discussed any more in the rest of the paper.
2. An interesting issue in the correction term $(u - u^t)$ of Eq. (18) is how to choose the "target" value u^t. A simple choice would be $u^t = \bar{u} + u^t_+$ where $\bar{u}$ is the target mean velocity and u^t_+ is the target unsteady velocity (either acoustic or vortical) imposed on the inlet patch. A better choice was proposed in [1,2] who pointed out that outgoing acoustic waves (inducing velocity fluctuations which will be called u_-) may also reach the inlet when they propagate from the computational domain to the inlet and should be accounted for in u^t. Fortunately, these outgoing waves can be evaluated in the limit of plane, low-frequency waves using the outgoing wave amplitude $\mathcal{L}_1$ which is readily available in all NSCBC methods. Therefore, the proper way to account for u_- is to add it to the target velocity to have $u^t = \bar{u} + u^t_+ + u_-$.
A last issue linked to Eq. (17) is the choice of the relaxation coefficient K (units: s^{-1}). The proper scaling for K is

[3] One aspect of this problem which is not discussed here is the need to also incorporate transverse terms in the ingoing wave expressions [11,30,37]. At an inlet, these terms play a limited role and they will be omitted throughout the present paper.

[4] A temptative explanation for this expression was actually proposed recently by Pirozzoli and Colonius [10], leading to a similar expression.

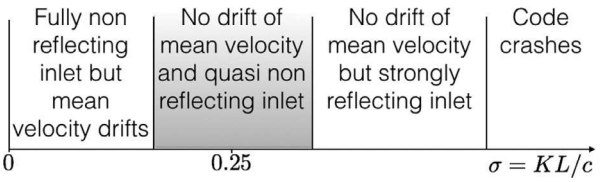

Fig. 3. Typical behavior of the solution for the classical NSCBC inlet condition (Eq. (18)) as a function of the reduced relaxation coefficient $\sigma = KL/c$. L is a typical domain length of the domain and c the sound speed. The shaded area is the desired operational zone.

the reduced factor $\sigma = KL/c$ where L and c are a characteristic length and a typical sound speed of the domain respectively [36,38]. Choosing an adequate value for K is a critical issue in many cases. Very large values of σ can lead to an unstable solution and a divergence of the simulation even in a stable flow (Fig. 3) because the wave amplitude becomes too large as soon as the velocity deviates from its target value: such instabilities are purely numerical and are due to the boundary condition. On the other hand, low values provide non-reflecting characteristics but will let the mean solution to drift from its target mean value $\bar{u}$ because of viscous and transverse terms affecting the solution in the system of Eqs. (1) to (5). Therefore, there usually is a range of σ values which provide both non drifting and quasi non-reflecting properties. Rudy and Strikwerda suggest that this occurs near $\sigma = 0.25$ but in practice, wide ranges of σ have to be tested by NSCBC users, leading to inefficient trial and error procedures. In some cases, large values of K are used, leading to inlets where the velocity is totally fixed but the boundary is fully reflecting.

3. Another and more surprising problem was pointed out by Prosser [39] and confirmed by Guezennec and Poinsot [40]. In the classical NSCBC approach, to inject a perturbation u^t, the incoming wave is expressed as:

$$\mathcal{L}_5 = -2\rho c\frac{\partial u^t}{\partial t} \tag{20}$$

This is a correct formulation to inject acoustic waves but Prosser [39] used a low Mach number expansion of the Navier–Stokes equations to show that the proper expression to inject vortical perturbations was different and that the factor 2 had to be suppressed to have:

$$\mathcal{L}_5 = -\rho c\frac{\partial u^t}{\partial t} \tag{21}$$

The fact that the factor 2 of Eq. (20) used for acoustic wave injection must be removed for vorticity injection in Eq. (21) was confirmed by the analysis of Polifke et al. [1] and tests [40] show that indeed, Eq. (21) is the proper wave expression to inject vortical perturbations (isolated vortices or fully developed turbulence) but raise a simple question: which expression (Eqs. (20) or (21)) should be used in practice? The present paper shows that they actually must be combined as discussed below.

These recent results suggest a generalized formulation for inlet boundary conditions which is the basis for the NRI-NSCBC condition described here[5] In this formulation, ingoing perturbations are split into two separate components which are superposed to the incoming wave amplitude: the vortical fluctuation, corresponding to a signal u_v^t and the acoustic fluctuation corresponding to a signal u_a^t. Each component is handled individually and superposed in the incoming wave as follows:

$$\frac{\mathcal{L}_5}{\rho c} = \underbrace{-2\frac{\partial u_a^t}{\partial t} - \frac{\partial u_v^t}{\partial t}}_{I} + \underbrace{2\ K[u-(\bar{u}+u_a^t+u_v^t+u_-)]}_{II} \tag{22}$$

where part I of expression (22) combines a term $2\partial u_a^t/\partial t$ to introduce acoustic waves and another one $\partial u_v^t/\partial t$ to inject turbulence, each of them with the correct factor (2 for acoustics and 1 for turbulence). Part II of expression (22) is the relaxation term. It is introduced to avoid drift and is not proposed by the characteristic theory. It includes u_a^t and u_v^t but also u_- as suggested by Polifke et al. [1]. This formulation allows to use exact terms for $2\partial u_a^t/\partial t$ and $\partial u_v^t/\partial t$ (satisfying properties P2 and P3 introduced in Section 1) while providing an expression for the relaxation term which should be zero as long as non acoustic terms remain small at the inlet (satisfying property P1). This should allow to use large relaxation factors K avoiding the drift of mean values while still being non reflecting for all normal acoustic waves: the relaxation term in Eq. (22) becomes non zero only when viscous and transverse terms become non negligible on the inlet. For all other cases, the relaxation term (II) is zero and Eq. (22) reduces to the exact NSCBC approach for $\mathcal{L}_5$: $\mathcal{L}_5 = -2\rho c\frac{\partial u_a^t}{\partial t} - \rho c\frac{\partial u_v^t}{\partial t}$.

In the expression of the incoming wave $\mathcal{L}_5$ (Eq. (22)), the acoustic velocity u_- associated to the reflected wave reaching the inlet from the computation domain must be evaluated. In the case of an outlet, Polifke et al. [1,41] used a method called CBF (characteristics based filter) to obtain a plane averaged value for the outgoing wave amplitude. This requires introducing a series of planes near the oulet of the computational domain where the outgoing wave can be evaluated. CBF is precise but can be difficult or impossible to implement in cases where the domain outlet has a complex shape or typically at an inlet as studied in the present work. Here an alternative technique is used where u_- is evaluated locally at each point of the inlet patch from the time integral of the acoustic wave amplitude $\mathcal{L}_1$ which is available in NSCBC:

$$u_- = \frac{1}{2\rho c}\int_0^t \mathcal{L}_1 dt \tag{23}$$

Expression (23) for u_- avoids using the PWM approach [1] and can be used in any code using NSCBC boundary conditions.[6]

The following sections compare the new NRI-NSCBC formulation to the classical NSCBC conditions [3,12]. Table 1 summarizes the wave expressions which will be used for both boundary conditions.

Table 1
Comparison of the classical NSCBC and the NRI-NSCBC conditions. $\bar{u}$ is the mean target velocity, u_a^t is the target acoustic fluctuation, u_v^t is the target vortical fluctuation and u_- is the reflected velocity fluctuation reaching the inlet from the computational domain.

Boundary condition	Transverse Waves $\mathcal{L}_3$ and $\mathcal{L}_4$	Axial Wave $\mathcal{L}_5$
NSCBC	$\mathcal{L}_3 = -\frac{\partial v^t}{\partial t}$ and $\mathcal{L}_4 = -\frac{\partial w^t}{\partial t}$	$\frac{\mathcal{L}_5}{\rho c} = -2\frac{\partial u_a^t}{\partial t} - 2\frac{\partial u_v^t}{\partial t}$ $+2K[u-(\bar{u}+u_a^t+u_v^t)]$
NRI-NSCBC	$\mathcal{L}_3 = -\frac{\partial v^t}{\partial t}$ and $\mathcal{L}_4 = -\frac{\partial w^t}{\partial t}$	$\frac{\mathcal{L}_5}{\rho c} = -2\frac{\partial u_a^t}{\partial t} - \frac{\partial u_v^t}{\partial t}$ $+2\ K[u-(\bar{u}+u_a^t+u_v^t+u_-)]$

[5] The reviewing phase of the present paper showed that this result could have been obtained also by combining results proposed by the group of Pr Polifke [1] with the work of Pr Prosser [39].

[6] In practice, for certain cases, Eq. (23) must be high-pass filtered to remove any continuous component.

4. Theoretical analysis of reflection coefficients in one dimension

A first method to analyze the differences between the standard NSCBC and the NRI-NSCBC conditions is to consider a simple case (Fig. 4) such as the inlet of a configuration where waves can be assumed to be one-dimensional. No vortical perturbation is introduced: $u_v^t = 0$. The inlet patch has a constant mean velocity $\bar{u}$ and is submitted to an acoustic harmonic forcing at pulsation ω with a target amplitude u_a^t. A reflected wave inducing an acoustic perturbation u_- associated to a wave amplitude $\mathcal{L}_1$ also reaches the inlet so that the exact velocity fluctuation at the inlet should be $u_a^t + u_-$. At this point u_- could be any signal: the only assumption is that u_- is a reflection due to the acoustic forcing and that it is therefore a harmonic signal at pulsation ω too.

This case allows to derive analytically, what the inlet velocity will be in a code using the boundary conditions of Table 1. To obtain this result, the two ingoing wave formulations of Table 1 are gathered in a single notation for this case with acoustic forcing only and no turbulence injection ($u_v^t = 0$):

$$\frac{\mathcal{L}_5}{\rho c} = -2\frac{\partial u_a^t}{\partial t} + 2\,K[u - (\bar{u} + u_a^t + \alpha u_-)] \tag{24}$$

When $\alpha = 0$, the standard NSCBC condition is obtained while $\alpha = 1$ yields the NRI-NSCBC condition. The reflected wave (amplitude $\mathcal{L}_1$) creates an acoustic velocity u_- which reaches the inlet and interacts with the inlet boundary condition. In general, u_- is never zero: reflected waves are found at the inlet of most compressible computations.

Assuming that all quantities fluctuate at pulsation ω and expressing all variables as $f(t) = Re[\hat{f}\exp(-i\omega t)]$, it is possible to combine Eqs. (24) and (13) to obtain the velocity fluctuations $u' = u - \bar{u}$ at the inlet. To do this, $\mathcal{L}_1$ is obtained from u_- using:

$$\frac{\partial u_-}{\partial t} = \frac{1}{2\rho c}\mathcal{L}_1 \quad \text{so that} \quad \hat{\mathcal{L}}_1 = -2i\omega\rho c\hat{u}_- \tag{25}$$

Eq. (13) can then be used to obtain the inlet velocity fluctuations $\hat{u}'$ using Eq. (24) for $\mathcal{L}_5$ and Eq. (25) for $\mathcal{L}_1$:

$$\frac{\partial u}{\partial t} = -\frac{1}{2\rho c}(\mathcal{L}_5 - \mathcal{L}_1) \tag{26}$$

which leads to:

$$\hat{u}' = \hat{u}_a^t + \frac{K\alpha - i\omega}{K - i\omega}\hat{u}_- \tag{27}$$

Eq. (27) conveys two messages:

- In general, the inlet velocity fluctuation $\hat{u}'$ is not equal to the acoustic forcing amplitude imposed on the boundary $\hat{u}_a^t$. For both boundary conditions ($\alpha = 0$ or 1), the only cases where $\hat{u}'$ is equal to $\hat{u}_a^t$ corresponds to situations where no outgoing wave reaches the inlet ($\hat{u}_- = 0$).
- The exact solution is that the inlet velocity should be the sum of the acoustic contributions coming from left and right: $\hat{u}' = \hat{u}_a^t + \hat{u}_-$. When $\alpha = 1$ (NRI-NSCBC condition), Eq. (27) shows that this property is always satisfied. For the standard NSCBC condition ($\alpha = 0$), the conclusion is opposite: the inlet velocity $\hat{u}'$ is never equal to its theoretical value except in rare cases where $K = 0$ or $\hat{u}_- = 0$.

Knowing $\hat{u}'$, it is also possible to express the inlet wave $\mathcal{L}_5$:

$$\hat{\mathcal{L}}_5 = \hat{\mathcal{L}}_5^t + R_1\hat{\mathcal{L}}_1 \quad \text{with} \quad R_1 = \frac{K(1-\alpha)}{K - i\omega} \tag{28}$$

where $\hat{\mathcal{L}}_5^t = 2i\omega\rho c\hat{u}_a^t$ is the target forcing wave and R_1 can be viewed as the reflection coefficient of the boundary condition: it measures how much of a left going wave $\mathcal{L}_1$ reflects into the ingoing acoustic wave $\mathcal{L}_5$. When $\alpha = 1$ (NRI-NSCBC), R_1 is exactly zero: the inlet is truly non reflecting and the injected wave $\hat{\mathcal{L}}_5$ contains only the imposed wave $\hat{\mathcal{L}}_5^t$. For the standard NSCBC condition ($\alpha = 0$), R_1 is never zero: the inlet is reflecting and any outgoing wave reaching it will be reflected back into the domain, making the inlet effectively more and more reflecting as K is increased. Note that, in this case, the reflection coefficient R_1 in Eq. (28) matches the expression obtained for the reflection coefficient by Selle et al. [34], Polifke et al. [1] and Pirozzoli and Colonius [10].

5. A one-dimensional duct with inlet acoustic forcing

The two boundary conditions of Table 1 are tested first on a one-dimensional duct of length L (Fig. 5) forced acoustically at its inlet ($x = 0$) and terminated by a fixed pressure outlet ($p' = 0$ at $x = L$). This is a direct application of the results of Section 4 where u_- will be specified: the inlet forcing is harmonic and corresponds to a velocity fluctuation $\hat{u}_a^t$. The outlet is fully reflecting so that ingoing waves will reflect at $x = L$ into outgoing waves (u_-) and interact with the inlet condition at $x = 0$. For all test cases presented in this section and the following ones, the compressible Navier–Stokes equations are solved using the fourth-order TTGC scheme (on regular meshes [42]) in the AVBP solver [43,44]. Time advancement is fully explicit and a CFL number of 0.7 is used for all runs.

Since the outlet reflection coefficient is -1 (to ensure $p' = 0$), the ratio between $\mathcal{L}_1$ and $\mathcal{L}_5$ is known ($\mathcal{L}_1/\mathcal{L}_5 = -\exp(2ikL)$ where $k = \omega/c$ is the wave number). Therefore the ratio I between the wave amplitude which the boundary condition should impose ($\mathcal{L}_5^t$) and the wave which will actually be imposed ($\mathcal{L}_5$) by Eq. (24) can also be expressed as:

$$I = \frac{\hat{\mathcal{L}}_5}{\hat{\mathcal{L}}_5^t} = \frac{1}{1 + R_1\exp(2ikL)} \tag{29}$$

I is a deterioration index: when it is equal to unity, the boundary condition is perfect, the injected wave is the one imposed by the user and the inlet velocity is $u = \bar{u} + u_a^t + u_-$ which is the exact solution. Any non unity I value indicates that the relaxation term in Eq. (24) is perturbing the inlet boundary condition and making it partially reflecting. Obviously for the NRI-NSCBC condition where $\alpha = 1$ and $R_1 = 0$, I is equal to unity for all K values while it is not for the standard NSCBC approach. To check this result, one-dimensional simulations of the configuration of Fig. 5 were performed for $\sigma = 0$, 2 and 5 at three forcing frequencies (100, 200

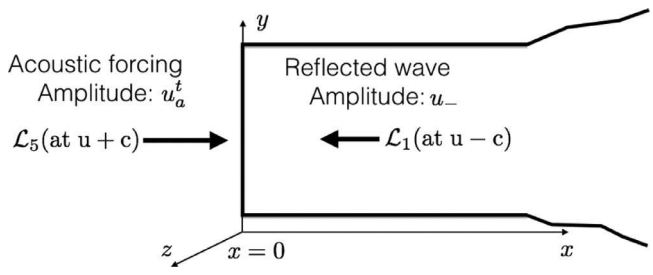

Fig. 4. Characteristic waves at a subsonic inlet (inlet at $x = 0$). The acoustic forcing induces a velocity fluctuation u_a^t. A longitudinal acoustic wave (amplitude u_-) is reaching the inlet from the computation domain.

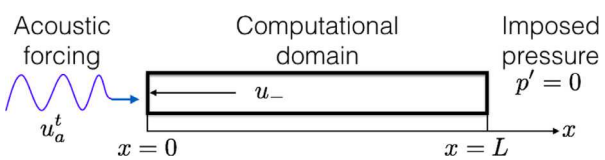

Fig. 5. Tests of inlet boundary conditions for a one-dimensional duct forced by a harmonic wave at the inlet and terminated by a pressure node at $x = L$.

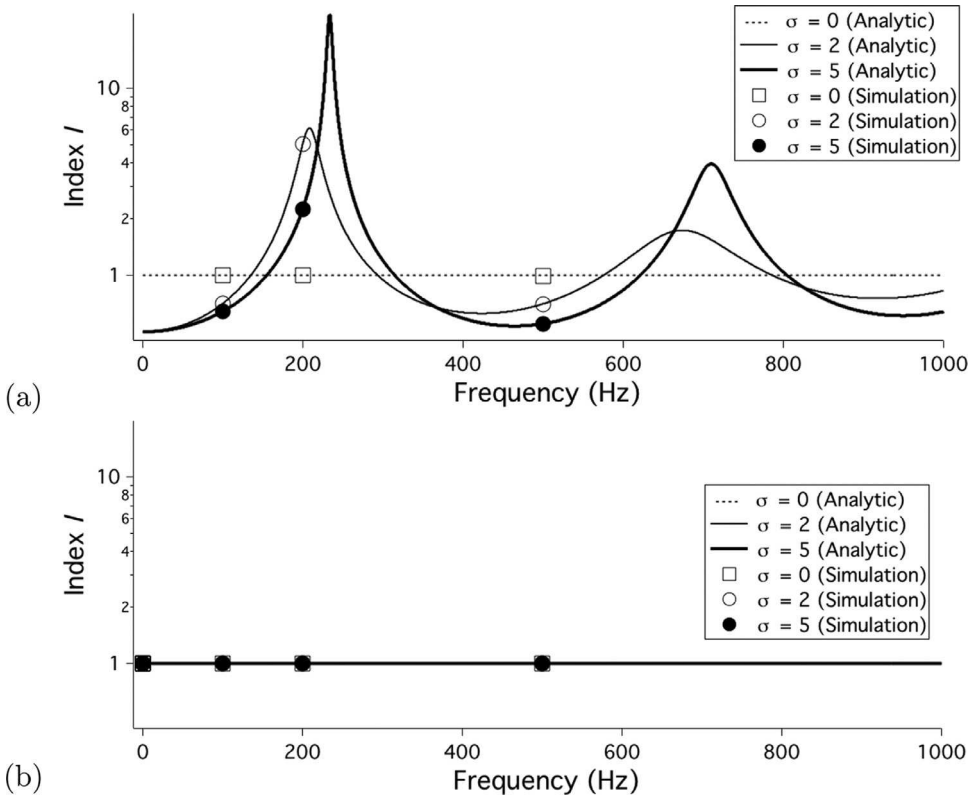

Fig. 6. Comparison of the quality index I (Eq. 29) in log scale, for the pulsated duct of Fig. 5: analytical result (Eq. (29)) vs compressible simulations. (a) standard NSCBC method, (b) new NRI-NSCBC method. Lines: analytical solutions; symbols: simulations.

and 500 Hz). The results obtained in terms of the index I as a function of the reduced relaxation coefficient σ are displayed in Fig. 6. The simulations match exactly the analytical result of Eq. (29) and confirm that for the NSCBC standard formulation, the deterioration index I can reach large values more than 20 for $\sigma = 5$), indicating that this method is much less accurate than the new NRI-NSCBC condition which offers a unity I index for all values of the relaxation coefficient σ. These results confirm the analysis of Polifke et al. [1] who pointed out the importance of taking u_- into account in the relaxation term.

6. Faster convergence for unforced compressible flows

The capabilities of the NRI-NSCBC can be illustrated in a second test, to demonstrate that it allows faster convergence in multi-dimensional, compressible, unforced flows because acoustic waves are perfectly evacuated through the boundaries while avoiding a drift of mean values, thanks to a large value of the inlet relaxation coefficient K. For an unforced flow ($u_a^t = u_\nu^t = 0$), the inlet wave of Eq. (22) becomes:

$$\mathcal{L}_5 = 2\ K\rho c[u - \tilde{u}] \quad \text{for NSCBC} \tag{30}$$

and

$$\mathcal{L}_5 = 2\ K\rho c[u - (\tilde{u} + u_-)] \quad \text{for NRI} - \text{NSCBC} \tag{31}$$

The test case is a two-dimensional subsonic nozzle (Fig. 7) where the inlet Mach number is 0.014, corresponding to an inlet velocity of 5 m/s. The outlet condition is $p' = 0$. The initial condition corresponds to a zero velocity field and constant pressure and temperature everywhere in the domain, including on the inlet patch. The shape of the nozzle is given by (unit m):

$$y = \begin{cases} 0.02\left[1.0 - 0.661514e^{\left(-\ln\ 2(x/0.6)^2\right)}\right], & x < 0 \\ 0.02\left[1.0 - 0.661514e^{\left(-\ln\ 2(x/6)^2\right)}\right], & x \geq 0 \end{cases} \tag{32}$$

When the simulation begins, the inlet boundary condition starts modifying the inlet variables. The objective of the test is to measure the physical time required for the simulation to reach steady state and to check whether acoustic modes of the configuration are triggered.

This flow is a good prototype of many compressible simulations. The initial conditions (zero velocity everywhere) combined with the inlet condition (which ramps rapidly to its target value) can generate strong perturbations and acoustic waves: with the standard NSCBC conditions (Fig. 3), low values of K lead to mean values which do not converge to the target values or drift away from them. On the other hand, large values of K avoid drifting mean

Fig. 7. Geometry of nozzle used for convergence tests to steady state. The domain length is $L = 0.6$m. The sound speed is $c = 345$ m/s.

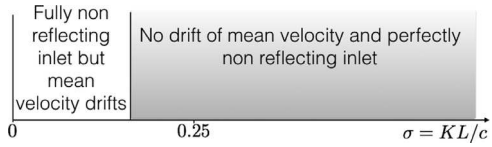

Fig. 8. Typical behavior of the solution for the new NRI-NSCBC inlet condition as a function of the reduced relaxation coefficient $\sigma = KL/c$. L is a typical domain length and c the sound speed. The shaded area is the desired operational zone.

values but induce reflections and undamped acoustic waves which delay convergence. With NRI-NSCBC, this problem disappears: it is possible to use large values of K and still be non reflecting so that convergence is reached very fast. Fig. 8 summarizes this observation and can be compared to Fig. 3.

Fig. 9 displays a typical time evolution of inlet velocity and pressure for a reduced relaxation coefficient $\sigma = KL/c = 0.017$. Since this coefficient is small, the inlet velocity (Fig. 9, left) increases slowly and no acoustic waves are triggered. However, convergence is reached after a long time for both methods (NSCBC in solid line and NRI-NSCBC in dashed line).

To increase the convergence speed, the natural solution is to increase the inlet relaxation factor: Fig. 10 shows the solutions for a reduced relaxation coefficient $\sigma = KL/c = 17$. The inlet velocity rapidly reaches its target (5 m/s) but acoustic oscillations are triggered using the classical NSCBC method (solid line) because acoustic waves are trapped within the domain: pressure and velocity oscillate at 150 Hz which is the frequency of the first mode of the setup with $u' = 0$ at the inlet and $p' = 0$ at the outlet. Inversely, the NRI-NSCBC method gives a solution (dashed line) which is stabilized after one acoustic time.

Increasing the relaxation coefficient even more (as often done by NSCBC users when they observe an oscillating inlet velocity) does stabilize the inlet velocity (Fig. 11, left) but makes the inlet even more reflecting, leading to pressure inlet excursions which actually grow in time (Fig. 11, right) and a boundary condition which is ill posed and will eventually lead to full divergence. NRI-NSCBC, as expected, is only weakly affected by the increase of σ and leads to a stable solution rapidly. This simple example reveals another interesting feature of the NRI-NSCBC condition, which provides fast convergence to steady state, using large relaxation coefficients, a useful property in all compressible solvers.

7. Simultaneous injection of turbulence and acoustic waves through a non-reflecting inlet

This test case corresponds to a situation where an inlet ($x = 0$ in Fig. 12) is used to inject both turbulence and an harmonic acoustic wave into a square section channel. The domain is a three-dimensional parallelepipedic box where the outlet is fully reflecting (imposed pressure: $p' = 0$ at $x = L$). Therefore, the inlet is submitted to three waves:

- vorticity waves associated to the turbulence injection u_v^t,
- an ingoing acoustic wave associated to the acoustic forcing u_a^t,
- an outgoing acoustic wave reflected from the outlet and propagating back to the inlet u_-.

The mesh is a pure hexahedra grid with $392 \times 98 \times 98$ points corresponding to a domain size of $L = 4 \times 1 \times 1$ mm. The mean inlet velocity is homogeneous in the $x = 0$ plane: $U = 100$ m/s. Periodicity conditions are applied in the two transverse directions y and z. Very large values of the relaxation coefficient K are used in both NSCBC and NRI-NSCBC: $K = 2.10^6 s^{-1}$ corresponding to a reduced coefficient $\sigma = KL/c = 23$. The inlet is submitted to two simultaneous outside excitations:

1. Three-dimensional turbulence: the RMS velocity of the injected turbulent field is $u_{v,RMS}^t = 5$ m/s and its most energetic wavelength is 0.5 mm. The turbulence spectrum has a Passot Pouquet expression [45].
2. One-dimensional planar acoustic wave: the acoustic forcing is a longitudinal harmonic wave introduced at the domain inlet, at a frequenc $f = 260$ kHz with a peak amplitude of $u_{a,peak}^t = 2$ m/s.

Note that the ratio between the two excitations levels can be fixed arbitrarily and is configuration dependent. It is measured here by the ratio of the excitation velocities $u_{v,RMS}^t / u_{a,peak}^t = 2.5$.

Fig. 13 displays fields of Q-criterion [46] for the standard NSCBC (left) and the NRI-NSCBC approaches (right), showing a usual decaying turbulent field. The same figure displays a pressure field in one plane, revealing that the axial plane acoustic forcing can be identified on the pressure signal. These qualitative results require more analysis to see the influence of the boundary condition. Fig. 14 shows the FFTs of pressure (left) and velocity (right) at the inlet ($x = 0$ m).

The two velocity spectra (right image) of Fig. 14 are close and both boundary conditions (NSCBC and NRI-NSCBC) produce inlet fluctuations which match the spectra of the target velocity u_t very well, confirming that the turbulent signal is correctly introduced. Note that no discrete peak is visible at the acoustic forcing frequency ($f = 260$ kHz). For the conditions chosen here ($u_{a,peak}^t / u_{v,RMS}^t = 0.4$), the acoustic forcing is not strong enough to dominate the turbulent forcing. For pressure (left image), however, the two spectra differ: both exhibit a peak at the acoustic forcing frequency (and its first harmonic) but the NSCBC results also

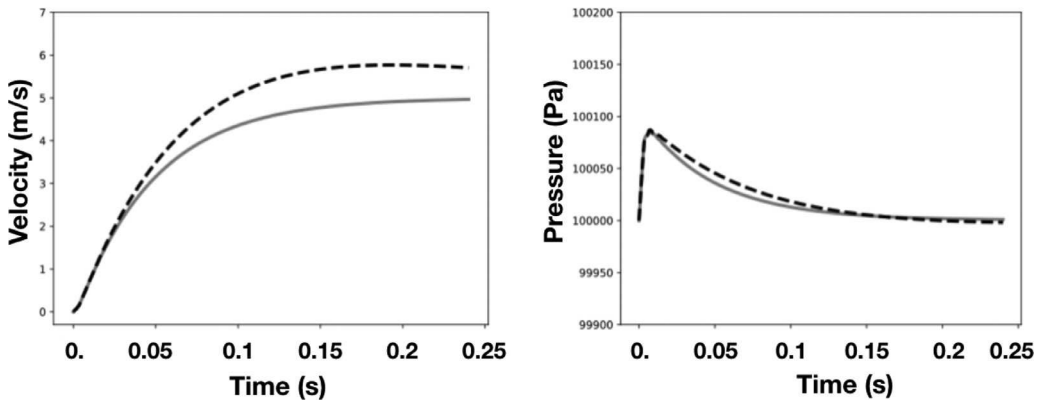

Fig. 9. Inlet velocity (left) and pressure (right) time evolutions for $\sigma = KL/c = 0.017$. NSCBC: solid line. NRI-NSCBC: dashed line.

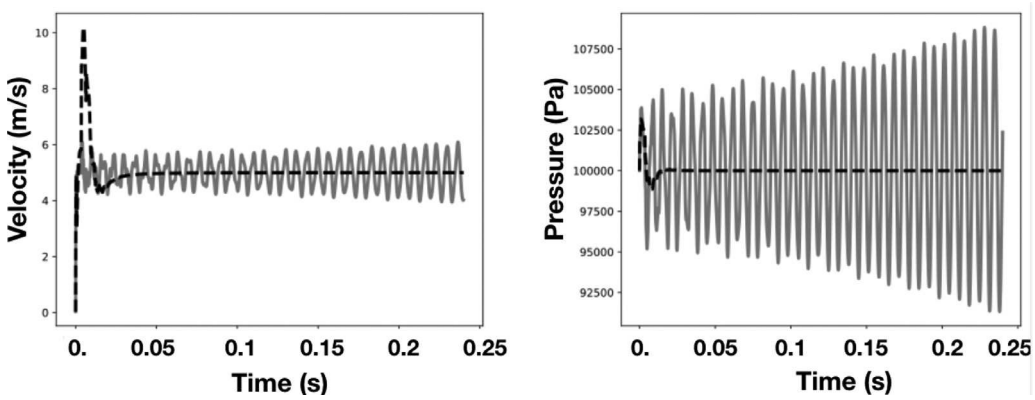

Fig. 10. Inlet velocity (left) and pressure (right) time evolutions for $\sigma = KL/c = 17$. NSCBC: solid line. NRI-NSCBC: dashed line.

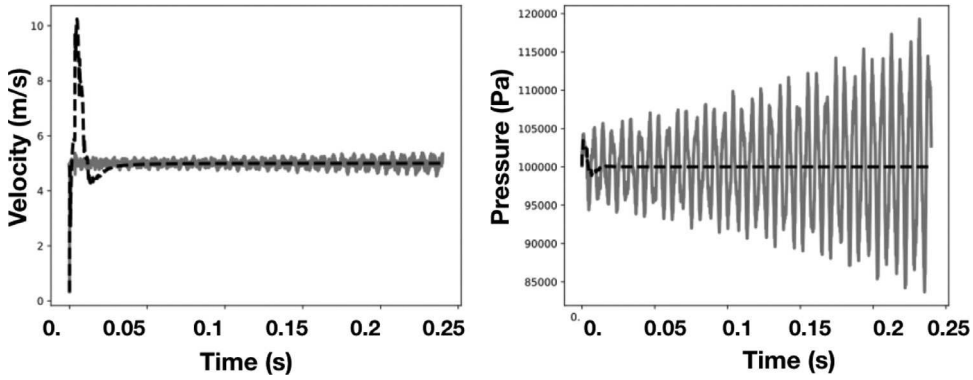

Fig. 11. Inlet velocity (left) and pressure (right) time evolutions for $\sigma = KL/c = 170$. NSCBC: solid line. NRI-NSCBC: dashed line.

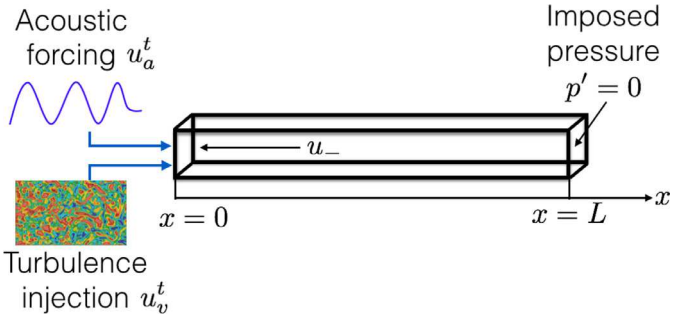

Fig. 12. Simultaneous injection of three-dimensional turbulence (velocity amplitude u_v^t) and one-dimensional acoustic forcing (velocity amplitude u_a^t) at the inlet of a domain with reflecting outlet ($p' = 0$).

reveal multiple other peaks due to non physical resonances. It is interesting to compare the pressure field obtained in the LES with the analytical solution corresponding to a forced inlet at frequency f and an outlet condition $p' = 0$. In a laminar flow (in the absence of turbulence injection), taking into account the correction due to non-zero Mach number, this solution is:

$$p'(x,t) = \rho c u_a \left(e^{-ik^+x} - e^{-i(k^+L + k^-(L-x))}\right) e^{i\omega t} \tag{33}$$

and

$$u'(x,t) = u_a \left(e^{-ik^+x} + e^{-i(k^+L + k^-(L-x))}\right) e^{i\omega t} \tag{34}$$

where $k^+ = \omega/(c+u)$, $k^- = \omega/(c-u)$ and $\omega = 2\pi f$. The variance of pressure p'^2 can be obtained by $p'^2 = p_a p_a^*/2$, with p_a^* the conjugate complex of p_a. Fig. 15 shows variations of $\sqrt{p'^2}$ along the duct axis for both boundary conditions and compares it to the analytical solution of Eq. (33). The NRI-NSCBC captures perfectly the analytical solution showing that for these conditions ($u_t/u_a = 2.5$), the unsteady pressure field is only weakly affected by the turbulence injection and that the NRI-NSCBC condition does not alter this property. On the other hand, similarly to the case of acoustic forcing in a laminar flow (Section 5), the classical NSCBC formulation modifies the acoustic field structure and fails to capture the analytic solution.

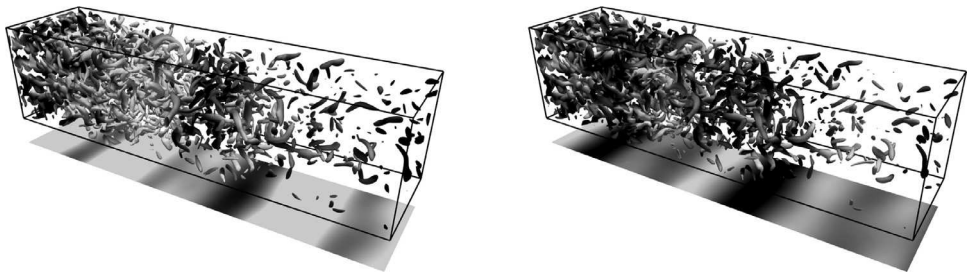

Fig. 13. Simultaneous injection of isotropic homogeneous turbulence and acoustic wave. Isosurface of Q criterion $Q = 2.5(U/L)^2$ colored by the axial velocity ($95 \leq u(m/s) \leq 105$) and fluctuating pressure in the range $-1.2e-2 \leq p/p_\infty - 1 \leq 1.2e-2$ in one plane. Left: NSCBC, right: NRI-NSCBC.

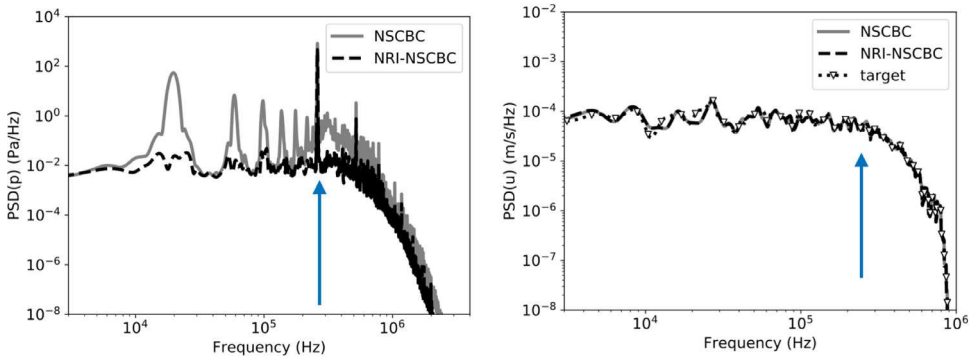

Fig. 14. Simultaneous injection of isotropic homogeneous turbulence and acoustic wave. Spectra of pressure (left) and velocity (right) at the domain inlet $x = 0$ m, $y = z = 0.005$ m. Solid line: NSCBC, dashed line: NRI-NSCBC. The arrows indicate the frequency ($f_a = 260$ kHz) at which the acoustic wave is introduced. The triangles on the right image correspond to the spectra of the injected turbulence target signal u_v^t.

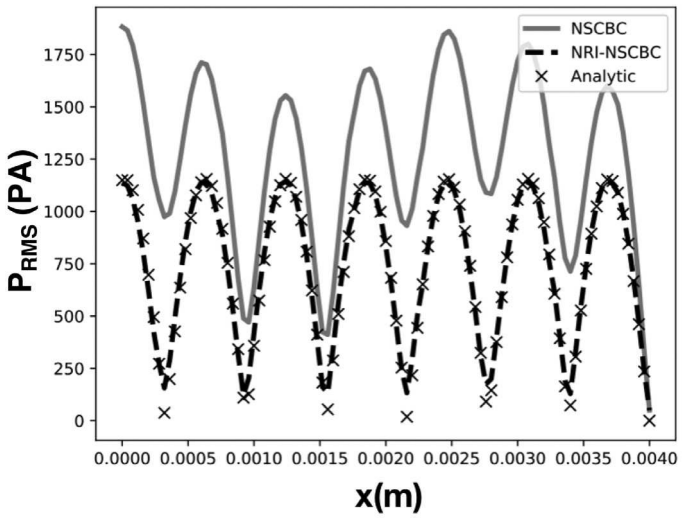

Fig. 15. Pressure perturbation structure along duct axis: field of $\sqrt{(p'^2)}$ vs x. Solid line: NSCBC, dashed line: NRI-NSCBC, symbols: analytical solution.

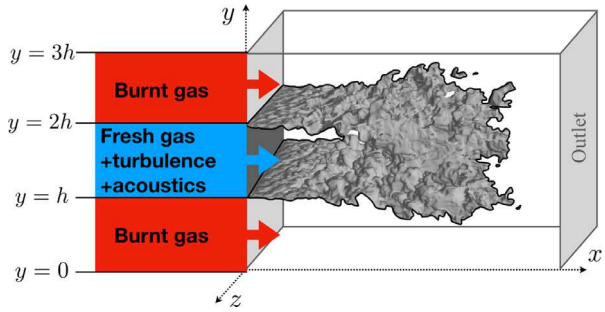

Fig. 16. Physical domain used for the DNS. At the inlet, a double hyperbolic tangent profile is used to inject fresh gases in a sheet ≈8 mm high, surrounded by a coflow of burnt gases. Top-bottom (along y) and left-right (along z) boundaries are periodic. The isosurface is a typical view of $T = 1600$ K.

8. A turbulent, acoustically forced premixed flame

The last example is a direct numerical simulation (DNS) of a stoichiometric, premixed turbulent flame stabilized in a slot-burner configuration. The inlet is forced by turbulence and by an harmonic acoustic wave introduced simultaneously, a usual situation for example to study Flame Transfer Functions in thermoacoustics.

The DNS is performed with the explicit, compressible solver (AVBP) for the 3D Navier–Stokes equations with simplified thermochemistry on unstructured meshes [43,47]. A Taylor–Galerkin finite element scheme called TTGC [42] of fourth-order in space and time is used. The acoustic CFL number is 0.7. The outlet boundary condition is handled using an imposed pressure, NSCBC approach [3] with transverse terms corrections [37]. The inlet is treated either with the standard NSCBC formulation or with the new NRI-NSCBC approach. Other boundaries are treated as periodic.

Methane/air chemistry at 1 bar is modeled using a global 2-step scheme fitted to reproduce the flame propagation properties such as the flame speed, the burned gas temperature and the flame thickness [48]. This simplified chemistry description is sufficient to study the dynamics of premixed turbulent flames. Fresh gases are stoichiometric: the laminar flame speed is $S_L^0 = 40.5$ cm/s. The flame thicknesses are $\delta_L^0 = 0.34$ mm (based on the maximum temperature gradient) and $\delta_L^1 = 0.7$ mm (based on the distance between reduced temperatures of 0.01 and 0.99). The mesh is a homogeneous hexahedra grid with a constant element size $\Delta x = 0.1$ mm, ensuring 7–9 points in the preheat zone and 4–5 in the reaction zone. With this resolution, the temperature and heat release profiles given by the DNS code match perfectly the results given by a specialized one-dimensional flame code (Cantera) for a laminar premixed flame. The domain size is 512 cells (5,12 cm) in the x direction and 256 cells (2,56 cm) in the y and z ones, for a total of 33.55 million cells (Fig. 16). The fresh gas injection channel has a height $h = 8.53$ mm ($h/\delta_L^0 \approx 25$).

The inlet stream is a central flow of stoichiometric fresh gases surrounded by a coflow of burnt gases at low injection velocity. Inlet temperatures are 300 and 2256 K in the fresh and burnt gases, respectively. The temperature and composition of the burnt gas coflow corresponds to the products of an adiabatic combustion of the fresh gases. Mean inlet velocity profiles are imposed as:

$$u(x=0,y,z) = u_{co} + (u_{in} - u_{co})\left(1 + \tanh\left(\frac{y-h}{2\delta}\right)\right) \times \left(1 - \tanh\left(\frac{y-2h}{2\delta}\right)\right) \quad (35)$$

where $u_{in} = 10$ m/s is the maximum speed in the fresh gases, $u_{co} = 0.1$ m/s is the minimum speed in the coflow of hot gases and δ is the momentum thickness of the shear layer ($\delta = 0.08$ mm) corresponding to a vorticity thickness of 0.36 mm. Turbulence is injected in the fresh gases only. The RMS velocity of the incoming flow is 1 m/s and the integral length scale is $l_F = 2$ mm. The spectrum of the injected turbulence corresponds to a Passot–Pouquet form [45]. Acoustic forcing is introduced at the inlet on the fresh gas stream. The forcing frequency is $f_a = 1$ kHz and the forcing amplitude is 2 m/s. For both NRI-NSCBC and NSCBC

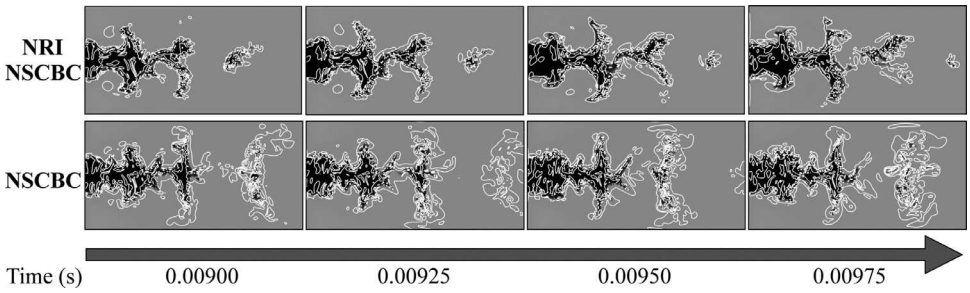

Fig. 17. Flame response at four instants of the acoustic forcing period ($f_a = 1$ kHz). Temperature field and isolevels of vorticity.

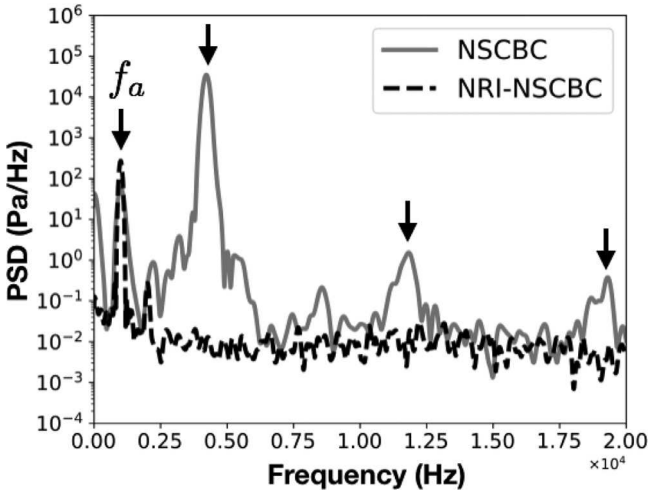

Fig. 18. Pressure spectra for NSCBC (solid line) and NRI-NSCBC (dotted line) at the domain inlet. The f_a arrow corresponds to the acoustic forcing at 1 kHz. The three other arrows are the first three longitudinal eigenmodes of the computational box at 4350, 12500 and 19500 Hz. The spectral resolution is 70 Hz.

conditions imposed at the inlet, the value of K is the same: $K = 100000$ s^{-1} (leading to $\sigma \simeq 15$). A series of 4 snapshots showing the flame response to turbulent and acoustic forcing is displayed in Fig. 17. Mushroom-shaped flame structures are created at 1 Khz as expected for acoustically forced flames [49]. These structures are separated spatially by $u_{in}/f_a = 1$ cm and interact with the injected turbulence.

The two DNS of Fig. 17, obtained by NRI-NSCBC and NSCBC, are obviously different but it is difficult to say which one is the best. A more quantitative result can be obtained by looking at the pressure spectra at the domain inlet in Fig. 18. The spectra observed for NRI-NSCBC corresponds to the expected result: a discrete peak at the acoustic forcing frequency f_a superimposed on broadband turbulent noise. On the other hand, for NSCBC, three additional high-level peaks also appear: they are due to the excitation by the flame of the eigenmodes of the computational domain. It is possible to verify that these modes are indeed acoustic modes by using an Helmholtz solver [50] taking into account the mean temperature distribution in the domain and the boundary conditions (imposed inlet velocity and imposed outlet pressure). The frequencies predicted for the first three acoustic modes given by the Helmholtz solver are marked by arrows in Fig. 18. The three acoustic modes which are excited when NSCBC is used are the longitudinal 1/4 wave (at 4350 Hz), 3/4 wave (at 12500 Hz) and 5/4 wave (at 19500 Hz) modes. Their frequencies, computed with the Helmholtz solver, match the frequencies observed in the LES with a 5 percent accuracy. These modes interact with the flame response at the acoustic forcing frequency ($f_a = 1$ kHz) and make the NSCBC run difficult to interpret: measuring the flame response at $f_a = 1$ kHz would be impossible for the NSCBC run because this response is polluted by the three acoustic eigenmodes forced by the boundary conditions. Clearly, NSCBC fails to inject acoustic forcing and turbulence without exciting the cavity modes of the computational domain while NRI-NSCBC succeeds in this task.

9. Conclusions

This paper has described a new boundary condition for subsonic inlet, based on a combination of the formalism proposed by Polifke and coworkers [1,2] to account for outgoing acoustic waves and an extension of the method of Guezennec et al.[40] to introduce both turbulence and acoustic waves simultaneously. The approach can be summarized in the expression of the ingoing wave:

$$\frac{\mathcal{L}_5}{\rho c} = -2\frac{\partial u_a^t}{\partial t} - \frac{\partial u_v^t}{\partial t} + 2\,K[u - (\bar{u} + u_a^t + u_v^t + u_-)] \tag{36}$$

where u_a^t is the velocity of the injected acoustic wave, u_v^t is the axial velocity of the turbulent signal, $\bar{u}$ is the mean target velocity, K is a relaxation coefficient and u_- is the velocity of the outgoing wave which is estimated locally using the outgoing wave amplitude $\mathcal{L}_1$:

$$u_- = \frac{1}{2\rho c}\int_0^t \mathcal{L}_1 dt \tag{37}$$

Analysis and tests show that this NRI-NSCBC condition performs better than the standard NSCBC approach: it allows to use large values for the relaxation coefficient K and to obtain non-drifting mean values and non reflective capabilities simultaneouslyecor. Tests were performed for one-dimensional acoustic forcing in a duct, for flow establishment in a compressible nozzle, for simultaneous injection of acoustic waves and turbulence in a three-dimensional channel terminated by a fixed pressure outlet and finally for a turbulent premixed flame forced acoustically. For all cases, NRI-NSCBC captured the expected solution accurately suggesting that this could become a standard approach in compressible codes.

Acknowledgments

We thank Dr L. Selle (IMF Toulouse, CNRS) for helpful discussions and the CERFACS CFD team staff for their scientific and technical support about the CFD code AVBP. The contribution of V. Bouillin to the development of NRI-NSCBC is gratefully acknowledged.

References

[1] Polifke W, Wall C, Moin P. Partially reflecting and non-reflecting boundary conditions for simulation of compressible viscous flow. J Comput Phys 2006;213(1):437–49.
[2] Tudisco P, Ranjan R, Menon S, Jaensch S, Polifke W. Application of the time-domain impedance boundary condition to large-eddy simulation of combustion instability in a shear-coaxial high pressure combustor. Flow Turbul Combust 2017;177:1–23.

[3] Poinsot T, Lele S. Boundary conditions for direct simulations of compressible viscous flows. J Comput Phys 1992;101(1):104–29. doi:10.1016/0021-9991(92)90046-2.
[4] Thompson KW. Time dependent boundary conditions for hyperbolic systems ii. J Comput Phys 1990;89:439–61.
[5] Grappin R, Léorat J, Buttighoffer A. Alfvén wave propagation in the high solar corona. Astron Astrophys 2000;362:342–58.
[6] Freund JB. Proposed inflow/outlow boundary condition for direct computation of aerodynamic sound. AIAA 1997;35:740–2.
[7] Colonius T. Numerically nonreflecting boundary and interface conditions for compressible flow and aeroacoustic computations. AIAA 1997;35(7):1126–33.
[8] Colonius T, Lele SK. Computational aeroacoustics: progress on nonlinear problems of sound generation. Prog Aerosp Sci 2004;40(6):345–416.
[9] Bogey C, Bailly C. Effects of inflow conditions and forcing on subsonic jet flows and noise. AIAA 2005;43(5):1000–7.
[10] Pirozzoli S, Colonius T. Generalized characteristic relaxation boundary conditions for unsteady compressible flow simulations. J Comput Phys 2013;248(C):109–26.
[11] Lodato G, Domingo P, L V. Three-dimensional boundary conditions for direct and large-eddy simulation of compressible viscous flow. J Comput Phys 2008;227(10):5105–43.
[12] Poinsot T, Veynante D. Theoretical and numerical combustion. 3rd ed; 2011. (www.cerfacs.fr/elearning)
[13] Albin E, D'Angelo Y, Vervisch L. Using staggered grids with characteristic boundary conditions when solving compressible reactive Navier–Stokes equations. Int J Numer Methods Fluids 2011;68(5):546–63.
[14] Coussement A, Gicquel O, Caudal J, Fiorina B, Degrez G. Three-dimensional boundary conditions for numerical simulations of reactive compressible flows with complex thermochemistry. J Comput Phys 2012;231(17):5571–611.
[15] Poinsot T. Prediction and control of combustion instabilities in real engines (invited hottel lecture). Proc Combust Inst 2017:1–28.
[16] Lourier JM, Stöhr M, Noll B, Werner S, Fiolitakis A. Scale adaptive simulation of a thermoacoustic instability in a partially premixed lean swirl combustor. Combust Flame 2017;183:1–15.
[17] Krediet HJ, Beck CH, Krebs W, Schimek S, Paschereit CO, Kok JBW. Identification of the flame describing function of a premixed swirl flame from les. Combust Sci Technol 2012;184(7–8):888–900.
[18] Duran I, Moreau S, Poinsot T. Analytical and numerical study of combustion noise through a subsonic nozzle. AIAA 2013;51(1):42–52.
[19] Dowling AP, Mahmoudi Y. Combustion noise. Proc Combust Inst 2015;35(1):65–100.
[20] Ihme M. Combustion and engine-Core noise. Ann Rev Fluid Mech 2016;49:1–35.
[21] Ni F, Miguel-Brebion M, Nicoud F, Poinsot T. Accounting for acoustic damping in a helmholtz solver. AIAA 2017;55(4):1205–20.
[22] Abom M. A note on the experimental determination of acoustical two-port matrices. J Sound Vib 1991;155(1):185–8.
[23] Polifke W, Poncet A, Paschereit CO, Doebbeling K. Reconstruction of acoustic transfer matrices by instationnary computational fluid dynamics. J Sound Vib 2001;245(3):483–510.
[24] Tournadre J, Förner K, Polifke W, Martínez-Lera P, Desmet W. Determination of acoustic impedance for Helmholtz resonators through incompressible unsteady flow simulations. AIAA 2016:1–9.
[25] Magri L, O'Brien J, Ihme M. Compositional inhomogeneities as a source of indirect combustion noise. J Fluid Mech 2016;799:R4–1.
[26] Livebardon T, Moreau S, Gicquel L, Poinsot T, Bouty E. Combining LES of combustion chamber and an actuator disk theory to predict combustion noise in a helicopter engine. Combust Flame 2016;165:272–87.
[27] Thompson KW. Time dependent boundary conditions for hyperbolic systems. J Comput Phys 1987;68:1–24.
[28] Giles M. Non-reflecting boundary conditions for euler equation calculations. AIAA 1990;28(12):2050–8.
[29] Yoo C, Wang Y, Trouvé A, Im H. Characteristic boundary conditions for direct simulations of turbulent counterflow flames. Combust Theor Model 2005;9:617–46.
[30] Yoo C, Im H. Characteristic boundary conditions for simulations of compressible reacting flows with multi-dimensional, viscous, and reaction effects. Combust Theor Model 2007;11:259–86.
[31] Berenger J-P. A perfectly matched layer for the absorption of electromagnetic waves. J Comput Phys 1994;114(2):185–200.
[32] Tam C. Advances in numerical boundary conditions for computational aeroacoustics. J Comput Phys 1998;6(4):377–402.
[33] Hu FQ, Li X, Lin D. Absorbing boundary conditions for nonlinear euler and Navier–Stokes equations based on the perfectly matched layer technique. J Comput Phys 2008;227(9):4398–424.
[34] Selle L, Nicoud F, Poinsot T. The actual impedance of non-reflecting boundary conditions: implications for the computation of resonators. AIAA 2004;42(5):958–64.
[35] Tudisco P, Ranjan R, Menon S, Jaensch S, Polifke W. Simulation of transverse combustion instability in a multi-injector combustor using the time -domain impedance boundary conditions. Flow Turbul Combust 2018;101:55–76.
[36] Rudy DH, Strikwerda JC. A non-reflecting outflow boundary condition for subsonic Navier Stokes calculations. J Comput Phys 1980;36:55–70.
[37] Granet V, Vermorel O, Leonard T, Gicquel L, Poinsot T. Comparison of nonreflecting outlet boundary conditions for compressible solvers on unstructured grids. AIAA 2010;48(10):2348–64.
[38] Rudy DH, Strikwerda JC. Boundary conditions for subsonic compressible Navier Stokes calculations. Comput Fluids 1981;9:327–38.
[39] Prosser R. Improved boundary conditions for the direct numerical simulation of turbulent subsonic flows i: inviscid flows. J Comput Phys 2005;207:736–68.
[40] Guezennec N, Poinsot T. Acoustically nonreflecting and reflecting boundary conditions for vorticity injection in compressible solvers. AIAA 2009;47:1709–22.
[41] Kopitz J, Brocker E, Polifke W. Characteristics-based filter for identification of acoustic waves in numerical simulation of turbulent compressible flow.. 12th Int'l Congress on Sound and Vibration (ICSV 12); 2005. Lisbon, Portugal
[42] Colin O, Rudgyard M. Development of high-order Taylor–Galerkin schemes for unsteady calculations. J Comput Phys 2000;162(2):338–71.
[43] Schønfeld T, Rudgyard M. Steady and unsteady flows simulations using the hybrid flow solver avbp. AIAA 1999;37(11):1378–85.
[44] Gourdain N, Gicquel L, Montagnac M, Vermorel O, Gazaix M, Staffelbach G, et al. High performance parallel computing of flows in complex geometries: I. Methods. Comput Sci Disc 2009;2(1):015003.
[45] Passot T, Pouquet A. Numerical simulation of compressible homogeneous flows in the turbulent regime. J Fluid Mech 1987;181:441–66.
[46] Hussain F, Jeong J. On the identification of a vortex. J Fluid Mech 1995;285:69–94.
[47] Selle L, Lartigue G, Poinsot T, Koch R, Schildmacher K-U, Krebs W, et al. Compressible large-eddy simulation of turbulent combustion in complex geometry on unstructured meshes. Combust Flame 2004;137(4):489–505.
[48] Franzelli B, Riber E, Gicquel LY, Poinsot T. Large eddy simulation of combustion instabilities in a lean partially premixed swirled flame. Combust Flame 2012;159(2):621–37.
[49] Poinsot T, Trouvé A, Veynante D, Candel S, Esposito E. Vortex driven acoustically coupled combustion instabilities. J Fluid Mech 1987;177:265–92.
[50] Nicoud F, Benoit L, Sensiau C, Poinsot T. Acoustic modes in combustors with complex impedances and multidimensional active flames. AIAA 2007;45:426–41.

Available online at www.sciencedirect.com

ScienceDirect

Proceedings of the Combustion Institute 37 (2019) 1953–1960

Proceedings of the Combustion Institute

www.elsevier.com/locate/proci

Impact of symmetry breaking on the Flame Transfer Function of a laminar premixed flame

T.L. Kaiser [a,*], G. Öztarlik [a], L. Selle [a,b], T. Poinsot [a,b]

[a] *IMFT (Institut de Mécanique des Fluides de Toulouse), 2 Allée Camille Soula, 31400 Toulouse, France*
[b] *CERFACS, 42 Avenue Gaspard Coriolis, 31057 Toulouse Cedex 1, France*

Received 1 December 2017; accepted 5 June 2018
Available online 28 June 2018

Abstract

This work presents a numerical study of the acoustic response of a laminar flame with tunable asymmetry. A V-shaped premixed flame is stabilised in the wake of a cylindrical flame holder that can be rotated. The configuration is symmetric when the flame holder is fixed but increasing its rotation rate breaks the symmetry of the flow. This configuration is submitted to acoustic forcing to measure the effect of rotation of the flame holder on the Flame Transfer Functions. It appears that the asymmetry of the two flame branches changes their respective time delays, resulting in interference in the global unsteady heat release rate fluctuations. Consequently, the Flame Transfer Function exhibits dips and bumps, which are studied via laminar Direct Numerical Simulation. Potential applications for the control of combustion instabilities are discussed.

Keywords: Laminar flame; Symmetry breaking; Interference; Laminar DNS; Rotating cylinder

1. Introduction

Combustion instabilities caused by a coupling of heat release fluctuations and acoustic modes of the combustion chamber are one of the key uncertainties in the development process of gas turbines. Their consequences may range from limiting the operating conditions to the destruction of the combustion chamber.

Combustion instabilities involve various complex physical mechanisms. Therefore, canonical test cases are often used to isolate certain phenomena. In this context, several configurations involving laminar flames in various shapes have been studied in the past. Besides V-flames and conical flames [1,2], the case of a flame anchoring in the wake of a bluff body in laminar cross flow, has been studied using numerical and analytical approaches. Using laminar Direct Numerical Simulations (DNS) validated by experiments, Brebion et al. [3] investigated the influence of the cylindrical flame holder's temperature on the flame anchoring mechanism. In their follow up study, Mejia et al. [4] investigated the influence of the cylinder's temperature on the Flame Transfer Function (FTF). The effect of rotation of the cylinder on the flame anchoring mechanism was explained by Xavier et al. [5] and Mejia et al. [6]. Their results

* Corresponding author.
E-mail address: tkaiser@imft.fr (T.L. Kaiser).

https://doi.org/10.1016/j.proci.2018.06.047

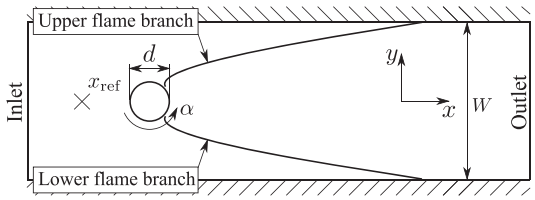

Fig. 1. Transverse cut of the computational domain.

showed that rotating the cylinder breaks the symmetry of both flame branches. Since the asymmetry of both flame branches is tunable by the rotation rate, it is a variable parameter to adapt the flame topology, without changing the flow velocity or the cold gas mixture. The dynamic response of both flame branches and their interaction nevertheless remain unknown.

This article focuses on influence of the cylinder rotation rate on the dynamic response of the flames to harmonic acoustic forcing. In Section 2 the setup and numerical strategy are laid out. Section 3.1 describes the influence of the rotation rate on the unperturbed flame topology and Section 3.2 discusses the FTF of the case without cylinder rotation. This FTF is compared in Section 3.3 to FTFs for various cylinder rotation rates. Section 3.4 discusses the flame branches topology in case of monochromatic forcing for several rotation rates. Finally, the results are concluded and discussed in Section 4.

2. Configuration and simulation framework

The configuration corresponds to that of Xavier et al. [5,7]: it consists of a constant-section rectangular channel (width $W = 34$ mm and depth 94 mm) at the center of which a stainless-steel cylinder (diameter $d = 8$ mm) serves as a flame holder (see Fig. 1). The cylinder is mounted on an electric motor with a controlled rotation speed ranging from 600 to 20, 000 rpm. The normalised rotation rate is defined as

$$\alpha = \frac{\omega d}{2u_b} \tag{1}$$

where u_b is the bulk velocity of the premixed gases in the channel.

As shown in previous studies on this experiment [3,5,7], because of its geometry and the laminar conditions, two-dimensional simulations are adequate. Laminar DNS are performed using the AVBP code [8], jointly developed by CERFACS and IFP Energies nouvelles, which solves the compressible Navier–Stokes equations for multicomponent reacting flows on unstructured grids. The numerical integration is performed by a two-step Taylor–Galerkin scheme called TTGC [9], which is of third-order in both space and time. In the current work, the combustion of methane and air is modelled via an analytically reduced skeletal mechanism accounting for 19 transported species and 11 quasi-steady species [10]. This mechanism, referred to as *LU19*, is based on the *GRI-mech3.0* mechanism [11] and reproduces the adiabatic temperature and flame speed over a wide range of operating conditions. It also includes low-temperature-chemistry, required to describe flame wall interaction at the flame holder interface.

The lateral walls are water-cooled and modelled by a no-slip iso-thermal boundary condition ($T_{wall} = 292$ K). The computational domain extends from $x = -35$ mm to $x = 97$ mm, where $x = 0$ corresponds to the center of the cylinder. The inlet and outlet boundary conditions are modelled via the Navier–Stokes characteristic boundary conditions (NSCBC) [12]. The inlet is fed by a methane-air mixture at equivalence ratio $\Phi = 0.75$ and temperature $T_u = 292$ K. The velocity profile is given by experimental measurements. The bulk speed is $u_b = 0.8$ m/s. A pressure of $p = 100,700$ Pa is imposed at the outlet. This operating point is far away from flame detachment of the cylinder.

The boundary condition at the cylinder's surface is a no-slip rotating wall, which was shown by Mejia et al. [7] to accurately account for the rotation of the flame holder. An estimation of the Biot number of the present cylinder is 0.01, meaning that the assumption of spatially uniform temperature is valid. Consequently, the cylinder temperature, T_{cyl}, can be obtained by solving [5]:

$$\frac{dT_{cyl}}{dt} = \frac{S}{C_p \rho V}(\dot{Q}_{cond} - \dot{Q}_{rad}), \tag{2}$$

where t denotes time, S the cylinder surface, ρ and V the density and the volume of the cylinder, and C_p the mass specific heat capacity. $\dot{Q}_{cond}$ and $\dot{Q}_{rad}$ are the conductive and radiative heat fluxes, respectively. $\dot{Q}_{cond}$ is obtained by integrating the laminar DNS heat flux long the cylinder surface. Radiation is governed by the Stefan–Boltzmann-radiation law [13]:

$$\dot{Q}_{rad} = \epsilon\sigma\left(T_{cyl}^4 - T_{wall}^4\right), \tag{3}$$

where σ is the Stefan–Boltzmann constant, and the emissiency coefficient, ϵ, is set to 0.9. The gas is assumed to be fully transparent and the temperature of the surroundings of the cylinder is supposed to be equal to the temperature of the cooled walls $T_{wall} = 292$ K. Since the time scales of the chemical reactions and that of the preheating of the cylinder are distinctively different, the transient heat up of the experiment can be accelerated following, for example the strategy presented in [14]. Also, because of the low Biot number and the high rotation rate, once in the permanent regime, the temperature of the cylinder is homogeneous and constant.

Finally, regarding spatial resolution, the coarsest cell size in the domain is $\Delta x = 500\,\mu$m, while it is $\Delta x = 70\,\mu$m close to the flame, which corresponds to 8 points in the flame [15]. Based on a

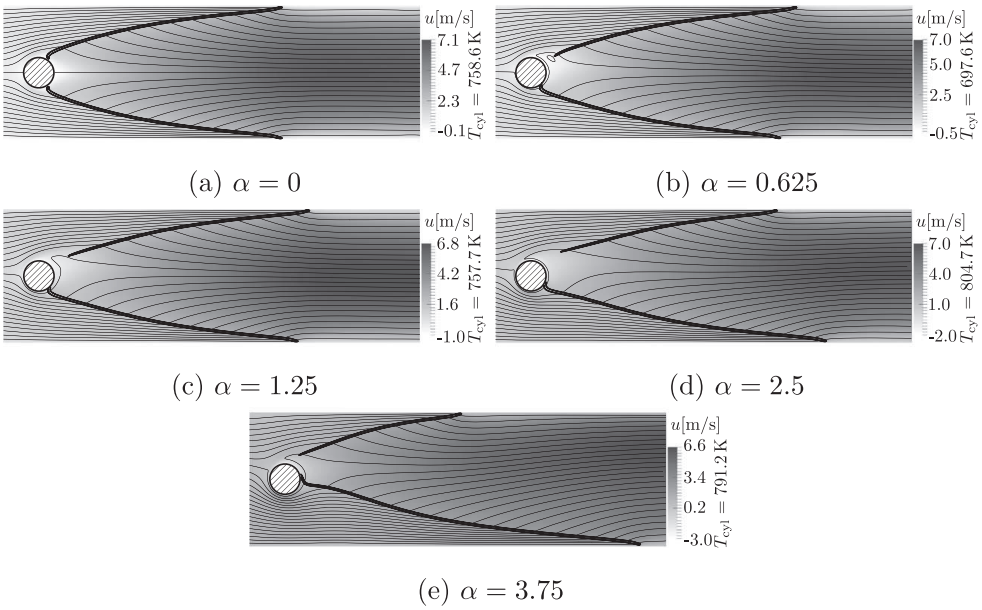

Fig. 2. Field of velocity component in main flow direction, u, with stream lines highlighted as thin black solid lines, iso-surface of heat release as thick solid line and cylinder temperature for various cylinder rotation rates, α.

mesh convergence study focusing on one dimensional flame head on quenching, the cell size at all solid walls is set to $\Delta x = 25\,\mu$m. The setup of the mesh convergence study is presented in [16].

This numerical strategy was successfully compared to experimental results in many previous studies [3,5,7], including investigations on flame wall interaction [16] and it is used here without modification.

3. Results

In this section, the influence of rotation of the flame holder on the response of the flame to acoustic waves is studied. This analysis is conducted in the framework of FTF, i.e., in the linear regime corresponding to low amplitude perturbations.

3.1. Steady-state analysis

First, the steady flame shapes are presented in Fig. 2, for all of which the fluctuations in heat release are smaller than 0.05% of the mean heat release value. As expected, without rotation the flame is symmetric (Fig. 2a) but this symmetry is broken by the rotation of the flame holder. With increasing rotation rates, the root of the upper branch detaches from the cylinder, but moves upstream again for very large values of α (cf. Fig. 2e). The tip of the upper branch moves downstream until $\alpha = 1.25$ but then goes back upstream, even past its location for the symmetric flame. Regarding the lower branch, it always remains attached to the cylinder and its tip is monotonously pushed downstream. A thorough investigation of the effect of bluff body rotation on the flame root is provided by Xavier et al. [5].

From the simple observation of the flame shape in the steady state, one can anticipate that the two branches will have a very different response to acoustic waves. Indeed, one can show from first principles [17,18] that the flame response is driven by its length and the dynamics of its root. While the length greatly impacts the delay, the dynamics of the flame root drives the gain of the FTF [4,6]. Moreover, the rotation of the cylinder breaks the symmetry of the flow so that the bulk velocities on both sides of the flame holder are different. This will change the speed at which perturbations travel on the flame front, also impacting the flame delay. Finally, because of the complex flow pattern around the cylinder, the temperature of the flame holder changes with the rotation rate (see right side of Fig. 2). It first decreases significantly at low rotation rates and increases again, past the reference value without rotation. The quantitative measurement of these changes is reported in Table 1, which gives the cylinder temperature, the flame root and tip positions and the bulk velocities for the two branches for various rotation rates.

All these changes in the flame front topology and the flow field point towards a modification of the FTF, which will be studied in the next sections.

3.2. Flame response without rotation

This section focuses on the FTF of the various flames, starting with the case without rotation. Under the assumption that the system is linear and invariant, it has been shown in many studies that the Wiener–Hopf Inversion (WHI) is a pow-

Table 1
Properties taken from the laminar DNS solution for different rotation rates, α.

α	T_{cyl} (K)	$x_{\text{root},y-}$ (mm)	$x_{\text{root},y+}$ (mm)	$x_{\text{tip},y-}$ (mm)	$x_{\text{tip},y+}$ (mm)	v_{y-} (m/s)	v_{y+} (m/s)
0	758.6	1.9	1.9	60.1	60.1	1.05	1.05
0.625	697.6	2.4	7.8	63.4	67.3	1.08	1.02
1.25	757.7	2.4	12.1	65.2	68.2	1.12	0.97
2.5	804.7	3.4	14.8	74.8	62.2	1.26	0.83
3.75	791.2	4.3	8.3	90.1	44.5	1.46	0.64

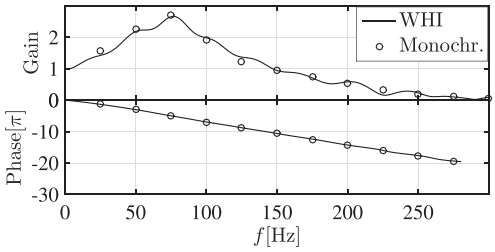

Fig. 3. FTF without rotation ($\alpha = 0$) based on WHI and monochromatic forcing.

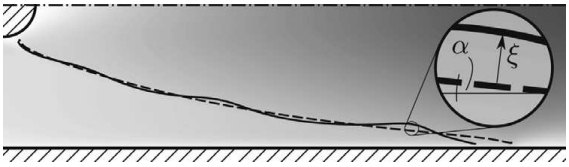

Fig. 4. Flame shapes behind a non-rotating cylinder; dashed line: unperturbed flame; solid line: flame forced at 80 Hz; Insert: definition of flame angle, α, and flame normal displacement, ξ.

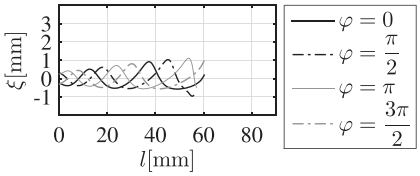

Fig. 5. Flame displacement, ξ, along the flame front without rotation for various phases at $f = 80$ Hz. Forcing amplitude: 5% u_b.

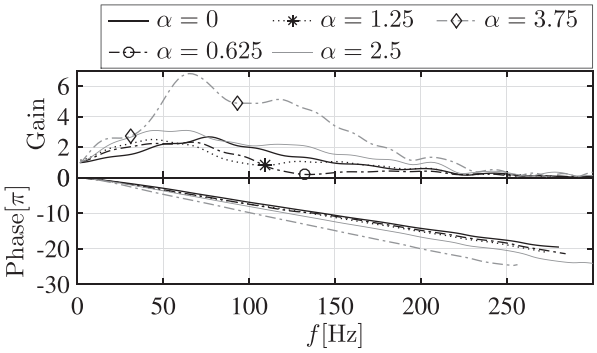

Fig. 6. Influence of flame holder rotation on the FTF.

erful methodology for the determination of FTFs [19–21]. In this method, the transfer function of a system is estimated by broad band forcing of the system and subsequent correlation analysis of its input and output signal. A detailed description of the method is provided in [22,23]. In order to remain in the linear regime, the forcing amplitude for the estimation of the FTF is kept at 1% of the bulk velocity. The reference point for the velocity perturbations is at $x = -10$ mm and $y = 0$. Figure 3 shows the FTF of the symmetric reference flame (i.e., $\alpha = 0$), obtained by a WHI analysis of laminar DNS data. As seen in previous studies of this configuration, this flame only responds under 250 Hz and shows a strong gain (> 2) at low frequencies, here around 80 Hz. The phase of the FTF is linear, corresponding to a constant time delay τ defined as the slope of the phase. For the present operating point, $\tau = 35.5$ ms. The accuracy of the WHI was tested by performing FTF evaluation at various discrete frequencies (see circles in Fig. 3).

We now investigate the motion of the flame front under harmonic forcing at 80 Hz, i.e., close to the frequency of the peak in the FTF. Figure 4 presents the mean and perturbed flame front and shows the definition of the normal displacement ξ between the two. In order to elucidate the dynamics of the flame, the evolution of ξ along the flame front is presented in Fig. 5 at four different phases of the harmonic excitation. It appears that the amplitude of the displacement increases weakly along the flame front but shows non-linear deformation close to the flame tip. It is also quite clear that a lot of the variation in the flame surface is caused by the flame-wall interaction at the flame tip.

3.3. Flame response with rotation

Figure 6 shows the FTFs for various rotation rates, up to $\alpha = 3.75$, including the case without rotation as the reference. The first observation is that the maximum gain is marginally affected up to $\alpha = 2.5$. However, between $\alpha = 2.5$ and $\alpha = 3.75$, it increases by at least a factor of 2. The location of the maximum gain remains in the low-frequency range (between 50 Hz and 80 Hz), but without clear trend.

The second observation is that for many rotation rates, the gains exhibit strong dips (see markers

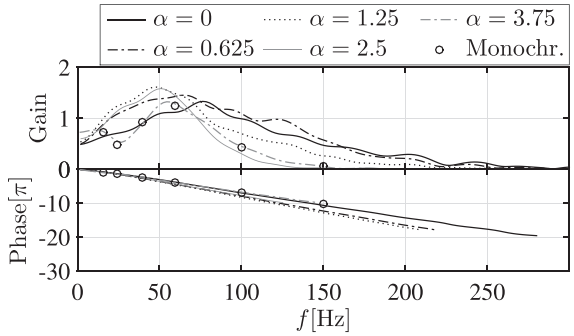

(a) Upper flame branch (y^+).

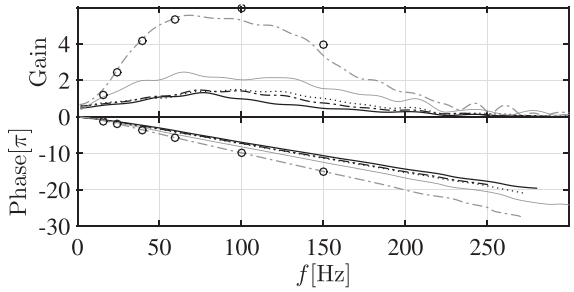

(b) Lower flame branch (y^-).

Fig. 7. FTF of individual flame branches versus rotation rate α; the circles mark results of monochromatic forcing at $\alpha = 3.75$.

in Fig. 6). It is anticipated that these dips could stem from the symmetry breaking of the flame, resulting in interference between the responses of the two flame branches. Regarding the phase of the FTF, it is linear in all cases and the corresponding delay monotonously increases with the rotation rate.

In order to investigate the dips in the FTF gain, the two flame branches are now analysed separately. The underlying assumption is that their dynamics are not, or sufficiently weakly coupled.

The FTF of the upper ($y > 0$, labelled y^+), respectively lower ($y < 0$, labelled y^-) branches are determined by integration of the heat release rate over one half of the domain. The reference point for the velocity is the same as for the global FTF and the heat release rate fluctuations are normalised by the total flame power. The resulting FTFs are displayed in Fig. 7a for the y^+-branch and in Fig. 7b for the y^--branch.

For the upper branch, the variations in maximum gain are limited but the cutoff frequency clearly decreases with α. It goes from 250 Hz without rotation down to around 130 Hz for $\alpha > 2.5$. The delay of the flame response first increases and then decreases with a maximum around $\alpha = 1.25$, which is consistent with the evolution of the steady upper-flame length shown in Fig. 2.

The evolution of the FTF of the lower branch is very different. First there is no decrease in the cutoff frequency but the striking feature is that the maximum gain increases drastically past $\alpha = 2.5$ over a broad frequency range. The delay of the FTF monotonously increases with α, replicating the increase in flame length concomitant with the bulk velocity increase for $y < 0$. Despite the high gains at $\alpha = 3.75$, results of monochromatic forcing, which are illustrated by the circles in Fig. 7, and WHI are in good agreement.

We now investigate the hypothesis that the breaking of the flame symmetry results in an interference between the two branches. A practical application for this modification of the FTF via rotation of the flame holder could be the control of combustion instabilities by tuning the location of the dips in the FTF. A simple model can be built to predict the frequency at which this dip occurs. It is based on the idea that the dip is the consequence of the interference between the responses in heat release fluctuation of the two branches. The total heat release fluctuation is equal to the sum of the heat release fluctuation of both branches, $q'_{\mathrm{tot}} = q'_{y^+} + q'_{y^-}$. Introducing the FTF using the notation of Crocco, the fluctuation in heat release can be related to a harmonic velocity fluctuation, u', which yields:

$$\frac{q'_{\mathrm{tot}}}{\overline{q}} = \frac{u'}{\overline{u}}\left(n_{y^+} + n_{y^-}\exp\left(i\omega\Delta\tau\right)\right)\exp\left(i\omega\tau_{y^+}\right). \quad (4)$$

Here, n are the gains of the respective branches and the difference in time delays is depicted as $\Delta\tau = \tau_{y^-} - \tau_{y^+}$. From Eq. (4) it is evident, that the gain of the global FTF is depending on the phase angle between the two branches, given by

$$\Delta\phi = \omega\Delta\tau. \quad (5)$$

The two extreme cases are ideal constructive interference and ideal destructive interference. For the former case, the phase angle between the both branches' heat release signals is 0 or an even multiple of π. Then the gain of the global heat release reduces to $n_{\mathrm{tot}} = n_{y^+} + n_{y^-}$. In the other case, the difference in phase angles is an odd multiple of π, so that the gain of the global heat release is equal to $n_{\mathrm{tot}} = |n_{y^+} - n_{y^-}|$. Therefore, the frequency at which destructive interference is maximal can be deduced from Eq. (5):

$$f_{\mathrm{d},n} = \frac{\Delta\phi}{2\pi\,\Delta\tau},\ \Delta\phi = (2n-1)\pi,\ n \in \mathbb{Z}. \quad (6)$$

The values, extracted from the laminar DNS, of the delays of the two branches (τ_{y^+} and τ_{y^-} for the upper and lower branch, respectively), their difference, $\Delta\tau$, and the first two frequencies of constructive and destructive interference ($f_{\mathrm{c},n}$ and $f_{\mathrm{d},n}$ for $n = 1$ and $n = 2$) are given in Table 2. For $\alpha = 0.625$ and $\alpha = 1.25$, the predicted values of $f_{\mathrm{d},1}$ correspond very well to the FTF of Fig. 6. For $\alpha = 2.5$, the first destructive interference occurs at a frequency where the gain of the upper-branch FTF is close to zero (cf. Fig. 7a). Consequently, the interference is not meaningful and no dip is observed in the FTF. Finally for the higher rotation rate ($\alpha =$

Table 2
Time delays of the two flame branches (τ_{y+} and τ_{y-} for the upper and lower branch, respectively) and values of the first two frequencies for destructive and constructive interference (cf. Eq. (6)).

α	τ_{y+} (ms)	τ_{y-} (ms)	$\Delta\tau$ (ms)	$f_{\mathrm{d},1}$ (Hz)	$f_{\mathrm{d},2}$ (Hz)	$f_{\mathrm{c},1}$ (Hz)	$f_{\mathrm{c},2}$ (Hz)
0.0	35.5	35.5	0	– –	– –	– –	– –
0.625	40.9	37.1	−3.8	132	395	263	395
1.25	42.5	37.9	−4.6	109	326	217	435
2.5	38.6	41.6	3.0	167	500	333	667
3.75	33.6	49.7	16.1	31	93	62	124

3.75), the value of $f_{\mathrm{d},1}$ is again very low and a dip is observed.

The frequency of the second dip, $f_{\mathrm{d},2}$, (Table 2) is much higher than the cutoff frequency of the flame response for all rotation rates except for $\alpha = 3.75$, which exhibits a dip around the expected value of 93 Hz. The frequencies $f_{\mathrm{d},n}$ are illustrated by the markers in Fig. 6, showing very good agreement with the location of the dips in the corresponding gains. It seems that the simple model of Eq. (6) gives an accurate prediction of this phenomenon, giving a posteriori confirmation of the hypothesis that there is indeed interference between the two flame branches.

Given the strong impact of symmetry breaking on the shape of the FTF, one may use the rotation rate of the flame holder to control combustion instabilities. However, it can be anticipated that only the low rotation rates, say $\alpha < 1.25$ can be of practical use for the present flame, first because of the strong decrease of the cutoff frequency of one of the branches, but also because of the large increase in gain of the other branch, which drives the gain of the total FTF and hinders the destructive interference.

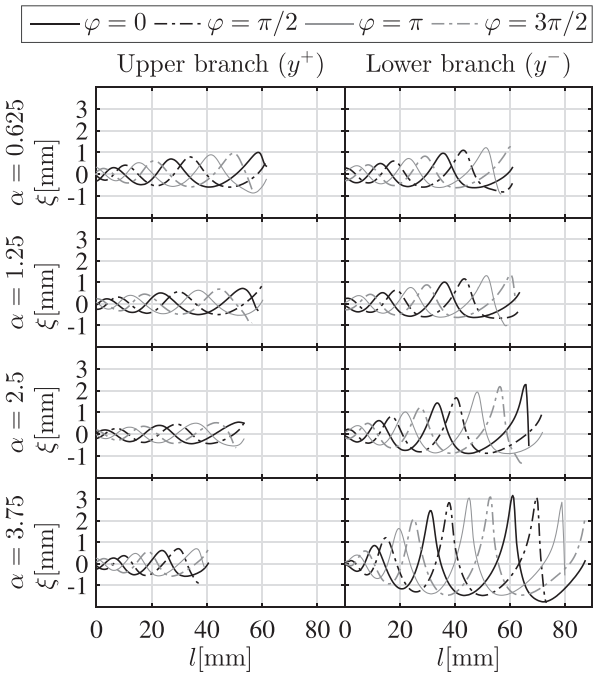

Fig. 8. Flame displacement, ξ, along the flame front at a velocity forcing of amplitude of 5% u_{b} and $f = 80$ Hz for various phase angles, φ, and rotation rates α.

3.4. Flame front dynamics

We pursue the analysis of the flame response by plotting the flame displacement along the flame front for the two branches in Fig. 8. As for the non-rotating case, the frequency of interest is 80 Hz, which lies close to the peak in the gain of the FTF for all rotation rates.

We start the analysis for the upper flame branch. For all rotation rates a growth of the flame displacement along the flame front is observed. With increasing rotation rate from $\alpha = 0$ to $\alpha = 2.5$, the flame displacement amplitude at the flame tip decreases moderately. It appears that the response in flame displacement amplitude increases again beyond this rotation rate. The same trend can be observed regarding the non-linear deformation close to the flame tip. This effect seems to decrease until a rotation rate of $\alpha = 2.5$ and increase again for higher rotation rates. Nevertheless, only a small variation of the flame displacement amplitude at the flame tip is observed. At the lower flame branch, the amplitude of the flame root displacement at $l = 0$ seems to decrease with increasing rotation rate. In contrast, the displacement growth along the flame front significantly increases, especially for rotation rates of $\alpha \geq 2.5$. This goes along with a considerable increase in non-linearity, as can be seen in the right half of Fig. 8. Note that the flame displacement monotonically grows along the flame front for both the upper and lower branch and all rotation rates until the flame tip, except for the lower branch at $\alpha = 3.75$. Here a saturation seems to occur and the fluctuation amplitude, while initially growing at the highest rate for low flame locations, stays approximately constant for $l > 40$ mm until the flame tip at $l = 87.4$ mm. Figure 8 suggests, that the lower branch's drastic increase in gain of the FTF for rotation rates $\alpha \geq 2.5$ might be due to some kind of convective instability mechanism which leads to a significant increase in flame displacement. The growth of perturbations artificially introduced into

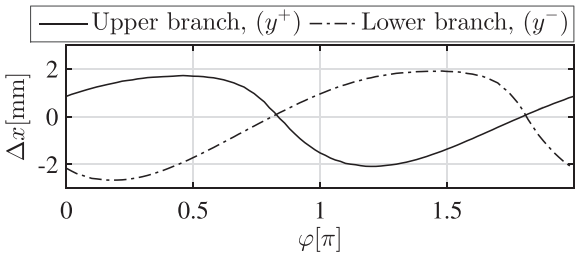

Fig. 9. Relative flame tip position with respect to the flame tip position of the steady flame, $\Delta x = x_{\text{tip}} - x_{\text{tip,s}}$, as a function of the phase angle of the velocity perturbation, φ, for a cylinder rotation rate of $\alpha = 0.625$; pulsation amplitude: 2% of bulk velocity; pulsation frequency: 132 Hz.

a laminar flame has been observed before (e.g., by Petersen [24] and Mejia et al. [4]).

Finally, the flame tip movement is analysed. Figure 9 shows the flame tip position of the perturbed upper and lower flame branches with respect to their positions in the unperturbed case for a cylinder rotation rate of $\alpha = 0.625$. The pulsation amplitude is at 2% of the bulk speed and its frequency is 132 Hz, i.e., at the frequency of ideal destructive interference. It appears that the tip movements are perfectly out of phase, which is expected since at these frequencies the FTFs show a phase difference of π and most of the heat release fluctuation is produced at the interaction of the flame tip and the lateral walls. Together with Fig. 6, Fig. 9 shows that introducing rotation of a flame holder can be used to build a flame which becomes almost insensitive to acoustic perturbation, suggesting that this could be used for combustion instability control. Note however that this result is obtained only in a limited frequency range.

4. Conclusion

The FTF of a laminar flame stabilised behind a rotating cylindrical bluff body is investigated for various rotation rates of the cylinder by the means of laminar DNS. The rotation causes a symmetry break between the two flame branches, where especially the flame tip positions vary significantly, especially for high rotation rates. FTFs are estimated for each branch separately, assuming that they can be described as two independent Linear Time Invariant (LTI)-systems. The results show a difference in time delays between the upper and the lower flame branch. This is mainly due to an independent modification of the flame tip positions of both branches, caused by two effects: a detachment of the upper branch from the cylinder and a modification of the bulk speeds in the two half domains due to the cylinder's viscous boundary layer. The resulting difference in time delay causes interference of the flames' heat release signals. At frequencies where destructive interference is maximal, the global FTFs, which include both flame branches, as a consequence show deep gaps in the gain. The difference in time delay and therefore the frequency at which destructive interference of both flame branches occurs can be tuned by adapting the rotation rate of the cylinder. In this context, the analysis suggests, that the rotation rate is a suitable and easily adaptable measure of open loop control of combustion instabilities. It is shown that for cylinder rotation rates, $\alpha \geq 2.5$, the flame displacement considerably grows along the flame front of the lower flame branch, leading to gains, that by far exceed the gain of the non-rotating configuration. This effect therefore limits the applicability of the method to moderate rotation rates and frequencies $f \geq 100$ Hz. Most practical flames are highly turbulent, and the existence of a corresponding effect in the turbulent regime remains unknown. Nevertheless, the present paper underlines the asset of decreasing the gain of the FTF significantly around a specific frequency by being able to tune the asymmetry of a combustion system which leads to destructive interference.

Acknowledgments

The research leading to these results has received funding from the European Research Council under the European Union's Seventh Framework Programme (FP/2007-2013)/ERC Grant Agreement ERC-AdG 319067-INTECOCIS.

This work was granted access to the high-performance computing resources of CINES under the allocation A0032B07036 made by Grand Equipement National de Calcul Intensif.

References

[1] R. Blumenthal, P. Subramanian, R. Sujith, W. Polifke, *Combust. Flame* 160 (2013) 1215–1224.
[2] T. Schuller, D. Durox, S. Candel, *Combust. Flame* 134 (2003) 21–34.
[3] M. Miguel-Brebion, D. Mejia, P. Xavier, et al., *Combust. Flame* 172 (2016) 153–161.
[4] D. Mejia, M. Miguel-Brebion, A. Ghani, et al., *Combust. Flame* 188 (2018) 5–12.
[5] P. Xavier, A. Ghani, D. Mejia, et al., *J. Fluid Mech.* 813 (2017) 127–151.
[6] D. Mejia, L. Selle, R. Bazile, T. Poinsot, *Proc. Combust. Inst.* 35 (2015) 3201–3208.
[7] D. Mejia, M. Bauerheim, P. Xavier, B. Ferret, L. Selle, T. Poinsot, *Proc. Combust. Inst.* 36 (2017) 1447–1455.
[8] T. Poinsot, The AVBP Handbook, CERFACS, Toulouse, 2005.
[9] O. Colin, M. Rudgyard, *J. Comput. Phys.* 162 (2000) 338–371.
[10] T. Lu, C.K. Law, *Combust. Flame* 154 (2008) 761–774.

[11] P.S. Gregory, D.M. Golden, M. Frenklach, et al., GRI-Mech, 2000. http://www.me.berkeley.edu/gri_mech/ (Accessed: 23 June 2018).
[12] T. Poinsot, S. Lele, *J. Comput. Phys.* 101 (1992) 104–129.
[13] L. Boltzmann, *Ann. Phys.* 258 (1884) 291–294.
[14] F. Duchaine, A. Corpron, L. Pons, V. Moureau, F. Nicoud, T. Poinsot, *Int. J. Heat Fluid Flow* 30 (2009) 1129–1141.
[15] M. Brebion, *Joint Numerical and Experimental Study of Thermo-acoustic Instabilities*, Institut de Mécanique des Fluides de Toulouse, 2016 Ph.D. thesis.
[16] A. Ghani, T. Poinsot, *Flow Turbl. Combust.* 99 (2017) 173–184.
[17] L. Boyer, J. Quinard, *Combust. Flame* 82 (1990) 51–65.
[18] A. Cuquel, D. Durox, T. Schuller, *C. R. Méc.* 341 (2013) 171–180.
[19] A. Giauque, T. Poinsot, F. Nicoud, 14th AIAA/CEAS Aeroacoustics Conference, Vancouver, British Columbia, Canada (2007) 2943.
[20] A. Gentemann, C. Hirsch, K. Kunze, F. Kiesewetter, T. Sattelmayer, W. Polifke, Proceedings of ASME Turbo Expo, Vienna, Austria(2004) 501–510.
[21] W. Polifke, A. Poncet, C. Paschereit, K. Döbbeling, *J. Sound Vib.* 245 (2001) 483–510.
[22] L. Ljung (Ed.), *System Identification (2nd ed.): Theory for the User*, Prentice Hall PTR, Upper Saddle River, NJ, USA, 1999.
[23] A. Huber, W. Polifke, *Int. J. Spray Combust. Dyn.* 1 (2009) 199–228.
[24] R.E. Petersen, H.W. Emmons, *Phys. Fluids* 4 (1961) 456–464.

Experiments in Fluids (2018) 59:33
https://doi.org/10.1007/s00348-018-2491-6

RESEARCH ARTICLE

Phosphor thermometry on a rotating flame holder for combustion applications

Pradip Xavier[1,2] · **Laurent Selle**[1] · **Gorkem Oztarlik**[1] · **Thierry Poinsot**[1]

Received: 22 September 2017 / Revised: 4 January 2018 / Accepted: 5 January 2018 / Published online: 24 January 2018

Abstract

This study presents a method to measure wall temperatures of a rotating flame holder, which could be used as a combustion control device. Laser-induced phosphorescence is found to be a reliable technique to gather such experimental data. The paper first investigates how the coating (thickness, emissivity and lifetime) influence the flame stabilization. While the low thermal conductivity of the coating is estimated to induce a temperature difference of only 0.08–0.4 K, the emissivity increases by 40%. Nevertheless, the transient and steady-state flame locations are not affected. Second, because temperature measurements on the rotating cylinder are likely to fail due the long phosphor lifetimes, we modify the classical point-wise arrangement. We propose to illuminate a larger area, and to correct the signal with a distortion function that accounts for the displacement of the target. An analytical distortion function is derived and compared to measured ones. It shows that the range of measurements is limited by the signal extinction and the rapid distortion function decay. A diagram summarizes the range of operating conditions where measurements are valid. Finally, these experimental data are used to validate direct numerical simulations. Cylinder temperature variations within the precision of these measurements are shown not to influence the flame location, but larger deviations highlight different trends for the two asymmetric flame branches.

1 Introduction

Performances and durability of combustion systems have been tremendously improved since Whittle's first turbojet, and regulations for pollutant emissions, noise and fuel consumption are driving future optimization and technological developments (Wulff and Hourmouziadis 1997; Lawrence 2009). Thermal efficiency improvement is crucial but limited by the thermal resilience of nozzle guide vanes used in gas turbines (Lefebvre 1999; Facchini et al. 2004; Duchaine et al. 2009; Berger et al. 2016). Moreover, the compactness of future systems is likely to enhance material stresses (Dreizler and Bohm 2015). The development of new materials that can withstand higher temperatures, raises the need to better understand their behavior in a combustion environment (Padture et al. 2002; Hooker and Doorbar 2000). Among others, flame–wall interactions and subsequent heat transfer in a combustor need to be carefully addressed as they can influence pollutant formation (Popp and Baum 1997; Mann et al. 2014; Jainski et al. 2017), flammability limits (Lakshmisha et al. 1991; Lamouroux et al. 2014; Xavier et al. 2017), flame stability (Guiberti et al. 2015; Mercier et al. 2016; Berger et al. 2016) or combustion instabilities (Tay-Wo-Chong 2013; Mejia et al. 2015; Kraus et al. 2017).

Wall temperature measurements in combustion systems are therefore mandatory but remain challenging due to the high-temperature and corrosive environment (Dreizler and Bohm 2015). Classical thermometry techniques suffer from several drawbacks. Thermocouples are intrusive and have their own thermal inertia, infrared thermometry (IR) relies on the knowledge of the material emissivity and the signal suffers from interferences with light emission from the flame (chemiluminescence). Thermal paints only provide

✉ Pradip Xavier
pradip.xavier@imft.fr; pradip.xavier@coria.fr

Laurent Selle
laurent.selle@imft.fr

Gorkem Oztarlik
gorkem.oztarlik@imft.fr

Thierry Poinsot
thierry.poinsot@imft.fr

[1] Institut de Mécanique des Fluides de Toulouse (IMFT), Université de Toulouse, CNRS, Toulouse, France

[2] Present Address: CORIA-UMR 6614, Normandie Université, CNRS, INSA et Université de Rouen, Campus Universitaire du Madrillet, 76800 Saint-Etienne du Rouvray, France

mean or peak information (Lempereur et al. 2008). Phosphor thermometry has appeared to be an interesting trade-off for these applications. Being semi-invasive as it requires to add a thin coating of phosphor particles, this technique—often named laser-induced phosphorescence (LIP)—uses rare-earth-doped ceramic phosphors whose spectroscopic properties are highly sensitive to temperature (Allison and Gillies 1997; Khalid and Kontis 2008; Chambers and Clarke 2009). In practice, this technique can be either implemented in the temporal domain, by measuring the phosphorescence glowing after excitation (Knappe et al. 2012), or in the spectral domain, by estimating a ratio of intensities (Feist et al. 2002). Fuhrmann et al. (2013) performed a systematic study of these two approaches and showed the advantages of the lifetime method, which is used in this study.

Despite the numerous applications of this technique to combustion (Kashdan and Bruneaux 2011; Alden et al. 2011; Brubach et al. 2013), some authors have studied how the surrounding environment can alter the spectroscopic properties of these particles. As an example, Brubach et al. (2013) investigated the influence of the dopant concentrations, laser energy, surrounding gas composition and pressure rise on a thermographic phosphor. However, to the authors' knowledge, the influence of this coating on flame stabilization has received little attention. For example, the coating is likely to change the material emissivity, the radiative heat transfer, the flame stabilization, and could even alter its stability (Miguel-Brebion et al. 2016; Kraus et al. 2017). This aspect will be treated in the first part of this paper.

Recently, Mejia et al. (2017) highlighted the possibility to perform active control of thermoacoustic instabilities of a flame stabilized on a rotating cylindrical flame holder. Xavier et al. (2017) numerically showed that the corresponding heat fluxes were more than three times larger, in comparison to classical flame–wall interaction cases (Poinsot and Veynante 2011; Ezekoye et al. 1992; Lu et al. 1990). The lack of detailed measurements in Mejia's experiment was the motivation for the implementation of LIP on this configuration. However, the rotating flame holder raises some questions on the data analysis: the classical point-wise laser excitation is likely to fail if the displacement of the moving target during the phosphorescence decay is larger than the typical size of the illuminated area. Several studies on moving surfaces have been reported, and the classical strategy consists in using phosphors with fast decay lifetimes (Mannick et al. 1987; Allison et al. 1988; Tobin et al. 1990; Alden et al. 2011). Thus, the object can be considered as a quasi-static object during the collection process. However, because this solution requires specific phosphors with adequate hardware, the authors want to evaluate the capabilities of a phosphor with longer decay lifetimes, by slightly modifying the point-wise static arrangement (second part of the paper).

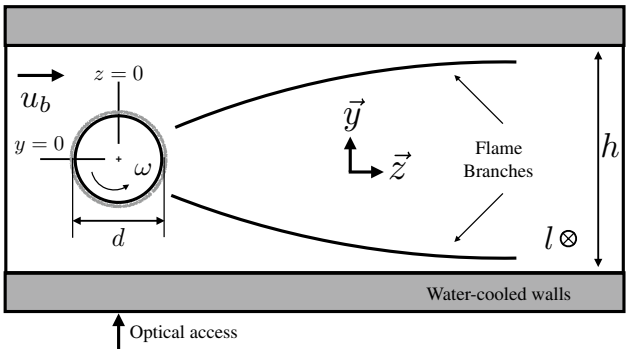

Fig. 1 Longitudinal cut through the combustion chamber (front view) and definition of the control parameters

The aim of this study is twofold: (1) evaluate the influence of the coating on the flame stabilization, and (2) provide a simple methodology for measuring temperatures on fast rotating parts with a phosphor having long decay lifetimes. Derived from the classical point-wise LIP arrangement, the methodology is implemented on the canonical case of a flame stabilized on a rotating cylindrical flame holder (Mejia et al. 2017).

The paper is organized as follows: the combustion test bench is briefly introduced in Sect. 2 while LIP implementation and validation are discussed in Sect. 3. Finally, the methodology for measuring temperatures on the rotating flame holder is described and validated in Sect. 4.

2 Setup and diagnostics

2.1 Combustion chamber

This study is performed on a confined laminar premixed methane/air flame, stabilized in the wake of a cylindrical flame holder. The setup, which is the same as that of Xavier et al. (2017), consists of a constant-section channel with a rectangular cross section: height, $h = 37$ mm and depth, $l = 94$ mm (cf. Fig. 1). The flame holder is a stainless-steel cylinder of diameter, $d = 8$ mm, which can be rotated at a constant angular velocity, ω, by a brushless electric engine (Faulhaber 2232S024BX4).The front side of the burner is equipped with a quartz window to allow direct flame visualization and the lateral walls are fitted with two optical slits for the passage of a laser sheet (not shown). The lateral walls are also water-cooled, which helps reducing the thermal inertia of the setup and allows a precise specification of boundary conditions for numerical simulations.

The bulk velocity and the equivalence ratio of the mixture are $u_b = 1.07$ m/s and $\phi = 0.7$, respectively. The Reynolds number, based on the cylinder diameter and the bulk velocity is $Re = 580$. In this regime, the reacting flow is steady.

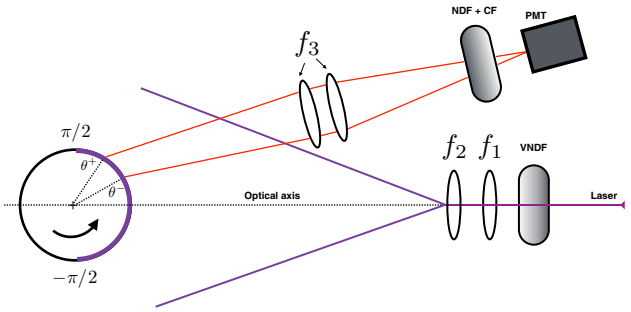

Fig. 2 Optical arrangement of the rotating laser-induced phosphorescence in the case of rotating cylinder. *VNDF* variable neutral density filter; *NDF* neutral density filter; *CF* colored filter; *PMT* photomultiplier; f_1 spherical lens (1000 mm); f_2 cylindrical lens (−22 mm); f_3 spherical lens (500 mm)

The control parameter of this experiment is the normalized rotation rate, α, defined as

$$\alpha = \omega d/2u_b. \tag{1}$$

The cylinder rotation speed ranges from 380 to 7600 rpm (rotation per minutes), corresponding to values of α between 0.15 and 3.

2.2 Laser-induced phosphorescence (LIP)

One objective of this study is to measure the temperature of the flame holder when it is rotating, via laser-induced phosphorescence. One issue with the classical point-wise laser excitation is that it is likely to fail if the phosphorescence decay time is much larger than the time the sensor views the illuminated spot. For instance, a rotating cylinder with $\alpha = 2$ (i.e., 5100 rpm) at room temperature has a displacement of ≈ 7 mm while the phosphor decays. This is definitely larger than the sensor field of view, which will experience a rapid signal extinction. Instead of using fast decay lifetimes' phosphor, the present setup produces a laser sheet rather than a point-wise excitation. Besides the increased collected signal, this solution also extends the phosphorescence collection time. Figure 2 presents the optical bench that can be applied to both steady and rotating cylinders. The laser beam first goes through a convergent lens ($f_1 = 1000$ mm) and is expanded through an additional cylindrical diverging lens ($f_2 = -22$ mm). Its optical axis is normal to the flame holder's rotation axis, so that the plane illuminates half of the cylinder's perimeter. The phosphorescence signal is collected on a set of two spherical lenses (diameter 50 mm, $f_3 = 500$ mm) and which increases the collected light on a photomultiplier (PM) tube (Hamamatsu H7422-50). The backward collection configuration is slightly tilted from the optical axis (Fig. 2). Because the cylinder is in the object plane of the first spherical lens, the PM sees a part of the cylinder.

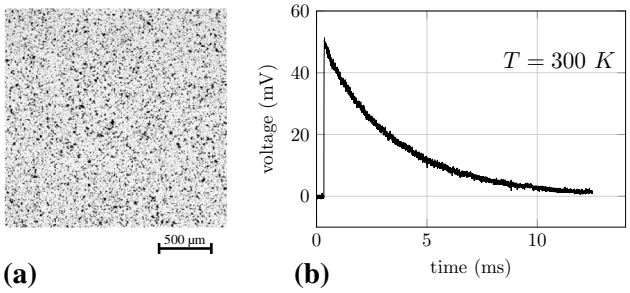

Fig. 3 **a** Microscopic image of the coating (binder+phosphor particles). **b** Typical phosphorescence decay curve obtained at room temperature $T = 300$ K

The viewing area is determined experimentally by replacing the pulsed laser source by a continuous diode source. The reflected light is collected on the PM and a mask is displaced in the streamwise direction until signal extinction occurs. The maximum amplitude of displacement is therefore converted to two angles, θ^- and θ^+. In this study, $\theta^- = 0.5$ rad and $\theta^+ = \pi/2$ rad, meaning that the PM sees the upper part of the cylinder.

Preliminary measurements using infrared thermography and thermocouples have shown that the temperature range for the steady flame holder lies between $T = 500$ K and $T = 800$ K for typical operating conditions. Therefore, we chose the commercial powder $Mg_4\,FGeO_{5,6}$:Mn (Osram SV067), which has an operating range from 300 to more than 900 K, corresponding to phosphor lifetimes from 3.3 ms to 5 µs (Brubach et al. 2008). The median diameter of the particles lies between 5.8 and 10.5 µm. The phosphor particles are mixed with a liquid ceramic binder (Zyp Coatings, Inc., HPC). The phosphor mass concentration is set to 5 % in this study, providing signal-to-noise ratios larger than 30 between 300 and 850 K (based on the maximum signal intensity and the mean background noise, see Fig. 3b). The resulting mixture is sprayed on the cylinder with an airbrush (Sotar Super Micron).

This coating is excited with the third harmonic (355 nm) of a Nd:YAG pulsed laser (at 10 Hz). The laser pulse energy is adjusted to 30 µJ per shot with a variable neutral density filter (Thorlabs NDC-50C-4-A). This level is in the linear range for the response of the coating and is low enough to prevent thermal damage (Atakan and Roskosch 2013; Linden et al. 2009). The PM is equipped with neutral density filters to prevent photocathode saturation (Brubach et al. 2008), and a set of colored optical filters: residuals from the laser excitation are removed with a high-pass filter (CVI LPF-550). The phosphorescence signal is transmitted by means of a narrow band-pass filter (CVI F10-660) at 660 ± 10 nm. The current output from the PM goes through an in-house current-to-voltage converter (load resistance of 10 kΩ) and is recorded by a 1 MHz acquisition card.

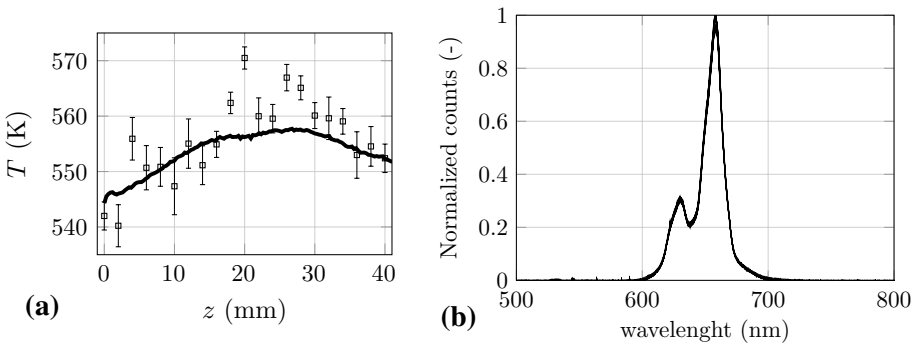

Fig. 4 **a** Comparison of the transverse temperature across the heated sample, between LIP data (square) and infrared thermography (solid line). **b** Series of ten emission spectra taken at room temperature (300 K) and spaced by a heating period of 10 min at 900 K between each measurement

3 Signal processing and validation

Measurements are performed in the temporal domain, by recording the phosphorescence decay after the coating has been excited by the laser. The collected signal is normalized by its maximum and a portion of the curve (between 10 and 90 % of the maximum) is extracted to get rid of fast fluorescence processes after the laser excitation and background noise when the signal has sufficiently decayed. Thus, the extracted data are fitted with an exponential function:

$$I(t) = \mathrm{e}^{-t/\tau}. \tag{2}$$

The principle of LIP is that the decay time τ depends on the temperature, T, of the material. A calibration procedure is required to establish the relation, $T(\tau)$, between the temperature and the decay time. For this calibration, we use a stainless steel heated sample by means of two heating cartridges, and whose temperature is controlled by a type K thermocouple. The sample temperature ranges from 300 to 850 K. For each temperature, 100 laser shots are recorded and the mean curve is fitted to estimate τ. The number of required data is determined by a sensitivity analysis to statistically converge the 1st and 2nd moments of τ. Prior to each measurement campaign, a calibration is performed on a newly coated sample.

The precision of the data is evaluated during the calibration procedure. For each temperature, the standard deviation due to shot-to-shot variations is converted to a temperature shift. This procedure is repeated over the entire range of temperature, which results in a precision of ± 7 K. The accuracy is determined by a comparison with infrared thermography. Figure 4a shows the transverse temperature profile across the sample with the two measurement methods. The infrared thermography measurements have an averaged standard deviation of 0.1% (not depicted in Fig. 4a), so that the mean IR temperature is used as the baseline for estimating the LIP accuracy. The averaged discrepancy (i.e., the average error) of the LIP to IR measurements is $\sim 1\%$.

The application of the coating is delicate and it is anticipated that it could be be user-dependent. Therefore, a series of tests is conducted to validate the coating technique. These tests are conducted on a coated piece of glass so that the distribution of phosphor particles can be visualized. The piece of glass is coated with the same procedure as the sample and the quality of the deposit procedure is checked with an upright transmission microscope (Zeiss A1 coupled with a $2000 \times 2000\,\mathrm{pix}^2$ Basler ace camera). A raw visualization of 2 by 2 mm^2 (Fig. 3a) shows that the airbrush technique produces a rather homogeneous coating. An example of a phosphorescence decay curve in Fig. 3b confirms the excellent signal-to-noise ratio with the settings described in Sect. 2.2. Without any specific procedure during the application, the airbrush technique produces a homogeneous coating while being inexpensive compared to more elaborated techniques (Brubach et al. 2013). The coating thickness is evaluated with a contact measurement gauge λ-Logitech (precision of $\pm 0.1\,\mu\mathrm{m}$). 40 point-wise measurements distributed over the sample gives an averaged thickness of 10 µm with a standard deviation 1 µm. The linear trend observed when applying several layers (i.e., a slope of 10 µm per layer) proves the good repeatability of the technique. The cylinder is coated while it is rotating at low speed, to ensure a good uniformity.

We anticipate that the coating may be altered or damaged by the harsh conditions of the reacting flow. to reproduce typical experimental conditions, several cycles of heating load are conducted: the sample is heated to 900 K during 10 min, and this procedure is repeated ten times. Between each heating load, an emission spectrum is recorded on a spectrometer (Ocean Optics USB 2000+, wavelength range from 330 to 1100 nm, optical resolution of 0.3 nm). Figure 4b presents ten successive spectra which have been normalized by the maximum of the first one. Both shape and amplitude of the spectra do not change with time so that neither spectroscopic nor signal-to-noise ratio are affected. An additional visual inspection confirms the excellent thermomechanical resistance to heat loads. It is therefore concluded that this coating is adequate for repeated use under reacting conditions, without measurable alteration of its performance.

The stabilization of the flame is known to depend on the material temperature, which is driven by the conductive and radiative properties of the flame holder. Knowing that the low thermal conductivity of the coating ($\lambda \approx$

Table 1 Emissivity of a polished stainless steel ϵ_p and a phosphor coating ϵ_c when varying temperature

T (K)	ϵ_p	ϵ_c
473	0.27	0.38
523	0.26	0.38
573	0.25	0.39

1–5 W/m K) can produce a temperature difference between the cylinder temperature, T_c, and the measurement, T_{LIP}, we use a simple resistance model to evaluate this shift, $\Delta T = \Phi R$ (the heat flux Φ is obtained from numerical simulations (Xavier et al. 2017), and R is the thermal resistance). The estimated temperature difference of 0.08–0.4 K is much lower than the precision of the technique and is not expected to play a major role in the flame stabilization process (Sect. 4.2). We also investigate the modification of the emissivity by the coating. Even if the coated surface is usually small, it might affect heat transfer and the flame location (Miguel-Brebion et al. 2016). The emissivity of the calibration sample's raw surface is compared to a coated one. The emissivity at a given temperature is,

$$\epsilon(T) = \frac{L(T) - L_e(T_e)}{L_0(T) - L_e(T_e)}, \tag{3}$$

where L is the luminescence of the surface (either raw or coated), L_0 is the luminescence of a black body (DCN 1000 N4, NHG), and L_e is the luminescence reflected from the environment at room temperature T_e. The transmission of air between the camera and the object is neglected as measurements are performed with a 14-bit infrared camera (Jade MWIR, CEDIP) operating with a spectral range of 3.6–5.2 µm, which corresponds to a high air transmittance window. The integration time is set to 20 µs to prevent sensor saturation at high temperatures.

Results are given in Table 1, where ϵ_p and ϵ_c are the emissivities of the raw and coated surface, respectively. The coated surface has an emissivity ~ 40% larger than the raw one: the coating application increases the wall roughness, which could be the main reason for the increased emissivity (not discussed here).

Because of the significant increase in ϵ, an a posteriori study is conducted: the influence of the coating on the flame anchoring location is conducted by temporally tracking the flame root location (FRL) of both branches. First, an uncoated cylinder is used as the reference for the FRL. Then, the cylinder is fully coated with the phosphor thereby varying the number of coating layers (from one to four layers). The flame is imaged on a Image Intense camera (LaVision), equipped with a $f/16$ 182 mm telecentric lens (TC4M64, Opto-engineering) to better resolve the vicinity of the cylinder. A colored optical filter, centered at 430 ± 10 nm, is placed in front of the sensor to collect the spontaneous CH* emission. Figure 5 presents the FRL (average of the two branches) during the transient heating. CH* chemiluminescence images are collected and the exact FRL is detected with a crest detector. After 400 s, the FRL has reached a steady state position. A slight difference is observed between the uncoated and the coated cylinder. The FRL of the coated cylinder is shifted downstream by approximately $0.35\delta_L^0$ (δ_L^0 is the planar unstretched adiabatic flame thickness), in comparison to the uncoated one. Modifications of the aerodynamics around the cylinder induced by the roughness of the coating and alteration of radiative properties would play a combined role to displace the steady-state flame stabilization. Moreover, increasing the number of layers does not change the FRL obtained for one layer. We therefore conclude the coating used in this study—especially the emissivity modification—is not significantly affecting the transient and steady flame stabilizations.

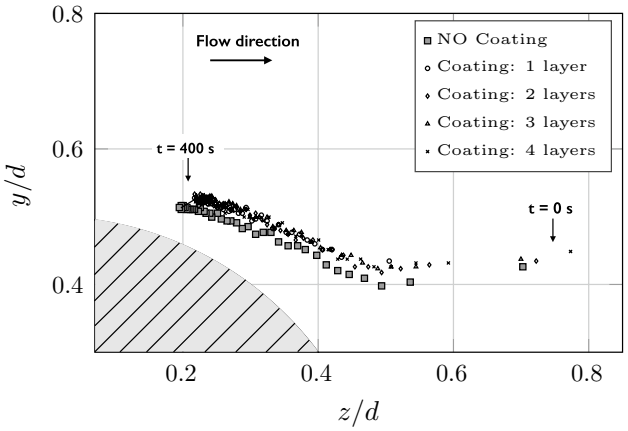

Fig. 5 Evolution of the flame root with time without rotation, for an uncoated cylinder (gray rectangles) and a coated cylinder (several layers)

4 Results

In Sect. 3, the LIP technique was calibrated on a non-rotating cylinder and it was checked that the coating did not affect the flame. In this section, the methodology for LIP measurement on the rotating cylinder is presented. As explained in Sect. 2.2, half of the perimeter is illuminated by the laser sheet and phosphorescence viewed by the photomultiplier is collected. Consequently, this setup measures the average temperature on the cylinder's surface. However, as the Biot number is 0.01, no temperature gradients are expected in the cylinder. Moreover, when the cylinder is rotating with $\alpha > 0.2$, the thermal time scale $\tau_s = d^2/D$ (D is the thermal diffusivity) is 6 s, which is 50 times larger than the rotation time scale $\tau_r = \pi d/\alpha u_b$

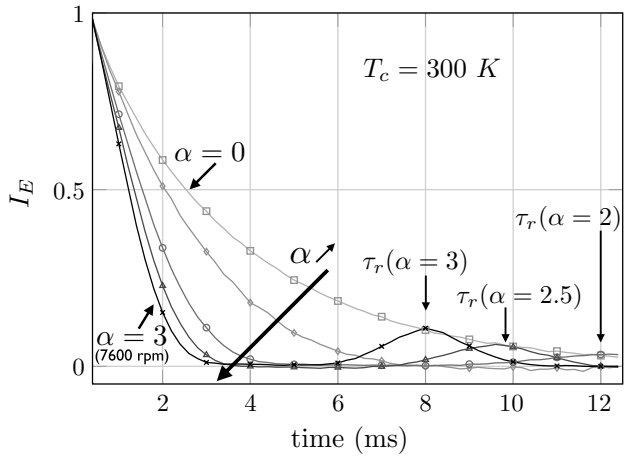

Fig. 6 Evolution of phosphorescence raw signals for different rotation rates α, without combustion, i.e., at room temperature $T_c = 300$ K. The secondary peak in the signal corresponds to the time τ_r for a full revolution of the cylinder

(one cylinder revolution). Thus, the temperature uniformity is enhanced by rotation.

4.1 Distortion function determination

Figure 6 shows typical phosphorescence signals recorded at ambient temperature (i.e., without flame) and for different rotation rates, α. For $\alpha = 0$, the signal exhibits an exponential decay. However, when α increases, the decay rate is smaller than without rotation because a portion of the illuminated area moves out of the PM field of view (i.e., signal extinction). This leads to a systematic error in the evaluation of the temperature because the LIP relies on the knowledge of a calibration curve $T(\tau)$ obtained without rotation. At high rotation rates ($\alpha > 2$), the cylinder performs a full revolution during the phosphorescence decay so that the PM signal goes to zero (when the cylinder has performed half of a revolution) and presents a secondary peak when the illuminated area has done a full revolution. It is therefore obvious that when LIP is performed on the rotating cylinder, a correction factor must be applied to the PM signal. We now propose an analytical evaluation of the distortion function, $\gamma(t, \alpha)$, that relates the phosphorescence signal when the cylinder is moving, $I(t, \alpha)$, to the one without rotation, $I(t, \alpha = 0) = I_0(t)$.

Figure 7a represents the portion of the cylinder that is illuminated by the laser sheet. As the diverging lens is 2 m away from the cylinder, the laser fluence I_L, received on the cylinder surface is assumed to be uniform between $-\pi/2$ and $\pi/2$.Consider a portion dl of the cylinder's surface, at an angle θ from the direction of the laser axis. The intensity received from the laser dI_R is

$$dI_R = I_L \cos(\theta) dl. \tag{4}$$

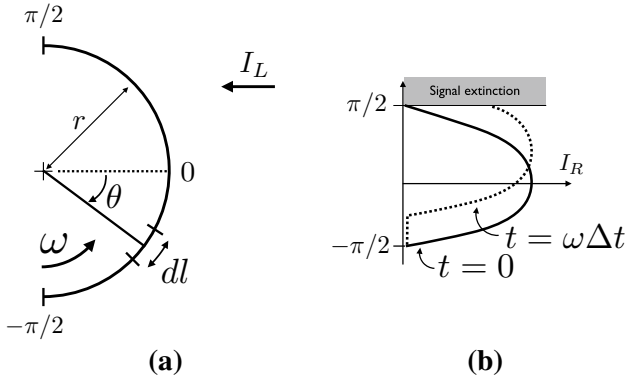

Fig. 7 Schematic representation of the modified LIP setup. **a** Definition of the different parameters. **b** Advection of the azimuthal intensity I_R received from the laser

Because the LIP is operated in the linear regime, the phosphorescence emission dI_E is proportional to the intensity received

$$dI_E = \beta I_L \cos(\theta) e^{-t/\tau} dl, \tag{5}$$

where β accounts for linearity between dI_R and dI_E. Because the PM is almost aligned with the optical axis of the laser, it collects the phosphorescence with an angle $\theta - \omega t$ (Fig. 7b). The term ωt accounts for the cylinder rotation. A Lambertian pattern (i.e., the off-normal emitted radiance follows a cosine law) is considered for the phosphorescence scattering, based on Allison and Gillies (1997) and Lee et al. (2007). Combining Eqs. (4) and (5) gives

$$dI_E = \beta I_L \cos(\theta - \omega t) \cos(\theta) e^{-t/\tau} dl. \tag{6}$$

Since dI_E is an amount of light, negative values must be discarded. This is performed with a sliding Heaviside step function $H(\theta)$,

$$dI_E = \beta I_L e^{-t/\tau} \cos(\theta - \omega t) \cos(\theta) H(\theta + \pi/2 - \omega t) dl. \tag{7}$$

The signal collected on the PM is the integral of dI_E over the field of view of the sensor (cf. Fig. 2):

$$I(t, \alpha) = \int_{\theta^-}^{\theta^+} dI_E, \tag{8}$$

where θ^+ and θ^- represent the maximum angles of the PM's field of view. Using the cylindrical coordinates (i.e., $dl = r d\theta$) yields,

$$I(t, \alpha) = r\beta I_L e^{-t/\tau} \int_{\theta^-}^{\theta^+} \cos(\theta - \omega t) \cos(\theta) H(\theta + \pi/2 - \omega t) d\theta. \tag{9}$$

Using Eq. (9), it is possible to define the distortion function $\gamma(t, \alpha)$, which is the ratio of the signal with rotation, $I(t, \alpha)$, and the one without rotation $I(t, \alpha = 0) = I_0(t)$,

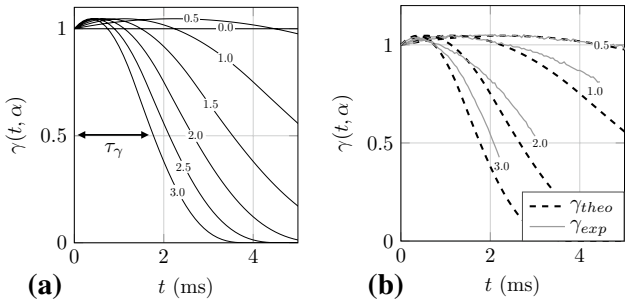

Fig. 8 **a** Theoretical efficiency function $\gamma(t,\alpha)$ from Eq. (10) for different α. **b** Evaluation of efficiency functions γ from theory (Eq. (10)) and experiments ($I(t,\alpha)/I(t,\alpha=0)$), taken for several rotation rates α

$$\gamma(t,\alpha)=\frac{I(t,\alpha)}{I_0(t)}=\frac{\int_{\theta^-}^{\theta^+}\cos(\theta-\omega t)\cos(\theta)H(\theta+\pi/2-\omega t)\mathrm{d}\theta}{\int_{\theta^-}^{\theta^+}\cos^2(\theta)d\theta}. \tag{10}$$

Equation (10) shows that the distortion function, $\gamma(t,\alpha)$, only depends on the PM's field of view and the cylinder's rotation rate.[1] Equation (10) can be numerically integrated so that a phosphorescence signal recorded on the rotating cylinder can be corrected for the rotation via the distortion function. Figure 8a shows the theoretical distortion functions for different rotation rates α. Obviously, the non-rotating case leads to a unit distortion function. When rotation is imposed, a slight overshoot above unity occurs before the function drops to zero: because the PM sees the upper part of the cylinder (positive θ), it records, with a delay, the maximum phosphorescence emitted at $\theta=0$. As the rotation rate increases, $\gamma(t,\alpha)$ drops more rapidly, confirming the signal extinction due to the rotation. The theoretical distortion function that is determined in the previous section can be validated by directly measuring the ratio of phosphorescence signals $I(t,\alpha)/I_0(t)$. However, this test needs to be done at the same temperature. In our experiment, the ambient condition at $T_c=300$ K is the only one that ensures a constant cylinder temperature. Indeed, as shown by Xavier et al. (2017), the steady-state temperature of the cylinder under reacting conditions depends on the rotation rate. The comparison between theory and experiments in Fig. 8b shows an excellent agreement for $\alpha=0.5$. However, discrepancies occur for larger rotation rates, which are not fully understood.

As the rotation increases, the time the PM sees the illuminated area $\tau_c=(\pi/2+\theta^+)r/\alpha u_b$ is shortened. If the phosphorescence decay is longer than the PM collection time (i.e., rotation timescale τ_c), it will clearly induce a bias, by reducing the fitting window (Tobin et al. 1990). Thus, one must ensure that the phosphorescence decay time $\tau_P=\ln(10)\tau$ (τ being the phosphorescence lifetime) is much smaller than the rotation timescale τ_c to prevent any information losses. Similarly, the correction we propose induces a post-processing bias as the recorded signal $I(t,\alpha)$ is divided by the efficiency function γ which tends to zero. With the intent to define the validity range of the correction procedure, we arbitrarily define τ_γ as the time at which the distortion function reaches half of its initial value. Consequently, we propose the following criteria under which the LIP measurements on moving objects are valid:

$$\begin{aligned}\tau_P &< \tau_\gamma\\ \tau_P &< \tau_c.\end{aligned} \tag{11}$$

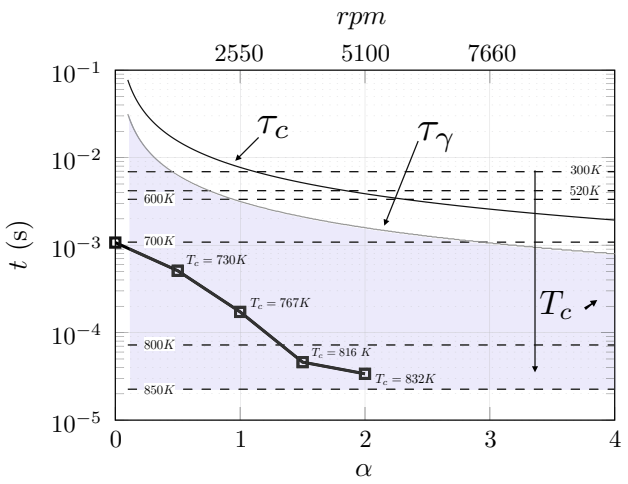

Fig. 9 Map showing the evolution of several timescales with rotation (τ_c: cylinder rotation, τ_γ: efficiency function, dotted lines: LIP). The shaded area corresponds to the range where LIP can be applied on rotating cylinders using Eq. (9)

Figure 9 represents the timescales of Eq. (11) as a function of the rotation rate α. Several phosphorescence decay times τ_P and their respective temperatures are highlighted (dashed horizontal lines). The criterion on the efficiency function τ_γ is more restrictive than the rotation timescale τ_γ. Therefore, the shaded area depicts the valid zone of measurements, where $\tau_P<\tau_\gamma$. The higher the rotation rate is, the higher the temperature of the surface needs to be to perform this type of measurements. The evolution of the cylinder temperature T_c is superimposed (black thick lines with square markers) and shows that the data of the present experiment lie within the valid range.

[1] This method can be derived with a point-wise arrangement: the distortion function, $\gamma(t,\alpha)$, is determined with Eq. (6) to be $\gamma(t,\alpha)=cos(\theta_i-\omega t)H(\theta_i+\pi/2-\omega t)/\cos(\theta_i)$, where θ_i is the position of excitation. However, this strategy reduces the signal on the PM as well as phosphorescence collection time, i.e., decreasing from $(\pi/2+\theta^+)r/\alpha u_b$ to $(\theta^+-\theta^-)r/\alpha u_b$ if the excitation point is near θ^- (see Fig. 2).

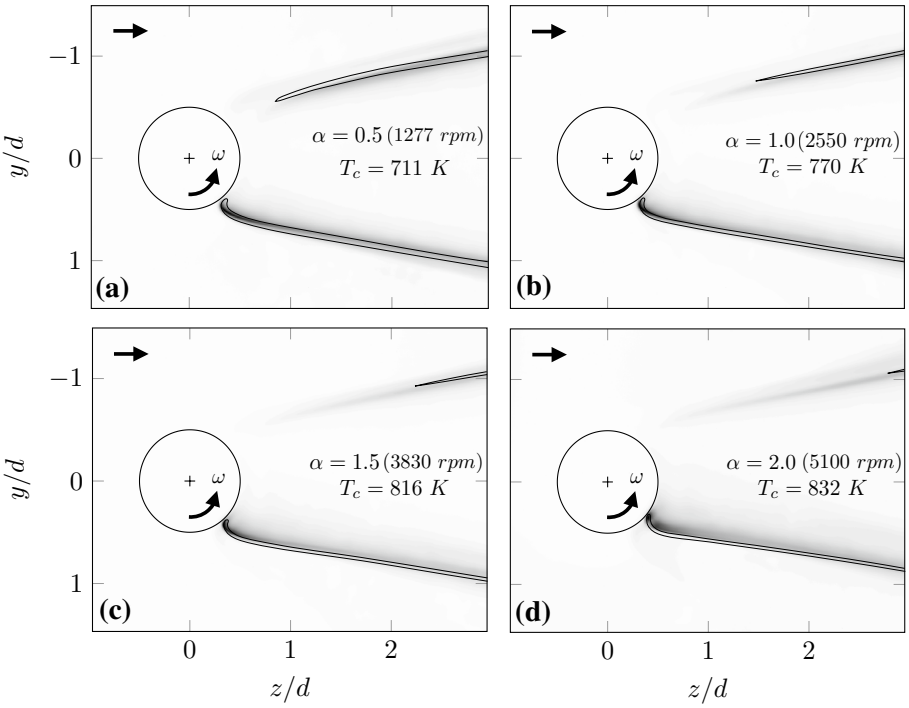

Fig. 10 Comparison between experiments (CH* chemiluminescence field) and DNS with isothermal boundary conditions (black iso-contours of 20% of the maximum heat release rate), for different rotation rates : **a** $\alpha = 0.5$, **b** $\alpha = 1.0$, **c** $\alpha = 1.5$, **d** $\alpha = 2.0$. The cylinder is fully coated with one layer

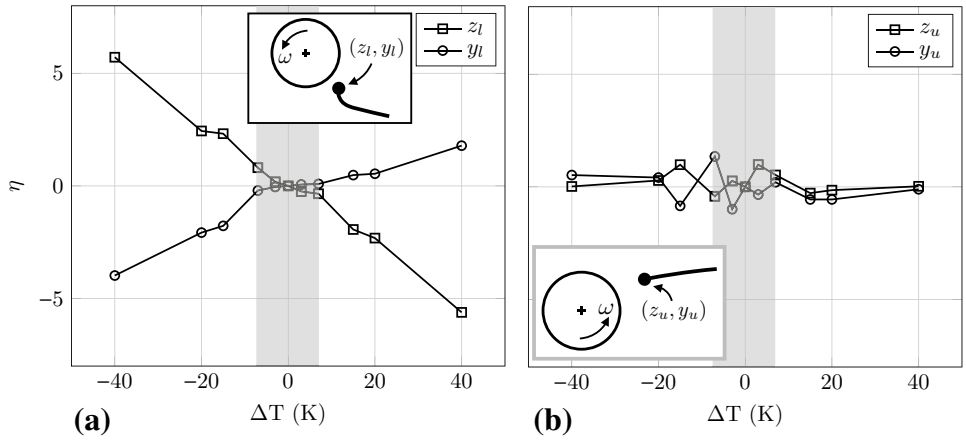

Fig. 11 Sensitivity analysis of the flame root location while varying the cylinder temperature, for the case $\alpha = 0.5$. $\Delta T = T_c^{ref} - T_c$ and $\eta = 100(x_i - x_i^{ref})/x_i^{ref}$ (x_i = z or y). Reference temperature and location are the ones obtained from Fig. 10a. **a** Lower branch. **b** Upper branch. The shaded area corresponds to the LIP precision

4.2 Validation of the temperature lumped model in numerical simulations

In contrast with previous numerical investigations, where adiabatic, coupled or lumped-adaptive conditions were implemented (Mejia et al. 2017, 2018; Xavier et al. 2017), the experimental value of the cylinder temperature is used as the boundary condition, to validate direct numerical simulations (DNS). Figure 10 shows the excellent agreement between experimental flame visualization (CH* chemiluminescence) and DNS (iso-contour of the heat release rate), for difference rotation rates α. This proves that the assumption of a uniform temperature is valid in terms of flame stabilization.

The sensitivity of the cylinder temperature on the flame root location (FRL) is evaluated by performing several DNS with a temperature shift, ΔT, ranging from −40 to 40 K (Fig. 11). The axial and radial FRL (z and y) are extracted with a crest detector on the heat release rate (set to 20% of the maximum). The spatial locations for each branch are normalized by the reference case (Fig. 10a) to give a deviation $\eta = 100(x_i - x_i^{ref})/x_i^{ref}$ ($x_i = z$ or y). The shaded area in Fig. 11 also shows the LIP precision of the present technique (i.e., ± 7K). A temperature deviation smaller than the LIP precision produces a FRL shift less than 3% for both branches. However, different trends occur when this shift is higher: the lower branch (Fig. 11a) is more sensitive to the cylinder temperature whereas the upper branch (Fig. 11b) is not affected. Indeed, as the FRL of the lower branch is

close to the cylinder, its reactivity is enhanced by the fresh gases that are pre-heated by the cylinder. In contrast, the upper branch is much more sensitive to the cylinder rotation, as depicted in Fig. 10. Therefore, in our case, a wrong estimation of the cylinder temperature could mainly lead to a change the location of the lower branch.

5 Conclusion

The accurate experimental determination of wall temperatures is crucial for the validation of numerical tools and the improvement of future combustion systems. The present work discusses the use of laser-induced phosphorescence (LIP) and shows how classical arrangements can be modified to measure the temperature of moving surfaces. Preliminary tests have been conducted to evaluate how the phosphorescent coating could affect the flame stabilization. Results show that the high temperature of the substrate does not alter the spectroscopic properties of phosphor particles, indicating that the coating can be used during several campaigns. The emissivity of the coated surface is increased by almost 40%, mainly due to the roughness increase. However, the transient and steady flame locations are weakly affected, enabling non-intrusive measurements. The classical point-wise LIP arrangement has been modified to allow temperature measurements at the surface of a moving object. A larger area is illuminated and the collected signal is corrected by a distortion function accounting for the displacement during the phosphorescence decay. The validity of this correction is assessed theoretically and experimentally. The main constraint stems from the velocity of the object and the phosphorescence decay rate. Eventually, measurements on a rotating cylindrical flame holder are compared with numerical simulations, and show an excellent agreement. A sensitivity analysis highlights that the lower branch is sensitive to the cylinder temperature, whereas the rotation rate α determines the location of the upper branch.

Acknowledgements The research leading to these results has received funding from the European Research Council under the European Union's Seventh Framework Programme (FP/2007-2013)/ERC Grant Agreement ERC-AdG 319067-INTECOCIS. The authors wish also to thank M. Marchal and S. Cazin from IMFT for their precious help with the experimental diagnostics, and Q. Douasbin (IMFT), C. Kraus (IMFT), B. Bedat (IMFT), and T. Schuller (IMFT) for useful discussions.

References

Alden M, Omrane A, Richter M, Sarner G (2011) Thermographic phosphors for thermometry: a survey of combustion applications. Prog Energy Comb Sci 37:422–461

Allison SW, Cates MR, Noel BW, Gillies GT (1988) Monitoring permanent-magnet motor heating with phosphor thermometry. IEEE Trans Instrum Meas 37:637–641

Allison SW, Gillies GT (1997) Remote thermometry with thermographic phosphors: instrumentation and applications. Rev Sci Instrum 68:2615–2650

Atakan B, Roskosch D (2013) Thermographic phosphor thermometry in transient combustion: a theoretical study of heat transfer and accuracy. Proc Combust Inst 34:3603–3610

Berger S, Richard S, Duchaine F, Staffelbach G, Gicquel LYM (2016) On the sensitivity of a helicopter combustor wall temperature to convective and radiative thermal loads. Appl Therm Eng 103:1450–1459

Brubach J, Feist JP, Dreizler A (2008) Characterization of Manganese-activated magnesium fluorogermanate with regards to thermographic phosphor thermometry. Meas Sci Technol 19(025):602–11

Brubach J, Pflitsch C, Dreizler A, Atakan B (2013) On surface temperature measurements with thermographic phosphors: a review. Prog Energy Comb Sci 39:37–60

Chambers M, Clarke D (2009) Doped Oxides for high- temperatures luminescence and lifetime thermometry. Ann Rev Mater Res 39:325–359

Dreizler A, Bohm B (2015) Advanced laser diagnostics for an improved understanding of premixed flame-wall interactions. Proc Combust Inst 35:37–64

Duchaine F, Corpron A, Pons L, Moureau V, Nicoud F, Poinsot T (2009) Development and assessment of a coupled strategy for conjugate heat transfer with large eddy simulation: application to a cooled turbine blade. Int J Heat Fluid Flow 30:1129–1141

Ezekoye OA, Greif R, Lee D (1992) Increased surface temperature effects on wall heat transfer during unsteady flame quenching. In: 24th Symp. (Int.) on Combustion. The Combustion Institute, Pittsburgh, pp 1465–1472

Facchini B, Magi A, Greco AS (2004) Conjugate heat transfer simulation of a radially cooled gas turbine vane. In: ASME Turbo Expo 2004: Power for Land, Sea, and air. American Society of Mechanical Engineers, pp 951–961

Feist JP, Heyes AL, Seefeldt S (2002) Thermographic phosphors for gas turbines: instrumentation development and measurement uncertainties. In: 11th International symposium on application of laser techniques to fluid mechanics, Lisbon, Portugal

Fuhrmann N, Brubach J, Dreizler A (2013) Phosphor thermometry: a comparison of the luminescence lifetime and the intensity ratio approach. Proc Combust Inst 34:3611–3618

Guiberti TF, Durox D, Scouflaire P, Schuller T (2015) Impact of heat loss and hydrogen enrichment on the shape of confined swirling flames. Proc Combust Inst 35:1385–1392

Hooker JA, Doorbar PJ (2000) Metal matrix composites for aeroengines. Mater Sci Technol 16:725–731

Jainski C, Ribmann M, Janicka J, Dreizler A (2017) Sidewall quenching of atmospheric laminar premixed flames studied by laser-based diagnostics. Combust Flame 183:271–282

Kashdan JT, Bruneaux G (2011) Laser-induced phosphorescence measurements of combustion chamber surface temperature on a single-cylinder diesel engine. In: SAE Technical Paper 2011-01-2049. SAE International

Khalid AH, Kontis K (2008) Thermographic phosphors for high temperature measurements: principles, current state of the art and recent applications. Sensors 8:5673–5744

Knappe C, Linden J, Nada FA, Ritcher M, Alden M (2012) Investigation and compensation of the nonlinear response in photomultiplier tubes for quantitative single-shot measurements. Rev Sci Instrum 83:034901

Kraus C, Selle L, Poinsot T, Arndt CM, Bockhorn H (2017) Influence of heat transfer and material temperature on combustion instabilities in a swirl burner. J Eng Gas Turb Power 129(051):503

Lakshmisha KN, Paul PJ, Mukunda HS (1991) On the flammability limit and heat loss in flames with detailed chemistry. In: Symposium (international) on combustion, vol 23. Elsevier, pp 433–440

Lamouroux J, Ihme M, Fiorina B, Gicquel O (2014) Tabulated chemistry approach for diluted combustion regimes with internal recirculation and heat losses. Combust Flame 161:2120–2136

Lawrence P (2009) Meeting the challenge of aviation emissions: an aircraft industry perspective. Tech Anal Strat Manag 21:79–92

Lee YK, Oh JR, Huh YRD (2007) Strong perturbation of the guided light within Y_2O_3 : Eu^{3+} thin film phosphors coated with two-dimensional air-hole photonic crystal arrays. Appl Phys Lett 91(231):908

Lefebvre AH (1999) Gas turbines combustion. Taylor & Francis, London

Lempereur C, Andral R, Prudhomme J (2008) Surface temperature measurement on engine components by means of irreversible thermal coatings. Meas Sci Technol 19(105):501

Linden J, Johansson B, Richter M, Alden M (2009) Investigation of potential laser-induced heating effects when using thermographic phosphors for gas-phase thermometry. Appl Phys B 96:237–240

Lu JH, Ezekoye O, Greif R, Sawyer F (1990) Unsteady heat transfer during side wall quenching of a laminar flame. In: 23rd Symp. (Int.) on Combustion. The Combustion Institute, Pittsburgh, pp 441–446

Mann M, Jainski C, Euler M, Bohm B, Dreizler A (2014) Transient flame-wall interactions: experimental analysis using spectroscopic temperature and CO concentrations measurements. Combust Flame 161:2371–2386

Mannick L, Brown SK, Campbell SR (1987) Phosphor-based thermometry of rotating surfaces. Appl Opt 26:4014–4017

Mejia D, Bauerheim M, Xavier P, Ferret B, Selle L, Poinsot T (2017) Stabilization of a premixed flame on a rotating cylinder. Proc Combust Inst 36:1447–1455

Mejia D, Miguel-Brebion M, Ghani A, Kaiser T, Duchaine F, Selle L, Poinsot T (2018) Influence of flame-holder temperature on the acoustic flame transfer function of a laminar flame. Combust Flame 188:5–12

Mejia D, Selle L, Bazile R, Poinsot T (2015) Wall-temperature effects on flame response to acoustic oscillations. Proc Combust Inst 35:3201–3208

Mercier R, Guiberti TF, Chatelier A, Durox D, Giquel O, Darabiha N, Schuller T, Fiorina B (2016) Experimental and numerical investigation of the influence of thermal boundary conditions on premixed swirling flame stabilization. Combust Flame 171:42–58

Miguel-Brebion M, Mejia D, Xavier P, Duchaine F, Bedat B, Selle L, Poinsot T (2016) Joint experimental and numerical study of the influence of flame holder temperature on the stabilization of a laminar methane flame on a cylinder. Combust Flame 172:153–161

Padture NP, Gell M, Jordan EH (2002) Thermal barrier coatings for gas-turbine engine applications. Science 296:280–284

Poinsot T, Veynante D (2011) Theoretical and Numerical Combustion, 3rd edn. (http://www.cerfacs.fr/elearning)

Popp P, Baum M (1997) An analysis of wall heat fluxes, reaction mechanisms and unburnt hydrocarbons during the head-on quenching of a laminar methane flame. Combust Flame 108(3):327–348

Tay-Wo-Chong L, Polifke W (2013) Large eddy simulation-based study of the influence of thermal boundary condition and combustor confinement on premix flame transfer functions. J Eng Gas Turb Power 135:021502

Tobin K, Allison S, Cates MR, Capps GL, Beashears DL, Cyr M, Noel BW (1990) High-temperature phosphor thermometry of rotating turbine blades. AIAA J 28:1485–1490

Wulff A, Hourmouziadis J (1997) Technological review of aeroengine pollutant emissions. Aerosp Sci Technol 1:557–572

Xavier P, Ghani A, Miguel-Brebion M, Bauerheim M, Selle L, Poinsot T (2017) Experimental and numerical investigation of flames stabilised behind rotating cylinders: interaction of flames with a moving wall. J Fluid Mech 813:127–151